Reliable durability assessment of welded yellow goods equipment.

Flynn, Dean

Reliable Durability Assessment of Welded Yellow Goods Equipment

Dean Flynn BEng (Hons) MRes

Submitted to the University of Wales in fulfilment of the requirements for the Degree of Doctor of Engineering.

Swansea University

2010

ProQuest LLC.
789 East Eisenhower Parkway
P.O. Box 1346
Ann Arbor, MI 48106 – 1346

Abstract

Weld fatigue performance is a main design consideration with Yellow Goods vehicles and can determine the overall product durability. Accurate fatigue life prediction is critical but current durability assessment involves extensive testing. This design process lacks efficiency and presents scope for a finite element (FE) based weld fatigue assessment method. Used early in the design stage, this method will improve time-to-market of products and achieve robust 'right-first-time' designs. Research work has been carried out into applying the 'Master S-N Curve' approach to thick-plate construction and agricultural equipment. Weld fatigue data was generated on a range of simple welded coupons and converted for the fatigue life prediction of welded structures using the structural stress damage parameter. Overall, a single Master S-N curve was achievable for a range of different weld joint configurations. The method achieved good condensation of the geometry dependent load-life fatigue curves into a single structural stress against life curve. The structural stress method was further extended to fatigue lives of weld throat failures with good condensation of the data. Excellent correlations were achieved between solid and shell element models. The concept proved to be effective and largely insensitive to FE mesh type and size. However, limitations were found with shell element models when predicting weld throat failures. The structural stress measurement technique was employed and a master curve generated, derived from coupon strain-gauge recordings. The Master S-N curve approach was applied in the fatigue assessment of a laboratory test component and production component for the construction industry with limited success. Predictions were compared with recorded values from component fatigue tests. More accurate predictions and improved correlations were found when using separate failure mode master curves. Overall the work showed some potential for the use of the Master S-N Curve approach in the early design stage of construction and agricultural welded structures.

DECLARATION

This work has not previously been accepted in substance for any degree and is not being concurrently submitted in candidature for any degree.

Signed.....(candidate)

Date.....

STATEMENT 1

This thesis is the result of my own investigations, except where otherwise stated. Where correction services have been used, the extent and nature of the correction is clearly marked in a footnote(s).

Other sources are acknowledged by footnotes giving explicit references. A bibliography is appended.

Signed.....(candidate)

Date.....

STATEMENT 2

I hereby give consent for my thesis, if accepted, to be available for photocopying and for inter-library loan, and for the title and summary to be made to outside organisations.

Signed.....(candidate)

Date.....

Contents

Acknowledgements

This thesis would not have been possible without the valued guidance, time and support from my supervisors; Prof W.J. Evans, Dr M.T. Whittaker, Dr Y. Gao, Mr T.B. Jones, Ms V. Cuddy and Dr D. Panni.

I am grateful to all at Corus Automotive Sector Unit including Jon King, Iain McGregor, Ray Long and Martin Batchelor.

I would like to thank everyone within the Research Department at J.C. Bamford Excavators Ltd including Iain Godwin, Lee Williams, John Dunkerly, Keith Clayton, Rod Latham, Luca Mangone, Emyr Hughes, Gordon Gray, George Painter, Pete Randel, Rob Scotchford, Tony Jeffries, Richard Usher, Seth Adams, Jim Easton, Paul Clulow, David Smith, Steve Bosworth and Chris Shenton.

I would like to thank the following industrial and academic members that provided the opportunity of the project; Engineering and Physical Sciences Research Council (EPSRC), the Materials Department at Swansea University, Corus Strip Products UK, Corus Automotive Sector Unit and J.C. Bamford Excavators Ltd.

I am also grateful for the assistance received from The Welding Institute (T.W.I.) and Safe Technology Ltd.

I owe my deepest gratitude to all my family and friends who have supported me along the way.

List of Figures

List of Tables

List of Equations

Definitions

E	Young's modulus
Hz	Hertz
l	Element length (mm)
f'	Element force
m'	Element moment
F	Nodal force
M	Nodal moment
N	Newton
kN	kiloNewton
ΔkN	Load range (kN)
k	Stiffness (force/displacement)
t	Material thickness
με	Microstrain
m	Metre
mm	Millimetre
M	Distribution matrix
M^{-1}	Inverse matrix
K_t	Stress concentration
ΔS_E	Weld material endurance limit range
$\Delta^e\sigma$	Endurance limit range
K	Stress intensity factor
da/dN	Crack growth rate
N_f	Cycles to failure
Reh	Yield strength (upper)
Rel	Yield strength (lower)
Rp0.2	0.2% proof strength
Rm	Tensile strength
a	Basquin equation fatigue co-efficient
b	Basquin equation fatigue curve gradient
P-t	Load-time history
σ-t	Stress-time history
D_i	Damage summation
n_l	Component recorded cycles
N_l	Component predicted cycles
R^2	R squared value - co-efficient of determination
$\Delta\varepsilon_{total}$	Total strain
$\Delta\varepsilon_{plastic}$	Plastic strain
$\Delta\varepsilon_{elastic}$	Elastic strain
Δσ	Stress range

$\sigma'f$	Fatigue strength co-efficient
$\varepsilon'f$	Fatigue ductility co-efficient
$\Delta\sigma$	Stress range
σ_m	Mean stress
R	Ratio of applied stress (or load)
σ_{max}	Maximum applied stress
σ_{min}	Minimum applied stress
σ_a	Stress amplitude
σ_{yield}	Yield stress
σ_{nom}	Nominal stress
$\sigma_{membrane}$	Membrane stress
$\sigma_{bending}$	Bending stress
$\sigma_{non\text{-}linear\ peak}$	Non-linear peak stress
$\sigma_{structural}$	Structural stress
σ_{notch}	Notch stress
σ_{total}	Total stress
σ_{ss}	Structural stress damage parameter
$Eqv.\sigma_{ss}$	Equivalent structural stress damage parameter
I(r)	Loading mode parameter
$\Delta\sigma_s$	Normal structural stress range
$\Delta\tau_s$	Shear structural stress range

1. Introduction

In the current state of the economy, construction equipment manufacturers are facing exciting challenges. The 'Yellow Goods' sector is required to provide a fast turnaround of robust new designs and meet high product demands in emerging markets. Furthermore, it is required to refine established designs and manufacture more profitable products in mature markets, where raw material and production costs are rising. There is a growing use of Computer Aided Engineering (CAE) to enable manufacturers to meet the difficult demands of efficient and robust designs.

A critical factor in the design of a Yellow Goods component is durability. In general terms, this defines how long the product will survive. The product must be able to perform the same task repeatedly without failure. Given the structural demands on Yellow Goods components, weld fatigue is one of the main design considerations when determining the overall durability of the product. Strip and plate steel is cut, pressed and welded into various configurations to make up the main structural bodies and parts. The manufacturing operations performed create harsh conditions and can detrimentally affect material performance. Fatigue failures are a major design concern and, given the detrimental effects of the welding operation, welded components have significantly reduced fatigue strengths compared with parent material. Hence, the overall durability of a component is determined by the fatigue strength of welded structures. A chain is only as strong as the weakest link and, in welded fabrications the welded joint is very much the weak link. For this reason, reliable durability assessments and accurate weld fatigue life predictions are crucial for design life requirements.

In design situations where CAE techniques are not fully developed, a popular method of fatigue life prediction in welded structures is a 'Design-test-build' approach. It relies on physical testing and prototype builds. It is an iterative, costly and time-consuming method. Accurate life estimations are achieved but the design philosophy lacks efficiency. There are many potential cost saving opportunities if a Finite Element (FE) based analysis could be introduced. Fatigue life predictions would then be numerically calculated for a welded structure under relevant boundary conditions. The role of CAE and its use for fatigue life predictions has been widely assessed and established for many industries such as automotive, aerospace, offshore and marine. Used early on in the design stage, an FE based fatigue life prediction can help reduce the length of the design process and the need for numerous costly

prototypes. The aim is to achieve a 'right-first-time' design, ultimately, minimising the number of iterations in the 'Design-test-build' process.

However, employing such a stress analysis approach to weld fatigue life prediction is associated with numerous challenges. Due to a 'stress singularity' effect at notch features, such as weld toe geometries, it is often the case that an FE analysis produces erroneous results that can depend on the parameters used in the analysis. Furthermore, there is a fatigue strength dependency associated with different welded geometries. This requires welded geometries to be grouped (subjectively) into a 'classification' based on a specific fatigue strength. There have been a number of alternative damage parameters proposed, and covered in the literature review, that aim to overcome these issues and allow consistent and accurate fatigue life predictions.

The overall aim of the work presented in this thesis, is to validate the applicability of an 'alternative' damage parameter for FE-based fatigue assessments of construction, agricultural and materials handling equipment. This required the generation of weld fatigue performance data for thick-plate welded Yellow Goods and their conversion into a suitable format for the FE-model. Once the fatigue assessment method was established, an analysis was undertaken and fatigue life predictions made for a welded component. Comparison of measured and predicted lives from the technique employed, were carried out to demonstrate the quality and effectiveness of the approach adopted. On this basis, recommendations are made on the choice of a reliable durability assessment procedure for the efficient and robust design of Yellow Goods structures.

2. Literature Review

2.1 Fatigue – Overview

It is estimated that around 75% of machine and structural failures are due to fatigue [1]. Therefore it is essential that fatigue is given great consideration during the design stage. The occurrence of fatigue failure in a material is due to repeated cyclic loading. Typically the repeated loading would not exceed the yield point of the material and therefore would not be enough to cause failure in one single application [2]. The material is said to weaken and tire from the localised cyclic plastic deformation that would result in a small crack. Ideally, an easier approach for design engineers would be to minimise the loads and increase the fatigue life of a component or structure, although this is not always possible. To achieve this, the engineer would have to analyse the geometry of the structure and redesign in order to minimise stress concentrations and crack initiation sites.

The study of fatigue originated in the early nineteenth century when parts such as steel axles or bolts were failing from in-service loads significantly under the tensile strength of the material. William Rankine found that steam train axles would fracture at sharp corners, and he described fracture surfaces similar to that of stage 2 crack growth striations and a final fracture area [3]. The first documented study into fatigue failures was conducted by a German engineer, August Wöhler, in the mid-nineteenth century. He studied the failure of railway axles subjected to a rotating bend fatigue test [4]. He then plotted the nominal stress applied to the axles against the number of cycles to failure, giving the Wöhler line, more commonly known today as an S-N curve. Since the early work done by Wöhler, much further research has been carried out in order to understand fatigue and how to design against it. The fatigue data is plotted on a graph as the relationship between the nominal cyclic stress S and the number of cycles upon failure, N. The axes used are generally S against $\log_{10}$ N, or $\log_{10}$ S against $\log_{10}$ N, (Figure 1). The number of cycles to failure at any stress level is termed as the endurance limit and this is typically associated with 10 million cycles or larger. Low Cycle Fatigue (LCF) is related to higher stresses and lower cycles ($<10^5$). Examples of LCF are experienced in picking up and dumping of a load in a crane arm or take-off/cruise/land cycles in aeroplanes. High cycle fatigue (HCF) is associated with low strains and high frequencies. Examples of HCF are experienced by components subjected to vibration such as exhausts on automotive engines.

Despite much research into fatigue, it remains a technical and engineering challenge to engineers and material scientists alike. One of the difficulties in fatigue studies lies with the large scatter of data associated with test results. Test conditions and environments can be identical from one test to another but still produce a large scatter of results. This is due to the random formation of defects in materials during manufacture and/or the grain to grain variations in properties in polycrystalline materials. Microcracks, dislocations and inclusions are statistically distributed within the microstructure.

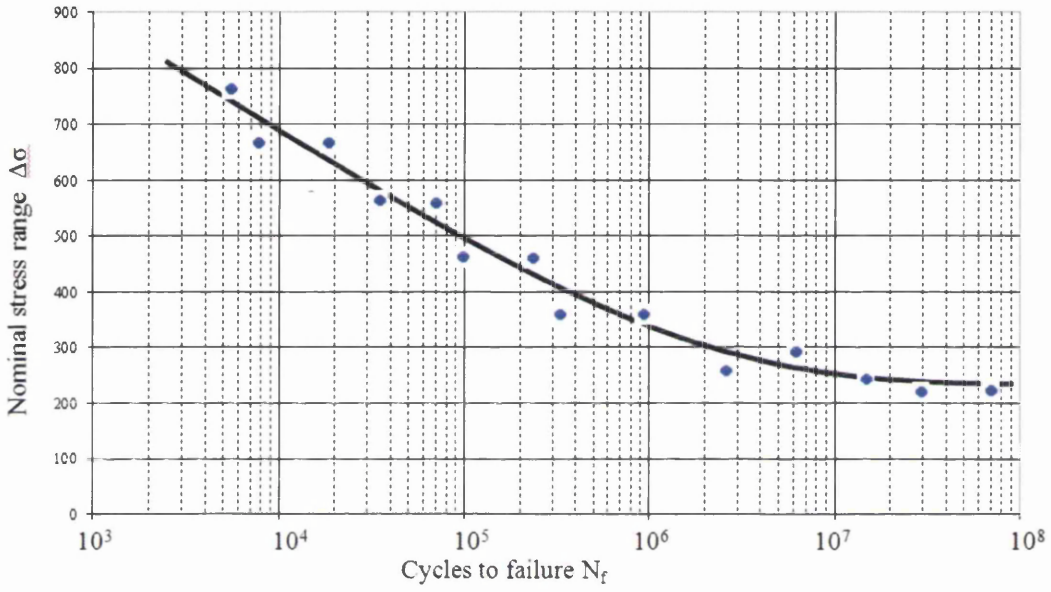

Figure 1: Fatigue S-N curve – plotted on nominal stress against log cycles scale

2.1.1 Failure mechanisms

Due to the development of the Scanning Electron Microscopy (SEM), it is possible to magnify material defects and fatigue cracks to analyse them more closely. The fatigue failure involves two distinct stages: crack initiation and crack propagation [5]. There are many circumstances in which fatigue crack initiation (stage 1) can take place. A crack can initiate from a surface defect due to a scratch or tool markings, a notch, hole or radius, or slip bands or dislocations and internal defects. Scratches due to manufacturing processes (such as tooling or small cracks from quenching) and stress concentrations (due to notches, radii and geometry features) are very common on engineering components. Fatigue performance can be significantly improved through surface treatments removing the crack initiation site and creating a smooth surface. Polished smooth plain test specimens used for fatigue testing contain no surface defects. When a smooth polished surface is present with no blemishes,

failure due to fatigue is caused by intrusions and extrusions from slip band formation. Under cyclic loading, slip bands move back and forth along the maximum shear planes to generate intrusions and extrusions, shown in Figure 2 [2].

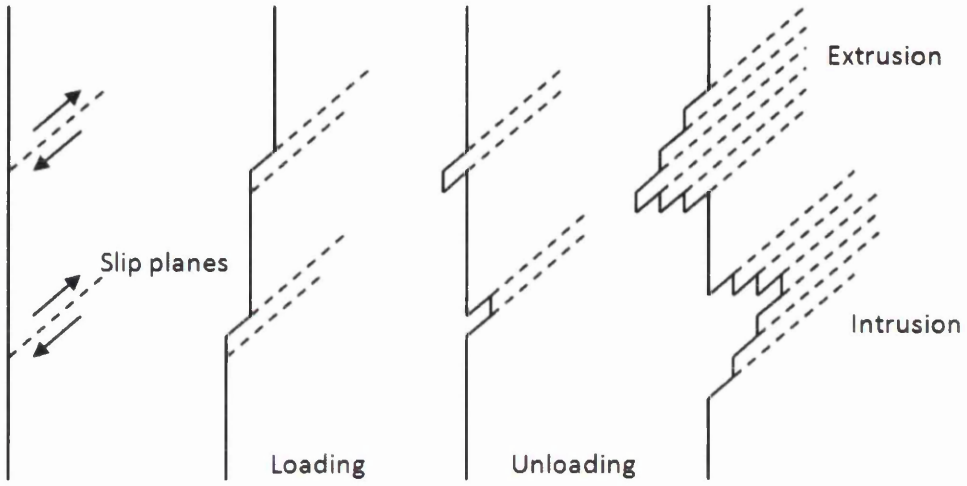

Figure 2: Intrusion and Extrusion slip bands from cyclic loading

The appearance is similar to that on the side of a deck of cards. The intrusion although very small in size still acts as a stress raiser and initiates the formation of a true fatigue crack. The crack grows at 45 degrees to the applied load, in the direction of the shear stress. It continues to grow up to a grain boundary and pauses until enough energy is applied to proceed into the neighbouring grain. Once the crack has initiated and has crossed through two or three grain boundaries, in stage 2 the crack grows perpendicular to the applied loading, Figure 3.

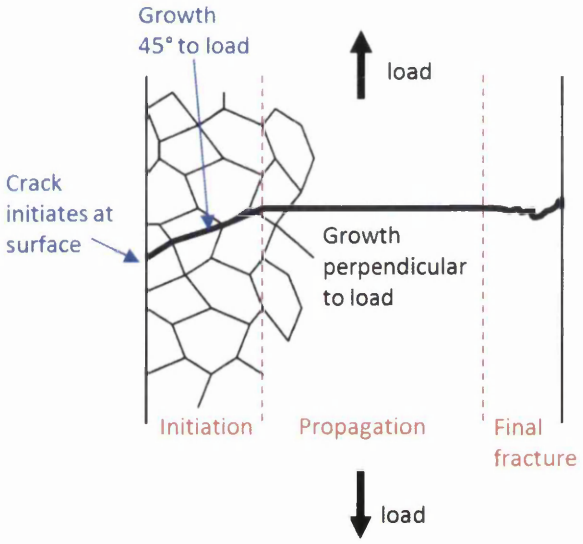

Figure 3: Stages of fatigue crack initiation and propagation until final failure

The crack growth mechanism differs from that of stage 1. In the crack propagation stage the crack tip creates a high stress concentration effect and undergoes localised plastic deformation. As the tensile stress increases the crack tip opens, local plastic shear deformation takes place with the crack growing into a new area of metal. As the load is reduced the crack tip closes, but the new permanent deformation remains and creates a saw tooth like striation. Repeated loading then causes the crack tip to continuously penetrate through the metal causing further striations. However, engineering components can contain a number of material defects. Defects within the local plastic zone will create holes and link up with each other and the crack tip advances through the holes, as shown in Figure 4.

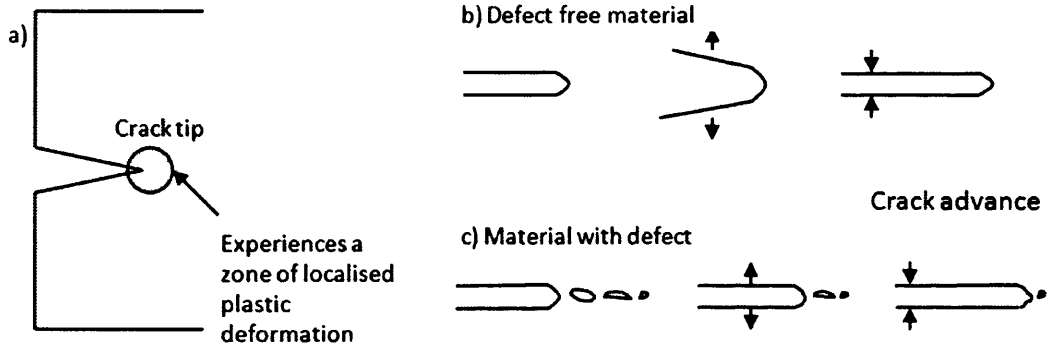

Figure 4: Crack propagation - a) localised plastic deformation zone, b) defect free material and c) material containing a defect

The stage 2 crack grows until the loading is too great for the remaining cross-section of the metal and fracture occurs, as in Figure 5.

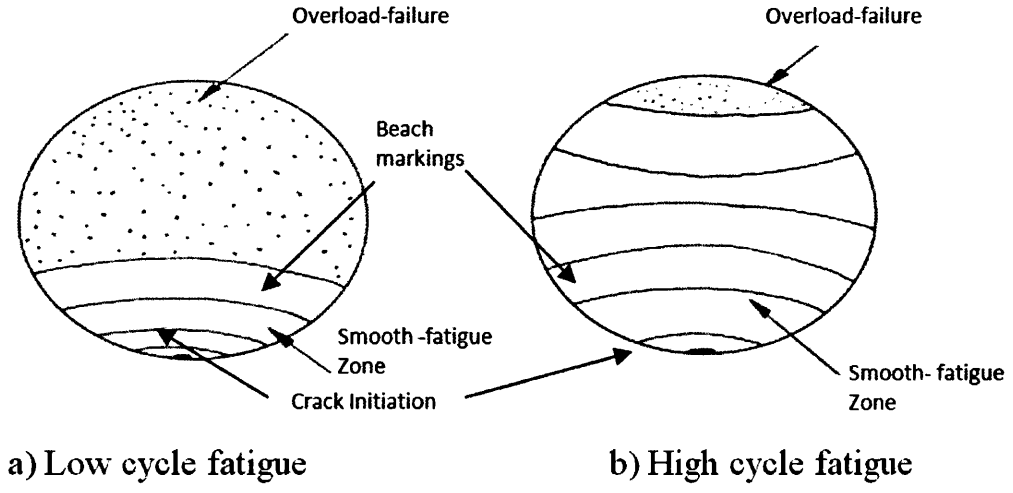

Figure 5: Failure striations of low cycle and high cycle fatigue [6]

The rate of crack growth is dependent upon various factors such as the stress range, mean stresses, surface finish, quality and surface treatments. The main driving forces affecting the fatigue life or crack growth rate are the stress or strain range and mean stress (Figure 6). It is fundamental, and can been seen on any S-N curve, (Figure 1), that the greater the increase in stress (or stress range $\Delta\sigma$), the lower the fatigue life of the metal.

The severity of the fatigue damage caused is different depending on whether the load cycle is positive or negative, i.e. loading cycles can be tensile or compressive. The mean stress of a cycle greatly alters the fatigue performance. Mean stress, $\sigma_m = (\sigma_{max} + \sigma_{min}) / 2$.

The stress ratio R, is the ratio of the minimum stress over the maximum stress applied, $R = \sigma_{min} / \sigma_{max}$. Loading cycles vary, such as fully reversed, R=1, where the applied tensile stress is equal to that of the compressive stress. When R= 0, the load applied is reversed back to zero stress (i.e. the stress is only tensile), or R=0.5, where the load reversed is equal to half of that applied. Similar R ratios apply to strain control fatigue testing.

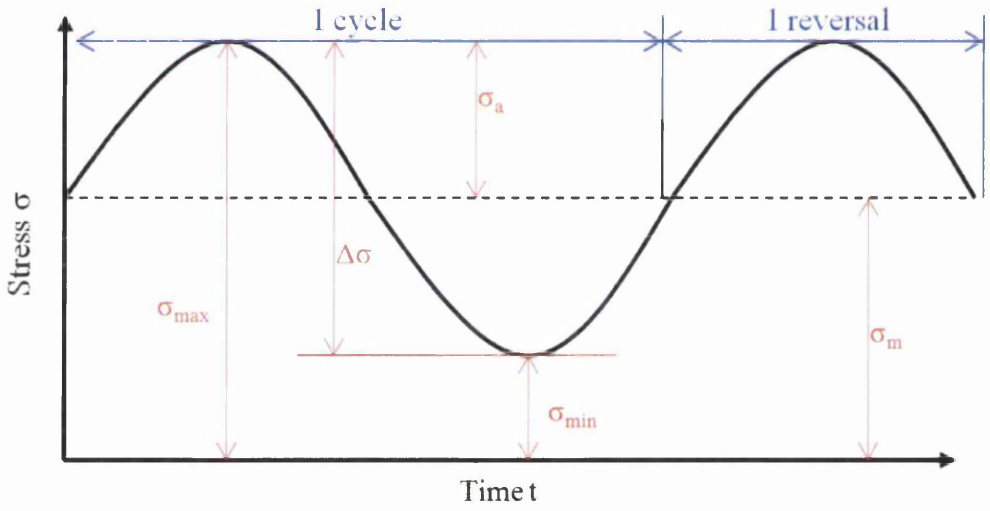

Where σ_{max} = maximum applied stress, σ_{min} = minimum applied stress

$\Delta\sigma$ = stress range, σ_m = mean stress, σ_a = stress amplitude

Figure 6: Stress-time fatigue cycle loading

2.1.2 Life prediction methods

There are various approaches for estimating fatigue life. The 3 main methods are:

Stress-life;

Strain-life;

Crack propagation – Linear elastic fracture mechanics.

The total fatigue life of a component is made up of the crack initiation and the crack propagation stage. Life estimation approaches are used for the prediction of an individual stage or the total fatigue life.

A stress-life approach is typically used for total fatigue life estimation. This is selected for situations where the nominal stress is elastic, under low loadings, and high cycle fatigue is the dominating failure mode. The structure under analysis is given consideration with regard to the load endured and the geometry of the design. Stress concentrations are identified as they impose a detrimental effect on the fatigue performance. A fatigue life is calculated from fatigue performance data of the material/component generated through laboratory fatigue tests. The results are plotted as nominal stress against life (cycles to failure), as shown in Figure 7. The S-N curve then allows a fatigue life estimate to be calculated for a given stress at a critical point of the structure using the Basquin line equation on a log scale [7].

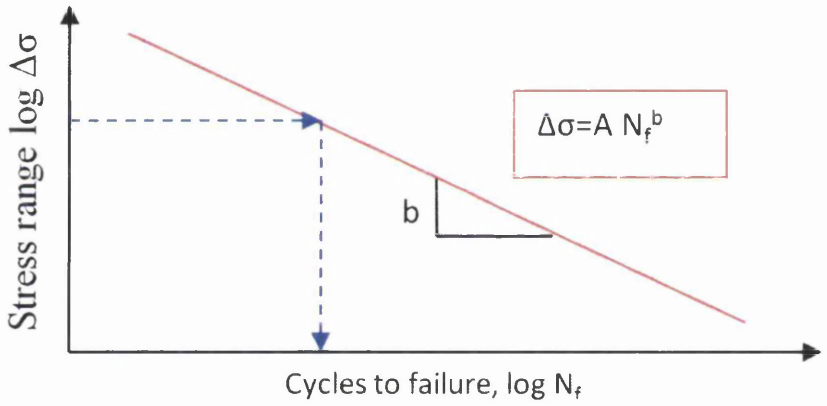

Figure 7: Stress-life S-N data - Basquin equation

Strain-life approaches are employed in loading conditions of higher stress/strain ranges than a stress-life approach. As a result of the higher loads and yielding, localised plastic deformation occurs around stress concentrations causing cracks to initiate. The strain-life concept assumes the life to initiation of a small crack is determined by the stress and strain loading experienced by the material local to the point of crack initiation. Therefore if the same stress-strain load conditions are experienced on a smooth plain specimen of the same material, it will fail in the same number of cycles, Figure 8. Fatigue performance data from tests on plain smooth specimens can be used to characterise a wide range of different stress concentrations due to notches and machined radii.

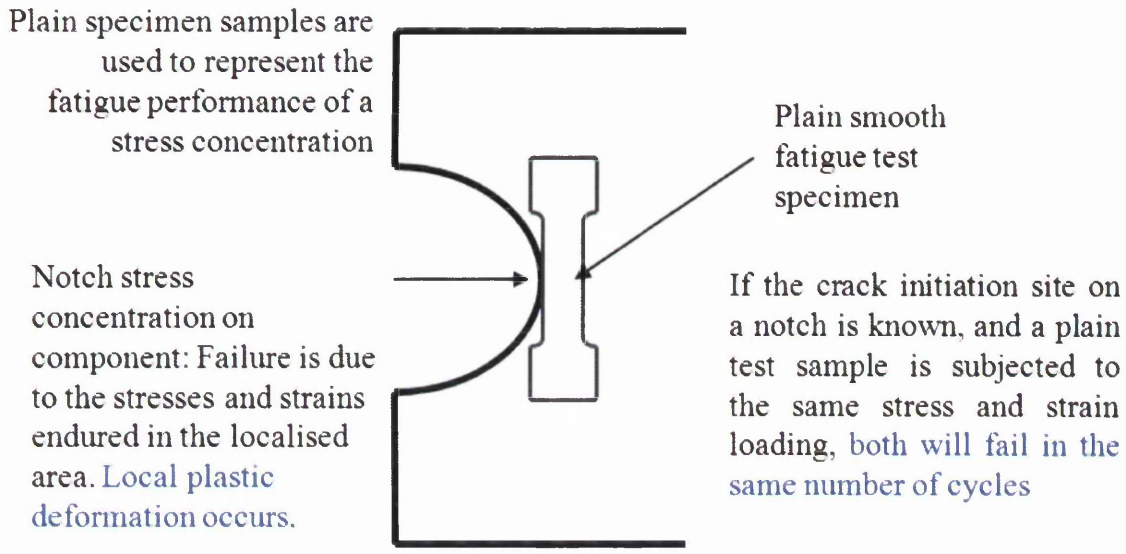

Figure 8: Strain-Life Approach (ε -n) Life prediction of Stress concentrations using plain specimens

A stress analysis of the notch under analysis is required and can be performed by computational (FEA) or a straightforward mathematical model (i.e. Neuber's Rule) in order to determine the localised plastic stresses and strains. The strain fatigue response of the plain specimens is expressed as a strain range versus cycles to failure. Using a particular method to analyse the results, such as the Coffin-Manson equation, a fatigue life can be calculated, Figure 9.

Where:

$\Delta\varepsilon_{total}$ = total strain

$\Delta\varepsilon_{plastic}$ = plastic strain

$\Delta\varepsilon_{elastic}$ = elastic strain

$\Delta\sigma$ = stress range

σ'_f = fatigue strength co-efficient

ε'_f = fatigue ductility co-efficient

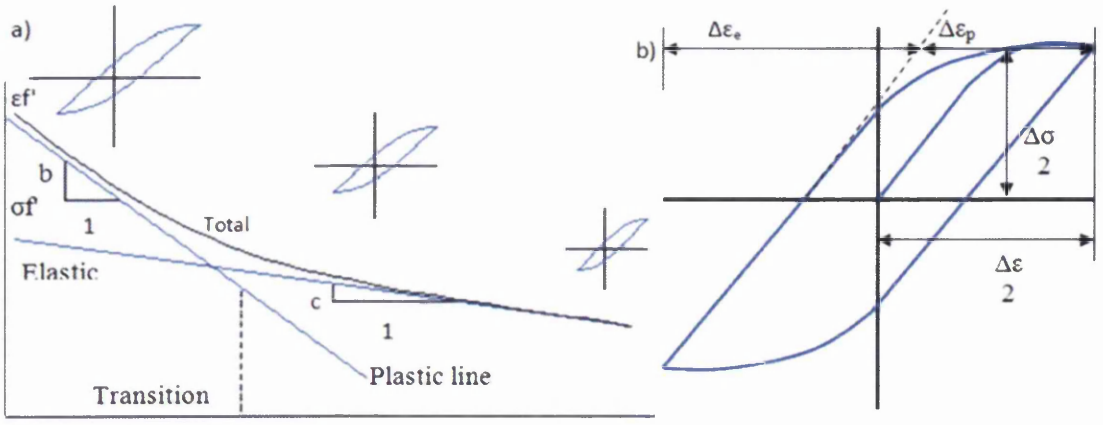

$$\frac{\Delta\varepsilon_{total}}{2} = \frac{\Delta\varepsilon_{el}}{2} + \frac{\Delta\varepsilon_{pl}}{2} = \frac{\sigma'_f}{E}.(2N_f)^b + \varepsilon'_f.(2N_f)^c$$

Figure 9: Strain controlled fatigue test data a) strain-life (ε-N) data and b) stress-strain hysteresis loop

Crack propagation models use fracture mechanics to firstly analyse the crack growth rate, and secondly determine how long a crack can grow until it proves to be critical and become catastrophic. This approach is based on calculating the crack growth rate depending on the crack length and nominal stress at the crack tip.

2.1.3 Design Philosophies

When designing against fatigue failures there are various design philosophies that can be followed. The method that is chosen depends on the component or structure and the required performance decided by the design engineer. The four methods are

Infinite design life;

Finite design life;

Fail-safe design;

Damage tolerant design.

If a durability target or required life has been defined by the engineer, there are two ways to design against fatigue. An infinite life design includes a known fatigue limit of the material/component. The component is designed to operate at a stress amplitude significantly below the fatigue limit, $\sigma_a < \sigma_f$, ensuring that the component would never fail, (see Figure 10 a). Yellow goods are designed using an infinite life approach. They are designed to never exceed the fatigue limit. This ensures excellent durability of the structure.

A finite life design (also known as safe-life) produces a component that exceeds the durability target required, $N_{design} > N_{target}$, (Figure 10 b). If a component is required to achieve 100,000 life cycles, the designer is confident of achieving a far greater life. This is a good approach to guarantee a certain level of durability if a warranty is provided with the component, ensuring the component never fails during its recommended fatigue life. However, there is always some uncertainty about the actual fatigue life of the component. There is also a lack of fatigue life optimisation as the component is over-designed to a life that is usually never actually achieved. A finite life design approach is used widely in automotive applications. For example, a motor vehicle will be expected to achieve 100,000 to 200,000 miles, although it is designed to reach a figure significantly beyond this with a factor of safety.

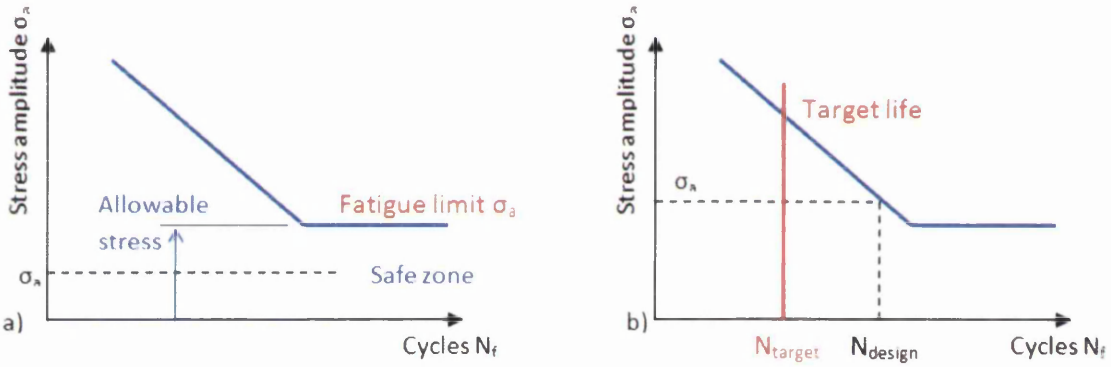

Figure 10: Fatigue design philosophies - a) infinite life approach and b) finite life approach

The fail-safe concept incorporates redundancies built-into the structure, giving safe operation if a component fails. Component failures are assumed, but failure of one part does not result in total failure of the structure. The damaged component would require replacing when found during inspection. The redundancies are provided by alternative load paths to withstand the load. This concept minimises the amount of over design associated with finite-life design. An aircraft wing contains numerous mechanical fasteners to hold the structure together. Upon one rivet failing, the remaining fasteners are still able to carry the load and maintain the structural integrity of the aircraft wing.

The Damage Tolerant design allows a structure to contain cracks. A structure can tolerate certain non-critical cracks until they reach a critical length. The component is inspected for cracks under a strict routine and then replaced when a critical crack length is reached. The method uses dye-penetrate inspection to find any flaws on the material surface and requires a

reliable prediction of the rate of crack growth between inspections. The designer must demonstrate that a flaw of a given size will not propagate to failure either before being detected, or before the structure is removed from service. Some components or areas of a structure are often difficult to inspect or inaccessible. Examples of damage tolerant concepts are found in the aviation industry. Various parts of the gas turbine engine such as compressor discs or turbine blades incorporate this design method. Failures cannot be tolerated therefore the parts are removed upon reaching a critical crack length.

2.1.4 Testing Methods

Various methods exist for fatigue testing. The basic methods involve applying a cyclic load to a test specimen through a servo-hydraulic test machine. This could be through repeated axial (tension or compression), repeated torsion or rotating bending loads. The test specimens can also vary and include a single or double edge notch, V- notch or a plain specimen. The applied loading can be of constant amplitude sinusoidal or other fluctuating waveforms to replicate more complex in-service loads. The results are then plotted together as the applied stress range against the number of cycles to failure, to form an S-N curve.

A servo-hydraulic testing machine, as shown in Figure 11, is powered through a pump and oil supply that feeds a loading actuator. The loading actuator applies the force onto the test specimen. The applied load is measured by a load cell in series with the specimen. The load cell output is compared in a differential amplifier with the original input signal. The differential amplifier output is relayed to a servo-valve controlling the oil pressure flow. This creates a closed-loop control circuit. The differential amplifier can also measure the output signal from a displacement transducer on the loading actuator, or from a strain gauge on the test specimen, as Figure 12.

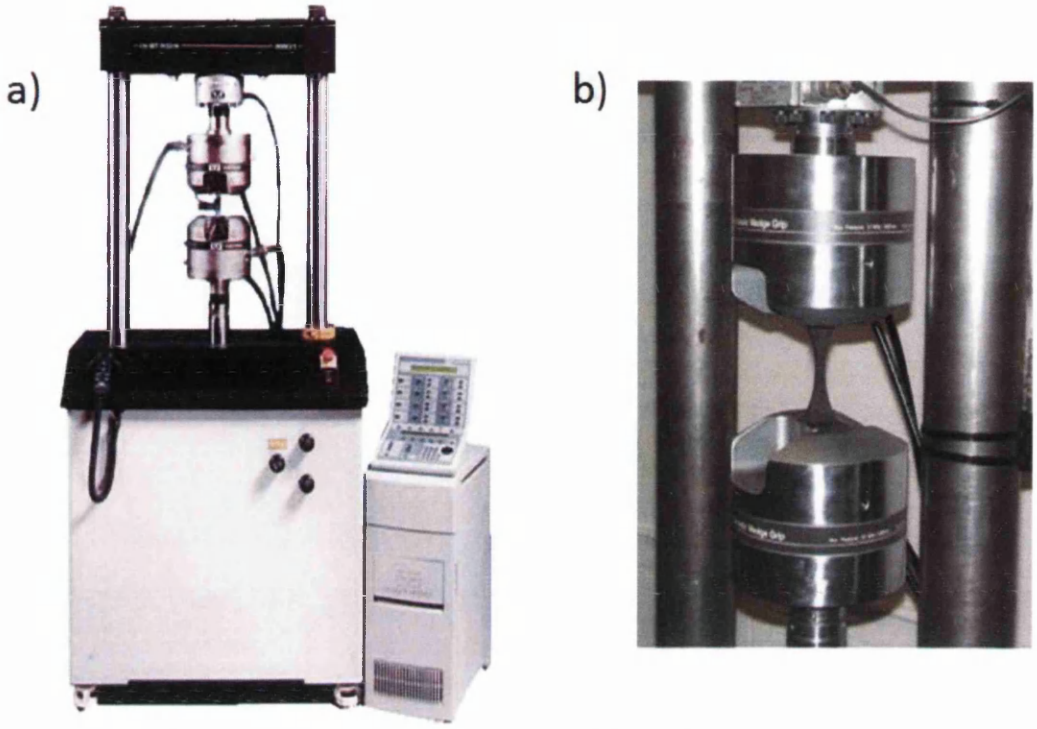

Figure 11: Fatigue testing a) Servo-hydraulic test machine, b) Test grips and smooth specimen

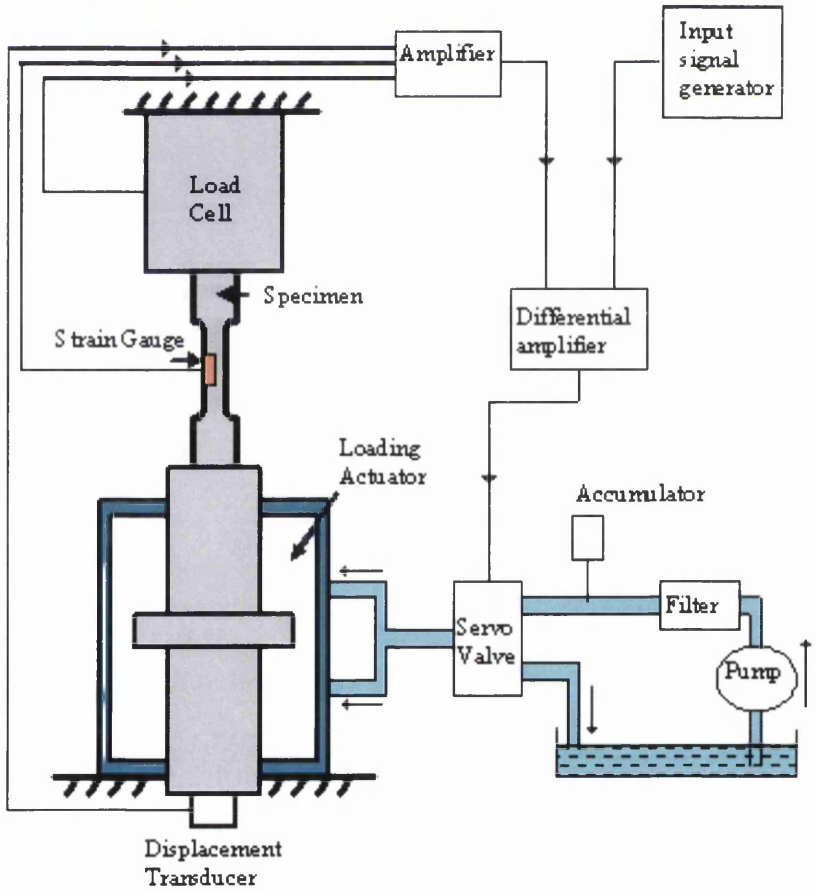

Figure 12: Schematic Diagram of a Servo-hydraulic test machine

Other than simple laboratory fatigue testing, full-scale testing of components and structures is used. This approach can be expensive and time consuming. However, in most cases, this is justified. Full-scale testing is used at various stages of design and development of a structure, such as a yellow-goods vehicle. In the initial stages of design of a component, full-scale testing is used to gather design data. For example, in a welded structure there might be insufficient fatigue data on a particular welded joint and so a full-scale test would be required to clarify its performance.

Full-scale testing is also used during the prototype development stage. Prototype structures of a new design are tested to give an idea of performance, fatigue life and reliability. Testing takes place in service conditions for the structure that duplicates working loads, e.g. an automotive vehicle driven around a test track. This is a very time-consuming and expensive process as it can take a long time to reach a lifetime of cycles. Alternatively, full-scale testing could be completed in a laboratory with the use of servo-hydraulic equipment and test rigs. The structure/component is set up in a rig in the configuration it is to be used in service. Servo-hydraulic actuators are used to apply the known service loads to give a realistic simulation. This method can be more beneficial as the conditions can be closely monitored and controlled. The simulation can also be readily repeated and accelerated to reduce the time scale and hence reduce costs.

The quantity of fatigue testing required can be easily overlooked and undermined due to the cost and time factors associated with it. Laboratory testing may be easily preferred to rectify a design without the added expense of full scale testing. There is some discrepancy when correlating laboratory data to predict actual fatigue lives due to the scatter band associated with fatigue. Without thorough research and characterisation, failure of components may occur in-service and the product could incur warranty claims. Upon failure, the redesign and validation of a part is needed as soon as possible. This is often in the form of full-scale testing to evaluate its effectiveness and improved performance. Timely investment in full-scale testing can save time and money.

2.1.5 Fatigue test data

Considerable variance and scatter in fatigue data is widely recognised. This is due to such aspects as chemical composition, randomly formed inclusions, varying levels of residual stresses, differences in manufacturing techniques and the simple variability of the fatigue crack initiation and propagation process. Careful consideration must be given to the analysis

of the results and the number of test samples required when generating fatigue data in order to establish a database that can be used effectively for the design of components.

Traditional methods for fatigue data under constant amplitude involve statistical analysis to estimate the probability of failure and survival. As in the British Standard BS7608 [8], linear regression analysis is used, on log S-log N curves to give 2.3% probability of failure or 97.7% survival. This method is widely used and is known as the Gaussian distribution. With Log N the dependent variable, a design line 2 standard deviations lines below the mean (M-2SD) is used as shown in Figure 13.

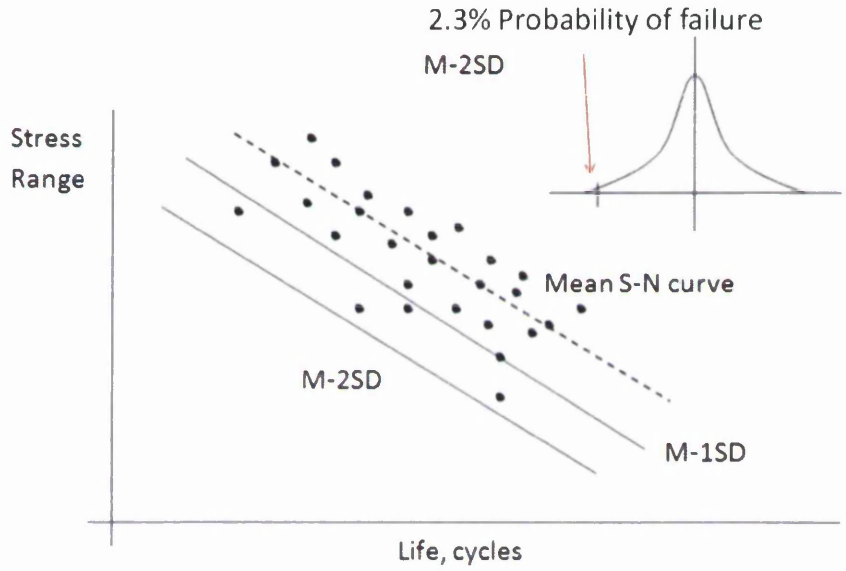

Figure 13: Statistical analysis of fatigue data showing mean minus 2 standard deviations

The reliability and confidence of the test results is dependent on the number of specimens tested. Greater reliability is achieved with a higher number of tests. The number of test results that can be achieved relies on the resources available in the project. The maximum number of test results, therefore, is determined by the costs incurred and the testing or design time requirements. A realistic figure should be proposed with additional samples produced for other chemical and microscope analysis and to cater for the unexpected.

Figure 14 shows the guidelines on the number of recommended tests from the British Standard BS 3518-1:1993 [9]. The number of tests required depends on use and purpose. The greater amount completed gives better definition = t/d, where t= number of tests and d= number of stress levels used.

Exploratory tests generally require fewer specimens, but repeatability is reduced. This would be useful for verification of an alternative manufacturing process or material. To determine a general form of an S-N curve, two fatigue tests at six different stress levels should be completed. A total of 4 tests should be run at each of the six stress levels for an accurate description of the S/N curve for design purposes. Using the results, life at a fixed stress level can be determined as recommended in the guidelines in BS3518-5:1993 [10]. The statistical analysis used to determine the lower fatigue limit uses the same Gaussian distribution method as previously described and found in BS7608 [8].

Test programme classification	Minimum number of test pieces	Minimum degree of replication
Exploratory tests	6 to 12	1.2 to 1.5
Research and development tests	6 to 12	1.5 to 2
Design data tests	12 to 24	2 to 4
Reliability tests	12 to 24	4 to 8
NOTE In each case the lower number refers to the situation where the general form of the *S/N* is known, and the higher number to where it is not.		

Figure 14: Sample number recommendations [9]

Following the guidelines from BS3518-1:1993, it is inevitably up to the judgement of the test engineer to decide on the number of tests used. There is no correct number, although it should be justified by the level of confidence required. Twenty tests may be intended for one S-N curve, although the scatter band may be defined after 12 test results. The remainder of the tests are not necessarily required if time is an issue.

The deciding factor for any test is dependent on the resources available. A judgement must be made by quantifying the number of tests and accuracy of the S-N curve required against the resources, time and budget available.

2.2 Fatigue of Welded yellow goods Equipment

Yellow goods generally consist of thick steel plate welded structures that are widely used for earthmoving equipment in construction, agricultural and materials handling environments. Vehicles include backhoe loaders, excavators, telescopic handlers, wheeled loaders, articulated dump trucks, forklift trucks and tractors, Figure 15.

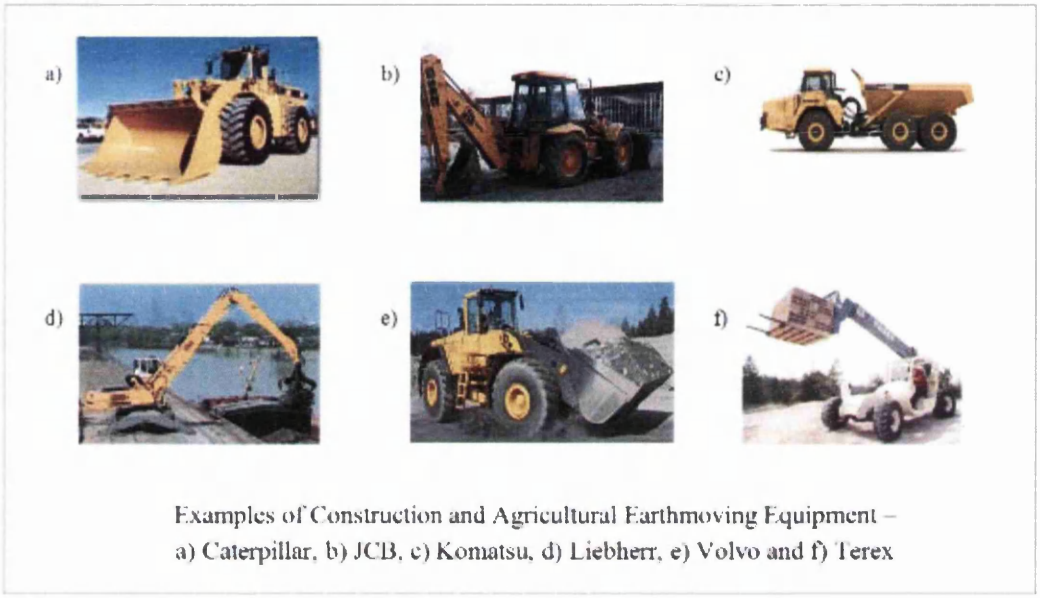

Examples of Construction and Agricultural Earthmoving Equipment –
a) Caterpillar, b) JCB, c) Komatsu, d) Liebherr, e) Volvo and f) Terex

Figure 15: Yellow goods equipment

The main structural parts of the chassis, frames and loading arms are welded together using strip and plate materials in the range of 5-25mm and even greater, substantially greater than other vehicles such as in the automotive industry. The main emphasis with automotive design is weight reduction in order to improve fuel economy and reduce costs. However, with earthmoving equipment, structural robustness and weight is a necessity for counter balance effects when excavating or loading.

Many aspects must be taken into consideration during the design stage of yellow goods so they achieve the intended service life. During the life of such structures, they experience variable cyclic loading which is difficult to predict. The extension of loading arms and booms used for excavating are constantly changing, creating variable loading cycles. Numerous weld seams on a structure create severe geometric stress concentration and crack initiation sites. Durability of the welded structure is a necessity in order to perform excavating tasks repeatedly and effectively without failure.

2.2.1 Weld fatigue

The fatigue performance of a structure is severely reduced when welded joints are incorporated into the design. This can be seen by the fatigue response of plain, notched, and welded sections, Figure 16.

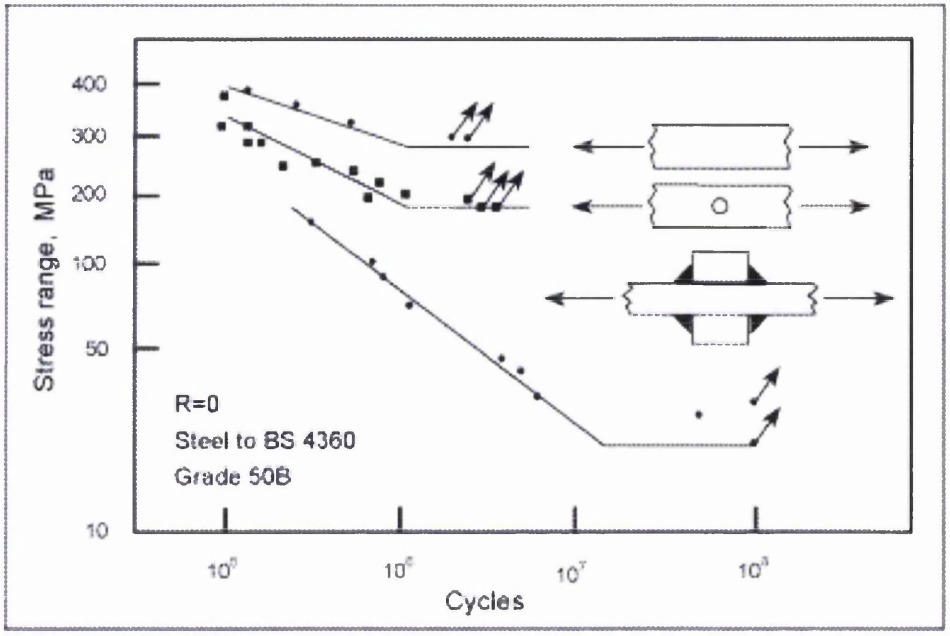

Figure 16: Effect of welding on fatigue strength. Curves for plain, notched and welded steel [11]

There are several contributors to the reduction in fatigue strength of welded components. The overall geometry of a welded joint creates a stress concentration, along with local notch effects and crack-like flaws at the weld toes, dramatically raising the local stress. It is said that the fatigue life of an un-welded specimen will consist of both fatigue crack initiation and crack propagation. However, in welded joints, upon the cooling and solidification of the welded process, micro-cracks form and act as crack initiation sites, thus the weld fatigue life consists only of the crack propagation stage as the crack already exists.

Second to this, high levels of residual stress are present in welded structures. Due to the heating and cooling cycles, the materials expand and contract inducing these high levels. The residuals can occur on both a local and long-range basis. Part of the residual stress will occur due to the local weld geometry cooling and contracting. Also from the long range fit-up of parts, increased residual stresses will be introduced. The residual stresses create a mean-shift effect, so even a relatively low stress range applied can prove to be detrimental due to the high mean stress ratio acting.

As the harsh effects of the welding procedure have been mentioned, weld durability is one of the main factors limiting the durability of the entire structure. Determination of the durability of a welded component demands accurate assessment of weld fatigue lives.

2.2.2 Factors affecting weld fatigue performance

A weld bead on a plate of material when under a transverse load will create a stress concentration. The stress distribution around the weld toe is greater than across the rest of the plate thickness. This is due to the geometric change where the material surface meets the weld bead. A fillet T-joint weld would therefore create a greater stress concentration than a butt weld as the change in geometry is greater and creates an increased peak stress at the toe, shown in Figure 17. Transversely loaded welds will have the greatest stress concentration, thus being the likely source of failure. Structures with a load parallel to the weld will also have stress concentrations in the form of surface imperfection such as crater/pinholes, start/stops, weld splatter. However, none are as severe as a weld toe.

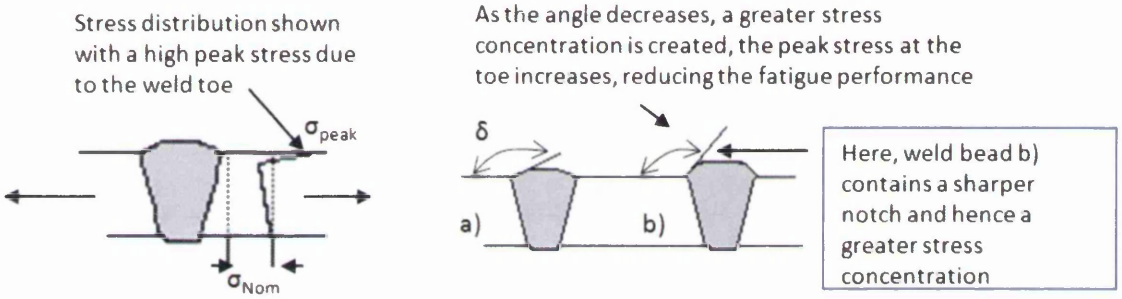

Figure 17: Effect of reinforcement angle. As the angle increases the notch and stress concentration is greater [12]

The fit up angle relative to the weld and applied forces can severely alter the fatigue response. Axial or angular misalignment in a simple butt weld in a plate, altering the angle of fit up between the two work pieces decreases the fatigue strength, Figure 18. Increases in stress level arise from imperfect weld geometries such as misalignment (axial or angular) and distortions. An increase is only present in axially loaded joints due to the introduction of a secondary bending stress. The fatigue strength will not be reduced in joints loaded longitudinally to the weld or in pure bending modes.

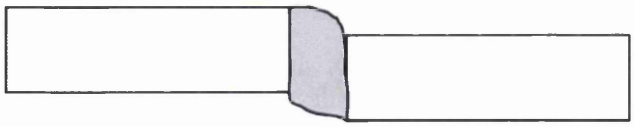

a) Axial misalignment – centre line of base materials mismatch

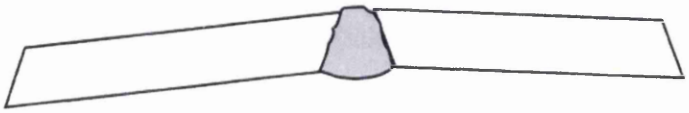

a) Angular misalignment – both base materials are not horizontal to each other

Figure 18: Angular and axial fit –up misalignment

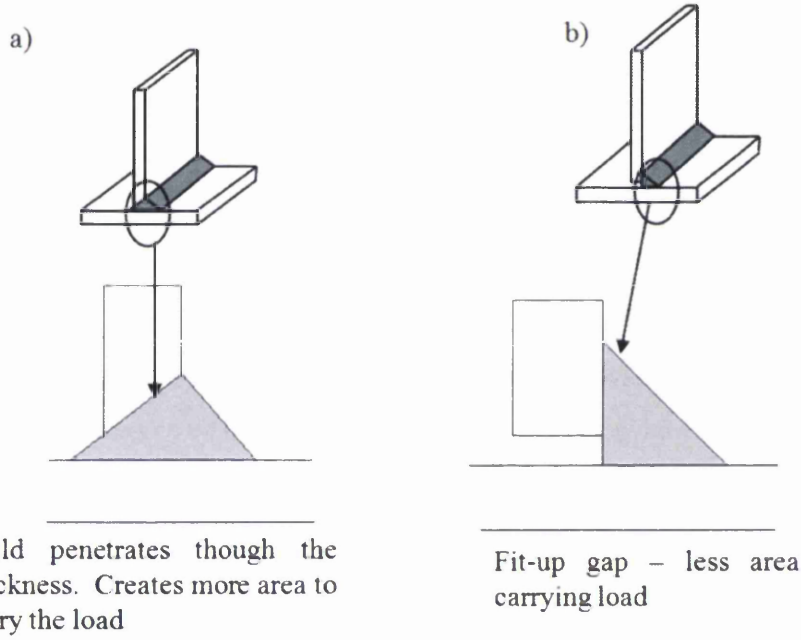

Figure 19: Weld Joint. a) Fillet T-joint full penetration weld & b) Fillet T-joint partial penetration weld

Certain welds exhibit a greater reduction in fatigue performance. Partial penetration welds create a second possible failure point along the weld root as shown in Figure 19. A crack can initiate at a weld root and then propagate through the throat. This is due to the fit-up gap made between the upright and base plate. A lack of penetration in the weld reduces the area to carry the load applied. As a result the stress increases and failure occurs. On a full penetration weld a greater cross-sectional area is used to carry the load therefore reducing the stress.

The fatigue strength can be greatly reduced due to the weld profile (i.e. toe undercut or convex weld bead). In addition, weld discontinuities also increase stress concentration effects.

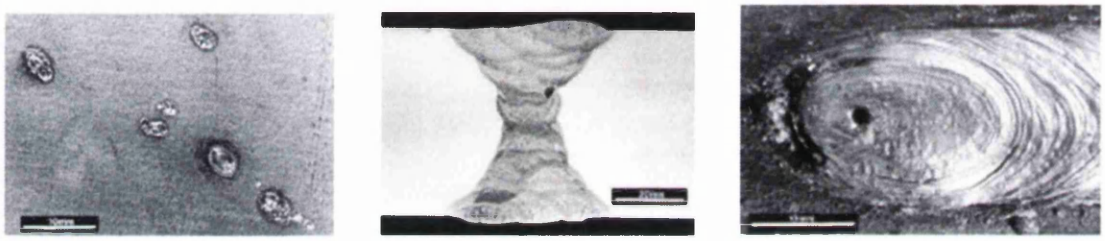

a) weld splatter b) slag inclusion c) gas pore crater

Figure 20: Types of weld discontinuities

Very small crack-like discontinuities and fatigue performance inhibitors exist as a consequence of the welding conditions selected, see Figure 20. Crack initiation can occur much sooner in a weld with inclusions, resulting in fewer cycles for the crack to initiate and propagate to failure. Upon welding, micro-cracks will grow at the fusion line of the weld bead and parent material. This is due to the intensity of the heat from the processes occurring around such a small area as the arc is struck. The local intense heat will cause the metal to melt and expand. Upon solidification, the molten metal will shrink and contract thereby forming cracks and defects. Given that total fatigue life consists of initiation and propagation, the fatigue life of a weld is much shorter as the crack initiation stage has been reduced or removed by the welding process. In other words, in an unwelded structure, fatigue crack initiation makes up a major contribution to the total life in the high cycle regime. However, in a welded joint, only a small proportion of the total fatigue life consists of the crack initiation; the major contribution is crack propagation.

As there is a large amount of scatter associated with fatigue performance in general, control measures should be put in place to further minimise the degree of scatter associated with welded joints, i.e. automation of the welding process in order to control the amount of toe undercutting and the quality of the weld.

There are two forms of residual stresses present in a welded structure, long-range and local residual stresses. Long-range residual stresses occur due to the assembly of the overall welded structure. The structure will have numerous tensile and compressive stresses locked in due to the fit-up of the various components.

Residual stresses can also occur locally due to the weld process. During welding the parent and weld metals undergo a range of thermal cycles. As the weld is heated up and cooled, the local material, the heat-affected zone (HAZ), alters its microstructure and material properties inducing residual stresses [13]. The main cause of residual stresses, however, is the contraction of the molten weld metal upon cooling.

When a weld is made, the material surrounding it will also heat up and expand. However, the bulk of the structure prevents this hereby causing the material local to the weld to be in compression. Then, on cooling, the underlying material contracts but because of constricting surrounding metal high residual stresses are created.

Residual stresses in a welded structure are generally assumed to be as high as the yield stress of the parent metal [14]. Where high residual stresses are present, the fatigue strength is dependent only on the applied stress range. There is no effect due to mean stress or varying stress ratio [15, 16]. No matter what stress ratio is applied, an effective stress range is produced that is much higher than the actual applied stress. Therefore it is conventional, and the practice in many design codes, to neglect any mean stress or stress ratio effects but only when the residual stresses equal the material yield strength.

There are many weld imperfections, flaws and discontinuities that can, and do, occur during the welding process. These imperfections have a detrimental effect on the fatigue strength. Such unwanted defects include misalignment, undercuts and overlaps, porosity, gas pores, slag inclusions and cavities, lack of weld fusion and lack of penetration, Figure 21.

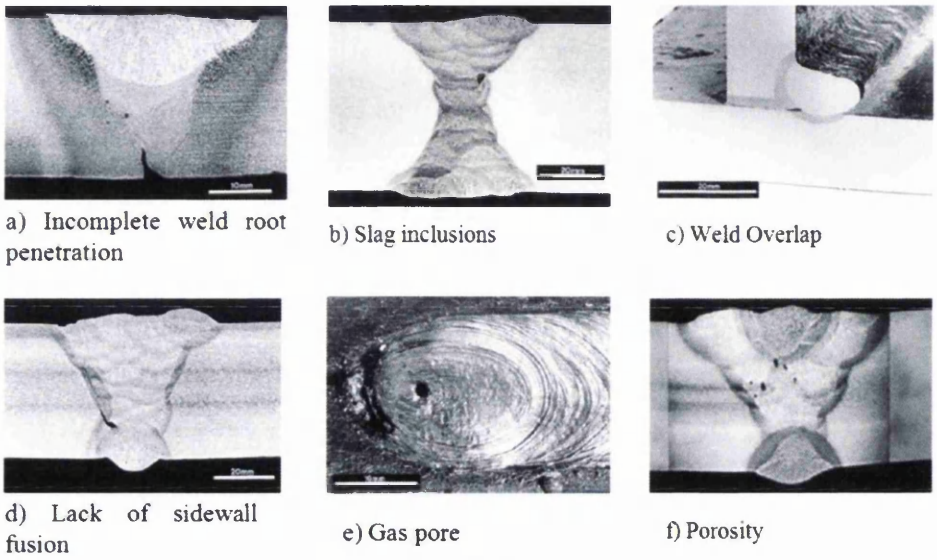

a) Incomplete weld root penetration

b) Slag inclusions

c) Weld Overlap

d) Lack of sidewall fusion

e) Gas pore

f) Porosity

Figure 21 Types of weld imperfections

A majority of weld flaws can often be put down to operator inexperience or incorrect welding parameters. However, as imperfections do occur, a 'fitness for purpose' and weld quality requirement is often established [17]. Under the loading and environment for which a weld is designed, defect levels are set so that failure of a weld is not due to weld quality. First visual inspection will take place for surface discontinuities, and then non-destructive testing (NDT) techniques such as ultrasonic, magnetic particle and radiographic techniques can be employed for embedded imperfections.

The fatigue resistance is also reduced by imperfections creating a local notch effect such as undercuts and overlaps, porosity and inclusions. There are two aspects of a local notch effect. In an 'additive' notch such as an undercut or overlap, it supplements any geometric discontinuities of the weld shape and lowers the fatigue strength of the welded joint by increasing the angle and sharpness of the toe. A 'competitive' notch effect, such as porosity or inclusions below the surface and away from any geometrical stress concentration, will act in competition to other notches. The porosity or inclusion creates another possible fatigue crack initiation site. A fatigue crack could propagate from either a porosity/inclusion flaw or, for example, a weld toe. The stress concentration with the greatest value and lowest fatigue life will be the principal failure location. Porosity creates a relatively round shape and a lower stress concentration than other flaws. Inclusions can be found that are more angular and crack-like. The shape and orientation will vary and likewise, the effect on fatigue strength can differ, but they are generally more damaging than porosity.

Fatigue strength is also reduced through planar discontinuities such as crack-like imperfections. These include lack of sidewall fusion and incomplete weld root penetration. These crack-like areas are associated with short crack initiation lives. Lack of fusion is due to poor welding technique, or inadequate joint preparation, resulting in no penetration of the weld and can create a severe stress concentration. Incomplete penetration is sometimes intentional e.g. for partial penetration welds. If there is a lack of penetration due to poor welding technique or fit-up, the fatigue strength can be significantly reduced due to the crack-like stress concentration created. The total load carrying area of the partial penetration welds is reduced, creating a higher local stress, and leading to premature failure. Providing the engineer inspecting the flaws can recognise them correctly, a 'fitness for purpose' approach can be implemented effectively to avoid fatigue failure from such imperfections.

In general, for the same stress range at the weld toe, an increase in the size of material thickness results in a reduction of the overall fatigue life in welded joints that crack from the toe [18]. This is due to the stress concentration of the weld detail creating a greater stress distribution across the thickness.

In traditional design codes employing S-N curves with a nominal stress approach [8], any thickness effect is included into the test data. There would be concern as to whether the test data is representative of a new structural design with different dimensions. If not, a necessary correction factor would have to be used. In more recent design codes, methods have been developed to allow for thickness effects when calculating the fatigue design stress. A correction factor is employed in the Eurocode [19], and also in IIW fatigue design rules [16] where the correction factor is better defined and takes into consideration the role of weld type, profile and mode of loading.

2.2.3 Fatigue life prediction of welded components

One popular method of product design and development is the 'build-test-fix' approach. A design or concept is created and a prototype made. The prototype then undergoes testing to determine its performance for a given design criteria. If the prototype meets the criteria, then the design can be approved for engineering sign-off and proceed to production of the component. Should the prototype not meet the set criteria, design modifications are made in order to 'fix' the problem areas. The re-design is then tested again to see if the modifications satisfy the criteria. This design process is highly iterative and not very efficient as lengthy design modifications and numerous prototypes increase costs and time. Given design stages have sign-off dates to adhere to, should there not be enough time to fix and test design modifications, then the changes are made and the revised structures proceeds straight to sign-off. The sign off dates are met but at the risk of warranty claims later on in the service life.

This is not always the case, and design stages can use many tools in order to avoid repeats of design-test-fix iterations. In the early design stage, before a prototype build is commissioned, time is spent in component design and using CAE modelling and engineering experience to achieve a 'right-first-time' design, and thereby minimise the number of 'test-fix' iterations. A flow chart model of a typical component design can be seen in detail in Figure 22. When applying this process in the design of welded components, early design stages can often be heavily reliant on engineer experience. Simulation methods may not be employed fully to model the effects of the welding process and stresses experienced in a component. FE stress

analysis of a component can provide accurate stress plots but cannot always simulate the welding process effects.

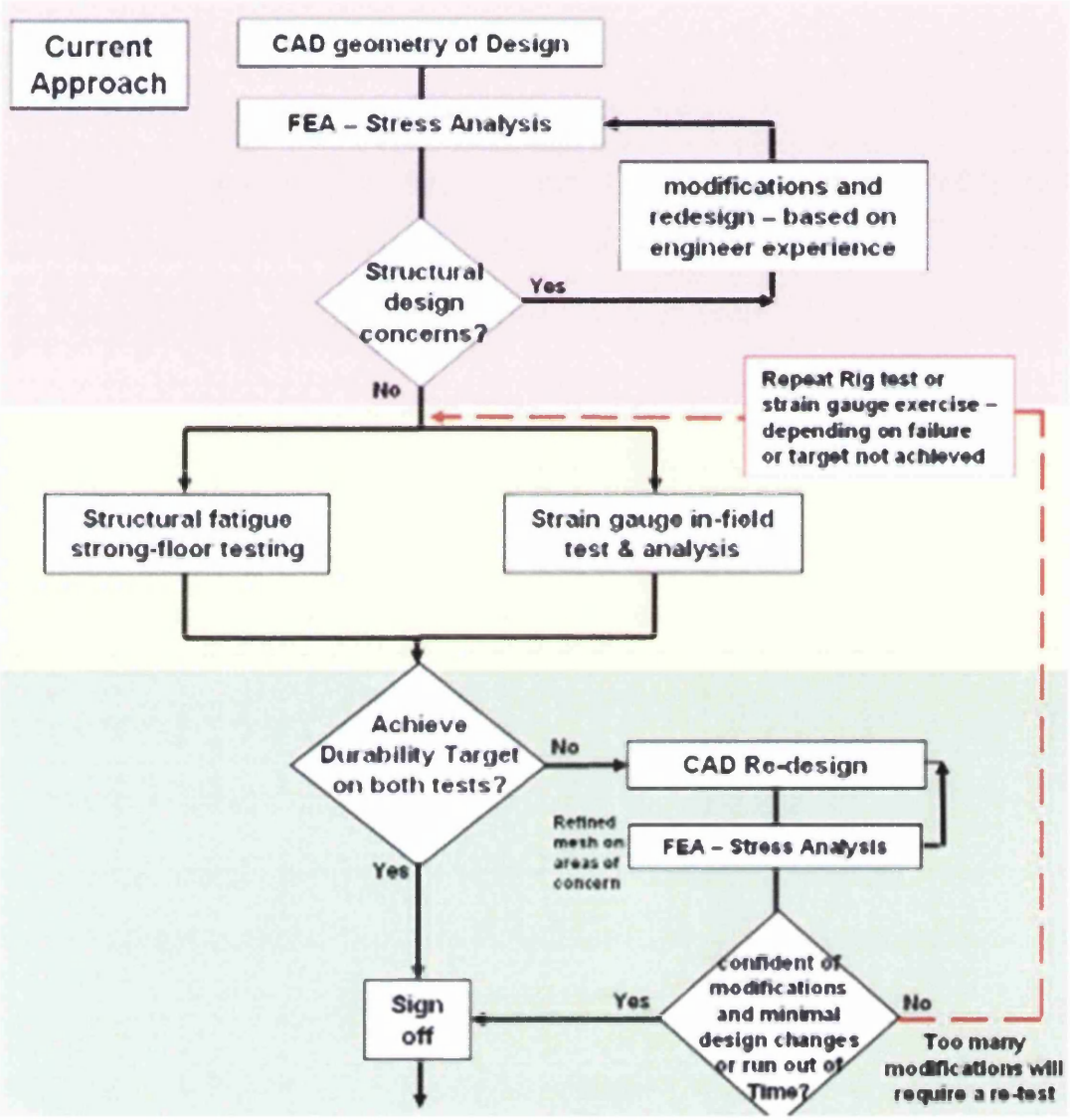

Figure 22: Engineering design sign-off process

Residual stresses contained in a welded component will affect the mean stress range applied and potentially be detrimental to the total service life. In this case it is difficult to model residual stresses on a component. A high stress area from the FEA might not necessarily coincide with the failure location of the weld fatigue crack. In order to characterise the stress behaviour in a welded structure significant amounts of time, resources and ultimately money, can be spent on analyses looking at the weld microstructure and properties, weld heat-flow simulations, residual stresses and distortion. Not all budgets can support such activities.

Frequently with welded components, while all that is possible to achieve a right-first-time design will be done, there is no guarantee of success. Relevant engineering experience may not be available and FE stress analysis does not directly quantify the fatigue performance of a component. So the build-test-fix design solution does not define all significant structural integrity issues before the commitment to a prototype build.

Once a prototype component has been built there are various methods for determining the durability and fatigue life of the welds. One method to obtain a fatigue life prediction is to complete an 'in field' strain gauge exercise. This uses the British Standard BS7608 -1993: Code of Practice for Fatigue Design and Assessment of Steel Structures. This standard provides guidelines for determining the fatigue life of a welded structure using a nominal stress method. Each type of weld joint and failure mode is classified and given a specific S-N curve for that class type. The actual welded structure is then analysed under field and service conditions. A strain gauge is placed 10mm away from the weld detail and its nominal stress is determined under load. The nominal stress range is related to the classification curves for that type of welded joint and a fatigue life obtained. The steps are defined in Figure 23.

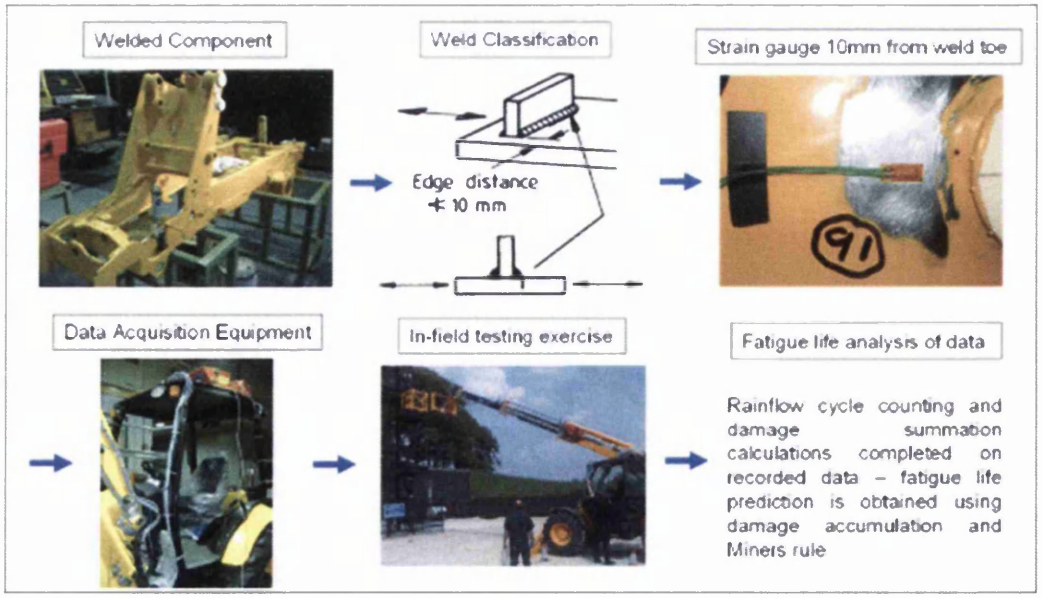

Figure 23: BS7608 Fatigue life prediction - Weld classification and strain gauging

Field tests and strain gauge exercises have benefits and concerns. The method can prove to be expensive as considerable resources are required including strain gauges, data acquisition equipment, analysis software and computing equipment. The method is representative as it uses real in-service testing regimes, but the fatigue life determination is only a prediction as

no actual fatigue failures are achieved. The method is appropriate for an infinite life design philosophy provided engineers are willing to accept that the structure might be over-designed. A limitation is that the standard does make a number of assumptions. All the weld classifications are for tensile loading only and not bending. In some cases, a weld joint geometry or loading mode of interest may not be included in the classification. Then questions are raised as to what is the best way of qualifying that type of joint? To ensure a suitable factor of safety it would be classified conservatively using engineering experience. However, the nominal stress method is a straightforward process and not as complex as other methods available. Life predictions can be reliable but the design process lacks efficiency. There is confidence in the structure achieving x amount of cycles but how far beyond x the structure will survive is unknown. If this issue could be addressed, the fatigue life could be optimised and used with greater confidence in defining the warranty for the structure.

As well as fatigue life prediction, it is also beneficial to complete some structural rig testing. The fully welded components are assessed under laboratory conditions and fatigue tested. Structural test equipment is required to provide loading power through rams and actuators, with measurements made through load cells and strain gauges. It is important to verify the test rig first with strain or load measurements from in service loading exercises in order to ensure accuracy when simulating in field conditions. The required load or stress range and loading regime is applied and a counter logs the number of cycles. The structure is inspected regularly for weld crack initiation sites.

The in-field testing and life prediction analysis is beneficial in this type of design process as it provides a life prediction under realistic loading but no actual failures are achieved. The rig testing is also very helpful as it provides actual failures and locations. However, the loading more often than not is constant amplitude. Questions might be raised about the relevance of constant amplitude loading in relation to service conditions. Both design tools are costly and time-consuming and also require a prototype build and possibly re-design and test if the structural integrity of the component is not adequate. For these reasons, the design-test-fix process is inefficient.

Alternatively, a right-first-time design approach can used in order to reduce the amount of redesign and retesting. However, the structural capability might be questionable and this could result in in-service failures later on. These issues are the main driving force behind the development of a numerical based life prediction method that can be used early on in the

design process. An FE fatigue analysis could be run to highlight fatigue prone areas of a design, thus allowing the model to be altered quickly without incurring the additional cost of manufacturing modified prototypes. This would increase the confidence of right-first-time designs. If greater confidence can be found in the definition of fatigue performance early on in the design programme, the amount of prototype testing could be significantly reduced, again reducing time and cost.

2.2.4 Fatigue testing of welded components

As discussed in the previous section, prototype component builds and full-scale model testing can often prove to be expensive. An alternative option is to test a small scale specimen with a detail or geometry representative of the full-scale model. A smaller scale test piece would not incur the full manufacturing and testing costs of a larger test piece. Small-scale specimens are tested in a column loading frame under the required loads and amplitudes. A large number of cycles can be applied in a relatively short time (compared with full-scale test rigs).

This approach is appropriate for generating design data or executing exploratory tests to support research and development. The main concern with such tests is how representative the small-scale test is compared with a full-scale component. Misrepresentation can easily occur and inaccurate data can be generated. These can be due to either the test-piece or the load applied.

In small welded coupons it is straightforward to represent a weld detail from a full-scale model. Some consideration should be given, though, to the loading mode seen in the actual component, and how to represent that in a tensile or bending load test. The main concern with coupons lies in the presence of residual stresses. The poor fatigue life of welded components has been discussed and the fact that it occurs due to the notch stress at the weld toe highlighted. The effects of residual stresses have also been raised. It is known that small-scale test pieces will not contain the significant residual stresses found in a full-scale component.

Work documenting residual stress effects [20], illustrates the influence that both welding residual and assembly stresses (long-range residuals) have on the fatigue strength of welded joints. In this work, fatigue response data is shown for samples with a range of maximum and minimum welding and assembly stresses. Significant differences can be seen in the fatigue strengths between a sample with maximum local and long-range residuals, one with only local residual stresses, and a sample containing no residual stresses. The effect of welding

and long-range residual stresses are given as the reason for the large difference in fatigue life between small test specimens and full-scale tests on welded structures. Work by Maddox [11] also suggests similar conclusions. Variations of residual stress levels in small welded joints affect the fatigue results significantly and can produce large scatter in the data. Correlation of small test specimen data and full-scale fatigue tests is then difficult. Designers and engineers would prefer to undertake full-scale tests but this is very costly and time-consuming.

When testing small welded joints to generate fatigue performance data the test specimens are evaluated using a traditional nominal stress approach as in BS7608. The effective stress range applied is used to establish the fatigue life. However, research has shown that with small welded specimens the assumption that residual stress is approximately equal to the parent material yield stress is not always true. Small specimens generally contain much lower levels of residual stresses than welded structures [21]. This is due to the release of residual stress when the specimens are manufactured from large plate material and cut to a smaller size.

Fatigue test results from small specimens do not necessarily provide an accurate representation of the fatigue performance in a welded structure. For small welded joints where high residual stresses are not present, the specimens can be tested at a maximum stress equal to the yield stress in order to represent the effect of the residual stresses in components [21]. Thus, the applied $\sigma_{max} = \sigma_{yield}$, with the $\Delta\sigma$ cycled down from the maximum stress, such that $\sigma_{min} = \sigma_{yield} - \Delta\sigma$. Using $\sigma_{max} = \sigma_{yield}$, results in lower fatigue lives [22] in a similar way to a welded joint containing residual stresses of yield strength magnitude.

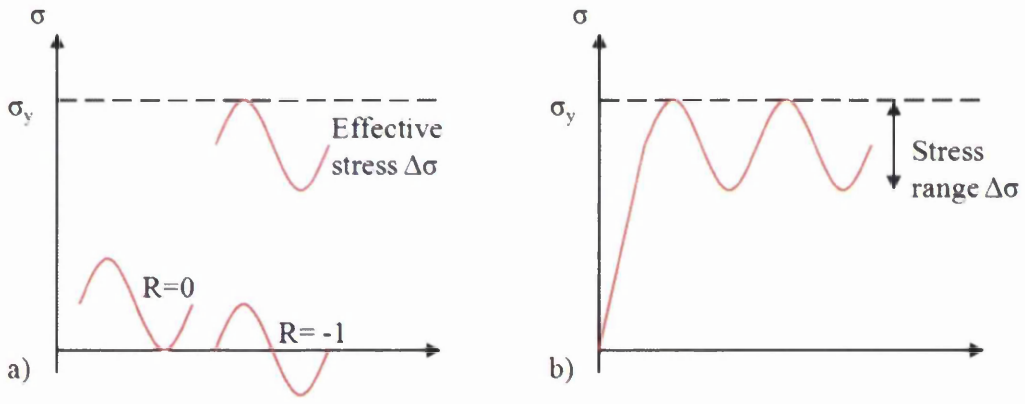

Figure 24: a) Effective stress range due to residual stresses, b) Test method for simulation of residual stresses in small welded joints

However, there are concerns when applying a high constant load to simulate residual stresses and then cycling at a high mean stress. The impact of a tensile load is different to that of residual stresses. Residual stresses are in equilibrium, which is not the case with an applied constant load.

The International Institute of Welding (IIW) recommends a similar method in which the fatigue tests are run at a high stress ratio, i.e. R=0.5 or to employ a fatigue enhancement factor is introduced for stress ratio, R<0.5 [16]. This modification takes into consideration both the release of residual stresses and mean stress effects where high residual stresses are not present.

Residual stress effects must be considered when using small specimens to develop compatible S-N curves for the predicting the fatigue lives of larger welded structures. Ideally test pieces should be manufactured sufficiently large as to contain the residual stresses.

2.3 Computer Aided Engineering (CAE)

Computer Aided Engineering (CAE) involves computer modelling in the design, development, performance evaluation, simulation and manufacturing of components. It encompasses, for instance, aerodynamic modelling of airflow around cars; CAD drawings of a component; simulation of a tooling process for input data on a CNC lathe machine.

As computing power advances, and cost saving opportunities are sought, an attractive solution for reliable and optimised designs is CAE and finite element analysis (FEA).

2.3.1 Finite Element Analysis (FEA)

Finite element analysis is a mathematical model that solves differential equations representing a physical problem. There are many different applications and techniques for this type of computer analysis. For the purpose of this literature review the Finite Element Displacement method is discussed. There are further sub-divisions depending on the environment e.g. non-linear, dynamic or linear elastic conditions. For a simple implicit model (structural linear elastic) $F(t) = Kx$, where both the input Force F, and component stiffness K values are known, simultaneous equation matrices are solved in order to determine the displacement of the structure under analysis. The solution provides the engineer with information on structural behaviour and performance before a component is made.

The component to be analysed is broken down into a finite number of elements and nodes in a mathematical model known as the mesh. This is achieved using a software package known as a pre-processor having a CAD-like user interface. The boundary conditions are then defined in the pre-processing stage and the physical quantities such as loads and constraints are defined to represent the real environment. Sets of equations are established for the component as a whole and the equations solved in the Analysis Solver. The solution of the finite element model calculates the unknown quantities from the simultaneous equations, giving the displacements and stresses or strains for each element and producing the deformation of a component. In the post-processing stage the results can be plotted to view the maximum stress or strain, stress concentrations and deformation.

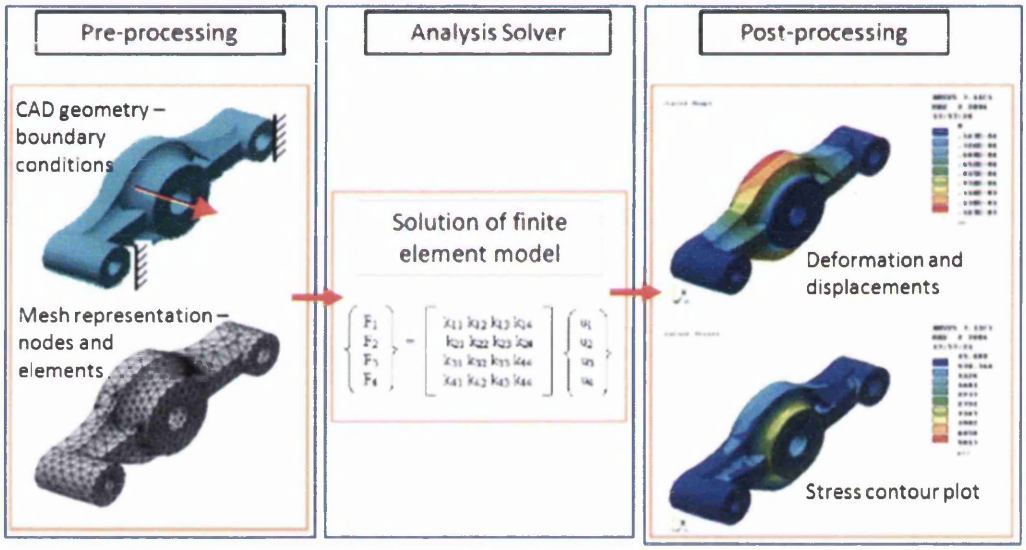

Figure 25: Finite element model process

This example is based on a linear structural finite element model. Other branches of FEA will require further steps to input material data and contact elements depending on the environment. These might include material or loading non-linearity. This durability assessment project is particularly concerned with a fatigue environment analysis.

2.3.2 Finite Element (FE) Fatigue analysis

As fatigue and durability are an important aspect of component design, it is often beneficial to complete a FE fatigue analysis to obtain an idea of the structure's performance. In its simplest form, a fatigue analysis can be described using a 'five-box trick', Figure 26.

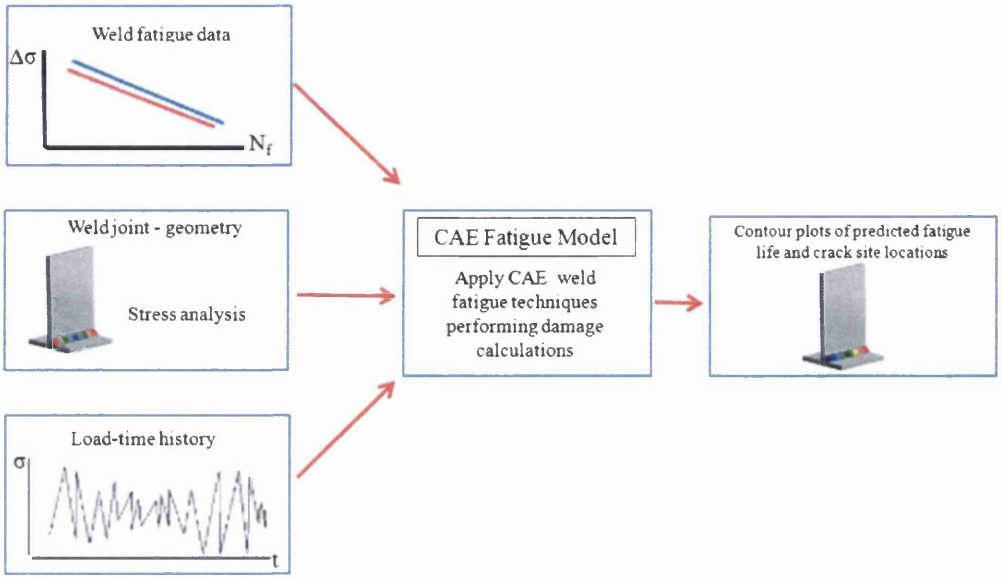

Figure 26: Finite element fatigue analysis - 5-box trick

A fatigue analysis, alongside a structural FE analysis (as described in the previous section), the fatigue model also requires material property data and a load-time history. To understand the steps taken in a fatigue analysis, the 5-box trick needs to be expanded. There are two approaches that can be taken:

Elastic-plastic FE analysis;

Linear-elastic FE analysis, scaling and super-positioning.

The main difference between the two is non-linear as opposed to linear analysis. In an elastic-plastic fatigue analysis a non-linear solver is used to establish localised plastic deformation associated with the fatigue failure. The load-time history data is entered into the FE-model along with material data, Figure 27, in the form of a stress-strain curve.

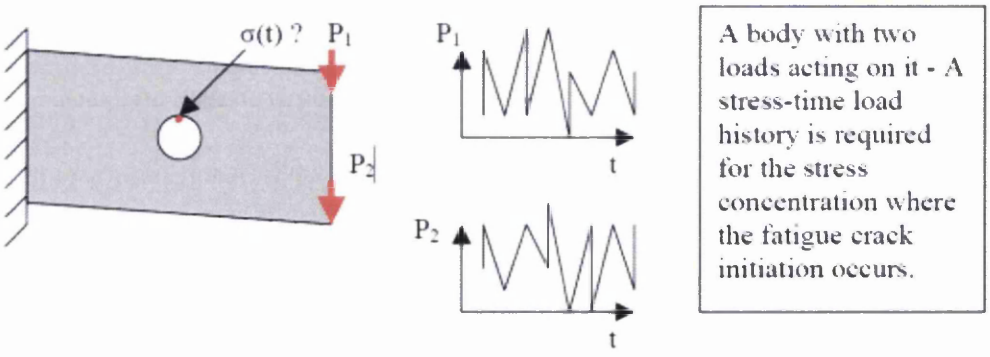

Figure 27: FE fatigue analysis - elastic plastic loading

An FE elastic-plastic analysis is run using the two load-time graphs to obtain a stress-time (or strain-time if a strain-life approach is used) history, σ_p (t). This is an ideal approach for obtaining the stress-time data. However, it is not very practical for large loads. Solution times for a non-linear analysis can be lengthy when using high overloads.

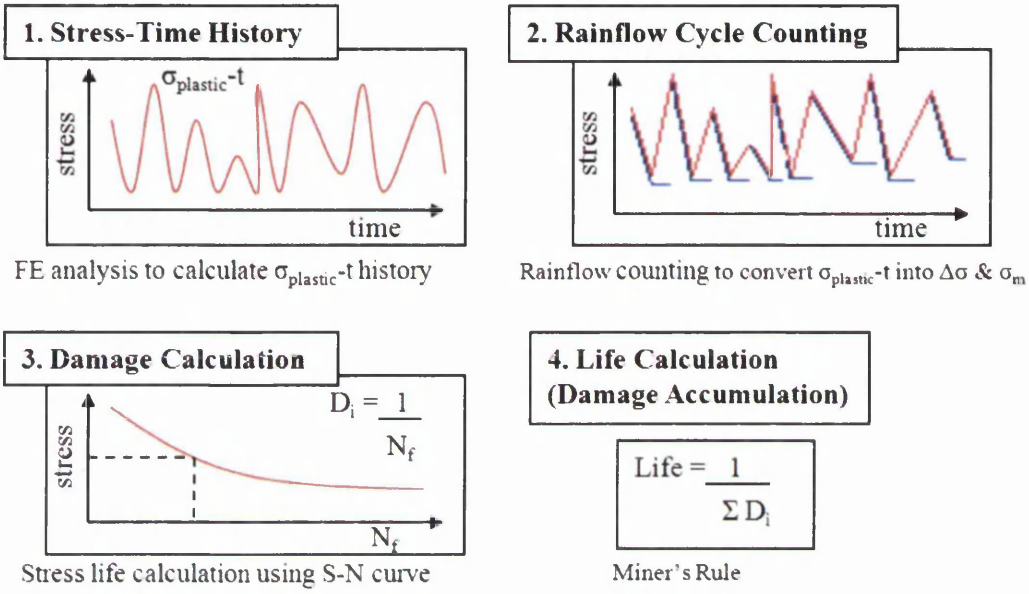

Figure 28: FE fatigue analysis damage calculations

Once a $\sigma_{plastic}$-t history is obtained, Figure 28, rain flow cycle counting is applied to reduce the range of varying stress cycles into a number of simple stress reversals. The stress ranges and mean stresses are calculated for the σ_p-t data. The next step involves a correction for any mean-stresses and then a damage calculation using fatigue performance data, i.e. an S-N curve. A life calculation completes the fatigue analysis. The fatigue life is estimated using Miner's Rule and states how many repeats of the loads, P_1-t and P_2-t, can be endured before failure occurs.

Due to the time-consuming non-linear solution process, an alternative and more practical approach is often adopted. The elastic-plastic analysis also demands a large amount of computing resource. The alternative is to carry out a linear-elastic fatigue analysis. Considering the simple model below in Figure 29, with two loads acting on the body, a straightforward linear elastic FE analysis is illustrated. Separate analyses are run with a single unit load replacing each load-time history. Two separate elastic stresses are calculated for the stress concentration at the fatigue crack initiation site.

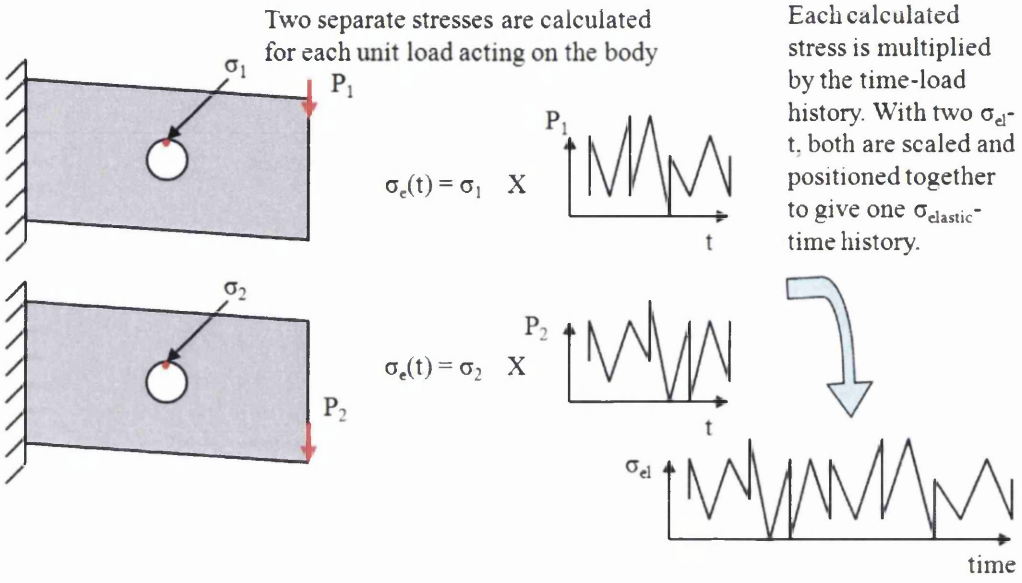

Figure 29: FE fatigue analysis - linear elastic scaling and positioning

Each calculated stress is multiplied by the load-time history to give the elastic stress-time history, $\sigma_{elastic}$-t. The two $\sigma_{elastic}$-t histories are then super-positioned to give the elastic stress versus time data.

The $\sigma_{elastic}$-t is used in a similar way to the elastic-plastic analysis. However, the stress-time data is in terms of elastic stress. The analysis must now take into consideration the material non-linearity and plasticity experienced at the local fatigue crack locations.

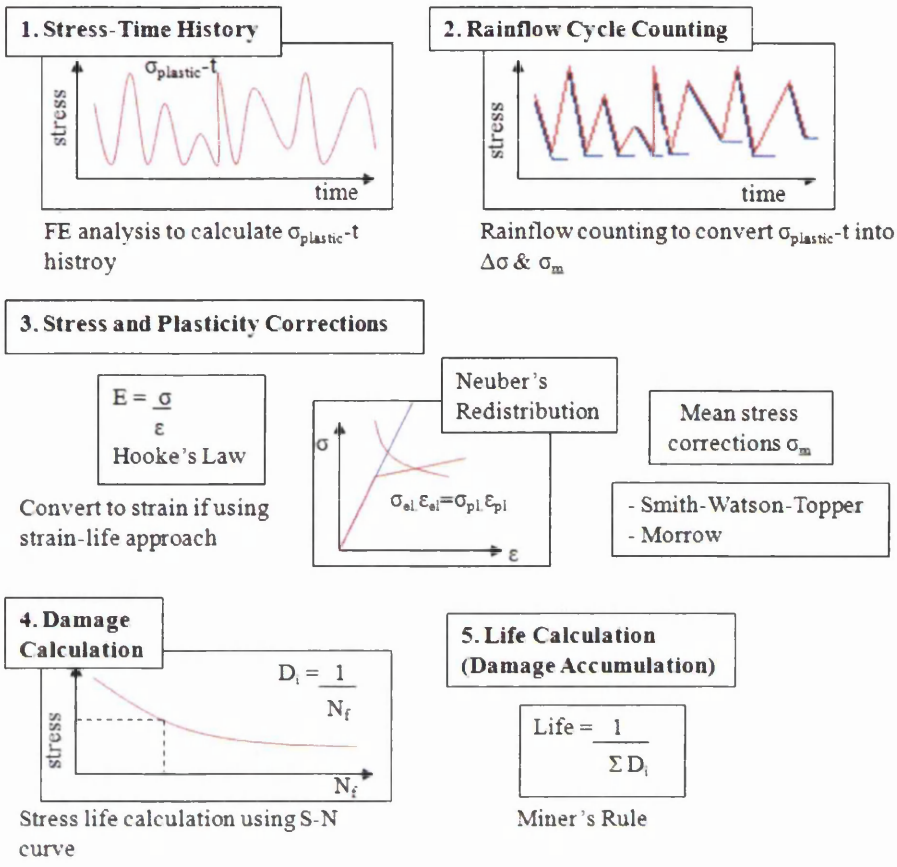

Figure 30: Linear elastic - scaling and super-positioning

Once a $\sigma_{elastic}$-t history is obtained through scaling and super-positioning, Figure 30, rainflow cycle counting establishes the stress range applied and the number of times each range is repeated. The total effective stress ranges and numbers of cycles are calculated, reducing the number of varying stress cycles to a set of simple stress reversals. The calculated stress range and mean stresses from the $\sigma_{elastic}$-t data are analysed to define the material non-linearity experienced during the localised plastic deformation. Neuber's approach [23] allows the plastic redistribution of stresses and strains to be established. The next step involves a correction for any mean-stresses and then a damage calculation is completed using an S-N curve. A life calculation completes the fatigue analysis. This estimates the fatigue life using Miner's Rule stating how many repeats of the loads P_1-t and P_2-t, can be endured before failure occurs.

To what extent FE-based fatigue analysis and calculations are needed and relied upon depends on the type of component and its service environment. If it is a critical component where failure could result in serious safety implications, the calculation and fatigue analysis are verified by fatigue testing. Full-scale or prototype testing is required if, for example, an

automotive vehicle is being designed and safety was a requirement. This is expensive and a prototype must be developed. However, if the FEA proves to be an accurate process, and the analyst is confident of the predictions, fewer modifications to the prototype are required.

2.3.3 FE – Weld fatigue analysis

In any welded structure the loading stresses and paths can be complex. When the structure consists of numerous welded joints, the analysis can become very intricate. Traditional standards of weld classification aim to simplify loadings into direct tensile or bending loads. However, in service load paths are much more complex. The actual stress at a weld is also difficult to determine but, through FE modelling, structural, nominal and even notch stresses can be established and used to predict fatigue performance. When using FEA to model the effects of welded joints, the ways in which welds and failure modes, etc are represented, depends on the method and software employed. In the previous chapter the requirements for a fatigue analysis were discussed: material data; loading history; the geometry stress analysis, Figure 26. For a weld fatigue analysis the critical characteristic is how to define and calculate an appropriate parameter for the fatigue strength. Before discussing how to calculate a weld fatigue damage parameter, it is important to consider the requirements of a FE weld fatigue analysis.

There are many challenges associated with establishing a reliable FE weld fatigue assessment method for welded components. To warrant the investment and time commitment, the life prediction should satisfy certain criteria. In essence, a weld fatigue analysis should be quick but also efficient and accurate.

In general, a finite element model with a coarse mesh presents limitations. Principally, the mesh is not fine enough to represent the component geometry adequately. With a finer mesh, greater accuracy in results should be achieved. However, the increased number of equations requires greater computing resources and involves longer solution times.

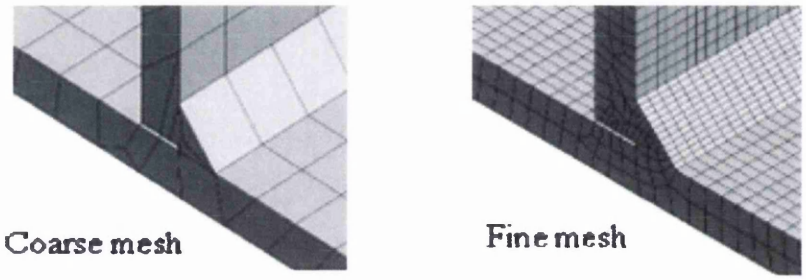

Figure 31: Weld representation - Coarse vs. fine mesh

At a crack initiation site such as a weld toe, an FE stress analysis requires a very fine mesh around the toe to predict accurately the stress. However, a notch effect can create misleading stress values due to the stress singularity. The finer mesh produces higher levels of stress. The notch tends to push the maximum stress towards infinity and will never fully converge. In essence, a different size mesh will calculate a different stress value. For a weld fatigue analysis to be reliable, the chosen method should give consistent results regardless of the mesh size and density and also the type of mesh element used and solution parameters employed.

For a reliable durability assessment to be consistent and applicable to a wide range of structures, the method must be geometry independent. For a nominal stress-life curve, the weld fatigue strength is geometry dependent. This poses a problem for a weld fatigue analysis as it is not practical to have numerous material data curves. In order to remove the geometry dependency an alternative damage parameter must be devised for the y-axis of the S-N curve. This parameter ought to correlate and collapse all of the data onto one master curve. Thus, the various coupon geometries such as T-joints, butt welds or lap joints should fit onto one curve. This is not possible if the defined parameter is geometry dependent.

2.3.4 Weld fatigue assessment methods

For the durability assessment to be reliable it should meet the criteria discussed previously; be fast, accurate and efficient. How well these criteria are met is dependent on the approach taken and fatigue damage parameter chosen. There are many methods that have been developed to calculate a weld fatigue parameter and these fall into one of the following approaches:

Nominal stress;
Structural stress;
Notch stress;
Linear elastic fracture mechanics.

Each approach uses different calculation techniques and damage parameters to obtain fatigue life predictions. The accuracy of the life predictions is often a product of the effort put into the model. As the accuracy of the life predictions increases so does the effort, complexity, and, ultimately, the time and costs.

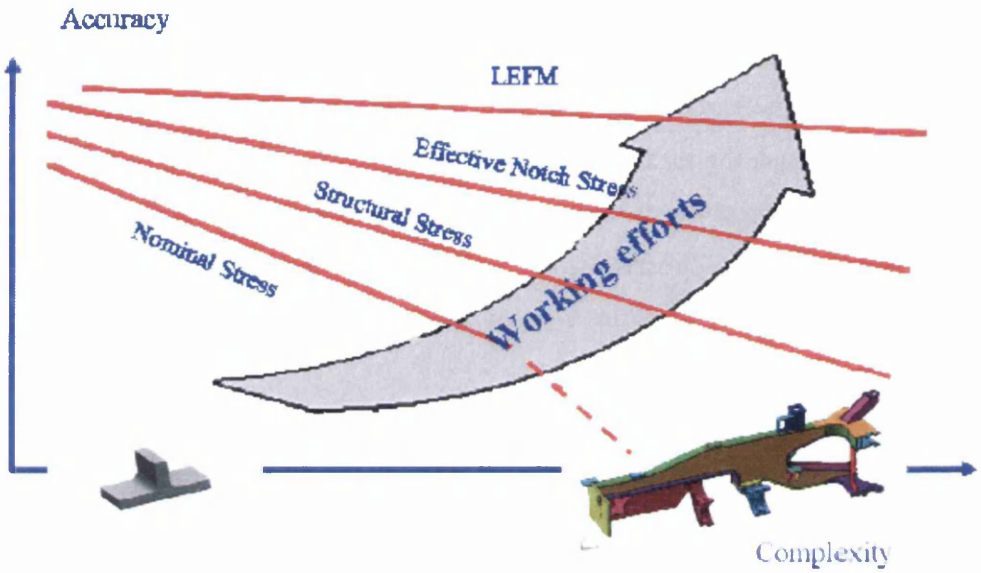

Figure 32: Accuracy vs. Complexity and effort required in a fatigue analysis [24]

The fatigue damage parameters differ for each approach. The definition of each stress parameter is defined in Figure 33.

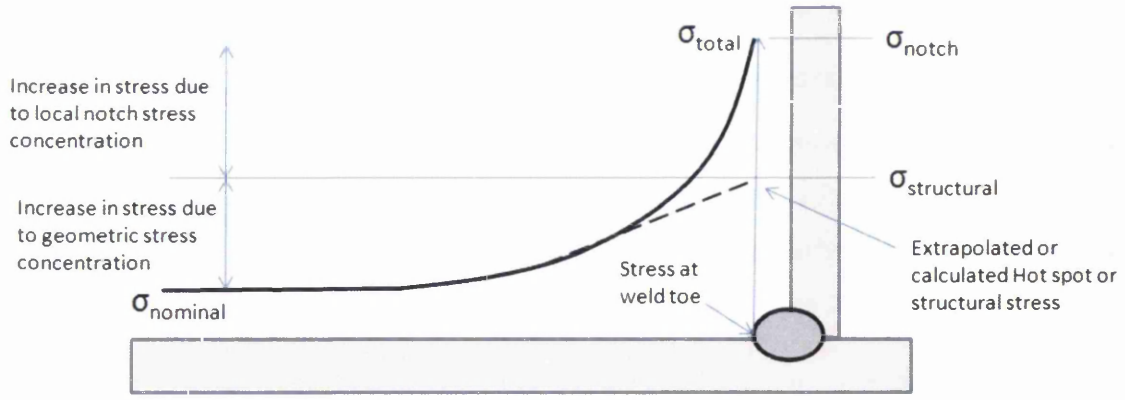

Figure 33: Weld fatigue damage parameters

The nominal stress ($\Delta\sigma_{nom}$) approach is a widely used method using S-N curves and the classification of welded joints. Traditionally, it formed the basis of the British Standard fatigue assessment codes [25]. Each welded part of a structure will be placed into a category depending on the loading mode, geometry, stress concentrations and more importantly, the engineers experience and judgement. The fatigue life is based on the nominal stress measured from a strain gauge, as shown in Figure 33, local to the welded joint. The nominal stress range is correlated to the fatigue life of the S-N data relevant to that category of weld. The IIW weld classification recommendations [16] and the Norwegian structural design code [26]

have been published more recently using the $\Delta\sigma_{nom}$. Modifications to the traditional nominal stress approach have been developed over time to account for various factors previously overlooked. Factors that affect fatigue life performance such as mean stresses and thickness effects, as previously discussed, are considered in order to achieve improved fatigue life estimations. Other research work [27] questions the use of test-piece developed S-N curves for the fatigue life estimation of welded structures. Due to the differences of material behaviour between laboratory specimens and a welded structure in service, only the crack initiation fatigue life can be represented by S-N curves. These modified 'crack initiation S-N curves' are based on local conditions at the weld. It is then suggested that subsequent crack propagation should be analysed individually considering the overall structure and loads experienced. The nominal stress approach is very much a practical application and holds all the costly and time-consuming implications in relation to the building and testing of a prototype component as discussed earlier.

The structural stress (σ_s) approach (or 'geometric' or 'hot-spot' stress) calculates the stress at the weld failure (i.e. weld toe), taking into account the stress due to the geometric stress concentration but not the effect of the local weld notch geometry (non-linear peak stress). The stress at the weld toe is a derived value representing the maximum stress and stress increase due to the structural geometry. Stress values are measured at certain distances away from the weld, allowing the hot-spot stress concentration factors to be calculated through extrapolation. The calculated structural stresses are then analysed against generated test data in the form of S-N curves and the fatigue performance is determined.

The method was originally developed for the assessment of offshore tubular joints. Various proposals exist for the extrapolation of the hot-spot stress [28] and more recently IIW recommendations have published a general international consensus [29] on its application. Despite the hot-spot stress being essentially a fictitious value, Niemi [30] defined the stress in plate structures at the weld toe to be the sum of the membrane and bending stress, see Figure 34.

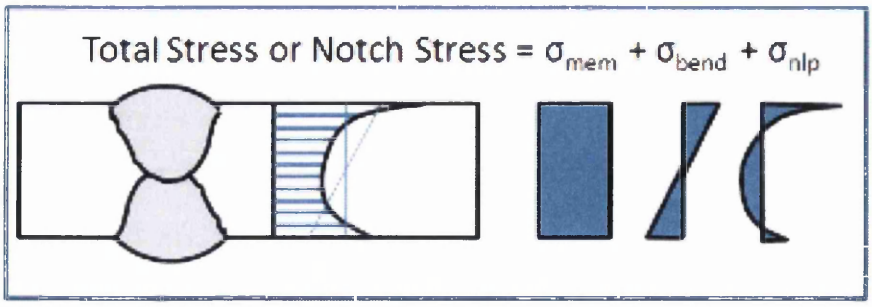

Figure 34: Components of total stress –membrane, bending and non-linear peak

The approach is greatly dependent on the mesh size in the FE analysis. The approach was further developed by Dong [31] using the derived membrane and bending stress and calculating the structural stress through FE nodal forces and moments. The technique proposes to be mesh insensitive using simple coarse elements.

Material performance data is required for welded joint specimens. Fatigue tests must be carried out on various weld geometries in order to generate the necessary S-N curves. The geometries of the welded joints are then modelled and analysed. FEA models highlight the stress-strain levels and stress concentration areas at the critical failure locations. Information is required on the loading modes and stress levels that are typically experienced on the structures in-service. Once all three sets of information and data have been gathered, the FE fatigue analysis of the weld structure can be run. The results give a prediction of the fatigue performance of the structure and of critical or likely failure locations.

The structural stress method has advantages over nominal stress methods as a result of its numerical pedigree. It does not require a prototype design to obtain a fatigue life estimate. The analysis can be completed early on in the design stage, highlighting any fatigue prone critical areas that can be modified before a prototype is made. Resources include only the computing power and operating labour. It is significantly less costly than manufacturing and altering a prototype. Despite satisfying the criteria of fast, accurate and efficient criteria, the method does historically have a limited number of applications to support its adoption. Extensive research is now taking place using the theory and has even met with some success [32, 33]. The method proposed by Dong [31] has gained ground since being accepted as a United States Patent [34]. It is also being included in a commercial software package, and the theory has more recently been acknowledged in the ASME Section VIII, Div.2 Boiler and Pressure Vessel Code [35].

Due to the various methods available for calculating structural or hot spot stress, a number of recent research papers have focused on a comparison with other techniques. Work completed by Poutiainen et al [36], Wei [37] and Fricke et al [38] carried out studies to calculate and apply different variants of the structural/hot-spot stress technique. All papers review the methods for calculating stresses for a number of different weld details, but lack the next step of achieving fatigue life predictions for real welded components.

Another popular approach involves the notch stress. The notch stress in a welded joint is defined as the total stress at the root of a notch. The stress concentration caused by the notch is assigned an effective notch root radius. A universal notch radius is used to describe the fusion zone of the weld and parent metal (radius = 1mm for thick metals and = 0.3mm for thin metals).

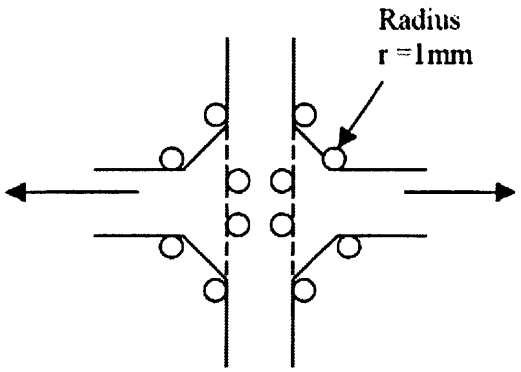

Figure 35 - Effective notch stress of a stress concentration

Notch effects caused by a welded joint such as a toe undercut or root are introduced and replaced by an effective notch radius, Figure 35. It is a fictitious parameter and so cannot be measured on specimens. The fatigue life prediction is based on formulae and an FE analysis of the notch stress which is correlated with an S-N curve. Material properties are back calculated from test data, taking into consideration the mean loads and scatter. FEA is then used to calculate the critical location stresses and the stress concentration factor, K_T, defined. From the fatigue tests of the components, the endurance limit range is determined and the weld material endurance limit range is derived by back calculation.

$$K_{T,r=1mm}\ \Delta S_E = \Delta^e \sigma\ E \qquad \text{Eq 2.1}$$

Where

K_t =stress concentration

ΔS_E= weld material endurance limit range

$\Delta^e\sigma E$ = endurance limit range.

The notch stress approach has the advantage that it considers the weld geometry, but requires a detailed FE model. It has much higher accuracy for complex structures but is only effective if the critical locations are known. The effective notch stress cannot actually be measured experimentally and it does need a much higher mesh density, increasing solution time and resources.

A linear elastic fracture mechanics approach can be employed to predict the crack propagation life. It describes the behaviour of the crack tip at the weld. Given that the weld will almost definitely contain a crack initiation site in the form of a weld flaw, this approach analyses the rate at which a crack will propagate causing complete failure of a component. As the generation of a flaw is unavoidable, the engineer must design against or try to control the propagation of a crack. Tests are required to determine the fracture resistance of a material and the assessment of a structure. The notch stress intensity factor K, describes the fatigue propagation behaviour of the crack tip depending on its shape and orientation. Linear elastic fracture mechanics (LEFM) is an analysis developed from early work completed by Griffith [39] where he described a crack in terms of an energy balance between stored energy and crack surface energy. Propagation is due to stored energy being released. This work was originally based on brittle materials until developments were made [40] to allow analysis for ductile metals. The stress intensity factor, K, analyses the stress at the crack tip caused by a remote applied stress, σ, and depends on the size of the crack, a (= half-length of the crack). In its basic form:

$$K = \sigma\,(\pi a)^{1/2} \qquad \textbf{Eq 2.2}$$

Further modifications of the equation are used depending on the loading and orientation of a crack. In fatigue, the crack growth rate, da/dN is related to the cyclic stress intensity range, ΔK. The method leads to the Paris crack growth law [41]:

$$da/dN = C(\Delta K)^n \qquad \textbf{Eq 2.3}$$

Formulae for K are available in terms of local geometry, crack shape and position and particular modes of cracking (opening, sliding or tearing). The prediction of fatigue life involves integrating growth rate equations such as equation 2.3, between the initial and final crack sizes for a given stress range.

Applications of LEFM are largely found in the fatigue assessment of many aerospace components. Structural parts undergo routine inspections at set intervals to detect cracks. The LEFM will have to predict the propagation of a crack before its next inspection. Parts are removed from service once a crack reaches a critical length.

2.4 Conclusions of Literature Review

Fatigue plays a crucial role in the design and service life of all engineering components. If it is not adequately designed against, it can cause early failures resulting in great financial and possibly even catastrophic loss. In this literature review, various aspects of welded components, weld fatigue performance, design process and testing methods have been discussed. Furthermore, the detrimental impact of various stress concentrations that affect the performance of welded joints in yellow goods equipment have been highlighted. There are various methods available when designing against the fatigue of welded goods. The advantages and disadvantages associated with current weld classification methods employing a nominal stress approach have been discussed. Alternative approaches have been reviewed, focusing on the techniques that involve a numerical Finite Element based procedure. This FE approach offers many advantages over traditional nominal stress methods. However, it is still under evaluation and yet to be established. This leaves scope for this project on 'Reliable Durability Assessment of Welded Yellow Goods Equipment'.

Main conclusions:

- Fatigue in general is a very challenging failure mode to design against, with many design criteria and life prediction models available.
- Yellow goods equipment are demanding structures enduring constantly changing loads and extensions.
- Welded joints have significantly reduced fatigue strength due to stress concentrations created by weld profile and welding induced residual stresses.
- Residual stresses (local and long-range) are very important in welded coupon joints. They must be handled with care in applying coupon data for designing and lifing welded structures.
- Other factors such as discontinuities and thickness effects also affect fatigue performance.
- The durability of a yellow goods structure relies on the overall durability of the welded joints.

- Various life prediction methods are available but nominal stress and weld classification methods are commonly used.
- There are concerns with BS7608 and 'nominal stress' approaches' including the facts that the design-test-redesign process creates uncertainty of time-to-market for the product and it is expensive to create numerous prototypes.
- There are concerns with an FE-based approach used for the life prediction of yellow goods which include accuracy vs. mesh size and density, geometry dependency, and mesh sensitivity.
- The uncertainty of an FE-based weld fatigue life prediction method creates great scope for this project to establish a reliable FE-based Durability procedure.

2.5 Program Objectives

When using an iterative 'design-test-redesign' and build method of product development, it can be beneficial to incorporate some degree of Computer Aided Engineering into the approach. Weld fatigue is one of the potential areas and the overall objective is to establish a reliable finite element (FE) based durability assessment procedure for welded yellow-goods vehicle structures.

The aims of the project are:

- Generate weld fatigue data (S-N curves) through testing small welded coupons of various geometries and loading modes.
- Complete FE structural stress and fatigue simulations of coupons to verify fatigue data.
- Complete FE stress and fatigue simulations of selected yellow goods equipment.
- Verify fatigue predictions by fatigue rig testing of selected yellow goods components.
- Evaluate the techniques used for prediction quality and produce best practice guidelines for FE weld fatigue life prediction.

Making use of CAE tools and implementing an FE-based weld fatigue life prediction method will supplement current life prediction methods used to potentially achieve right-first-time designs. They will minimise the emphasis on, and requirements for costly prototype builds.

There are certain issues to overcome in order to use an FE-based method and these will govern the effectiveness of the approach and establish if an FE weld fatigue package can be used at all. The main issue is how the stress is calculated at a welded geometry. It is very

difficult to model and calculate the actual 'real' stress at a weld. It is also just as difficult to physically measure the real stress at the weld. For this reason, current fatigue life prediction methods measure or calculate the nominal stress away from the weld, then relate that stress range to a set of predefined curves. In order to adopt an accurate and efficient FE-based method this project had to adopt a different method of calculating the weld stress using an alternative damage parameter. How well this damage parameter can be used can only be found out through the research proposed.

Undoubtedly, the project aims and objectives could potentially reduce the time-to-market of products and significantly lower design-development costs.

3. Experimental Methods

In order to complete an FE fatigue analysis and obtain accurate predictions, material data has to be input into the FE-model, containing information on the fatigue strength properties. The material data is generated by cyclically loading material or welded joints at a range of stress levels until failure occurs. For the case of welded joints, various configurations are made by welding small plates of sheet steel together to make a 'coupon'. The joint configuration is essentially a small-scale representation of a similar type of weld geometry from a larger structure. This gives an indication of the fatigue performance of that type of weld without incurring the costs of full-scale component fatigue testing.

3.1 Health and Safety

All the testing was carried out according to the site Health & Safety rules, guidelines and appropriate safe operating procedures (SOPs). Personal Protective Equipment (PPE) was supplied and used in the form of safety gloves, goggles and shoes. Safeguards were in place before any testing commenced in order to minimise the risk of harm to personnel and damage to equipment.

3.2. Data generation – coupon testing

3.2.1 Fatigue test equipment

The general fatigue test principles are shown in Figure 36. The stress range is defined as the maximum applied stress minus the minimum applied stress.

$$\Delta\sigma = \sigma_{max} - \sigma_{min} \qquad \textbf{Eq 3.1}$$

The stress ratio R, is the ratio of the minimum stress applied divided by the maximum stress.

$$\mathbf{R} = \sigma_{min} / \sigma_{max} \qquad \textbf{Eq 3.2}$$

Where:

$\Delta\sigma$ = stress range

σ_{max}= maximum stress

σ_{min}= minimum stress

Loading cycles vary, such as fully reversed, R=-1, where the applied tensile stress is equal to that of the compressive stress. When R= 0, the load applied is reversed back to zero stress

(i.e. the stress is only tensile), or R=0.5, where the load reversed is equal to half of that applied.

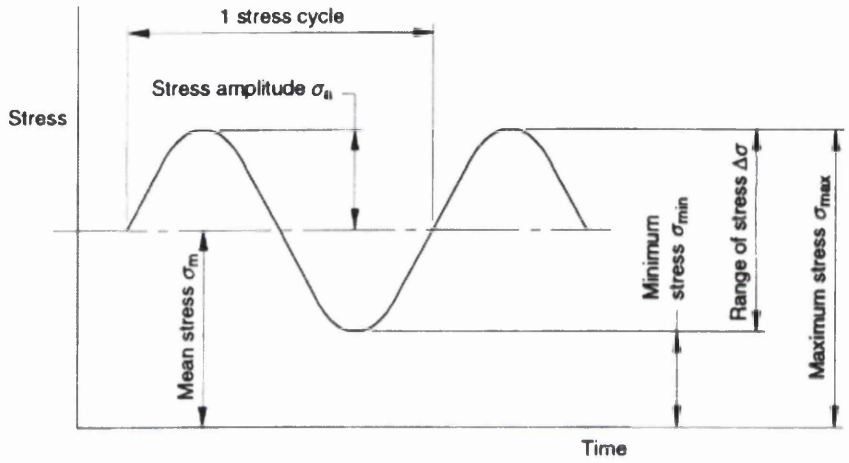

Figure 36: Fatigue test principles

The fatigue test machine used was a Schenck 400kN servo-hydraulic twin-column loading frame with MTS 500kN hydraulic grips, as shown in Figure 37. The loading frame operates via a Kelsey Instruments K7500 servo controller.

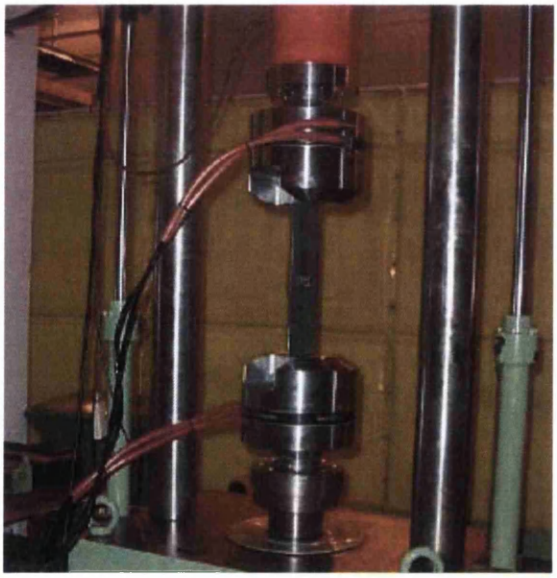

Figure 37: Schenck 400kN Servo-hydraulic loading frame

All of the equipment was in good working order and calibrated with all the relevant certificates prior to the testing commencing. As the hydraulic grips are a new addition to the loading frame, a Health & Safety risk assessment (RA) was completed and SOP proposed.

3.2.2 Test parameters

There are no set rules for the fatigue testing of welded coupons, specimen sizes or geometries. The coupon fatigue tests were run following the guidelines set in British Standard BS3518 for constant amplitude fatigue testing of metallic materials [9].

The load controlled fatigue tests were all run with constant-amplitude sine wave at varying stress ratios. The tests were completed in ambient air temperature and at the maximum possible operating frequency. Tests were completed at a frequency of 5-10 Hertz, depending on the overall stiffness of the coupon. Tests completed have shown that a frequency of 12 Hertz (Hz) is easily achievable without any large signal errors or compromise to the test conditions.

In order to achieve repeatability and consistency in the test methods, the same set-up procedure is used on all tests. The test coupon is placed in the hydraulic grips at 90 degrees to the test bed using a calibrated inclinometer and clamped up. The strain gauge readings are recorded with the test piece in-situ and no loading applied. The test loads are then entered into the servo controller and the test is begun.

Each test was ended after complete separation and 'through' failure of the joint had occurred. The number of cycles was recorded. Data logging equipment was used to record the servo-controller feedback loading and displacement for the peak and trough of each sine wave cycle. Calculating the loading range divided by the displacement defines the stiffness parameter, K of the test coupon. As a crack propagates through the test coupon the stiffness decreases as shown in Figure 38. Plotting the stiffness against the cycles to failure displays the stiffness drop over the life of the test. Upon analysis of the results, a defined percentage stiffness drop (10 or 20%) can be set as the effective fatigue life.

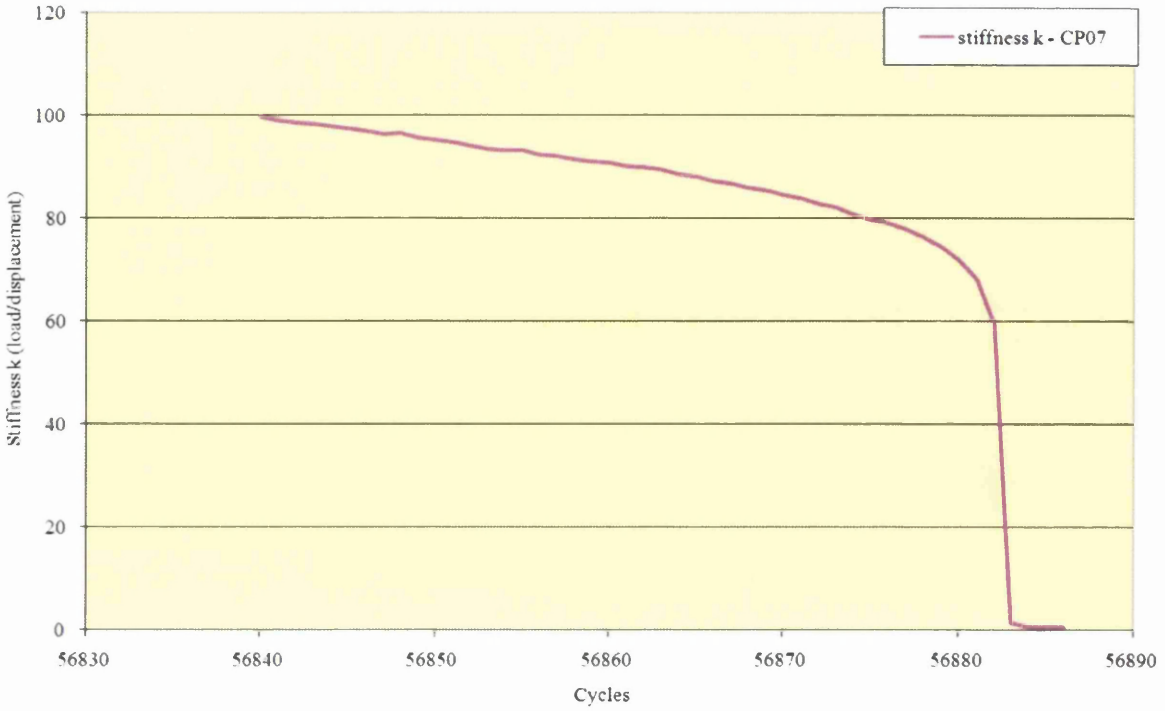

Figure 38: CP07- Example of coupon stiffness drop over cycles to failure

3.2.3 Material specification

The material used was 8mm or 12mm thick S355 carbon-manganese structural steel (EN10025:1993 grade). This hot-rolled product has good strength and welding properties and is widely used by yellow goods manufacturers. The mechanical properties and chemical composition are listed in Table 1 and Table 2.

Mechanical properties – S355					
	Upper yield strength (Reh)	Lower yield strength (Rel)	0.2% proof (Rp0.2)	Tensile (Rm)	% Elongation
Specification	355MPa (min)	-	-	470-630MPa	20% (min)
Measured	437MPa	420MPa	429MPa	522MPa	27

Table 1: S355 mechanical properties

Chemical properties – S355 (% composition)						
	Carbon C	Manganese Mn	Phosphorous P	Sulphur S	Silicon Si	Nitrogen N
Specification (Maximum)	0.240	1.600	0.035	0.035	0.550	0.012
Measured	0.131	1.050	0.012	0.019	0.007	0.003

Table 2: S355 chemical composition

Tensile test samples of the material yielded the true stress-true strain curve shown in Figure 39.

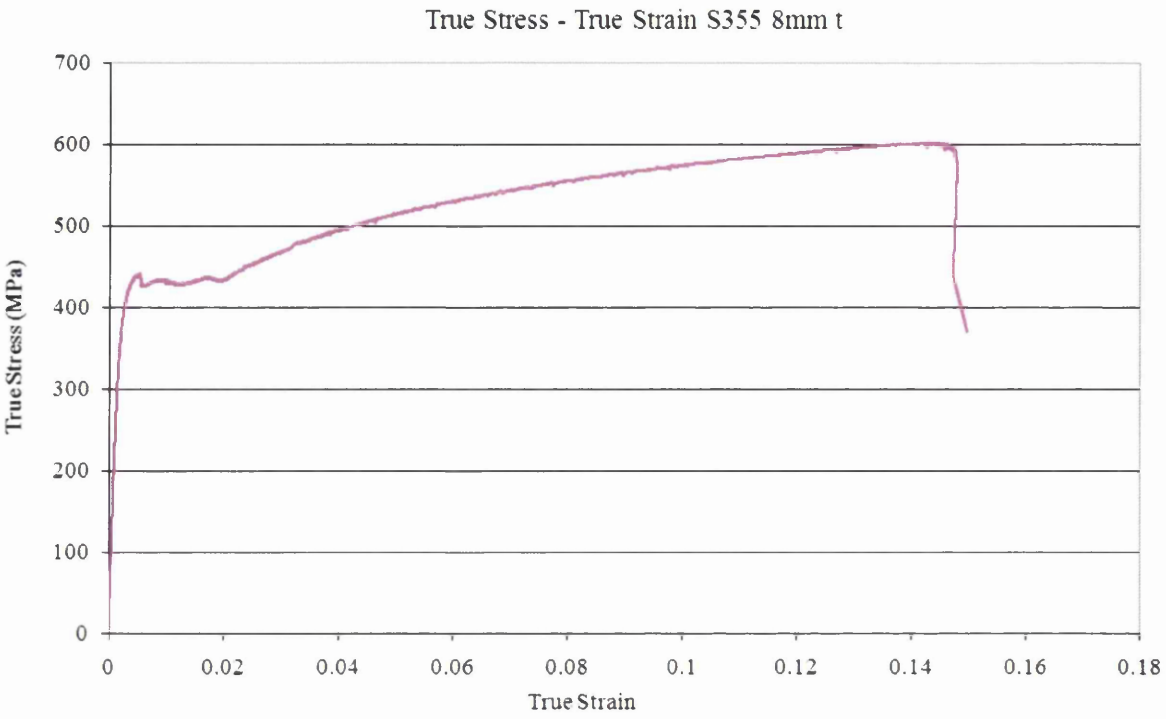

Figure 39: True Stress-Strain curve - S355 8mm thick hot-rolled structural steel

All the test coupons were welded with a semi-automatic MAG welding machine using an Argon/CO_2 (88/12%) gas mix. The welding parameters were kept consistent with those used for welding yellow goods components shown in Table 3.

Welding Parameters			
Current	Voltage	Travel speed	Gas feed
300 amps	30V	11metres/min	15p.p.m.

Table 3: Welding parameters - test coupons -8mm thick material

3.2.4 Tensile load Tee-joint

The coupon geometries were chosen to best represent popular and typical joint configurations found on yellow goods equipment. One of the most popular configurations is the tee joint single-sided fillet weld. Two plates align together to form a 'tee' shape as detailed in Figure 40. The single-side weld is common practice as in many configurations access to the underside of the plate is restricted.

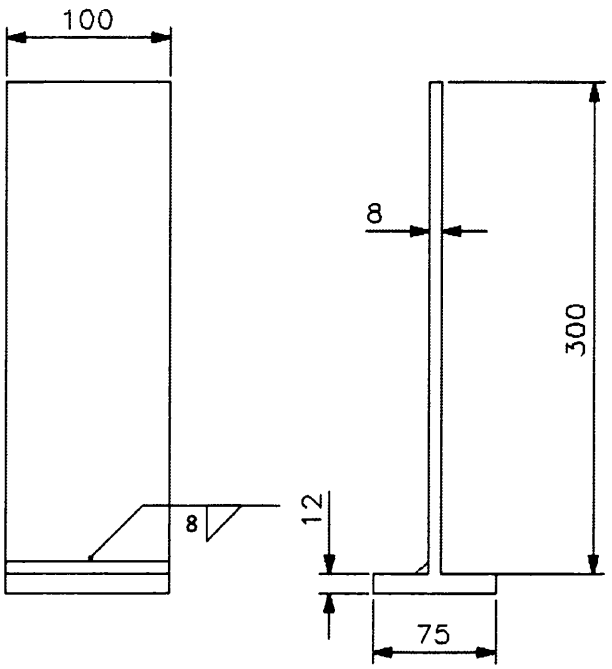

Figure 40: Tee joint single sided fillet weld - tensile load

The coupons were fabricated (with an 8mm partial penetration fillet weld) from 1m lengths of steel and sectioned on a horizontal flat bed band saw into 9 x 100mm wide coupons, removing the weld start/stop (50mm off each end). Due to the manufacturing process, the finished coupons were produced with varying levels of distortion. Ideally the upright plate would be perpendicular to the base plate. However, when the weld seam is cooling and contracting, the upright plate will become offset from 90 degrees. The upright can be tack welded into a pre-offset angle i.e. at -5 degrees so when the weld cools, the upright pulls over and is perpendicular, but this is very difficult to control accurately. The coupons tested had a range of distortion levels from around 1 degree to 5 degrees. In total 20 test coupons were made.

In order to account for the distortion created in the coupons during the manufacturing process, the fatigue test used two coupons in a back-to-back configuration. This ensured the loading path would be purely tensile accounting for the misalignment and bending of the coupon. Failure was defined as complete separation of the joint.

Two brace straps and M16 cap screws were clamped over each flange of the base and hand-tightened ensuring the correct alignment of the uprights, shown in Figure 41. Next the

required pre-load torque was applied to the four bolts, tightening in increments and sequentially to ensure an even clamping force.

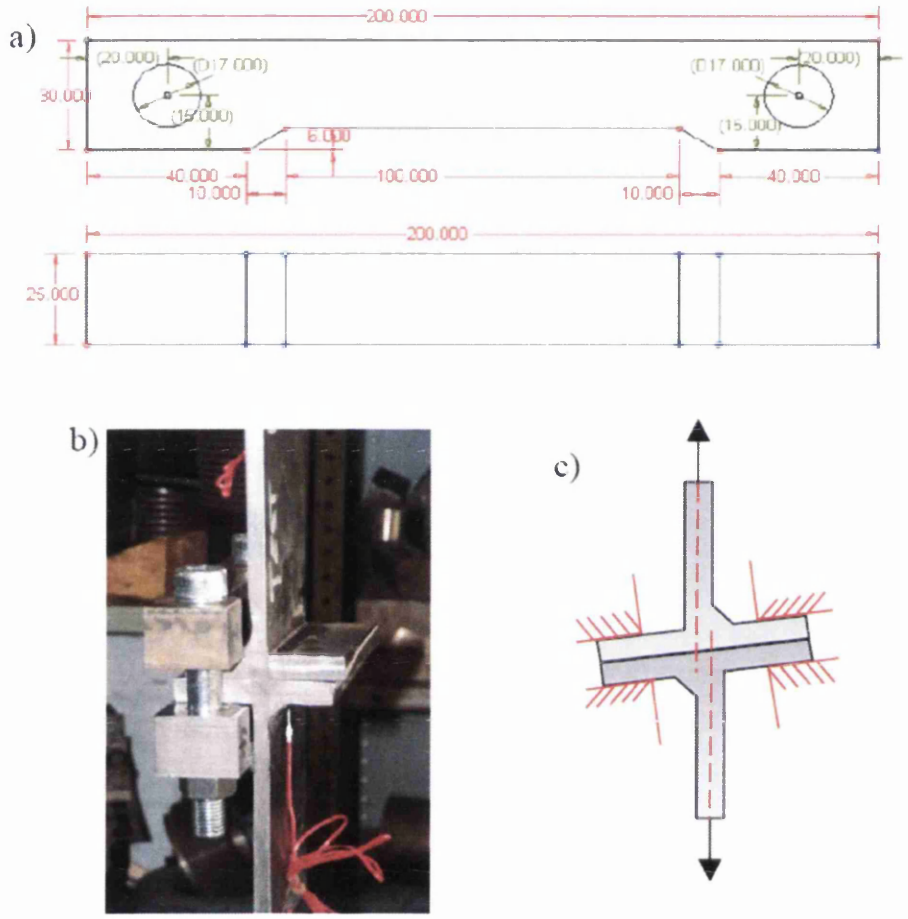

Figure 41: Tee testing - a) Strap dimensions, b) Strap and coupon setup and c) Coupon mis-alignment

This configuration removes any misalignment keeping the loading path tensile and reducing any possible bending moment. The back-to-back coupons were then placed in the test machine and the upper and lower jaws clamped.

3.2.5 Bending load Tee-joint

The bending load tee-joint coupon is similar to the previous geometry, although the test configuration was modified to change the loading mode and crack location. Thus, while the first tee coupon experienced a predominantly tensile load, in this case a bending load was required. The coupon geometry is detailed below in Figure 42.

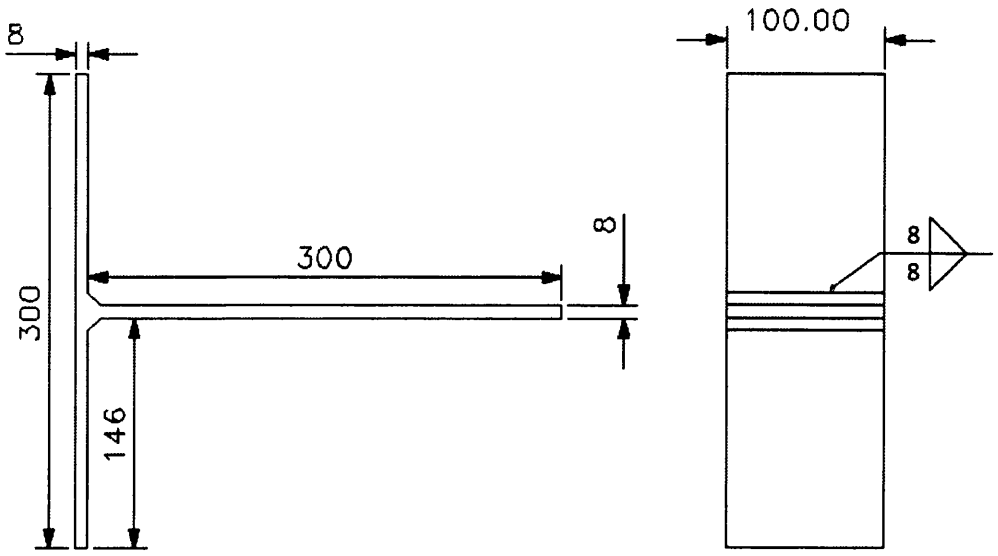

Figure 42: Tee-joint double sided fillet weld - bending load

The coupons were fabricated from 120mm by 300mm laser cut steel plate and welded individually. Two 8mm partial penetration fillet welds were created each side of the upright. Due to the manufacturing process and heat input, the base plate of the coupon was slightly distorted. Each side of the base rose by an angle of ~0.5 degrees into the upright as the weld runs cooled. The 120mm wide coupons were then placed in a milling machine and 10mm of material removed from each side. This ensured consistent widths and parallel edges. The weld start/stops were removed. To prevent fatigue cracking at the edge of the coupon, the edges of the weld toe notches were prepared with an abrasive wheel. The notch was ground using a coarse (60 grit) and fine (240 grit) grinding disc, leaving any grinding marks parallel with the loading path. 12 test coupons were made in total.

Figure 43: Tee-joint bending load test configuration

The base of the tee-joint was clamped to the loading frame actuator with a brace-to-brace distance of 100mm, Figure 43. The upright was clamped in the hydraulic grips. This test configuration created a high bending moment and promoted failure along the bottom weld toe.

3.2.6 Load carrying Lap joint

The load bearing lap joint geometry consists of two plates, 337.5mm by 100mm wide, with an overlap of 75mm. An 8mm leg length fillet weld is laid on each side. The weld detail, Figure 44 is typical of the type of attachment found in welded yellow goods structures.

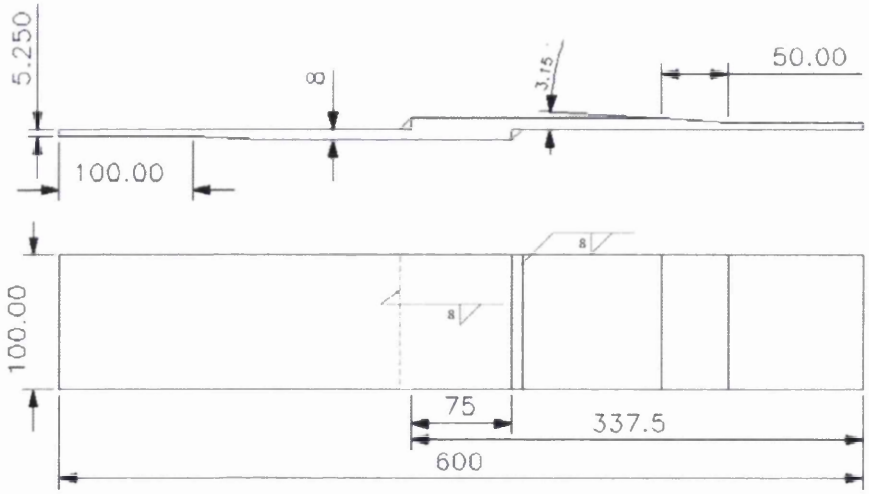

Figure 44: Load bearing lap joint

The material for the coupon test pieces was first laser cut to 120mm widths. The coupons were fabricated individually and the two welding runs created. Each coupon was placed in the milling machine and the material removed evenly leaving a 100mm wide coupon. This ensured consistent widths and parallel edges for each sample. The weld start/stops were removed. The thickness capacity of the hydraulic test grips is 10.9mm (max material thickness). Due to the double plates on the lap joint (total thickness 16mm) the clamp area of the coupon required a milling machine operation to remove 3mm from each outer edge. A packing block of 5mm was inserted in the grip along with the coupon to ensure an aligned loading path in the test frame.

To prevent fatigue cracking at the edge of the coupon due to any edge effects, the edges of the weld toe notches were prepared with an abrasive wheel. The notch was ground with a coarse (60 grit) and fine (240 grit) grinding disc leaving any grinding marks parallel with the loading path. 16 test coupons were made in total.

3.2.7 Non-load carrying transverse cover plate

The non-load carrying cover plate geometry consists of a main plate strip, 600mm by 100mm wide, and a cover plate attachment, 100mm in length, with a double 8mm leg fillet weld, Figure 45. The weld detail is typical of fillet weld attachments found in welded yellow goods components.

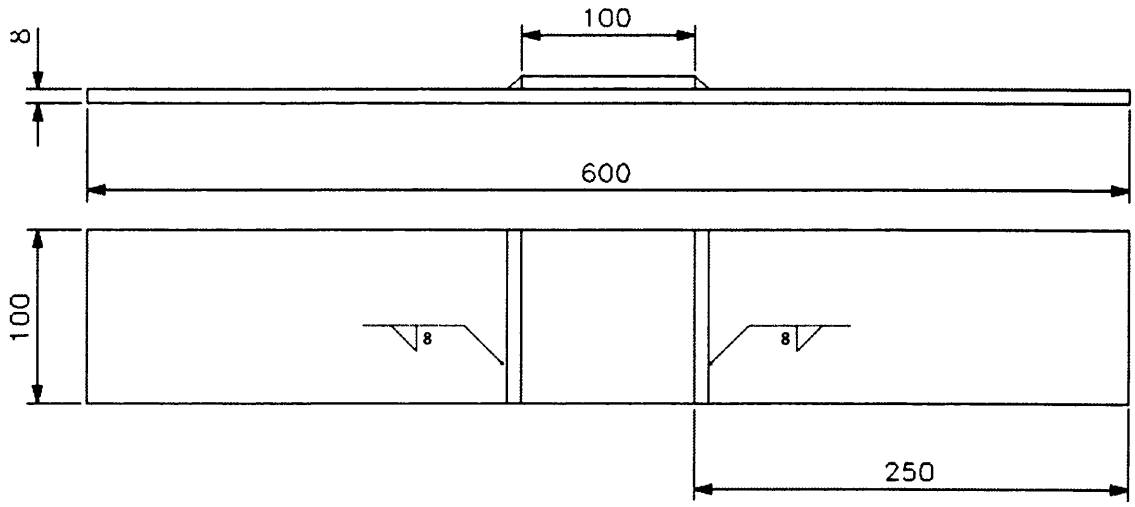

Figure 45: Non-load carrying cover plate coupon

The coupon geometry was initially welded from a 1000mm long test-piece. The attachment was tack welded in place and the two fillet weld runs laid down. The 1000mm length was

sectioned into individual widths approx 120mm wide and each had material removed down to 100mm wide coupons on the milling machine. Due to the manufacturing process and heat input, the base plate of the coupon was slightly distorted. Each side of the base rose by an angle of ~1.5 degrees towards the cover plate side as the weld runs cooled.

To prevent fatigue cracking at the edge of the coupon due to any edge effects, the edges of the weld toe notches were prepared with an abrasive wheel. The notch was ground with a coarse (60 grit) and fine (240 grit) grinding disc leaving any grinding marks parallel with the loading path. 16 test coupons were made in total.

3.2.8 Non-load carrying horizontal attachment

The non-load carrying horizontal attachment coupon consists of one main back plate, 6000mm by 100mm wide, and a single transverse attachment 100mm by 100mm. The attachment is fabricated with an 8mm leg length fillet weld, some with a single weld and others with a weld run on both sides of the plate, Figure 46. A second coupon was created, 600mm by 100mm but with a double attachment (60mm long) and four weld runs in total, Figure 47. These weld details are typical of non-load carrying horizontal welded attachments in yellow goods structures.

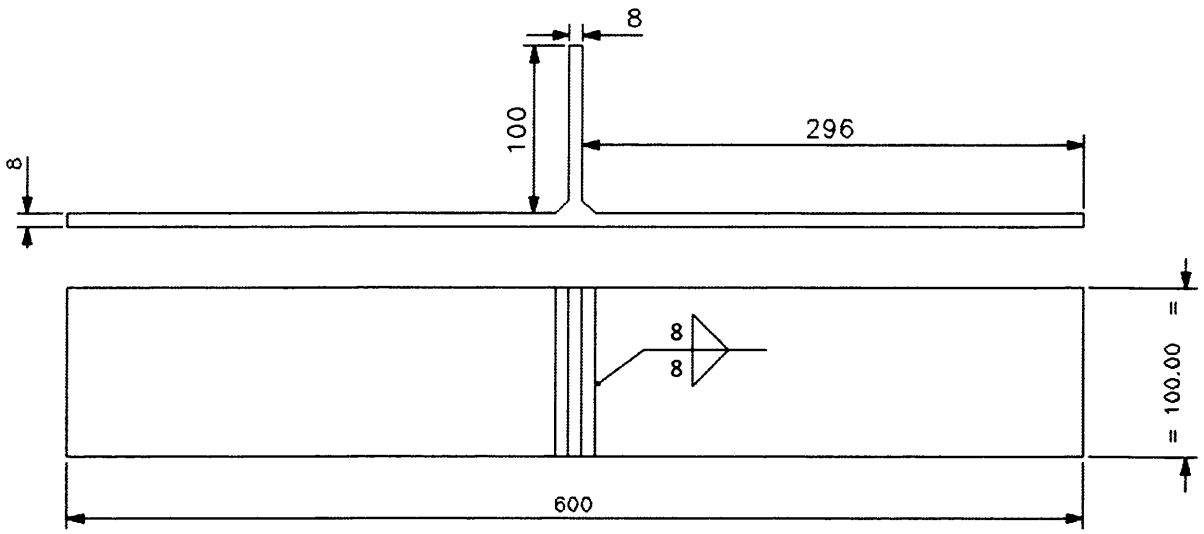

Figure 46: Single sided non-load carrying attachment

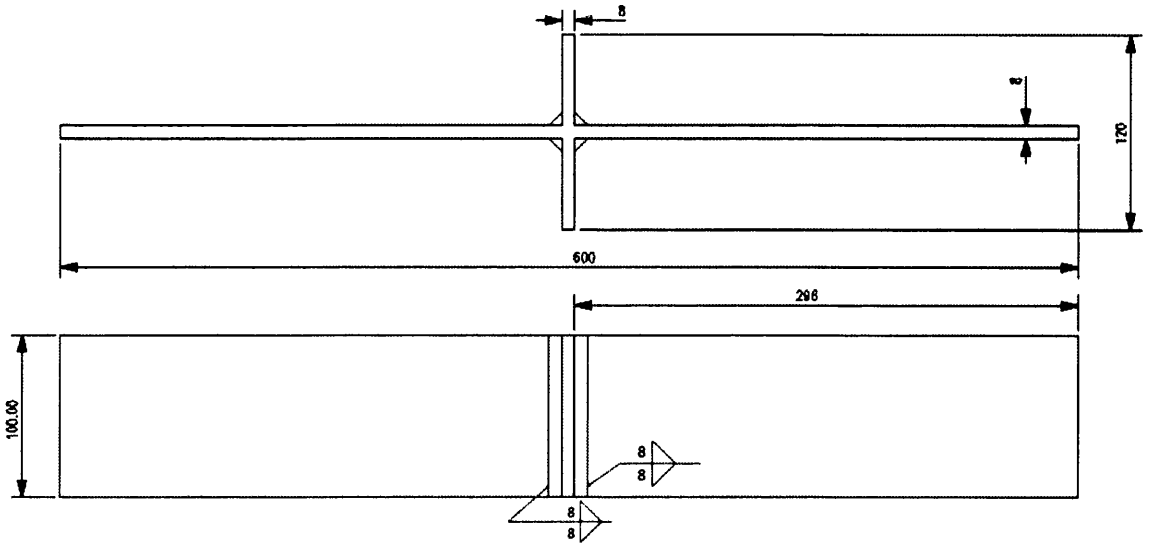

Figure 47: Double sided non-load carrying attachment

The material for the coupons was first laser cut to 120mm widths. The welding operation fabricated each coupon individually. The milling machine operation removed material evenly leaving a 100mm wide coupon with consistent and parallel edges. Due to the joint configuration and welding process, the single-side attachment coupons were slightly distorted. Each side of the base became elevated by an angle of ~2° into the attachment plate as the weld runs cooled. The double-sided coupons were welded sequentially and opposite to the previous weld run to minimise the distortion. Each weld contracted equally with little distortion. 4 single-sided welded coupons and 8 double-sided welded coupons were made.

To prevent fatigue cracking at the edge of the coupon due to edge effects, the edges of the weld toe notches were prepared with an abrasive wheel. The notch was finished with a coarse (60 grit) and fine (240 grit) grinding disc leaving any grinding marks parallel with the loading path. 16 test coupons were made in total.

3.2.9 Load carrying cruciform joint

The load carrying cruciform joint consists of two main uprights, 300mm by 100mm wide, welded to a middle single horizontal plate 120mm by 100mm, Figure 48. Two coupon types were fabricated, the first with an 8mm leg length fillet weld, and the second with a 10mm leg length fillet weld.

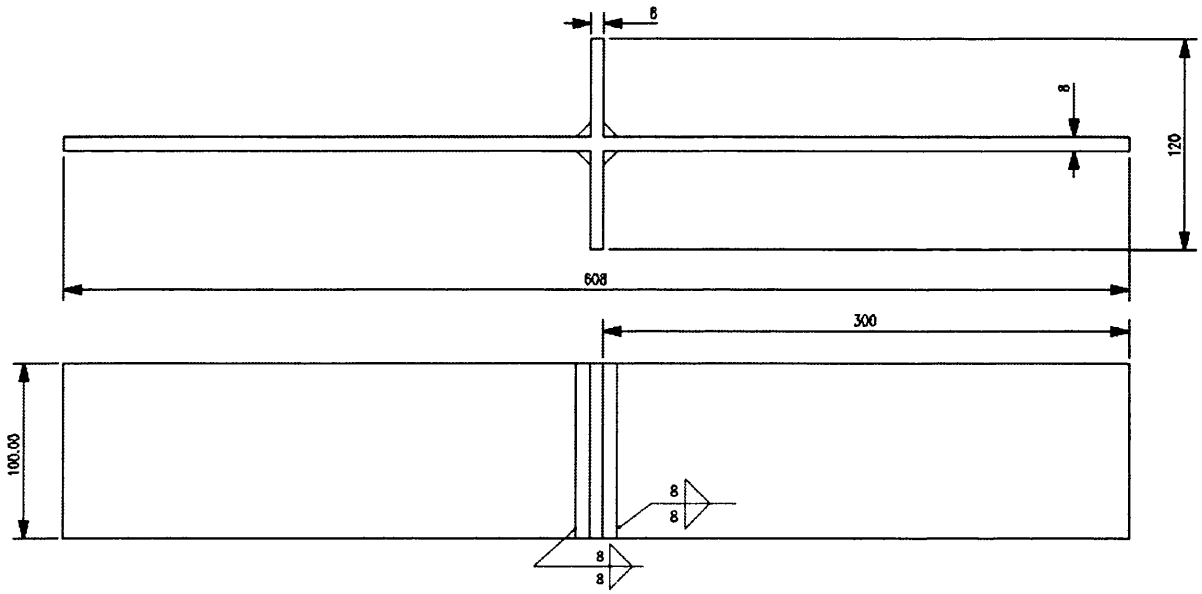

Figure 48: Load carrying cruciform joint

The material for the coupons was first laser cut to 120mm widths. The welding operation fabricated each coupon individually. The milling machine operation removed material evenly leaving a 100mm wide coupon with consistent and parallel edges.

The cruciform coupons were welded sequentially and opposite to the previous weld run in order to minimise the distortion. Each weld run contracted evenly with little distortion. Eight 8mm leg length fillet cruciforms and six 10mm leg length fillet cruciforms were made.

To prevent edge effect fatigue cracking of the coupon, the edge of the weld toe notches was prepared with an abrasive wheel. The notch was ground with a coarse (60 grit) and fine (240 grit) grinding disc leaving any grinding marks parallel with the loading path. 14 test coupons were made in total.

3.3 Welded Test Component - structural testing

The previous section covered the types of geometries used to generate basic weld fatigue data to input into the finite-element model and to facilitate the fatigue durability assessments. The approach is being applied to new applications here, and in order to have confidence in the fatigue predictions they must be validated, as with any kind of finite element modelling.

The optimum validation is against physical testing of the same component under similar boundary conditions. Structural fatigue testing in a laboratory, controlled environment provides a fast and accurate assessment of the integrity of components. In a short length of

time, a large number of known loads and cycles can be applied and failure locations obtained. Potentially, the loading conditions are not fully representative of in-service conditions. However, the ability to precisely control the boundary test conditions provides a vital step towards validating any new methods or approaches. The predictions can be compared against the actual measurements recorded during testing and analysed for quality and accuracy. As the testing equipment moves from permanent loading frames to assembled test fixtures and rigs and larger components, the sources of variability in fatigue results are ever more possible. This requires careful consideration of the actual loadings seen by the component in order to achieve accurate correlations between predicted and measured fatigue lives.

3.3.1 Component design

As an intermediate step between the data generation stage on relatively simple test pieces and fatigue assessments of an actual sub-assembly or component, a test component was used to initially validate the Structural Stress approach. This test component is a simplified component related to a part, but only a small section of the full assembly. The aim is predominantly to validate the assessment method using similar loading conditions, materials and failure modes rather than obtaining fatigue life predictions for an in-service component.

The design of the test component was based to some extent on a section of the 'dipper' which is part of an excavating arm from a Backhoe Loader, Figure 49. The dipper component is attached to the boom arm by a pivot pin and has an excavating bucket at the other end. It plays a vital part in the main excavating operation.

Figure 49: J.C. Bamford Ltd. Backhoe loader - excavator arm at rear of vehicle

The test component, Figure 50, is made from 8mm thick plate pressed into a U-section, 190mm high by 150mm wide and 1000mm long. Along one length of the section there is a mouse-hole semi-circle cut out with a 35mm radius, 240mm along the length. This is to create an unsymmetrical loading path causing a non-uniform stress distribution. The U-section is then welded to a wider and longer 12mm thick base plate (250mm by 1100mm). The weld runs have a 6mm 45 degree chamfer weld preparation. A capping weld is added on top with a weld leg length of 10mm. The weld run stops over the length of the mouse hole and restarts until the end of the U-section.

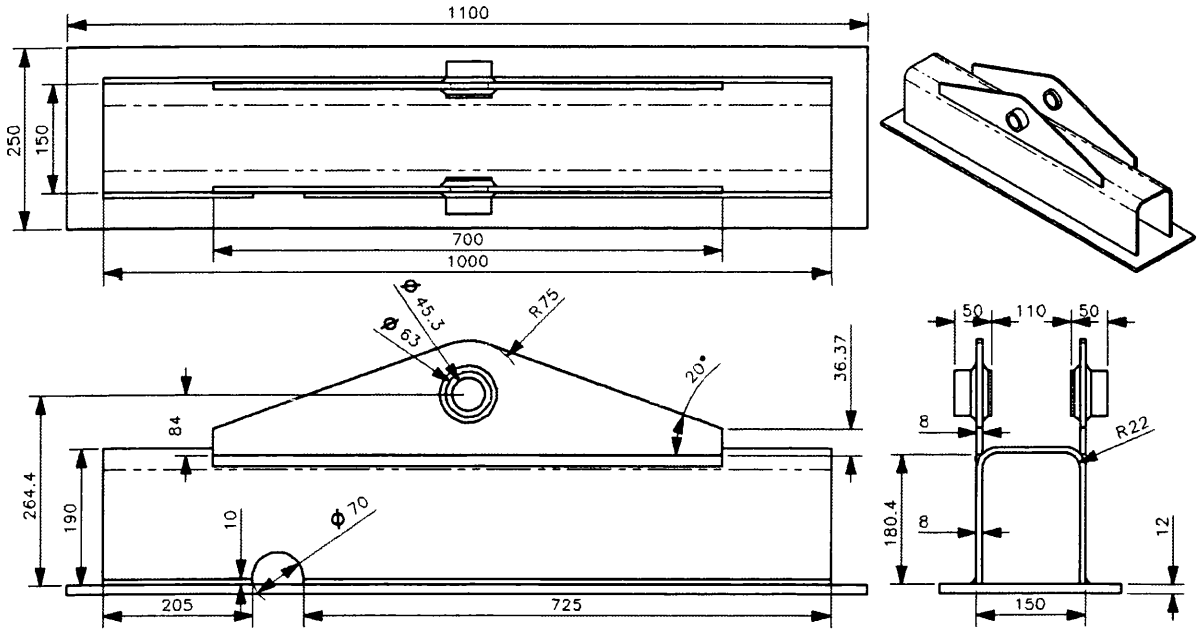

Figure 50: Test component design – mini dipper

Welded along each radius of the U-section pressing, were two attachment plates, 700mm long by 150mm high with a chamfer of 20 degrees on the top edge. A double weld run was used to achieve a full penetration weld at the radius. In the centre of the attachment plate is a 63mm diameter hole with a boss tube 50mm wide (45.3mm dia.) and set into the plate 10mm. The attachment plate was prepared with a 6mm chamfer and 3 weld runs.

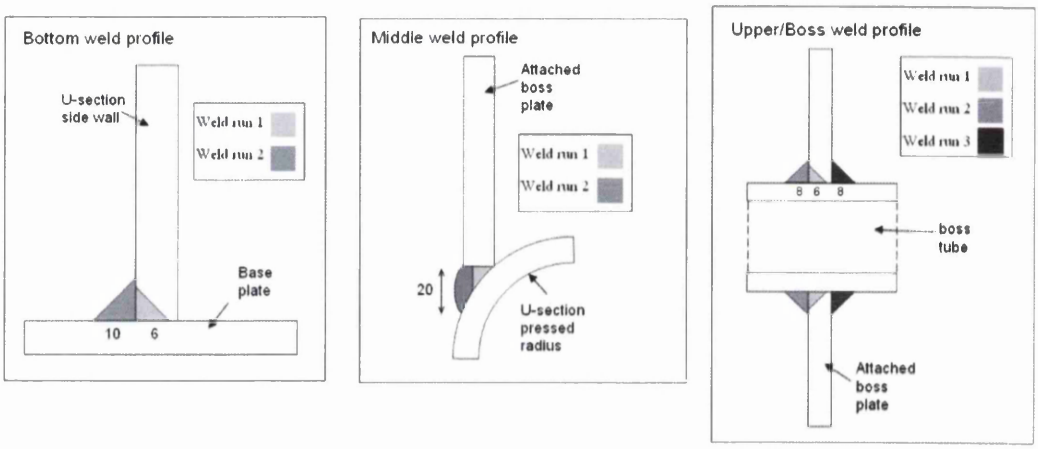

Figure 51: Test component weld run profiles

The weld profiles represent popular joint configurations on actual yellow goods equipment: partial penetration fillet, full penetration and boss and pin weld details, Figure 51. The test components were manufactured using stock material S275 (43A grade) Carbon-Manganese structural steel. All the test coupons were manually MAG welded and gas shielded using an Argon/CO_2 (88/12%) gas mix at a feed of 15p.p.m. The welding used a spray transfer mode with a current of 300 Amps, 30V and a travel speed of 11metres/min. The material and welding practices are typical of those used on yellow goods equipment. The final welded component is shown in Figure 52 of which 4 samples were made for testing.

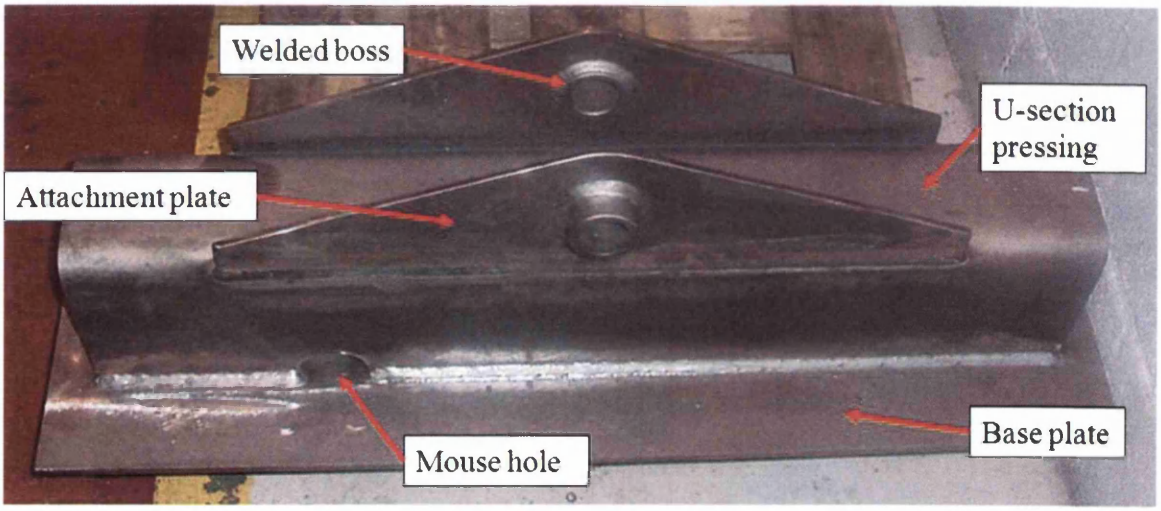

Figure 52:- Fabricated test component

3.3.2 Fatigue test equipment

The on-site fatigue test equipment is generally used for determining the structural integrity of a range of construction, material handling and agricultural equipment. Through experience in this type of heavy machine industry, engineers are able to replicate a large number of in-service conditions and environments. The test equipment encompasses Schenck test frames and Kelsey servo-hydraulic controllers. Most test fixtures are manufactured through a work instruction in-house, allowing freedom to devise and modify different tests.

The component was tested on a load-controlled basis. It is loaded by means of a hydraulic ram and two base fixtures. The component is braced to one of the bases by clamps and the load is applied by a pin and ram at the welded boss lug, Figure 53. The ram is connected at 90 degrees to the component and attached to the other base fixture. A load cell was used on the end of the hydraulic ram to measure the load acting on the component during cycling. All of the equipment was in good working order and calibrated, and fully certified prior to testing.

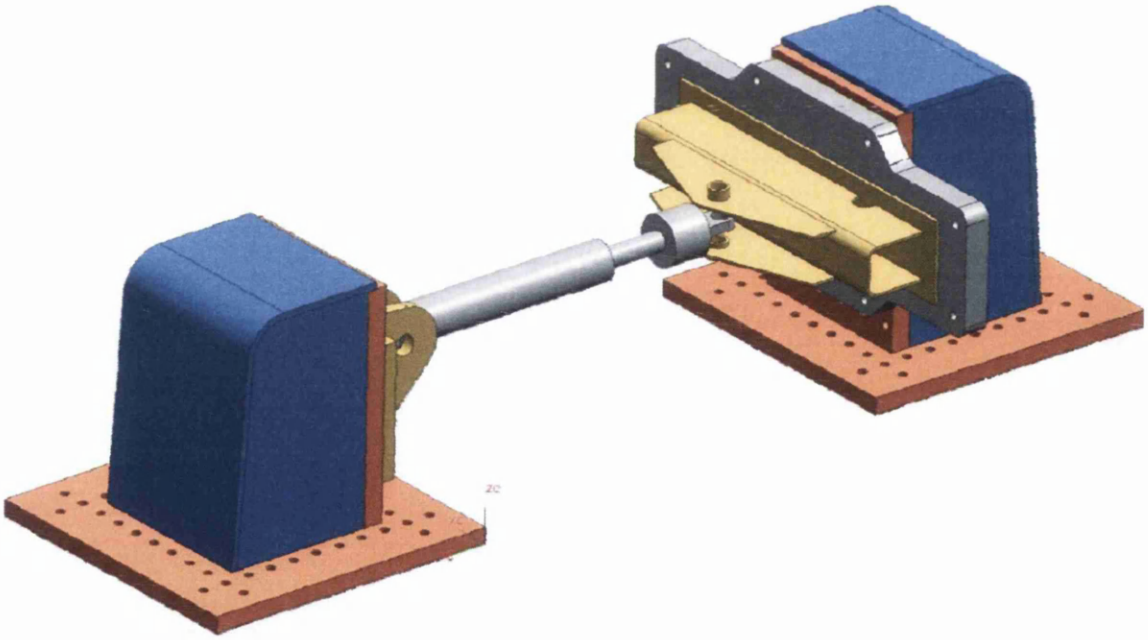

Figure 53: Test component test configuration

3.3.3 Test parameters

The load controlled fatigue tests were carried out under constant-amplitude sine wave loading regimes and a stress ratio of R=0.1. The tests were completed in ambient air temperature and at a maximum possible operating frequency until the command and feedback following error became compromised. Tests were completed at a frequency of 2 Hertz.

The load range was initially determined from a finite element analysis of the component and test model under the relevant boundary conditions. Approximate load values were calculated from the stress output. For a desired fatigue failure around $1x10^5$ cycles, from the S-N curves in the standard BS7608, an F2 class weld would need a stress range of approximately 150MPa. From the FE-model this is calculated as ~230kN.

For the first test component, electrical resistance strain gauges were fitted around the weld detail as highlighted in the FE stress analysis. 13 gauges were fitted to the first sample to verify the loads at the local weld toe. This also provided strain readings to verify the FE stress analysis of the model. The further 3 test components were fitted with fewer gauges just measuring strains at the areas of interest.

In order to achieve repeatability and consistency in the test methods, the same set-up procedure was used on all tests. The test component was placed on the base fixture, measured for correct alignment and clamped up. The clamping bolts were pre-loaded to the values defined in the bolt installation standard. Initial strain gauge readings were recorded under static loads and to correlate against the load cell readings. After verifying the required load, the test was set to run and the number of cycles recorded.

Over the period of the test, the weld locations and any possible stress concentrations were inspected twice daily for any potential fatigue cracks. The stiffness of the component was also monitored by a dial test indicator through displacement changes of the hydraulic ram. The tests were run until a fatigue crack grew to a critical length (engineering crack 20mm in length) and the test could not be run further without compromising safety.

3.4 Finite element weld fatigue assessment

As defined in the programme objectives, there is potential for the iterative design-build-test product development stages for yellow goods equipment to benefit from Finite Element based durability assessment methods. The programme objectives also highlighted the critical issues in using a traditional finite element stress analysis to determine a weld fatigue damage parameter. It is generally very difficult to characterise the stress at a weld toe, be it through calculation or physical measurement. The problems to overcome in an FE analysis are notably, mesh-sensitivity, fast and accurate FE-model solutions, geometry dependent fatigue curves and classification subjectivity.

3.4.1 FE weld fatigue life predictions

The critical issue with a linear finite element weld fatigue analysis is the notch stress singularity effect created at the weld toe. Stresses are calculated within each element of the mesh and extrapolated to nodes at the notch and weld toe. The results are then sensitive to the size of the meshed elements. The finer the mesh the higher the calculated stress at the notch. Two models with identical geometries, loading and boundary conditions are shown in Figure 54. The only difference was size of element mesh used to fill the geometry. The stress results for the first model are approximately 33% lower compared to the second model. This is an infinite stress singularity.

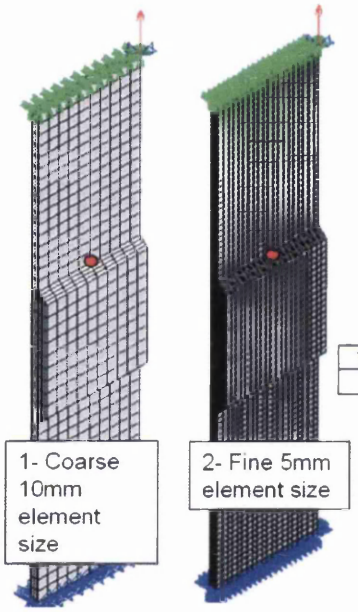

Test coupons under a 1kN unit load and identical boundary conditions

Centre node at weld toe

Stress (MPa) - Centre node at weld toe

	Max Princ σ	Mid Princ σ	Min Princ σ	Von Mises
1- Coarse	1.108	0.1229	0.0431	1.037
2- Fine	1.687	0.3273	0.1561	1.453

Figure 54: Stress singularity in an FE stress analysis

Completing a non-linear finite element analysis will overcome this problem as material σ-ε curves are input into the model. As the analysis exceeds the yield point, the material can proceed to deform plastically. However, a non-linear fatigue solution will consist of a more complicated analysis and take longer to solve, requiring more computing power. In order for a weld fatigue analysis method to be effective and efficient, it must provide accurate results fast in order to be repeated quickly. Non-linear FE-models do not fit this criterion.

As seen in any of the numerous weld fatigue design codes, fatigue lives of welded joints are geometry dependent, Figure 55.

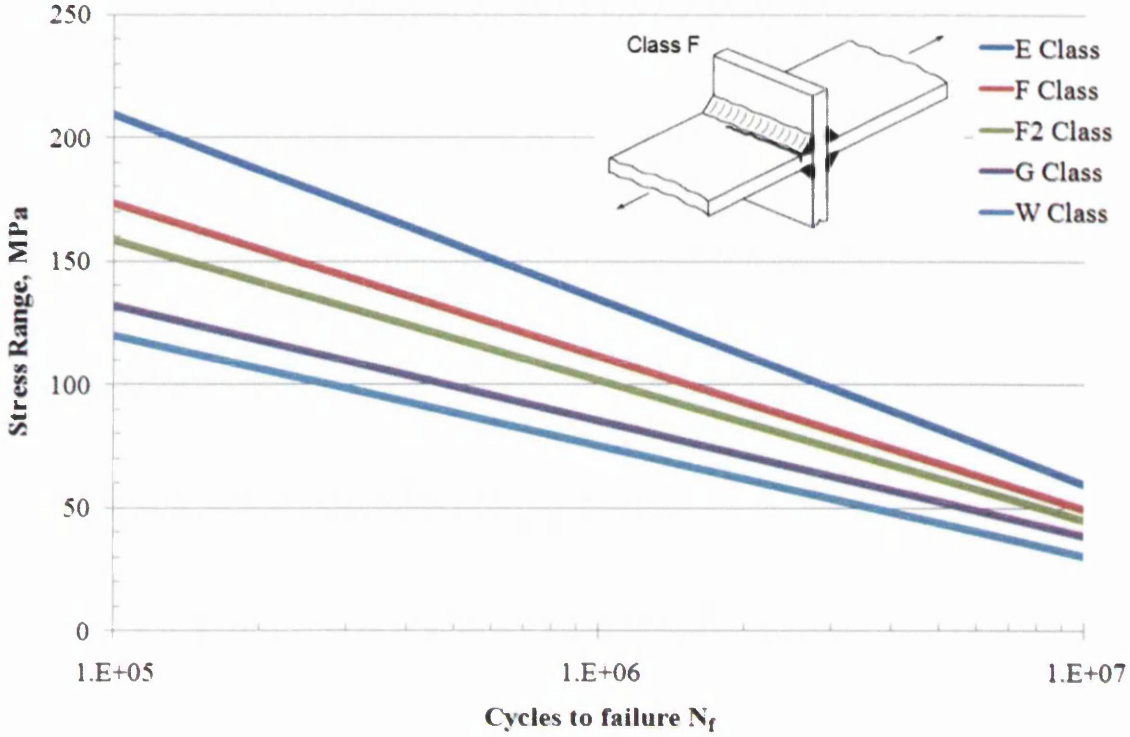

Figure 55: BS7608 geometry dependent weld fatigue design curves

Each type of joint geometry is classified and is assigned a specific fatigue curve. This approach is very subjective and not every type of joint or loading mode might be included. More importantly, having a number of different fatigue curves is difficult to input into an FE model as every millimetre of weld seam would have to be classified, which is unfeasible. Due to the impracticalities of using a nominal stress based weld fatigue analysis, an alternative damage parameter is sought to satisfy the above concerns.

3.4.2 Structural stress analysis method

The alternative fatigue damage parameter chosen for the durability assessment is the Structural Stress. This is the stress arising due to the overall geometry of the structure. Niemi [30] defined the total stress at a weld toe failure as made up of three stress components, membrane, bending and non-linear peak stresses, Figure 56.

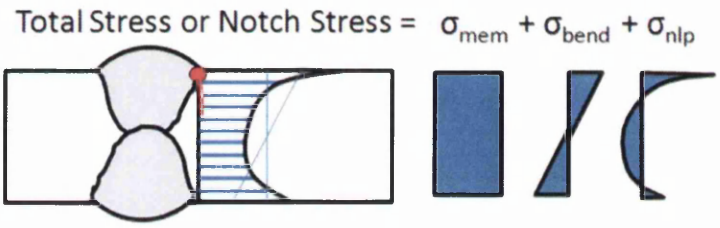

Figure 56: Total stress at a weld toe failure - membrane, bending and non-linear peak

The membrane and bending stresses arise from the tensile load or bending moments applied, respectively. These are both linear components and increase due to the geometry of the structure. Only if there is load acting on the structure will membrane and bending stresses occur. The non-linear peak stresses occur due to the weld notch effects such as the local notch stress and residual stresses. The non-linear peak stresses are in equilibrium and are still present if there is load acting on the body or not.

Dong [31] proposed distinguishing between the linear load dependent stresses and the non-linear peak stresses. The non-linear peak stresses are assumed to be contained within the fatigue test data and a damage parameter is calculated based only on the geometry and the applied linear loading. Excluding non-linear peak stresses, a damage parameter is defined as:

Structural stress σ_{ss}

$$\sigma_{ss} = \frac{f_{y'}}{t} - \frac{6m_{x'}}{t^2} \qquad \textbf{Eq 3.3}$$

Where t = thickness, $f_{y'}$ = forces acting perpendicular to the weld and $m_{x'}$ = moments parallel with the weld. As an example, if the structural stress is calculated for a non-welded geometry, i.e. a section with no weld notch (no non-linear peak stresses), the structural stress would be the same as the nominal stress or $K_t\sigma_{nom}$ elastic stress, Figure 57.

Consider a simple plate 300mm by 100mm and 2mm thick, with a 30mm diameter hole in the centre. The plate is fully restrained at one end and a 10kN load applied on the other. Calculating a structural stress as defined above, the value is 167.84MPa, compared with elastic theory $K_t\sigma_{nom}$ =167.78MPa and FE-model 8 node element= 168.60MPa. All values show very similar results.

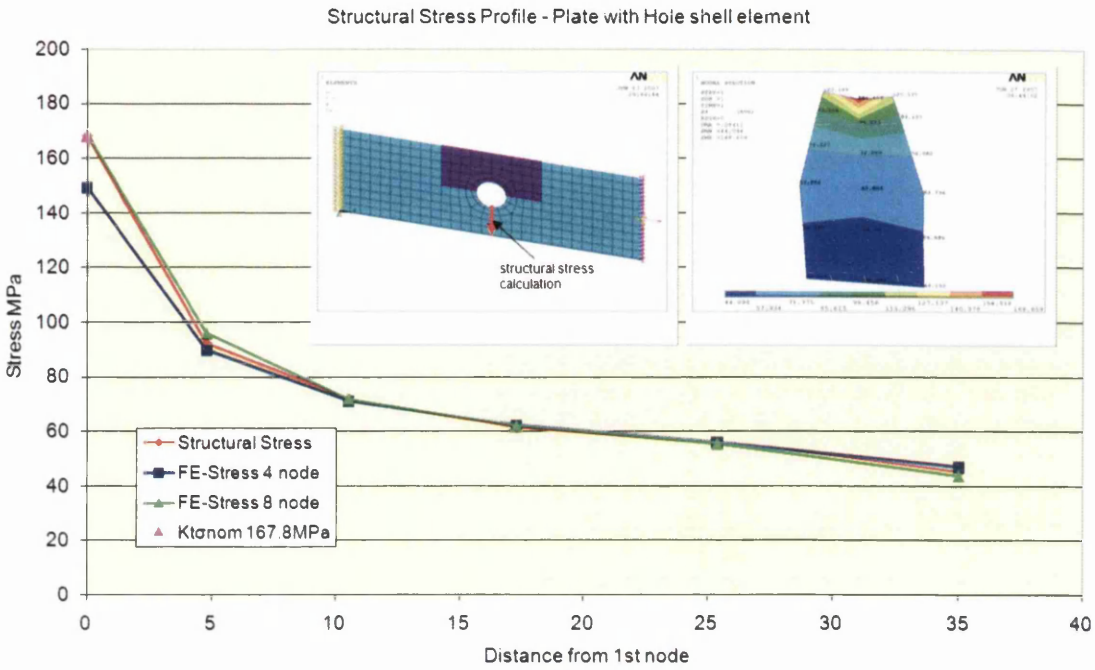

Figure 57: Calculation of Structural stresses for a non-welded geometry

This demonstrates that structural stress theory can calculate a stress based on linear loading stresses only (excluding non-linear peak stresses). Having the stress calculation based on linear geometry only will allow a number of fatigue curves to condense into one single master curve.

After generating fatigue test data for test coupons, structural stress σ_{ss} values for each geometry must be calculated for a 1kN unit load. Plotting the fatigue curves on a σ_{ss} against N_f instead of $\sigma_{nominal}$ against N_f, would then redistributes the geometry dependent fatigue data and condenses all the points on to one curve. This curve can then be used as the basis of the FE fatigue prediction model. After defining the curve, the same structural stress calculation procedure using a static 1kN unit load must be completed for the structure or component. This can be a new design or an un-common geometry type. A structural stress value is determined for the new component. An FE linear fatigue analysis (as discussed in the literature review) is completed next, superimposing a fatigue life loading regime. Ultimately a damage summation is achieved but based on a structural stress range. This damage summation, $\Delta\sigma_{ss}$ can then be read off the master-curve generated and a fatigue life prediction obtained at each node location.

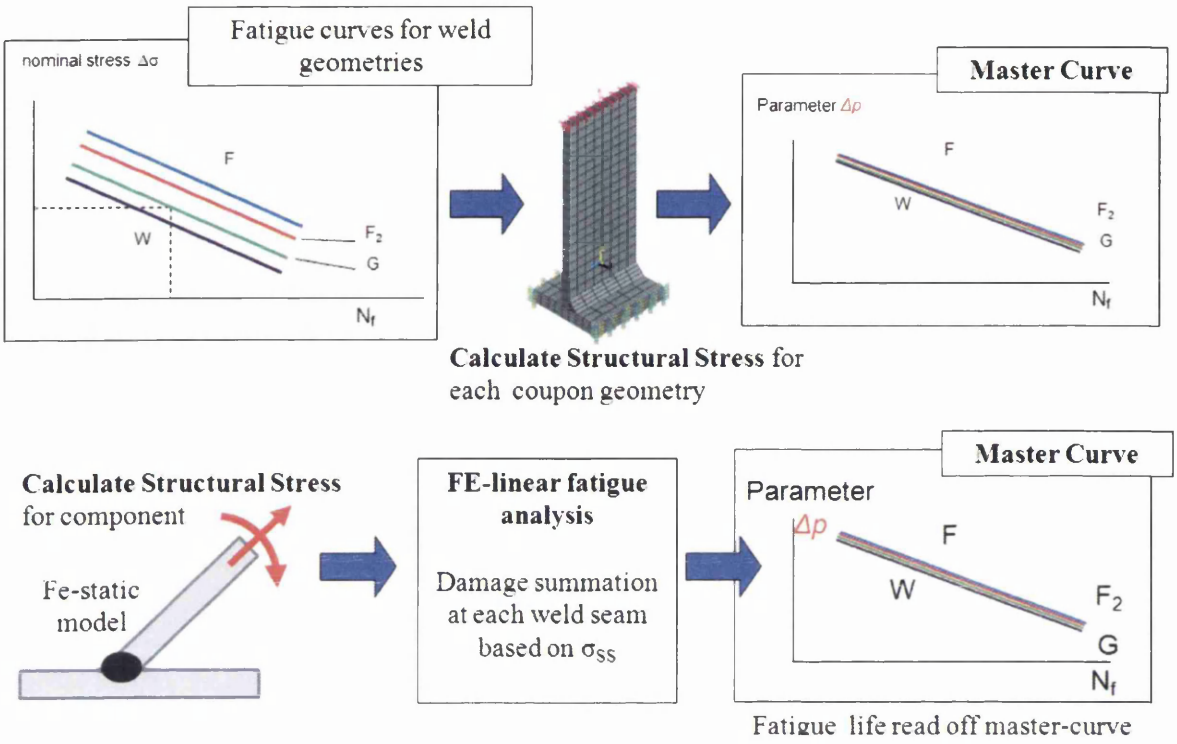

Figure 58: Structural stress fatigue assessment

3.4.3 Validation of Method

Once a fatigue damage parameter using the structural stress has been calculated and fatigue lives determined, all predictions must be validated by fatigue test measurements as discussed earlier. As well as comparing fatigue measurements and predictions, strain readings can be taken from test coupons and test components in order to validate the FE models and highlight any discrepancies in the analysis that might lead to possible sources of error.

Along with measuring nominal stresses and strains for comparison, strain gauges were used on coupons and components to obtain *Structural Stress* measurements. It is possible to measure the level of membrane and bending stresses (excluding non-linear peak stresses) at a weld detail with a series of strain gauges. This allows comparison of the measured and calculated structural stresses and provides further validation of the fatigue damage parameter.

4. Results

4.1 Coupon fatigue test results – Data Generation

In this research programme, it was recognised that an accurate weld fatigue life prediction method would benefit from referenced and traceable fatigue data. Generating weld fatigue data specific to the application of the prediction method can produce numerous benefits. The fatigue data will be representative of the manufacturing processes and materials used and enable tighter control to minimise unwanted variability in the test results. More accurate fatigue predictions can be obtained, specific to a developed design curve as opposed to published data from a range of un-known sources and this eliminates any conservatism of the predictions. It is also beneficial to have access to information on the coupon geometries when creating a finite-element model. Coupon geometries, test parameters, loads and strain gauge measurements can help create an accurate finite element analysis and simulation.

A range of welded joint configurations have been selected to best represent typical welded fabrications of construction and agricultural equipment. These welded coupon test pieces have been presented and discussed in the previous chapter.

4.1.1 Tensile load tee-fillet weld

Using the back-to-back configuration as shown in Figure 59, seven load controlled fatigue tests were completed for the tensile load tee joint.

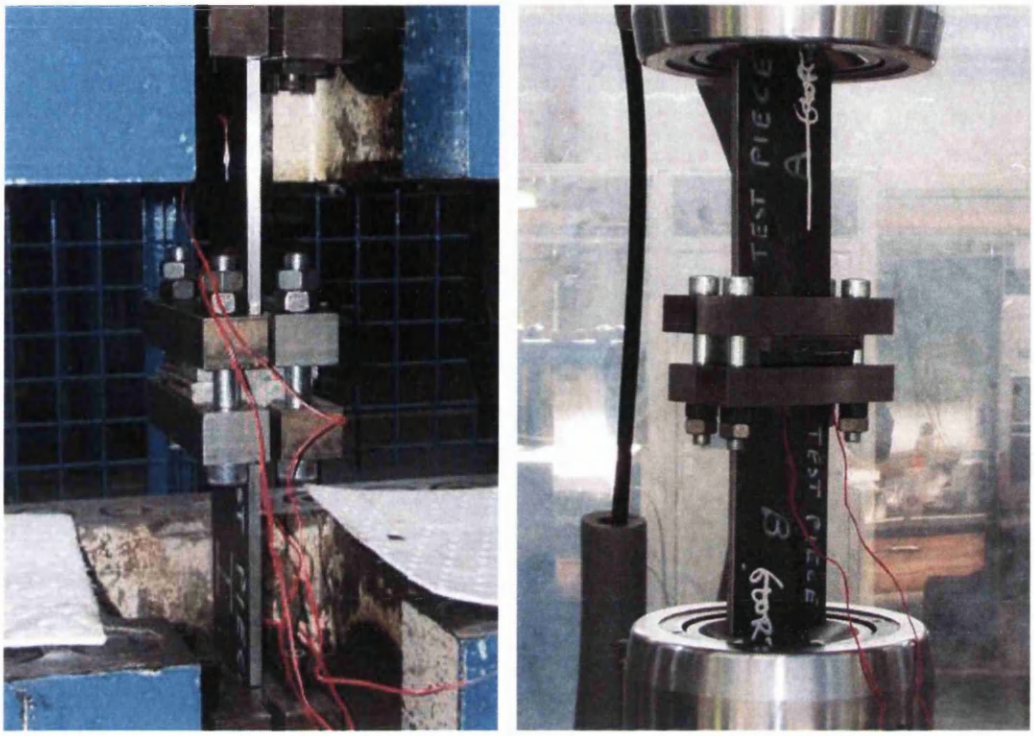

Figure 59: Tensile load tee joint testing configuration

Prior to testing, two 5mm KYOWA 120Ω electrical resistance strain gauges were placed on the weld side of each coupon at 5mm and 100mm away from the weld toe, to take a reading of the true strain and correlate with the load cell output of the testing frame. The back-to-back coupons were then placed in the test machine and the jaws clamped up. The strain gauge readings were recorded with the test piece in-situ and no loading applied. The strain gauges were calibrated and balanced to zero and a static load applied. The strain readings were correlated with the applied load. Assuming a plane stress condition, the force divided by area and the equating stress divided by Young's modulus, E, provides a calculated strain for comparison to the measured readings. The recorded nominal strains and calculated strains are given in Figure 60.

	Applied load	Measured Micro Strain
Sample 1	**kN**	**με**
1	165	**1025**
2	86	**560**
3	80	**467**
4	60	**288**
5	60	**385**
6	50	**307**
7	40	**231**

Stress Force / area	Microstrain Stress / E
MPa	**με**
206	**1006**
108	**524**
100	**488**
75	**366**
75	**366**
63	**305**
50	**244**

Young's Modulus E = 205000MPa E = Stress / strain Area = 800mm^2

Figure 60: Measured micro-strain values and calculated micro-strain for Tee joint coupons

The tests were completed at load ranges between 36kN and 77.4kN on the DARTEC 2000kN and INSTRON 100kN twin column loading frames. A test running frequency between 5 Hertz and 10 Hertz was achieved based on the stiffness of the coupon but also depending on the capability of the machine used. The following error of the load feedback signal was always kept within approximately 10% of the command controller. All of the tests were conducted at a stress ratio of R=0.1 in an ambient air environment.

The test was completed and a fatigue life recorded when complete separation of one of the test samples occurred as shown in Figure 61. The remaining un-failed coupon was removed and not used in any further testing.

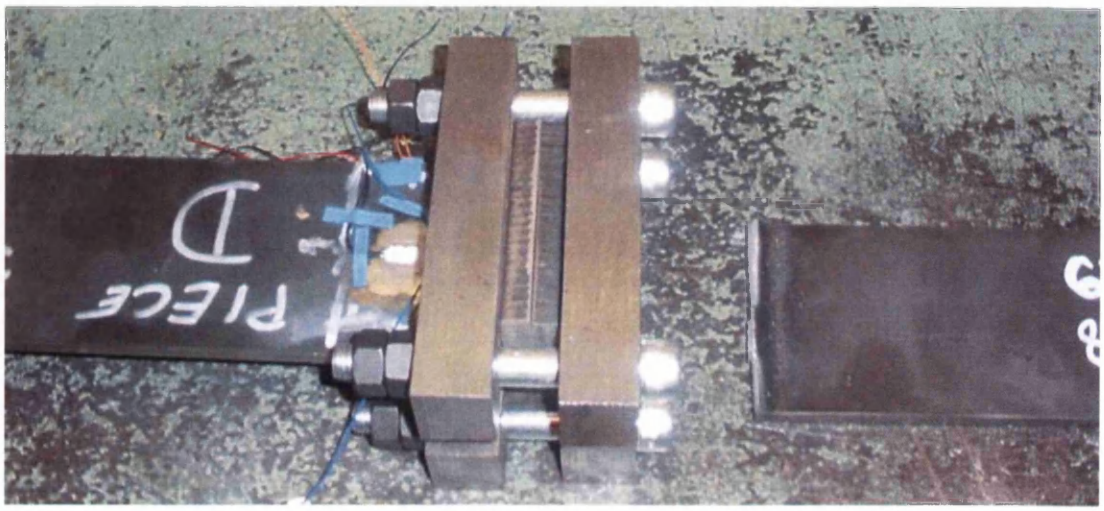

Figure 61: Tee joint failed coupon

During testing the servo-controller peak feedback load and displacement signals were recorded using data logging equipment. Using Microsoft Excel the peak load values were divided by the displacement (kN/mm) and a calculated stiffness value, k, obtained. The stiffness reduction of sample 7 is plotted against the number of cycles (k against N_f), in Figure 62.

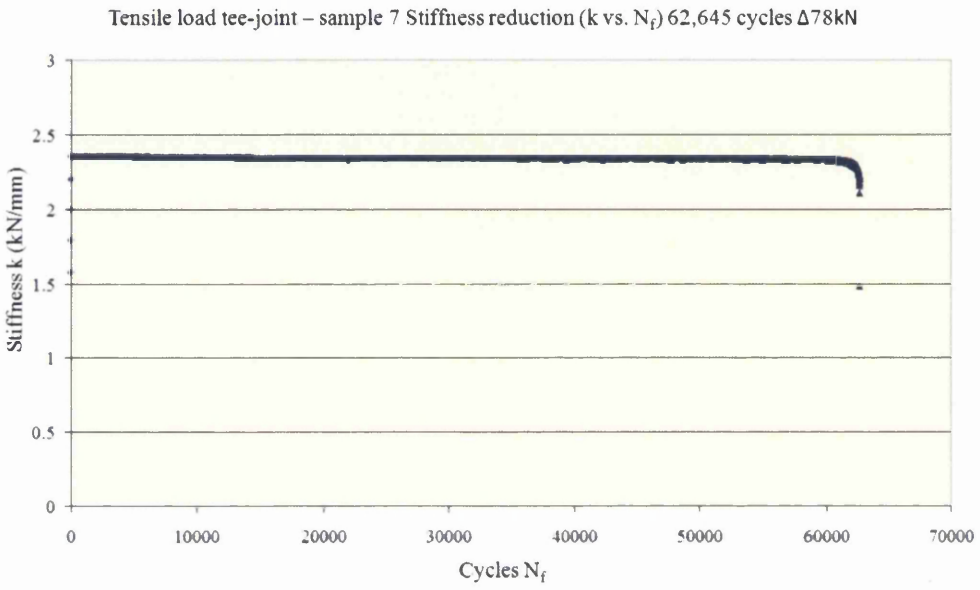

Figure 62: Stiffness (k) reduction curve for Tensile load tee joint sample 7

It is common practice to use a failure criterion of a 10% or 20% stiffness reduction of the original stabilised stiffness (after initial cyclical hardening or softening). All of the coupon geometries tested in this research work (with exception of the tee joint bending load), produced a full separation failure before reaching a 10% stiffness drop. Full separation typically occurred between 3-5% reduction in stiffness. For this reason, the failure criterion for N_f here is defined as a 3% reduction from the original stabilised stiffness, k. These 3% stiffness drop fatigue lives were then used for further analysis in this work. The 3% stiffness reduction fatigue lives are plotted on the log-log scale, Load range against Cycles to failure (ΔkN against. N_f) curve in Figure 63.

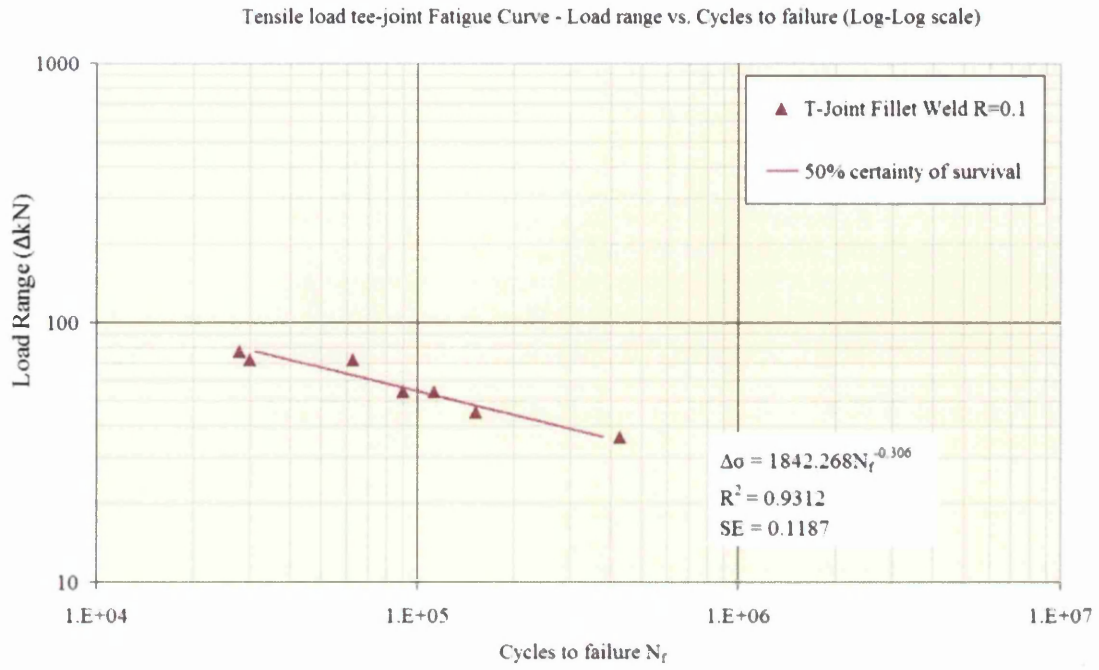

Figure 63: Tensile load tee joint fatigue data - Load range against cycles to failure (Log ΔkN against Log N_f)

A statistical analysis was completed using a log-linear regression analysis on the y-axis (N_f) of the fatigue data, the fatigue lives being the variable. A 50% certainty of survival curve is created with a standard error =0.1189 and R^2 value = 0.9312. There is excellent correlation in the data from the regression analysis. It is assumed that Weld-fatigue S-N curves generally have a slope of $m = 3$, where m is the inverse slope of the log S (or log Load) against log N curve. The test results for the tensile load tee joint have an inverse gradient = 3.06. This is consistent with data reported in the literature.

More coupon samples were available for testing, but the decision was taken not to run any further tests on the single-sided fillet weld tee joint. The seven tests clearly defined the S-N curve adequately and reflecting on the loads used, any further test would be at a very low load and possibly result in a run out. Therefore, it would not produce a significant data point or further distinguish the S-N curve.

All of the test failures occurred through the throat of the fillet weld seam. The crack initiated at the base of the weld where the two plates meet. With only a single-sided fillet weld, only a low level of penetration is achieved. The fit-up gap between the two plates creates a severe stress concentration and crack-like feature, where the failure originated, Figure 64.

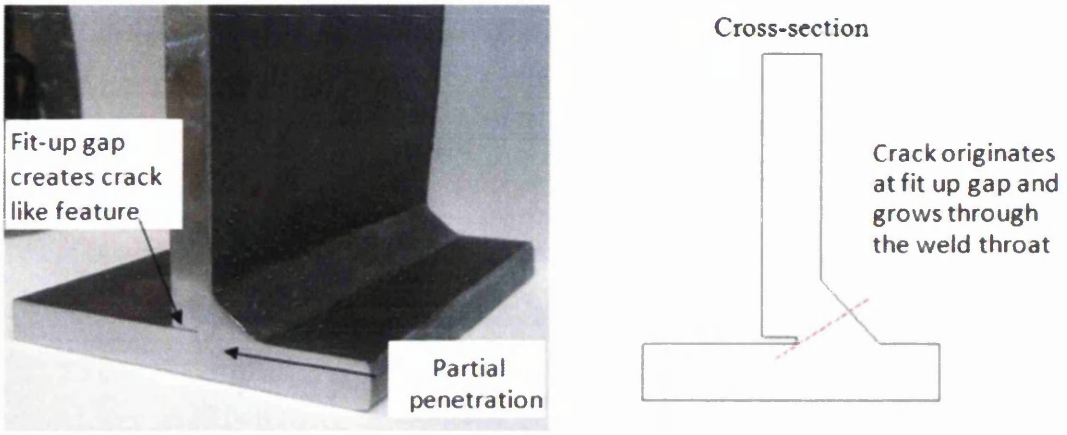

Figure 64: Tee joint coupon - crack initiation location at weld throat

The fracture surfaces of the coupons demonstrate characteristics of a typical fatigue failure, shown in Figure 65.

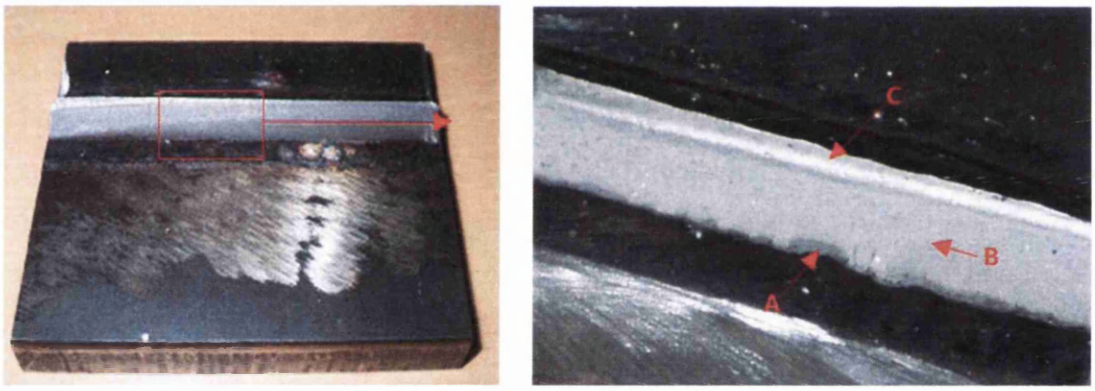

Figure 65: Tensile load tee joint fracture surface

The darker shaded areas at location A and all along the base of the fracture area show the crack initiation sites. At B the lighter burnished marks demonstrate the typical beach mark effects of fatigue crack growth. Finally at location C the coarse fast fracture area is visible where the remaining surface area is no longer able to support the load and fails. Of the discarded coupons, the base and the upright were separated to look for fatigue crack initiation and crack growth. It is clear from the image in Figure 66 that crack initiation occurred at point A and all along the base of the weld throat. At B stage 2 crack growth has occurred. At C the coarse fracture surface is where the upright was separated from the base after the fatigue test was stopped.

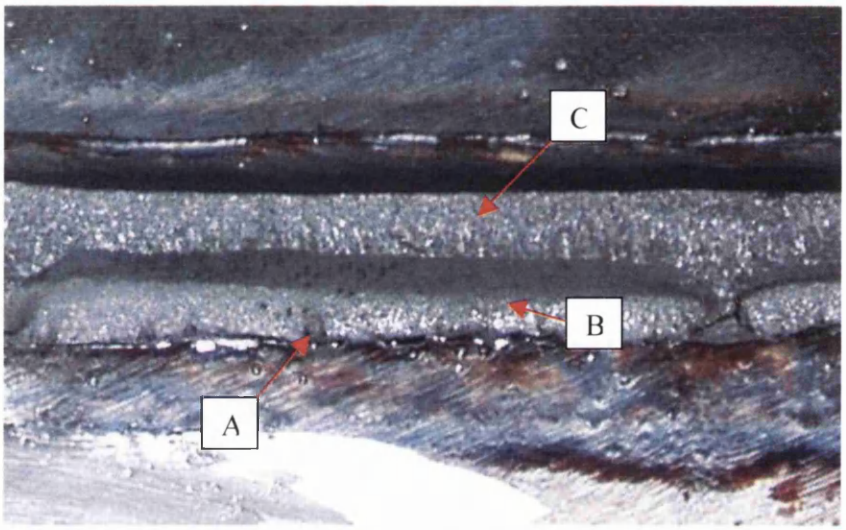

Figure 66: Un-failed Tee joint coupon - upright removed and crack initiation is visible

It is possible that the results of the coupon tests are slightly conservative as of the two coupons used in a test, only the first to fail was recorded and the second coupon was discarded. It is clear that crack initiation and propagation occurred on the un-failed coupon. The crack propagation stage can proceed quickly and account for only a small part of the fatigue life. Once the crack does propagate, the remaining fatigue life is associated with an insignificant number of cycles. Hence the test data are not wildly conservative.

The single-side fillet weld represents a high percentage of the total welds in yellow goods structural components. The predominant failure mode of this weld is a crack initiating at the weld toe, not the throat as is the case is these tee joint tests. Considering the test data in terms of load range against cycles to failure, the fatigue strength for the net cross-section of the coupon is poor. Where the failure occurs through the throat, despite a low load range, there is a high stress range and bending moment acting about the weld seam. The back-to-back configuration of single side welded coupons creates an offset in the load path, Figure 67. In a welded structure, a similar joint configuration would have the longer-range material restraining the base of the tee joint and preventing the bending moment. The load path in a larger structure would transmit further into the structure, unlike the tee-joint coupon, where the load is driven directly underneath to the adjoining coupon.

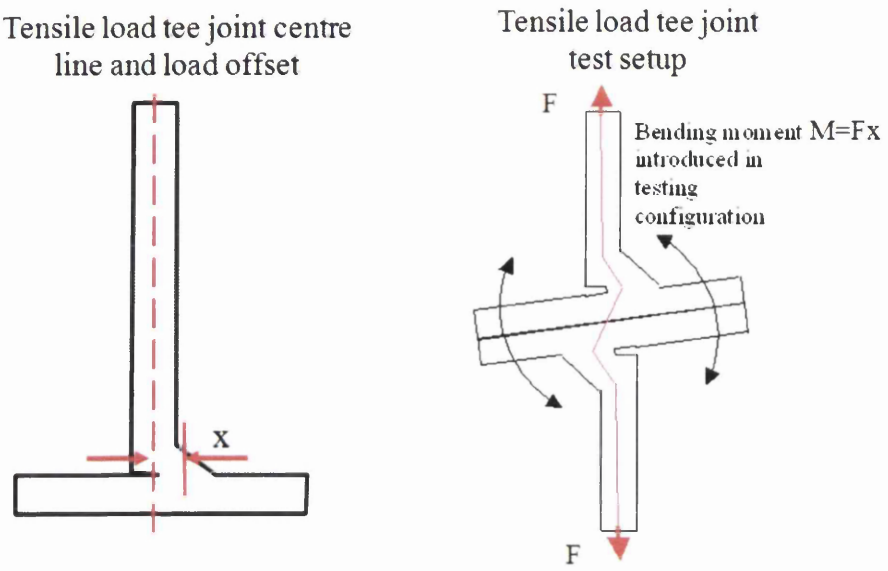

Figure 67: Tee joint test configuration- Low load but high stress range

It is generally assumed that residual stress levels in welded components are approximately equal to the yield strength of the material. The issue of whether or not welded coupons contain residual stresses of that magnitude has been discussed earlier in the literature review. During the project, the opportunity arose to measure the residual stress levels in the tee joint coupon. Three samples were selected and the X-ray diffraction technique was applied to obtain residual stress levels.

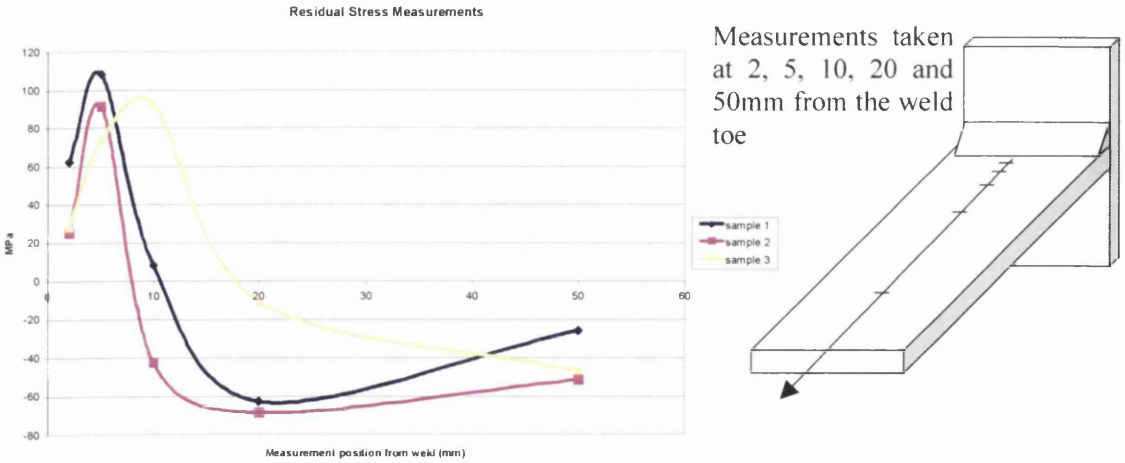

Figure 68: Tee joint residual stress measurements using X-Ray diffraction

Figure 68 shows the residual stress measurement in the MPa on the y-axis, against the distance away from the weld toe (mm) on the x-axis. It suggests the residual stresses are significantly below the material yield point of ~400MPa. This is likely to be due to the

medium-range residual stresses released when the coupons are cut to 100mm widths. The three samples generally follow the same pattern of residual stress measurements, although there is still some scatter between the three coupons. It is significant to note the levels of residual stresses in the coupons as this can affect the fatigue life.

4.1.2 Non-load-bearing cover plate

The non-load-bearing cover plate was tested as depicted in experimental methods in chapter 3.1.5. Electrical resistance strain gauges were placed on the weld side of each coupon at 15mm and 100mm away from the weld toe. During the test set-up, micro-strain measurements were taken to record the pre-load effects of the hydraulic grips actuation (no tensile force applied). The strain gauges were calibrated and balanced to zero and then a tensile load applied. The micro-strain values were correlated with the applied load. The strain gauge data at 15mm away from the weld toe during clamp-up of the test grips and on applying tensile load are given in Figure 69.

	Applied load	**Measured Micro Strain**	Stress Force / area	**Microstrain** Stress / *E*
Run	**kN**	**με**	**MPa**	**με**
clamp grips	0	435	0	0
balance gauges	0	0	0	0
1	66.8	545	84	407
2	167.2	1330	209	1020

Young's Modulus E = 205000MPa E = Stress / strain Area = 800mm^2

Figure 69: Non-load-bearing cover plate micro-strain readings - 15mm away from weld toe

In total, twenty-one fatigue tests were completed for the non-load-bearing cover plate coupon. Of the tests completed, 16 were run in the as-welded state at load ranges between 50kN-225kN all at a ratio R=0.1. There were 15 full separation failures and 1 run out. A further 3 were completed in the as-welded state at load ranges between 60kN-100kN at a higher mean load ratio R=0.5, with all tests running to full separation failures, Figure 70. A further two test coupons underwent post-weld heat treatment and were placed in the stress relieving oven. The samples were taken to a critical temperature in order for the internal residual stresses to redistribute and were left to cool to room temperature. The 2 stress-relieved samples were run at 99kN and 157.5kN load ranges with a ratio R=0.1. Both tests terminated with complete separation.

Figure 70: Non-load-bearing cover plate original test piece (top) and weld toe failure (bottom)

A test running frequency between 6 Hertz and 12 Hertz was achieved without compromising the following error of the load feedback signal. All of the tests were conducted in an ambient air environment. A fatigue life failure was recorded when complete separation of the test coupon occurred as in Figure 70. The stiffness parameter k was determined for the test coupon by dividing the peak load by the peak displacement (kN/mm). The stiffness reduction of sample 11 is plotted against the number of cycles (k against N_f), in Figure 71. The fatigue life at 3% stiffness drop was determined from the original stabilised k value. The 3% stiffness drop fatigue lives were then used for further analysis in this work.

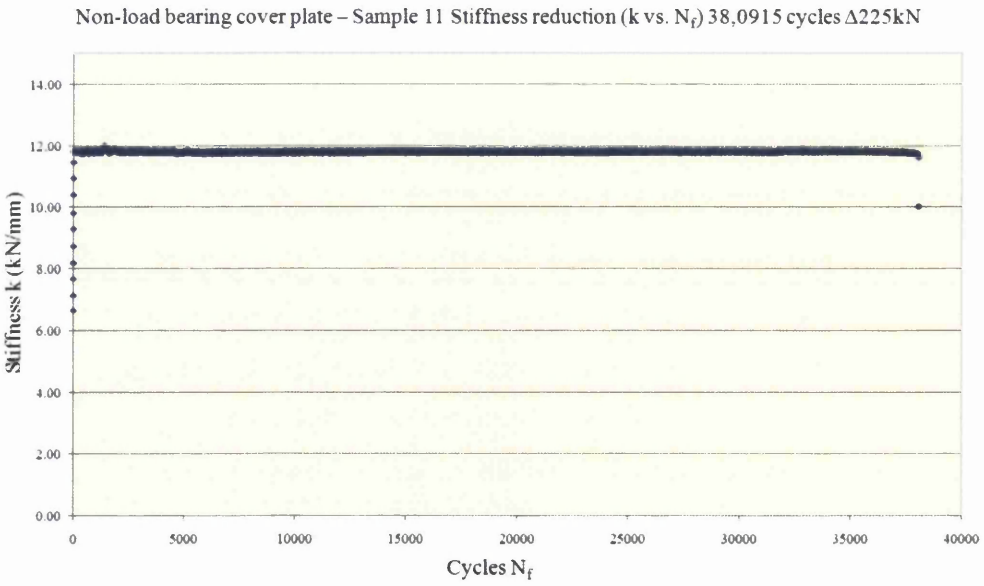

Figure 71: Stiffness (k) reduction curve for Non-load-bearing cover plate sample 11

The 3% stiffness reduction fatigue lives are plotted on a log-log scale as Load range against Cycles (ΔkN against N_f) curve in Figure 72. A statistical analysis was completed using a log-linear regression analysis on the y-axis (N_f) of the fatigue data, the fatigue lives being the variable. A 50% certainty of survival curve is created and an R^2 value = 0.9812. This is excellent correlation of the data.

Test sample 10 completed 10 million cycles without failing or any indication of a visible crack. The test coupon was removed and was regarded as a 'run out' where failure did not occur. This is highlighted conventionally in the fatigue curve as a slanting black arrow next to the data point.

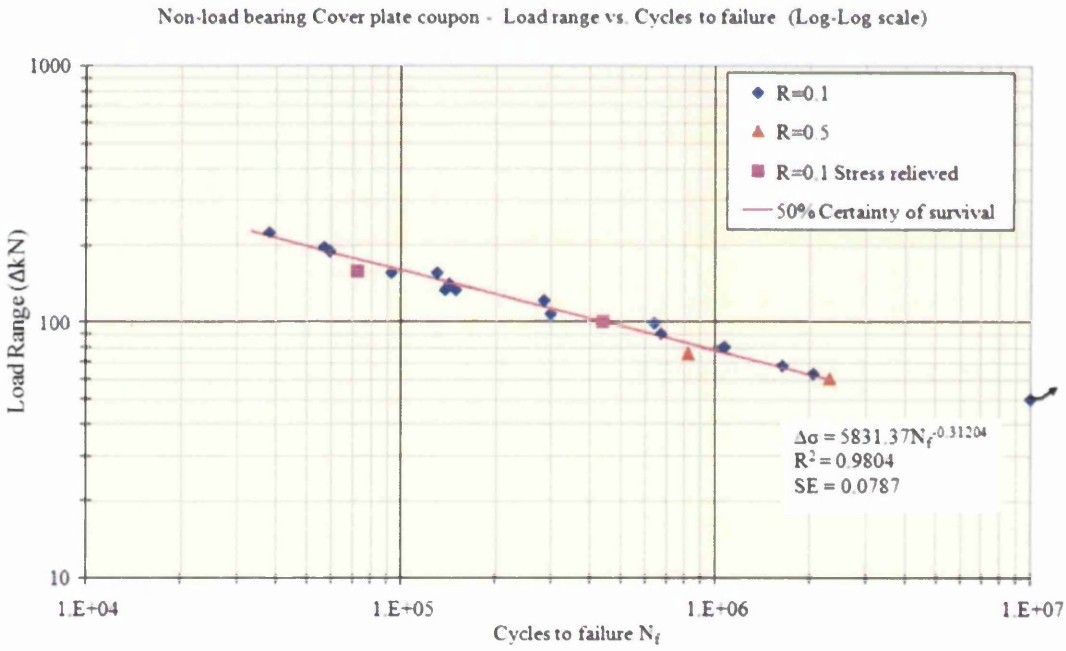

Figure 72: Non-load-bearing cover plate fatigue data- Load range against cycles to failure (Log ΔkN against Log N_f)

The remainder of the test failures occurred through the weld toe. Fatigue cracks initiated at the stress concentrations and notch effects caused by the welding process. Crack initiation could be seen across the width of the coupon (except at the edges where the weld details were ground flush to prevent premature failures from higher stresses due to an edge effect).

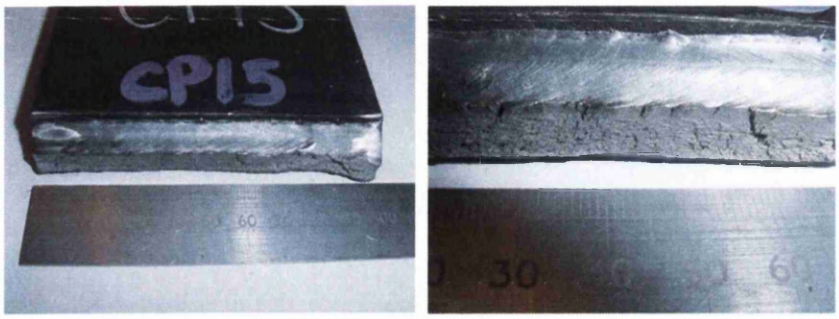

Figure 73: Non-load-bearing cover plate coupon fracture surface

The fracture surface of cover plate test piece 15 is shown in Figure 73. The small dark shaded lines at the top of the fracture surface demonstrate fatigue crack initiation from the weld toe, across the width of the coupon. A smooth burnished appearance is visible on the fracture surface, from the weld toe down through half the thickness of the plate, demonstrating fatigue crack growth. A coarse and much rougher surface is visible on the lower half of the fracture area where final separation has occurred due to insufficient cross-sectional area to support the test load.

Two tests were completed at a high mean load ratio of R=0.5 to further investigate the effects of residual stresses in small welded coupons. It has been discussed previously that some believe small welded coupons do not contain sufficient welded residual stresses to accurately represent the weld fatigue behaviour of full size structures. Welded components with residual stresses will show no fatigue strength dependency on the load or stress ratio R used. In the load-life curve in Figure 72 it is apparent the tests completed at R=0.5 produce a fatigue strength with a similar performance and curve fit to the tests completed at R=0.1. This suggests sufficient residual stresses are contained within the 100mm wide test coupons. Tests were also completed on stress-relieved coupons, but it has been shown in research that this post-weld heat treatment is only beneficial for compressive or fully reversed loading ratios [42].

4.1.3 Load-bearing lap joint

Fourteen load-bearing lap joint fatigue tests were completed as defined in experimental methods in chapter 3.1.6. Electrical resistance strain gauges were placed on the weld side of each coupon at 15mm and 35mm away from the weld toe. During the test set-up, micro-strain measurements were taken and recorded against a set static tensile load applied via the

hydraulic servo-controller. The strain gauge data at 15mm and 35mm away from the weld toe for a corresponding tensile load applied are given in Figure 74.

	Applied load	Measured Micro Strain 15mm	35mm
Run	kN	με	με
1	66.8	1315	1315
	176.2	2558	2558
2	66.8	1200	1200
	140	2342	2342
3	66.8	1195	1195
	140	2325	2325

Figure 74: Measured micro-strain values for Load-bearing lap-joint

11 samples were tested and fully separated in the as-welded state at load ranges between 45kN-135kN and a load ratio R=0.1, Figure 75. An additional sample was tested (as-welded) at a load range of 50kN and a higher mean load ratio R=0.5. This test failed at full separation. 2 test coupons were placed in the stress-relieving oven for post-weld heat treatment. The samples were left to cool to room temperature. The 2 stress-relieved samples were run at 50kN and 90kN load ranges and a ratio R=0.1 with both tests terminating in complete separation.

Figure 75: Load-bearing lap joint coupon - original test piece (left) and weld toe failure (right)

A test frequency between 4 Hertz and 8 Hertz was achieved without compromising the following error of the load feedback signal. All of the tests were conducted in an ambient air

environment. A fatigue life failure was recorded when complete separation of the test coupon occurred as shown in Figure 75. The stiffness parameter k was determined for the test coupon by dividing the peak load by the peak displacement (kN/mm). The stiffness is plotted against the number of cycles (k against N_f) for sample 11 in Figure 76.

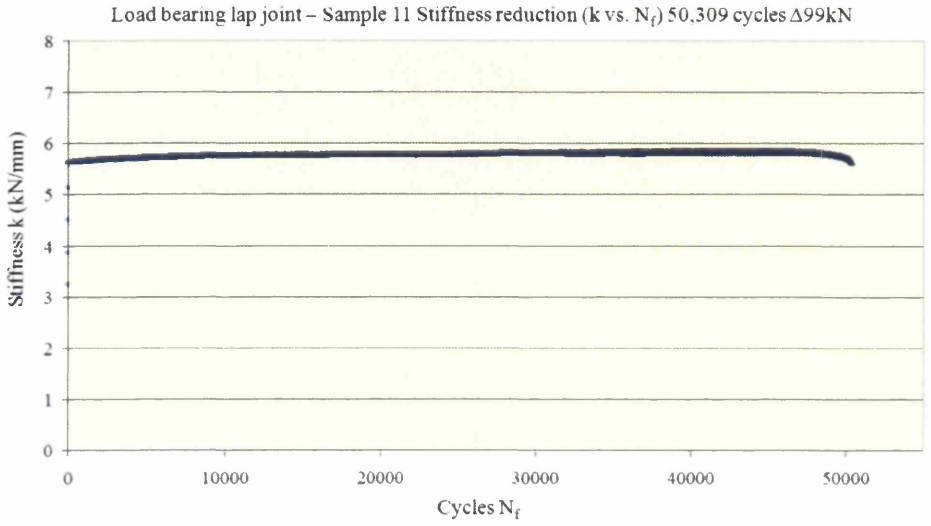

Figure 76: Stiffness (k) reduction curve for Load-bearing lap joint sample 11

The 3% stiffness drop fatigue lives were then used for further analysis in this work. The 3% stiffness reduction fatigue lives are plotted on a log-log scale as Load range against Cycles to failure (ΔkN against. N_f) curve, Figure 77.

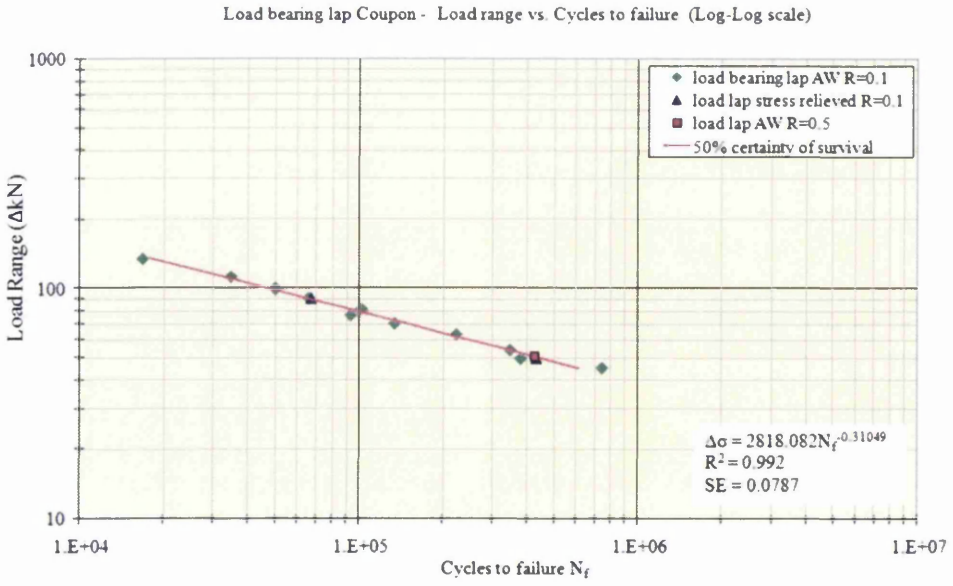

Figure 77: Load-bearing lap joint fatigue data-Load range against cycles to failure (LogΔkN against Log N_f)

A statistical analysis was completed using a log-linear regression analysis on the y-axis (N_f) of the fatigue data, the fatigue lives being the variable. A 50% certainty of survival curve is created with a determined R^2 value = 0.992. This is excellent correlation of the data .

The failure mode of the lap joint welds occurred from the weld toe. Fatigue cracks initiated typically at the stress concentrations and notch effects caused by the welding process. Crack initiation could be seen across the width of the coupon, Figure 78. The small dark shaded vertical lines at the top of the fracture surface demonstrate fatigue crack initiation from the weld toe. Typical beach marks on the fracture surface represent the fatigue crack growth from the weld toe down through the thickness of the plate. The coarse fast fracture area is visible where the remaining surface area is no longer able to support the load and fails.

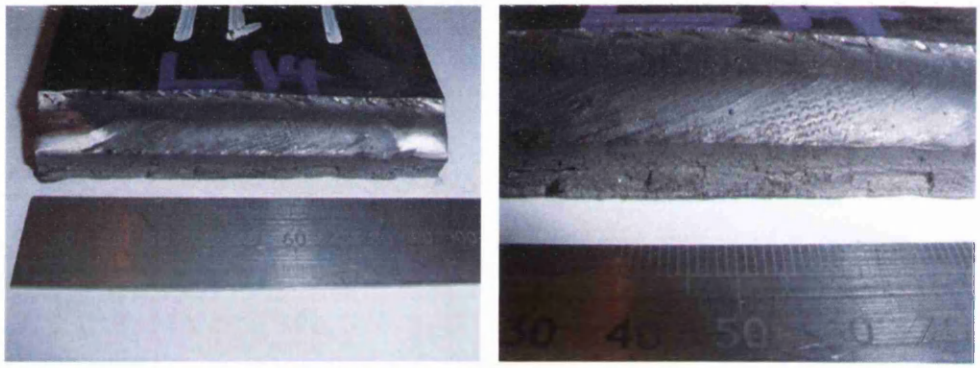

Figure 78: Load-bearing lap-joint coupon fracture surface

Of the two weld runs on a lap joint coupon, fatigue crack propagation was also present on the opposing weld run that did not fully fracture and separate, Figure 79.

Figure 79: Load-bearing lap joint coupon sample 2 - weld toe failure (left) and underneath, opposite weld run with significant crack propagation (right)

Sample 7 was completed at a high mean load ratio of R=0.5 to further investigate the effects of residual stresses in small welded coupons. A coupon with insufficient residual stresses would produce a shorter fatigue life when tested at a higher mean stress ratio compared with the life of a sample with load ratio of R=0.1. The load-life curve in Figure 77 compares the R=0.5 test with samples 10 and 14 tested at R=0.1. At the same load range there is little scatter to distinguish between the three measurements. This again suggests there are sufficient residual stresses contained within the 100mm wide test coupons.

4.1.4 Non-load-bearing transverse attachment

An initial batch of non-load-bearing transverse attachment samples was manufactured to the drawing shown in Figure 80. The welding detail consists of a single-sided non-load-carrying attachment, with a single weld run. Similar welding detail is commonly found in welded structures where access is only possible to one side of the welded section and a weld toe failure is the predominant failure mode.

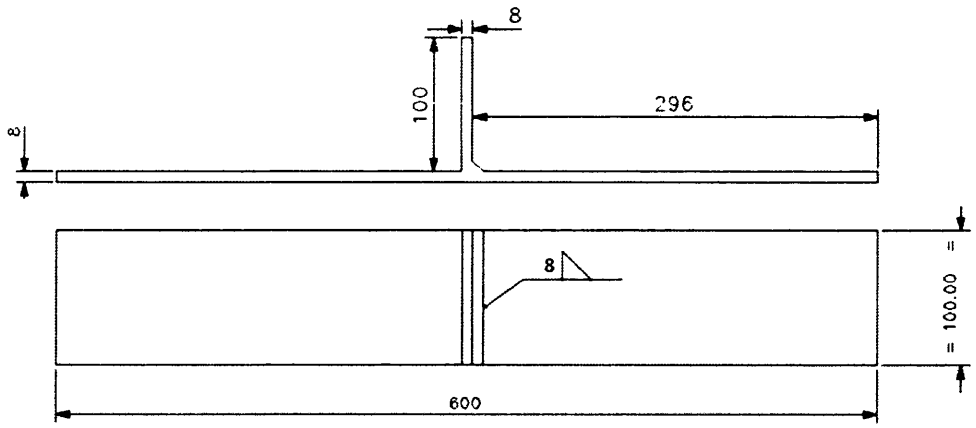

Figure 80: Non-load-bearing transverse attachment drawing

Seven coupon tests were completed using a twin column loading tower. The failure mode occurred from the root of the weld and propagated into the main plate, Figure 81.

Figure 81: Non-load-bearing transverse attachment - batch 1 root failure mode

Upon inspection of the fatigue fracture surface and polishing of the cross-section of the weld profile, it was evident that there was excessive sulphur segregation in the parent material plate in four of the seven coupons tested, Figure 83. Plotting the fatigue test results on a log-log scale, Load range against Cycles to failure (ΔkN against N_f), Figure 82, suggests the sulphur segregation can potentially have an effect on the two lower load ranges tested (112.5kN and 90kN). However, the difference is still within a reasonable range of scatter as expected in fatigue lives.

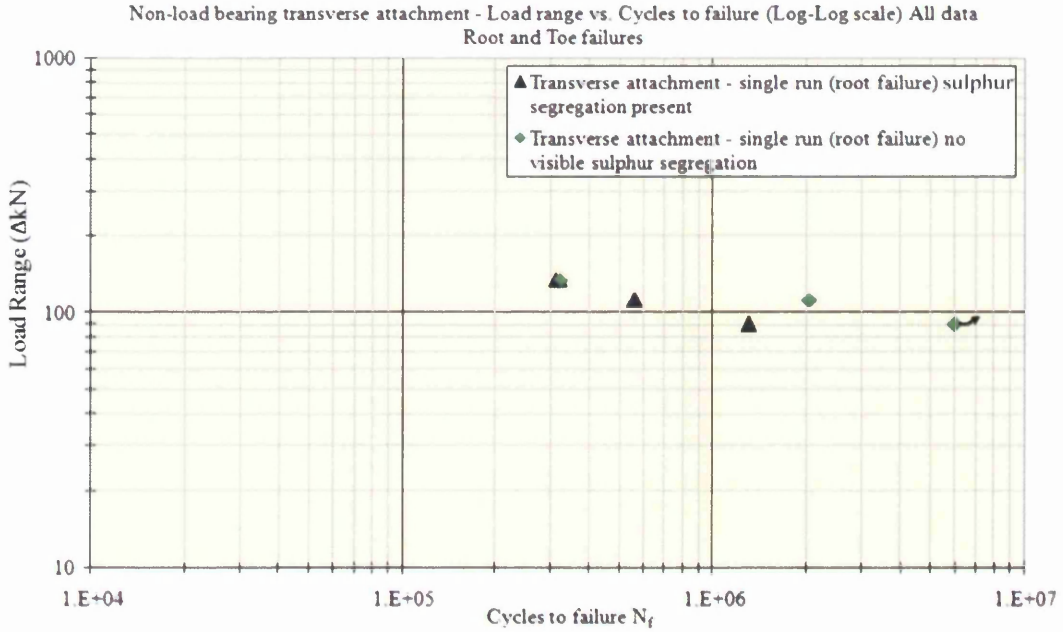

Figure 82: Non-load-bearing transverse attachment (Batch 1) fatigue data- Load range against cycles to failure (Log ΔkN against Log N_f)

The three data points (two with visible sulphur segregation, one without) at the higher load range all fail at $3x10^5$ cycles. At the 135kN load range, presence of sulphur segregation

clearly has no effect on the fatigue strength. This leaves uncertainty as to whether sulphur segregation affects the fatigue performance or whether the scatter is due to discontinuities and impurities at the root crack initiation site. Despite the weld detail representing a commonly found joint configuration, the root failure mode observed is a rare occurrence. The failure mode can sometimes take place from welding details such as load-bearing lap joints or puddle welds where a hole or gap in a cover plate attachment is filled with weld metal. Ultimately the root failure is not the intended weld toe crack initiation site. For this reason, additional weld fatigue samples were manufactured and tested.

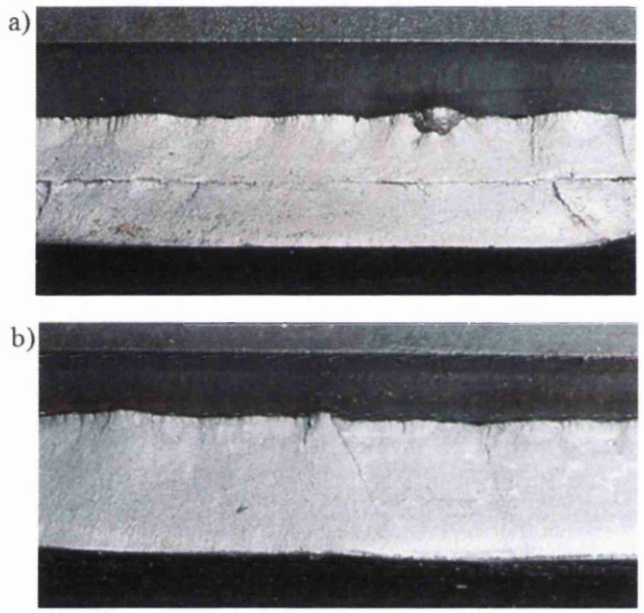

Figure 83: Non-load-bearing transverse attachment Root failure fracture surface - a) Sample 3 with sulphur segregation and b) Sample 5 without

The next batch of non-load-bearing transverse attachment coupons consisted of 12 samples, eight of which had a double sided attachment and the remaining four a single-sided attachment. The double-sided coupons were welded with four weld passes, and the single-side coupon with two weld passes. Each attachment consisting of two weld runs, Figure 84.

Figure 84: Double (left) and-single (right) welded attachments

Electrical resistance strain gauges were placed on the weld side of each coupon at 15mm and 35mm away from the weld toe. During the test set-up, micro-strain measurements were taken to record the pre-load effects of the hydraulic grip actuation (no tensile force applied). The strain gauges were calibrated and balanced to zero and then a tensile load applied. The strain gauge data at 15mm and 35mm away from the weld toe for a corresponding tensile load applied are given in Figure 85.

		Measured Micro Strain		Measured Micro Strain			
	Applied load	Double sided coupon 15mm	35mm	Single sided coupon 15mm	35mm	Stress Force / area	Microstrain Stress / E
	kN	με	με	με	με	MPa	με
Grips clamped up	0	10	18	145	208	0	0
Gauges zeroed							
1	25	164	159			31	152
2	50	327	316	503	425	63	305
3	70.88	459	445	697	589	89	432
4	100	644	625	875.5	811	125	610
5	150	974	943	1362	1169	188	915
6	177.2	1150	1114	1502	1304	222	1080

Young's Modulus E = 205000MPa E = Stress / strain Area = 800mm^2

Figure 85: Measured micro-strain values and calculated micro-strain for double and single non-load-bearing attachment

From previous tests of other coupon geometries it was apparent that stress relieving and high mean test ratios had no effect on the fatigue performance and sufficient residual stresses are contained in the welded coupons. Based on this, all twelve non-load-bearing transverse attachment samples were tested in the as-welded state. The tests were completed at load ranges between 90kN and 225kN at a load ratio R=0.1 All twelve samples tested failed at full separation, Figure 86.

Figure 86: Non-load-bearing transverse attachment weld toe failures -Double (left) and single (right)

A test running frequency between 4 Hertz and 8 Hertz was achieved without compromising the following error of the load feedback signal. All of the tests were conducted in an ambient air environment. A fatigue life failure was recorded when complete separation of the test coupon occurred. The stiffness parameter k was determined for the test coupon by dividing the peak load by the peak displacement (kN/mm). The stiffness is plotted against the number of cycles (k against N_f) for the double-sided sample 2 in Figure 87.

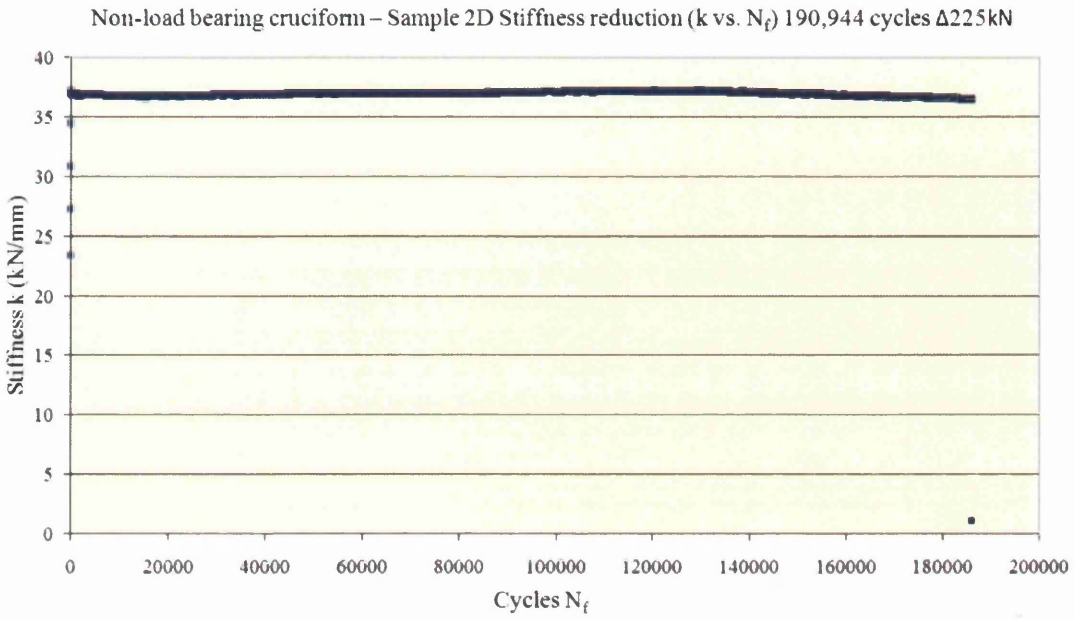

Figure 87: Stiffness (k) reduction curve for Non-load-bearing transverse attachment- double-sided sample 2

The 3% stiffness reduction fatigue lives are plotted on a log-log scale as Load range against Cycles to failure (ΔkN against N_f) curve. A statistical analysis was completed using a log-linear regression analysis on the y-axis (N_f) of the fatigue data, the fatigue lives being the variable and a 50% certainty of survival curve created. The fatigue data curves have been analysed for a number of different scenarios. Firstly, all of the fatigue tests (root failure coupons, single-sided and double-sided coupons) are considered as one data set, Figure 88.

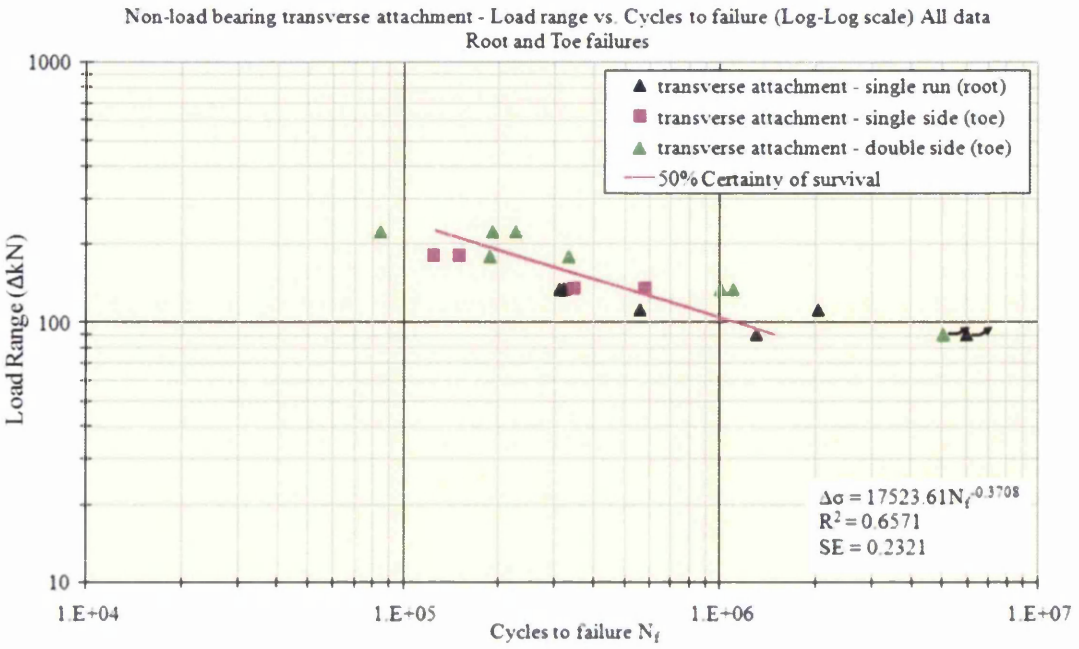

Figure 88: Non-load-bearing transverse attachment- All fatigue data- Load range against cycles to failure (Log ΔkN against Log N_f)

Next the fatigue lives are plotted on a log-log scale as Load range against Cycles to failure (ΔkN against N_f) curve using only the weld toes failures (not including the initial batch of root failures) single and double-sided coupons shown below in Figure 89.

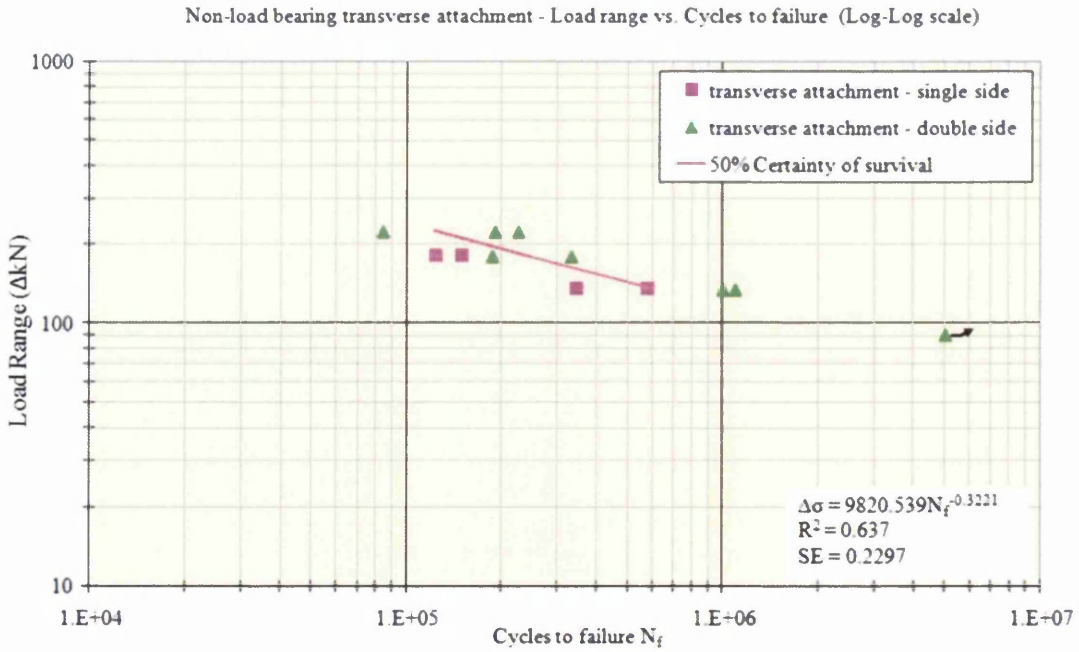

Figure 89: Non-load-bearing transverse attachment- Double and single-sided coupons Weld toe failures- Load range against cycles to failure (Log ΔkN against Log N_f)

The non-load-bearing transverse attachment weld toe failures have been analysed separately based on the joint configuration, single-sided and double-sided weld attachments, Figure 90 and Figure 91 respectively. Completing individual statistical analyses on the single- and double-sided coupons indicates there is a difference in fatigue strength depending on the joint geometry and improved fitted curve despite the similar welding detail and same failure mode. Compared with the original R^2=0.637, Figure 89, the R^2 values increased to 0.9031 for the single-sided and 0.828 for the double-sided coupon. There is a lower fatigue strength for the single-sided coupon.

The single-sided coupon contains an un-symmetrical weld detail (weld runs on only one side of the coupon creating a distorted test piece). This potentially creates two detrimental effects on the fatigue performance. Firstly, a mean stress shift is likely to be introduced into the coupon on clamping the test grips with the micro-strain recordings in Figure 85 supporting this. However, the effects can be considered negligible as the results of tests for previous coupons at different mean stress ratios show there is no effect on the fatigue strength, Figure 72, suggesting there are sufficient residual stresses contained in the small-scale welded coupons. Secondly and most likely, the distorted coupon creates an eccentric loading path to the tensile load applied in the loading frame. Upon deformation the coupon tries to achieve concentricity while inducing a bending moment around the weld toe, and ultimately a moment reducing the fatigue strength of the coupon.

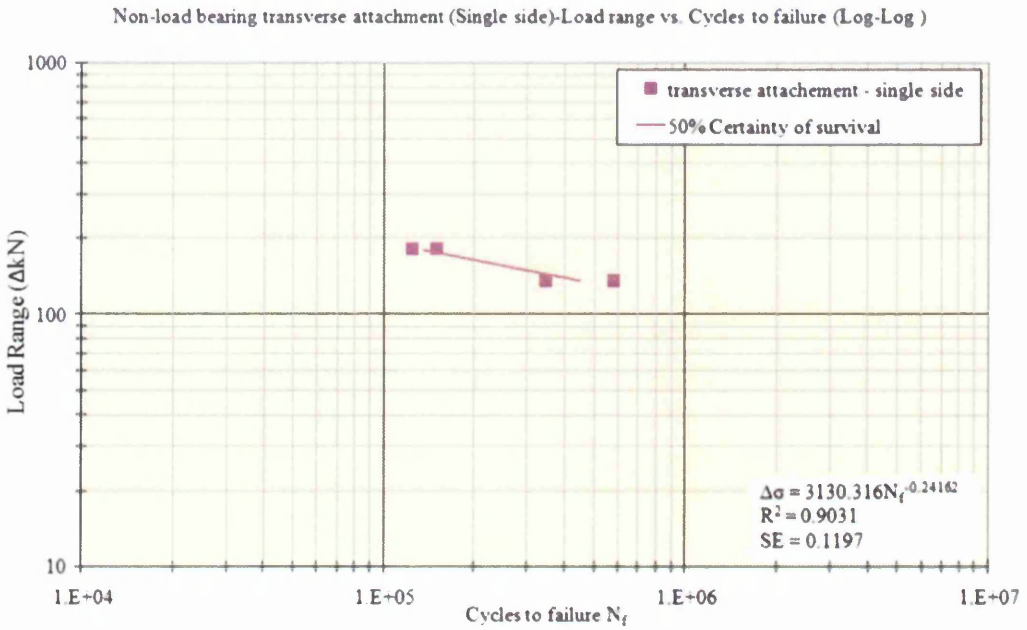

Figure 90: Non-load-bearing transverse attachment- Single-sided coupon- Load range against cycles to failure (Log ΔkN against Log N_f)

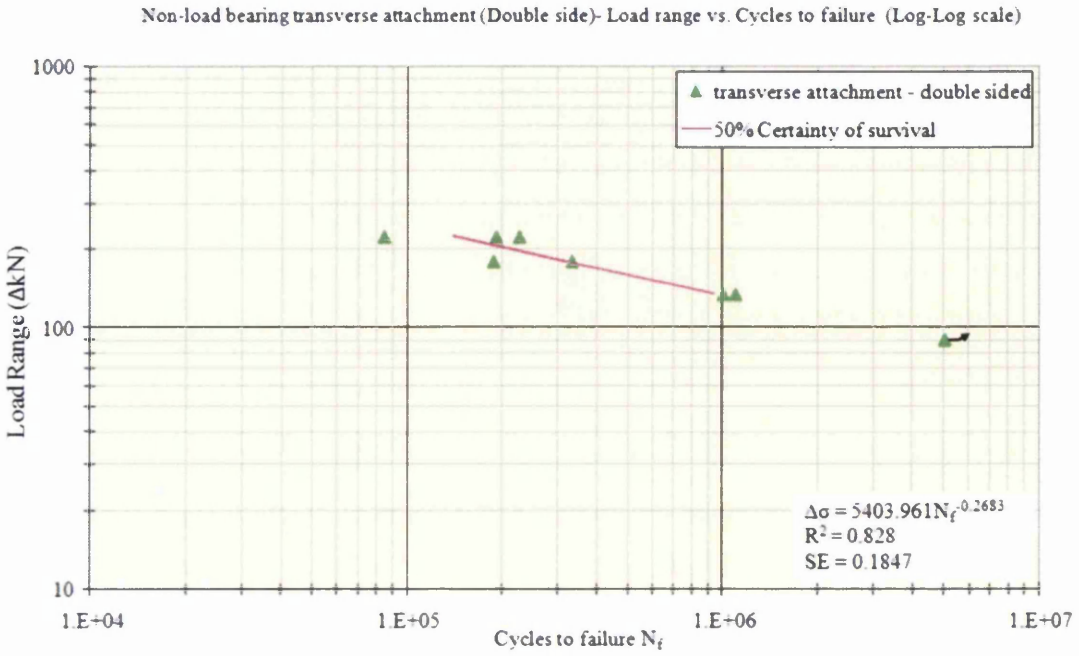

Figure 91: Non-load-bearing transverse attachment- Double-sided coupon- Load range against cycles to failure (Log ΔkN against Log N_f)

The difference in fatigue strength between a double- and single-sided welded coupon, despite having similar welding detail and failure modes, should be considered and analysed separately.

The final fracture surfaces of the single- and double-sided coupons NLT1S and NLT8D are shown in Figure 92. Both coupons demonstrate typical fatigue crack initiation and propagation characteristics on the fracture surface. Crack initiation occurred across the width of the coupon except at the plate edge where the weld detail had been removed.

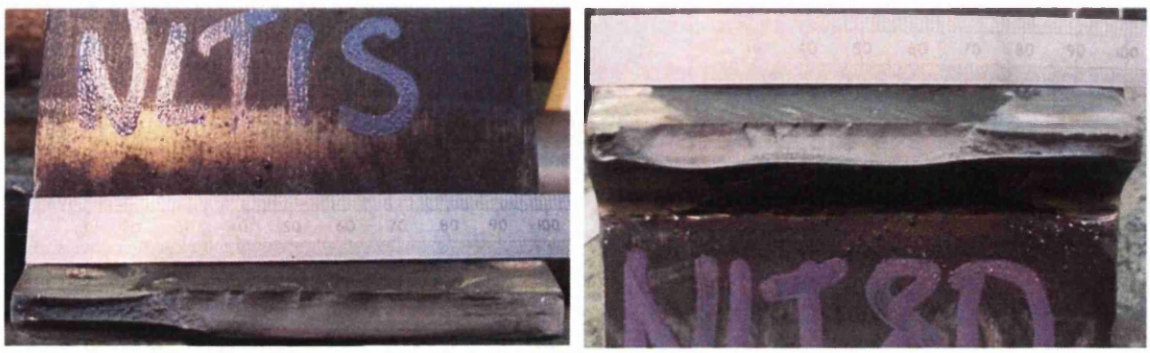

Figure 92: Non-load-bearing transverse attachment fracture surfaces - single (left) and double-sided (right)

4.1.5 Load carrying cruciform joint

Two sets of load-bearing cruciform joints were manufactured. The initial set consisted of 8 samples with an 8mm weld leg length, Figure 93. Six samples were manufactured in the second batch with a weld leg length of 10mm.

Figure 93: Load-bearing cruciform coupon - 8mm weld leg length sample

Electrical resistance strain gauges were placed on the weld side of each coupon at 15mm and 35mm away from the weld toe. During the test set-up, micro-strain measurements were taken and recorded against a set static tensile load applied via the hydraulic servo-controller. The strain gauge data at 15mm and 35mm away from the weld toe for a corresponding tensile load applied are given in Figure 94.

	Applied load	Measured Micro Strain 8mm weld leg 15mm	Measured Micro Strain 8mm weld leg 35mm	Measured Micro Strain 10mm weld leg 15mm	Measured Micro Strain 10mm weld leg 35mm	Stress Force / area	Microstrain Stress / E
	kN	με	με	με	με	MPa	με
Grips clamped up	0	8	12	6	5	0	0
Gauges zeroed							
1	50	286	296	313	313	63	305
2	66.8	380	392	420	419	84	407
3	100	574	593	623	624	125	610
4	150	863	891	924	927	188	915
5	167.2	963	995	1025	1028	209	1020
6	200	1151	1189	1225	1229	250	1220

Young's Modulus E = 205000MPa E = Stress / strain Area = 800mm^2

Figure 94: Measured micro-strain and calculated micro-strain values for 8mm and 10mm weld leg load-bearing cruciform

The 8 samples with an 8mm leg length were tested in the as-welded state at load ranges between 90kN-225kN and a load ratio R=0.1, all tests terminating at full separation, Figure 95. Of the eight samples tested, seven had a failure mode through the weld throat. The remaining sample failed at the weld toe.

Figure 95: Load-bearing cruciform joint 8mm leg failure modes - toe failure (left) and throat failure (right)

The 6 samples with 10mm leg length were tested in the as-welded state at load ranges between 90kN-225kN and a load ratio R=0.1, all tests terminating at full separation, Figure

96. Of the six samples tested, four had a failure mode through the weld throat. The two remaining samples failed at the weld toe.

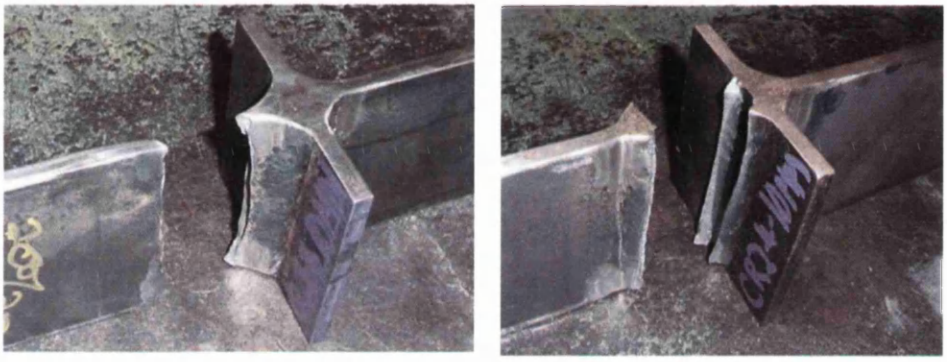

Figure 96: Load-bearing cruciform joint 10mm leg failure modes - toe failure (left) and throat failure (right)

A test running frequency between 4 Hertz and 6 Hertz was achieved without compromising the following error of the load feedback signal. All of the tests were conducted in an ambient air environment. A fatigue life failure was recorded when complete separation of the test coupon occurred as shown in Figure 96. The stiffness parameter k was determined for the test coupon by dividing the peak load by the peak displacement (kN/mm). The stiffness is plotted against the number of cycles (k against N_f) for the 8mm leg length coupons sample 5 (throat failure) and 6 (toe failure) in Figure 97 and Figure 98 respectively.

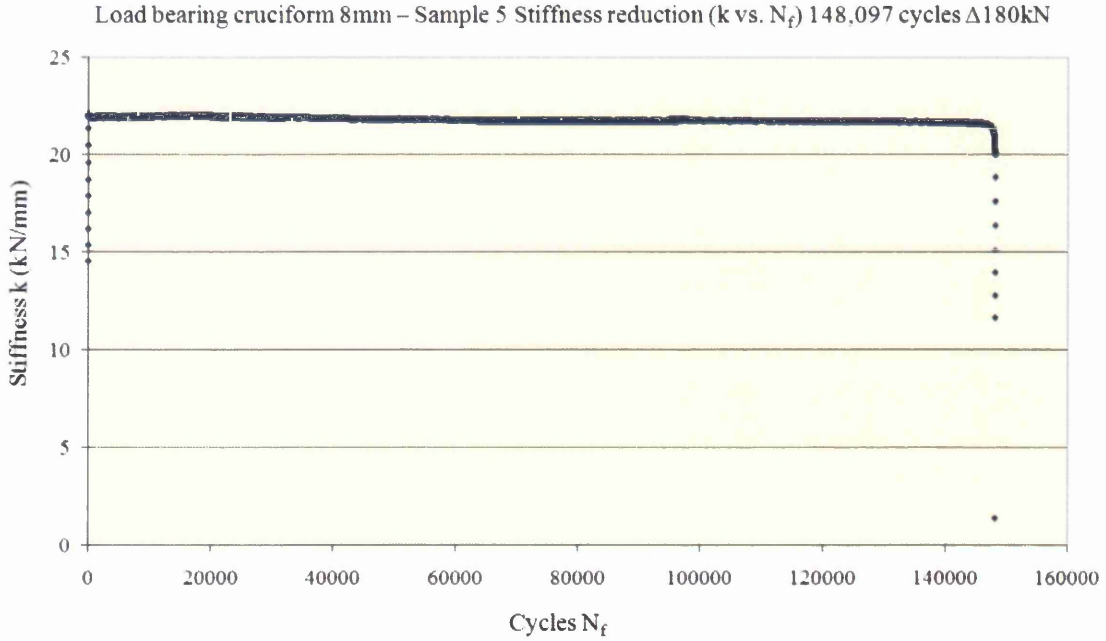

Figure 97: Stiffness (k) reduction curve for Load-bearing cruciform 8mm leg length sample 5

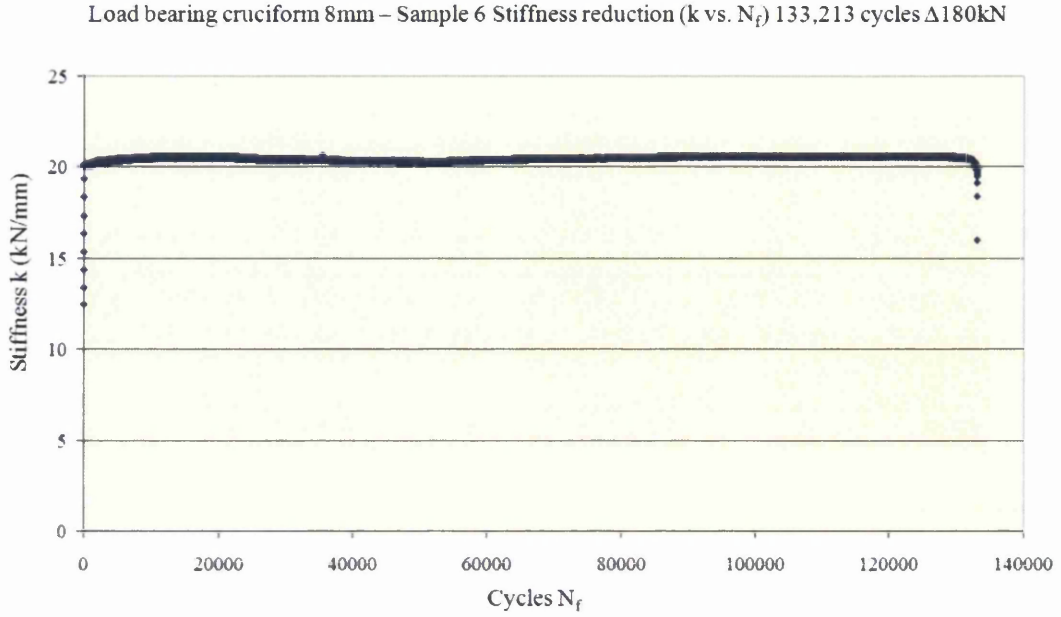

Figure 98: Stiffness (k) reduction curve for Load-bearing cruciform 8mm leg length sample 6

The stiffness is also plotted for the 10mm weld leg length coupon sample 6 in Figure 99. The 3% stiffness drop fatigue lives were derived and then used for further analysis in this work. The 3% stiffness reduction fatigue lives are plotted on a log-log scale as a Load range against Cycles to failure (ΔkN against N_f) curve for both the 8mm and 10mm weld leg length coupons, Figure 100.

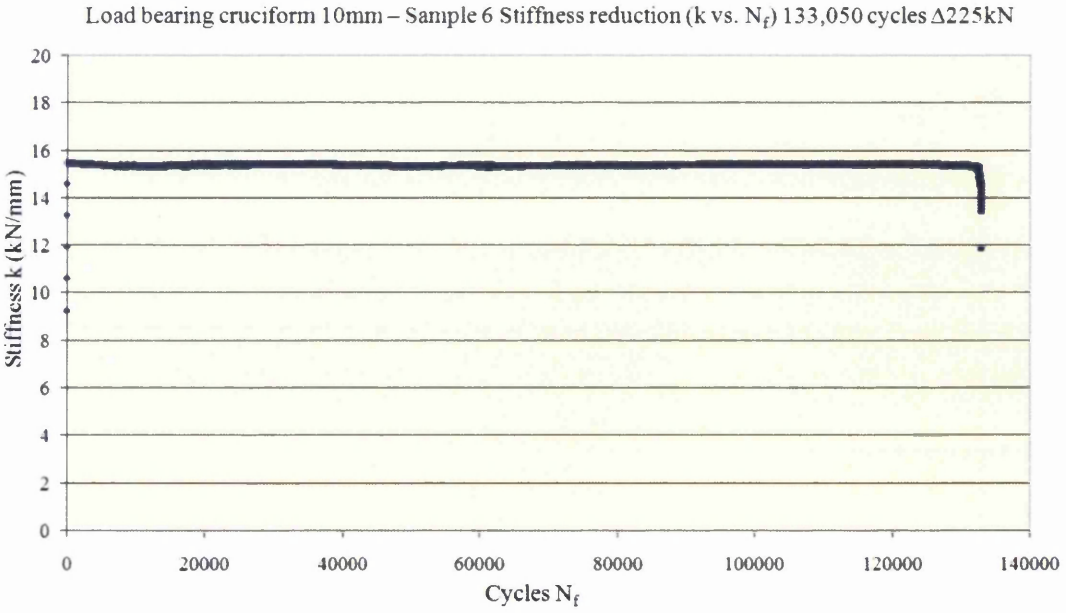

Figure 99: Stiffness (k) reduction curve for Load-bearing cruciform 10mm leg length sample 6

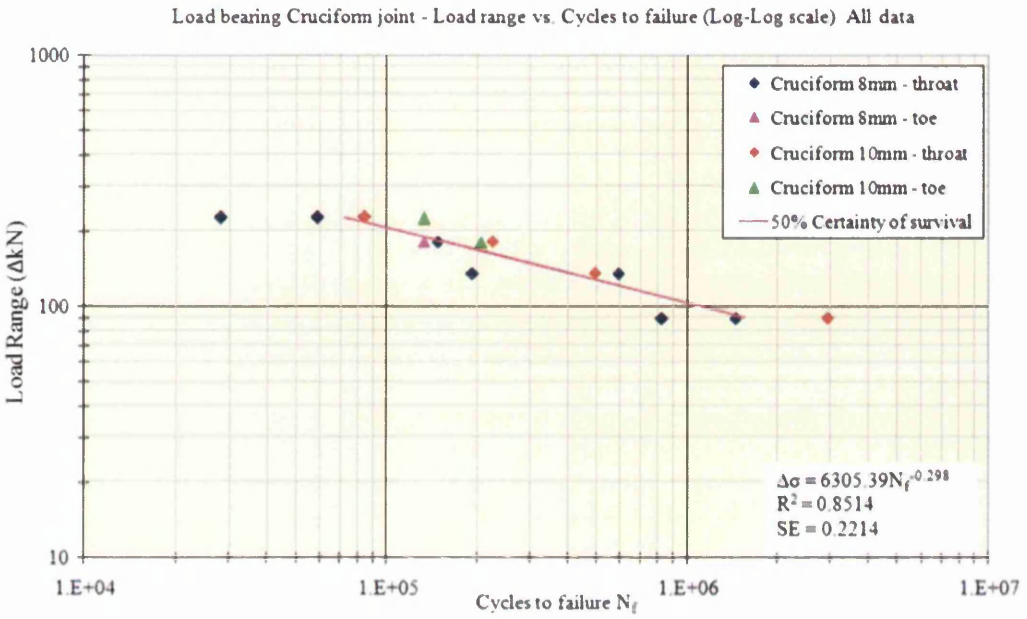

Figure 100: Load-bearing cruciform 8mm and 10mm weld leg - Load range against cycles to failure (Log ΔkN against Log N_f)

The Load range against Cycles to failure (ΔkN against N_f) curves have also been represented whilst considering the 8mm and 10mm weld leg length coupons separately. These are shown in Figure 101 and Figure 102 respectively. Considering the cruciform fatigue data under separate conditions will show any dependency of fatigue strength on the basis of weld configuration. A statistical analysis was completed using a log-linear regression analysis on the x-axis (N_f) of the fatigue data for each condition. Considering all of the fatigue tests as one data set the determined R^2 value = 0.851 with a standard error = 0.221. A statistical analysis on the 8mm and 10mm leg length coupons calculates a R^2 value = 0.895 and 0.977 respectively. It is evident that the strength of association in the regression model is improved for both data sets from the original R^2 value = 0.851. The standard error is also improved for 0.221 originally to 0.2 for the 8mm coupon data and 0.09 for the 10mm data.

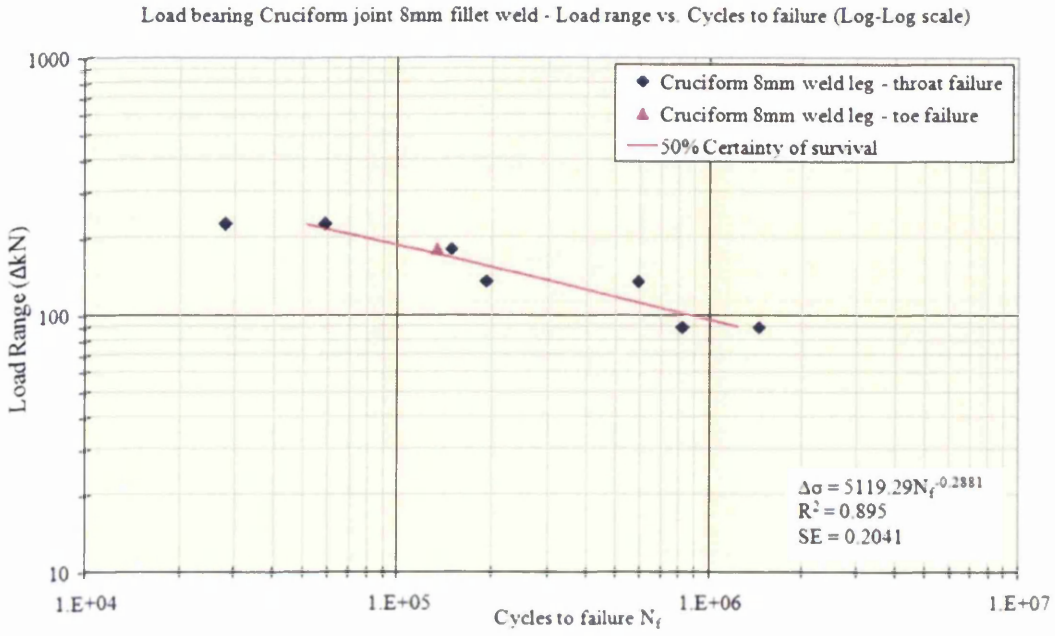

Figure 101: Load-bearing cruciform 8mm weld leg - Load range against cycles to failure (Log ΔkN against Log N_f)

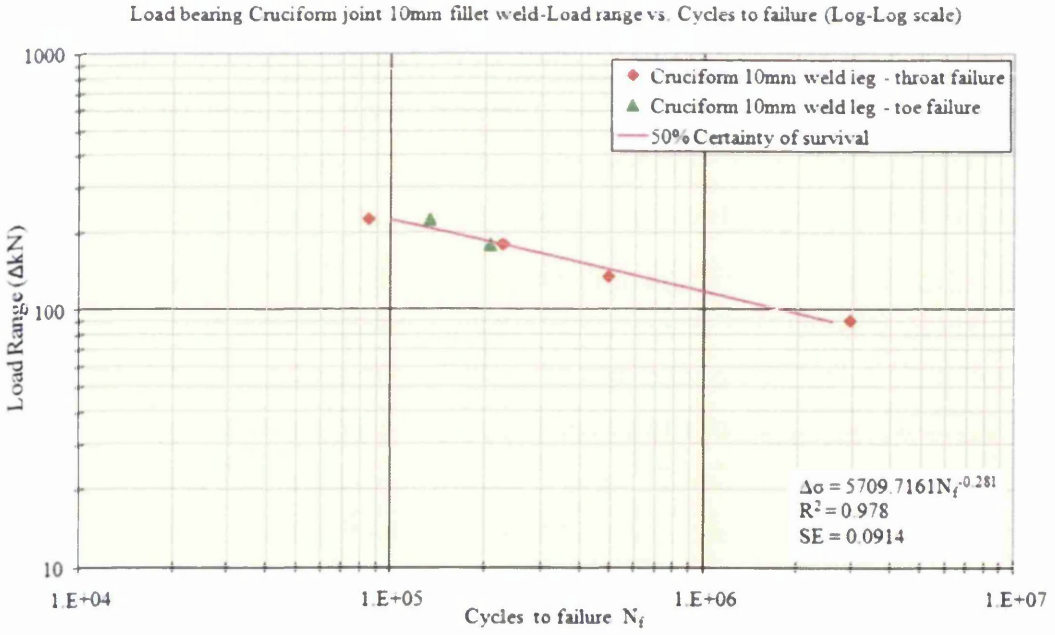

Figure 102: Load-bearing cruciform 10mm weld leg - Load range against cycles to failure (Log ΔkN against Log Nf)

Analysing the fatigue data under separate conditions suggests the 8mm leg length coupons have a reduction in fatigue life compared to the 10mm leg length coupons. This is expected since the fatigue life will be influenced by the throat area and ultimately is a function of the weld leg length. For the same load range applied, the fatigue life of the larger weld area will

be longer as the crack propagation will take longer to final fracture. The fatigue curves would have a slightly different distribution if considering a nominal stress range against cycles to failure. For the same load range applied, a reduced throat fracture surface area would result in a higher stress.

The crack initiation occurred at the throat of the weld penetration where the load carrying plate met the base plate. Initiation could be seen across the width of the coupon throat base. The crack propagated out through the weld throat on both weld runs on either side of the load carrying plate. The crack plane of the weld was approximately 18 degrees from the horizontal base. The final fracture surfaces of the 8mm cruciform samples 1 and 2 are shown below in Figure 103. A significant difference can be seen in weld penetration achieved between the two samples in Figure 103(a) and (b).

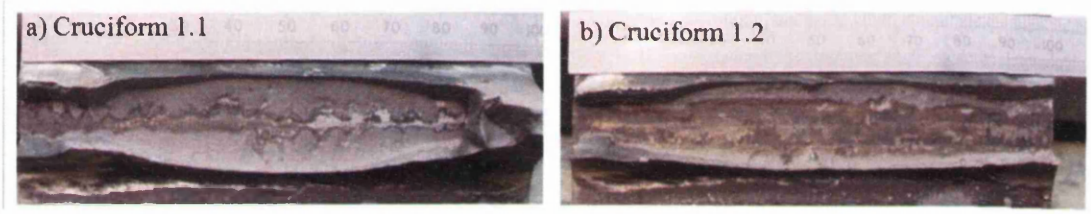

Figure 103: Load-bearing cruciform 8mm weld leg throat failure- weld penetration of sample 1.1 (left) against sample 1.2 (right)

Figure 104: Load-bearing cruciform 8mm weld leg toe failure- sample 1.6

The 8mm cruciform weld toe failure is shown in Figure 104. Crack initiation locations were found on the upper weld toe in Figure 104. The crack propagated through the thickness of the material plate, until the load could not be supported by the remaining coupon area. Final fracture of the specimen occurred as shown by the coarse fracture surface on the right hand side of Figure 104.

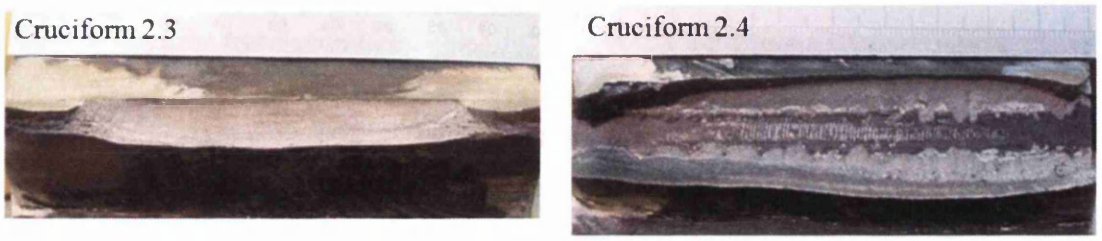

Figure 105: Load-bearing cruciform 10mm weld leg failure modes- sample 2.3 weld toe (left) and sample 2.4 weld throat (right)

The fatigue fracture surfaces of the 10mm cruciform joint are shown in Figure 105. The weld toe failure is shown on the left hand side and the weld throat failure on the right. Weld toe crack initiation occurred on the upper notch. The crack initiated at a number of locations across the coupon, propagating through the plate material evenly. Typical beach marks and burnish striations are seen on the final fracture surface. Final fracture of the coupon occurred on the edges of the plate and is evident through the necking of the material and coarse fracture area. Crack initiation on the throat failure sample occurred at the base of the weld penetration and propagated out through the weld at approximately 18 degrees.

4.1.6 Bending load tee joint

The bending load tee joint is a load-bearing fillet weld similar to previous joint configurations. However an increased bending moment is induced to create an alternative failure mode. The upright plate is welded to the centre of the 300mm wide base plate with two 8mm leg length weld runs.

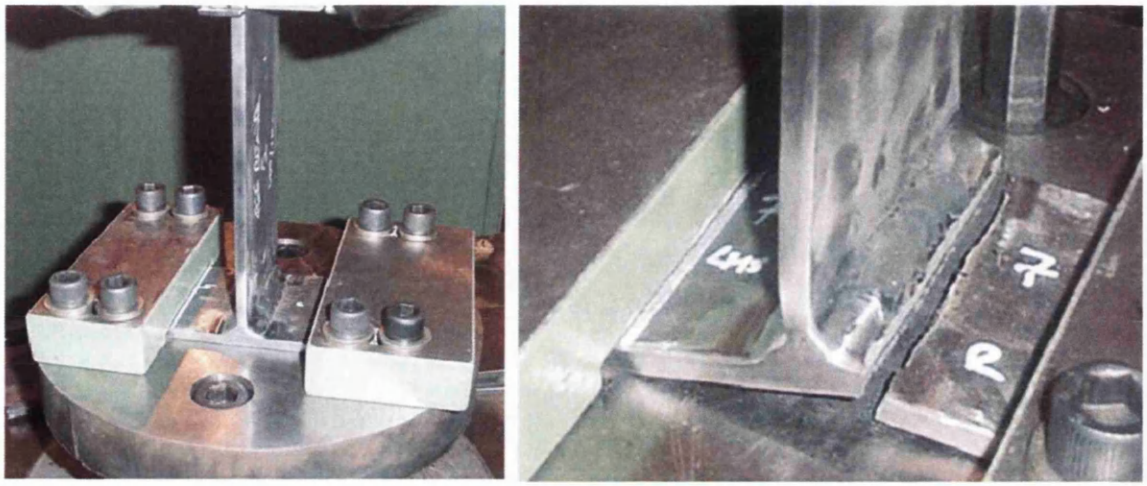

Figure 106: Bending load tee joint testing configuration

The tee joint upright was placed in a set of hydraulic grips and the base was restrained to an attachment plate on the actuator ram with two clamp blocks and M16 bolts, Figure 106. A jig was employed to space the clamp blocks equally 34mm away from the weld toe each side of the upright plate (100mm block to block). Electrical resistance strain gauges were placed on the upright and base plate of each coupon at 15mm and 35mm away from the weld toe. During the test set-up micro-strain measurements were recorded during sample installation and clamp up and under static tensile load applied via the hydraulic servo-controller. The strain gauge data at 15mm and 35mm away from the weld toe for a corresponding tensile load applied are given in Figure 107.

		Measured Micro Strain			
	Applied load	Upright 10mm from toe	Base plate 10mm from toe	Stress Force / area	Microstrain Stress / E
Run	**kN**	**με**	**με**	**MPa**	**με**
Clamp up		13	985	-	-
1	5	33	58	6	30
2	10	66	116	13	61
3	15	100	174	19	91
4	20	133	233	25	122
5	25	165	292	31	152
6	30	198	356	38	183
7	35	233	422	44	213
8	40	267	489	50	244

Young's Modulus E = 205000MPa Area = 800mm^2

E = Stress / strain

Figure 107: Measured micro-strain and calculated micro-strain values for bending load tee joint coupon

12 samples in total were manufactured with an 8mm leg length and tested in the as-welded state at load ranges between 36kN-72kN and a load ratio R=0.1. Out of the 12 samples, 10 tests terminated at full separation, Figure 106 (left hand side). The failure mode and crack initiation occurred at the weld toe on the base plate of the samples. Despite a low load range applied there was obvious panting and gaping between the coupon base plate and the test fixture. A large bending moment is induced and hence high stresses at the weld toe due to the test configuration. The remaining two samples were run outs.

A test running frequency around 4 Hertz was achieved without compromising the following error of the load feedback signal. All of the tests were conducted in an ambient air environment. A fatigue life failure was recorded when complete separation of the test coupon occurred as shown in Figure 106. The stiffness parameter k was determined for the test coupon by dividing the peak load by the peak displacement (kN/mm). Unlike previous

coupon tests where the stiffness reduction has been relatively small before experiencing full separation, the tee joints under a bending load display a longer stage of stiffness reduction and slower crack propagation. The stiffness is plotted against the number of cycles (k against N_f) for samples 3 and 8 in Figure 108 and Figure 109 respectively. The stiffness reduction for samples for a 63kN load range and above, exhibit a slow, long and smooth stiffness reduction. At load ranges below 63kN the stiffness reduction show some temporary crack arrest and a reduction in the rate of crack propagation as shown in Figure 110 and Figure 111 for tee joint samples 9 and 10.

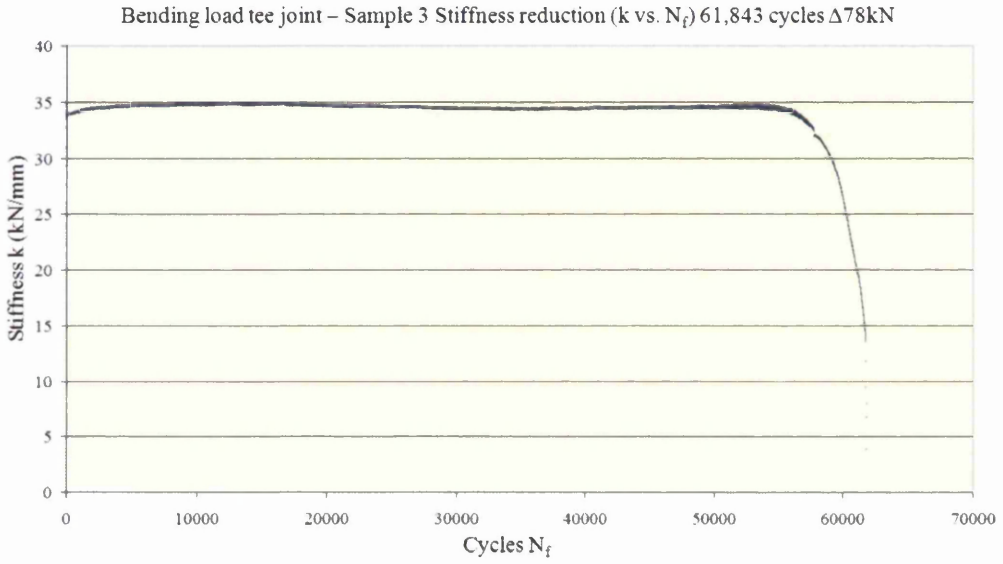

Figure 108: Stiffness (k) reduction curve for Bending load tee joint sample 3

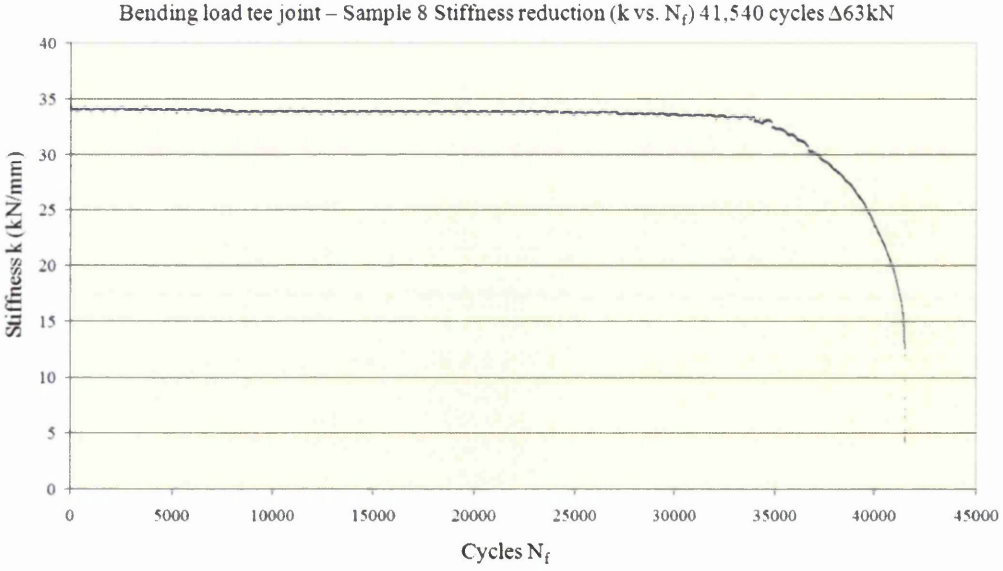

Figure 109: Stiffness (k) reduction curve for Bending load tee joint sample 8

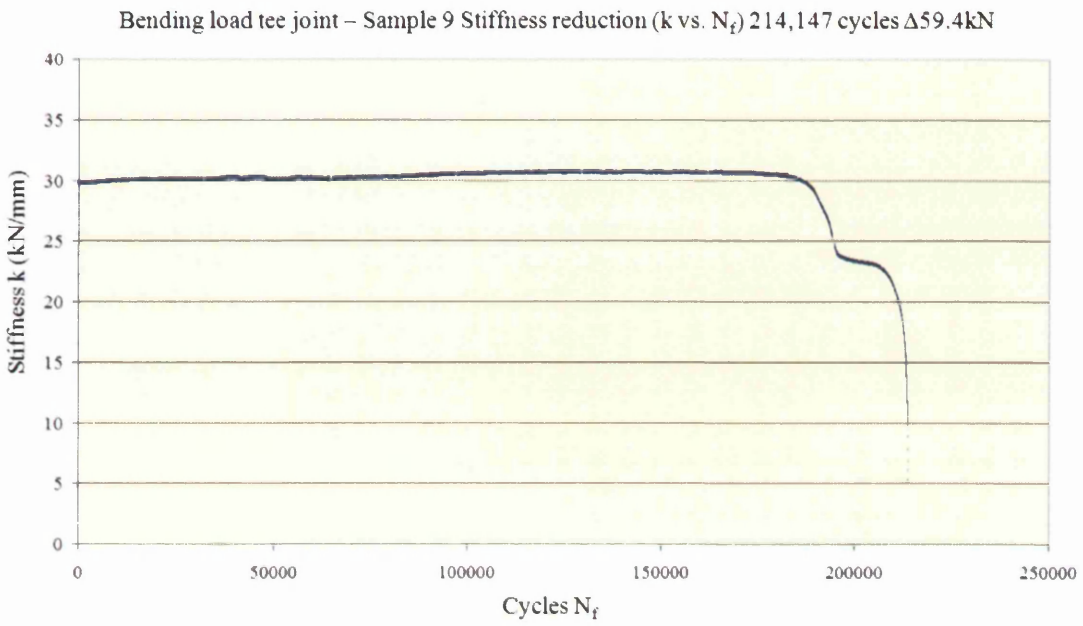

Figure 110: Stiffness (k) reduction curve for Bending load tee joint sample 9

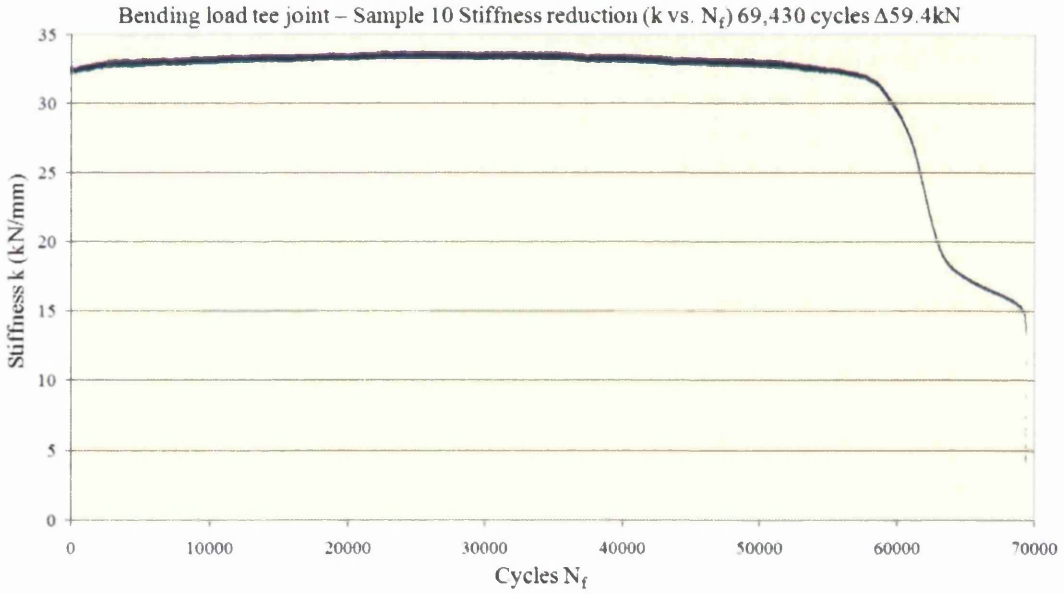

Figure 111: Stiffness (k) reduction curve for Bending load tee joint sample 10

The 3% stiffness drop fatigue lives were derived and then used for further analysis in this work. As the crack propagation in the tee joints is much slower, the 3% stiffness drop failure criterion has a significant impact on the fatigue life unlike previous stiffer coupon geometries. The 3% stiffness reduction fatigue lives are plotted on a log-log scale as a Load range against Cycles to failure (ΔkN against N_f) curve in Figure 112.

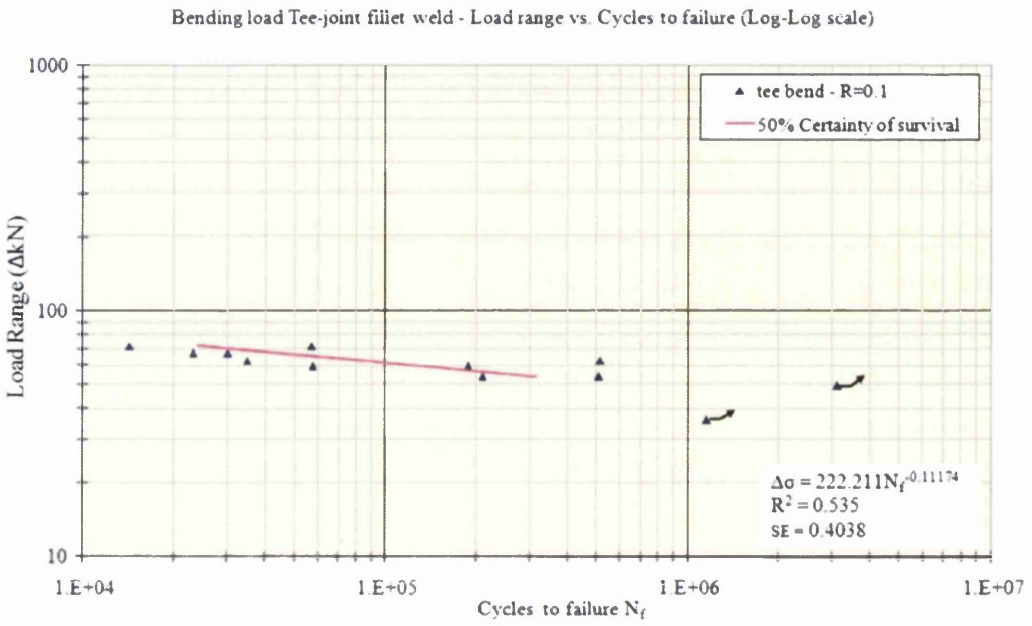

Figure 112: Bending load tee joint coupons - Load range against cycles to failure (Log ΔkN against Log N_f)

A statistical analysis was completed using a log-linear regression analysis on the y-axis (N_f) of the fatigue data, the fatigue lives being the variable. A 50% certainty of survival curve is created and a determined R^2 value = 0.535. The linear association of the regression model is reasonable. As the test configuration used a clamping fixture there are more potential sources of error and reasons for an increase in scatter in the fatigue data. The gradient of the curve is also noticeably different from that of previous coupon test data and the generally assumed 1 in 3 slope for weld fatigue data.

Considering the two test results samples 9 and 10 at the 59.4kN load range, there is a factor of 3 difference in fatigue strength. The stiffness drop behaviour exhibits similar characteristics and k reduction rates between the two samples. Using the measured 3% reduction failure criteria compared with the original full-separation recorded lives, the reduction in fatigue life is 88% and 83% respectively, compared with the average 85% of the original recorded values. The fracture surfaces also demonstrate similar characteristics and the final fracture surface areas are comparable, Figure 113 and Figure 114.

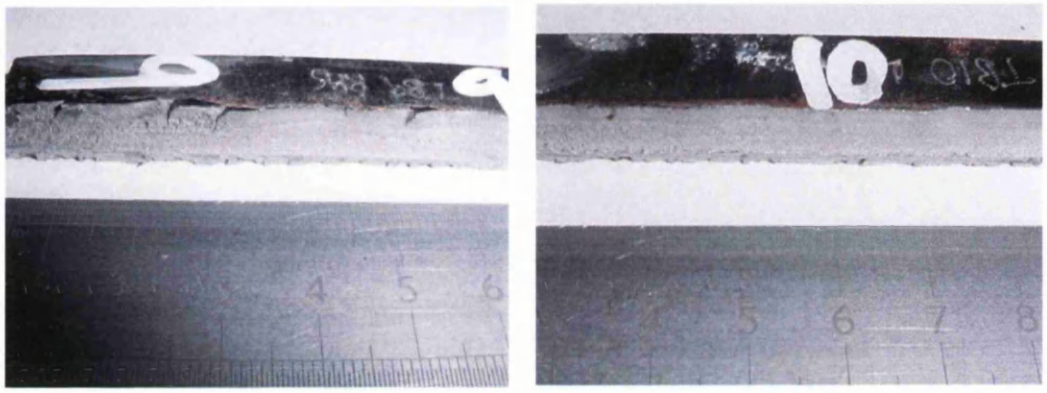

Figure 113: Bending load tee joint fracture surfaces 59.4kN load range- sample 9 (left) and sample 10 (right)

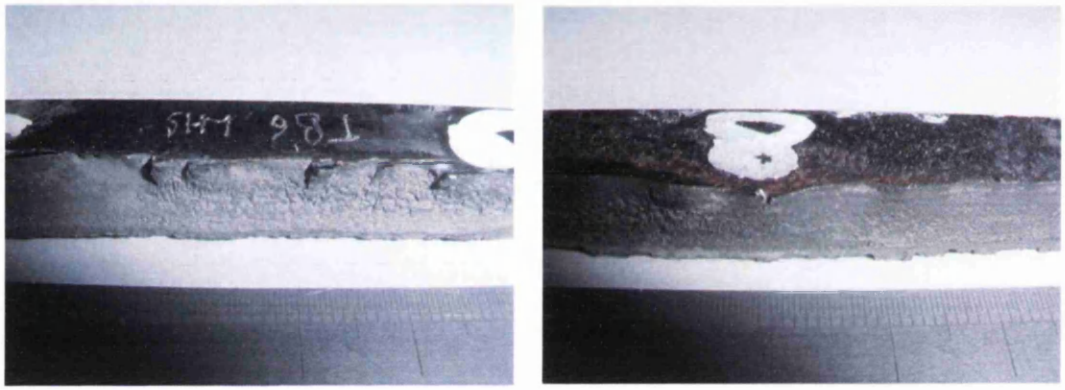

Figure 114: Bending load tee joint fracture surfaces 63kN load range- sample 6 (left) and sample 8 (right)

When comparing the samples 6 and 8 tested at 63kN loads, there is a significant factor of ~12 difference of fatigue strength between the two measurements. The stiffness drop behaviour of sample 6, Figure 115, exhibits an uncharacteristic phenomenon where the displacement feedback decreases dramatically causing the stiffness to increase.

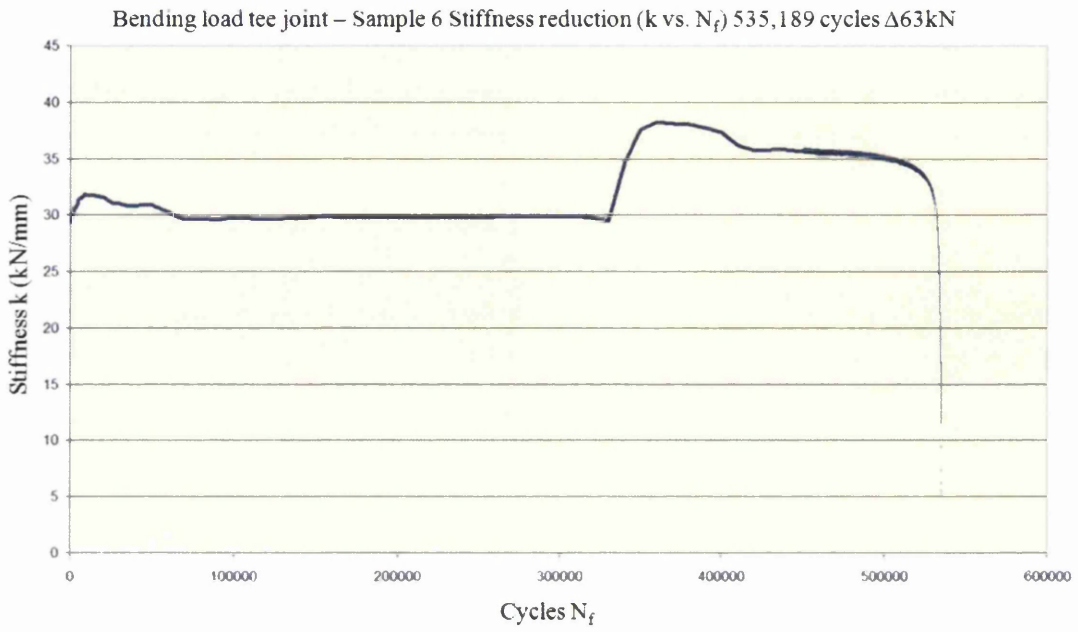

Figure 115: Stiffness (k) reduction curve for Bending load tee-joint sample 6

This is only seen in the one sample and is not consistent with sample 8, Figure 109, for the same load range. Using the measured 3% reduction failure criteria compared with the original full-separation recorded lives, the reduction in fatigue strength is 92% and 84% respectively (of the original measured life), compared with the average 85%. The fracture surfaces demonstrate dissimilar characteristics, particularly the final fracture surface areas as compared in Figure 116. The final fracture area of sample 6 was considerably smaller at approximately 0.5mm depth compared with sample 8 which had a depth of 1mm. Sample 6 also displays much smoother cracks from the base of the coupon, unlike sample 8 where the appearance is a significantly more jagged edge suggesting a difference in force was used to cause the final separation. It is evident that there is a difference in the behaviour of the samples despite being tested at the same load range. It is possible that one of the samples is a rogue result due to the increased potential causes of variability from the test fixture arrangement, as well as the standard sources from differences in the servo-hydraulic controller, test piece material and manufacturing issues. It might also be feasible to suggest that a change of load path or stress distribution occurred. Due to the clamping arrangement of the double fillet weld base plate, the crack propagation may only have penetrated part way through one side of the material thickness. Then, a change in load distribution to the other fillet weld took place. Further to this, it would also be plausible to suggest interference from an unknown source. This might include interference from an unauthorised operator in the vicinity of the test frame and controller or even a blackout of power supply. However, the

fact that the increase in stiffness is not instantaneous, and increase happens over approximately 25,000 cycles, would suggest this is unlikely.

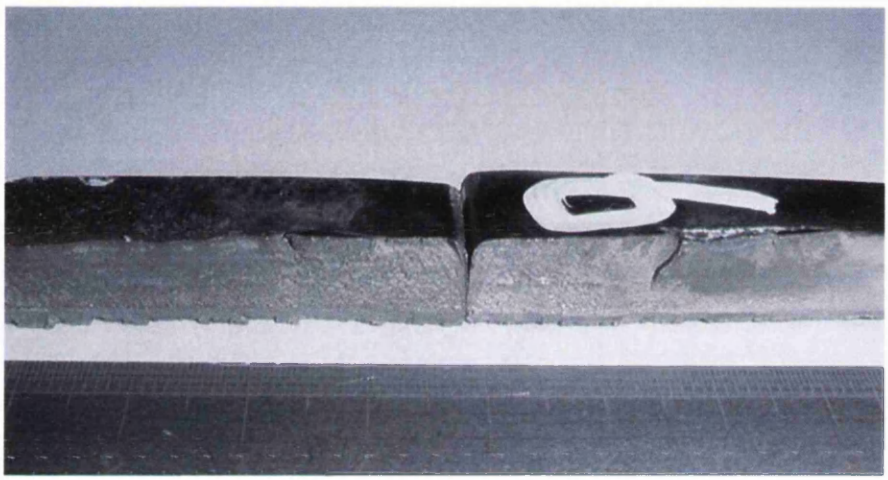

Figure 116: Bending load tee joint fracture surfaces comparison 63kN load range- sample 8 (left) and sample 6 (right)

The uncharacteristic failure aspects of test sample 6 would suggest it is an unexplainable data point and could be excluded from the fatigue curve. Despite this, it would be plausible to accept the test result and put it down to a factor of variability in the weld fatigue phenomenon.

4.1.6 Summary – Coupon data generation

A wide range of welded coupon geometries and loading modes have been tested. Failure modes at the weld toe, weld throat and the weld root have been recorded. The final Load range against cycles to failure (Log ΔkN against Log N_f) fatigue data curves are shown in Figure 117. It is clear that the fatigue performance is geometry dependent. A range of different weld curves is not practical for carrying out a finite-element based weld fatigue life assessment. The coupon geometries show no sensitivity to different load R ratios used, suggesting sufficient welding-induced residual stresses exist. Hence, the test data has captured the weld-induced effects seen (and therefore is potentially suitable for the design stage) in construction and agricultural equipment.

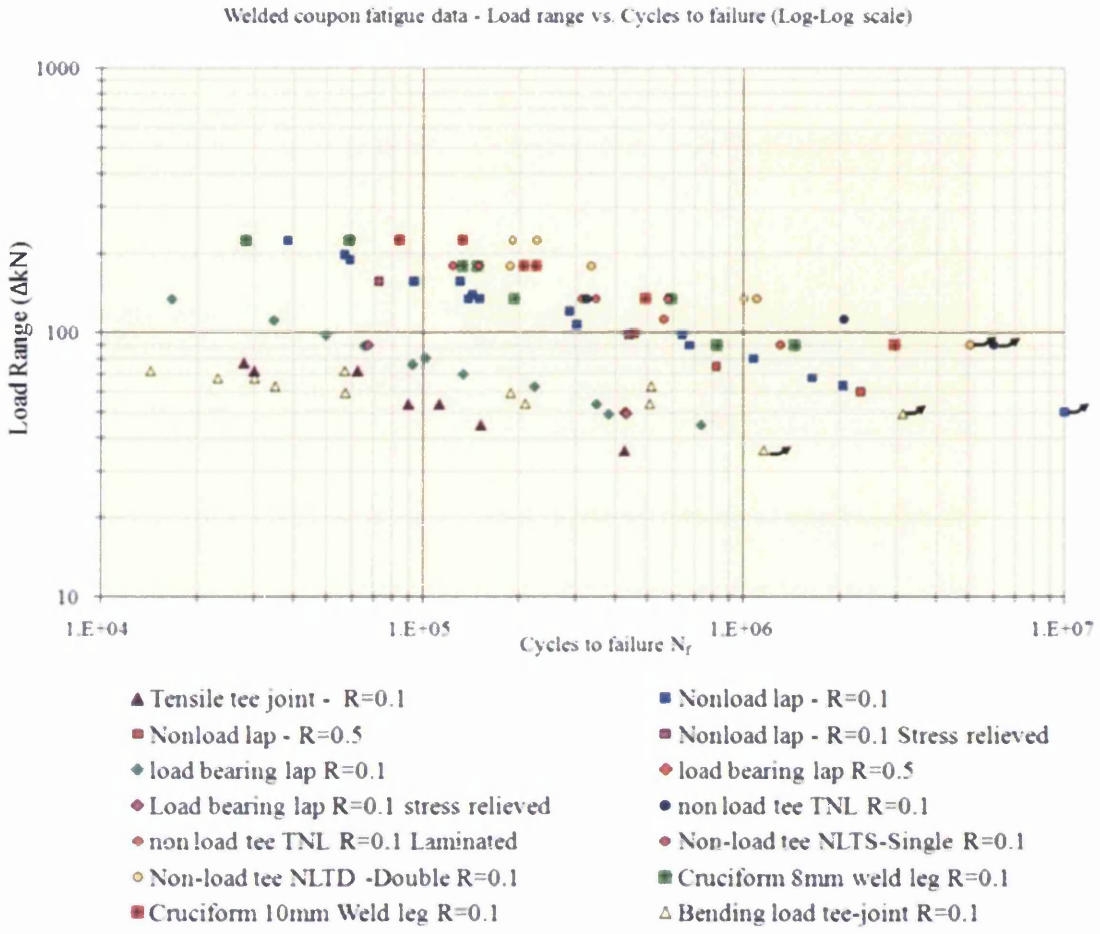

Figure 117: Coupon weld fatigue data -Load range against cycles to failure (Log ΔkN against Log N_f)

The next step is to assess the weld fatigue data using an alternative fatigue damage parameter as opposed to a nominal stress or load for the reasons above. Before determining the new damage parameter or even discovering if it exists, we must analyse the above coupon geometries in a finite-element simulation under an elastic scaling unit load.

4.2 Coupon Finite-Element Models

After generating the geometry-dependent weld fatigue data presented in the previous chapter, the next step in the data generation process is to model the weld fatigue coupon test pieces in a finite element simulation. Each type of coupon geometry and test configuration will be represented using adequate boundary conditions in a linear-elastic static solution analysis. The nodal forces and moments from the solution can then be further used in an attempt to establish a geometry-independent fatigue damage parameter.

The linear-elastic solution will help minimise the computer and modelling effort required compared with a more complex non-linear or dynamic analysis. A static unit load is applied to the coupon and is scalar as the fatigue loading is within the elastic modulus of the material.

4.2.1 Tensile load tee joint

The tee joint coupon is modelled using solid brick and shell plate elements in Figure 118a) and b) respectively. In order to represent the loading frame test configuration a tensile 1kN unit load is applied at one end of the coupon and fixed degrees of freedom at the other end.

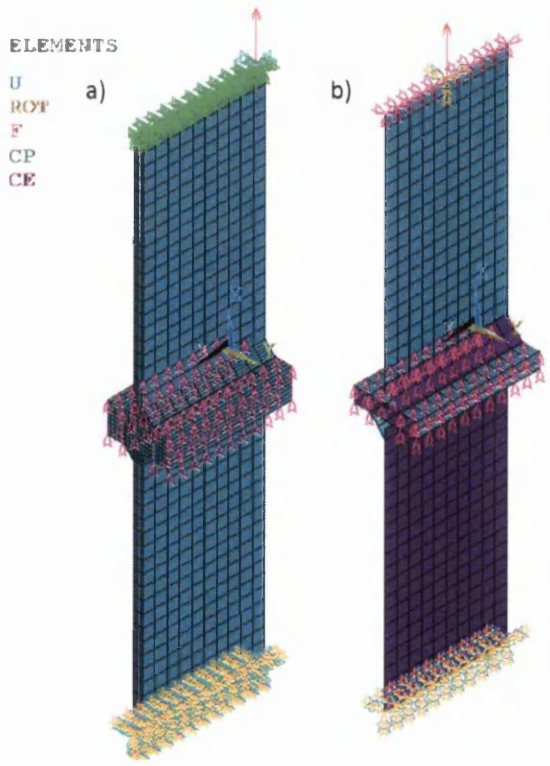

Figure 118: Tensile load tee joint FE-model using a) Solid brick and b) shell plate elements

The tensile tee joints represent the two coupon samples used in the back-to-back test configuration. The two base plates of the coupons are coupled together to simulate the bracing used to clamp the coupons together. In Figure 119 a close up of the weld detail is shown. The coupon upright plate is only connected to the weld metal and not the base plate to represent the partial penetration weld on the coupon.

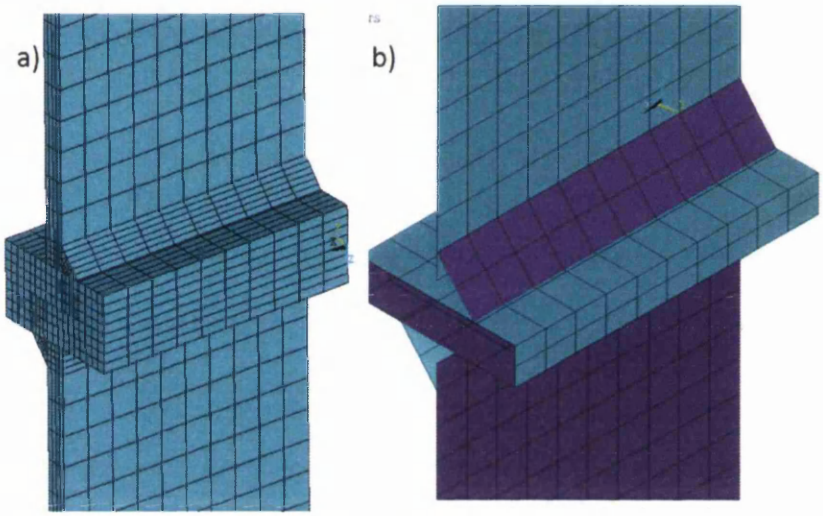

Figure 119: Tee joint FE-model weld detail using a) Solid brick (Cross-section) and b) shell plate elements

In the models shown above a global element size of 10mm is used. The solid brick elements have a through thickness size of ¼ *t* (t= thickness 8mm upright and 12mm for the base plate). The shell plate elements have a real constant set of 8mm for the upright and 12mm for the base plate. In Figure 119, a single diagonal shell element is used to represent the weld bead plate, with a thickness of 8mm. The shell element model is created using automotive model principles for welded shell element structures. A node is placed on the mid-surface thickness of the parent material. The node correlates with the location of the weld toe crack plane, shown in Figure 120.

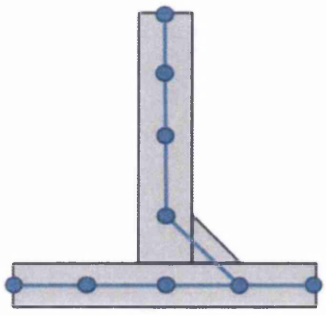

Figure 120: Shell element modelling technique

The element sizes and real constant thicknesses are varied and altered in an attempt to explore the effects on the results of the fatigue damage parameter calculation and whether any mesh sensitivity exists (i.e. coarse- 20mm global and ½ t through thickness element sizes). This is covered in chapter 4.3.

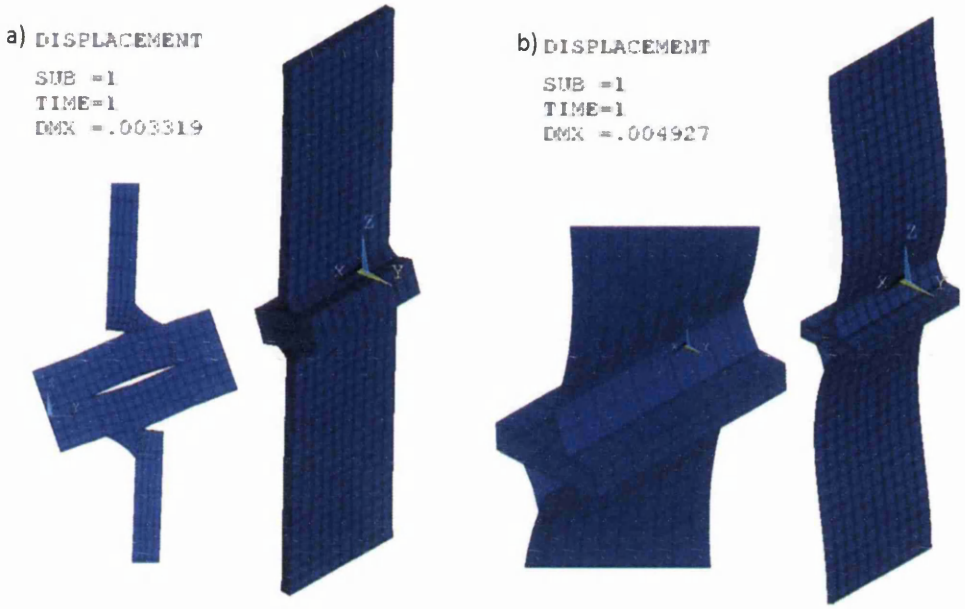

Figure 121: Tee joint FE-model results - displacements a) Solid brick and b) shell plate elements

Due to the potential stress singularity created at a weld toe, we are not concerned with any kind of FE-calculated stress from the solution output. Instead the deformation of the model is reviewed to see if the results are representing similar behaviour to that found in the test coupons. The deformation results are shown in Figure 121 for both the solid and shell element models. As seen in the test coupon results, an offset fillet weld introduces a bending moment. The upright plates bend and the base plate swivels around the horizontal centre line.

Despite the same loading and constraint boundary conditions, there is a difference in maximum displacement between the solid and shell elements. This is expected, due to the challenge presented when using shell plate elements to accurately represent the weld detail. The solid brick element can represent the actual physical geometry of the weld detail whereas the shell plate elements can only calculate a constant uniform theoretical thickness.

4.2.2 Non-load-bearing cover plate

The non-load-bearing cover plate coupon is modelled using solid brick and shell plate elements in Figure 122 a) and b) respectively. In order to represent the loading frame test

configuration a tensile 1kN unit load is applied at one end of the coupon and all degrees of freedom are fixed at the other end. The coupon is modelled in the as-designed state with no distortion of the material, i.e. perfectly flat parent material.

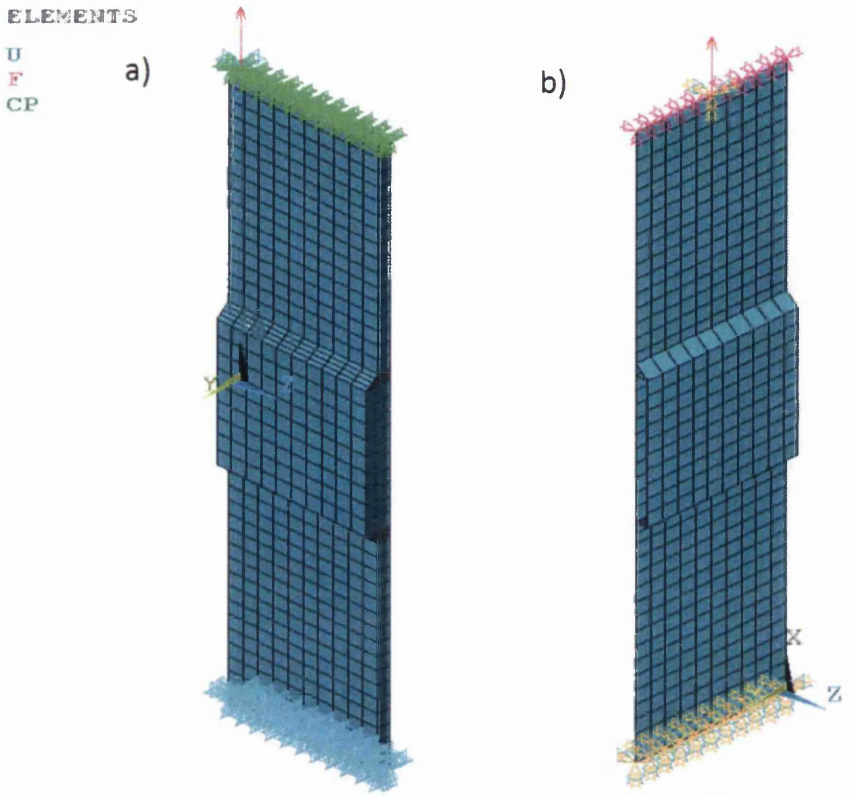

Figure 122: Non-load-bearing cover plate FE-model a) Solid brick and b) shell plate elements

Figure 119A close up of the weld detail is shown in Figure 123. The cover plate attachment is only connected to the weld bead metal and not the load carrying plate parent material.

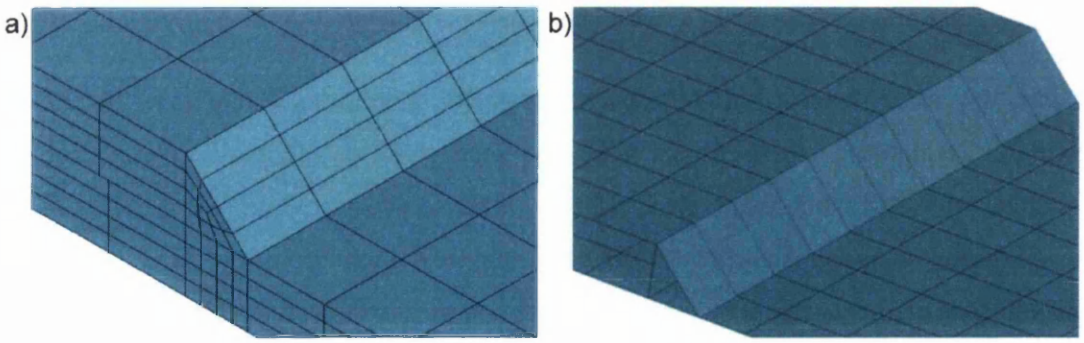

Figure 123: Cover plate FE-model weld detail using a) Solid brick (Cross-section) and b) shell plate elements

In the models shown above a global element size of 10mm is used. The solid brick elements have a through thickness size of ¼ *t* (t= thickness 8mm upright). The shell plate elements of

the parent plate and the weld bead both have a real constant set material thickness of 8mm. The element sizes and real constant thicknesses are varied and altered in an attempt to explore the effects on the results of the fatigue damage parameter calculation and whether any mesh sensitivity exists. This is covered in chapter 4.3.

Figure 124: Cover plate FE-model results - displacements a) Solid brick and b) shell plate elements

The displacement results are shown in Figure 124 for both the solid and shell element models. The solid and shell models under the same loading and constraint boundary conditions, show a small but negligible difference. A displacement of 0.003708mm and 0.003726mm is recorded for the solid and shell models respectively. The difference is expected due to theoretical thickness of the shell plate elements and the inability to accurately represent the weld detail. The difference is very small compared to the previous solid and shell element models of the tee joint coupon geometry. The effect is less significant for the cover plate as the weld shell elements are only an attachment and not a load carrying structural member. This will have less of an influence on the displacement and stiffness of the coupon.

During test set-up of the coupon in the loading frame, distortion of the welded geometry is evident when the coupon does not fit into the grips centre line. The single-sided weld runs cause distortion and curvature in the coupon plate. The cross-sectional area of the coupon

was determined (out of the test frame) using a co-ordinate measurement machine. The co-ordinates of the area were plotted into the finite-element software and a mesh created.

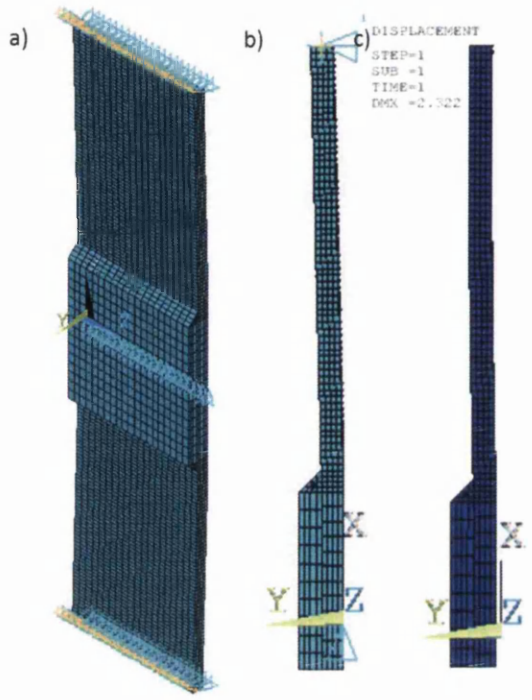

Figure 125: Cover plate FE-model -distorted geometry and test grips clamp-up

The finite element model in Figure 125 a) and b) represents the actual distortion of the coupon and fixed displacements and rotations are applied to the coupon ends to simulate the actuation of the hydraulic grips closing and clamping up. In c) after the solution is run, the geometry shows some slight distortion and mis-alignment from the centre line load path of the load-carrying back plate. The geometry is different to the initial cover plate 'perfect' as-designed geometry of the coupon shown in Figure 122.

The actuation of the test grips will cause a mean shift in the stress state of the coupon inducing residual stresses. This is unlikely to greatly affect the fatigue performance as it is a common assumption that welded components already containing high residual stresses. The geometry of the coupon will, however, need to be accurately modelled. The nodal displacements from the solution in Figure 125 c) are used to create an updated finite element simulation for the distorted cover plate coupon in-situ in the test configuration. The FE model is again run with the loading frame test configuration and a tensile 1kN unit load, Figure 126 a).

Figure 126: Non-load-bearing cover plate distorted FE-model

In Figure 126b) the displacement results of the cover plate static tensile unit load are plotted. Compared with the original undistorted coupon displacement results in Figure 124, although exaggerated, it is clear that the loading path changes due to the distortion in the welded coupon. In the un-distorted coupon, the cover plate attachment is forced into the tensile loading path. In the distorted coupon, the cover plate attachment is being forced away from the loading path. It is therefore highlighted how important it is to model the geometry accurately to that in the physical test.

4.2.3 Load-bearing lap joint

The lap joint coupon solid-brick and shell-plate element models are shown in Figure 127 a) and b) respectively. The model is created simulating the loading frame test configuration under a tensile 1kN unit load. The coupon is modelled in the as-designed state with no distortion of the material. Due to the symmetrical nature of the weld runs, the distortion in the actual coupon geometry was small and any change in coupon geometry during test set-up are considered negligible not requiring any further modelling.

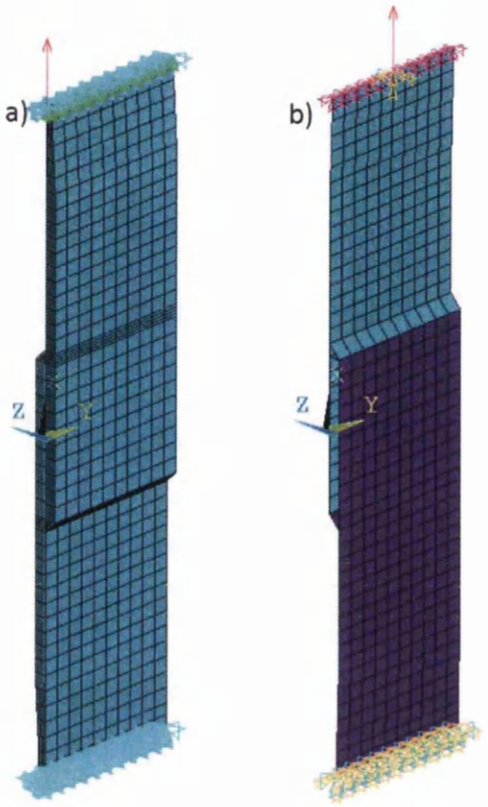

Figure 127: Load-bearing lap joint FE-model a) Solid brick and b) shell plate elements

The displacement results are shown in Figure 128 for both the solid and shell element models under a unit load. The solid element model has a recorded maximum displacement of 0.009875mm and the shell model 0.009465mm. There is a small difference between the two types of element model. Due to the offset lap configuration, a high bending moment is experienced at the weld toe.

Figure 128: Load-bearing lap joint FE-model results - displacements a) Solid brick and b) shell plate elements

4.2.4 Non-load-bearing attachment

The first batch of non-load-bearing attachment coupons made consisted of a transverse plate welded with a single fillet pass as shown in Figure 81. The resulting failure mode occurred at the root of the weld and the crack propagated into the parent material. This was not the intended failure mode and further modified coupons were manufactured.

In an attempt to assess the capabilities and effectiveness of the structural stress approach, the root failure coupons have been modelled. The non-load-bearing attachment-single weld run coupon is modelled using solid brick elements. The geometry shown in Figure 129 uses the dimensions measured from the co-ordinate measurement machine. To determine the actual coupon geometry in the test configuration an initial FE simulation is run to model and represent the closing and actuation of the hydraulic grips in the test frame. This is done through fixed displacements and rotations applied to the coupon grip-to-grip distance.

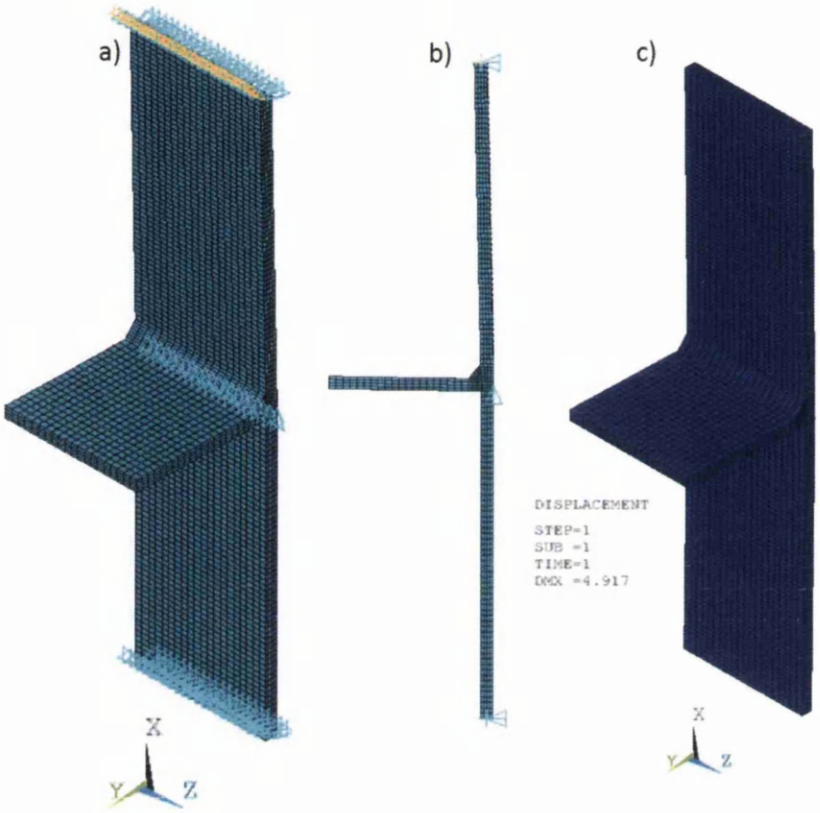

Figure 129: Non-load-bearing transverse attachment root failure - test grips clamp-up model

In Figure 128 c) after the solution is run, the geometry shows distortion and mis-alignment from the centre line load path of the load-carrying back plate. The geometry is therefore different to the intended perfectly straight coupon due to the heat-up, cooling and contraction cycle of the fusion welding process. The final nodal displacements shown in Figure 129c) are used for the means of structural stress calculation and a more accurate representation of the actual coupon geometry. The updated geometry is used in a unit load FE static analysis with simulation of the testing frame configuration.

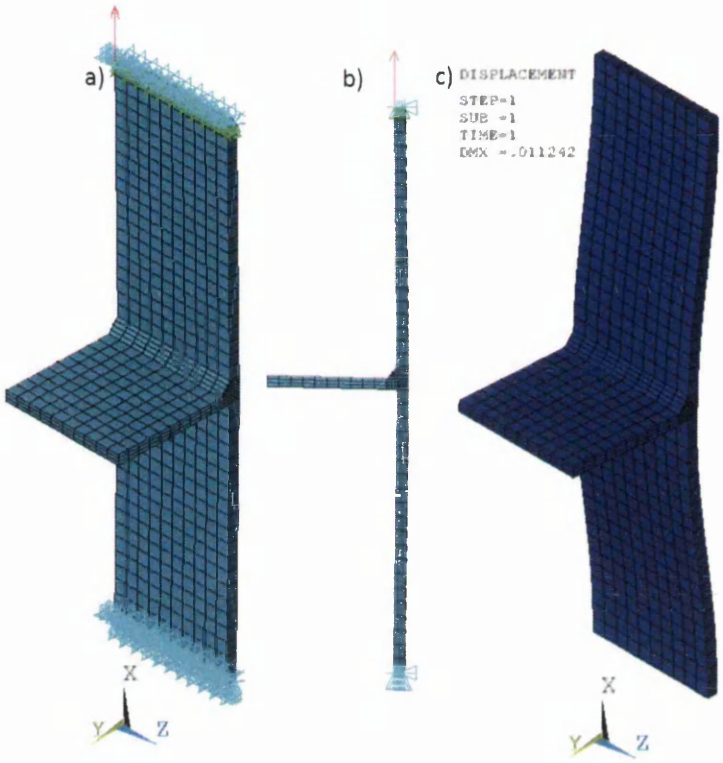

Figure 130: Non-load-bearing transverse attachment root failure - test frame tensile unit load

The solid brick elements have a global element size of 10mm and a through thickness size of ¼ *t* (t= thickness 8mm upright). The displacement results are shown above in Figure 130c). From this model, forces and moments can be extracted and a structural stress factor per unit load calculated for the weld root failure, found in Chapter 4.3.

The second batch of non-load carrying transverse attachment coupons manufactured consisted of a double-sided attachment with four weld runs as shown in Figure 84. The coupon is modelled using solid and shell elements shown in Figure 131a) and Figure 132a) respectively.

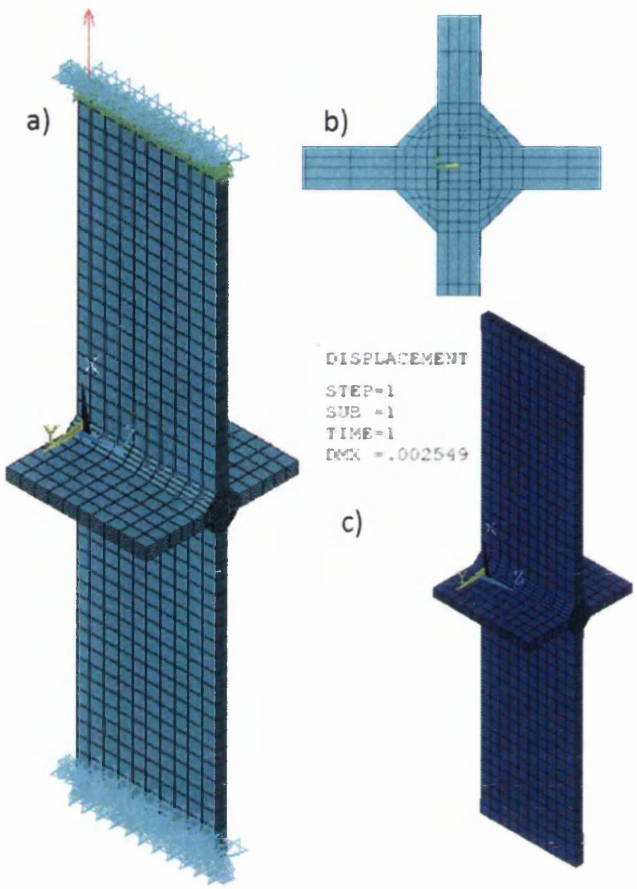

Figure 131: Double-sided non-load-bearing attachment- Solid brick elements

The loading frame test configuration was simulated with a tensile 1kN unit load applied. The coupon is modelled in the as-designed state with no distortion of the material. Due to the symmetrical nature of the weld runs, the distortion in the actual coupon geometry was small and any changes in coupon geometry during test set-up are considered negligible not requiring any further modelling.

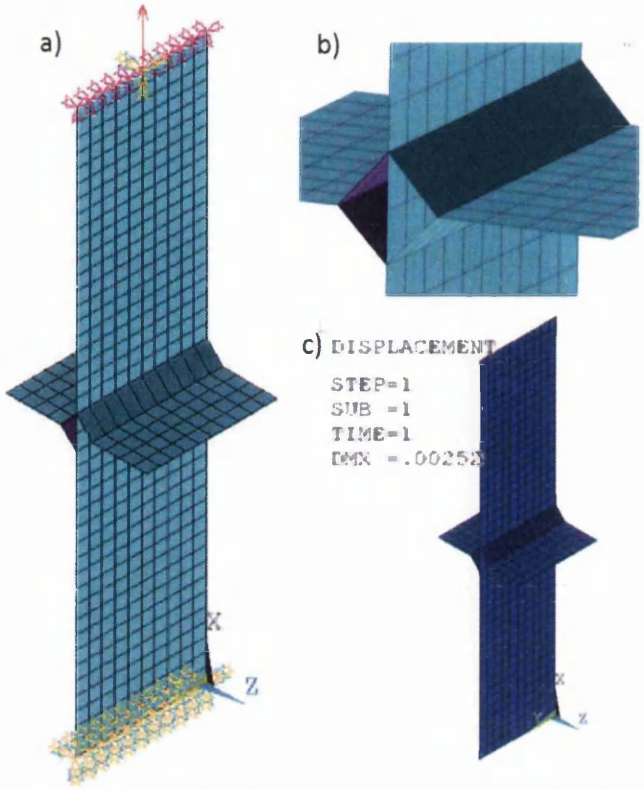

Figure 132: Double-sided non-load-bearing attachment – Shell plate elements

The displacement results are shown in Figure 131c) and Figure 132c) for both the solid and shell element models. There is a small difference in displacement between the solid and shell element results. The weld attachment will have only a small influence on the deformation. In the tensile load tee joint, the load is fully carried through the weld and a clear difference exists between the shell and solid element results. Unlike the difference here, where it is negligible.

The non-load-bearing transverse attachment single-sided coupon is modelled using solid brick and shell plate elements in Figure 133 a) and Figure 134 a) respectively. The boundary conditions replicate the conditions seen in the test coupon with a tensile 1kN unit load applied. The coupon is modelled in the as-designed state with no distortion of the material due to the heat and cooling of the weld cycle.

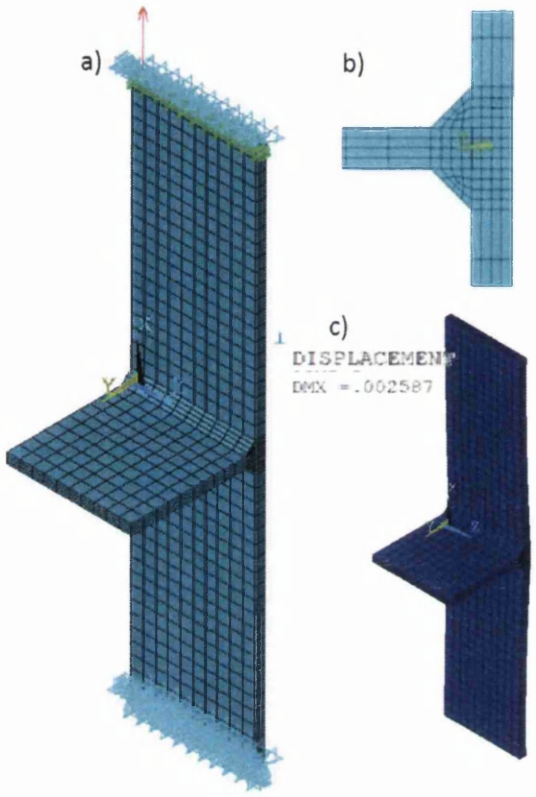

Figure 133: Single-sided non-load-bearing attachment- Solid brick elements

A close up of the weld detail is shown in Figure 133 b) and Figure 134 b). The solid elements fully represent the weld geometry, with some defeaturing of the weld bead and penetration. The shell element model only simulates the mid-plane material geometry with a theoretical thickness.

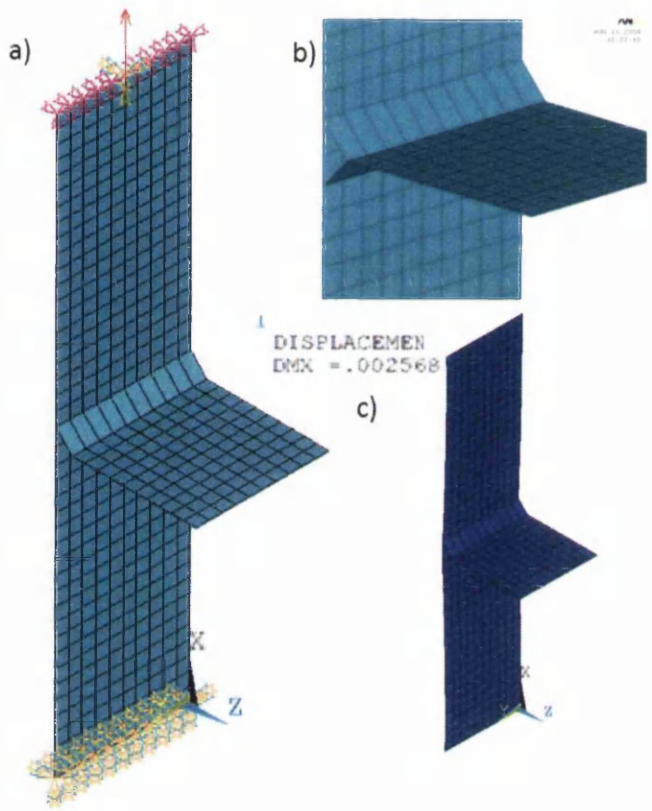

Figure 134: Single-sided non-load-bearing attachment- Shell plate elements

The displacement results are shown in Figure 133 c) and Figure 134c) for both the solid and shell element models. The load carrying upright plate deforms away from the attachment, as the weld is forced into the tensile load path. The load carrying plate becomes a curved, concave shape. The same loading and constraint boundary conditions are used but there is a small difference between the solid and shell elements, with displacements of 0.002587mm and 0.002568mm respectively. This is again caused by differences in the modelling techniques of solid and shell elements. The theoretical thickness of the shell plate element has limitations in accurately representing the weld detail.

During test set-up of the coupon in the loading frame, distortion of the welded geometry is obvious when the coupon does not fit into the grips centre line. The single-sided weld runs cause distortion and curvature in the coupon plate. The cross-sectional area of the coupon was determined using a co-ordinate measurement machine. The co-ordinates of the area were plotted into a finite-element software package and a mesh created.

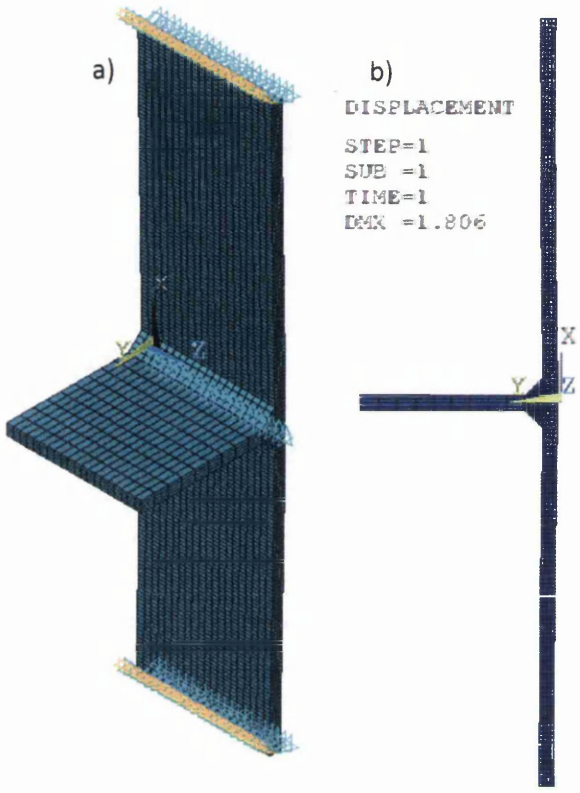

Figure 135: Single-sided non-load-bearing attachment FE-model -distorted geometry and test grips clamp-up

The finite-element model in Figure 135 represents the actual distortion of the coupon and fixed displacements and rotations are applied to the coupon ends to simulate the actuation of the hydraulic grips closing and clamping up. In b) after the solution is run, the geometry shows some slight distortion and mis-alignment from the centre line load path of the load-carrying back plate i.e. the load carrying plate is concave and curved into the weld. The geometry is different to the initial 'perfect' as-designed geometry of the coupon and so the geometry must be accurately modelled. The nodal displacements from the solution in c) are used to create an updated finite element simulation for the distorted geometry in-situ in the test configuration. The FE-model is again run with the loading frame test configuration and a tensile 1kN unit load applied, Figure 136 a).

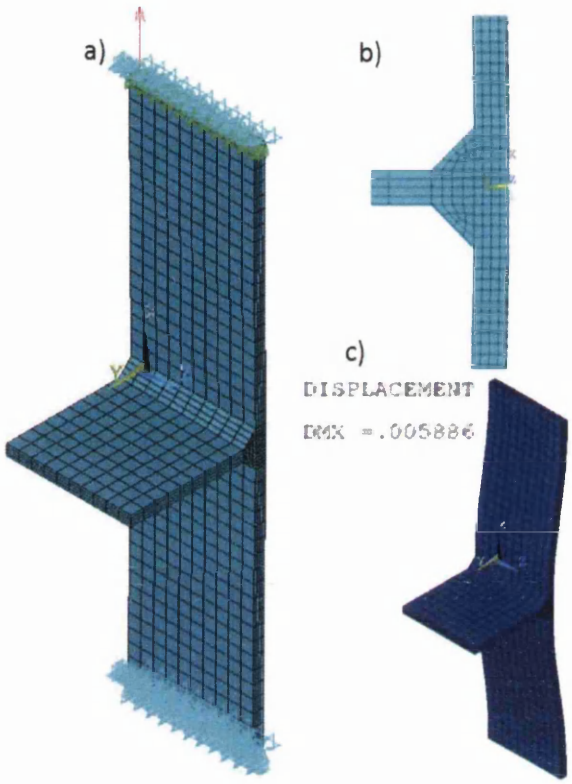

Figure 136: Single-sided non-load-bearing attachment distorted coupon FE-model and unit load

In Figure 136 c) the displacement results of the cover plate static tensile unit load are plotted. Compared with the original undistorted coupon displacement results in Figure 133, although exaggerated, it is clear that the loading path changes due to the distortion in the welded coupon. In the un-distorted coupon, the plate attachment is forced into the tensile loading path and the plate becomes a concave shape. In the distorted coupon, the plate attachment is being forced away from the loading path into the weld attachment. The main load carrying plate experiences a slightly different load (and stress) distribution and is forced into a convex shape. It is therefore highlighted how important it is to model the geometry accurately to that in the physical test.

4.2.5 Load carrying cruciform joint

The load-bearing cruciform joint coupon is modelled using solid brick and shell plate elements in Figure 137a) and Figure 138a) respectively. The FE models were run using the test frame boundary conditions under a 1kN unit load.

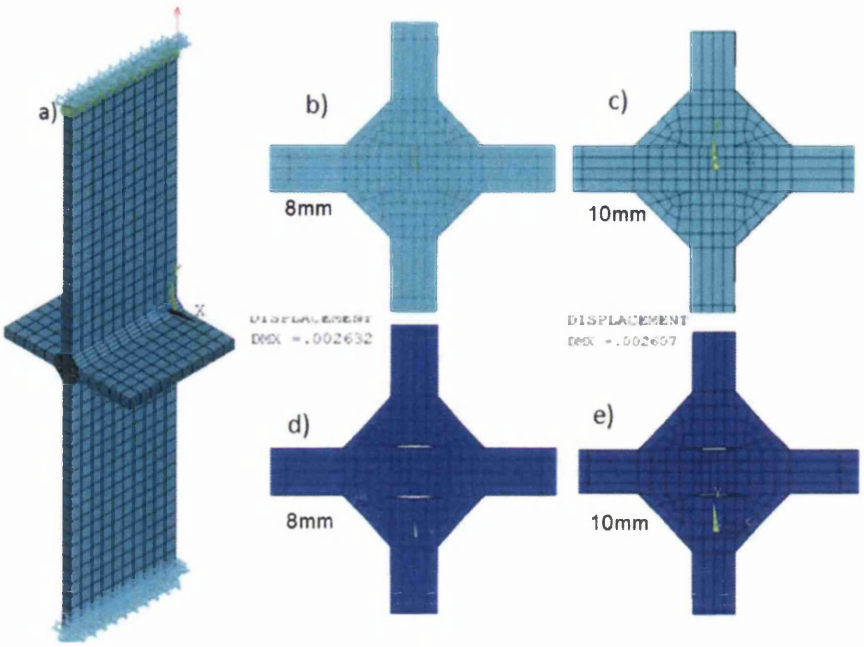

Figure 137: Load-bearing cruciform joint FE-model solid brick elements

The coupon is modelled in the as-designed state with no distortion of the material. There were negligible levels of distortion in the coupon geometry during test set-up. This was confirmed with the micro-strain values recorded upon installation (<12με), shown previously in chapter 4.1.8.

A close up of the weld detail is shown in Figure 137b) and c) for the 8mm and 10mm weld leg solid element model, and Figure 138b) for the 8mm weld leg shell element model. A shell model was also created with a 10mm shell thickness at the weld material. The nodes at the intersection of the plate uprights and horizontal load carrying plates are not connected. The parent plates are only connected to the weld bead metal, not each other creating a fit-up gap as found in the actual coupon.

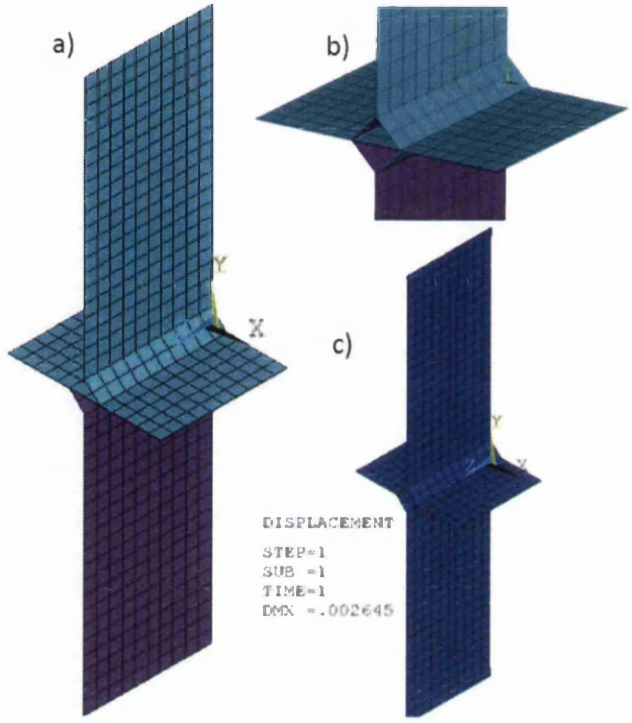

Figure 138: Load-bearing cruciform joint FE-model shell plate elements

In the models shown above a global element size of 10mm is used. The solid brick elements have a through thickness size of ¼ *t* (t= thickness 8mm upright). The levels of penetration achieved in the test coupon were varied, creating different sizes of fit-up gaps at the weld root. This was replicated in the FE models; initially with idealised weld geometry with no penetration. Subsequent models were then created with 1mm, 2mm, and 3mm penetrations and sidewall fusion into the parent plate. The effects of which were explored during the structural stress calculation in chapter 4.3.

The displacement results are shown above for both the solid and shell element models. There is a difference in displacement between the 8mm and 10mm weld leg length solid models due to the increased cross-sectional area. There is a slight discrepancy between the solid and shell elements again due to theoretical thickness of the shell plate elements and the inability to accurately represent the weld detail. Due to the type of failure, the location of the shell weld element is critical in simulating the test coupon load path. A majority of the load flows around the crack at the root of the weld. In the shell mid-plane geometries this feature is not present and load is transferred through the weld toe node on the horizontal base. Again, the effects of the modelling techniques are explored in the structural stress calculation in chapter 4.3.

4.2.6 Bending load tee joint

The bending load tee joint is modelled using solid brick and shell plate elements in Figure 139a) and Figure 140a). In order to represent the loading frame test configuration a tensile 1kN unit load is applied at the upright plate of the coupon. The braced section of the base plate is restrained in the translational y and z degrees of freedom. The translational y DOF of the nodes under the clamped area, are unrestrained in order to simulate the material flow accurately. A node along the centre line of the coupon is fixed in the translational x direction to stop the model moving along the x axis and behaving erratically.

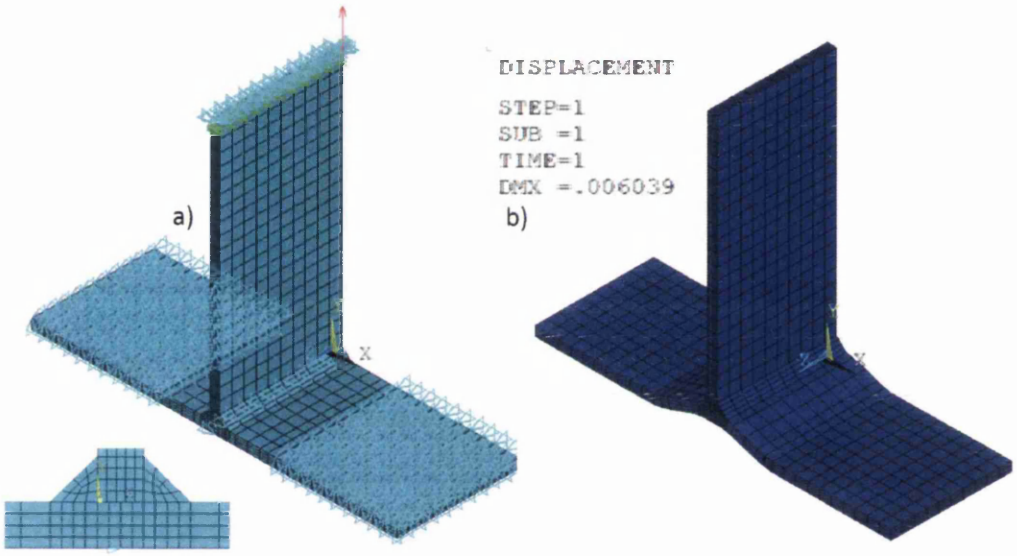

Figure 139: Bending load tee joint FE-model - solid brick elements

A close up of the weld detail is shown. The nodes at the intersection of the plate uprights and the horizontal base plates are not connected. The parent plates are only connected to the weld bead metal, not each other, creating a fit-up gap as found in the actual coupon. In the models shown above a global element size of 10mm is used. The solid brick elements have a through thickness size of ¼ *t* (t= thickness 8mm upright). The shell plate elements of the parent plate and the weld bead both have a real constant set material thickness of 8mm.

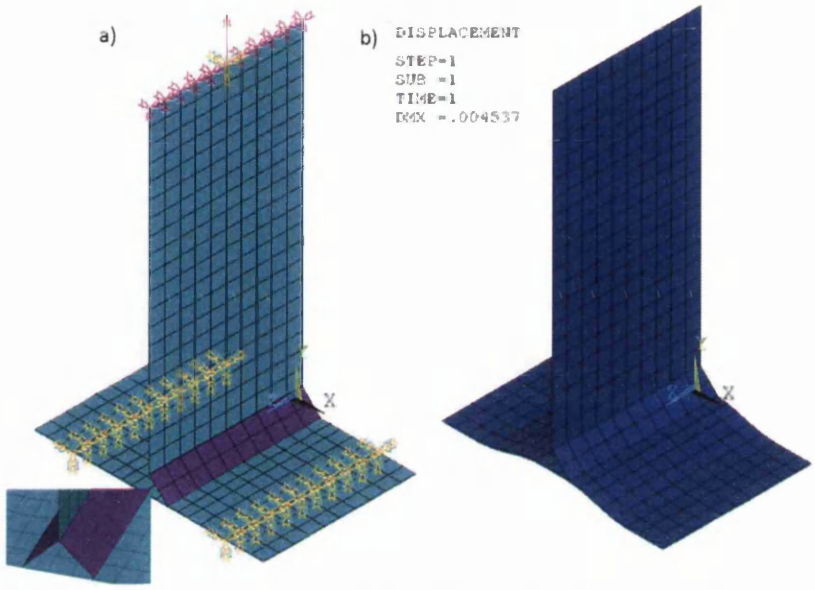

Figure 140: Bending load tee joint FE-model - shell plate brick elements

The displacement results are shown above in Figure 139b) and Figure 140b) for both the solid and shell element models. Under a 1kN unit load, the recorded displacement (in the y-axis) at the test grip end is 0.006039mm and 0.004537mm for the solid and shell models respectively. There is a difference between the displacement values, again, due to mid-plane geometry of the shell plate elements. This has an increased effect on the load-carrying weld and hence a larger difference between the solid and shell element models. Unlike the double-sided non-load-bearing attachment (section 4.2.4) where only a negligible difference is seen between the two element model types.

The coupon models shown above are in the as-designed state with no distortion of the material simulated. The cross-section of a coupon (out of the test frame) was taken using a co-ordinate measurement machine. The cross-section was modelled in the FE software and a mesh extruded to create a distorted model, Figure 141a). Boundary conditions were applied to the model to simulate the clamp up of the bracing used on the test configuration. Rotations in the z-axis were applied on the nodes at the 100mm brace-to-brace distance. The nodal displacements of the solution are displayed in Figure 141b).

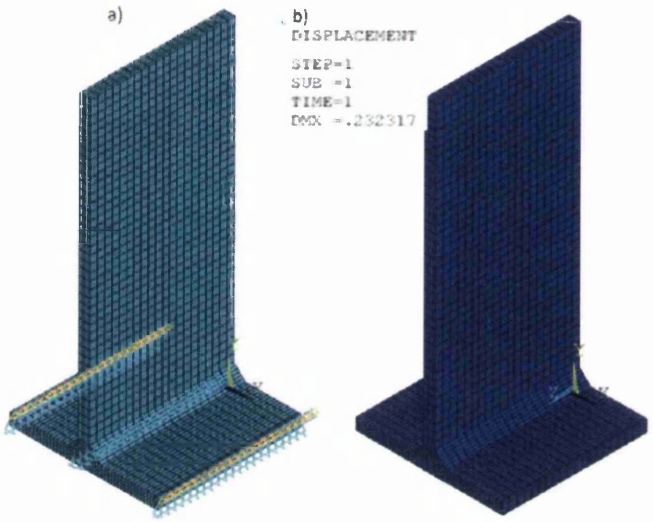

Figure 141: Bending load tee joint distorted model - test frame clamp-up simulation

The final nodal displacements above are used to update the tee joint geometry and a further analysis is completed on the geometry data. The static unit load boundary conditions are applied as shown in Figure 142a) and the solution is run.

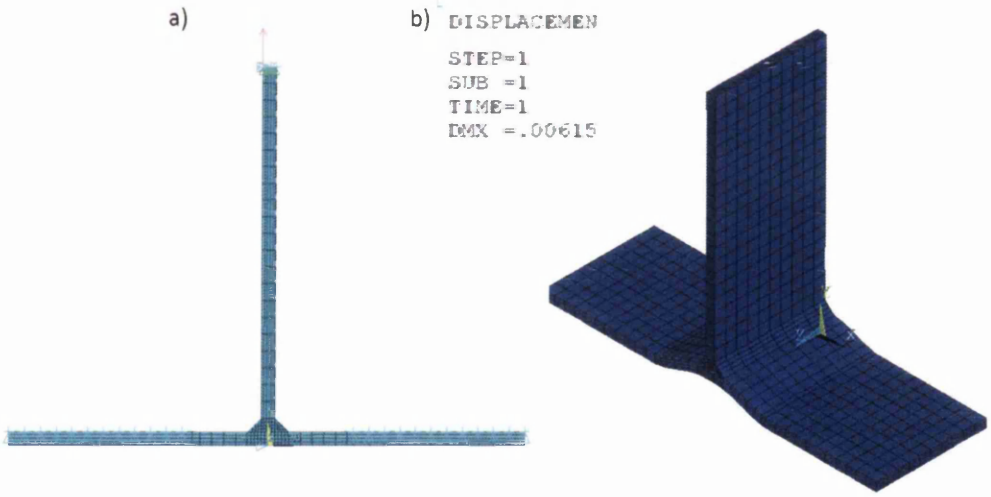

Figure 142: Bending load tee joint distorted model - static 1kN unit load

There is only a slight distortion in the updated coupon geometry and could be potentially considered negligible. In the displacement results shown in Figure 142b), there is a slight difference in comparison to the initial un-distorted model in Figure 139b).

4.2.7 Validation of Coupon Models

The validity of the FE models produced in this chapter was checked prior to using the models for structural stress calculations. This gave confidence in the models before using the coupon

data and converting into a single master S-N curve. Checking was carried out by comparing micro-strain values obtained from the FE model against those measured by strain gauges placed on the coupons. All strain gauges were placed 10mm away from the weld toe on the main load carrying plate. Elastic micro-strain values were extracted from each coupon model at the corresponding gauge positions. In the case of the bending load tee joint, a strain gauge was placed on the base plate at 10mm away from the lower weld toe. The micro-strain comparisons are shown in Figure 143.

	Load kN	FE-Model Microstrain με	Strain gauge measured microstrain με
Tensile load tee joint	86	522	560
Non load bearing cover plate	167	1115	1330
Distorted model	167	1801	1330
Load bearing lap joint	67	1057	1315
Non load bearing transverse attachment			
Double	177	1079	1150
Single	100	621	876
Single - distorted model	100	1044	876
Cruciform			
8mm	200	1218	1151
10mm	200	1218	1225
Bending load tee joint			
Upright	40	272	267
base	40	1128	750

Figure 143: Validation of coupon models - FE micro-strains vs. recorded micro-strains

The entire coupon FE models gave reasonable correlation with the recorded micro-strain values. Some errors were produced, but as to be expected given variables in the material properties, misalignment and accuracy of gauge positioning, and calibration errors in the test and measurement equipment.

Where distortion was present in the coupon geometries, the as-designed undistorted models initially gave optimistic micro-strain levels, compared to the recorded values. Upon simulation of the distortion levels in the coupon, an increase in strain levels were calculated, and higher than the strain gauge measurements. This suggests the distorted as-welded geometries are too pessimistic compared with the test data. A further judgment can be made as to which model is correct, based on the correlation and condensing of data into the single

master S-n curves. The FE micro-strain values for the bending load tee joint coupon do not fare as well in comparison of measured micro-strain values, however, the coupon and test geometry has far greater sources of error. There is a large stress gradient across the coupon base plate and hence, results will prove very sensitive to any misalignment of gauge positioning than the other coupons. Furthermore the clamping test arrangement is dependent on hand and eye measurements to clamp the tee into place, unlike the other coupons that rely on upper and lower test grip fixtures on a fixed concentric spigot arrangement.

4.2.8 Summary

The six coupon types and relevant geometry variations have all been modelled in a linear static finite element simulation. Where applicable, the distorted as-welded geometries have also been modelled and analysed and prove to have an important effect on the load distribution. Both the use of solid brick and shell plate elements has been explored. Where non-load-bearing coupon joints are modelled, there is only a small difference found between the two element types. However, in load-bearing weld applications the shell element results clearly differ from the solid element. This is because of the mid-plane geometry of the shell element and not fully representing the weld bead geometry in the test coupons. This will possibly create a difference in the analysis and conversion of test data when generating an alternative fatigue damage parameter.

Due to the singularity created at a notch, any stress results from the solution does not provide robustness for a suitable parameter to assess weld fatigue strength. To convert the weld fatigue data (documented in chapter 4.1) into a useable format the next step requires extraction of the forces and moments from the finite element coupon models. The force and moment data provides information acting through a weld location based on the overall geometry of the structure. This excludes information or any kind of stress concentration arising from the peak stresses at the weld toe (or stress singularity in the FE-model).

The force and moment data can be used in the Structural Stress approach to calculate and explore if a robust weld fatigue damage parameter exists.

4.3 Coupon Structural Stress Calculation

After generating and solving a suitable and accurate finite element model of a component a further 'post-processing' step outside of the standard FE software is required. As any calculated FE stress can give erroneous results at stress singularities, it is advantageous to use forces and moments as an output from the FE model. Forces and moments are largely insensitive to mesh densities and singularities as they are calculated at nodal positions as opposed to stresses calculated at Gaussian positions within the element, which are extrapolated to nodes.

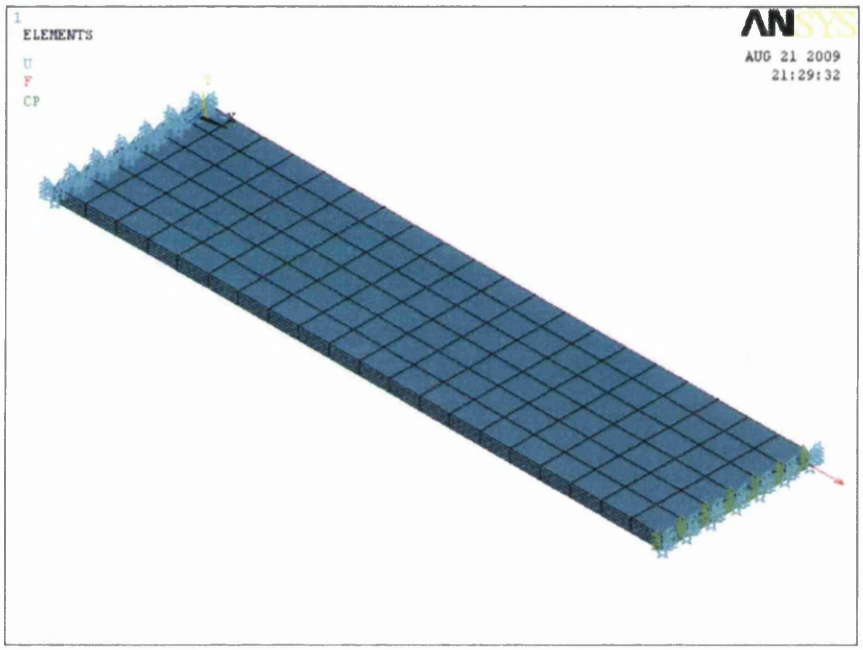

Figure 144: Structural Stress calculation example- un-welded coupon under unit load

There are a number of steps required to calculate a structural stress fatigue damage parameter. Assuming a linear-static analysis with a unit load is completed, Figure 144, the following 'post-processing' steps are carried out.

From the FEA software package of the solved model, the weld fatigue crack path must be defined. This is achieved by sectioning the model at potential weld crack path positions and selecting only the elements up to the crack plane, Figure 145. The nodes positioned on the crack plane must then be highlighted and selected, Figure 146.

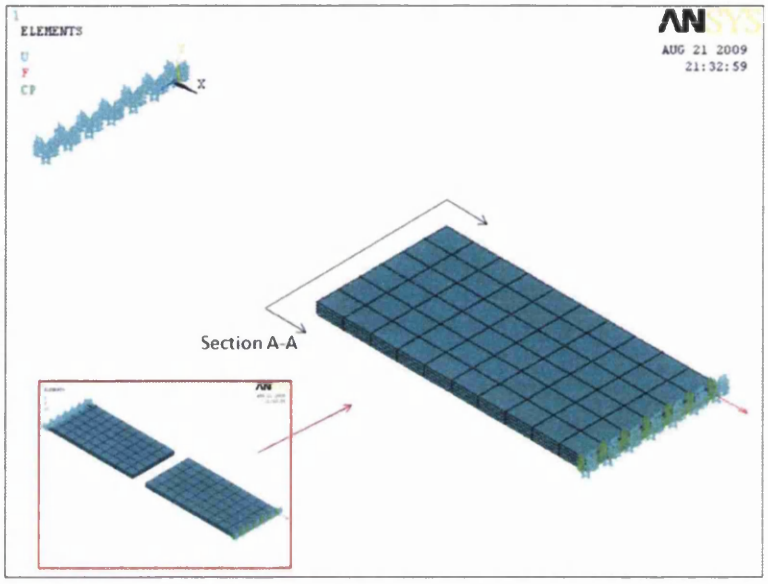

Figure 145: Crack plane definition -sectioned model at weld failure crack path

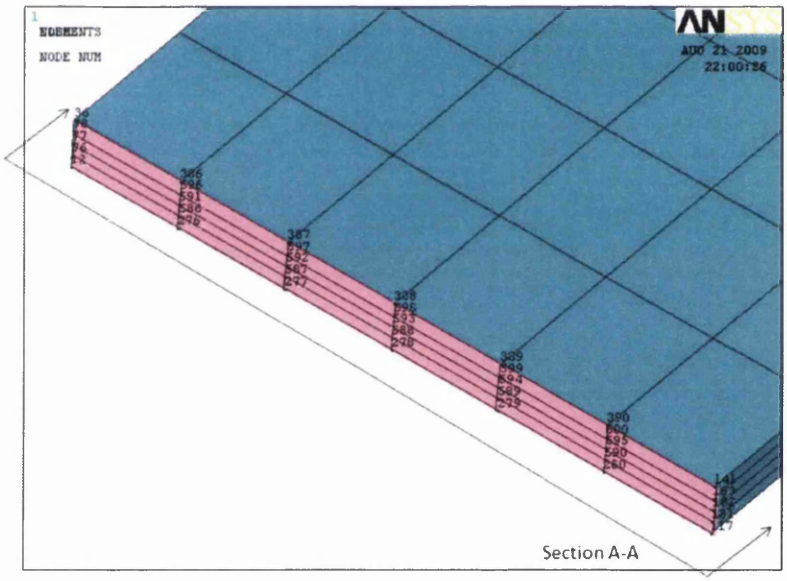

Figure 146: Crack plane definition -selected nodes on weld failure crack path

After selecting the appropriate nodes, the relevant command prompt is given to the FE-software to obtain force and moment data for each node. This creates a 'free body diagram' of the component and determines the forces and moments passing through the weld nodes under the applied load. A list or text file output is given of the nodal values for the forces and moments in the x, y, z directions, Figure 147. Values of the element size along the weld line are also required from the model.

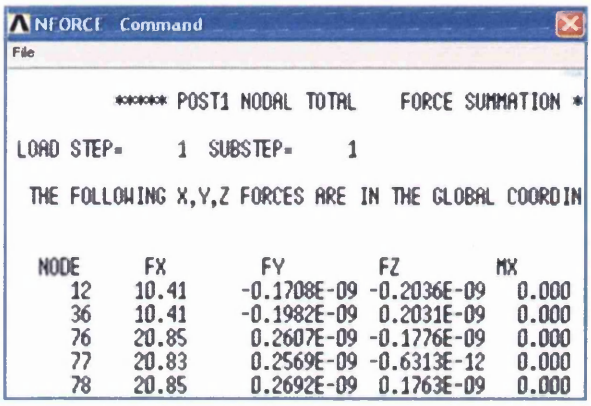

Figure 147: FE model text file output- nodal forces and moments

Using a spreadsheet or calculation based software, the nodal force data are distributed along the weld crack plane, changing the normal point (node) forces F into line (element) forces f', Figure 148.

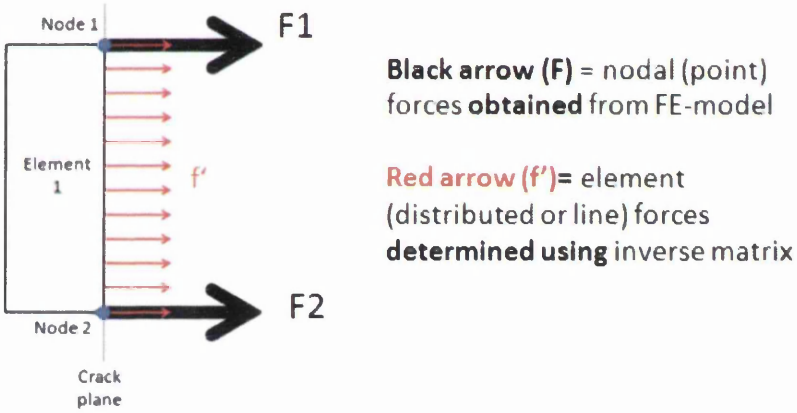

Figure 148: Nodal (point) forces from FE model distributed into element (line) forces

The nodal forces are summed up through the thickness of the FE model, and a station point or nodal column is created for each column of nodes across the width of the crack plane. There are 6 element divisions along the width of the crack area and therefore 7 nodal column station points. Station points 1 and 7 are at either edge of the coupon.

a)

Nodal Column	element length	distance across width
1	16.67	0.00
2	16.67	16.67
3	16.67	33.33
4	16.67	50.00
5	16.67	66.67
6	16.67	83.33
7		100.00

b) node numbers down column

1	36	78	77	76	12
2	386	596	591	586	276
3	387	597	592	587	277
4	388	598	593	588	278
5	389	599	594	589	279
6	390	600	595	590	280
7	141	183	182	181	117

c) NFORCE FX (values from FE output)

1	10.41	20.85	20.83	20.85	10.41
2	20.82	41.7	41.65	41.7	20.82
3	20.82	41.69	41.65	41.69	20.82
4	20.82	41.68	41.65	41.68	20.82
5	20.82	41.69	41.65	41.69	20.82
6	20.82	41.7	41.65	41.7	20.82
7	10.41	20.85	20.83	20.85	10.41

d) Total sum of column

	FX	MZ
1	83.35	0
2	166.69	0
3	166.67	0
4	166.65	0
5	166.67	0
6	166.69	0
7	83.35	0

Figure 149: Structural Stress calculation - element and node data entered from FE model

Each element length (distance between station points) across the width of the coupon is entered Figure 149a). A grid with each node number as defined on the crack plane is created Figure 149b) relating to the node numbers in Figure 146. A corresponding grid is created and the relevant node force values normal to the weld are entered with the values (Fx) obtained from the FE model output Figure 149c). The total force through the thickness of the model is summed for each node column in Figure 149d).

$$\begin{Bmatrix} F_1 \\ F_2 \\ F_3 \\ \cdot \\ \cdot \\ F_n \end{Bmatrix} = \begin{bmatrix} \frac{l_1}{3} & \frac{l_1}{6} & 0 & 0 \\ \frac{l_1}{6} & \frac{(l_1+l_2)}{3} & \frac{l_2}{6} & 0 \\ 0 & \frac{l_2}{6} & \frac{(l_2+l_3)}{3} & \frac{l_3}{6} \\ 0 & 0 & \cdots & \cdots \end{bmatrix} \begin{Bmatrix} f_1 \\ f_2 \\ f_3 \\ \cdot \\ \cdot \\ f_n \end{Bmatrix}$$

where $F_1, \ldots, F_n$: element nodal force

$f_1, \ldots, f_n$: line force

$l_1, \ldots, l_n$: element length

Figure 150: Structural Stress theory - element length matrix

The structural stress element length matrix was discussed earlier in the literature review and is displayed in Figure 150 above. The nodal forces and element lengths are known, resulting in the inverse line (distributed) forces to be calculated ($f=M^{-1}F$). In Figure 151, distribution matrix (M) and the inverse matrix (M^{-1}) are created in a spreadsheet.

	1	2	3	4	5	6	7
1	5.56	2.78	0.00	0.00	0.00	0.00	0.00
2	2.78	11.11	2.78	0.00	0.00	0.00	0.00
3	0.00	2.78	11.11	2.78	0.00	0.00	0.00
4	0.00	0.00	2.78	11.11	2.78	0.00	0.00
5	0.00	0.00	0.00	2.78	11.11	2.78	0.00
6	0.00	0.00	0.00	0.00	2.78	11.11	2.78
7	0.00	0.00	0.00	0.00	0.00	2.78	5.56

	1	2	3	4	5	6	7
1	0.208	-0.056	0.015	-0.004	0.001	0.000	0.000
2	-0.056	0.111	-0.030	0.008	-0.002	0.001	0.000
3	0.015	-0.030	0.104	-0.028	0.008	-0.002	0.001
4	-0.004	0.008	-0.028	0.104	-0.028	0.008	-0.004
5	0.001	-0.002	0.008	-0.028	0.104	-0.030	0.015
6	0.000	0.001	-0.002	0.008	-0.030	0.111	-0.056
7	0.000	0.000	0.001	-0.004	0.015	-0.056	0.208

Figure 151: Element length matrix (M), left and Inverse matrix (M^{-1}), right.

The distributed forces are calculated in Figure 152(a) using the product of the inverse matrix in Figure 151 and the total sum of forces in Figure 149(d) where $f=M^{-1}F$.

line distributed	f_x'	m_y'	b) Structural Stress	c) σnominal force/area	d) FE-Stress (S1)
a) 1	10.002	0	1.2503	1.25	1.2503
2	10.001	0	1.2502	1.25	1.2501
3	10.000	0	1.2500	1.25	1.2499
4	9.998	0	1.2498	1.25	1.2498
5	10.000	0	1.2500	1.25	1.2499
6	10.001	0	1.2502	1.25	1.2501
7	10.002	0	1.2503	1.25	1.2503

Figure 152: Structural Stress calculation per unit load

The distributed line forces f can then be entered into the structural stress equation 3.3 presented in chapter 3:

$$\sigma_s = \frac{f_{x'}}{t} + \frac{6m_{y'}}{t^2}$$

Where f = distributed force
m = distributed moment
t = thickness

The structural stress factor, σ_s (MPa per unit load applied), as calculated in Figure 152(b), is calculated using membrane and bending (loading) components and ignoring any non-linear peak stresses at the weld toe, as discussed in chapter 2 (see figure 2.34). The FE model example used above contains no weld toe or non-linear peak stresses, therefore the structural stress should be the same as the nominal stress. For comparison, the nominal stress (force/area) Figure 152(c) and maximum principal stresses (from the FE model) Figure 152d) are given.

The structural stress calculation method discussed above can be employed on weld failures such as the weld toe, throat and root or fusion line. The process is repeated here for the welded coupon models defined in the previous chapter (4.2) and using the appropriate failure modes recorded in chapter 4.1.

Traditionally, a finite element model and its mesh density should be carefully considered if results are mesh sensitive. As shown in chapter 3.4.1, a coupon with the same geometry and boundary conditions, but modelled with two different mesh densities can give two different stress results. The proposed structural stress method is unique in its approach as it is always asserted to be insensitive to the mesh density. Potentially, there are, however, different parameters associated with the finite element model that can affect the structural stress

calculation, such as element type and size. It is also possible to model the geometry and weld crack path in different formats with further effect on the structural stress calculation.

Finite element models were generated concentrating on the effects of mesh density and element type and calculation order. The range of different element types and sizes were used to explore the structural stress mesh insensitivity claim. The mesh densities used were 3.125, 5, 10, 16.67, 25 and 50mm across the width of the coupon (element length along the weld). The through thickness element sizes were ¼, ½ and 1t, with t the thickness of the coupon plate material. Element types used were shell and solid models linear 1st and quadratic 2nd order elements with both reduced and full integration methods. Examples of different global element sizes and through thickness element sizes are shown for the non-load-bearing coupon in Figure 153. The range of different element types and sizes were applied for each of the coupon geometries in the data generation programme.

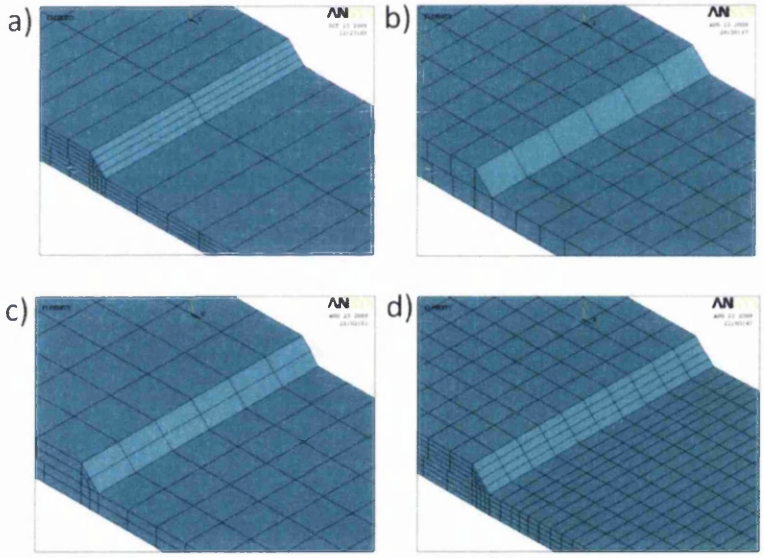

Figure 153: Non-load lap coupon mesh density -a) 50mm global and ¼ through thickness element size, b) 16.67mm and 1t, c) 16.67mm and ½t and d) 10mm and ¼t

4.3.1 Tensile load tee joint

Nodal forces and moments were extracted from the tensile load tee FE solid-model at the crack path defined in Figure 154. The crack plane of the weld originates at the root of the weld bead 'fit up' gap and propagates out through the weld throat at approximately 33 degrees from the horizontal coupon base.

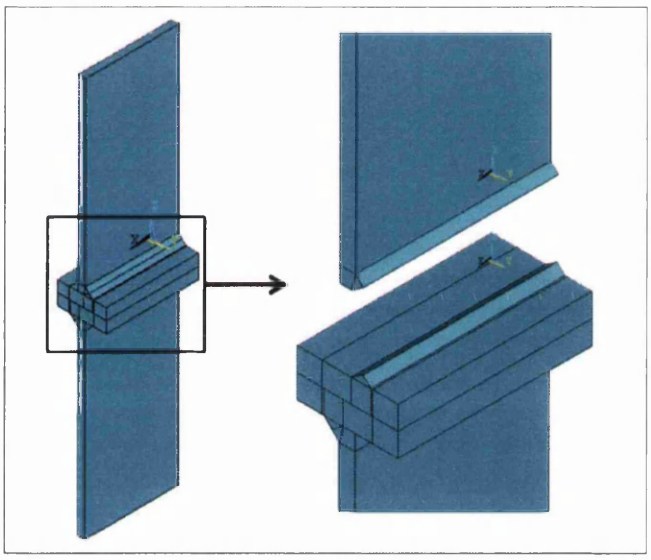

Figure 154: Tensile load tee joint – FE solid model throat crack plane 33 degrees

Nodal forces and moments were also extracted for the tensile load tee FE shell model at the equivalent 33 degrees crack path defined in Figure 155.

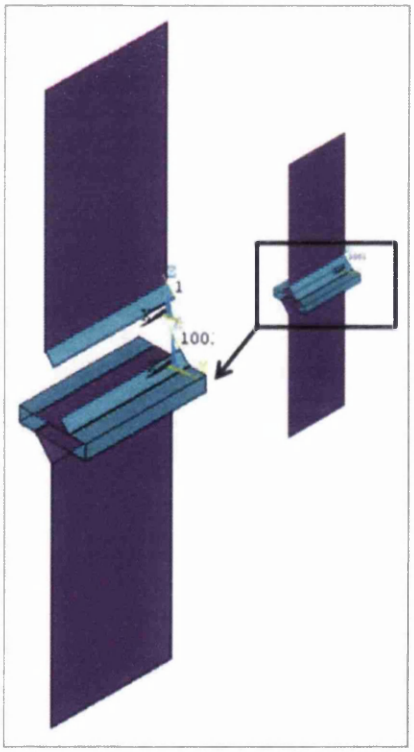

Figure 155: Tensile load tee joint - FE shell model throat crack plane 33 degrees

The main consideration for the tensile load tee joint is the weld throat failure mode. Work applying the structural stress method has been explored and well documented for use with weld toe failures but less so, (and with less consistency) for weld throat failures. In this part

of the research work, the capability of the method has been investigated with consideration given to the effects of element type and crack plane location rather than factors less sensitive to the calculation procedure such as mesh density. Comparisons of the effects of different mesh densities are reviewed and covered later on in this chapter (4.3.2 and subsequent) for other coupon geometries with definitive results (justifying the exclusion of mesh density effects here).

The structural stress calculation procedure described above was applied to both solid brick elements and shell plate elements with a crack plane angle of either 33 degrees (actual throat crack angle) or 45 degrees (minimum weld throat area i.e. maximum nominal stress). Where solid elements were used, a review was completed on the effect that different levels of weld penetration have on the structural stress calculation. Where shell elements were used, a review was completed of the effect that different weld throat element real constant thicknesses have on the structural stress calculation. The different solid and shell element models are shown in Figure 156 and Figure 158 respectively.

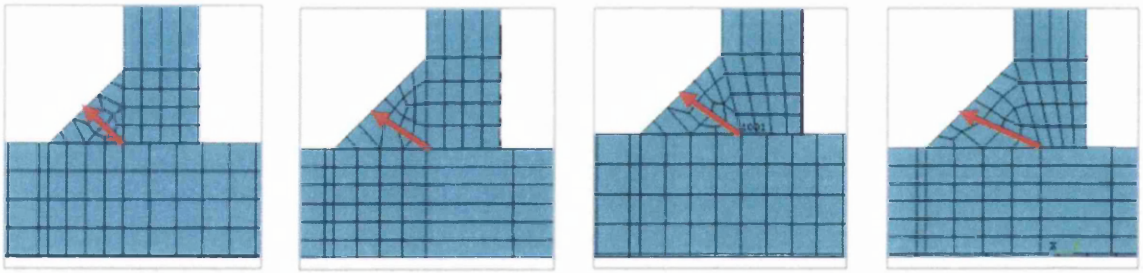

a) No penetration with 45 degree crack plane

b) No penetration with 33 degree crack plane

c) 1mm penetration with 45 degree crack plane

d) 1mm penetration with 33 degree crack plane

Figure 156: Tensile load tee joint - Solid models 1, 2, 3 and 4– varying penetration and crack path

The results of the structural stress calculation for the tensile load tee solid element models under a 1kN unit load are shown in Figure 157. The structural stress (MPa per unit load) is plotted on the y-axis against the distance across width of the coupon (mm) on the x-axis. The structural stress peak values of interest lie at the centre of the coupon (50mm from the edge) where the crack initiation occurred in the test coupon.

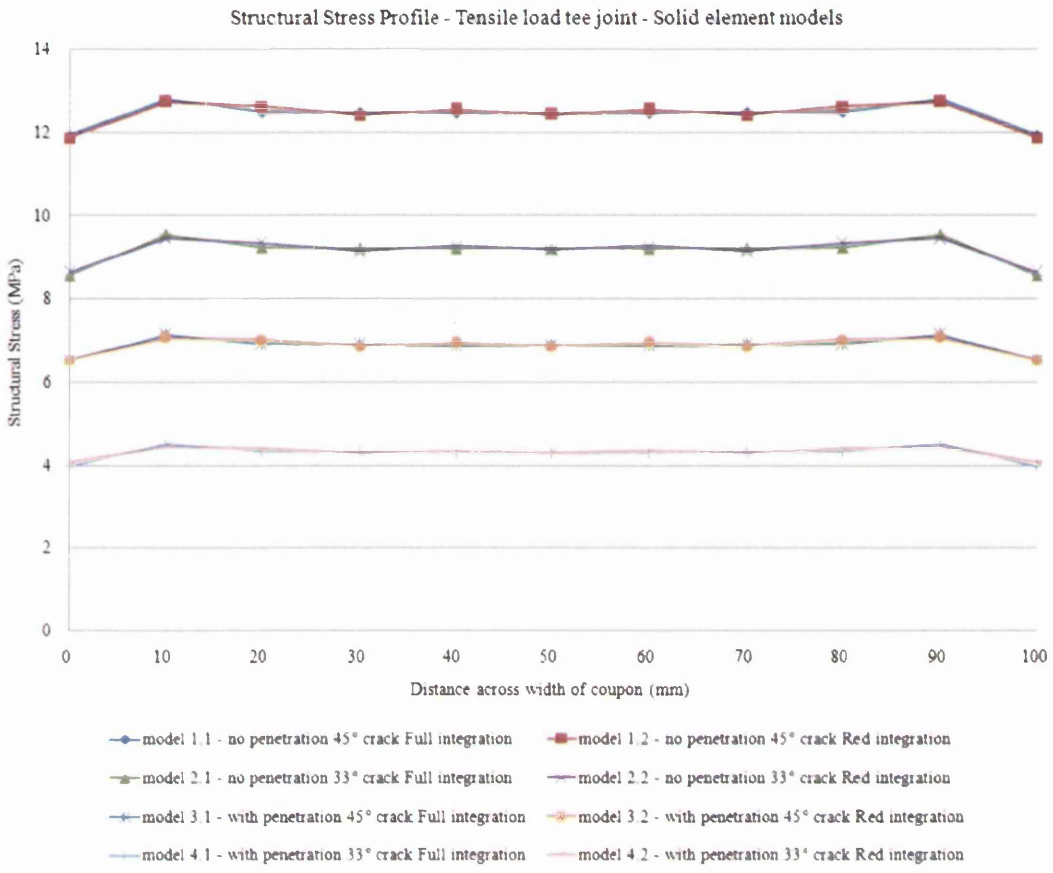

Figure 157: Tensile load tee joint - Structural stress profile using solid element models

The tee joint solid element model results are sensitive to the level of weld penetration and crack plane modelled in the finite element model. The results differ significantly by a factor of 3. This could potentially prove to be a problematic area for fatigue life prediction of weld throat failures and produce erroneous results. Model 4 is the most realistic and representative geometry of the test coupon weld and failure. The results of which are assumed to be the most accurate or 'correct' value to take forward for further analysis.

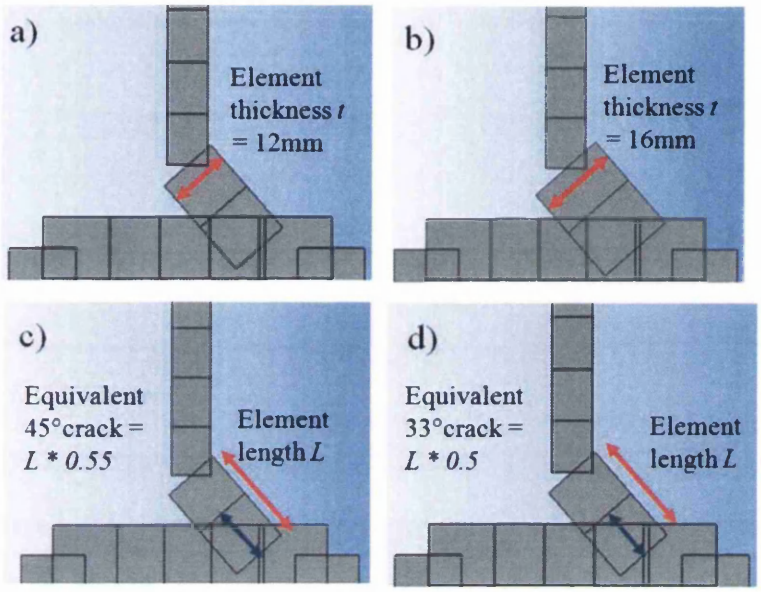

Figure 158: Tensile load tee joint - Shell model examples a) weld throat element thickness 12mm, b) weld element throat thickness 16mm, c) equivalent 45 degree crack and d) equivalent 33 degree crack

The results of the structural stress calculation for the tensile load tee shell element models under a 1kN unit load are shown in Figure 159. The structural stress is plotted on the y-axis against the distance across width of the coupon, x-axis. The structural stress peak values of interest lie at the centre of the coupon (50mm from the edge) where crack initiation occurred. The structural stress theory proposes that the forces and moments extracted from the FE model are divided by the element thickness used. For an analysis of a weld throat failure, this can be problematic and an area of uncertainty. Four tee shell models have been created using different weld throat element thicknesses of 8, 10, 12 and 16mm. In the structural stress calculation, the corresponding weld throat element thickness has been used.

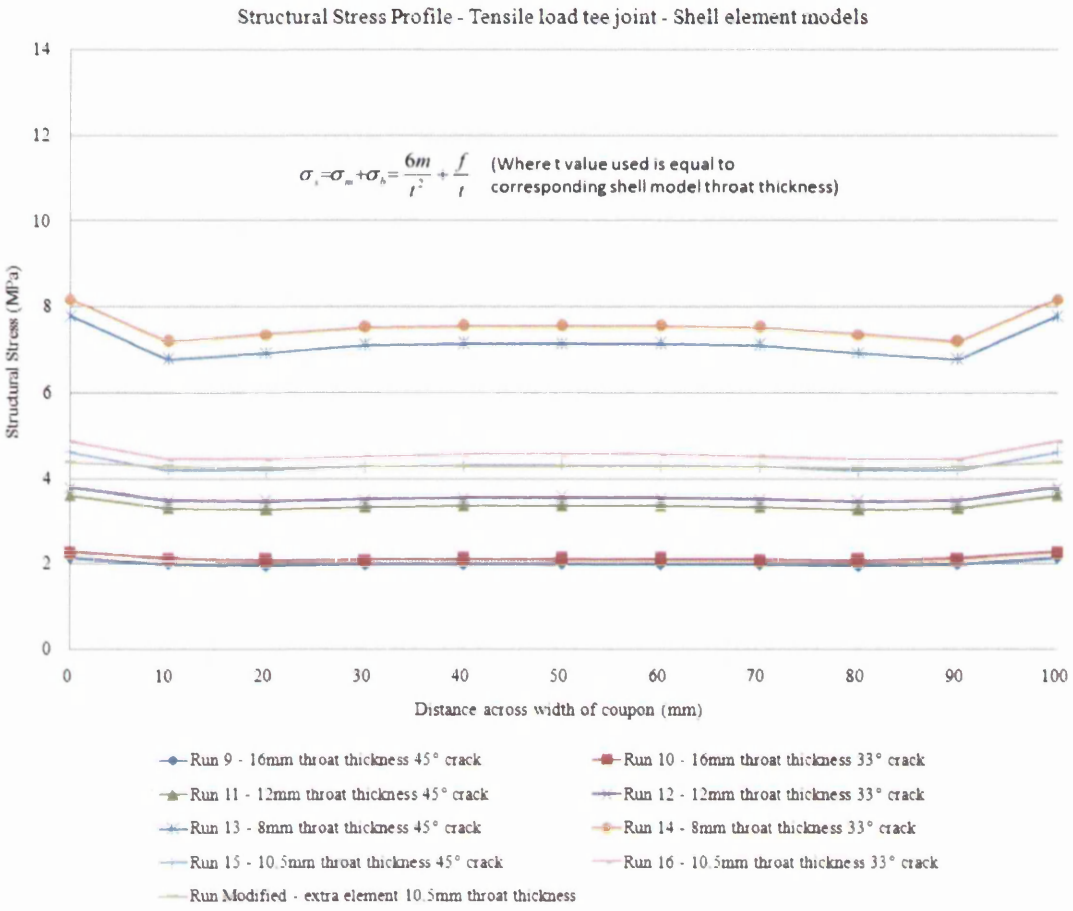

Figure 159: Tensile load tee joint - Structural stress profile using shell element models

The structural stress profile results show sensitivity to the element thickness and the corresponding thickness t value used in calculation. There is a minimal or negligible difference in the results due to the varying crack path of 45 degrees or 33 degrees. A further shell element model was created to explore the effects of weld thickness representation. An additional shell element was modelled into the weld throat region as shown in Figure 160. This is to increase the shell thickness area of the theoretical weld throat. It is possible that under certain loading conditions, the weld representation will play a crucial role in calculating the structural stress. This is dependent upon the way the load path is distributed through the coupon body, and whether shell elements are able to replicate the distribution accurately.

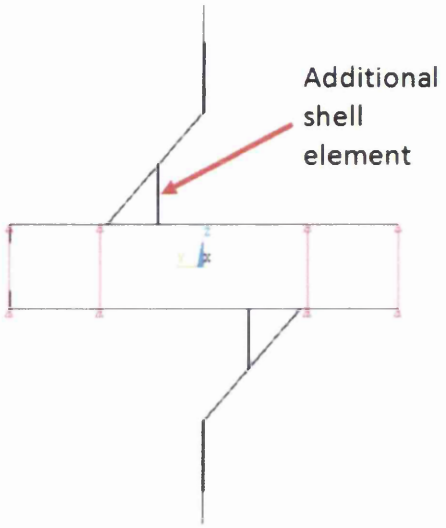

Figure 160: Modified tensile load tee-joint model - additional weld throat elemnet

The modified weld model for the tensile load tee joint has no effect on the calculated structural stress. It will be discussed in detail later on in the chapter, how the weld representation is critical for cruciform throat failure shell models.

Figure 161 shows a comparison of extracted nodal forces and moments from the four shell element models (8, 10, 12 and 16mm throat thickness). It is evident that there is little variation in the extracted forces and moments. This would be expected, as the shell geometries are identical except for the throat thickness. The unit load (1kN) applied to the top of the model is distributed through the four models in a similar load path. It is the final structural stress calculation that creates the differences in the final structural stress factors.

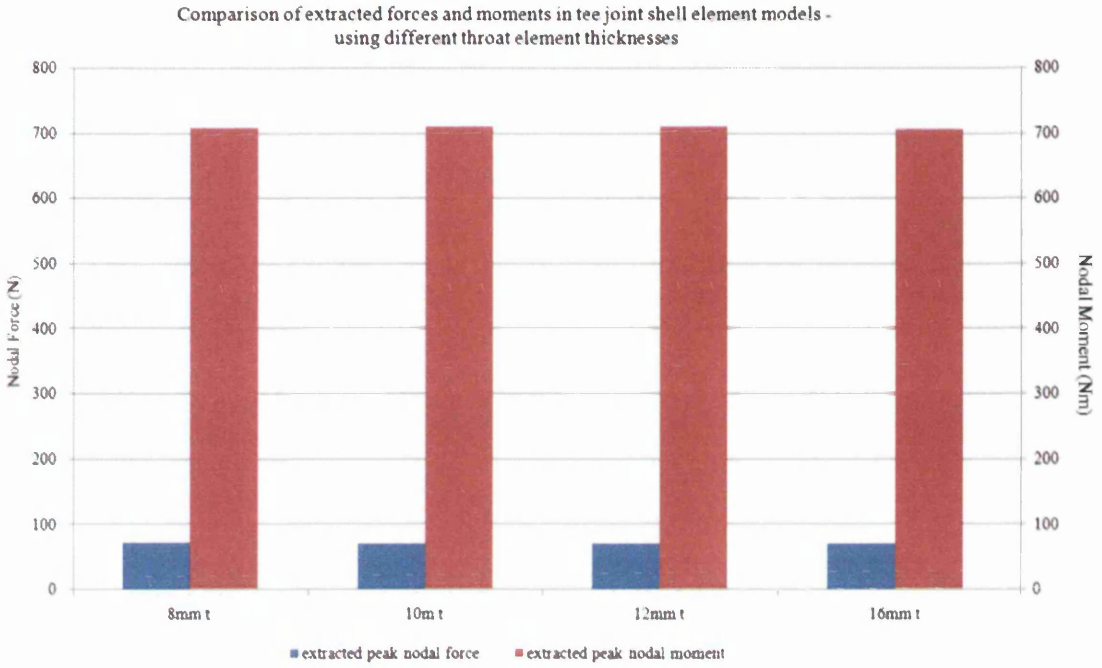

Figure 161: Comparison of extracted nodal forces and moments of the tee joint shell element models

As the forces and moments show little sensitivity to the FE model throat element thickness *t*, the actual throat failure area of the test coupon was used in the final structural stress calculation. The structural stress profiles of the four models are shown in Figure 162. There is a much better improved correlation between the four FE models. Again, the Structural Stress (MPa per unit load) on the y-axis is plotted against the distance across the width of the coupon (mm) on the x-axis.

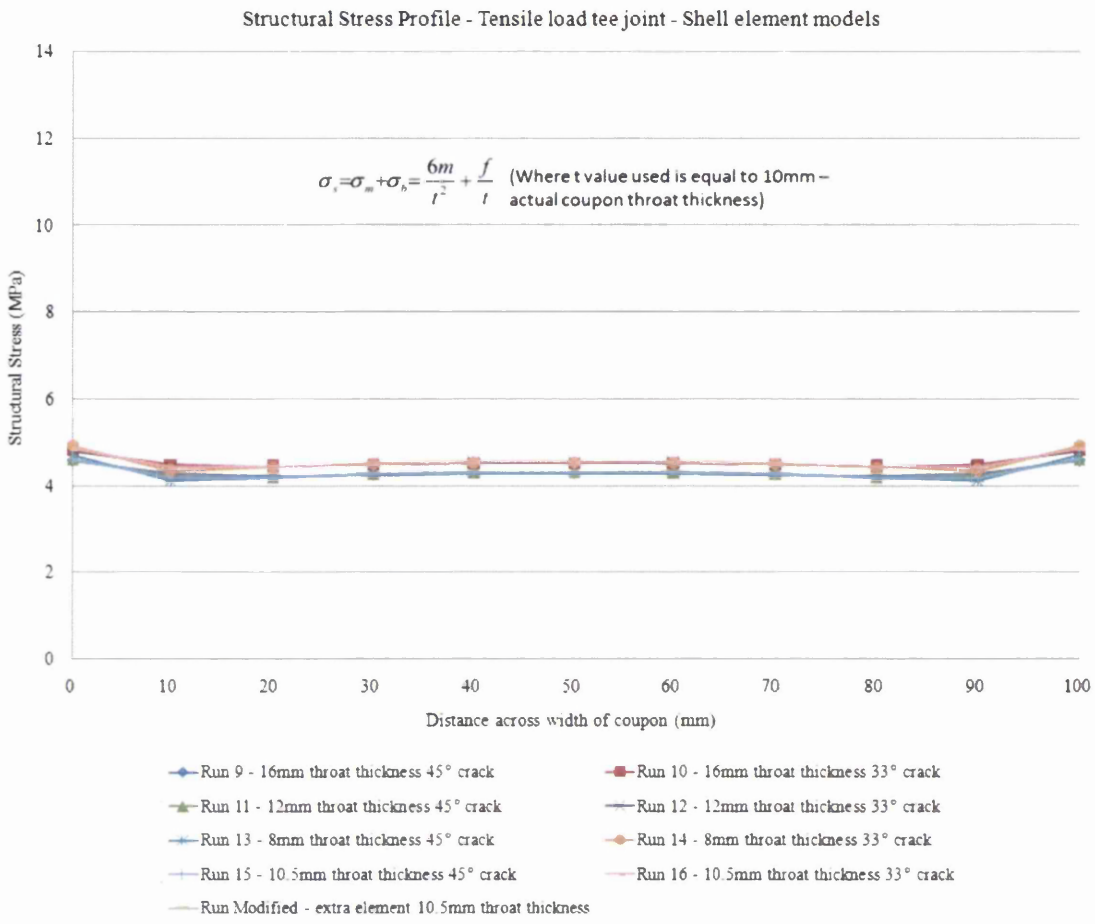

Figure 162: Tensile load tee joint - Structural stress profile using shell element models – using actual weld throat failure thickness in the structural stress calculation

There is a question regarding the use of shell elements for 'thick' plate structures for non-automotive applications (i.e. components greater than 2mm thickness). It is questionable if a shell element can truly represent the geometry of a solid brick element. The structural stress calculation used here can be broken down into membrane and bending components (membrane governing the level of structural stress and bending governing the gradient of stress, as shown in Figure 2.34). This has been completed for the tee joint solid and shell element models, Figure 163, using values from solid model type 4 and the shell element model with weld throat t of 10mm. The level of stress components correlate well with a negligible difference given the limitations of the shell element capability, which is to be expected.

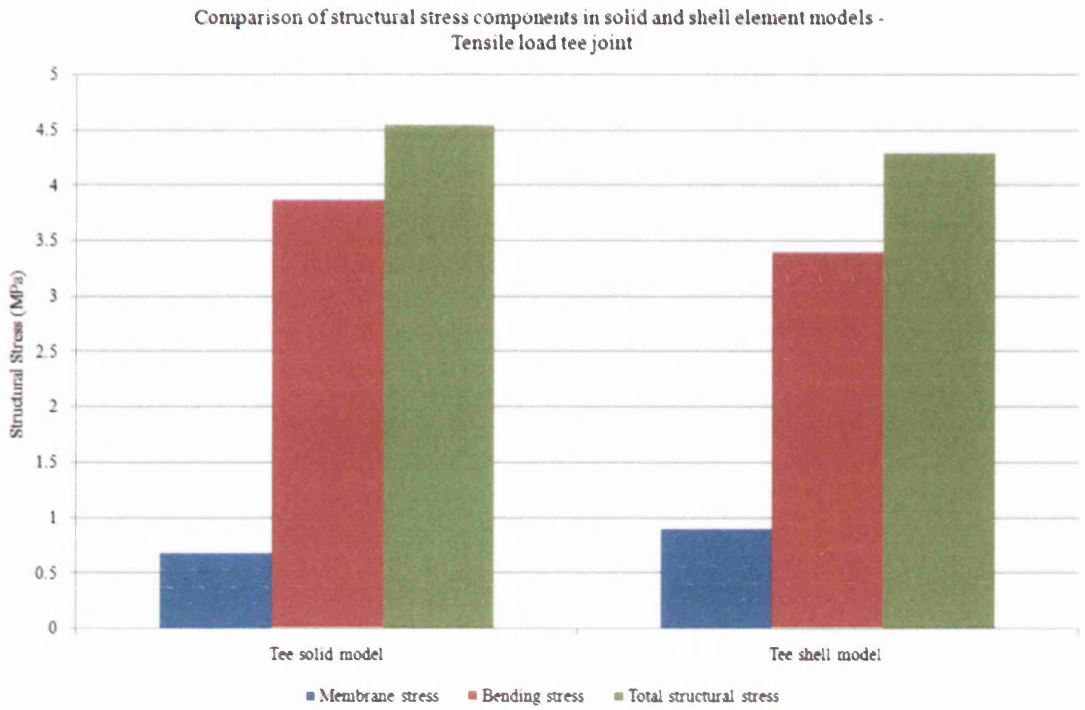

Figure 163: Comparison of calculated structural stress components in the tensile load tee joint - solid against shell element models

4.3.2 Non-Load-Bearing Transverse Cover Plate

The non-load-bearing cover plate crack path is defined in Figure 164 and Figure 165 for solid and shell element models respectively. The crack plane of the weld originates at the weld toe and propagates down through the thickness of the plate. The structural stress calculation procedure is applied for a range of different element types and sizes. The investigation of the proposed mesh-insensitive structural stress approach concentrated on effects of mesh density and element type and calculation order. The mesh densities used were 3.125, 5, 10, 16.67, 25 and 50mm across the width of the coupon. The through thickness element sizes were ¼, ½ and 1t, t being the thickness of the coupon plate material. Element types used are linear 1st and quadratic 2nd order elements employing reduced and full integration methods. Structural stress factors were calculated for the coupon in 'as-designed' un-distorted geometry condition and 'as-welded' distorted geometry.

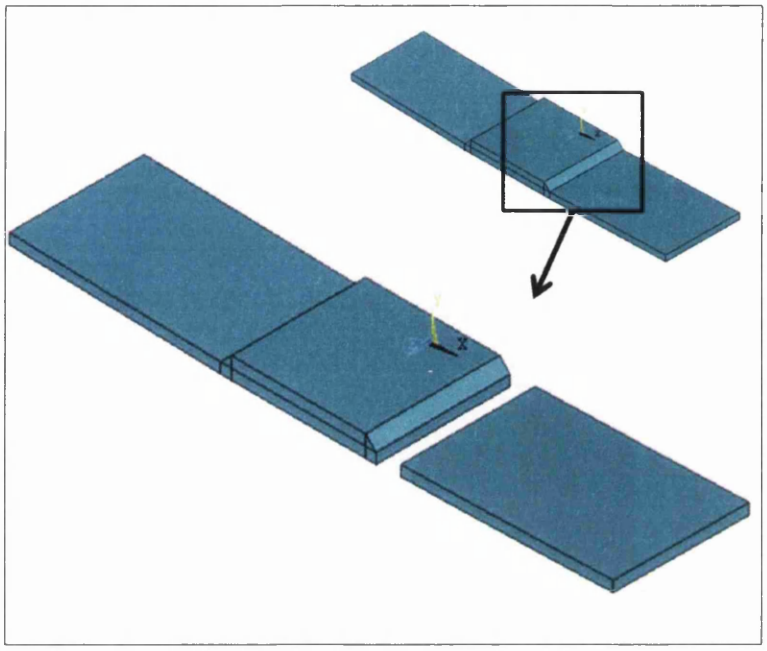

Figure 164: Non-load-bearing cover plate - FE solid model crack plane

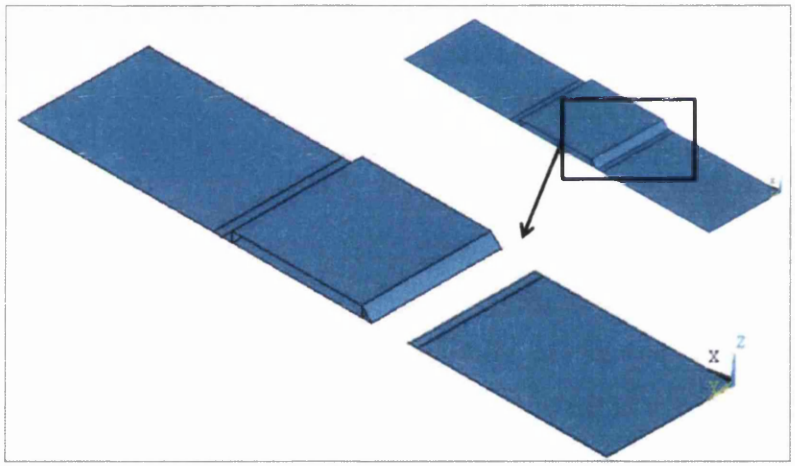

Figure 165: Non-load-bearing cover plate - FE shell model crack plane

The structural stress is calculated along the weld toe across the width of the coupon. The structural stress concentration factor per unit load (1kN) is displayed in Figure 166 and Figure 167 for the un-distorted and distorted solid element models respectively. The Structural Stress (MPa per unit load) on the y-axis is plotted against the distance across the width of the coupon (mm) on the x-axis.

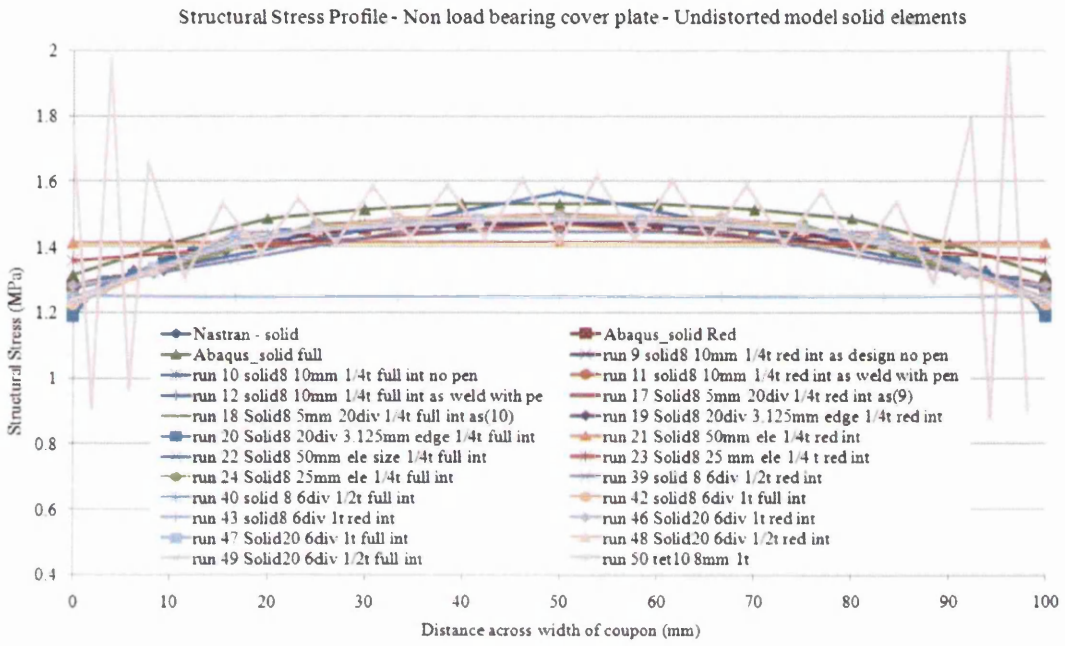

Figure 166: Non-load-bearing cover plate - Structural stress profile using un-distorted solid element models

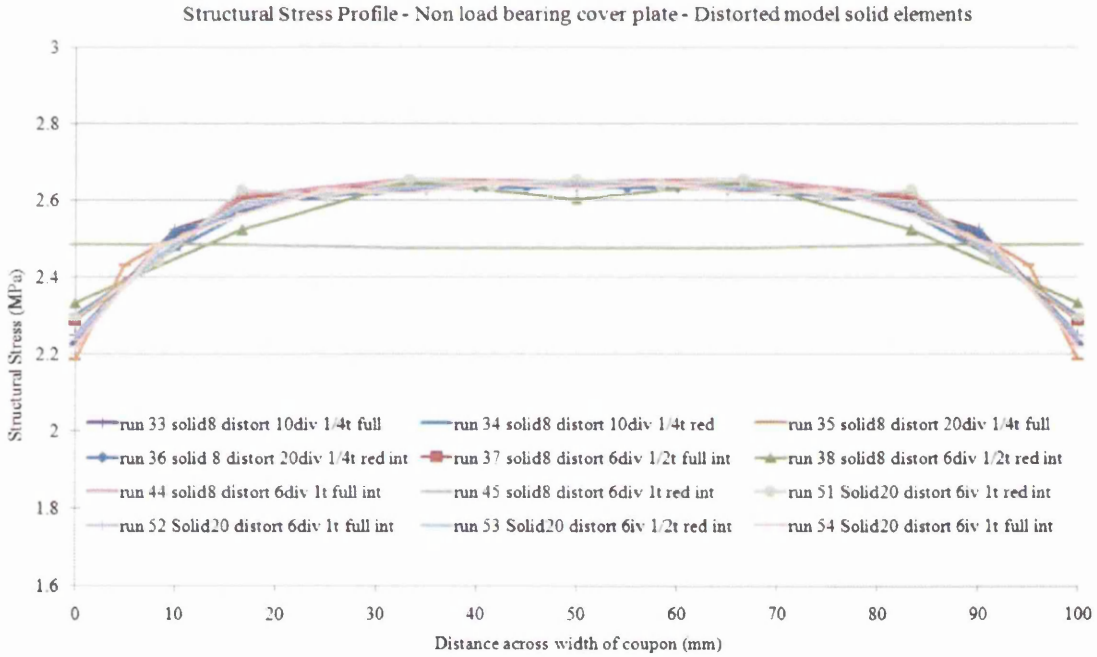

Figure 167: Non-load-bearing cover plate - Structural stress profile using distorted solid element models

The structural stress profiles show a distinct difference between the undistorted and distorted welded coupon geometries. Considering the various element types and calculation methods used, there is good correlation and minimal mesh sensitivity to the structural stress results.

There is reasonable correlation between three different software vendor packages used. The same FE model analysed in the Nastran, Abaqus and Ansys packages have a structural stress unit load calculation of 1.48MPa, 1.54MPa and 1.48MPa respectively at the centre of the coupon using a full integration method. A reduced integration option is not available in the Nastran package. Where it was used for Abaqus and Ansys, both unit load factors calculated values of 1.47MPa.

There are a few exceptions, such as the 1st order element with a through thickness of 1t (1 element through the thickness of the coupon) and a reduced integration calculation procedure. This arrangement would not be considered a reasonably realistic mesh; it is a severely coarse mesh. It is limited in calculating effects due to bending as it has fewer Gaussian integration points than the full method. Ideally, 3 or 4 elements should extend through the geometry thickness. However, the final results are still within a satisfactory margin of error. The un-distorted and distorted coupon structural stress values are within 16% and 4% of the mean results respectively.

A finite element model was created using a 10-node tetrahedral mesh. The structural stress profile of which, in Figure 166, behaves very erratically. The stress fluctuates up and down between 1.6MPa-1.4MPa at the centre of the coupon. The increase is most noticeable at the edges, between 0.9MPa-2.0MPa. This suggests that the locations of the nodal force summations and line element matrix (from which the structural stress is calculated) are incorrect, as the FE model total force acting through the crack plane is equal to the unit load applied (i.e. in equilibrium).

The structural stress factor per unit load is 1.6MPa for the un-distorted coupon and 2.6MPa for the distorted coupon. These values are based on the FE models with the highest density mesh of 10 divisions across the coupon width, and 4 elements through the plate thickness using a full integration. This would be considered the most accurate representation of the geometry with the highest order and efficient mesh available.

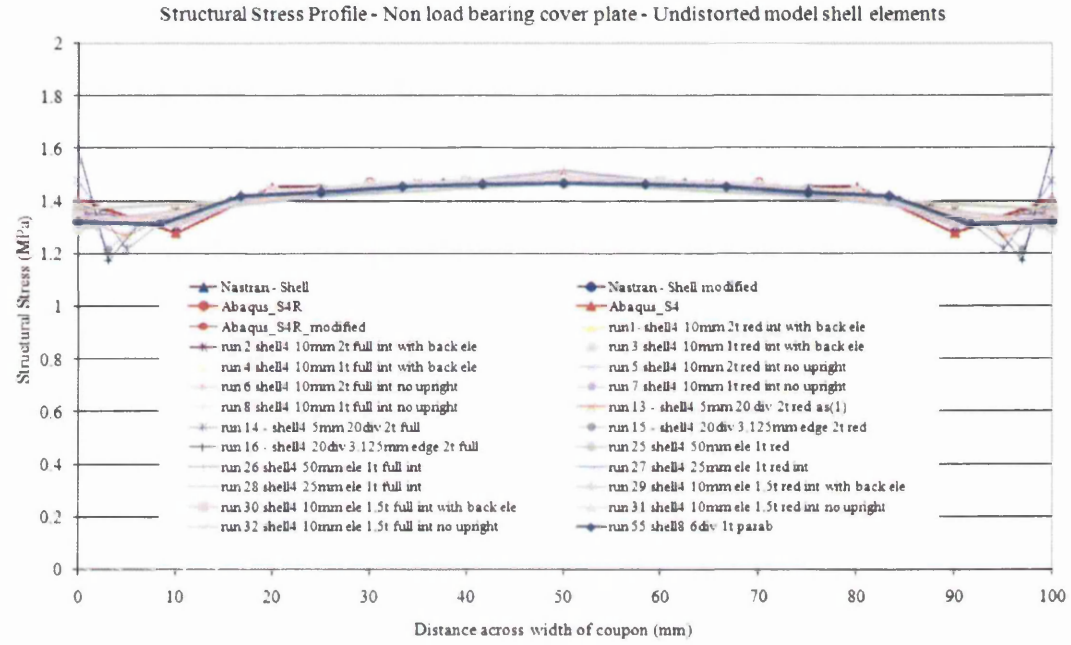

Figure 168: Non-load-bearing cover plate - Structural stress profile using un-distorted shell element models

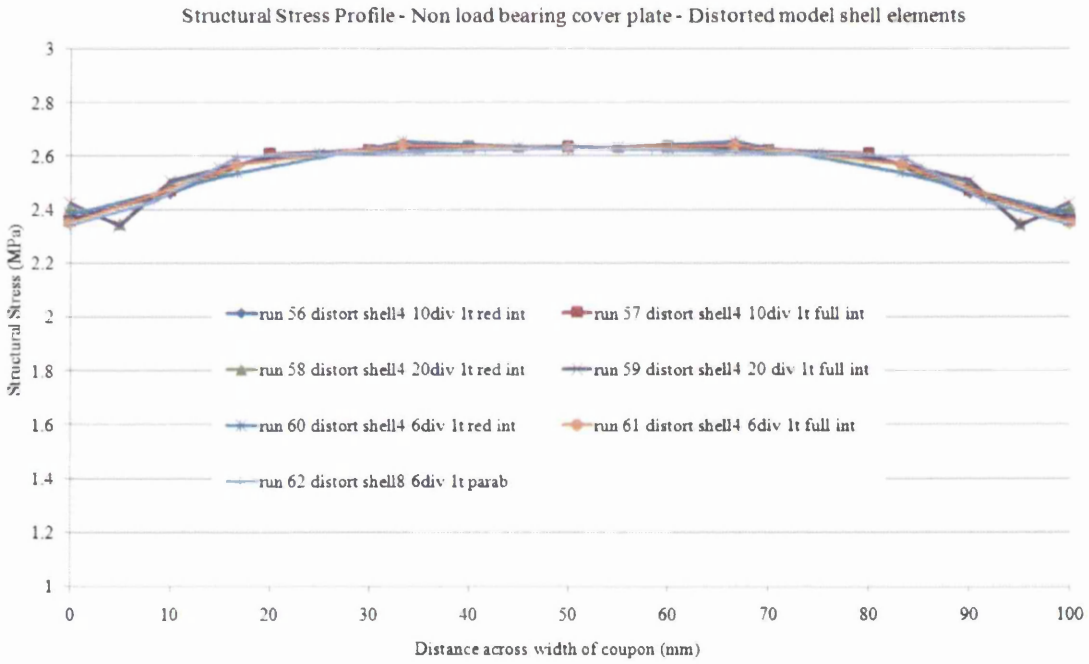

Figure 169: Non-load-bearing cover plate - Structural stress profile using distorted shell element models

The structural stress concentration factors per unit load (1kN) are displayed in Figure 168 and Figure 169 for the un-distorted and distorted shell element models respectively. In a similar way to the solid element models, there is a distinct difference between the undistorted and distorted welded coupon geometries with a peak structural stress factor per unit load of

1.5MPa and 2.6MPa respectively. When calculating the structural stress using shell elements, there is an erratic step in value towards the edge of the coupon. This is only shown when using a full integration method for element sizes >10mm. A jump in value is visible in both full and reduced integration methods for element sizes 5mm and smaller, with a larger and more apparent step occurring for full integration. There is, however, excellent correlation between the solid and shell element calculations.

There is some deviation in the results calculated with models using reduced integration methods and a coarse element number of divisions across the width of the coupon. This is due to the inability to model bending effects across the width of the coupon. These solution and modelling parameters would be advised against. However, despite showing a marginal difference in the results, an efficient answer can be achieved with only a slight compromise on accuracy.

The peak structural stress unit load factors of 1.5MPa and 2.6MPa for the shell un-distorted and distorted models are to be taken forward for further analysis. These values are obtained from what is considered the most representative, efficient and accurate, high capability mesh. This is found from using a 10 division full integration model. Confidence can be taken from the fact there is no, or only a very small deviation, seen in the results using a coarser or finer mesh from the model values taken forward.

In an attempt to determine where maximum efficiency can be obtained, a relative convergence curve is shown in Figure 170. This is a convergence check from one model to the next giving the peak structural stress (MPa) at the centre of each model plotted on the y-axis against the various model types on the x-axis. Convergence would be considered complete or achieved when the target (y-axis) displays only a small change in value in the subsequent iteration. So if the structural stress value changes by less than 10% with the iteration, there would not be much benefit from modifying the mesh or completing the next solution.

12 runs were completed for the non-load-bearing cover plate distorted geometry solid element model and 7 for the shell. The details of the solution and model parameters in each model are displayed in Table 4. There is an increased difference in the solid model results due to the added variable of through thickness mesh densities. The highest solid model inaccuracies are displayed at runs 1 to 3, where very coarse element densities are used. This

effect is not seen on the shell element models as there is no variant possible for a through thickness mesh.

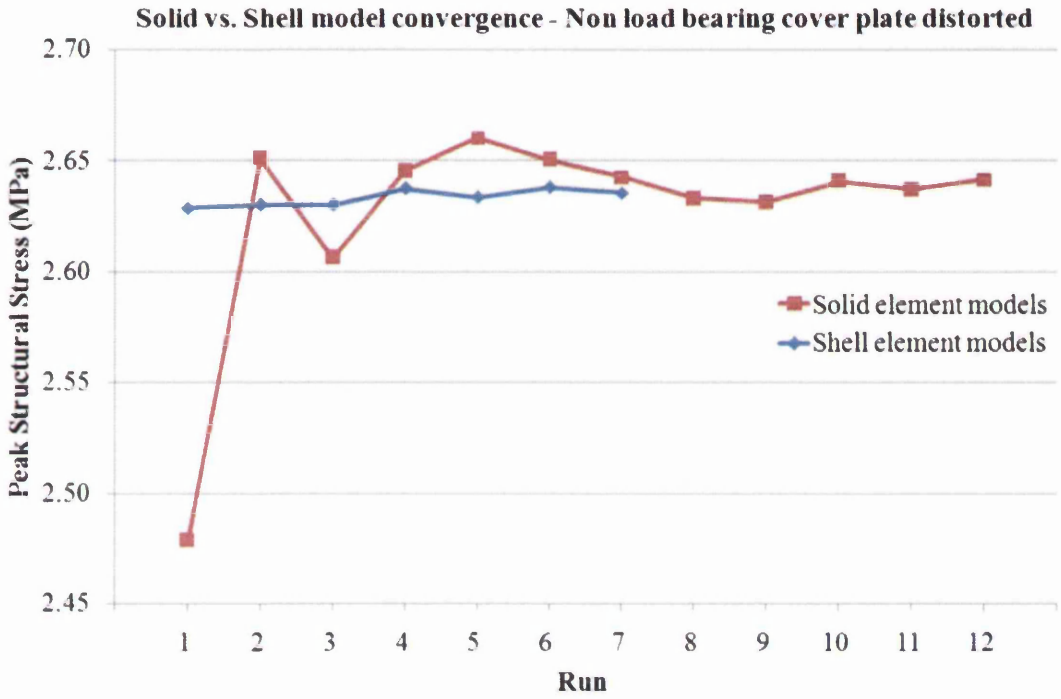

Figure 170: Solution convergence – non-load-bearing cover plate solid element distorted model

Run	No. of divisions along weld	No. of divisions through thickness	Integration type	Element order	No of. nodes	Peak SS (Mpa)
1	6	1	reduced	1	8	2.4779
2	6	1	full	1	8	2.6507
3	6	2	reduced	1	8	2.6058
4	6	2	full	1	8	2.6452
5	6	1	reduced	2	20	2.6600
6	6	1	full	2	20	2.6500
7	6	2	reduced	2	20	2.6425
8	6	2	full	2	20	2.6326
9	10	4	reduced	1	8	2.6309
10	10	4	full	1	8	2.6404
11	20	4	reduced	1	8	2.6366
12	20	4	full	1	8	2.6413

Table 4: Solid element distorted model solution parameters used in Figure 170

The convergence graph suggests full integration methods obtain the most accurate calculation. Only a very small, negligible, change is seen in the solid models after solution run 8 and up to 12. Observing the very small y-axis range, an efficient solution with only a slight compromise on accuracy, can still be achieved using models 2 to 6. Based on the convergence graph it is recommended that Model 1, reduced integration with 1 element

division through thickness, be avoided. The low levels of scatter observed also provide confidence in the mesh insensitive theory applied. Depending on the time scales and solution power available, the analyst could make a subjective decision depending on the accuracy, efficiency and time constraint imposed.

Run	No. of divisions along weld	Integration type	Element order	No of. nodes	Peak SS (MPa)
1	6	reduced	1	4	2.6288
2	6	full	1	4	2.6302
3	6	-	2	8	2.6302
4	10	reduced	1	4	2.6375
5	10	full	1	4	2.6337
6	20	reduced	1	4	2.6381
7	20	full	1	4	2.6356

Table 5: Shell element distorted model solution parameters used in Figure 170

The shell element model runs display only a small difference in the calculated structural stress between runs 3 and 7. This is a similar trait seen in the solid element model convergence between runs 7 and 12. There is only a slight increase seen, in both cases, between a 6 divisions and 20 divisions element mesh across the width of the coupon. It is evident that the finer mesh density increases the bending seen across the width of the coupon. Although the result of using a 6 division mesh is only a small error here, in a larger or complex sub-assembly under multiple loading modes, the error could be greatly increased. This could give rise to more inaccuracies in the fatigue life prediction. The shell element models here converge faster and more efficiently than the solid element models, largely due the lower number of variable FE parameters (i.e. no through thickness mesh). In this case of a non-load-bearing attachment weld, the shell model displays excellent correlation with the solid model.

4.3.3 Load-Bearing Lap Joint

Nodal forces and moments were extracted from the load-bearing lap joint FE model at the crack path defined for the solid model in Figure 171 and the shell model in Figure 173. The crack plane of the weld originates at the weld toe and propagates down through the thickness of the plate. The structural stress calculation using Excel was repeated for different element types and sizes discussed at the beginning of this chapter.

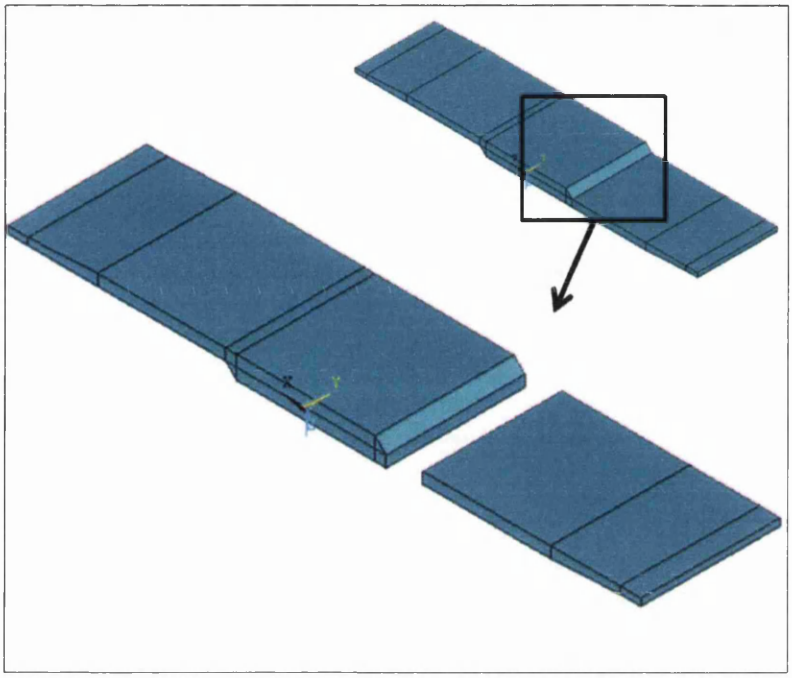

Figure 171: Load-bearing lap joint - FE solid element model crack plane

The structural stress concentration factors per unit load at the weld toe across the width of the coupon are displayed in Figure 172 and Figure 174, for the solid and shell element models respectively. The Structural Stress (MPa) on the y-axis is plotted against the distance across the width of the coupon (mm) on the x-axis.

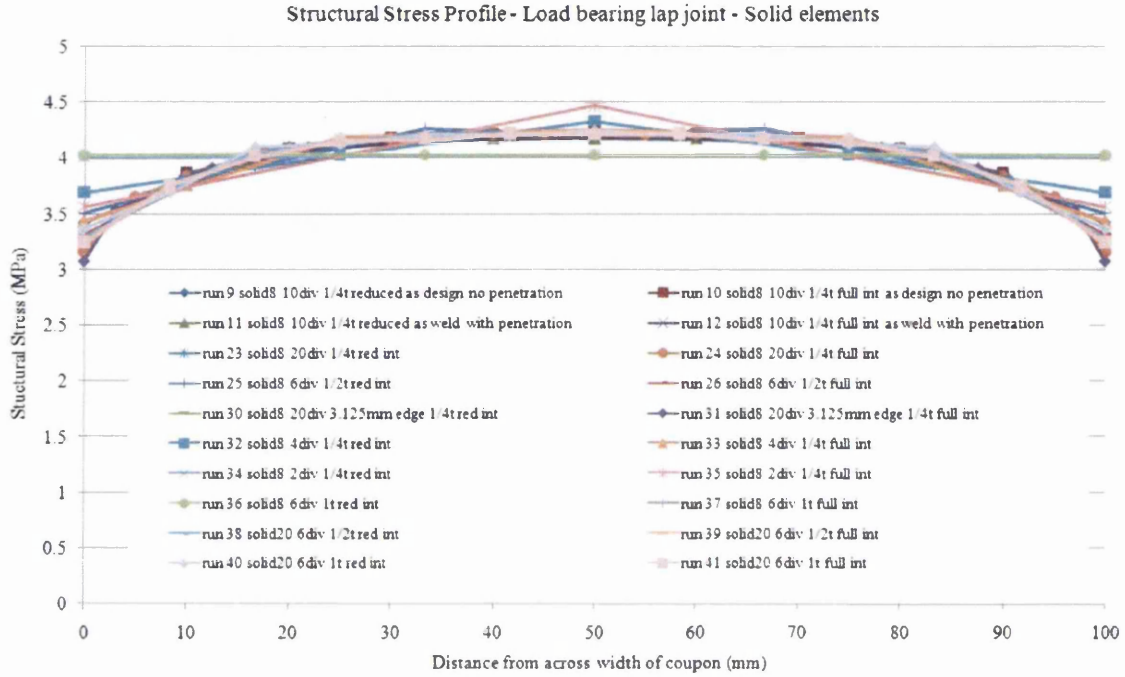

Figure 172: Load-bearing lap joint - Structural stress profile using solid element models

The structural stress factor per unit load is approximately 4.2MPa for the solid element coupon geometry. Considering the various element types and calculation methods used, there is very good correlation with little mesh sensitivity to the structural stress results. There are a number of exceptions with structural stress values calculated at approximately 4.0MPa and 4.5MPa. There are 2 models calculating structural stress values of 4MPa. The model parameters used are; 6 element divisions across the weld, 1 element through thickness and reduced integration; and 2 divisions across weld, 4 elements through thickness and reduced integration. For the 4.5MPa unit load factors, the model used consists of 2 element divisions across weld, 4 elements through thickness and a full integration solution. These measures are considered a very coarse and unrealistic mesh that should be avoided due to its limitations in representing bending. This mesh approach could lead to a slight compromise on accuracy but might be feasible given the time saved in solution. Despite this, the approach can be considered to support the mesh insensitivity claim. The final peak structural stress values are all still within a satisfactory margin of error, 5% of the mean values of the most representative and accurate mesh. Excluding the coarse mesh exceptions described above, the peak structural stress factor of 4.2MPa is to be taken forward for the solid element model.

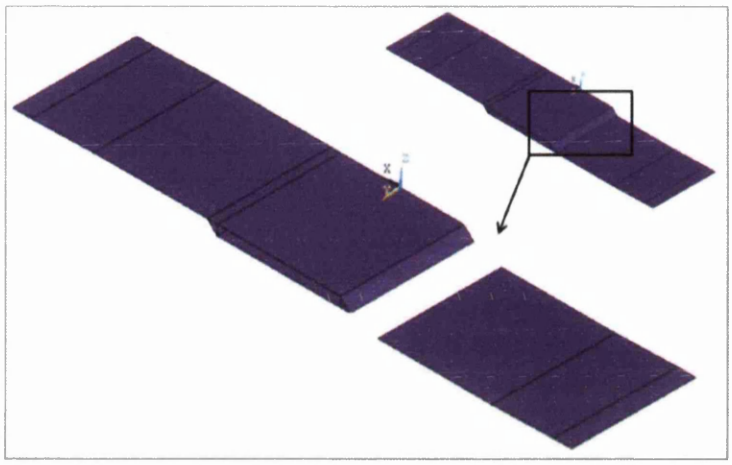

Figure 173: Load-bearing lap joint - FE shell element model crack plane

When calculating the structural stress using shell elements, there is a noticeable step in value towards the edge of the coupon. This is again, as per the previous coupon, only shown when using a full integration method for element sizes >10mm. An increase in the step is in both full and reduced integration methods of element sizes 5mm and smaller. Of the two, the step is larger and more apparent for full integration.

At the centre of the coupon stress profile, there is excellent correlation between the calculated factors. Models with a coarse mesh, of 2 and 4 divisions across the wide of the coupon, and a reduced integration method calculate a slightly higher unit load factor of 4.3MPa and 4.45MPa respectively. This only a slight error compared with the peak structural stress factor of 4.2MPa for the high density meshes. The 2 and 4 divisions gave element sizes of 50mm and 25mm respectively. Across a 100mm coupon, these values are considered very coarse and will be excluded from any further analysis. However, there is confidence in the method if comparable answers, with only a slight degradation in accuracy, can be achieved using extremely coarse models. Second to this, when using the same mesh sizes with a full integration type, there is very good correlation of peak structural stresses with the most accurate high-density mesh.

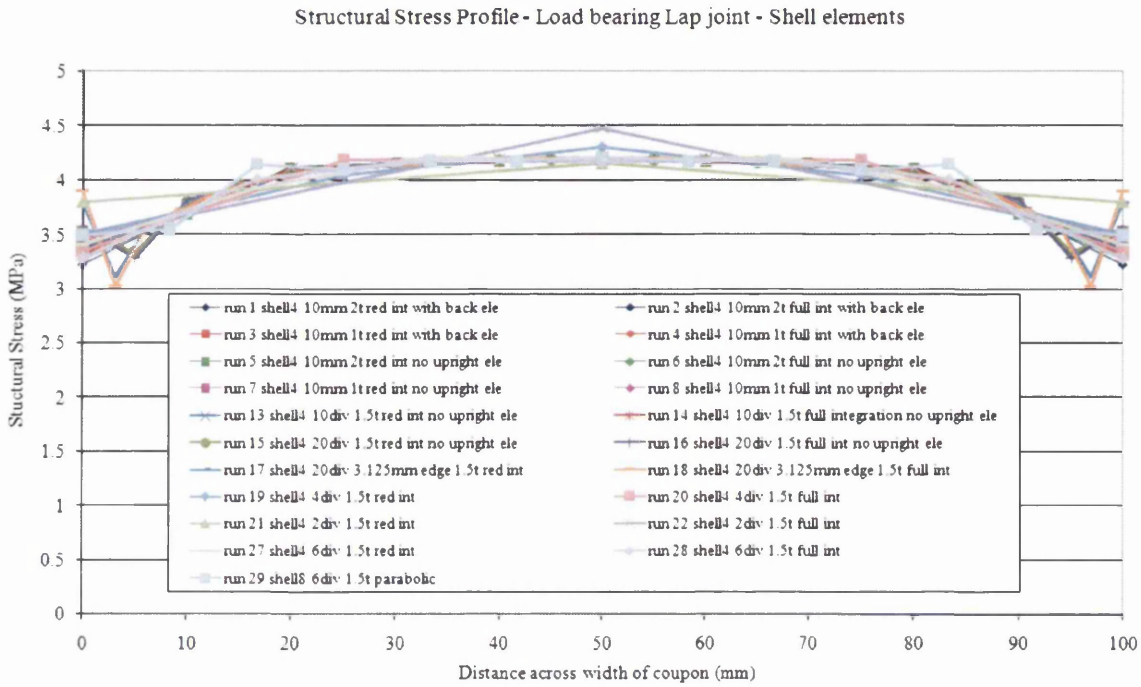

Figure 174: Load-bearing lap joint - Structural stress profile using shell element models

There is excellent correlation and little deviation between the solid and shell element calculations, both with unit load factors of 4.2MPa.

4.3.4 Non-load-bearing Transverse Attachment

The first non-load-bearing transverse attachment coupon with the root failure crack path is defined in Figure 175 and Figure 176 for the solid and shell element models respectively. The crack plane of the weld originates at the weld bead root where the attachment meets the load carrying plate and propagates down through the thickness of the plate. The structural stress calculation procedure is applied for a range of different element types. The structural stress is calculated for a weld toe failure, to compare against the weld root failure. If the calculation theory supports a weld root failure, the weld toe will see a lower structural stress parameter. Should a similar situation arise in an authentic design environment, the structural stress approach could be optimised to then avoid a root failure by altering the weld geometry design.

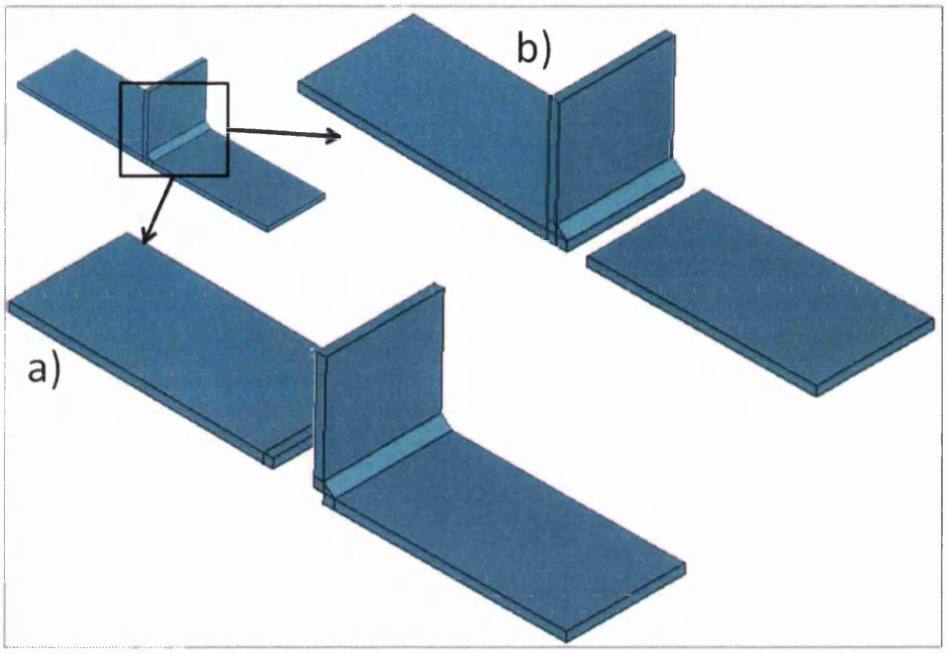

Figure 175: Non-load-bearing transverse attachment – FE solid model crack plane a) plate root failure and b) weld toe failure

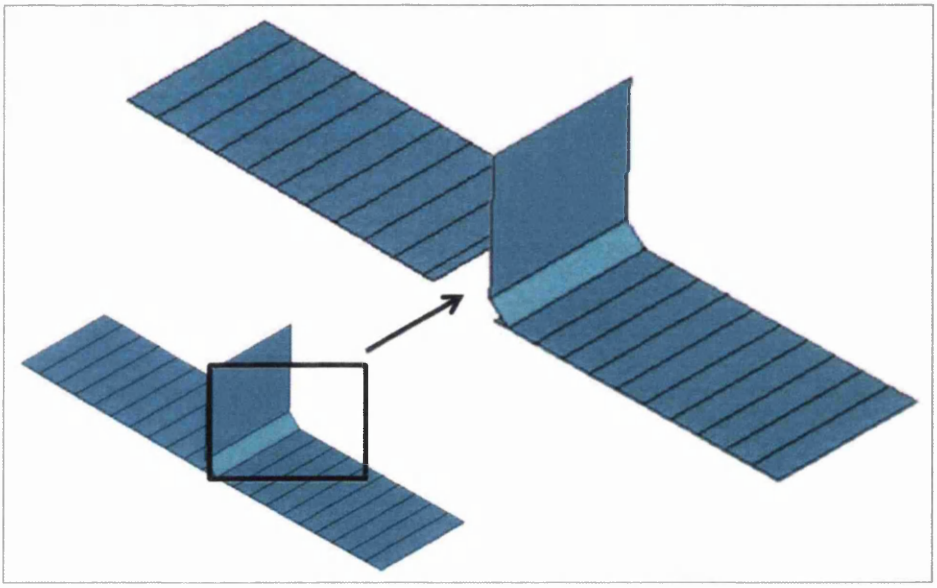

Figure 176: Non-load-bearing transverse attachment FE shell model – root failure crack plane

Solid and shell element FE models were generated for both the as-designed and as-welded (distorted) coupon geometries. The structural stress profile was generated using the calculation procedure described at the beginning of this chapter. The structural stress factors per unit load at both the weld toe and weld root are displayed below across the width of the coupon. The Structural Stress (MPa) on the y-axis is plotted against the distance across the

width of the coupon (mm) on the x-axis for the un-distorted coupons in Figure 177 and the distorted coupons in Figure 178.

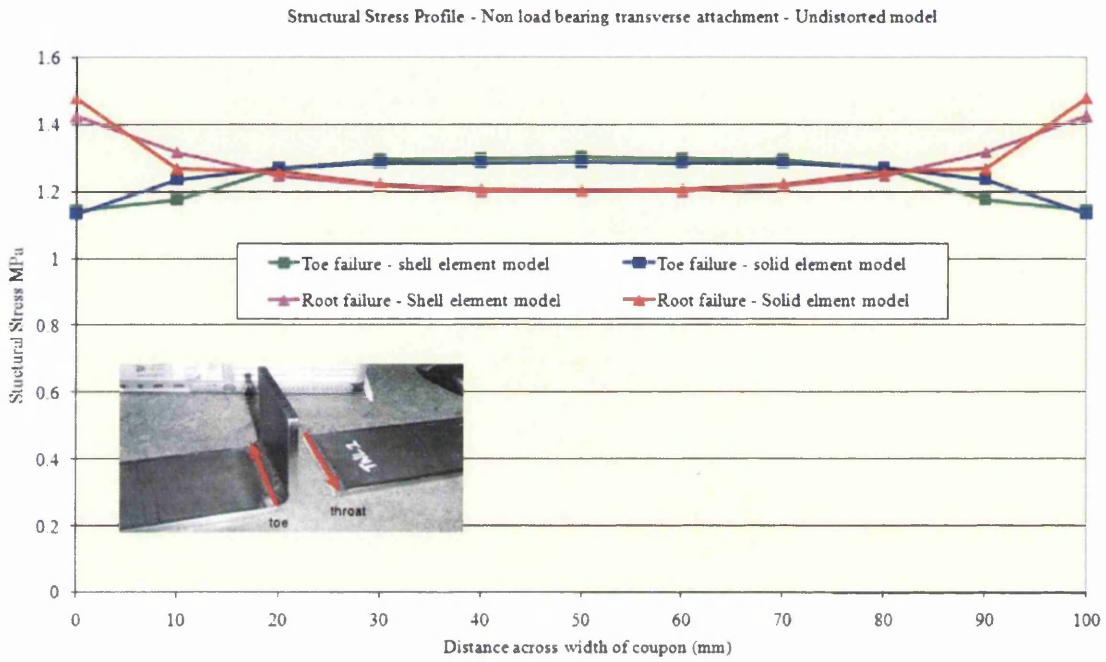

Figure 177: Non-load-bearing transverse attachment root failure – un-distorted structural stress profile

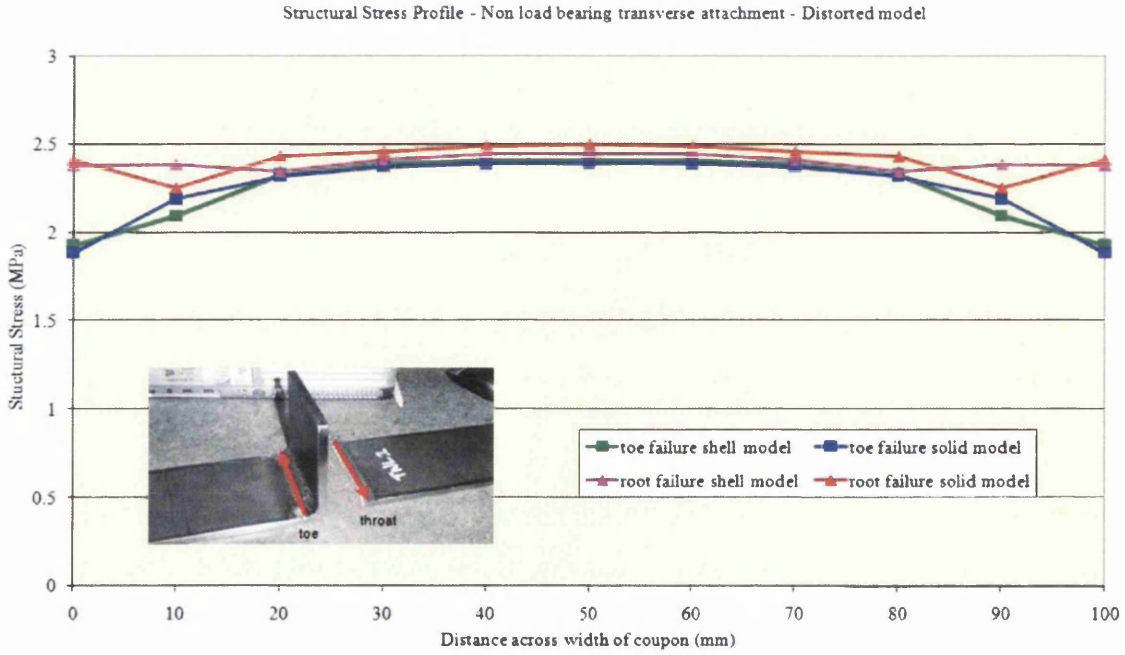

Figure 178: Non-load-bearing transverse attachment root failure - distorted structural stress profile

In the un-distorted coupon geometry, the weld toe failure mode calculated a slightly higher structural stress than the root failure mode that was actually observed in the test coupon, 1.3MPa compared with 1.2MPa at the centre (where crack initiation occurred). Having modelled the distorted geometry of the actual welded coupon, the structural stress concentration factors calculated are 2.39MPa for the weld toe failure and 2.49MPa for the root failure. A more realistic representation of test coupon is seen in the distorted geometry, and a higher factor is then calculated for the actual root failure mode.

Nodal forces and moments were extracted for the second batch of non-load-bearing transverse attachment coupons at the crack paths positions defined in Figure 179 and Figure 180 for the solid and shell element doubled sided coupon models. The crack plane of the modelled weld is typical of a common weld toe failure.

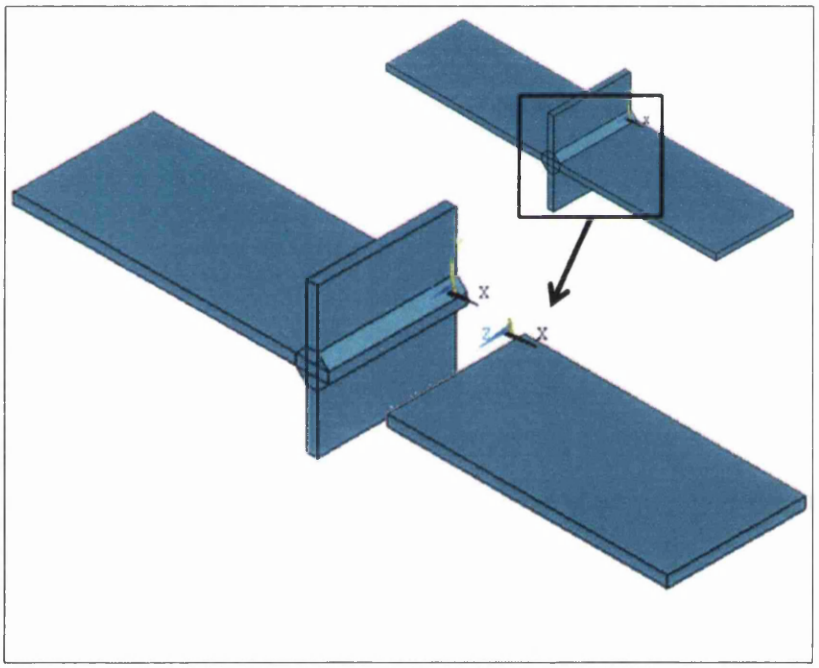

Figure 179: Double non-load-bearing transverse attachment - FE solid model crack plane (NLT1D)

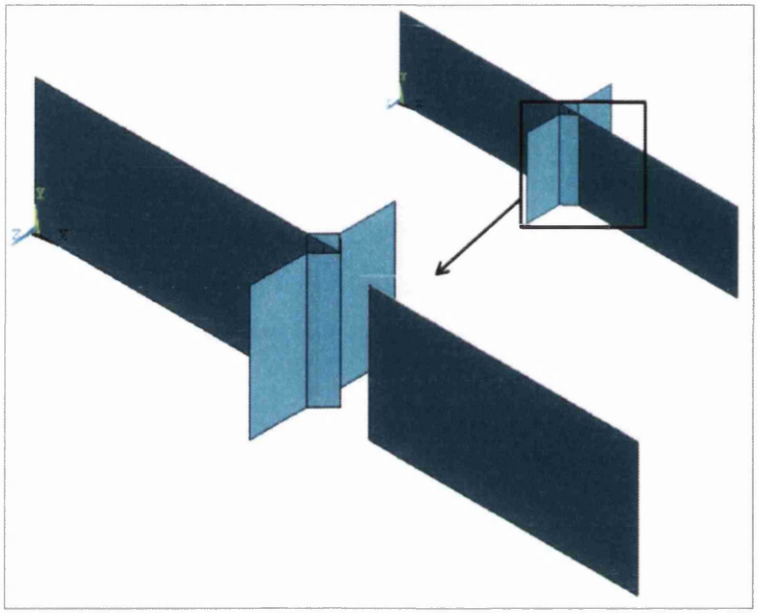

Figure 180: Double non-load-bearing transverse attachment - FE shell model crack plane (NLT1D)

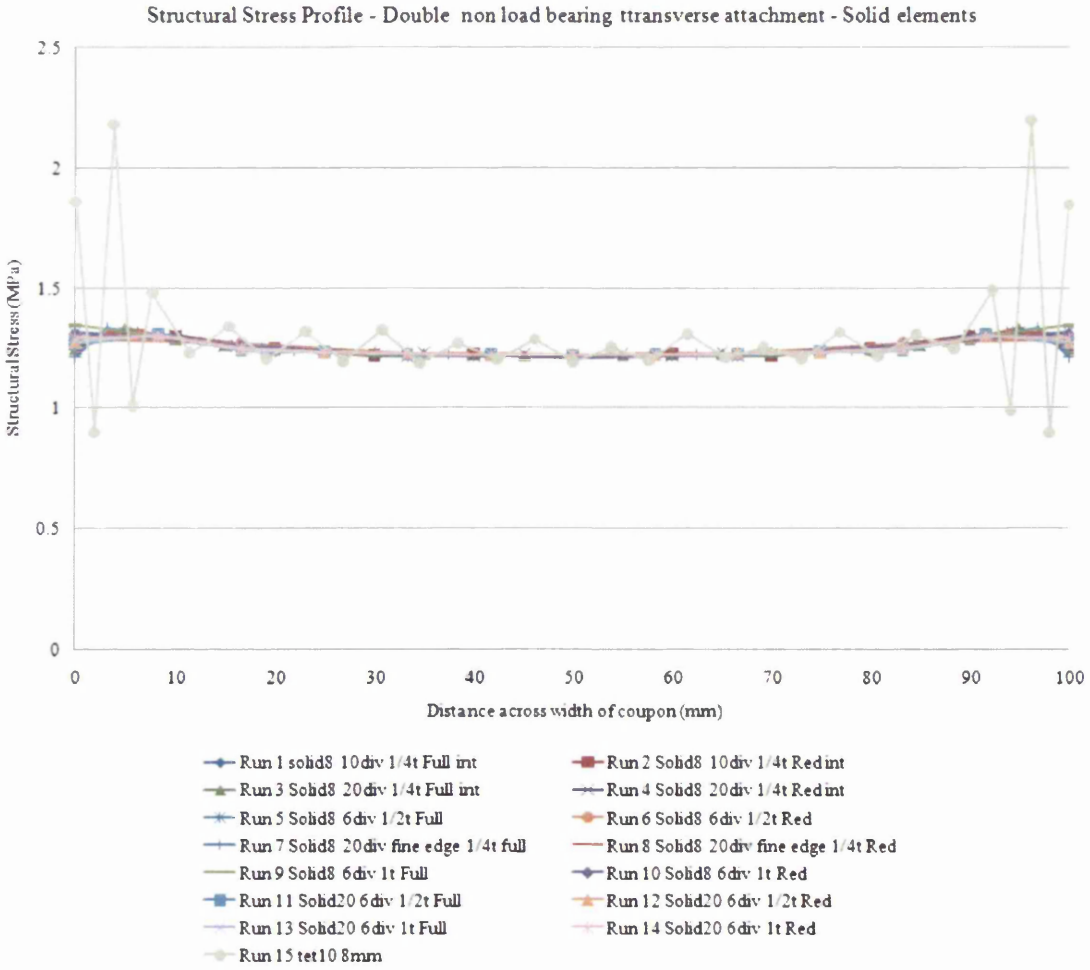

Figure 181: Non-load-bearing transverse double attachment (NLT1D) - structural stress profile using solid element models

The structural stress concentration factor per unit load is calculated at the weld toe across the width of the coupon. The structural stress profiles for the double non-load-bearing attachment solid element models are displayed in Figure 181. The peak structural stress factor per unit load is approximately 1.22MPa at the centre of the solid element coupon geometry. There is a wide range of differing FE model parameters used but all with very good correlation and little mesh sensitivity to the structural stress results. A 10-node tetrahedral element model was created and the structural stress plotted. The stress profile is inconsistent and uneven with the stress value fluctuating between 1.2 and 1.29MPa. The values get considerably worse at the edges lying between 0.9 and 2MPa

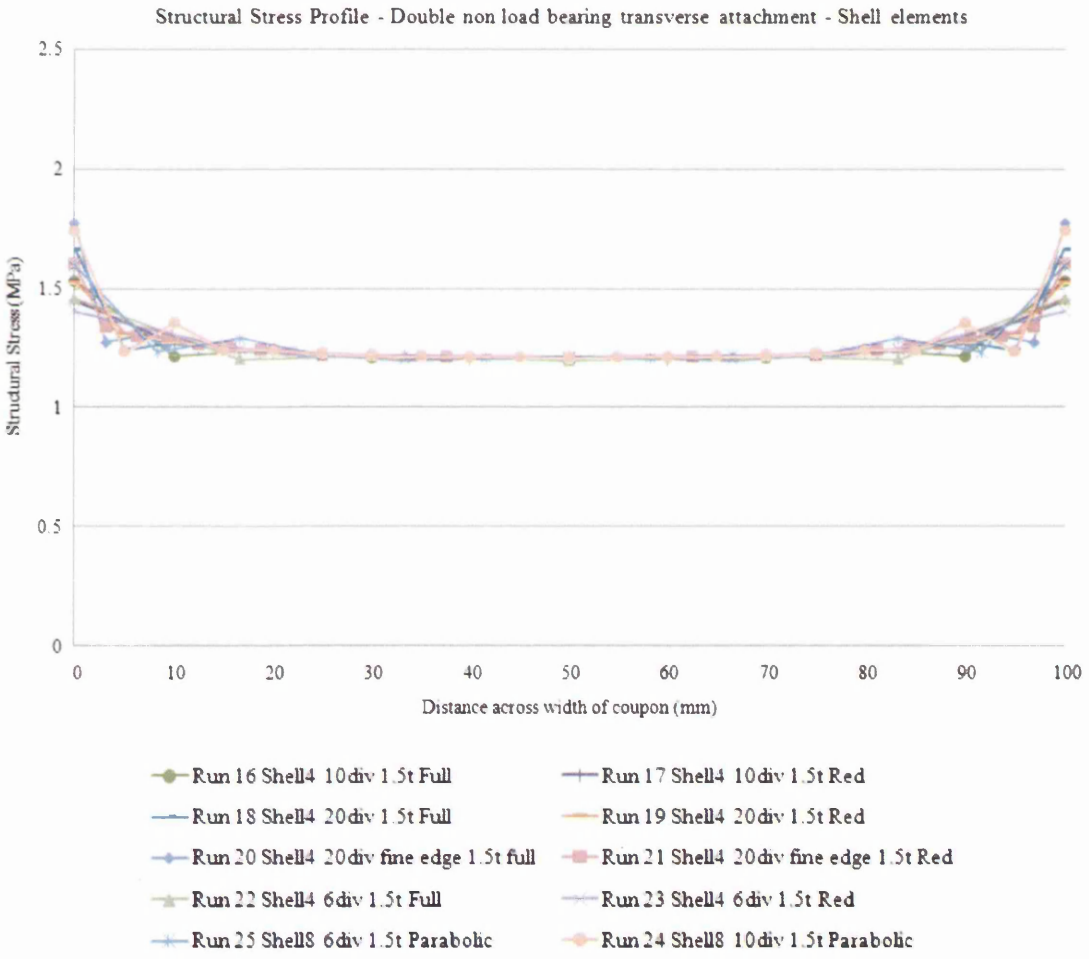

Figure 182: Non-load-bearing transverse double attachment (NLT1D) - structural stress profile using shell element models

The structural stress profiles for the double non-load-bearing attachment shell element models are displayed in Figure 182. The shell element models show a peak structural stress factor per unit load of 1.2MPa. When calculating the structural stress using shell elements,

there is a noticeable increase in value towards the edge of the coupon. The increase occurs for both full and reduced integration types of all element sizes. The difference in stress profile towards the edge of the coupon is noticeable. The calculated values become irregular at the edge of the coupon for finer element mesh densities and become more exaggerated when full integration is used. Comparing the solid against the shell element calculations there is excellent correlation and little deviation between the two.

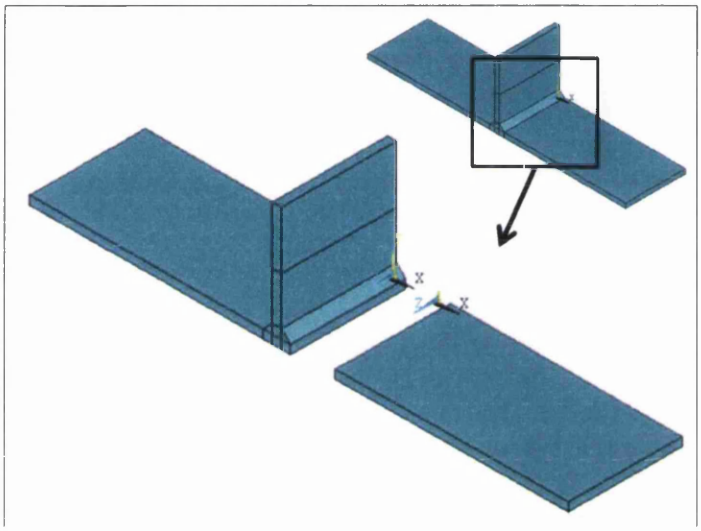

Figure 183: Single non-load-bearing transverse attachment - FE model solid element model crack plane (NLT1S)

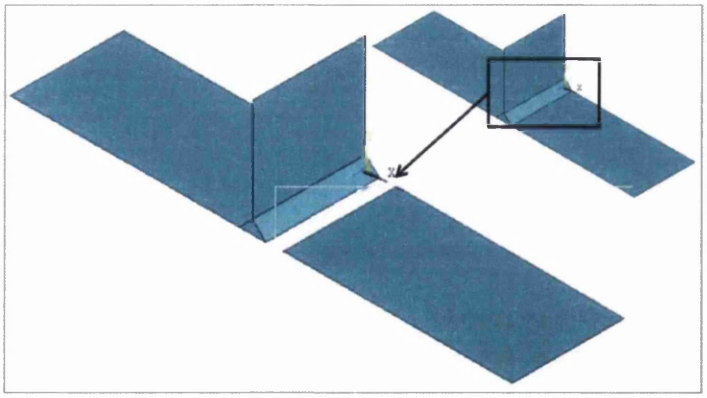

Figure 184: Single non-load-bearing transverse attachment - FE model shell element model crack plane (NLT1S)

Nodal forces and moments were extracted for the non-load-bearing single transverse attachment coupons at the crack paths positions defined in the solid element and shell element models, Figure 183 and Figure 184. The range of FE model parameters, as used on the double attachment coupon, was also applied to the single attachment coupon, as per the summarised element mesh size and densities at the beginning of chapter 4.3. Due to the

single-sided welding runs, the final coupon manufactured was distorted. The load carrying back plate was convex and curved into the weld. Two model geometries were created, in the un-distorted and distorted form.

The structural stress concentration factor per unit load was calculated at the weld toe across the width of the coupon. The structural stress profiles for the single, non-load-bearing attachment, un-distorted model using solid elements are displayed in Figure 185.

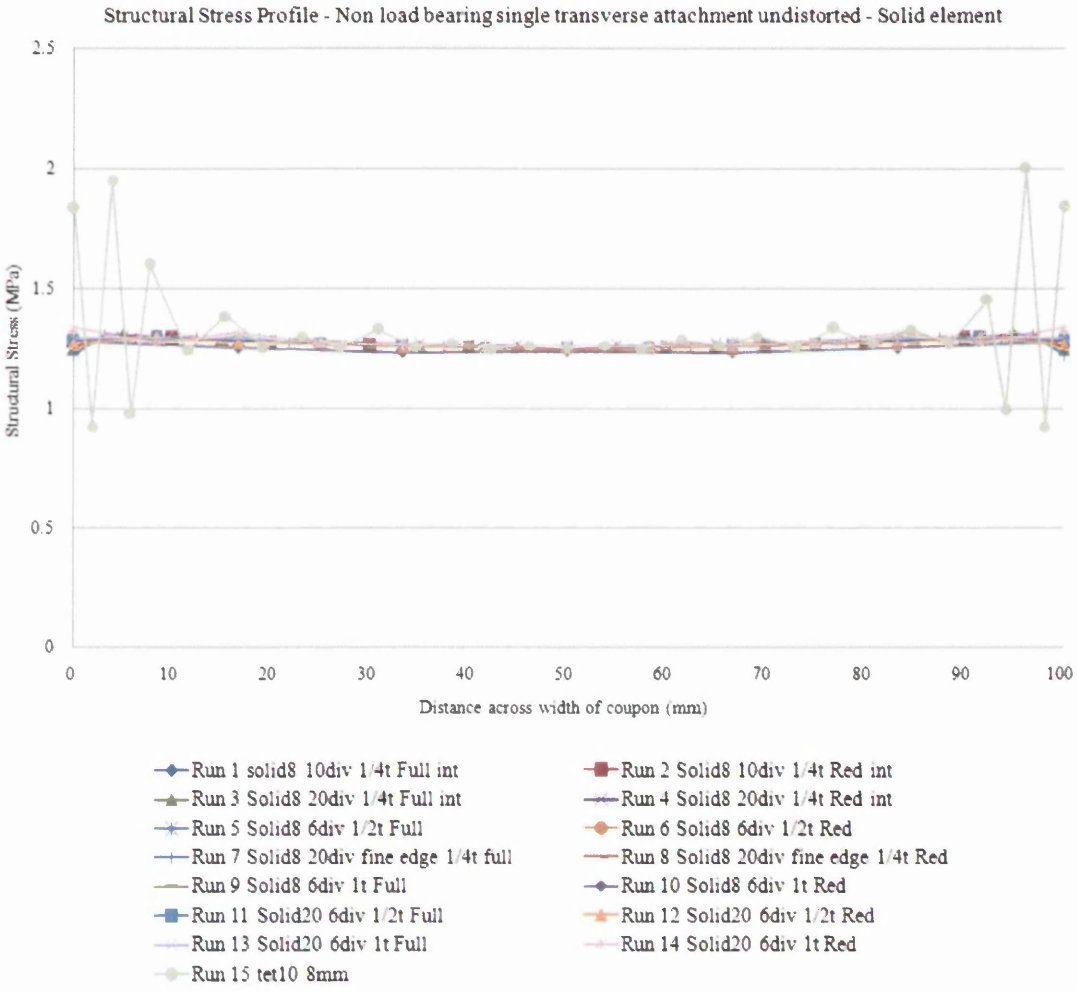

Figure 185: Non-load-bearing transverse - single attachment un-distorted (NLT1S) - structural stress profile using solid element models

The peak structural stress factor per unit load is approximately 1.26MPa at the centre of the solid element coupon geometry. The structural stress calculation displays very little sensitivity to the different FE model parameters: mesh density and element type used (solid brick or plane shell, 1st or 2nd order). A 10-node tetrahedral element model was created and the structural stress plotted. The stress profile for this is inconsistent and uneven. The stress at

the centre region of the coupon has a similar profile with a magnitude of 1.25MPa. Towards the edges of the coupon the structural stress profile gets very erratic and differs between 0.93 and 2MPa.

The structural stress profiles for the single, non-load-bearing attachment, un-distorted model using shell elements are displayed below in Figure 186. The Structural Stress (MPa) on the y-axis is plotted against the distance across the width of the coupon (mm) on the x-axis for the un-distorted coupons.

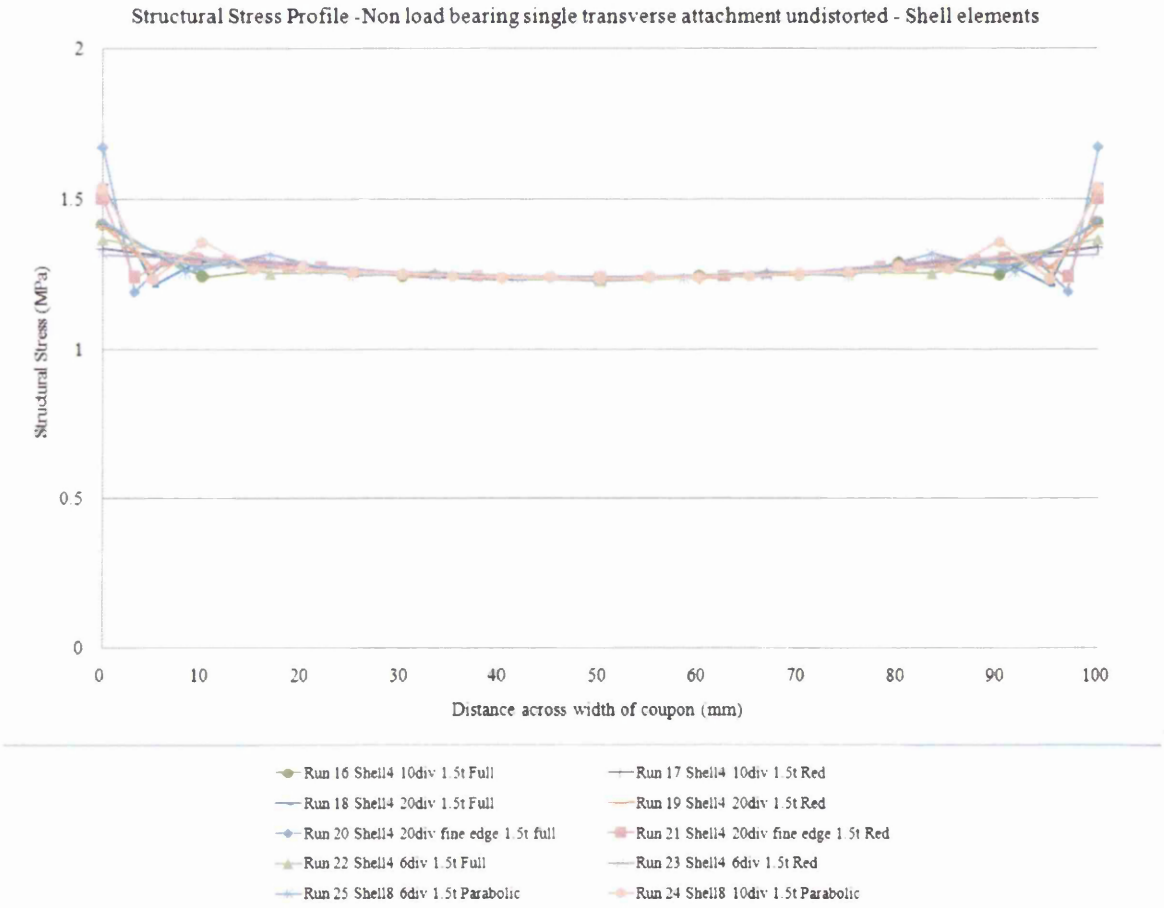

Figure 186: Non-load-bearing transverse - single attachment un-distorted (NLT1S) - structural stress profile using shell element models

The shell element models show a peak structural stress factor per unit load of 1.24MPa. When calculating the structural stress using shell elements, there is a noticeable increase in value towards the edge of the coupon. An increase occurs for both full and reduced integration methods and all element sizes. There is a noticeable difference in stress profile towards the edge of the coupon. The calculated values become irregular at the edge of the

coupon for finer element mesh densities particularly when full integration is used. This is not a major concern as crack initiation in the coupons occurred in the centre region of the coupons. The outer edge weld toes were also ground flush with a 240 grit abrasive grinding wheel. Comparing the structural stress profiles of the solid element models against the shell element profiles, there is excellent correlation and little deviation at the centre region peak values. There is some divergence in the stress profile at the edge of the coupon in the solid element models.

In an attempt to investigate the effects of modelling the designed weld coupon geometry, as opposed to the distorted or 'real' coupon geometry, the structural stress profiles for the single, non-load-bearing attachment, distorted solid element models are displayed below in Figure 187.

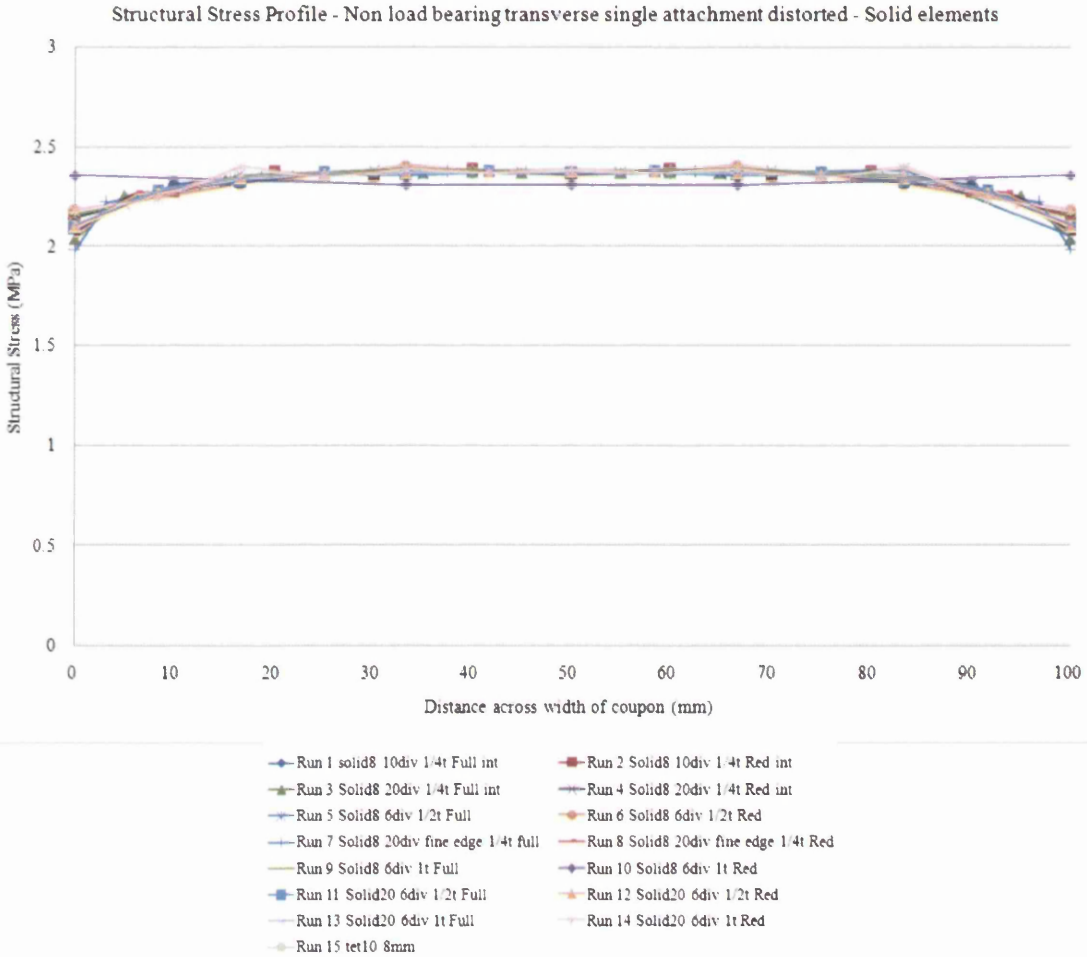

Figure 187: Non-load-bearing transverse - single attachment distorted (NLT1S) - structural stress profile using solid element models

The structural stress profiles for the single, non-load-bearing attachment, distorted shell element models are displayed below in Figure 188.

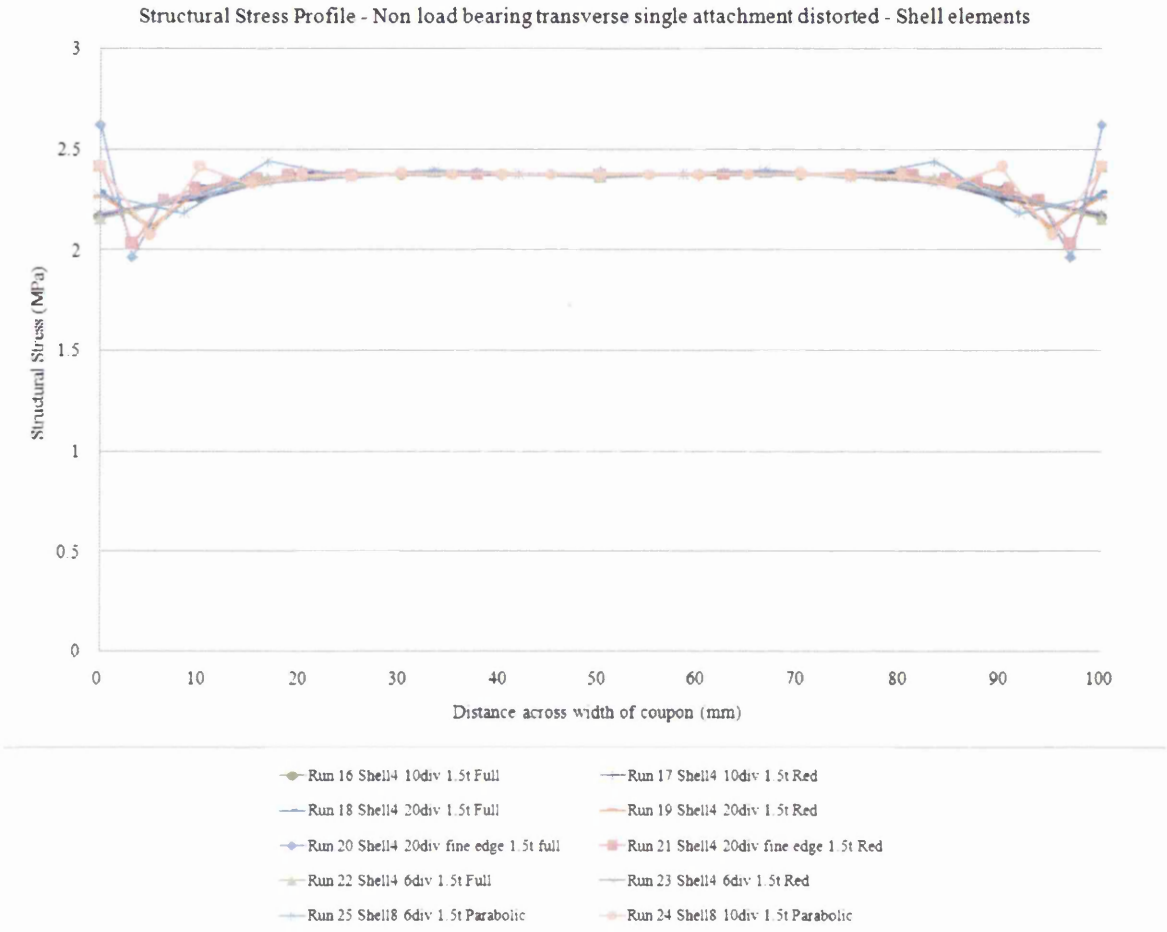

Figure 188: Non-load-bearing transverse - single attachment distorted (NLT1S) - structural stress profile using shell element models

The structural stress factor per unit load is calculated at the weld toe across the width of the coupon. The Structural Stress (MPa) on the y-axis is plotted against the distance across the width of the coupon (mm) on the x-axis. When modelling the distortion of the coupon geometry, the load-carrying back plate is bent due to the weld runs position at the centre of the coupon. Applying a tensile load, the load follows a different path to that of the un-distorted geometry (Figure 133). Significantly more bending moment is introduced (Figure 136). This is shown in the distorted geometry structural stress profiles above. The peak structural stress values at the centre region are 2.39MPa and 2.38MPa for the solid and shell element models, compared with 1.26MPa and 1.24MPa for the un-distorted coupon geometries. Similar mesh-insensitivity traits are shown here as found in previous stress profiles of the non-load-bearing double and single (un-distorted) attachment coupon. There is

excellent correlation throughout, except for the 1st order solid element model with 1 element through thickness, which has limitations in representing bending across the coupon width, while shell elements profiles become uneven towards the edge of the coupon.

4.3.5 Load Carrying Cruciform Joint

The structural stress calculation procedure was applied to the both the cruciform FE models with 8mm and 10mm weld leg lengths. The crack paths are illustrated in Figure 189 and Figure 190 for solid and shell element models (10mm weld leg models shown). The crack plane originates at the root of the weld bead 'fit up' gap and propagates out through the weld throat at approximately 18 degrees to the horizontal base plate.

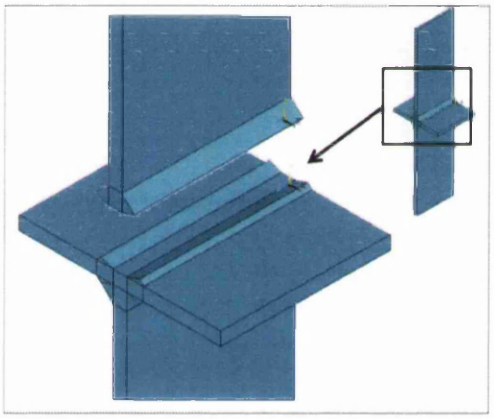

Figure 189: Load-bearing cruciform coupon - FE solid element model crack plane 10mm weld leg

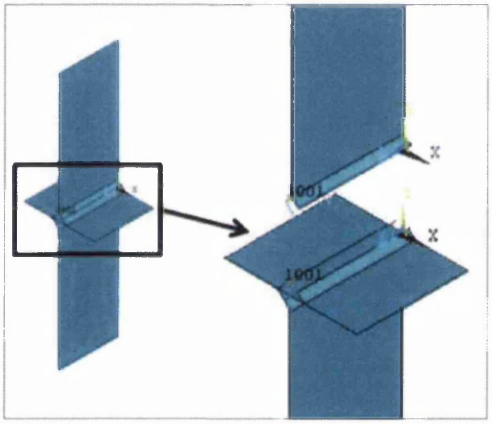

Figure 190: Load-bearing cruciform coupon - FE shell element model crack plane 10mm weld leg

The main consideration of the load carrying cruciform joint is the weld throat failure mode. Sensitivity effects in the calculation procedure due to factors such as mesh density have been explored extensively earlier on in this chapter with consistent results. The capability of the method for the cruciform joint has been investigated; with consideration given to the effects

of element type (solid brick or shell plane), crack plane location and weld penetration. These are factors that are potentially more influential on the structural stress results. Solid brick elements were used to model with a crack plane angle of either 18 degrees (actual throat crack angle – shallow) or a generic 45 degrees (minimum weld throat area i.e. maximum nominal stress). A review was completed on the effects of different weld penetration levels and the bearing it has on the structural stress calculation. From the tensile load tee joint stress profiles, shell element models are not sensitive to the different theoretical crack planes used. Thus a single shell crack plane model was used for the cruciform joints. A review was completed on the effect that different weld throat element thicknesses have on the structural stress calculation. Taking these issues into consideration, separate FE models were created for both the 8mm weld leg and 10mm weld leg cruciform joint. Structural stress profile plots were created for both coupon geometries.

The structural stress profile per unit load (MPa) is plotted against the distance across the width of the coupon (mm) in Figure 191 for the 8mm cruciform joint solid element models and Figure 192 for the shell model.

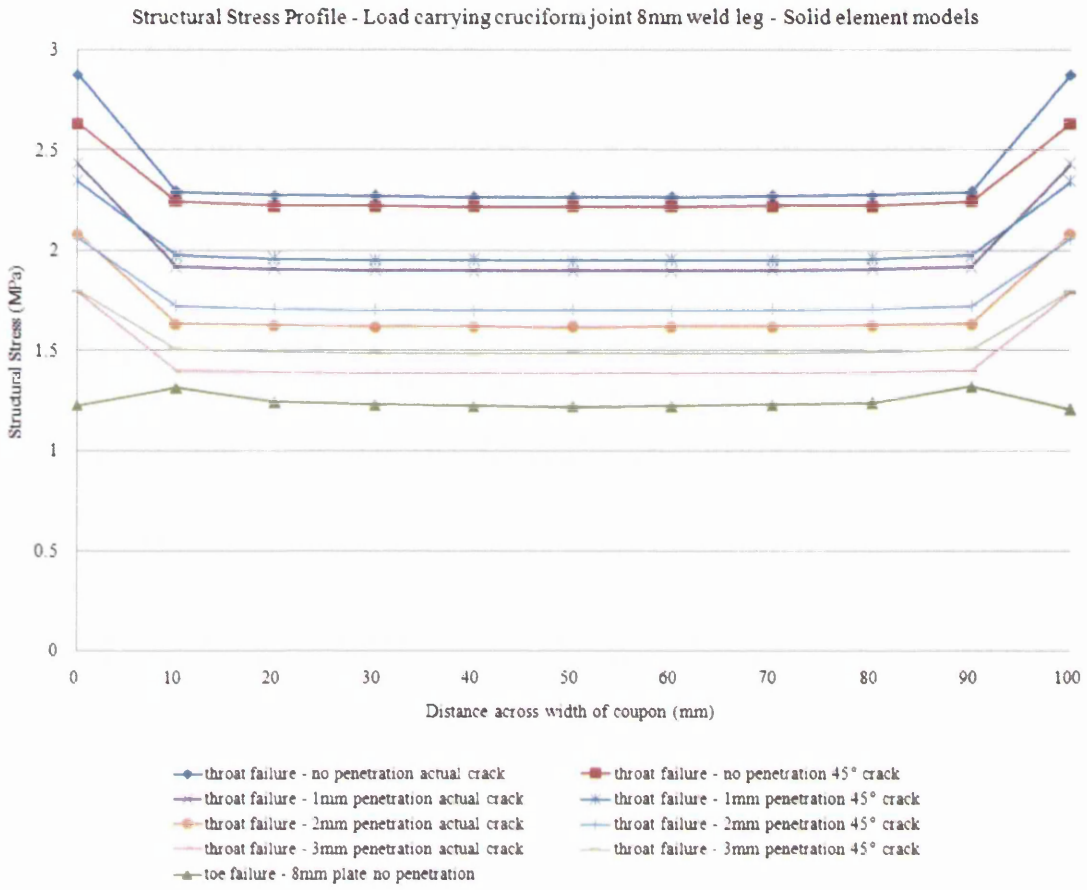

Figure 191: Cruciform joint 8mm weld leg- Structural stress profile using solid element models

The structural stress peak values of interest lie at the centre of the coupon (50mm from the edge) where the crack initiation was observed to occur on the test coupon. The results for the tee joint solid element model are sensitive to the level of weld penetration and crack plane position. The results differ, ranging from 1.4MPa to 2.3MPa per unit load (1kN). This could potentially prove to be a problematic area for fatigue life prediction of weld throat failures and produce conservative or over predicted lives. In the actual fatigue test coupon failures, there were varying and inconsistent levels of weld penetration achieved. The structural stress profile for a toe failure is also calculated with a centre peak unit load factor of 1.25MPa. This is below the lowest calculated throat failure value and suggests a throat failure value should occur before a weld toe cracking.

For the shell element models, the structural stress theory proposes that the forces and moments extracted from the FE model are divided by the value of the element thickness used. For an analysis of a weld throat failure, this can be problematic and an area of uncertainty. Four tee shell models were created using different weld throat element thicknesses of 8, 10,

12 and 16mm. In the structural stress calculation, the corresponding weld throat element thickness has been used.

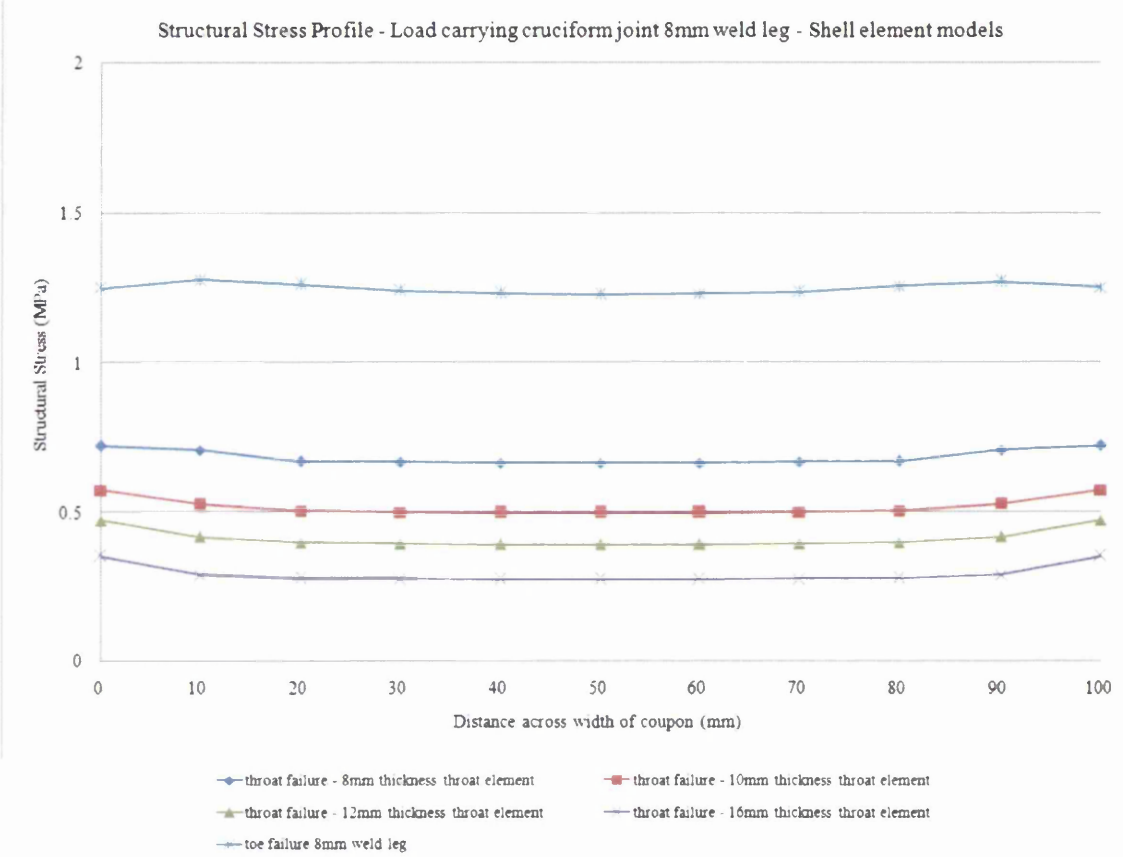

Figure 192: Cruciform joint 8mm weld leg - Structural stress profile using shell element models

The structural stress profile results show sensitivity to the element thickness and the corresponding throat element thickness t value used in calculation. The structural stress values are also very low (0.27 to 0.66MPa per unit load) in comparison with the solid model peak stresses (1.4 to 2.25MPa per unit load). In Figure 193 the structural stress profiles are plotted using the final fracture area thickness t, as seen in the coupon test. This value ranges between 6.3mm and 9.2mm. Plotting the modified structural stress profiles shows there is a much-improved correlation between the four FE-shell models. Again, the Structural Stress (MPa) is plotted against the distance across the width of the coupon (mm). The centre region peak structural stresses range from 0.4 to 0.6MPa per unit load. A unit load factor is calculated for a toe failure mode. The value of 1.25MPa is considerably high than the calculated throat failure modes. Based on this a weld toe failure should occur before a weld throat crack. In the test coupon results this was not the case and would suggest the cruciform shell structural stress calculation is incorrect.

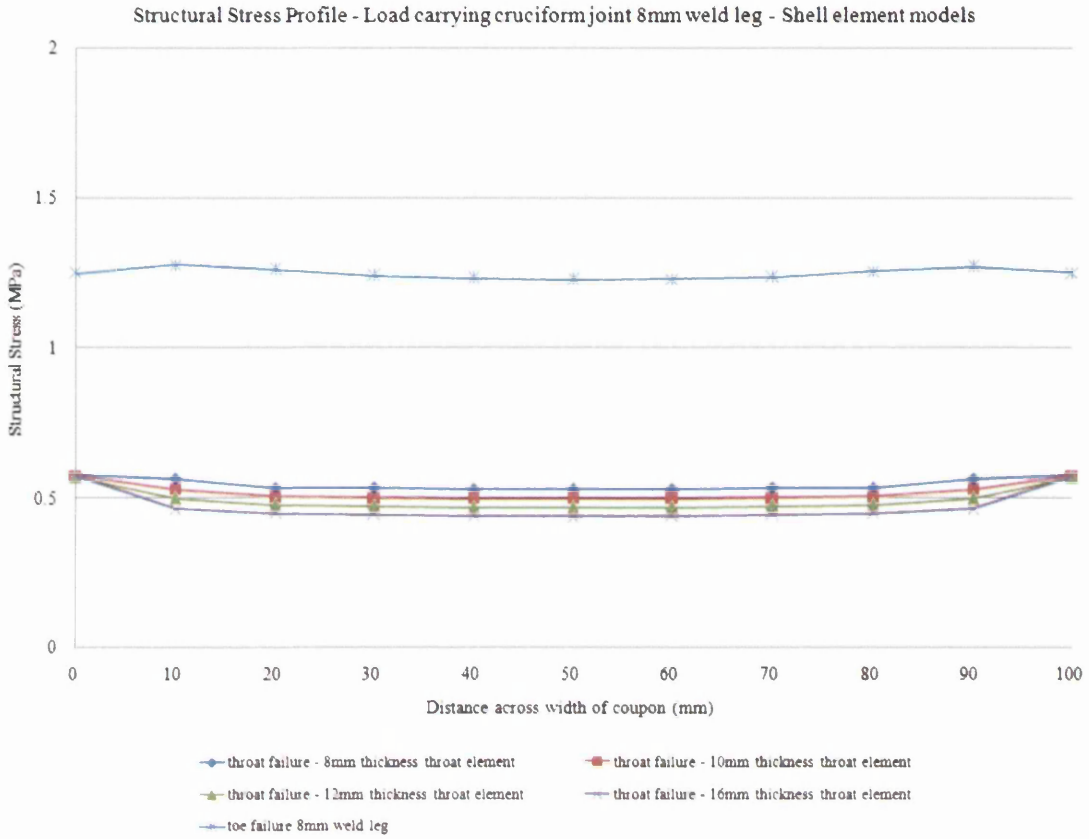

Figure 193: Cruciform joint 8mm weld leg - Structural stress profile using shell element models – using actual weld throat failure thickness in the structural stress calculation

The same approach has been applied to the 10mm weld leg cruciform joint. The structural stress profile per unit load (MPa) is plotted against the distance across the width of the coupon (mm) in Figure 194 for the 10mm cruciform joint solid element models and Figure 195 for the shell model.

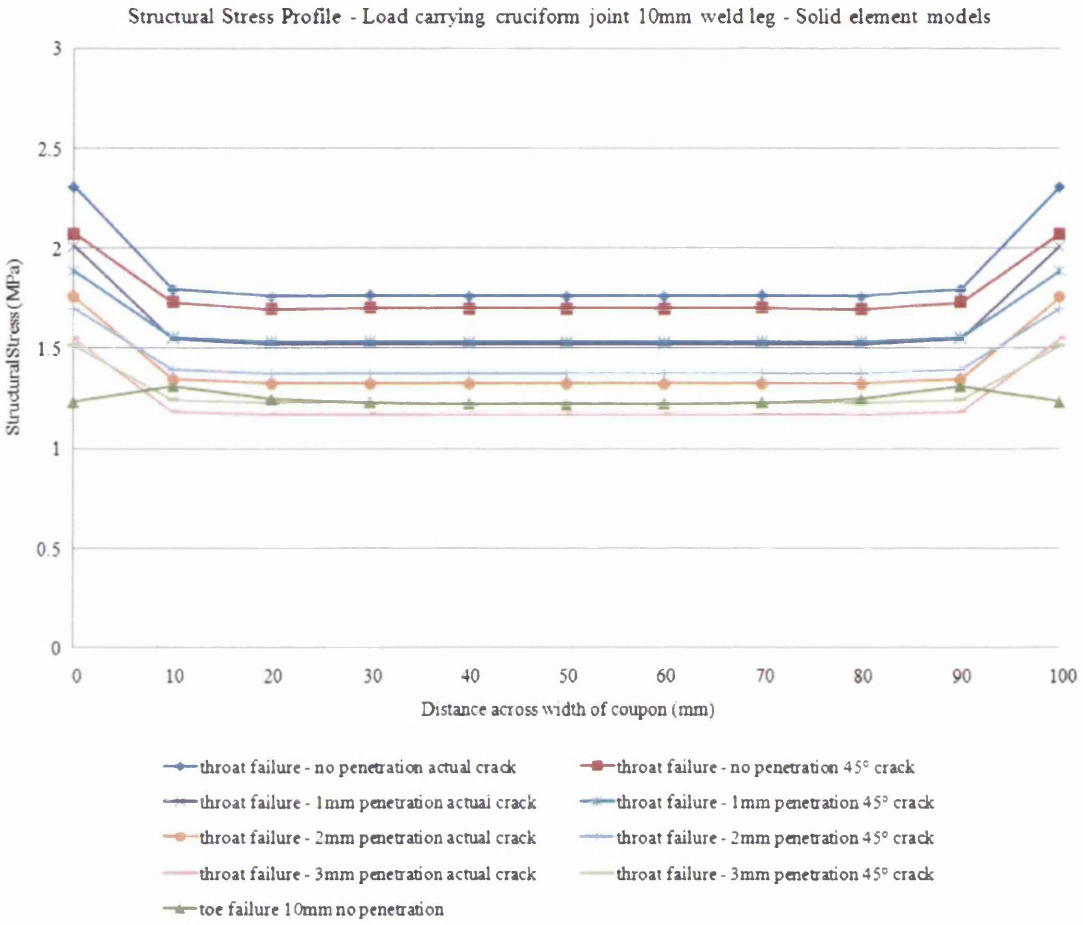

Figure 194: Cruciform joint 10mm weld leg- Structural stress profile using solid element models

The tee joint solid element model results are sensitive to the level of weld penetration and crack plane modelled in the finite element analysis. The results differ ranging from 1.16MPa to 1.76MPa per unit load (1kN). This could be a source of conservative or over prediction in fatigue lives. In the actual fatigue test coupon failures, there were varying and inconsistent levels of weld penetration achieved.

In the stress profiles for the four tee shell models above, the weld throat element thicknesses of 8, 10, 12 and 16mm were used as *t* in the structural stress calculation. The structural stress profile results show sensitivity to the element thickness and the corresponding throat element thickness t value used. The structural stress values are also very low (0.28-0.68MPa per unit load) in comparison with the solid model peak stresses (1.16-1.76MPa per unit load)

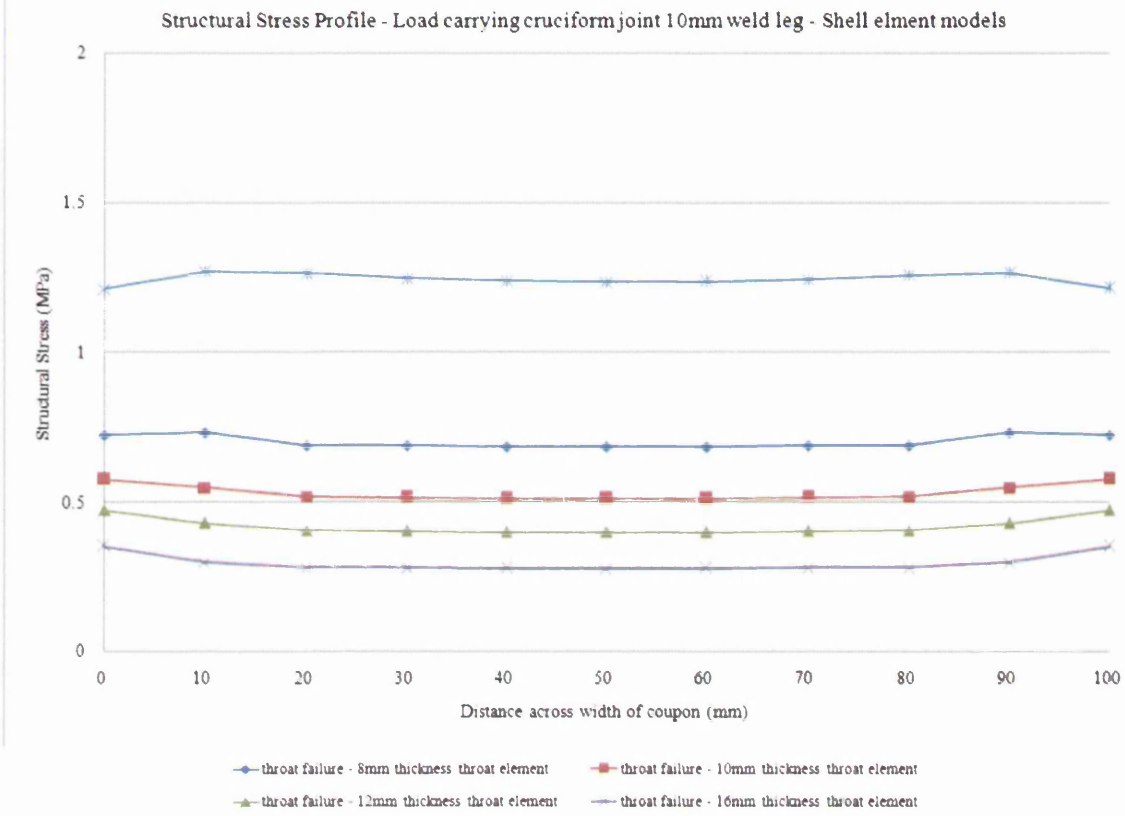

Figure 195: Cruciform joint 10mm weld leg - Structural stress profile using shell element models

The shell model structural stress profiles in Figure 196 below used the final fracture area thickness t, as seen in the coupon test. This value ranges between 8mm and 10.8mm. Plotting the modified structural stress profiles shows there is a much-improved correlation between the four differing FE shell models. The Structural Stress (MPa) on the y-axis is plotted against the distance across the width of the coupon (mm) on the x-axis. The centre region peak structural stresses range from 0.4MPa to 0.68MPa per unit load.

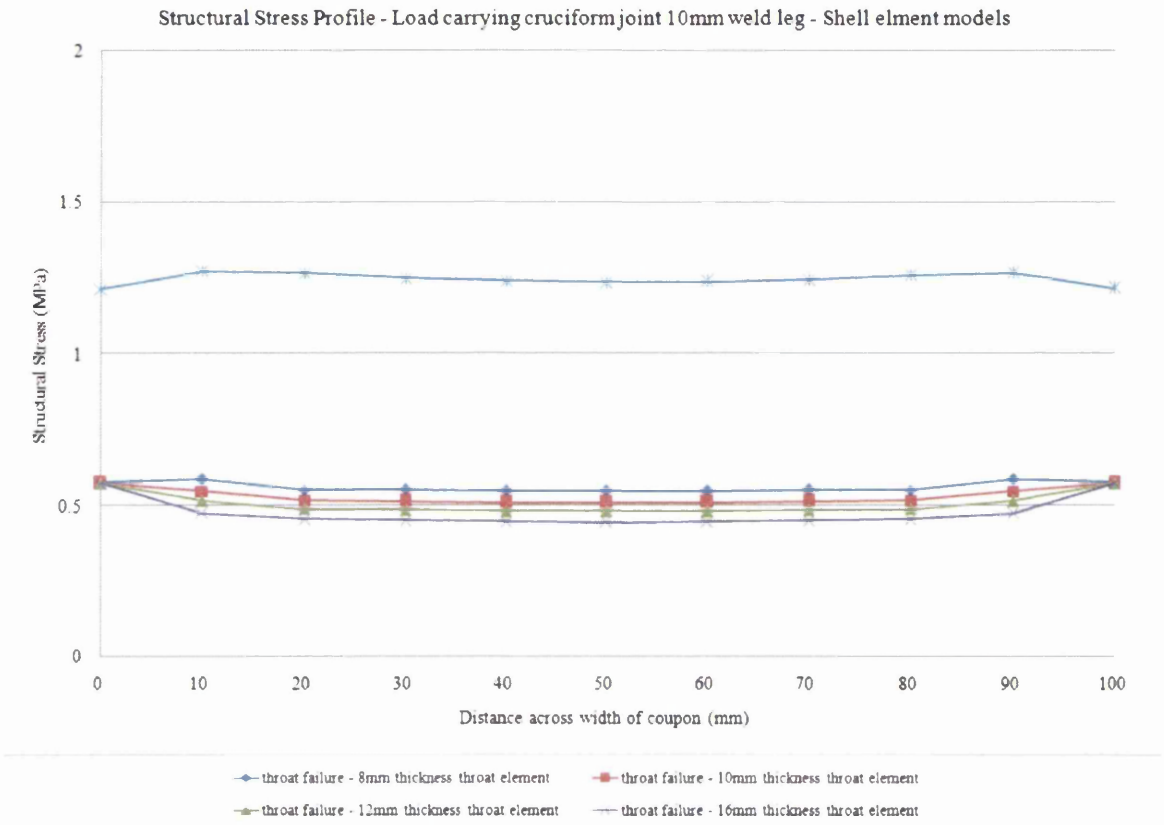

Figure 196: Cruciform joint 10mm weld leg - Structural stress profile using shell element models – using actual weld throat failure thickness in the structural stress calculation

There is little correlation in solid and shell element models of both the 8mm and 10mm weld leg cruciform throat failures. The calculated peak structural stress has been divided into the membrane and bending stress components for comparison between the solid and shell element models. This has been done for both the 8mm and 10mm weld leg cruciform joints in Figure 197 and Figure 198 respectively. In both cases it is clear that there is zero bending stress components calculated. The total structural stress is equal to the total membrane stress. This is due to the inability of the shell mesh to accurately represent the real weld geometry.

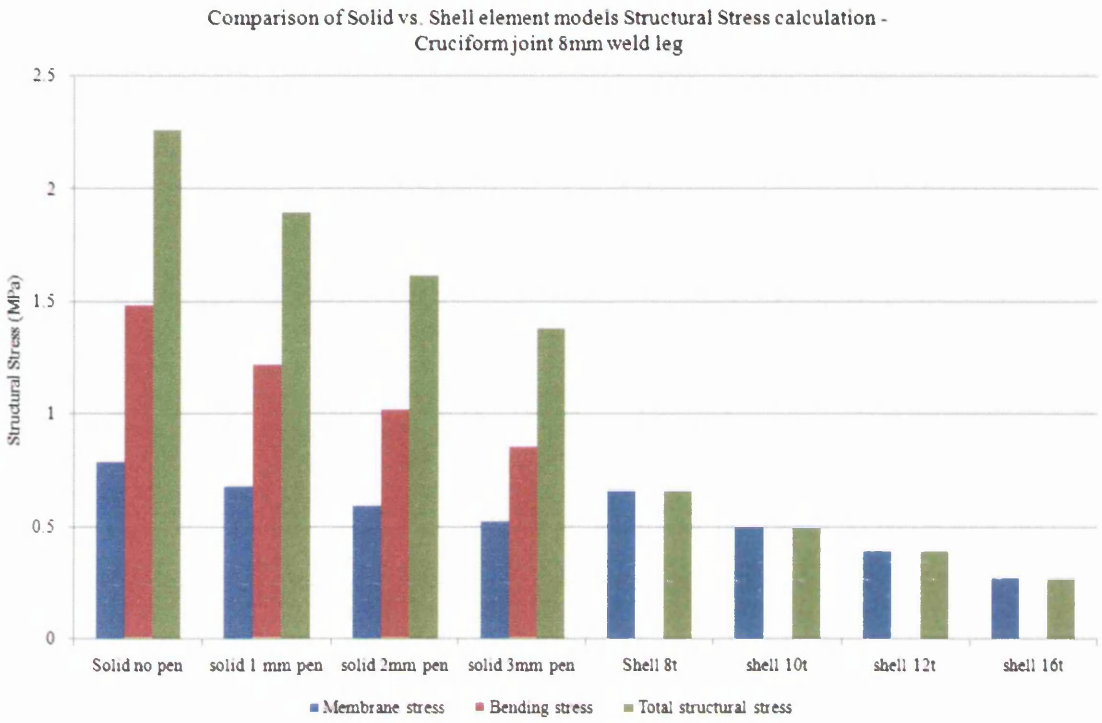

Figure 197: Comparison of structural stress components in the 8mm weld leg Cruciform joint - solid against shell element models

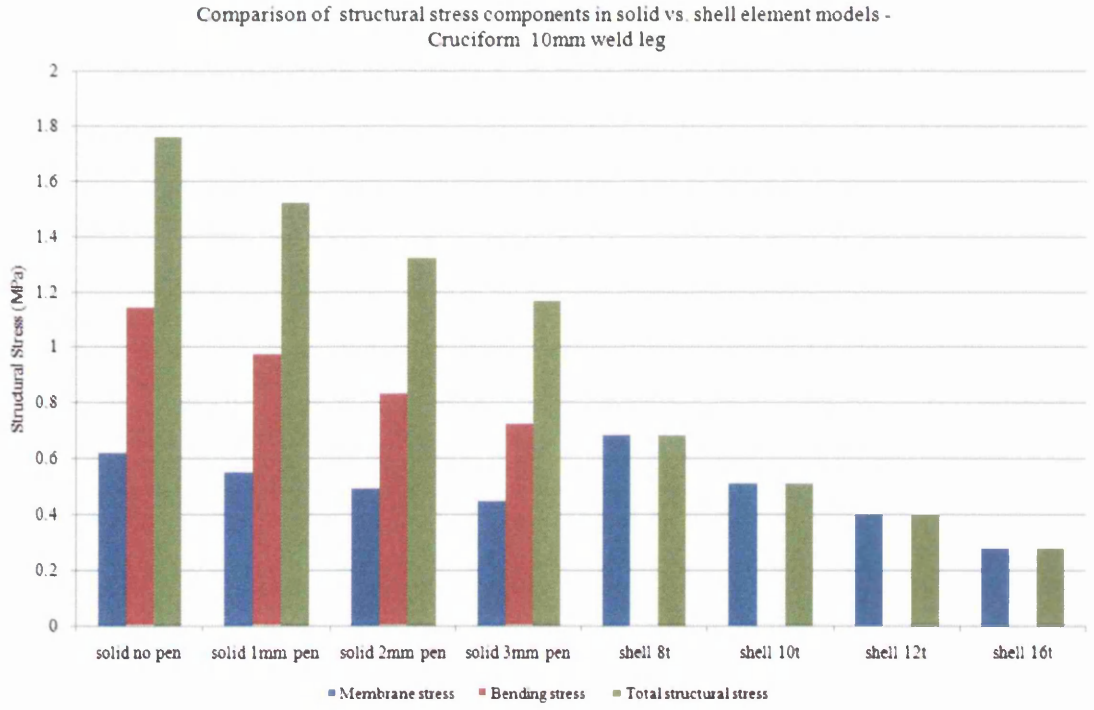

Figure 198: Comparison of structural stress components in the 10mm weld leg Cruciform joint - solid against shell element models

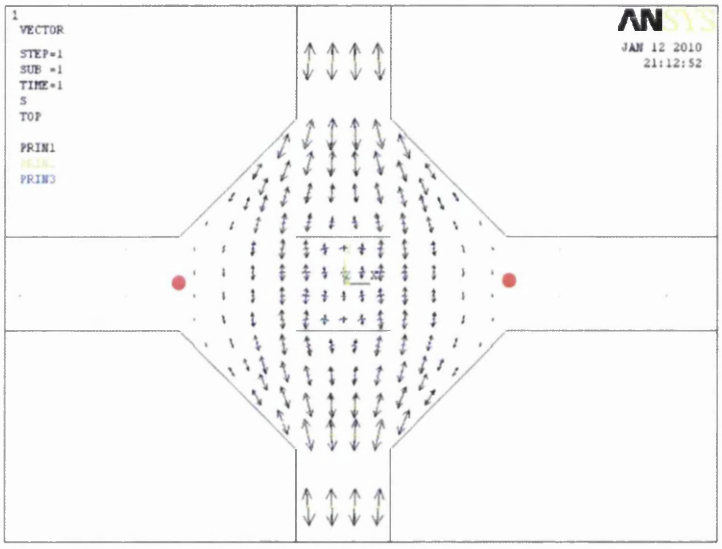

Figure 199: Cruciform joint 10mm weld leg solid model cross-section - Vector plot of principal stresses

A vector plot of the principal stresses is shown in Figure 199 for the cross-section area of the 10mm weld leg cruciform joint. The black arrows show the tensile principal stresses and are a good indication of the load path running through the cruciform joint. The two red dots indicate the superimposed location of the node positions from the weld throat element in a shell cruciform model as shown in Figure 200. In the shell element model the tensile load path applied is transferred, from the upper plate to the lower plate, through these two nodes.

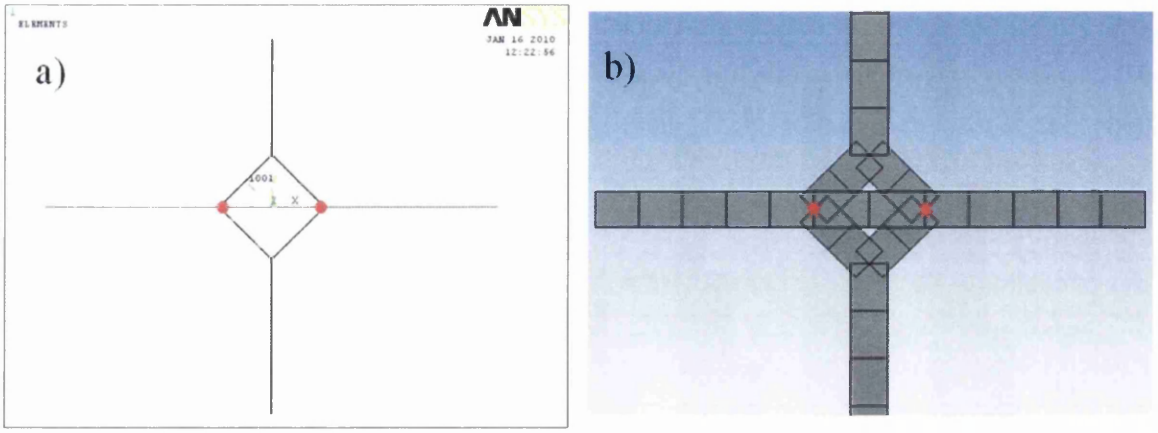

Figure 200: Cruciform joint 10mm weld leg shell model cross section a) shell plane mesh and b) shell plane mesh with theorectical real constants applied

It is misleading to suggest the shell element geometry is representative of the solid model or real test coupon. It is evident the solid model load path is transmitting load through all of the weld geometry and weld penetration, i.e. approximately 4mm each side of the coupon vertical centreline. In comparison, the shell model load path is only distributing load through the

nodes approximately 14mm away from the coupon vertical centre line. It has been proposed earlier on in the chapter that similar structural stress factors can be achieved using both solid and shell elements for characterising weld toe failures. The comparative results show that this is the case. For weld throat failures this has proved to be more difficult. In an attempt to address this and create a comparable shell element model for weld throat failures, a number of different concept options have been proposed. In essence, the structural stress calculation is exactly the same for a toe, throat or root weld failure. The problem lies with constructing a shell element model akin to the real structure; the load path cannot be portrayed adequately.

Shell element geometries have been presented with different FE model parameters to try and represent the load path more accurately. The models are shown in Figure 201.

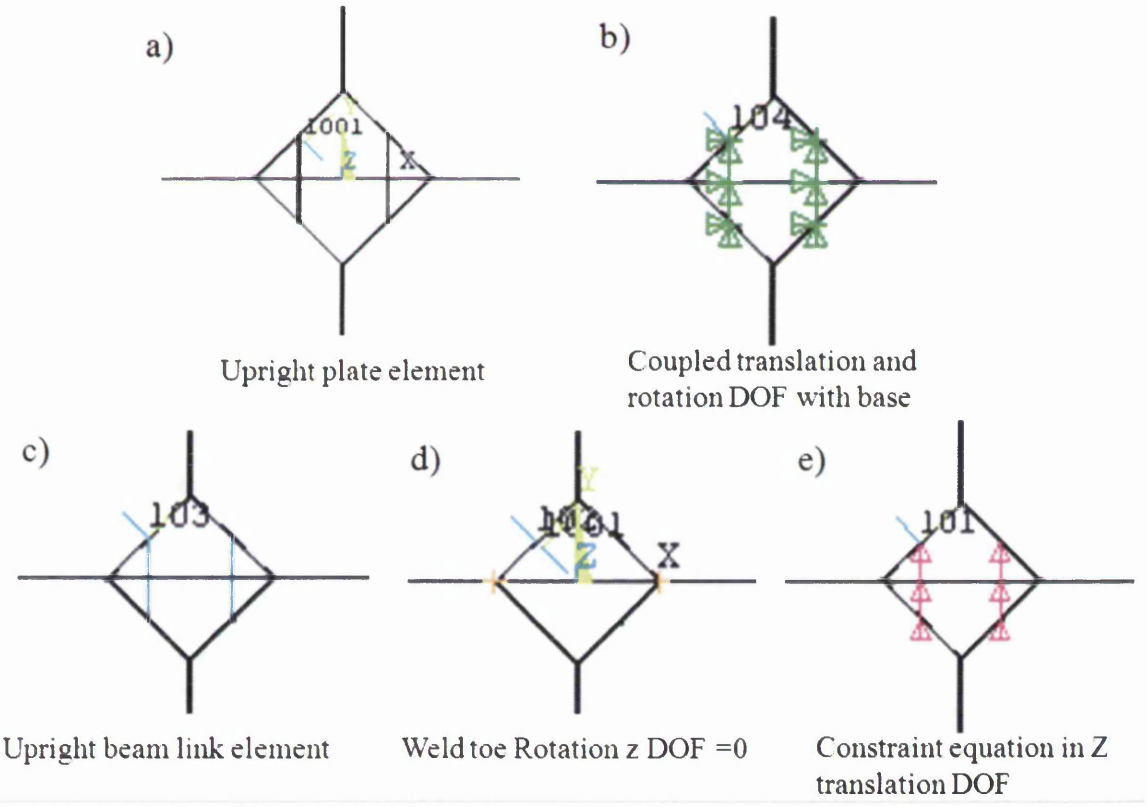

Figure 201: Modified cruciform shell element models

The models suggest different methods to try and distribute the load path in a similar manner to the real coupon. This is achieved by distributing the load through a larger area of the horizontal plate. Concept a) uses a mesh shell element, b) the nodes in the weld throat are coupled with the nodes in the base plate (so all the nodes translate and rotate in a similar manner) and c) a beam or link element is used to transmit load through the base plate.

Concept d) has a fixed rotation (about z-axis) constraint on the nodes in the weld toe to try and stiffen the base geometry. Finally, in concept e) the translation of the nodes in the weld throat is fixed with the base nodes to stiffen up the weld geometry. The structural stress calculation process has been repeated for the above options. The peak structural stress values at the centre of the coupon are recorded and compared against the solid element model values in Figure 202. The components of the total structural stress, membrane and bending stresses are also displayed.

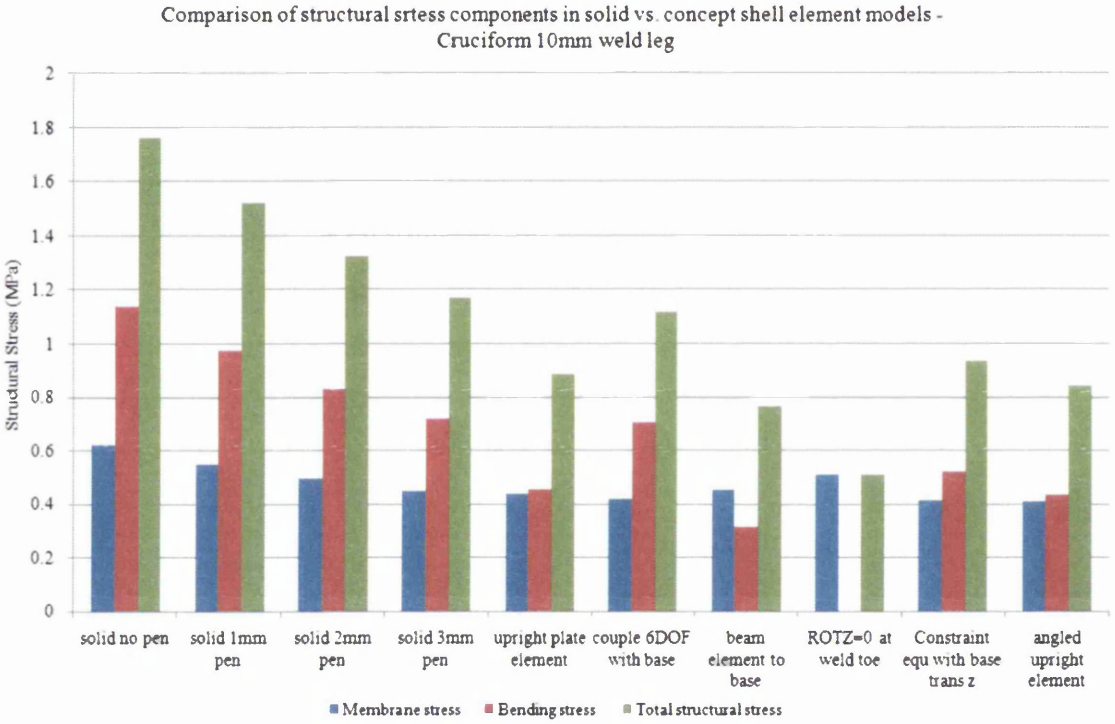

Figure 202: Comparison of structural stress components in the 10mm weld leg Cruciform joint - solid against concept shell element models

The modified shell element models have a higher value of total, membrane and bending structural stress, compared with the original shell values shown in Figure 198. However, the peak structural stresses are still lower than the solid element models. The solid and shell element models will both be considered in the data generation process and the effects the unit load values have on the correlation of the final structural stress master curve. This will give an indication on the effectiveness of shell element models in the analysis of weld fatigue throat failures.

A further point for consideration will be given to the levels of weld penetration achieved. The structural stress calculation method is sensitive to this when modelled in the FE geometry.

The effects of using a single or multiple structural stress unit load values will be considered when constructing the master curve in chapter 4.5. The use of multiple cruciform structural stress factors will be beneficial in condensing the single master curve and improving correlation. This is supported by analysing the coupon weld fatigue data of both the 8mm and 10mm weld leg length. Previously in chapter 4.1, Figure 100 the cruciform weld fatigue date was presented on a Load range against cycles to failure (Log ΔkN against Log N_f) plot. From the statistical analysis the R-squared value of the 50% mean curve is 0.851. Alternatively, by presenting the fatigue data on a stress range against cycles to failure (Log Δσ against Log N_f) plot, Figure 203 the correlation is improved and the R-squared value from the statistical analysis is 0.963. The stress range is calculated by dividing the applied load by the actual crack plane area and, hence, taking into consideration the levels of weld penetration achieved. Separate structural stress values are calculated depending on the levels of penetrations observed in the test coupon and modelled in the FE analysis. The different values will have an effect on the scaling and superposition stage when converting the weld fatigue data into the master curve.

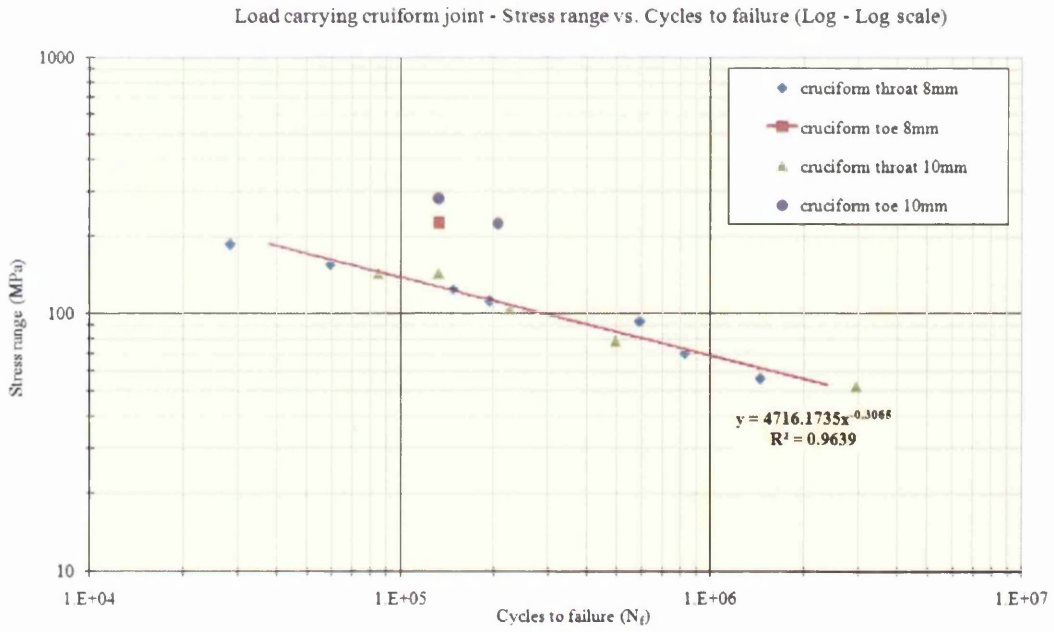

Figure 203: Cruciform joint 8mm and 10mm- Stress range against cycles to failure (Δσ against N_f)

4.3.6 Bending Load Tee joint

The bending load tee joint crack planes are defined in Figure 204 and Figure 205 for the solid and shell element models. The crack plane of the weld originates at the weld toe of the base plate and propagates down through the thickness of the plate. Due to the clamping arrangement and bending moment, a low load but a high stress is created. The structural stress calculation procedure is applied for a range of different element types and sizes.

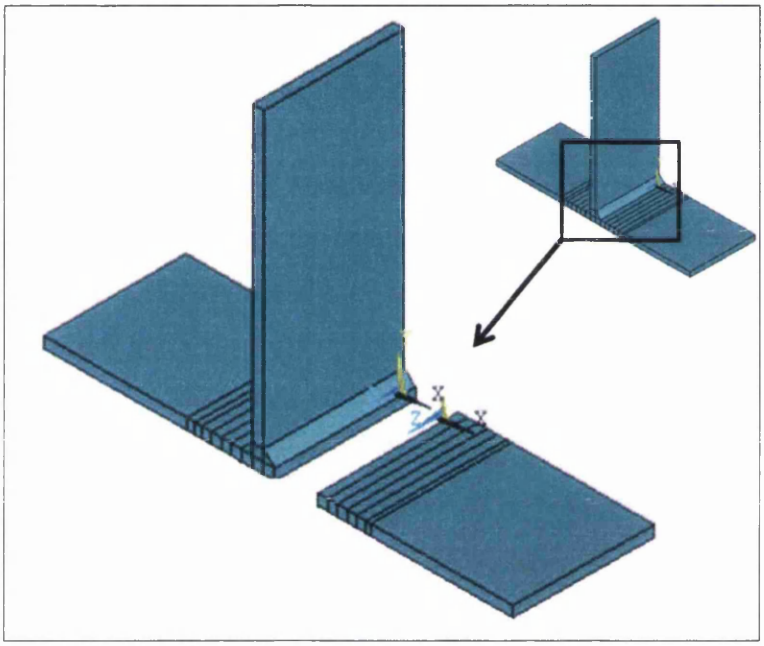

Figure 204: Bending load tee joint – Solid element FE model crack plane

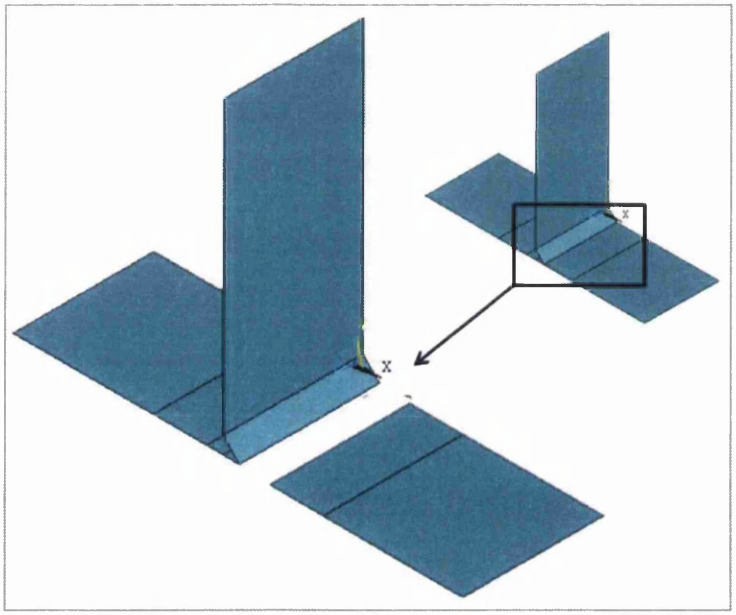

Figure 205: Bending load tee joint - Shell element FE model crack plane

The structural stress profiles per unit load at the weld toe are displayed in Figure 206 and Figure 207 for the solid and shell element models. The Structural Stress (MPa) is plotted against the distance across the width of the coupon (mm).

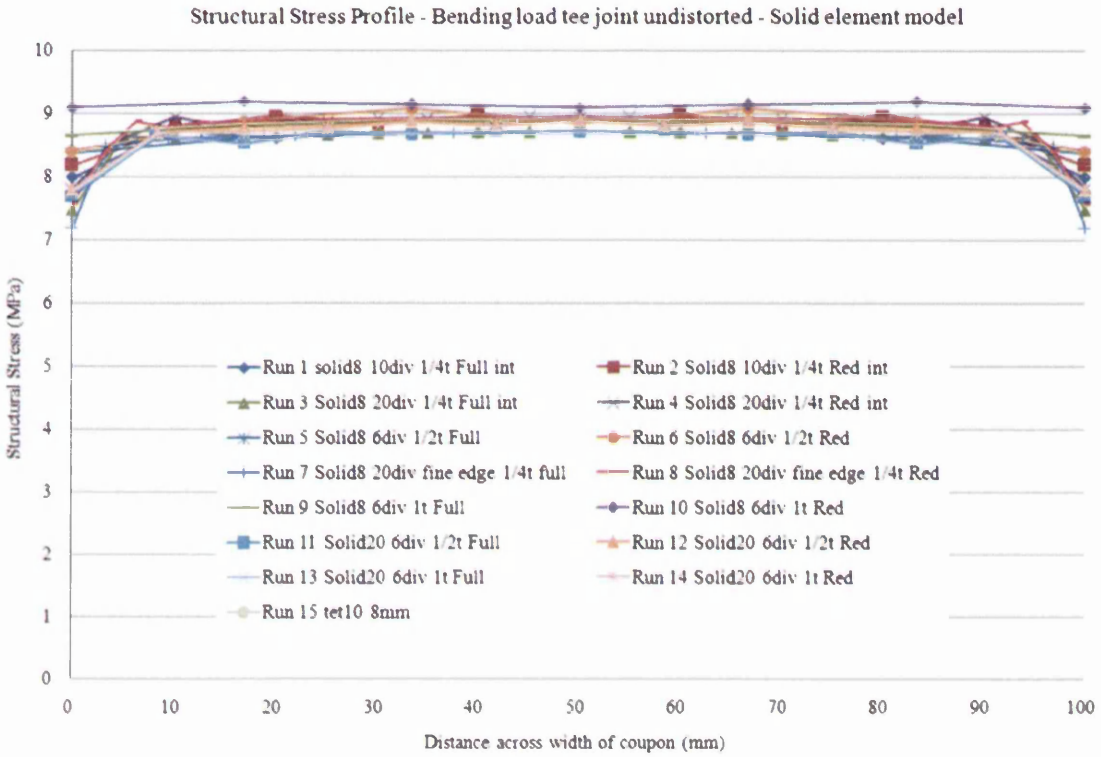

Figure 206: Bending load tee joint - structural stress profile using solid element models

The peak structural stress factor per unit load is approximately 8.9MPa for the solid element coupon geometry. Considering the various element types and calculation methods used, there is very good correlation and little mesh sensitivity to the structural stress results. There is a small difference when using a 1st order element with a through thickness density of 1t and a reduced integration calculation. This is a very coarse and unrealistic mesh that should be avoided due to its limits in representing bending moments and an experienced stress engineer would know to avoid this mesh. Despite the poor mesh, the structural stress profile calculated is reasonable and consistent with the fine mesh or high-density models, supporting the mesh-insensitive background to the method.

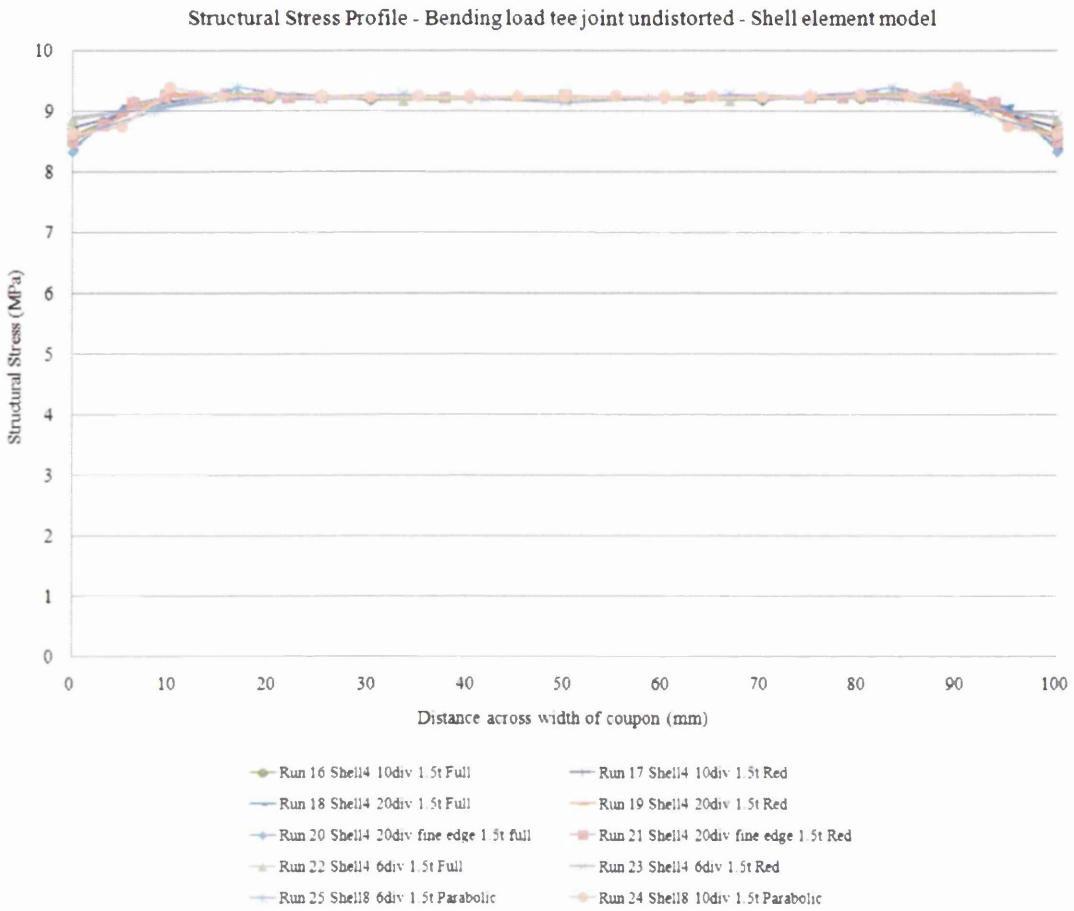

Figure 207: Bending load tee joint - structural stress profile using shell element models

The shell element models show a peak structural stress factor per unit load of 9.2MPa. When calculating the structural stress using shell elements, there is some unbalanced behaviour towards the edge of the coupon. This is similar to the previous shell coupon models. The erratic behaviour is greater when using a full integration method and a finer mesh density. Comparing the solid against the shell element calculations there is reasonable correlation with a small level of deviation between the two. The weld geometry created is a load-bearing coupon. The meshed shell geometry has potential issues in its ability to represent actual weld geometries and can give rise to error. However, the results are reasonably straightforward to use and are within <5 % of the solid model stress profiles.

4.3.7 Summary

FE based structural stress calculations have been completed on all test coupon geometries using a range of mesh sizes, density, element type and solution parameters. A majority of the results achieve excellent correlation between these different parameters supporting the theory

of a mesh insensitive FE-based approach. The greatest correlation is shown for weld toe failure modes. The structural stress method was extended to weld throat failures. However, there is less consistency between the different element types when calculating a fatigue damage parameter for weld throat failure modes. In these cases, the range of structural stress factors will be used in generating a single master curve, and their effectiveness in condensing a wide range of scatter will be assessed.

Unit load factors for each geometry type have been calculated. This is the first step in completing the elastic scaling and super-positioning weld fatigue analysis. Here the structural stress damage parameter has been established. The 'structural stress factor per unit load' for each coupon to be taken forward in an attempt to generate a single master S-N curve are summarised below:

Coupon Geometry	**Shell element model**	**Solid element model**
1. Tensile load tee joint	**4.29**	**4.55**
2. Non-load-bearing cover plate		
Un-distorted	**1.5**	**1.56**
Distorted model	**2.6**	**2.6**
3. Load-bearing lap joint	**4.2**	**4.2**
4. Non-load-bearing transverse attachment		
Non-load tee - root failure	**2.44**	**2.49**
Double transverse attachment	**1.2**	**1.22**
Single transverse attachment – un-distorted	**1.24**	**1.26**
Single transverse attachment - distorted	**2.38**	**2.39**
5. Load carrying cruciform joint		
8mm weld leg (Weld penetration dependent)	**0.5-0.6**	**1.4-2.25**
10mm weld leg (Weld penetration dependent)	**0.4-0.68**	**1.17-1.76**
Modified shell model	**0.8-1.1**	-
6. Bending load tee joint	**9.2**	**8.9**

Table 6: Structural Stress (MPa) unit load factors - FE based calculation

4.4 Coupon Structural Stress Measurements

The structural stress method is targeted at iterative design procedures where significant amounts of resource, time and money are spent on fatigue life prediction techniques employing in-field testing and prototype building of components. The structural stress theory is a FE-based fatigue life prediction method that can assess the fatigue performance of a component before it has been manufactured. The work completed by Dong [43] demonstrates that this theoretical method can be taken a step further to allow a structural stress factor to be determined from real components. This allows designers to validate, verify and correlate calculated values against measurements made with strain gauges.

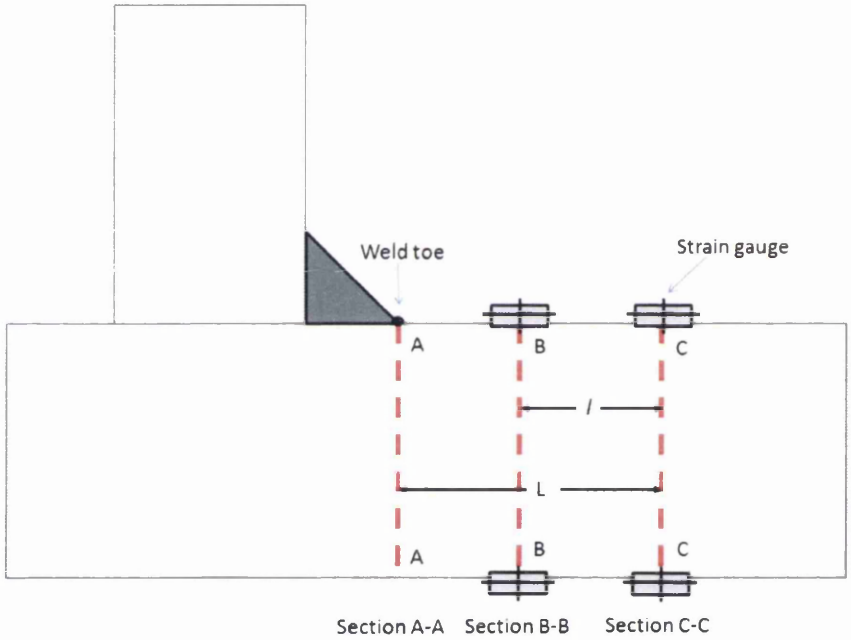

Figure 208: Schematic diagram of strain gauge positioning for the measurement of a structural stress fatigue damage parameter

Section A-A in the Figure 208 above is a weld section under analysis where a toe failure would occur and propagate down through the plate section. A minimum of four electrical resistance strain gauges should be used and placed on the upper and lower section of the parent material plate adjacent to weld toe under analysis at section C-C and B-B. The structural stress parameter has previously been broken down into membrane and bending components. A double row of opposite strain gauges will enable the calculation of the gradient of the bending stress component at two locations, and the difference or ratio of each will determine the membrane structural stress. The resistance of the strain gauges under

elastic loading are recorded, converted using the Young's elastic modulus rule and entered into the following equations as a stress:

First the stress values are entered into the equation to determine the level of bending stress components at section B-B and section C-C:

$$\sigma^{B\text{-}B}{}_{bending} = \tfrac{1}{2}\,(\sigma^{B}{}_{top} - \sigma^{B}{}_{bottom}) \qquad \textbf{Eq 4.4.1}$$

$$\sigma^{C\text{-}C}{}_{bending} = \tfrac{1}{2}\,(\sigma^{C}{}_{top} - \sigma^{C}{}_{bottom}) \qquad \textbf{Eq 4.4.2}$$

From this, bending, membrane and structural stress values can be calculated for section A-A:

$$\sigma^{A\text{-}A}{}_{bending} = \sigma^{B\text{-}B}{}_{bending} + L/l\,(\sigma^{C\text{-}C}{}_{bending} - \sigma^{B\text{-}B}{}_{bending}) \qquad \textbf{Eq 4.4.3}$$

$$\sigma^{A\text{-}A}{}_{Structural} = \sigma^{B}{}_{top} + L/l\,(\sigma^{C\text{-}C}{}_{bending} - \sigma^{B\text{-}B}{}_{bending}) \qquad \textbf{Eq 4.4.4}$$

$$\sigma^{A\text{-}A}{}_{Membrane} = \sigma^{A\text{-}A}{}_{Structural} - \sigma^{A\text{-}A}{}_{bending} \qquad \textbf{Eq 4.4.5}$$

Using the above $\sigma^{A\text{-}A}{}_{bending}$ and $\sigma^{A\text{-}A}{}_{Membrane}$ values the Structural Stress unit load ratio at the weld toe A-A can be calculated:

$$= \frac{\sigma_{bending} + \sigma_{membrane}}{\sigma_{membrane}} \qquad \textbf{Eq 4.4.6}$$

Where

$\sigma^{B}{}_{top}$ = recorded stress upper gauge section B
$\sigma^{B}{}_{bottom}$ = recorded stress lower gauge section B
$\sigma^{C}{}_{top}$ = recorded stress upper gauge section C
$\sigma^{C}{}_{bottom}$ = recorded stress lower gauge section C
L = distance from weld toe to section B
l = distance from section B to section C
$\sigma^{B\text{-}B}{}_{bending}$ = bending stress at section B
$\sigma^{C\text{-}C}{}_{bending}$ = bending stress at section C
$\sigma^{A\text{-}A}{}_{bending}$ = structural stress component - bending stress at weld toe
$\sigma^{A\text{-}A}{}_{membrane}$ = structural stress component - membrane stress at weld toe
$\sigma^{A\text{-}A}{}_{structural}$ = total structural stress at weld toe

The strain gauge measurement technique has been applied to all the coupon test geometries discussed in the experimental methods chapter. The measured structural stress values are directly comparable with the unit load structural stresses calculated in chapter 4.3.

4.4.1 Tensile load tee joint

An example of the calculation method is completed for the tensile load tee joint. The upright plate was fitted with electrical resistance strain gauges in the centre across the coupon width. The gauges were placed at section C-C and B-B at distances of 15mm and 35mm respectively, Figure 209. Strain gauge readings were recorded from the test coupon using data logging equipment under a static load of 67kN (approximately 20% of the nominal yield stress) in the servo-hydraulic test frame. The strain readings were converted into stresses and entered into the structural stress equation. The results are given in Figure 210 below.

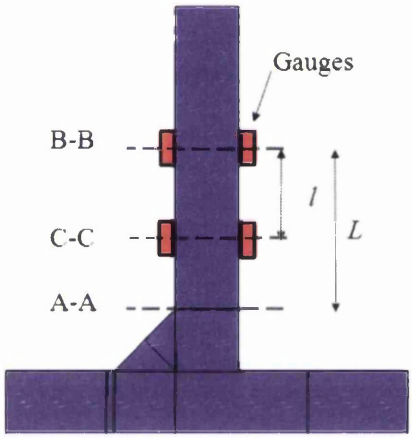

Figure 209: Tensile load tee joint - strain gauge positions

The actual test coupon failed through the weld throat. It is not possible to record strain gauge readings for a throat failure but the measured structural stress values can be correlated with the FE-based calculated weld toe values to verify the approach.

distance (mm) from weld toe	15		35	
Section	C-C		B-B	
upper strain gauge	50.43		51.25	l= 20 mm
lower strain gauge	40.80		42.64	L= 35 mm
$\sigma^{C-C}_{bending}$ =	4.82	$\sigma^{B-B}_{bending}$ =	4.31	

Weld toe Section A-A

$\sigma_{bending}$	$\sigma_{structural}$	$\sigma_{membrane}$
5.20	52.15	46.95

Structural Stress Value per unit load (MPa) =	1.11

Figure 210: Tensile load tee joint - recorded stress values and measured structural stress value

The measured structural stress factor per unit is 1.11MPa compared with the calculated value of 1.23MPa for a toe failure. Given the possible sources of variability, such as errors in the test frame, material and gauge positioning, the overall comparison of the measured and calculated values is satisfactory.

4.4.2 Non-load-bearing cover plate

The calculation method as described in section 4.4.1 was applied to the non-load-bearing cover plate coupon. The same strain gauge locations, recordings and loading method were repeated. The measured structural stress for the non-load-bearing cover plate is 1.75MPa per unit load. In the original structural stress calculation, two finite element geometries were constructed, representing the as-designed un-distorted coupon and the as-welded distorted coupon. There was a difference in the result with values of 1.56MPa and 2.6MPa respectively using both shell and solid element models. The measured unit load factor value lies in between the calculated un-distorted and distorted geometry values. There is potentially an issue in determining which of the measured and calculated 'theoretical' structural stress parameters is correct. Deciding on the correct value of the parameter is difficult. This decision can be made when the effectiveness of the measured and calculated values are assessed based on their ability to condense several fatigue data curves into a single master curve, providing accurate fatigue life predictions.

4.4.3 Load-bearing lap joint

The load-bearing lap joint coupon measured a structural stress value of 3.16MPa per unit load. In the original FE-based calculation, the load-bearing lap joint had a structural stress factor per unit load value of 4.2MPa when using both shell and solid element FE models. Comparison of the two values suggests the FE-based calculation is too severe in the stress determination. The measured result, although lower than the would-be expected correct result, is not necessarily the correct value as it is still a calculation of a theoretical structural stress parameter.

4.4.4 Non-load-bearing transverse attachment

The non-load-bearing transverse double attachment measured structural stress value is 1.15MPa per unit load. In the FE-based calculation, the structural stress factor per unit load was 1.2MPa when calculated using both shell and solid element models. The lower measured value compares well with the ideal symmetric geometry FE model. The lower strain gauge

readings from the measurement technique suggest there is potentially some gauge misalignment, material variations or test frame and instrumentation errors.

The measured structural stress value for the non-load-bearing single attachment is 1.81MPa per unit load. The theoretical structural stress calculation was based on two different FE models. The first was generated using the as-designed un-distorted coupon dimension and the second based on the as-welded distorted coupon geometry. There was a significant difference between the two with a value of 1.25MPa for the un-distorted and 2.4MPa for the distorted geometry, for both shell and solid element models. The measured structural stress value lies between the calculated un-distorted and distorted geometry values of 1.25MPa and 2.4MPa respectively. There is potentially an issue in determining which structural stress is correct. Comparing the FE-based calculations, the as-designed un-distorted geometry is lower and the distorted geometry is higher than the measured structural stress. Once again, a decision on the correct value to use can only be made through construction of an S-N master curve and obtaining fatigue life predictions.

4.4.5 Load carrying cruciform joint

The majority of cruciform test coupons failed through the weld throat except for 3 recorded results. It is not possible to record strain gauge readings for throat failures but the measured structural stress values can still be correlated with weld toe failure results and related to calculated structural stress values. The measured structural stress value for the 8mm weld leg cruciform joint is 0.95MPa per unit load. This value is low compared with the calculated structural stress value of 1.2MPa. The measured structural stress value for the 10mm weld leg cruciform joint is 1.10MPa per unit load. Although lower, the results correlate well with the calculated FE-based value. It is possible that some discrepancies arise due to differences in the material properties, strain gauge positioning, test equipment and unsymmetrical or distorted test coupons.

4.4.6 Bending load tee-joint

The bending load tee joint test coupons failed through the lower weld toe. Measured structural stress values were recorded for the upper weld toe to be correlated with the calculated values in order to explore and verify the method. The measured structural stress method was applied and a value determined for the bending load tee upright plate at 0.98MPa per unit load, compared with the calculated structural stress value of 1.2MPa.

The base plate of the bending load tee joint coupon was fitted with strain gauges at distances of 12mm and 25mm away from the weld toe. This was due to the geometry of the test coupon and clamping arrangement test setup. The measured structural stress value of the base plate is 12.49MPa per unit load. This is compared with a calculated structural stress value of 8.9MPa and 9.1MPa for the solid and shell element models respectively. There is a significant difference between the measured and calculated values – approximately a factor of 1.39. There is a greater potential for error in the bend load tee joints due to the clamping arrangement of the base plate. The other coupons use an upper and lower set of test grips that are concentric to each other. The bend load tee coupon uses an upper test grip and a clamping fixture where alignment is achieved using a set square and steel rule. Consistent measurements and set up is not always guaranteed and even representation of the test grip in the FE model may not correctly model the actual assembly.

4.4.7 Summary

Measured structural stress factors have been recorded for weld toe failures in each test coupon. In general, measured values showed some levels of correlation with the FE-based calculated structural stress values. However, there are some discrepancies. In these cases both the measured and calculated values will be taken forward for the construction of a single S-N master-curve in order to assess their respective effectiveness. A judgment can be made later on whether the measured values are too optimistic or pessimistic based on the accuracy of the calculated fatigue life predictions. A summary of the strain gauge based measured structural stress values are given in Table 7.

	$\sigma_{membrane}$	$\sigma_{bending}$	$\sigma_{structural}$	σ_{ss} (MPa per unit load)
Tensile load tee joint	46.95	5.20	52.15	1.11
Non load bearing cover plate	83.53	62.30	145.83	1.75
Load bearing lap joint	84.77	183.32	268.09	3.16
Non load bearing attachment double	119.60	18.41	138.01	1.15
Non load bearing attachment single	88.13	71.01	159.14	1.81
Load bearing cruciform - 8mm weld	205.75	-9.98	195.78	0.95
Load bearing cruciform - 10mm weld	197.85	19.39	217.24	1.1
Bending load tee joint - Upright	84.47	82.44	-2.03	0.98
Bending load tee joint - Base	2.15	24.73	26.88	12.49

Table 7: Measured structural stress unit load factors (MPa)

4.5 Structural Stress Master-Curve – Data Conversion

FE-based structural stress concentration values have been calculated in chapter 4.3, and measured values reported in chapter 4.4, for each of the coupon test geometries. The next process is to combine these values to the raw fatigue test data obtained. The objective is to define a new fatigue damage parameter with the potential of superimposing the fatigue test data for all the coupons within a single scatter band. This will provide the designer with a more FE-user friendly weld fatigue standard.

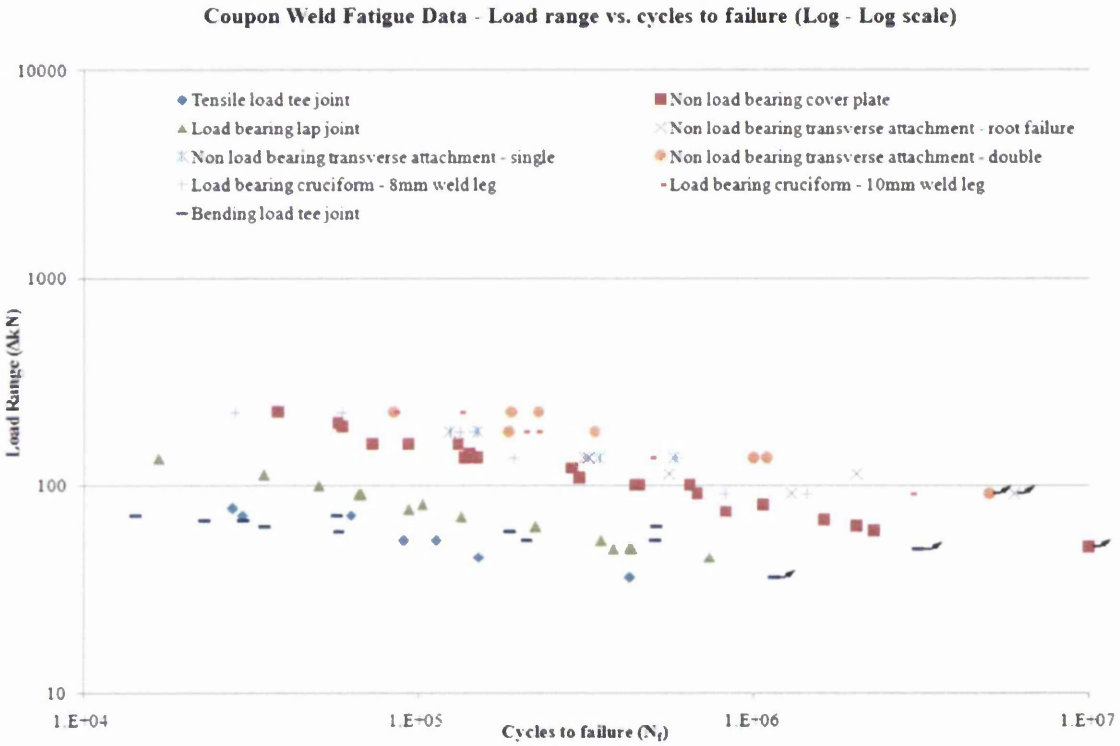

Figure 211: Coupon weld fatigue data - Load range against cycles to failure (ΔkN against N_f)

Figure 211 presents the basic fatigue data on a load range against Cycles to failure (ΔkN – N_f) plot. It is evident that the weld fatigue strength performance is geometry dependent. This method of presentation, therefore, poses significant problems as far as a generalised FE weld fatigue analysis is concerned.

In order to condense a range of data points into a single scatter band or master-curve, the coupon fatigue data has to be plotted using the alternative damage parameter 'Structural Stress' as calculated previously. The fatigue data points are taken for each coupon and multiplied by the Structural stress concentration factor per unit load calculated for the appropriate coupon geometry in chapter 4.3. This produces a scaling effect for each curve.

Thus a high fatigue strength coupon (e.g. non-load-bearing attachment) has a low structural stress concentration whereas, a low fatigue life coupon (e.g. bending load tee joint, high stress) is associated with a high structural stress concentration value. As a consequence, there should be a reduction in the scatter and an improved correlation.

In essence, this means that the load range for each coupon and data point (Load-Life curves) in Figure 211 is multiplied by the structural stress values in Table 6. For example, a coupon subjected to a 100kN load range and with a calculated structural stress factor of 1.2MPa per unit load, has a structural stress range of 120MPa. The calculated 120MPa SS range is then plotted against the original number of cycles to failure. The resultant weld fatigue curves are presented on a Log-Log scale with structural stress range (load range multiplied by structural stress value, MPa) against cycles to failure, N_f.

While one single master curve is the objective, there are a number of issues to consider during calculation of a structural stress factor per unit load as previously highlighted. The values of the structural stress factors depend on the calculation method. Variations in magnitude will impact on the correlation of the data point and the effectiveness of the resultant master curve. The different approaches encompass shell or solid element FE-based models, un-distorted (as-design) or distorted (as-welded) coupon geometries and calculated versus measured structural stress values. Each of these alternatives, in relation to failure and loading mode for each test coupon, is presented below and the resultant impact on the master curve correlation considered.

4.5.1 FE-Based calculated structural stress curve

Figure 212 illustrates a structural stress against cycles to failure master curve generated using unit load factors from the FE shell element models and un-distorted coupon geometries. There is a redistribution of the original load range against cycles to failure curves. There is also a noticeable grouping of the curves towards the centre of the scatter band. The lower bound consists of the cruciform 8mm and 10mm coupon results. The cruciform structural stress unit load factors were cause for concern as they were drastically different from the solid element model factors. The bending load tee joint coupon data are placed towards the upper bound of the master curve with a distinct and different gradient compared with the other fatigue curves. A statistical assessment was carried out employing a log-linear regression analysis with the cycles to failure as the variable. The calculated 50% certainty of

survival curve has a standard error =0.44 and R^2 value = 0.34. The equation for the curve is $y=12800000N_f^{-0.9}$, with 'y' the structural stress range.

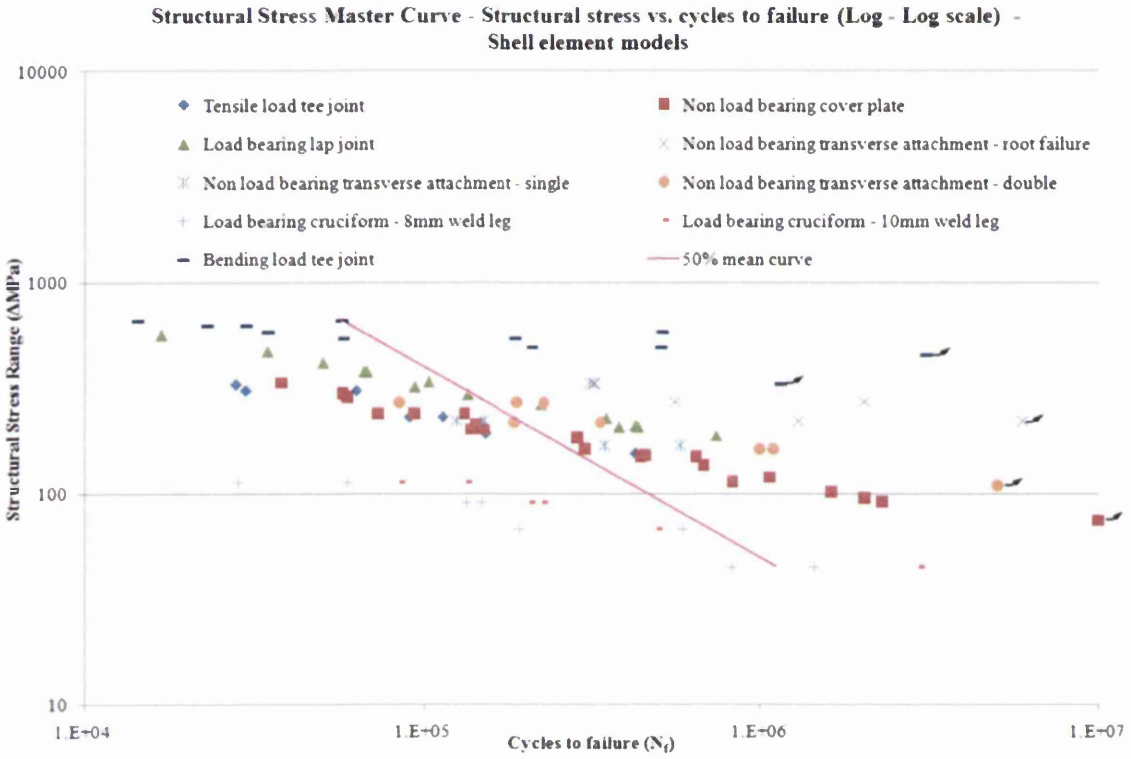

Figure 212: Structural stress master curve - FE-shell element un-distorted models

(In all of the statistical analyses completed none of the run out, i.e. did not fail, data points are included in the calculation).

A structural stress against cycles to failure master curve was also constructed using unit load factors from the FE solid element models and un-distorted coupon geometries as shown below in Figure 213. The redistribution of the original load range against cycles to failure data is again evident. There is noticeable grouping of the curves towards the centre of the scatter band with an improved correlation compared with the shell element models. The cruciform 8mm and 10mm coupon curves are now within the main trend of the data points. The bending load tee joint data lies towards the upper bound of the data points and outside the general trend for all of the remaining data. They also have a distinct and different gradient. The statistical analysis defined a 50% certainty of survival curve with a standard error =0.35 and R^2 value = 0.57. The curve equation can be expressed as $y = 94009N_f^{-0.48}$.

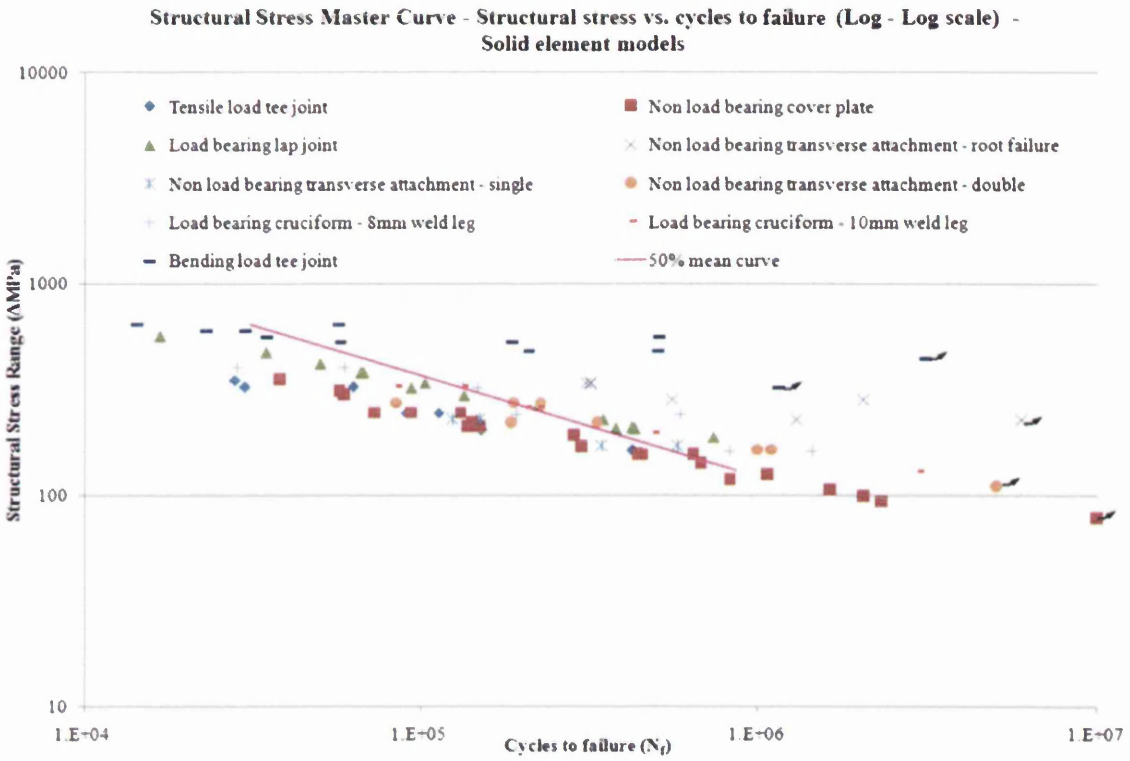

Figure 213: Structural stress master curve - FE-solid element un-distorted models

A modified structural stress master curve was generated using the solid element un-distorted models but eliminating the data points from the bending load tee joint coupon due to its positioning away from the main scatter band. The curve is displayed in Figure 214 below on a structural stress range against cycles to failure plot. The 50% mean curve generated from a statistical analysis is also shown. The equation for the curve is $y = 27863N_f^{-0.39}$. The data has a calculated R^2 value = 0.66 and a standard error = 0.30.

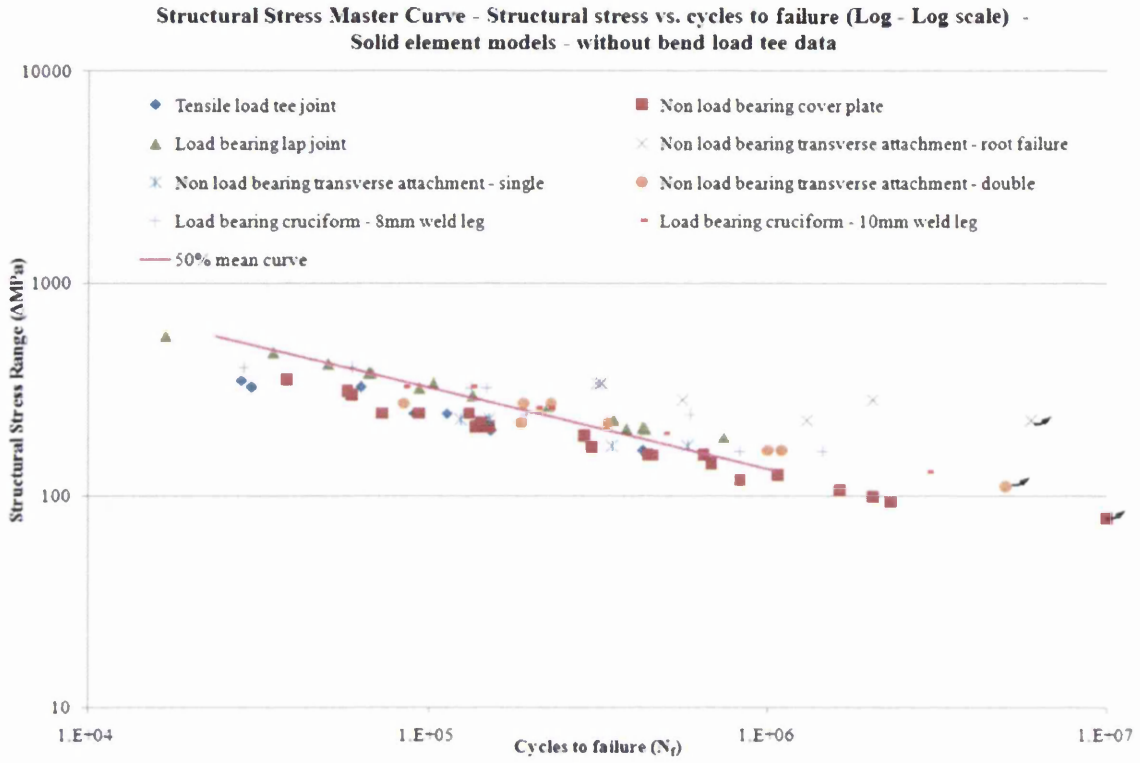

Figure 214: Structural stress master curve - FE-solid element un-distorted models without bending load tee data

The modified master curve presents an improved correlation of the data with an R^2 value = 0.66 compared with a previous value = 0.57 for the master curve that included the bending load tee data, as shown in Figure 213. This suggests that calculation of an effective fatigue damage parameter would require consideration of separate loading modes.

4.5.2 Distorted coupon geometries calculated Structural stress curve

Due to the weld configuration for the non-load-bearing cover plate and non-load-bearing single attachment coupons (unsymmetrical welding runs), the final geometries were distorted. To achieve a more accurate stress distribution for the coupons, the distortion was modelled in the FE model and the structural stress per unit load factor re-calculated. The structural stress values of the modified distorted coupons (both shell and solid element models) were updated and the structural stress curves re-plotted. For coupons with little or no distortion, the original structural stress values are used. A structural stress against cycles to failure master curve generated using unit load factors from FE shell element models and the updated distorted coupon geometries is shown in Figure 215.

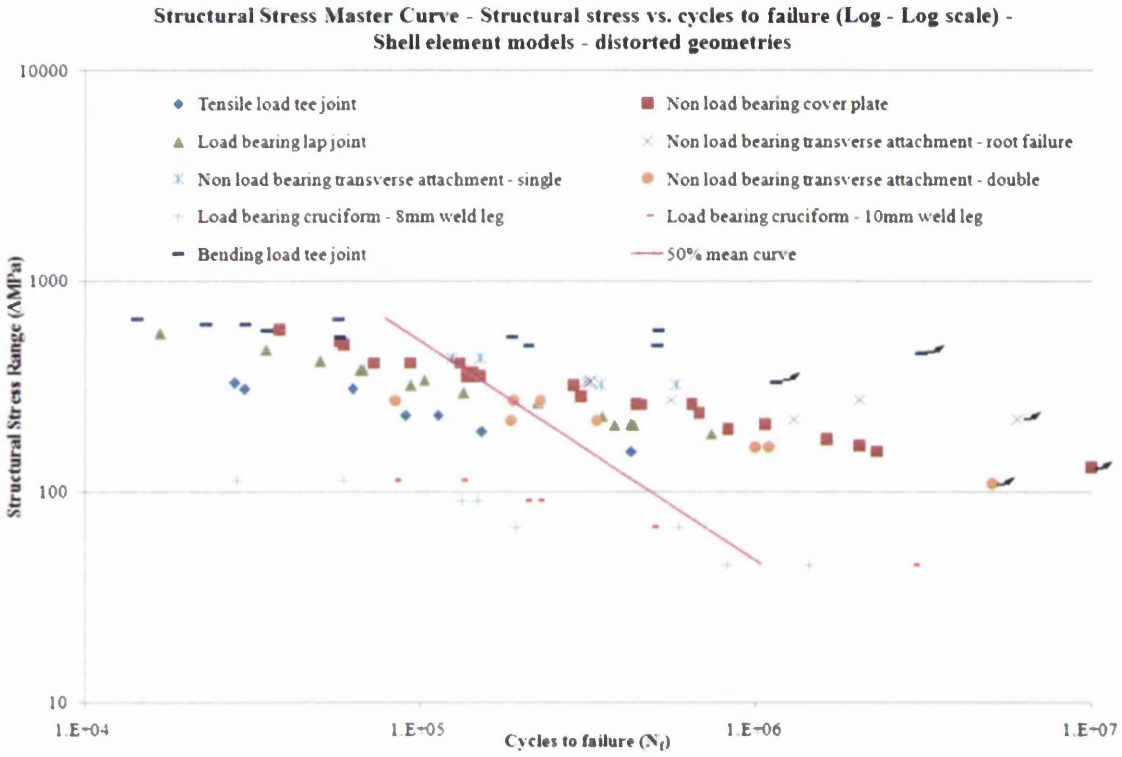

Figure 215: Structural stress master curve – FE shell element distorted models

There is a redistribution of the original load range against cycles to failure data. The distorted coupon structural stress curves show some improvement in fatigue strength being positioned higher than the original un-distorted curves based on the shell elements as recorded in Figure 212. The curves for the distorted geometry move higher up on the graph towards the bending load tee joint data. As a result, the low cycle fatigue failures ($<10^5$) appear to have an improved correlation with the main trend for other geometries. However, for lives greater than 10^5 cycles the bending load tee joint data are displaced from the main scatter band and have a different gradient. As per the previous shell structural stress curve, the cruciform coupons are positioned below the main scatter band. The statistical analysis gave a 50% certainty of survival curve with a standard error = 0.47 and $R^2 = 0.26$. The equation for the curve is expressed as $y = 81000000N_f^{-1.04}$.

A structural stress against cycles to failure master curve based on unit load factors from the FE solid element models and the updated distorted coupon geometries is presented in Figure 216.

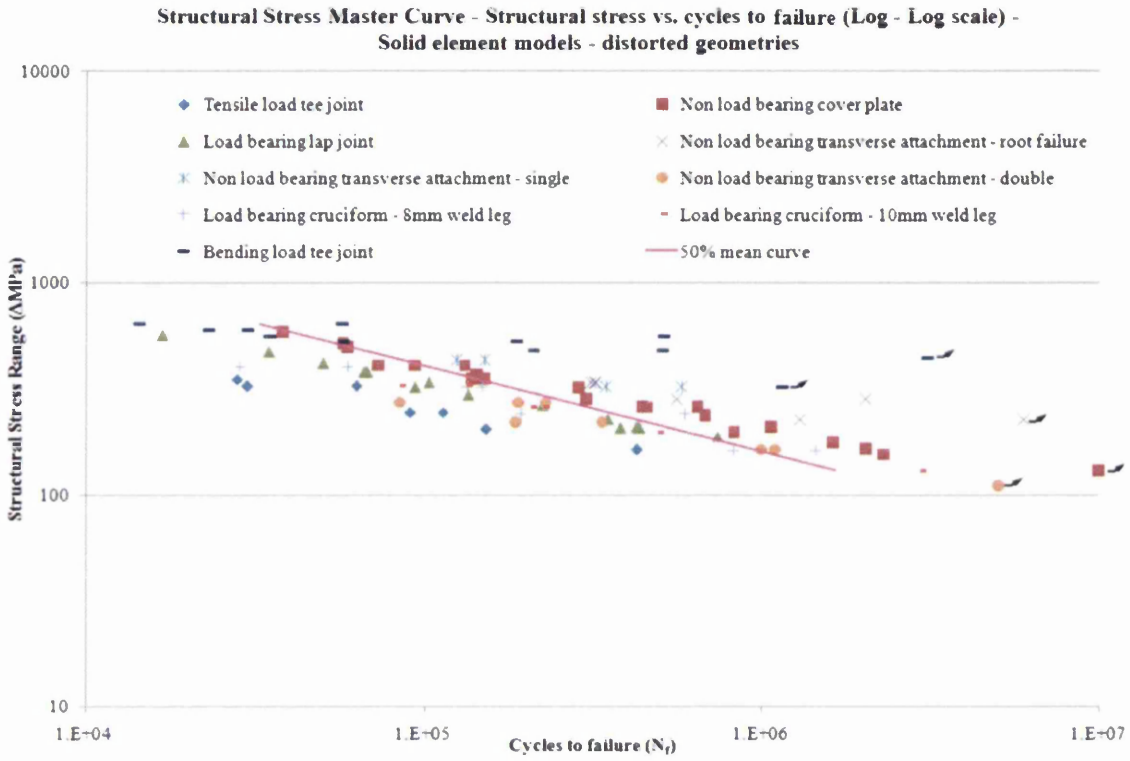

Figure 216: Structural stress master curve - FE-solid element distorted models

There is a shift in the original load range against cycles to failure data. The distorted coupon structural stress curves reinforce the concept of a universal master curve. The curves are positioned higher than the original solid un-distorted curves in Figure 213. This is a similar trend to the shell element distorted models. The distorted coupon curves are situated higher up towards the bending load tee joint data and have an improved correlation with the general trend for the low cycle fatigue failures ($<10^5$). The bending load tee joint data points at lives greater than 10^5 are situated away from the main scatter band and suggest a curve with a different slope. The cruciform coupons are now positioned within the main scatter band. The statistical analysis provided a 50% certainty of survival curve with a standard error =0.34 and R^2 value = 0.60. The R^2 for the distorted coupon values is an improvement on that for the un-distorted coupon model curve at R^2 =0.6 compared with 0.57. The equation for the curve in Figure 216 is $y = 43405N_f^{-0.41}$.

As per the calculation of the un-distorted model master curve, a further master curve was generated with the exclusion of the bending load tee data due to the distinct slope of the curve. The master curve is displayed in Figure 217 with a structural stress range against cycles to failure on a log-log scale. A 50% mean curve is displayed with an equation of y =

$20419N_f^{-0.35}$. The correlation of the data is improved with a R^2 value =0.66, compared with an original value = 0.6, when considering the bending load tee joint data.

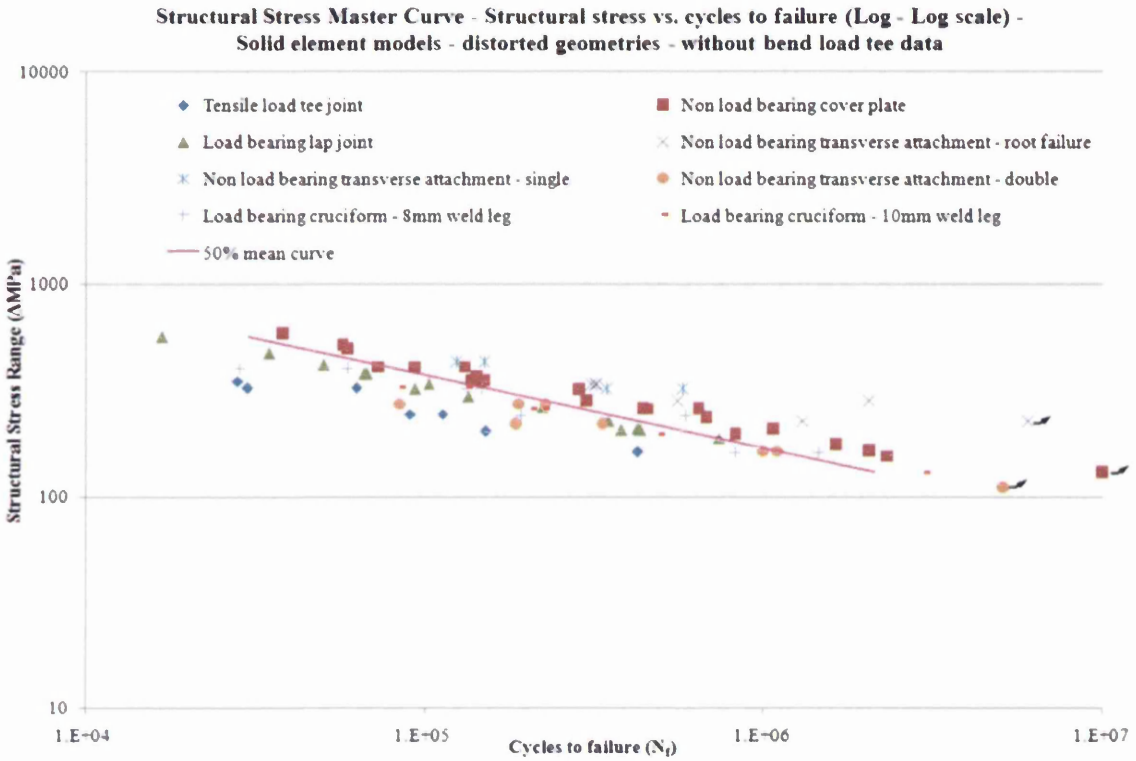

Figure 217: Structural stress master curve - FE-solid element distorted models without bending load tee data

As per the un-distorted structural stress master curve calculated, the exclusion of the bending load tee joint results suggests that master curves exist based on the applied loading mode.

4.5.3 Measured Structural Stress Curve

Measured structural stress values of the test coupons were determined from electrical resistance strain gauges and suitable data logging equipment under static tensile loading conditions. This provides an equivalent theoretical measured structural stress ratio for each coupon. A structural stress curve was constructed using these measured values. The measured values are only possible for the weld toe failures. Where other failure modes are recorded, the FE-based solid element calculated structural stresses are used for comparison. A structural stress against cycles to failure master curve generated using unit load factors based on the measured structural stresses for weld toe failures (solid element calculated values are used for throat failures), is shown in Figure 218.

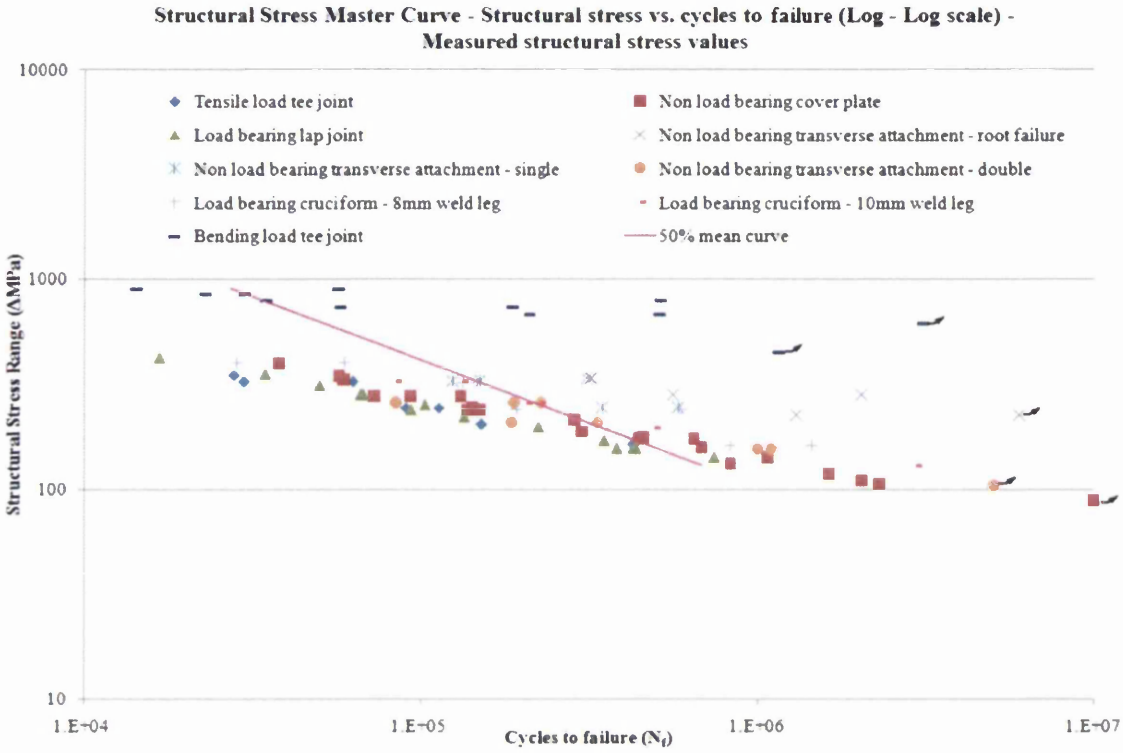

Figure 218: Structural stress master curve - Measured structural stress values

There is a shift in the position of the original load range against cycles to failure data. A majority of the data are situated in one main scatter band in the centre of the graph. There is very good correlation. However, the bending load tee joint data is an exception. In a similar manner to the FE-based calculated structural stress curves, the tee bend data sits higher than the central scatter band approximately by a factor of 2. Similarly, the curve appears to have a different gradient to the more general 1 in 3 slope. The statistical analysis of the data gave a 50% certainty of survival curve with a standard error =0.40 and R^2 value = 0.47. The equation for the curve is expressed as $y = 430512N_f^{-0.6}$. The measured structural stress curve provided similar and consistent results to the calculated structural stress values. A measurement based master curve was generated with the exclusion of the bending load tee data. The curve is shown in Figure 219 on a measured structural stress against cycles to failure plot. Again the curve displays more common traits expected with weld fatigue data. An R^2 value = 0.65 and a slope of -0.31. This is a marked improvement in correlation with a previous R-squared value of 0.47 with the tee bend data included in the statistical analysis.

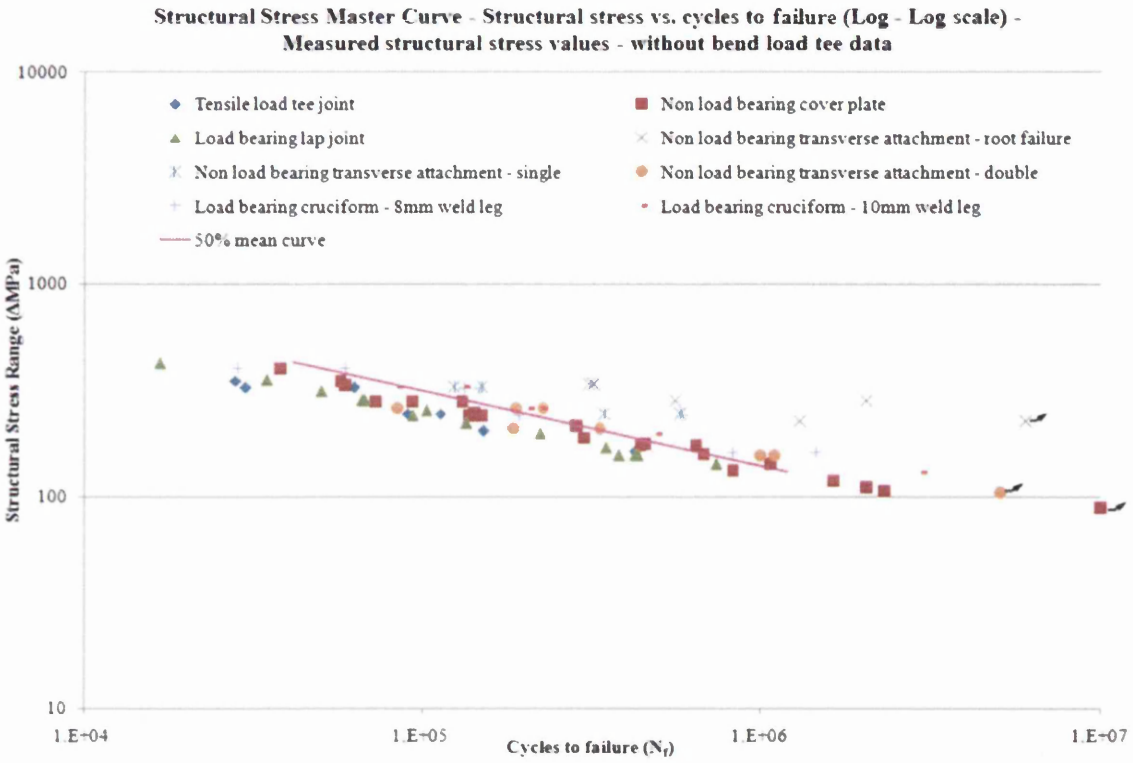

Figure 219: Structural stress master curve - Measured structural stress values without bending load tee data

4.5.4 Structural stress curve – loading mode dependency

It is clear that irrespective of the method used to construct a master curve, the bending load tee joint coupons have consistently shown anomalous behaviour. In particular, there has been a significantly different gradient not only from the general trend for the other geometries but also from the norm of -0.3, typical of welded steels. It is feasible to assume that generation of a master curve should be dependent on the loading mode, particularly when dealing with predominantly bending or tensile loads. The structural stress against cycles to failure master curve in Figure 220 has been generated with data from coupon geometries with a dominant bending mode and using unit load factors from FE solid element models. The coupon tests included are the tensile load tee joint, load-bearing lap joint and the bending load tee joint. These are all low load, high stress tests. (The tensile load tee joint - despite its name- endures a high bending moment due to the back-to-back testing arrangement, clamping fixture and single-sided fillet welds.)

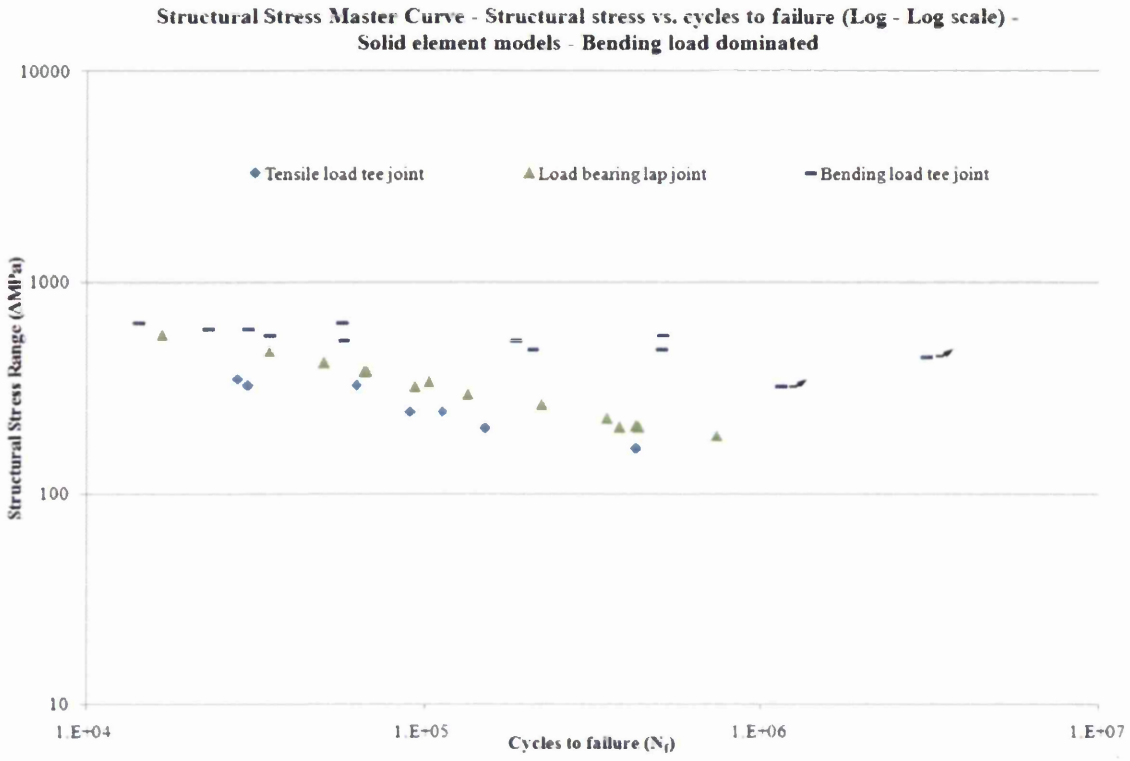

Figure 220: Structural stress master curve – Bending load mode dominated (solid element models distorted geometries)

The master curve for the bending load coupon geometries provides little evidence to support an effect due to loading mode dependency. The tensile tee and load-bearing lap joints do not naturally display similar characteristics to the bending load tee joint data, particularly in relation to the gradient. The tensile tee and load-bearing lap data correlate well with other tensile dominated loading coupons despite having high bending moments associated with the coupon failure. The tensile tee and load-bearing lap also show similar features to tensile loaded coupons in relation to the stiffness drop plots shown in chapter 4.1, short crack propagation periods and full separation of coupon before the stiffness drop reaches ~3%. In contrast, for the bending load tee joint, the crack propagation stage is long and slow. This is good reason to develop a separate structural stress master curve for the bending load tee joint coupons. It is unclear when, at what level of a given ratio of bending, or only above a certain stress threshold should a separate 'bending' master curve be required. This will be discussed in more detail later in chapter 5.

4.5.5 Weld Toe failures - Structural Stress Curve

To investigate the sensitivity of the master curve approach to failure mode, the different weld fatigue failure modes have been grouped separately. A structural stress against cycles to failure master curve was generated using unit load factors from FE solid element models and un-distorted coupon geometries for weld toe failures only, Figure 221.

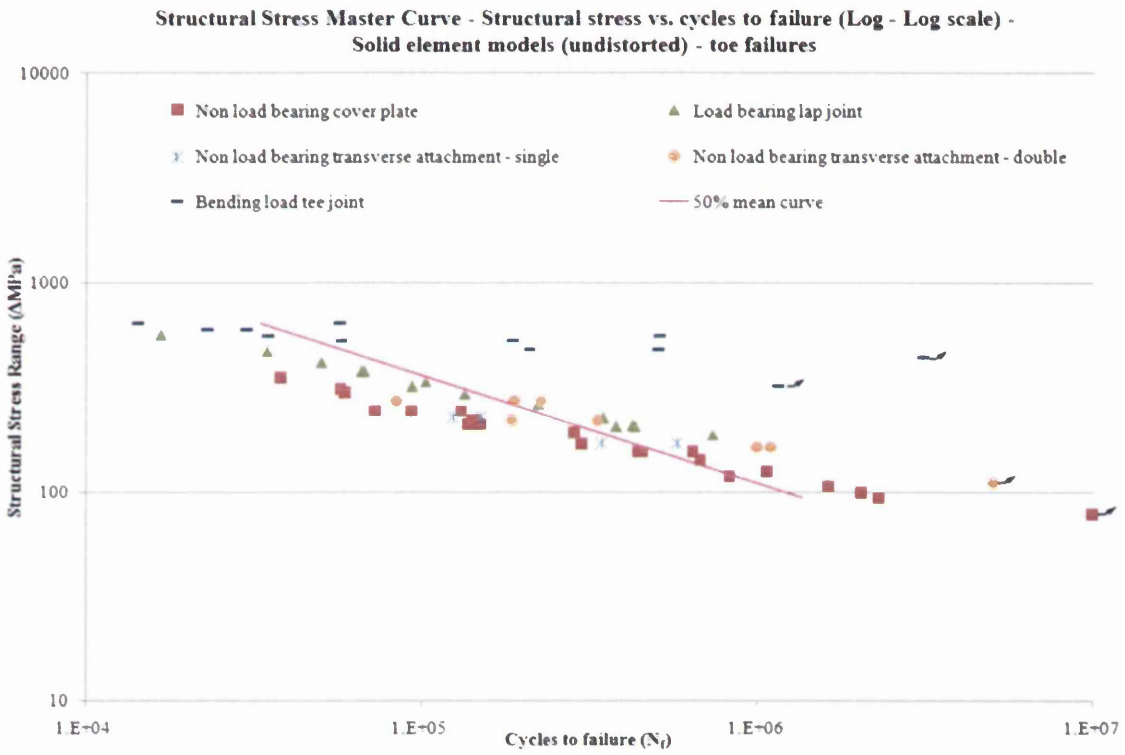

Figure 221: Structural stress master curve - Weld toe failures (solid element models un-distorted geometries)

The fatigue curves are redistributed compared with the original load-life data. There is a tightly correlated central scatter band consisting of four different weld geometries. However, the bending load tee joints, as per previous master curves, have a structural stress fatigue parameter with a distinct slope. The statistical analysis of the central band gave a 50% certainty of survival curve with a standard error =0.318 and R^2 value = 0.654. The equation for the curve is expressed as $y = 139316N_f^{-0.517}$.

A structural stress against cycles to failure master curve was generated using unit load factors from FE solid element models and representing distorted coupon geometries (non-load cover plate and single attachment) for weld toe failures, Figure 222.

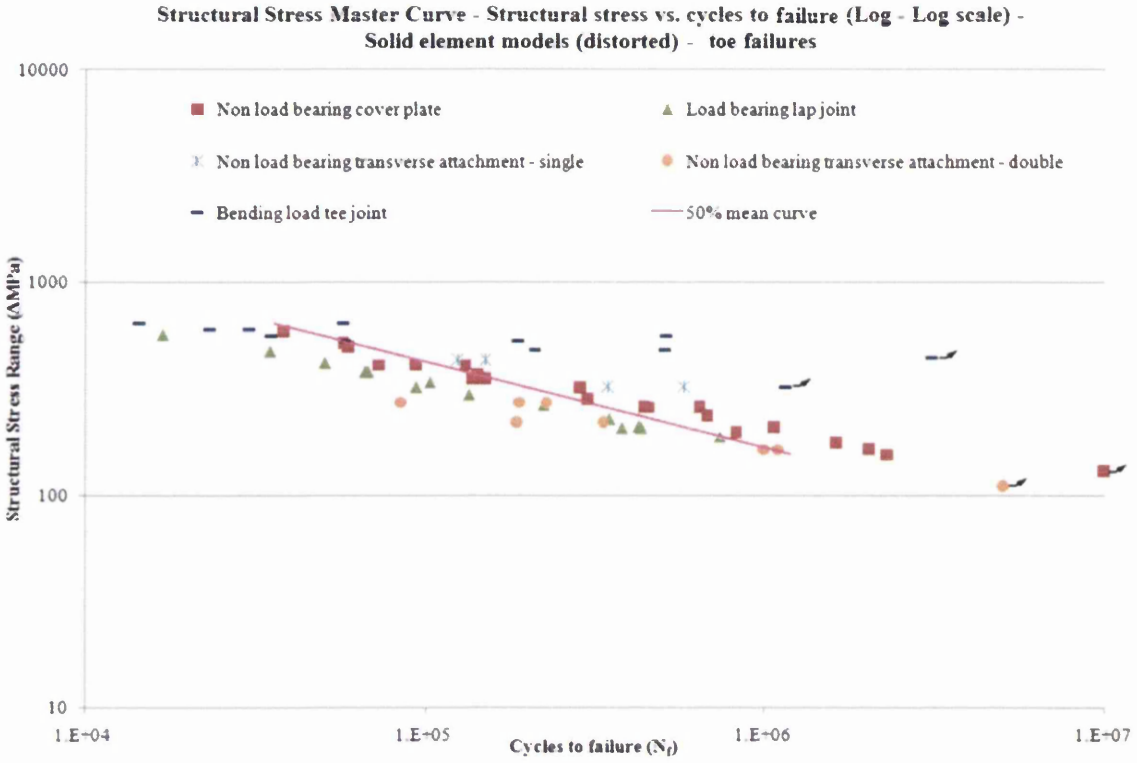

Figure 222: Structural stress master curve - Weld toe failures (solid element models distorted geometries)

The data are repositioned when compared against the original load-life curves and the un-distorted coupon geometries, with higher per unit load structural stress value. This increases the apparent fatigue strength of the curve but also improves the spread and scatter for all the weld geometries. The bending load tee joints display the usual distinct slope. The distorted geometry coupons have increased stress value and a slightly improved correlation with the bending load tee data. The statistical analysis of the data provided the 50% certainty of survival curve and confirms the improved correlation with an R^2 value = 0.685 compared with 0.654 in Figure 221. The standard error = 0.304 with the equation for the curve expressed as $y = 43905N_f^{-0.403}$.

The effectiveness of the toe failure master curve was further explored to observe the effects of excluding the un-characteristic bending load tee joints. The master curve generated is displayed in Figure 223 on a structural stress against cycles to failure plot.

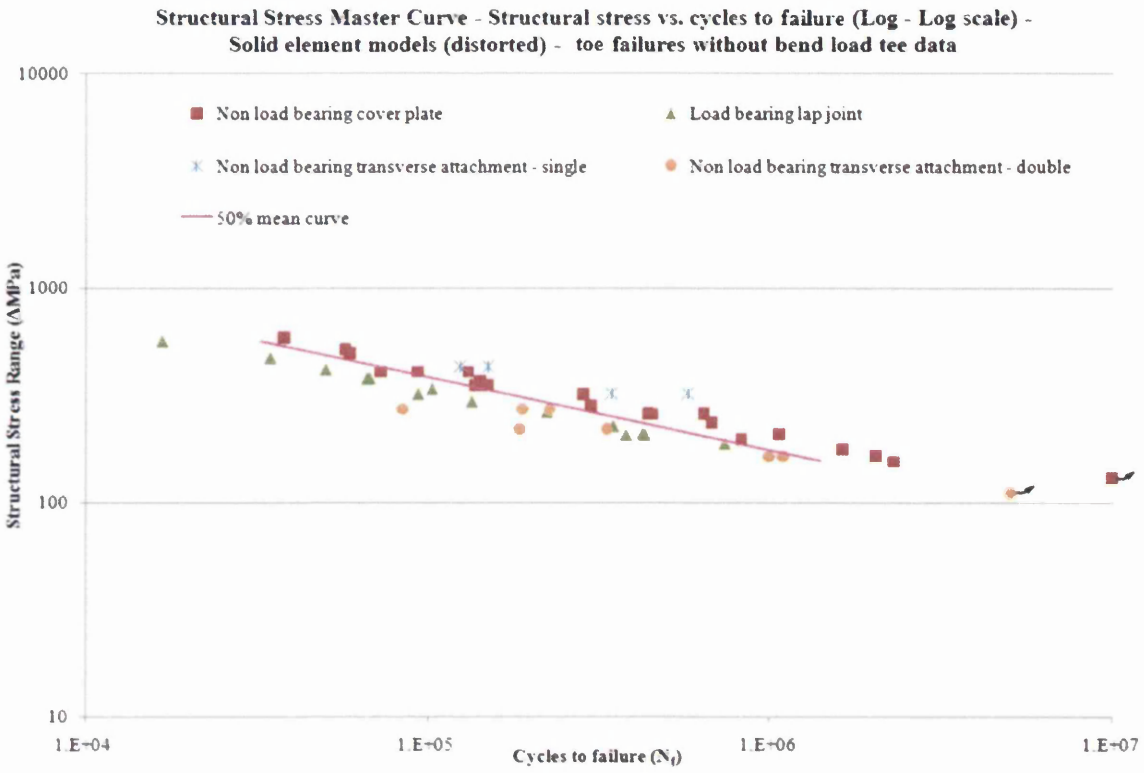

Figure 223: Structural stress master curve - Weld toe failures (solid element models distorted geometries) excluding bending load tee data

Despite the omission of the bending load tee data, there is no calculated improvement in correlation for the weld toe failure master curve. The statistical analysis of the data gave an R^2 value of 0.685 and a curve equation $y = 20419N_f^{-0.347}$. There is a slight change in the gradient of the fatigue curve slope. The curve is flatter and therefore calculates lower low-cycle fatigue strength. The shallower slope of -0.34 is more in-line with typical weld fatigue data.

This analysis contradicts the results of the combined failure mode master curves generated previously. The exclusion of the bending load tee joint data has a smaller impact on the weld toe failure mode curve and is not as severe as that seen in previous curves in Figure 214, Figure 217 and Figure 219 for the un-distorted, distorted and measured structural stress master curves respectively. This suggests that the structural stress parameter is not purely dependent on loading mode, but also there is some dependency arising due to failure mode. Ultimately, further judgement is necessary on the accuracy of the weld fatigue life prediction obtained from each curve.

4.5.6 Weld Throat failures - Structural Stress Curve

There were different levels of penetration achieved when manufacturing the welded cruciform coupons. The various levels of penetration were modelled into the solid element geometries and a structural stress value calculated for each. The resultant effects are explored in the throat failure master curve. A structural stress against cycles to failure master curve was constructed using unit load factors from FE solid element models and un-distorted coupon geometries for weld throat failures only, Figure 224. An average penetration level is assumed and the same structural stress value is used for the corresponding cruciform coupon. These are 1.75MPa for the 8mm weld cruciform coupons and 1.44MPa for the 10mm weld cruciform coupons.

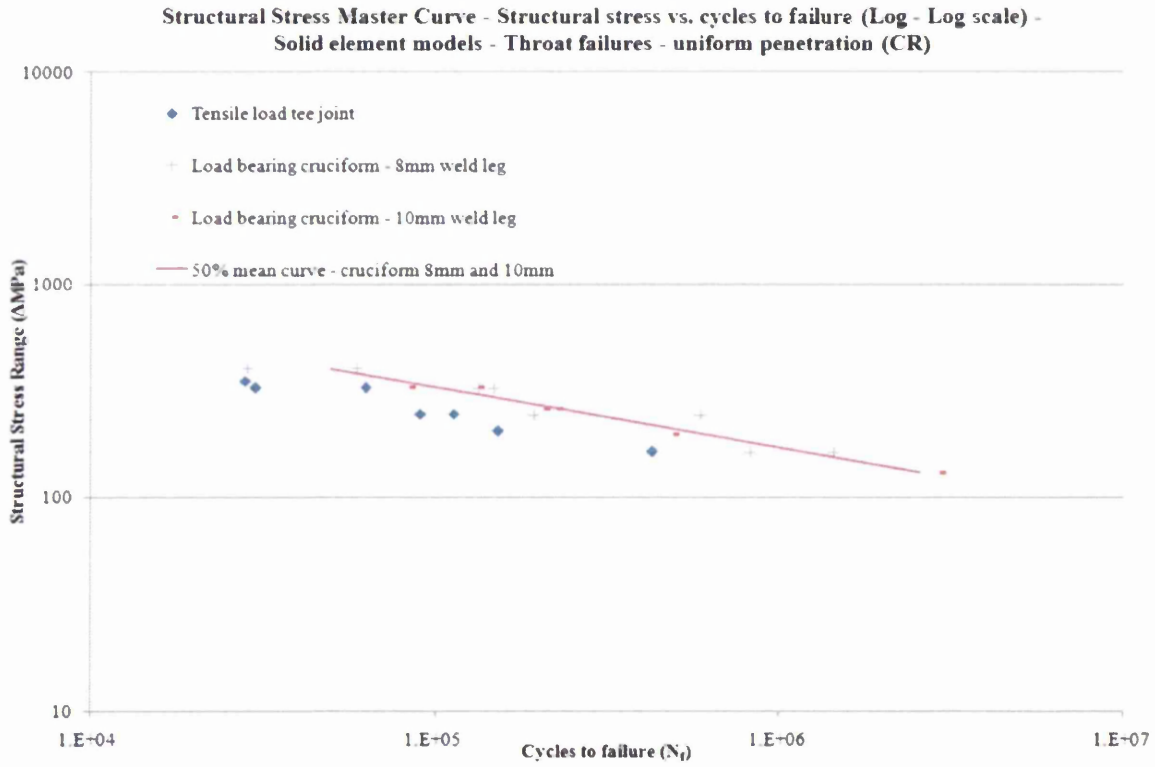

Figure 224: Structural stress master curve - Throat failures (solid element models with averaged weld penetration)

The statistical analysis of the data provided the 50% certainty of survival curve with an R^2 value = 0.793 and standard error = 0.255. The equation for the curve is expressed as $y = 8151N_f^{-0.287}$.

A structural stress against cycles to failure master curve was generated using unit load factors from FE solid element models and un-distorted coupon geometries for weld throat failures

only, Figure 225. The corresponding weld penetration level was modelled into the FE coupon geometry and the structural stress value calculated for each. This was done for the 8mm and 10mm cruciform specimens with 0.5, 1, 2 and 3mm levels of sidewall fusion into the parent plate. The structural stress values were correlated with each failed test coupon and the level of penetration noted. The structural stress values range between 1.4-2.25MPa for 8mm and 1.16-1.76MPa for 10mm weld cruciform coupons.

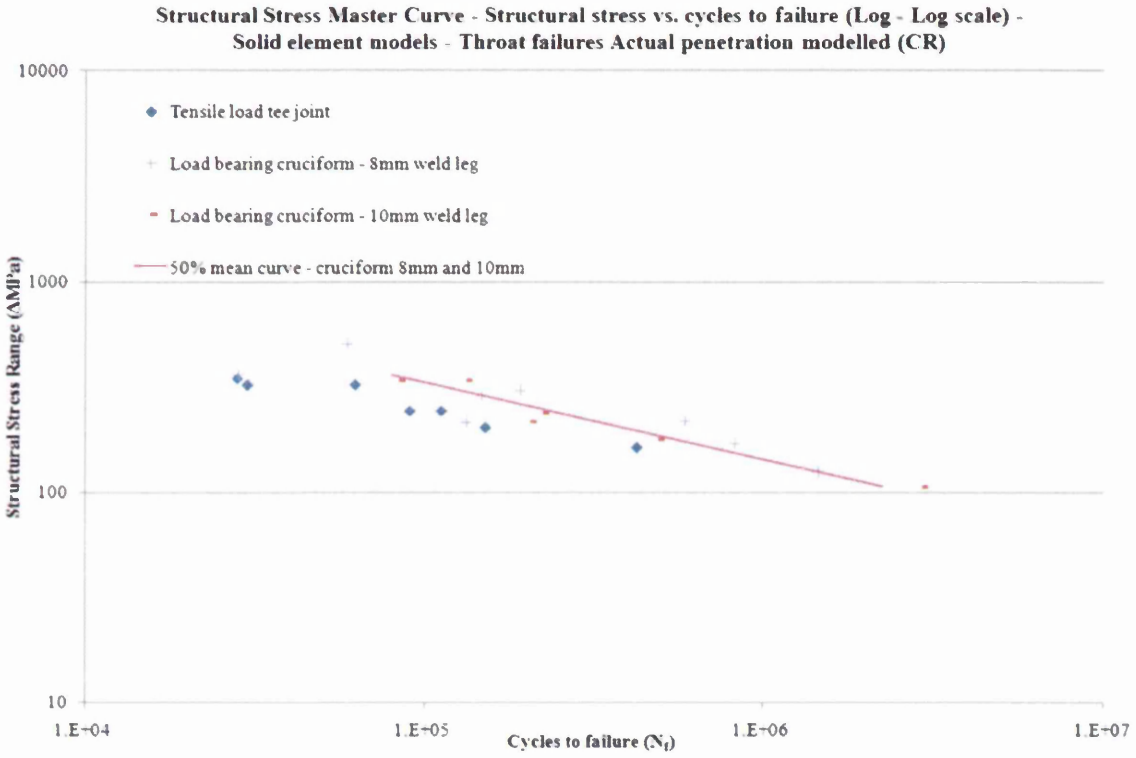

Figure 225: Structural stress master curve - Throat failures (solid element models with relevant weld penetration)

The statistical analysis of the data gave a 50% certainty of survival curve with an R^2 value = 0.779 and standard error = 0.263. The equation for the curve is given as $y = 15632N_f^{-0.344}$. On comparison there is no improvement in correlation when modelling the actual weld penetration over an assumed average value. In fact the degree of correlation is reduced as evidenced by R^2 values, which decreases from 0.793 to 0.779. Even so, there is still good correlation between the different weld coupon geometries.

In Figure 226 the weld toe and throat failure mode master curves generated have been plotted on the same axis. Both weld toe failure curves, including and excluding the bending load tee data are displayed.

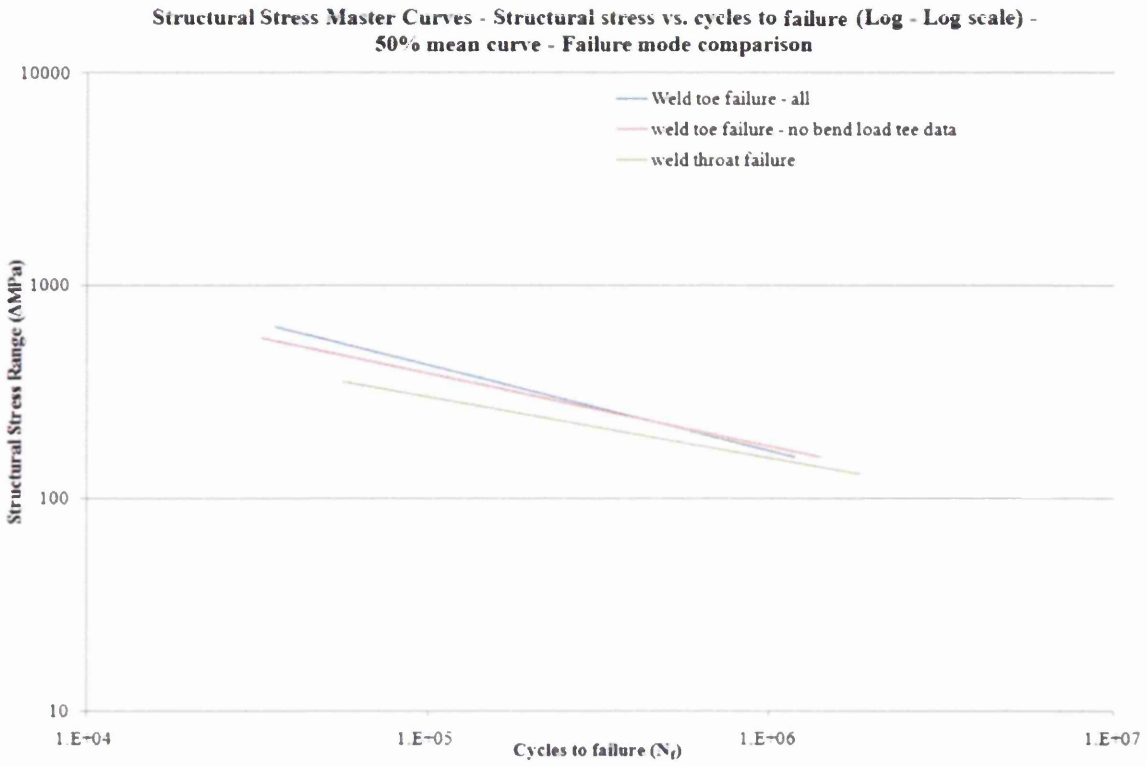

Figure 226: Structural stress master curves generated – Weld toe and throat failure modes – 50% mean curves

From the displayed 50% mean curves, it is evident there is a slight change in the weld toe failure data with the bend load tee data removed. With either weld toe curve, there is a significant difference between them and the weld throat failure master curve. Based on these curves it is adequate to suggest that the structural stress master curve is also failure mode dependent. Should a single master curve be used for all failure modes, the weld toe fatigue predictions would be pessimistic, and hence over designed. As a result they are not robust, efficient designs. In contrast, weld throat failure predictions would be optimistic and structures risk being under designed, thus limiting the confidence in its performance.

4.5.7 Weld Root failures - Structural Stress Curve

A structural stress against cycles to failure master curve was generated using unit load factors from FE solid element models and un-distorted coupon geometries for weld root failures only, Figure 227. Since there is only one set of coupon geometries with a root failure, it is not possible to compare correlations as in the previous cases. It is possible to consider the root failures as not viable data for the structural stress graph. It is inconclusive whether or not the

excessive sulphur banding of the parent material played a part in the onset of the fatigue failure. This provides sufficient cause to eliminate the fatigue data from any further analysis.

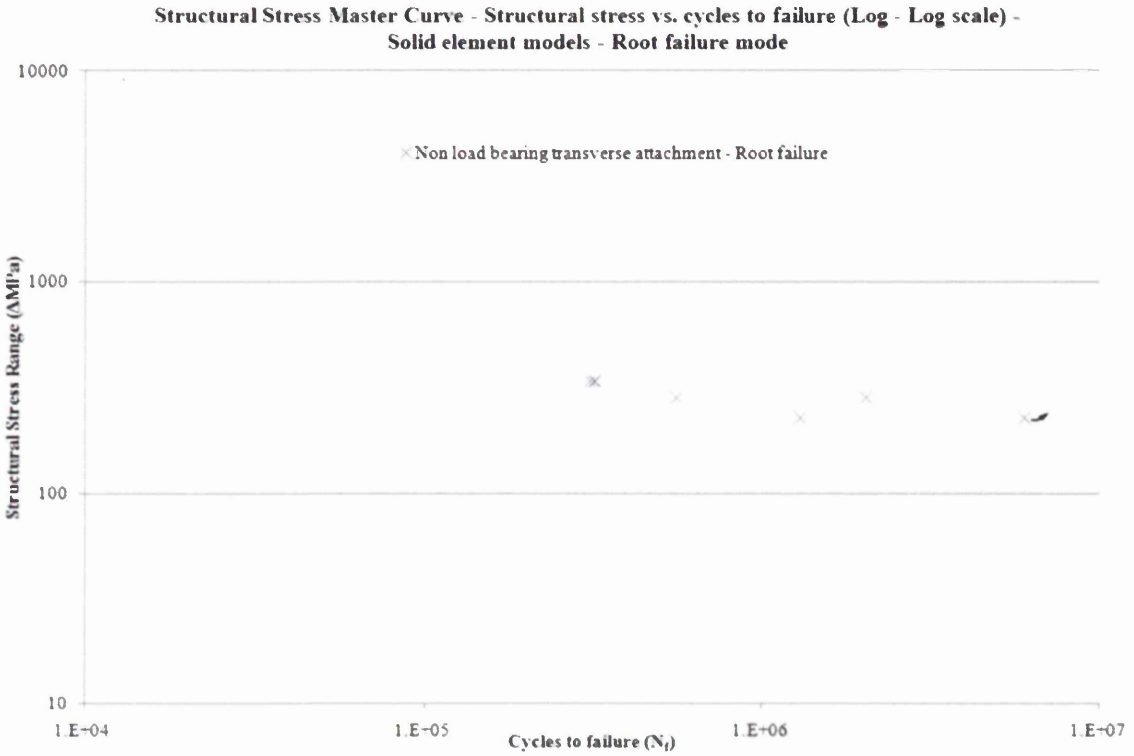

Figure 227: Structural stress master curve - Root failures (solid element models distorted geometries)

The statistical analysis of the data gave a 50% certainty of survival curve with an R^2 value = 0.621 and standard error = 0.243. The equation for the curve is expressed as $y = 8628N_f^{-0.253}$.

4.5.8 Summary - Structural stress master curve

The structural stress calculation shows a low sensitivity to failure modes, element size, element type and mesh density for solid element models. There is some discrepancy for shell element models when analysing throat failures but this is due to the limitations of the shell element representing bending moments and the weld geometry of thick plate structures. An improved correlation is also achieved when modelling the distortion of actual coupon geometries.

Upon deciphering the range of coupon fatigue data and presenting master curves based on separate failure and loading modes, it is perfectly feasible to suggest the damage parameter is sensitive to each mode.

Ultimately there is a wide range of master curves available for use in the weld fatigue life prediction as shown in Figure 228, where the structural stress against cycles to failures (Log-Log scale) is plotted and based on FE solid element distorted models. Also displayed on the graph is the 50% mean curve and 99% certainty of survival curve. The equation describing the master S-N curve will now be input into the FE weld fatigue analysis package in order to obtain an appropriate life prediction.

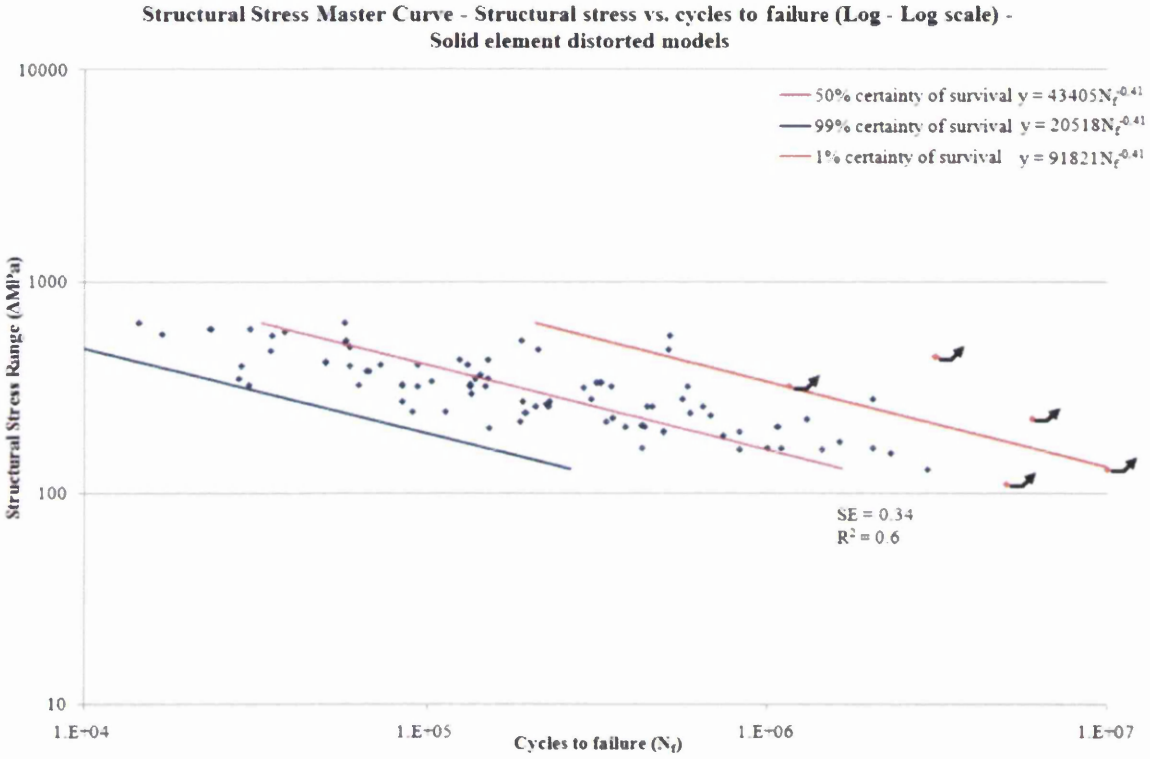

Figure 228: Master S-n Curve - Structural stress against Cycles to failure (Log-Log scale) – Solid element distorted models

The FE modelling and structural stress calculation technique will have an effect on the master S-N curve generated. Using different modelling and calculation parameters, the nine distinct curves created are listed below. To identify and analyse the variation between each curve type, the nine different curves are brought onto a single graph in Figure 229. The structural stress range (ΔMPa) is plotted on the y-axis against the cycles to failure (N_f) on the x-axis. The curves that are considered for a fatigue life prediction analysis are based on a number of different calculation parameters:

Solid element, distorted geometry models;

Solid element, un-distorted geometry models;

Solid element, distorted geometry models – excluding the bending load tee data;
Solid element, un-distorted geometry models - excluding the bending load tee data;
Measurement based data;
Measurement based - excluding the bending load tee data;
Weld toe failures;
Weld toe failures - excluding the bending load tee data.;
Weld throat failures.

The fatigue master curves presented are based on the 50% certainty of survival mean curve generated from the list above.

It is evident that some variation in the master curves exists. The most noticeable is the measured base master curve with the included bending load tee joint data. The unit load measured value was significantly higher than the FE-based calculation. The tee bend data was also positioned higher than the general scatter band, with a distinct slope. These factors create a much steeper placed fatigue master curve. The measurement based master curve without the bend load tee data is placed reasonably well within the various FE-based calculated structural stress master curves.

The FE-based structural stress curves are all placed together with similar behaviour. Including the bending load tee data increases the gradient of the curve (~1/5). A master curve not including the bend tee data has a flatter gradient approximately ~1/3, more representative of a typical weld fatigue curve.

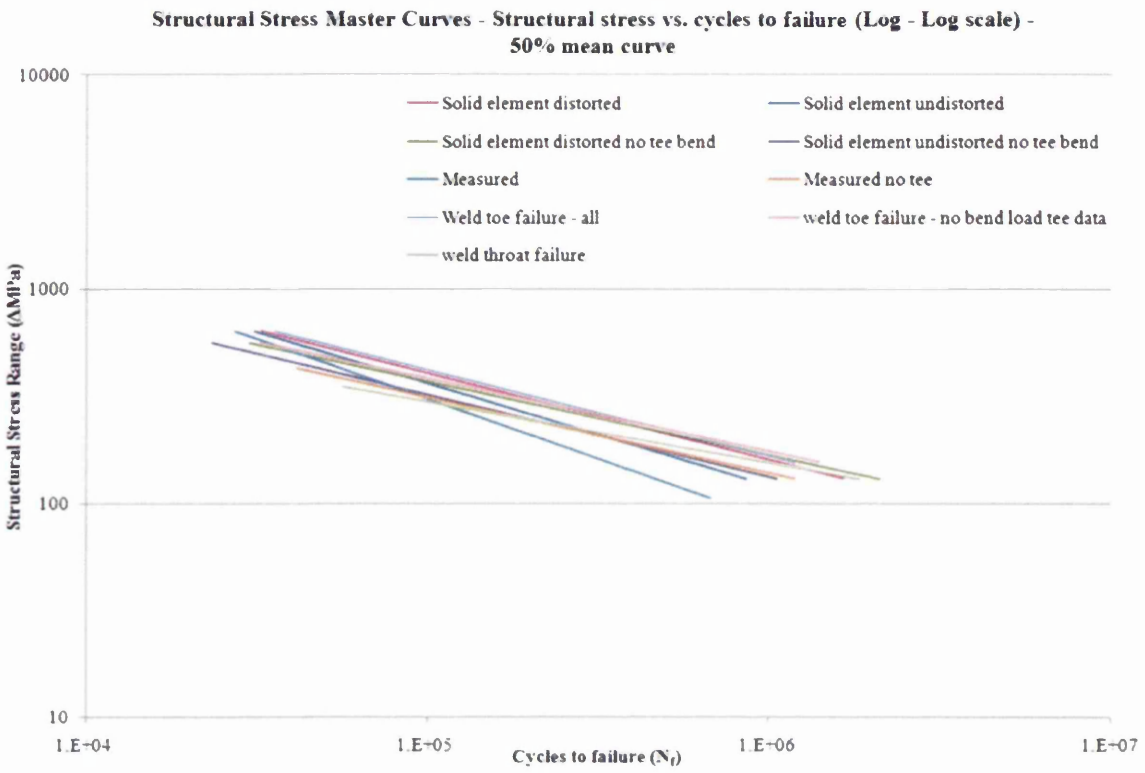

Figure 229: Comparison of structural stress master curves generated – All 50% mean curves

All of the various fatigue curves will be taken forward for a component fatigue analysis. It is promising to see that only a slight difference exists between the wide range of curves. Naturally there is some variation and exploiting the differences between the fatigue curves could prove crucial in obtaining a robust design and maximising cost saving opportunities should the application of the structural stress method prove accurate and efficient.

4.6 Equivalent Structural Stress Master Curve - Data Conversion

The structural stress fatigue parameter has been established for a range of different coupon geometries in order to generate a single master curve suitable for FE-based weld fatigue life predictions. Complementary to the theory of the structural stress alternative damage parameter, Dong [44] proposes that weld fatigue data can be further consolidated into a single master curve with improved condensing of test data. This is a separate fatigue damage parameter obtainable when taking into consideration crack growth effects of the loading mode and material thickness. The 'Equivalent Structural Stress' (Eqv.SS) is defined as:

$$Eqv.SS = \frac{\sigma_s}{t^{\frac{2-m}{2m}} I(r)^{\frac{1}{m}}} \qquad \text{Eq 4.6.1}$$

Where:

σ_s= structural stress
t = plate thickness (mm)
m= fatigue crack growth exponent
I(r) = loading mode correction
r = bending ratio

Entering the structural stress unit load values generated from the FE based calculations in the above equation, the 'Equivalent structural stress' damage parameter is derived. There are two variables used to optimise the scatter of the fatigue data. The term $I(r)^{(1/m)}$ has a value between 1.1 for tensile loaded welds and 1.13 for predominantly bending load coupons. The thickness, t, is relevant to the thickness of the welded plate under analysis. Then, using the elastic scaling method applied to the coupon test data (chapter 4.1), an equivalent structural stress against cycles to failure curve is generated.

4.6.1 FE-Based calculated equivalent structural stress curve

An equivalent structural stress against cycles to failure master curve is generated using unit load factors from FE solid element models with un-distorted coupon geometries and is displayed in Figure 230. There is a redistribution of the original load range against cycles to failure curves, and a different (not comparable – separate damage parameter) distribution to the conventional structural stress master curve. There is a noticeable grouping of the curves towards the centre of the scatter band. The bending load tee joint coupon data is placed towards the upper band of the data points and has a distinct and different curve gradient

compared with the other fatigue curves as seen previously in the structural stress master curve in chapter 4.5. The values of $I(r)^{(1/m)}$ used are related to the coupon loading regime. For predominantly tensile loading coupons, such as the non-load cover plate, single and double transverse attachment and load-bearing cruciform joints, a value around 1.1 is used. The tensile load tee joint, bending load tee joint and load-bearing lap joint, which endured a high bending moment, have an $I(r)^{(1/m)}$ value of 1.13.

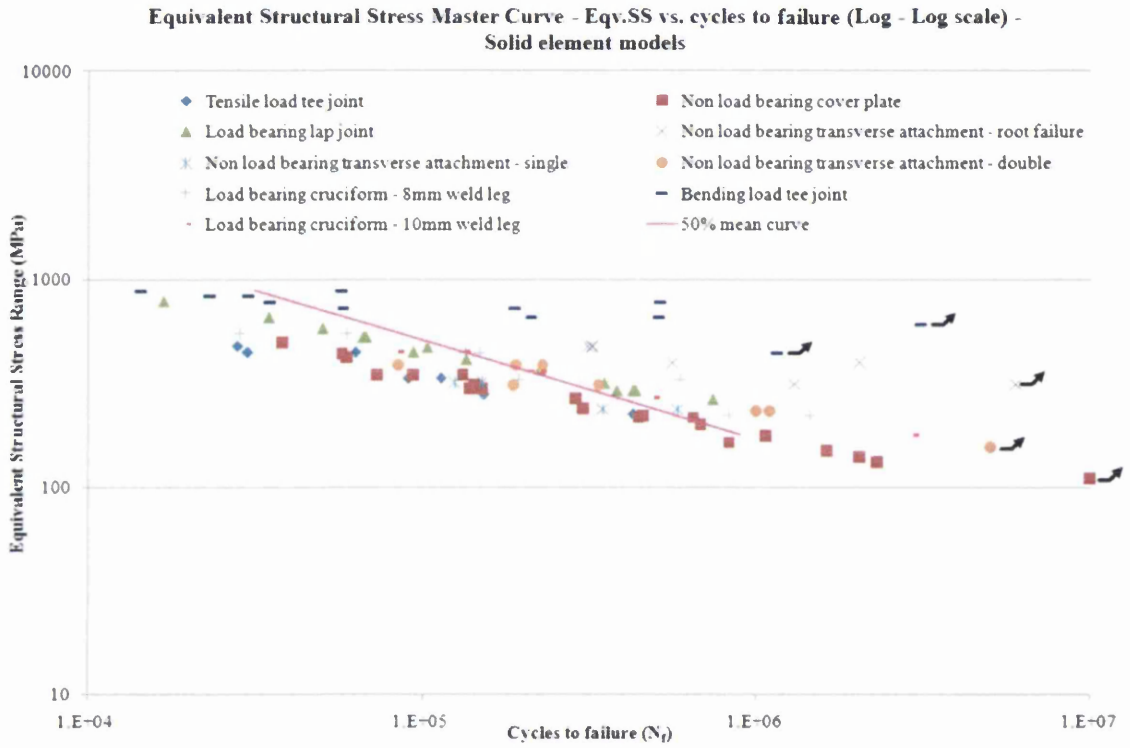

Figure 230: Equivalent structural stress master curve - FE-solid element un-distorted models

A statistical analysis was completed and gave a 50% certainty of survival curve expressed as $y = 50545N_f^{-0.48}$. The values for the standard error = 0.36 and R^2 = 0.57, show little improvement of correlation compared with the original structural stress approach. The statistical analysis completed for the standard structural stress master curve gave a correlation in the data with values for SE = 0.35 and R^2 = 0.57. As there is little variation in thickness of the coupons, there is only a slight improvement in the correlation of the data based on the standard structural stress.

Repeating the above substitution process, but now employing unit load factors from FE solid element models for distorted coupon geometries (i.e. the non-load-bearing cover plate and

non-load-bearing single transverse attachment) a revised equivalent structural stress against cycles to failure master curve is obtained, Figure 231.

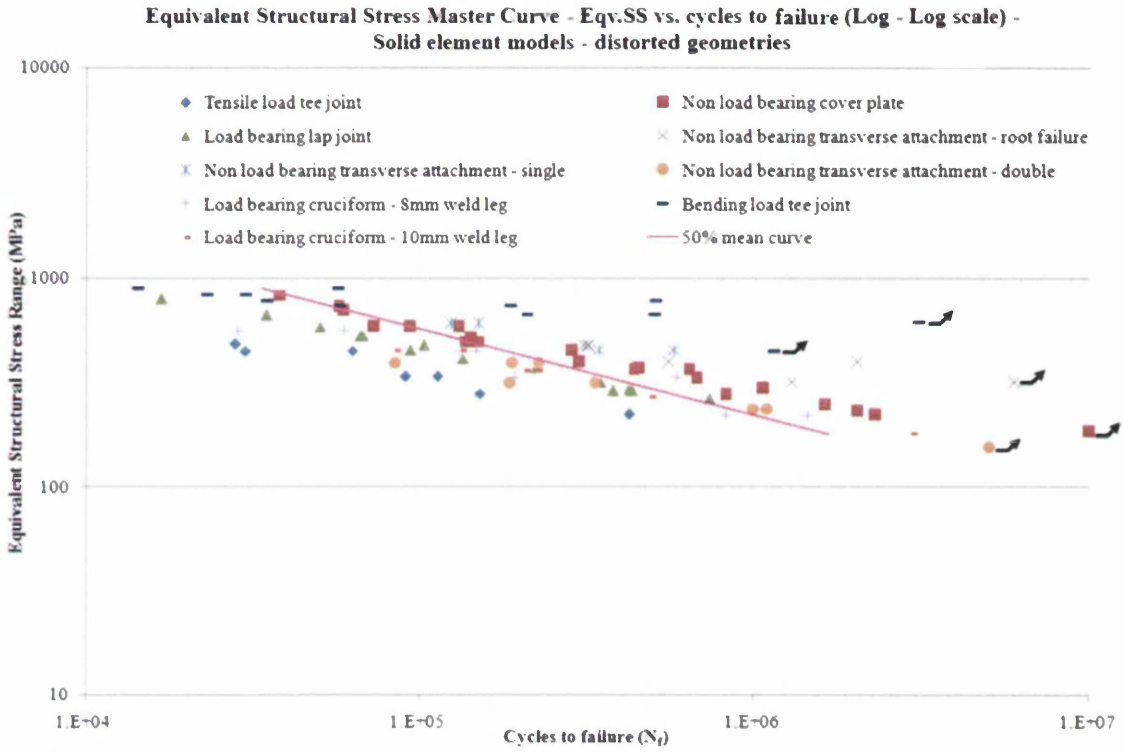

Figure 231: Equivalent structural stress master curve - FE-solid element distorted models

There is an apparent increase in the fatigue life for the non-load-bearing cover plate and non-load-bearing single transverse attachment distorted geometries. A higher structural stress unit load factor is calculated for the distorted coupon geometries and, hence for the same cycles to failure, a higher stress is calculated compared with the un-distorted coupons. This approach improves the correlation between all coupons. Most noticeably, it improves the correlation with the bending load tee joint data. The revised standard error = 0.35 with $R^2 = 0.59$. These compare with a standard error =0.36 and R^2 value = 0.57 for the un-distorted equivalent structural stress master curve in Figure 230. From the statistical analysis, the equation of the new curve is $y = 62600N_f^{-0.41}$.

4.6.2 Measured Equivalent Structural Stress Curve

The measured structural stress values recorded in chapter 4.4 were used to generate the equivalent structural stress against cycles to failure master curve in Figure 232. The measurements were entered into the above equation instead of using the calculated values. The measured values are only possible for the weld toe failures. Where other failure modes

are observed (such as throat failures where it is not possible to obtain a measured value), the FE-based solid element calculated structural stress values are included for comparison. There is an excellent correlation between the majority of the coupon data. The bending load tee joint data lies above the main scatter band by an approximate factor of 2.

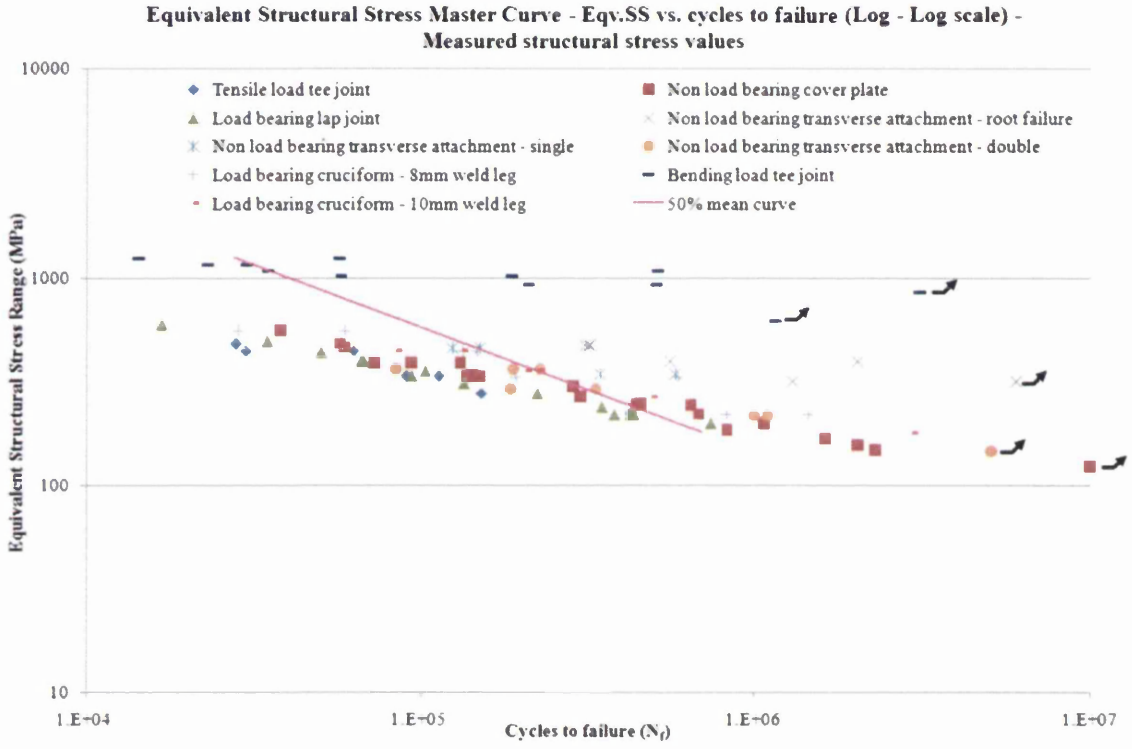

Figure 232: Equivalent structural stress master curve - Measured structural stress values

A statistical analysis provided the 50% certainty of survival curve with the equation $y = 576926N_f^{-0.6}$. The standard error value = 0.4 and $R^2 = 0.46$ were calculated. There is little improvement in the correlation of data, compared with the measured structural stress fatigue curve shown in chapter 4.5.3.

4.6.3 Sensitivity on equivalent structural stress parameters

The equivalent structural stress parameter has a minimal effect on the correlation of the data, primarily due to the fact that all the welded coupon geometries have similar weld specifications and material thicknesses. However, the $I(r)^{(1/m)}$ loading mode variable could potentially have a significant effect on the data correlation and the scatter between the different fatigue data sets. Using the same calculated structural stress unit load factors for the solid element distorted geometries in the equivalent structural stress equation but with a modified $I(r)^{(1/m)}$ value, an alternative equivalent structural stress against cycles to failure

master curve can be constructed. An example with an $I(r)^{(1/m)}$ value of 1.1 for all coupon geometries is shown in Figure 233.

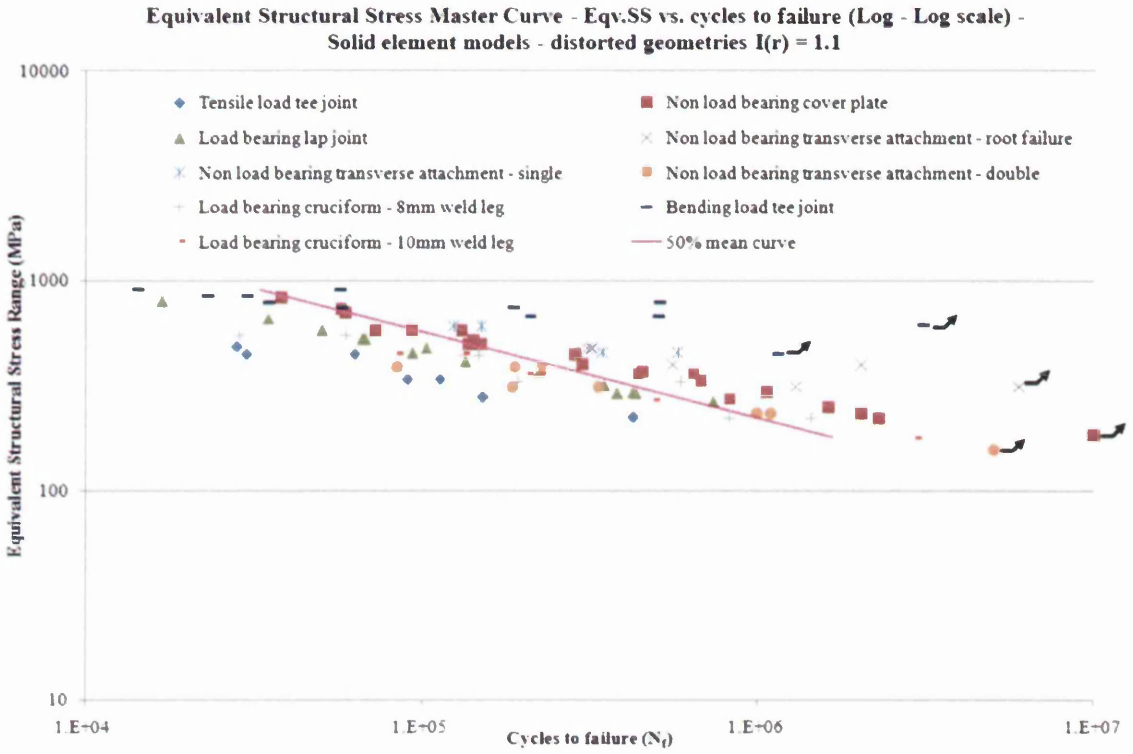

Figure 233: Equivalent structural stress master curve - FE-solid element distorted models – Modified $I(r)^{(1/m)}$ value = 1.1

The statistical analysis gave a 50% mean curve equation of $y = 65866N_f^{-0.412}$, and a standard error = 0.349 and $R^2 = 0.587$.

This process was extended to the calculated structural stress unit load factors for the solid element distorted geometries in conjunction with a modified $I(r)^{(1/m)}$ value. The resultant equivalent structural stress against cycles to failure master curve with an $I(r)^{(1/m)}$ value of 1.13 for all coupon geometries is shown Figure 234. The modification to the $I(r)^{(1/m)}$ value has a very small effect on the correlation of the data. The equation for the 50% mean curve is $y = 64700N_f^{-0.412}$ with a standard error = 0.349 and $R^2 = 0.587$. There is no change from the 50% mean curve of the previous master curve with an $I(r)^{(1/m)}$ value of 1.1. Using different loading mode $I(r)^{(1/m)}$ ratios had little further effect on the correlation of coupon data. The equivalent structural stress damage parameter has a higher fatigue strength master curve. Based on the original structural stress curve, the fatigue data is multiplied by a factor of ~1.4. It is higher at 1.41 for fatigue data with a predominantly tensile loading mode and $I(r)^{(1/m)}$ = 1.1. The

multiplication factor is 1.38 for fatigue data with a predominantly bending loading mode and $I(r)^{(1/m)} = 1.13$.

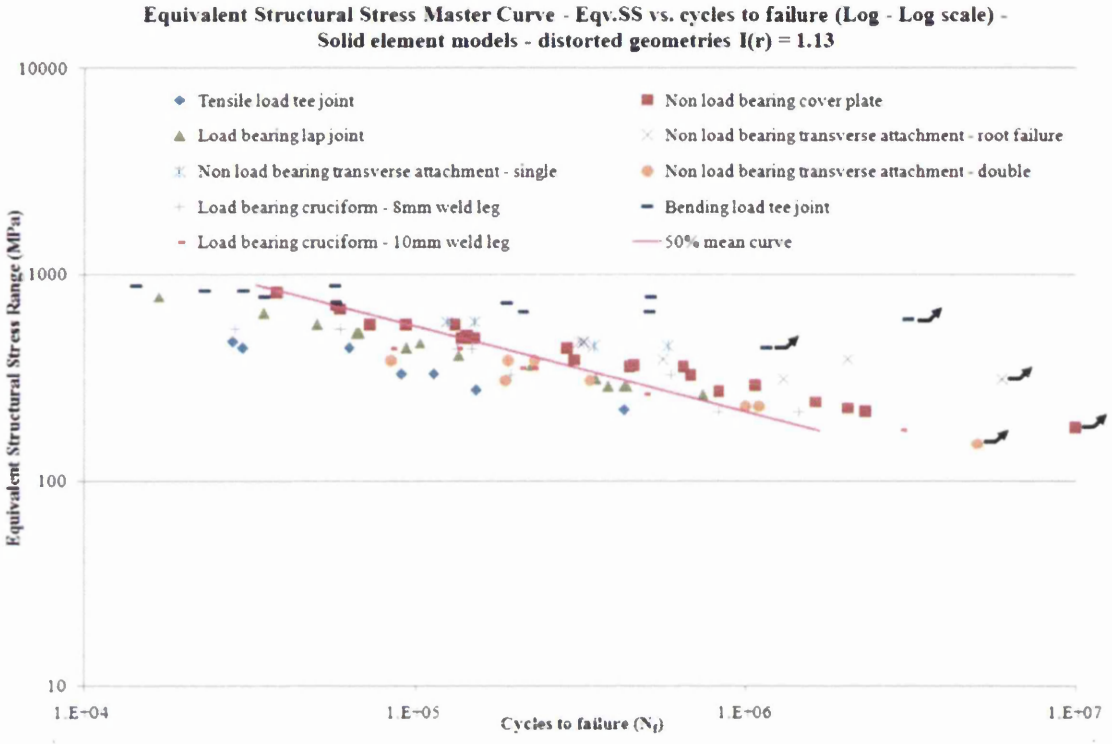

Figure 234: Equivalent structural stress master curve - FE-solid element distorted models – Modified $I(r)^{(1/m)}$ value = 1.13

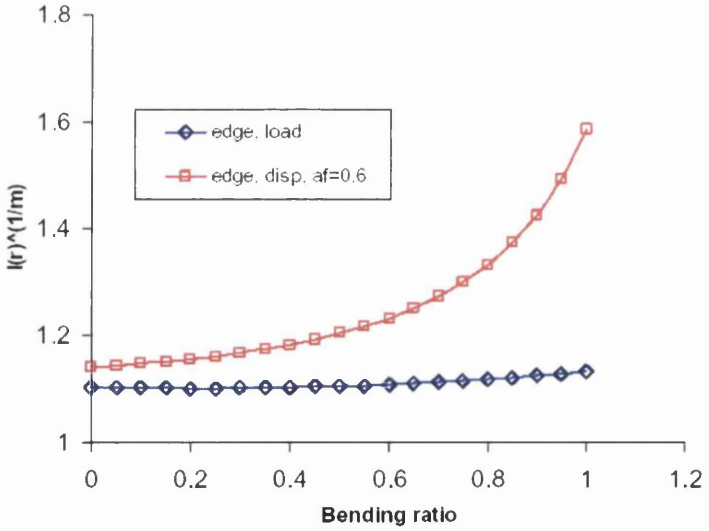

Figure 235: $I(r)^{(1/m)}$ Value against Bending ratio

The derived $I(r)^{(1/m)}$ value is derived figure from the structural stress theory as defined by Dong, Figure 235. The value for load controlled test conditions is $I(r)^{(1/m)}$= 1.1 to 1.13. The $I(r)^{(1/m)}$ value differs for displacement controlled fatigue test conditions with $I(r)^{(1/m)}$ = 1.14 to

1.6. This is because displacement controlled conditions are very sensitive to the R value and degree of bending. Even though all the fatigue test coupons in this present research work were subjected to load-controlled conditions, the bending load tee joint displayed some important differences compared with the other geometries.

The bending load tee joint exhibited a significantly longer fatigue crack propagation stage (Chapter 4.1- Figure 108) before final separation occured, compared with the other coupons, in which final separation occured before a stiffness drop of ~3%. The gradient of the S-N curve was -0.11, compared with a approximate -0.33 slope for the other test coupon results. The slope of -0.33 is generally observed in other work on welded coupons. The test setup used an upper test grip and lower clamping base where the tee joint base plate was restrained with a 100mm wide clamp-to-clamp distance (i.e. clamped each side of the base plate 50mm away from the centre of the upright plate). This creates a high stress low load condition. The test setup for the other coupons used both an upper and lower test grip. It is conceivable that the bending load tee joint was more sensitive to bending effects in a similar way to the conditions seen under displacement controlled testing.

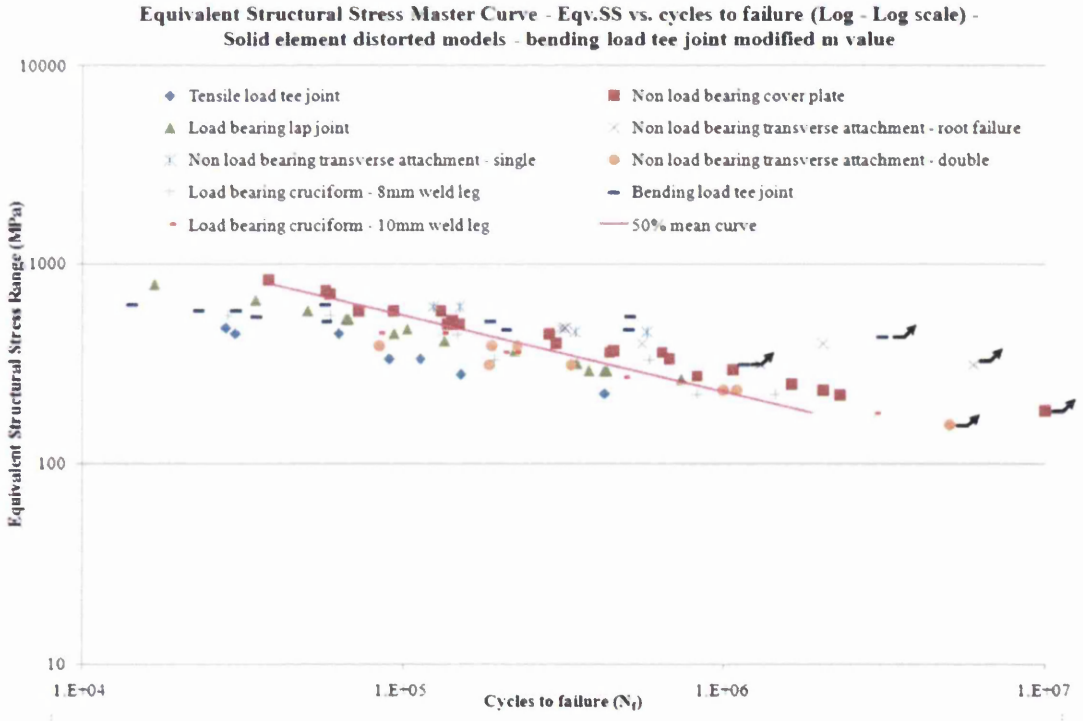

Figure 236: Equivalent structural stress master curve - FE-solid element distorted models – Modified $I(r)^{(1/m)}$ value = 1.6

The master curve shown in Figure 236 is based on the calculated structural stress unit load factors for the solid element distorted models but with a modified $I(r)^{(1/m)}$ value for the bending load tee-joint coupon. The equivalent structural stress against cycles to failure master curve is generated with $I(r)^{(1/m)}$ of 1.6 for the bend load tee joint and 1.1- 1.13 for all other test coupon geometries. The bend load tee joint data is reduced in equivalent structural stress fatigue strength and the data lie within the main scatter trend. The statistical analysis gave a 50% mean curve with a standard error = 0.339 and an $R^2 = 0.61$. The equation for the mean curve is $y = 43997N_f^{-0.38}$. There is a slight improvement in correlation when using the $I(r)^{(1/m)} = 1.6$ value for the bending load tee joint.

4.6.4 Weld failure modes

It has been shown in chapter 4.6.3 that the equivalent structural stress damage parameter can accommodate any effects due to applied loading modes – the effectiveness of which is dependent on the parameter values used. Subsequently, as per the structural stress master curve analysis, the equivalent structural stress parameter is explored to find whether any possible sensitivity exists due to the failure mode type. A weld toe failure master curve has been generated for 3 separate conditions:

1. Weld toe failures - including bending load tee data with $I(r)^{(1/m)} = 1.13$;
2. Weld toe failures - including bending load tee data with $I(r)^{(1/m)} = 1.6$;
3. Weld toe failures - excluding bending load tee data.

The three master curve conditions are presented in Figure 237, Figure 238 and Figure 239 respectively. The equivalent structural stress is plotted against the cycles to failure. A statistical analysis was completed of the data for each master curve condition, also displayed on the graphs. The curve equations and corresponding R^2 correlation values are summarised in Table 8.

Weld toe failure 50% mean curve statistical analysis			
Master curve	**R squared**	**a**	**b**
1	**0.69**	**58121**	**-0.40**
2	**0.74**	**22233**	**-0.32**
3	**0.81**	**28147**	**-0.34**

Table 8: Summary of weld toe failure master curves – 50% mean curve values

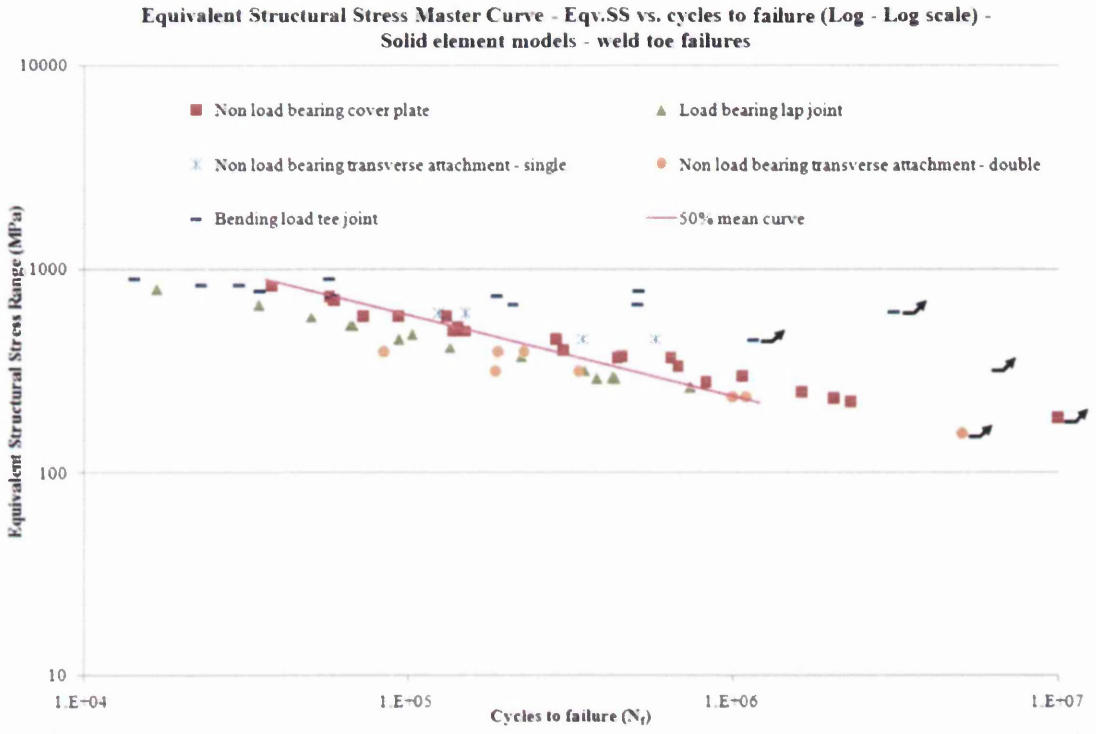

Figure 237: Equivalent structural stress master curve - Weld toe failures (bend tee joint $I(r)^{(1/m)}$ value = 1.13)

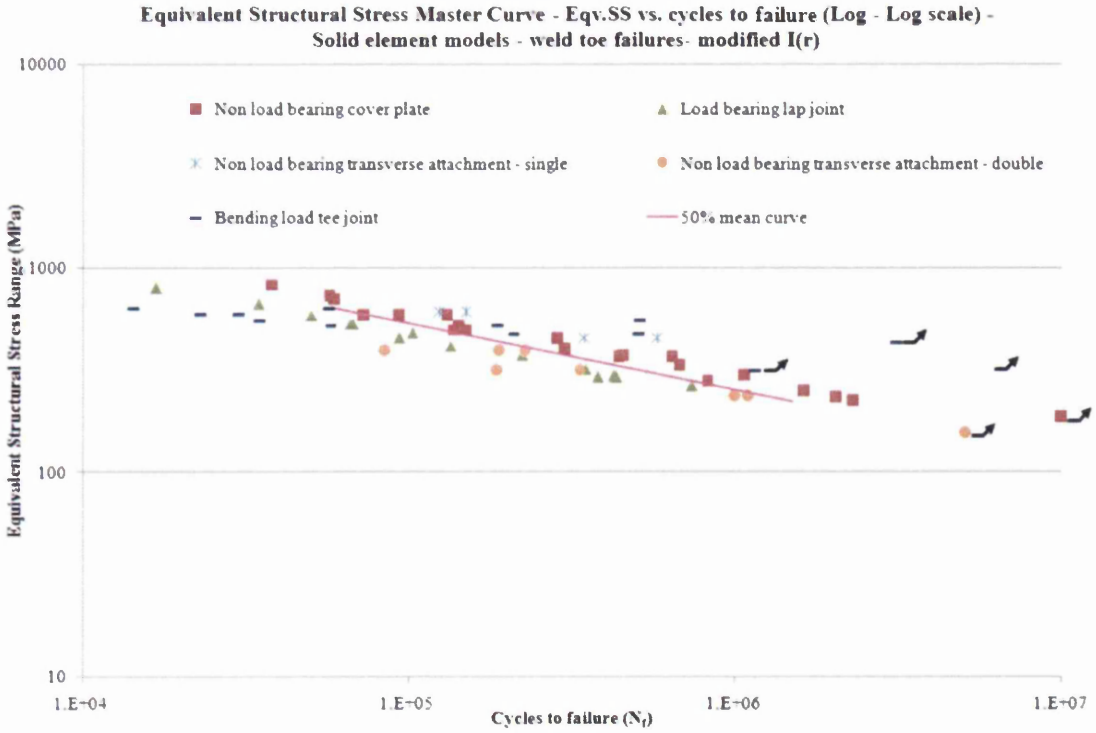

Figure 238: Equivalent structural stress master curve – Weld toe failures (bend tee joint modified $I(r)^{(1/m)}$ value = 1.6)

It is visibly apparent upon using a modified I(r) value that the bending load tee data sits within the main scatter of weld toe failures in Figure 238. This is supported further by an improved R^2 value of 0.74.

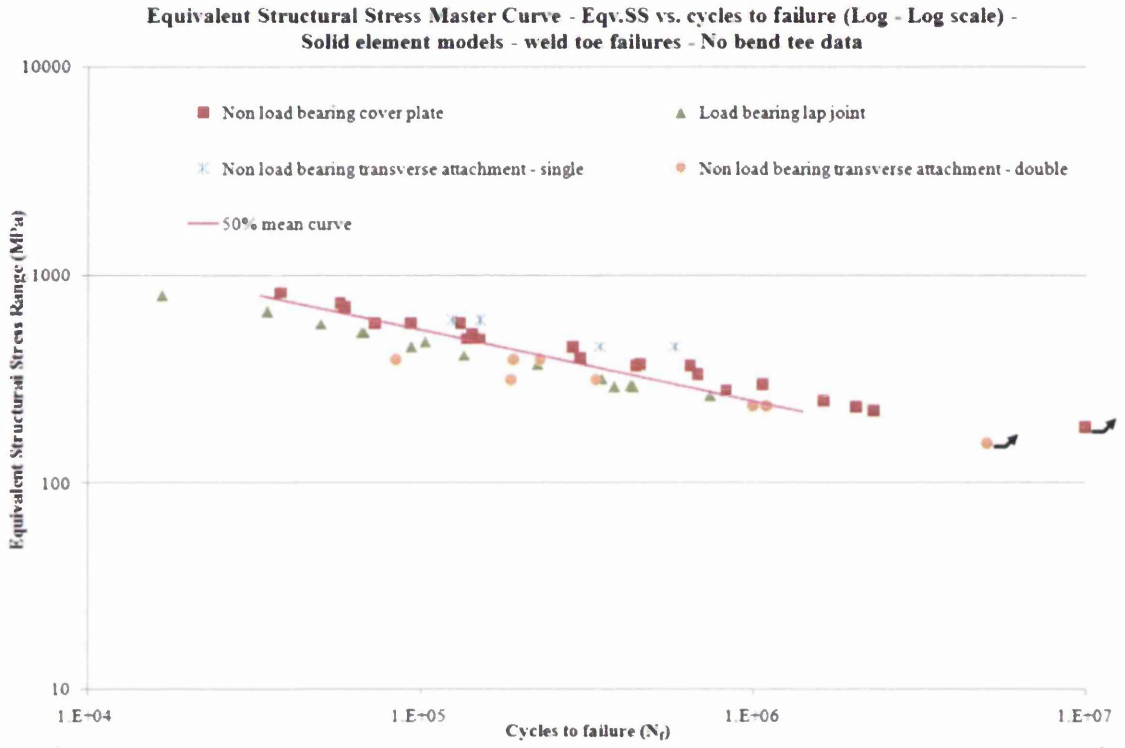

Figure 239: Equivalent structural stress master curve – Weld toe failures (no bend load tee joint data)

The correlation of the weld toe failures is further improved with the exclusion of the bending load tee joint data. The R^2 value is only a slight improvement at 0.81, up from 0.74. Despite the improvement on discounting the bending load tee joint, preference would be to include the fatigue failure in the weld toe master curve. This would further support the effectiveness of the equivalent structural stress fatigue damage parameter and its ability to condense all data into a single scatter band, but with some compromise on data correlation.

The weld fatigue throat failures are displayed in Figure 240 with equivalent structural stress against cycles to failure. The calculated 50% mean curve is also displayed, with an equation $y = 19918N_f^{-0.342}$ and R^2 value of 0.785.

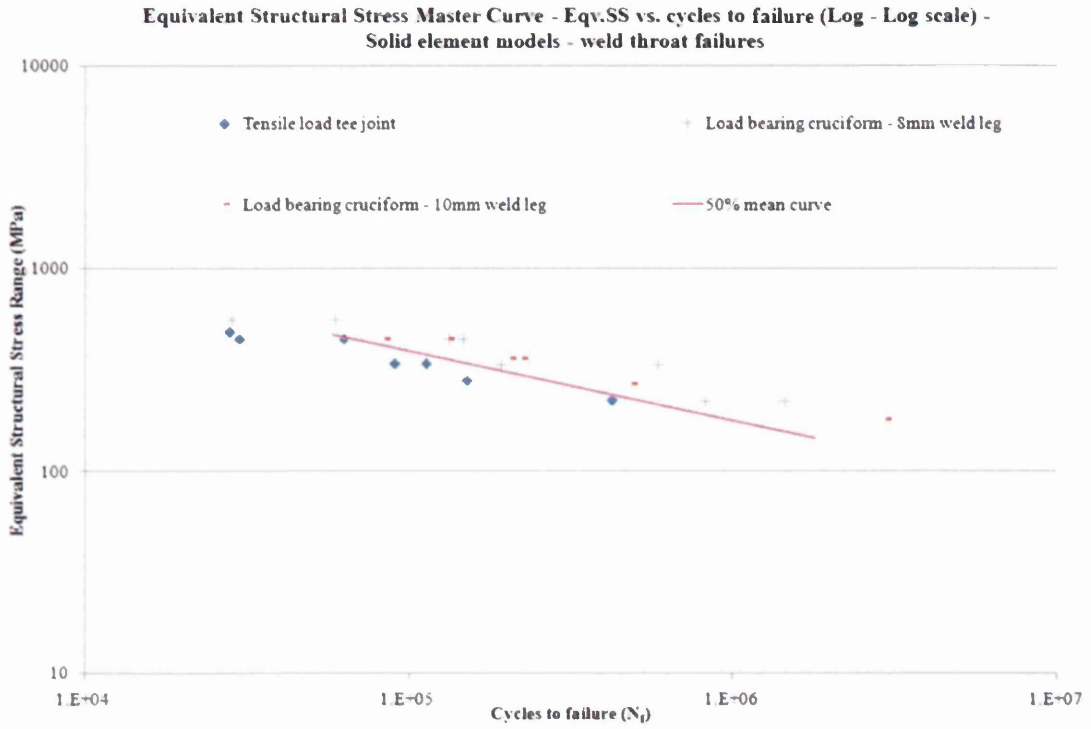

Figure 240: Equivalent structural stress master curve – Weld throat failures

Displayed on the same axis in Figure 241 are both the weld toe and throat failure mode master curves generated.

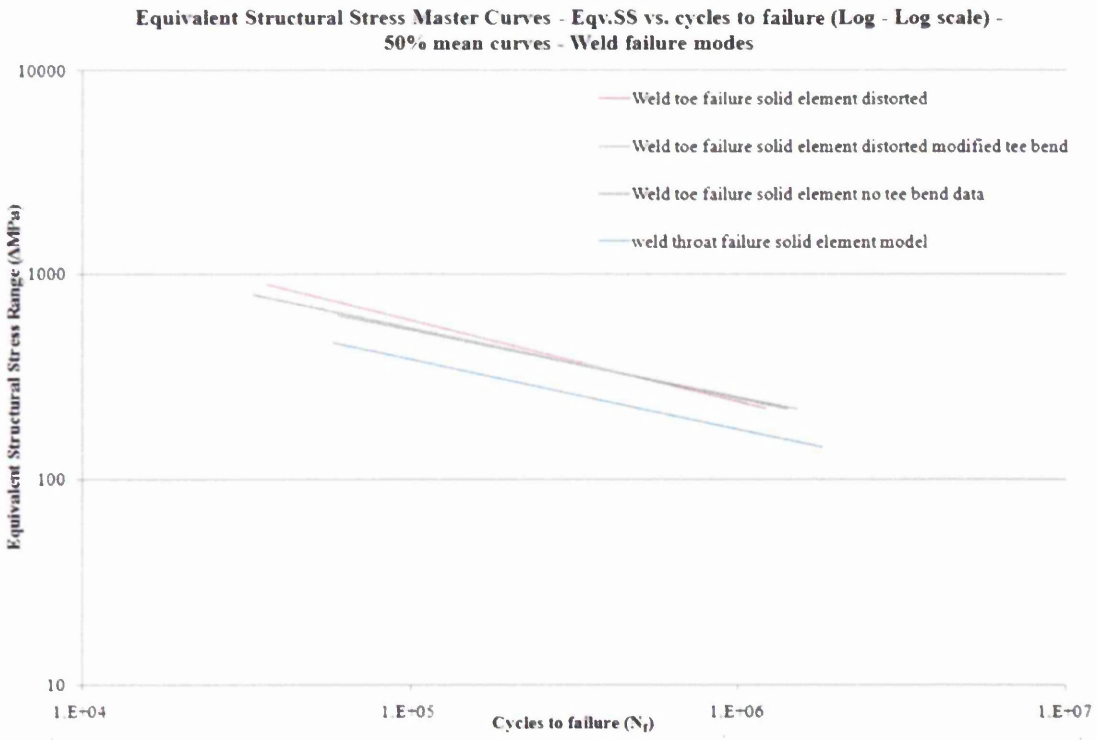

Figure 241: Weld failure mode master curves - 50% mean curves

All three modified weld toe failure curves are displayed along with the throat failure master curve. There is a significant difference between the failure mode toe and throat master curves. It shows there is a higher calculated fatigue strength for weld toe failures. Of the weld toe master curves generated, there is only a slight sensitivity shown. For the toe failure curves of conditions 2 and 3, (2 with tee data and modified I(r), and 3 excluding tee data) there is a very small, marginal difference seen between the curves. Positioning of the curves is almost directly on top of each another. This is only achieved when a modified I(r) value of 1.6 is used. As the master curve is the same with or without the bending load tee data, this provides very strong support that a different I(r) value should be used from the suggested 1.1-1.13.

4.6.5 Summary

In a similar way to the structural stress damage parameter, a number of different equivalent structural stress based master curves have been generated. The data for the range of master curve conditions will be taken forward for fatigue life prediction such as that based on solid element distorted models displayed in Figure 242.

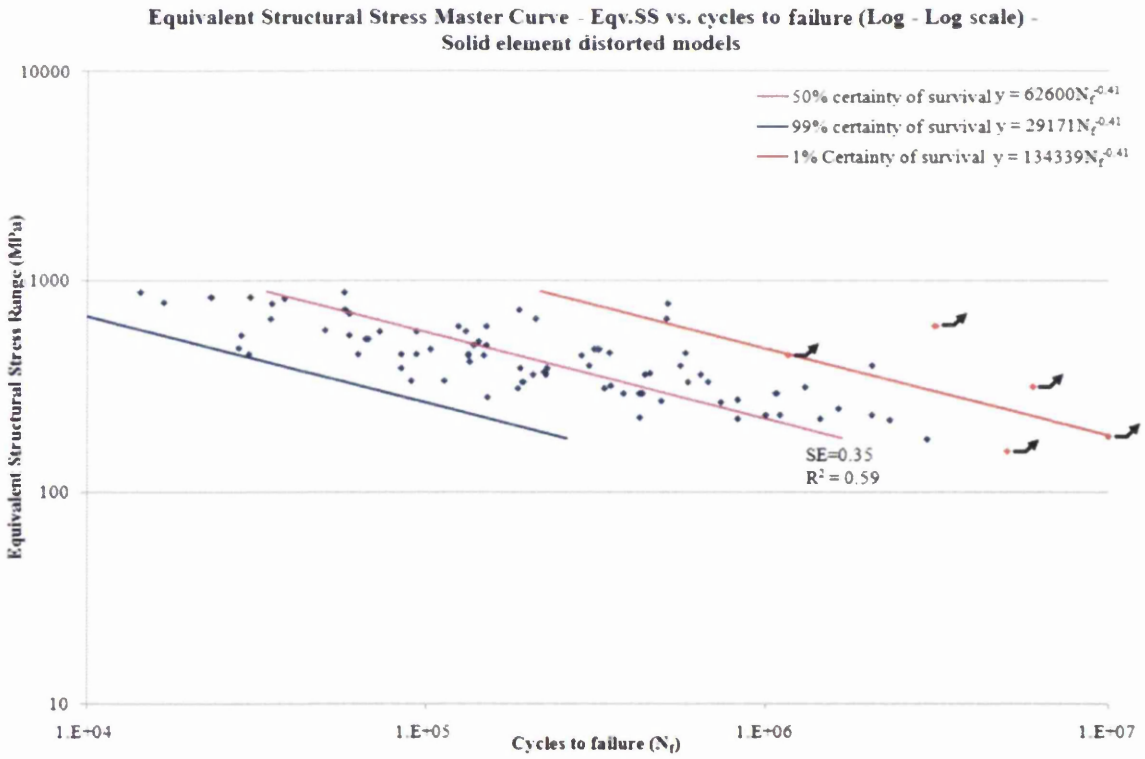

Figure 242: Master S-n Curve - Equivalent structural stress against Cycles to failure (Log-Log scale) – Solid element distorted models (bend tee I(r)(1/m) value = 1.13)

Also displayed on the plotted graphs is the 50% mean curve and 99% certainty of survival curve. The range of master curves generated are compared in Figure 243 and listed below.

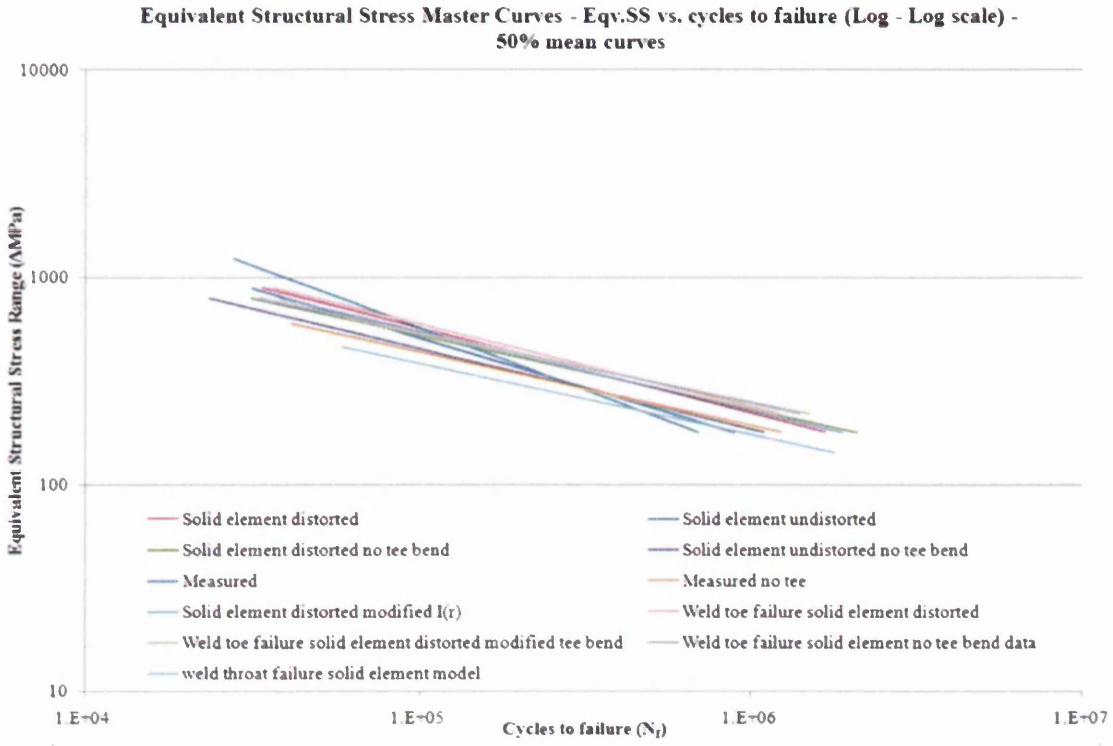

Figure 243: Comparison of structural stress master curves generated – All 50% mean curves

As per the structural stress master curves, there is some variation when comparing all of the equivalent structural stress curves. Given the range of parameters and variables present, this is expected. The curves that are considered for a fatigue life prediction analysis are based on a number of different calculation parameters;

Solid element, un-distorted geometry models;
Solid element, distorted geometry models;
Measurement based data;
Solid element, un-distorted geometry models - excluding the bending load tee data;
Solid element, distorted geometry models – excluding the bending load tee data;
Measurement based - excluding the bending load tee data;
Solid element, distorted geometry models – with modified I(r) value 1.6;
Weld toe failures;
Weld toe failures - bending load tee data modified I(r) value 1.6;
Weld toe failures - excluding the bending load tee data;
Weld throat failures.

The master S-N curve fatigue curves will be required for input into the weld fatigue life prediction analysis in the following chapter and a decision made on the 'correct' curve depending on the accuracy of results.

4.7 Yellow Goods Test Component

4.7.1 Component fatigue testing

The test component shown in Figure 50 was subjected to load-controlled fatigue testing to determine its structural performance. A ram applied a tensile load through a 45mm diameter pin into the welded boss lugs in the attachment plates. The base plate was restrained 25mm away from the fillet weld across the length of the component and bolted with 40mm wide restraining bars and M24 cap screws. The restraint bars were clamped to the test fixture plate connected to a base that was secured to the guttering in the test bed floor as shown in Figure 244.

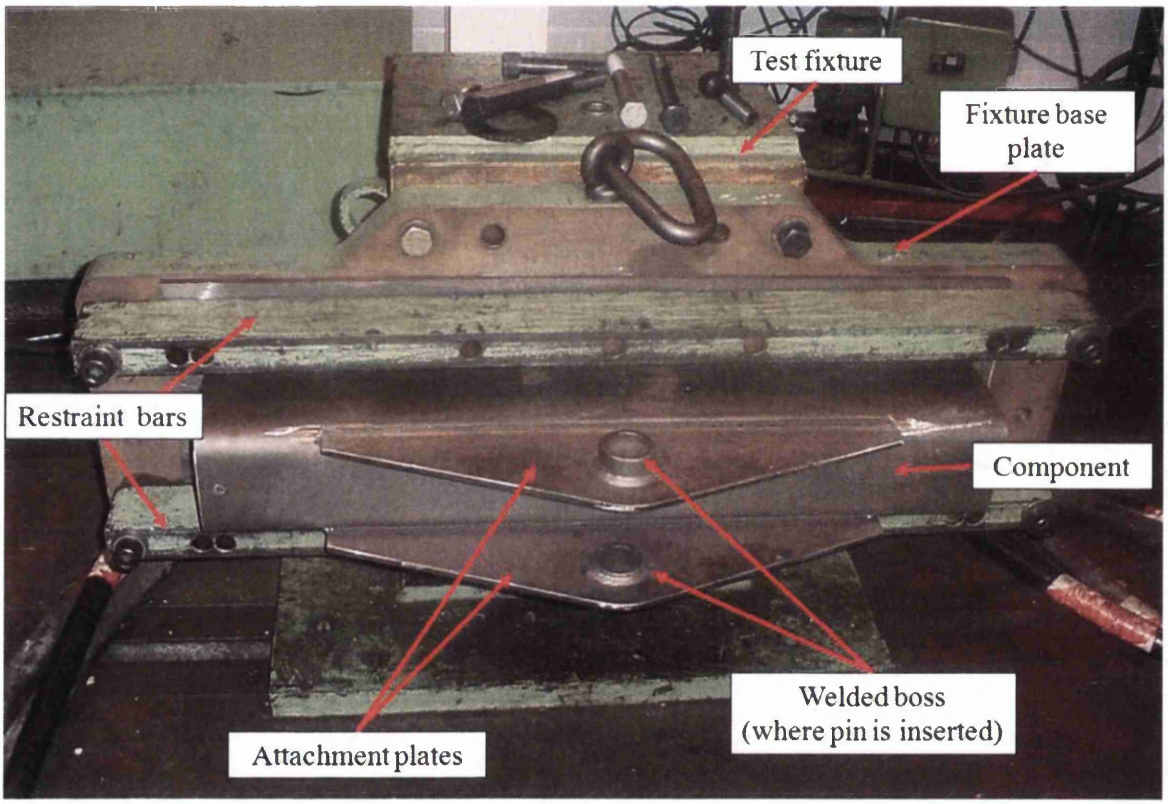

Figure 244: Test component - fatigue test fixture

The welded areas of the component were painted yellow to allow easier crack identification. A 120kN hydraulic ram was available for use initially and completed 2,000,000 cycles on test sample 1 but was later removed and replaced with a larger 300kN ram for the remainder of the test, Figure 248. A higher load than 120kN was required but the ram was not initially available. Electrical resistance strain gauges were attached to the test component to record deformation under loading. Strain gauge readings were recorded under both static and cyclic

loading regimes. The recording procedure was implemented for both the 120kN and 300kN hydraulic rams.

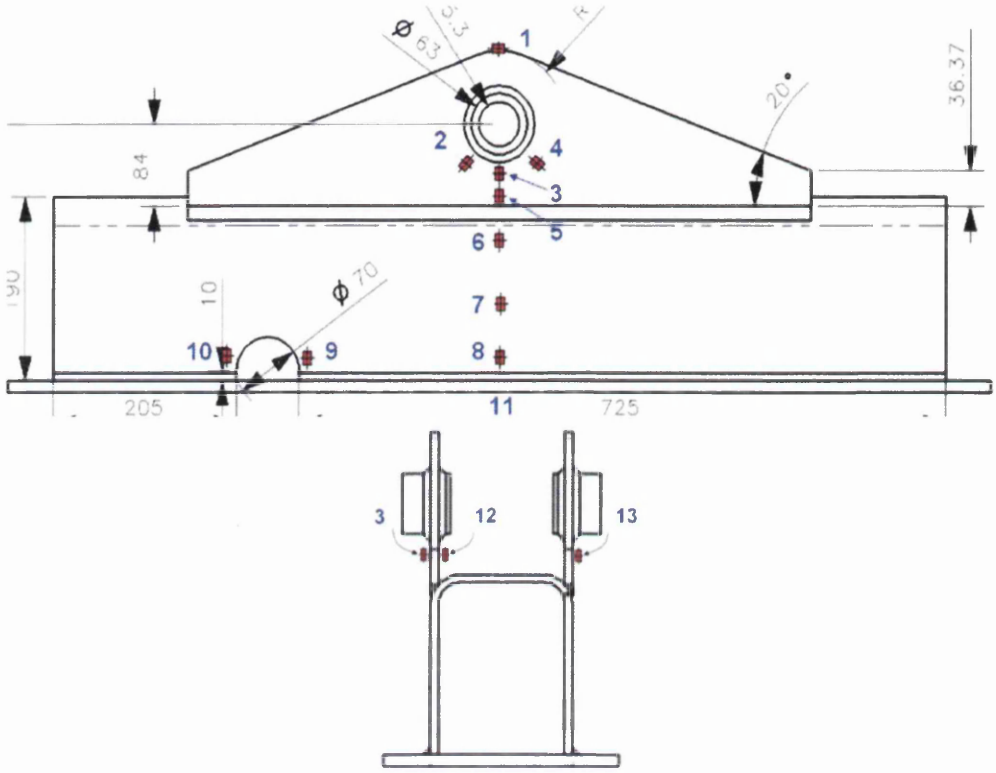

Figure 245: Test component sample 1 - strain gauge positions

The gauge positions in Figure 245 are defined as:

1. Top edge of the LHS attachment plate – centre of the component
2. Welded boss LHS 45 degrees to horizontal centre line – 10mm from weld toe
3. Welded boss horizontal centre line – 10mm from weld toe
4. Welded boss RHS 45 degrees to horizontal centre line – 10mm from weld toe
5. 10 mm from middle weld run – top toe
6. 10 mm from middle weld run – bottom toe
7. Centre line of U-plate pressing
8. 10 mm from bottom weld run – centre line
9. RHS of mouse hole feature – 10mm from weld toe
10. LHS of mouse hole feature – 10mm from weld toe
11. Base plate centre line – 10mm from weld toe
12. Opposite gauge 3 – on the same attachment plate
13. Mirror of gauge 3 – on other attachment plate

The static strain gauge recordings are recorded in Figure 246 for the gauge locations at 3, 10, 12 and 13. The micro-strain values (με) are plotted on the y-axis against the load (kN) on the x-axis.

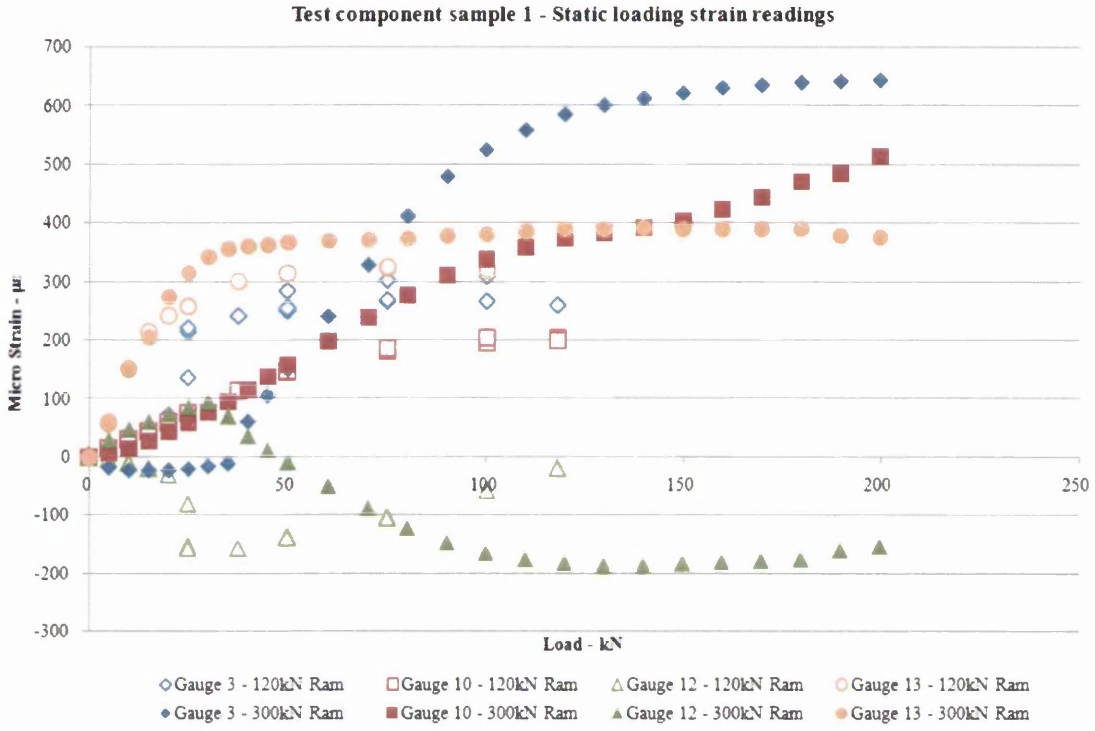

Figure 246: Test component sample 1 - static strain gauge readings

Sample 1 strain gauge readings (Δμε) under cyclical loading are shown below in Figure 247.

		Micro strain range Δμε	
	Test component cyclic loading	95kN load range	195kN load range
1	top edge on attachment	323	610
2	45° at boss LHS	130	276
3	10mm from boss toe - CL	121	512
4	45° at boss RHS	191	449
5	10mm from middle weld top toe	83	112
6	10mm from middle weld lower toe	30	65
7	centre line of U-plate pressing	44	112
8	10mm from bottom weld toe CL	108	273
9	RHS of Hole	78	183
10	LHS of hole	214	345
11	CL base plate	33	-
12	opposite gauge 3 (same attachment plate)	140	406
13	mirror of gauge 3 (other attachment plate)	113	110

Figure 247: Test component sample 1 - cyclical strain gauge readings

It is evident that some of the strain gauge readings recorded in Figure 246 are non-linear. For example, gauge 10 with the 120kN ram is linear until approximately 150με and the strain measurement decreases and levels off at approximately 100kN. Gauge 10 with the 300kN ram is linear until approximately 300με and the recorded strain decreases and begins to level off thereafter. It is possible the non-linear load versus recorded strains, are a result of geometric or pin to component contact non-linearity. The strain gauge readings will be use for comparison with the FE models later on, chapter 4.7.3.

Sample 1 initially underwent 2,000,000 cycles using the smaller hydraulic ram with a sinusoidal 95kN load range applied at 1 Hertz. On changing to the larger 300kN, the test resumed under a 195kN sinusoidal load range tested at 2 Hertz, Figure 248. Sample 1 completed a further 841,789 cycles at 195kN before a 20mm crack appeared (the defined failure criterion) at the base of the outside weld toe on the boss to the weld attachment lugs. The crack appeared on the same side as the mouse hole feature.

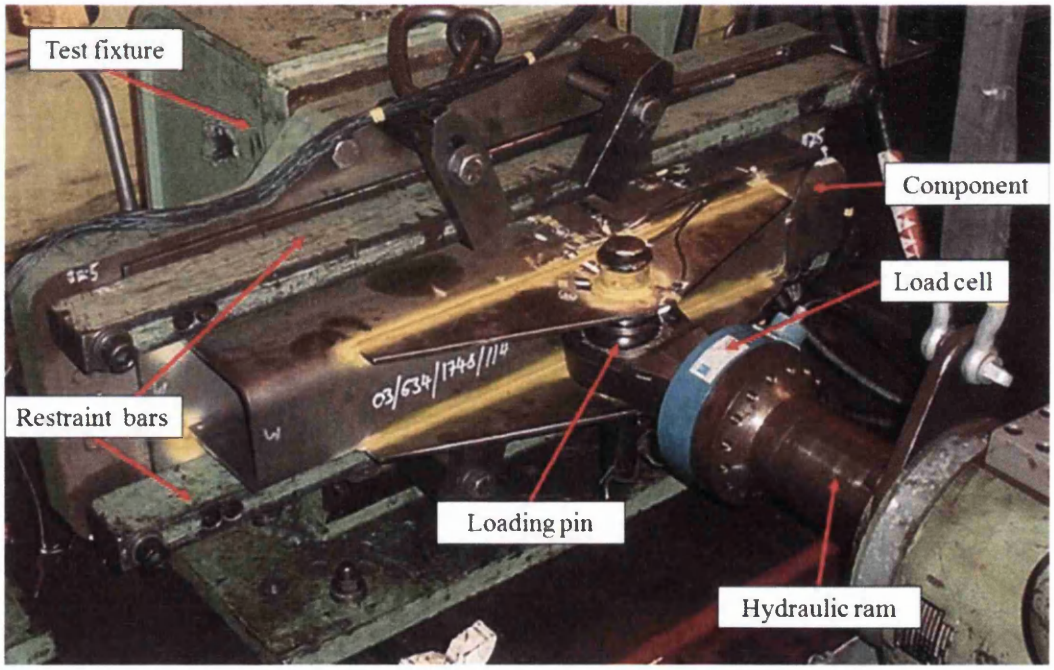

Figure 248: Component testing - 300kN ram in-situ

The test continued until the crack size was considered significant enough to compromise the integrity and safety of the facility. The sample was removed at 1,052,840 cycles. The crack location is show below in Figure 249 at the base of the outside boss weld toe, in the centre region, highlighted by the red arrow.

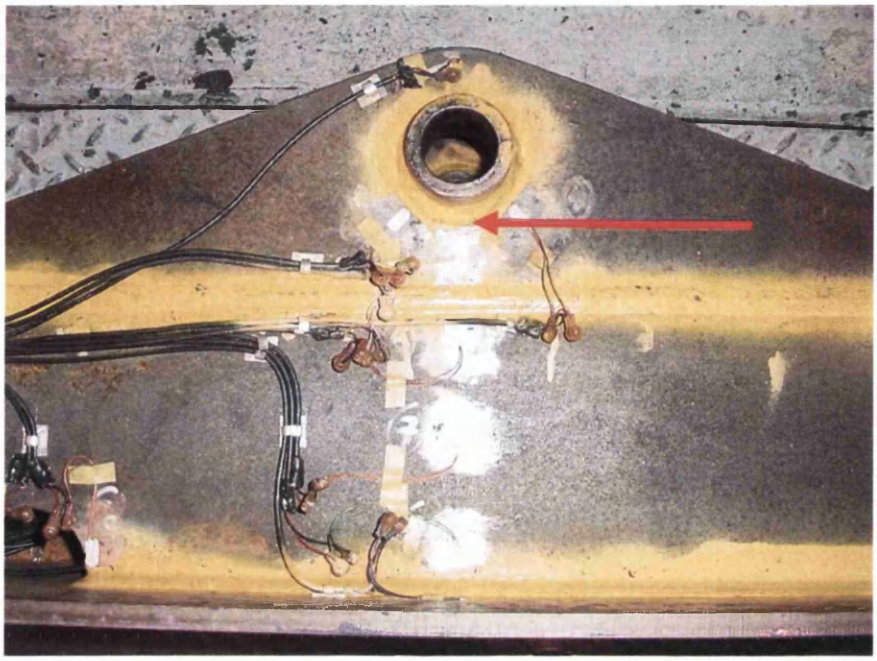

Figure 249: Test component sample 1 crack location - base of outside weld toe

A close up image of the crack is shown below in Figure 250. The lug plate containing the weld failure was cut and sectioned to reveal the fatigue fracture surface, Figure 251.

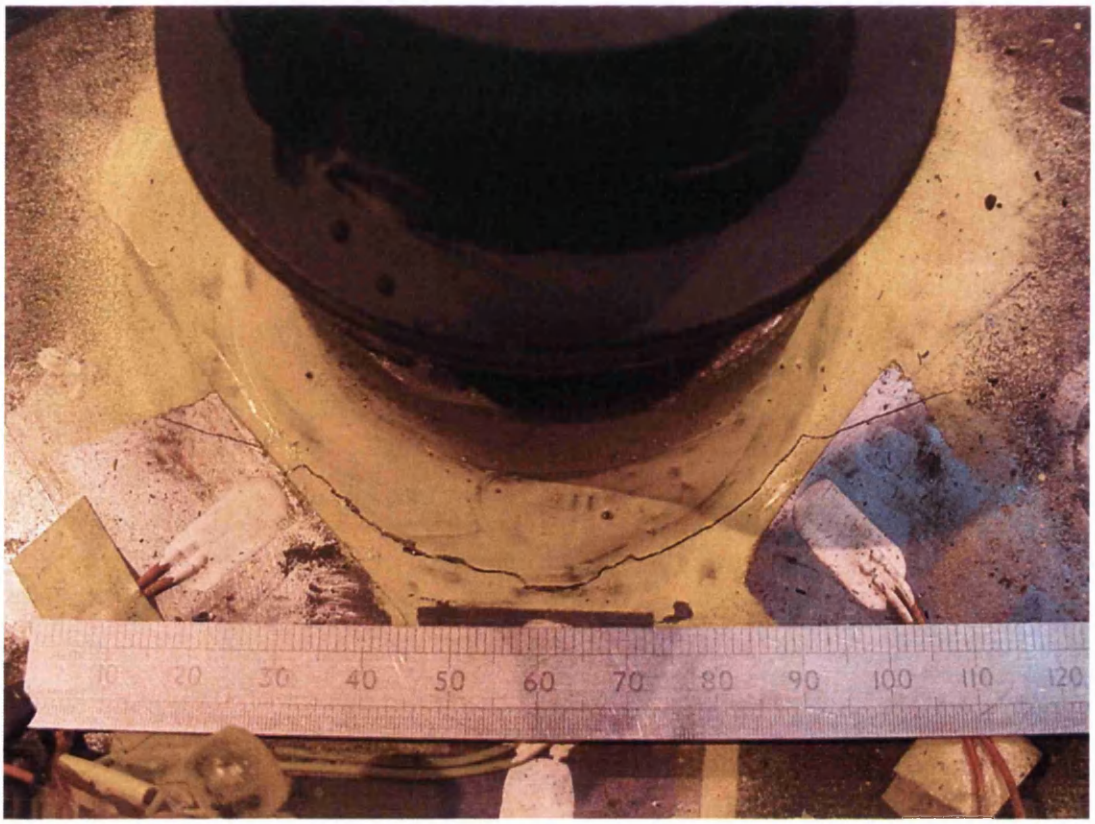

Figure 250: Test component sample 1 - boss outside weld toe failure upon removal at 1,052,840 cycles

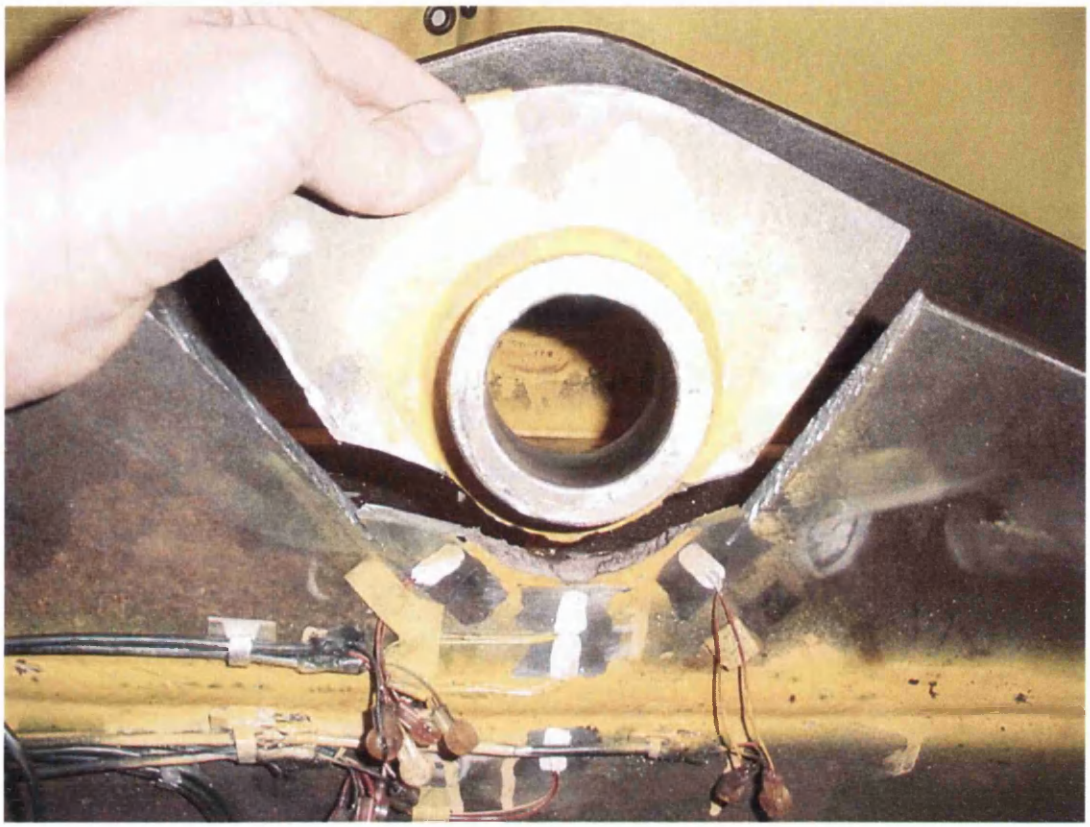

Figure 251: Test component sample 1 - sectioned attachment lug of boss weld toe failure

A close up of the fracture surface is shown in Figure 252 and Figure 253. A number of fatigue crack initiation points can be seen across the weld toe. The prominent initiation sites are highlight by the red arrow markers. There is also an indication of sulphur banding in the middle of the parent plate material, towards the left hand side of the picture.

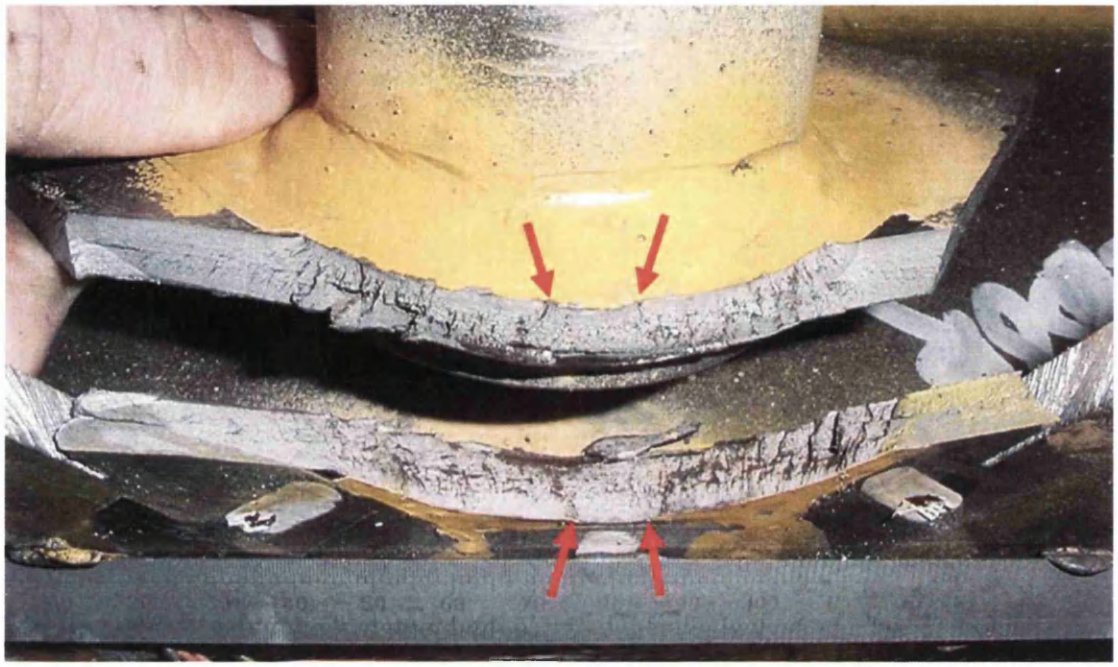

Figure 252: Test component sample 1 - boss weld toe failure fracture surface 1

Figure 253: Test component sample 1 - boss weld toe failure fracture surface 2 - fatigue crack initiation sites

In total, 4 test components were manufactured and all were tested in the same configuration. Due to availability of the test apparatus, a requirement to complete the cycles in a faster time and attain higher loads, sample numbers 2, 3 and 4 were tested in the twin column loading frame shown in Figure 254.

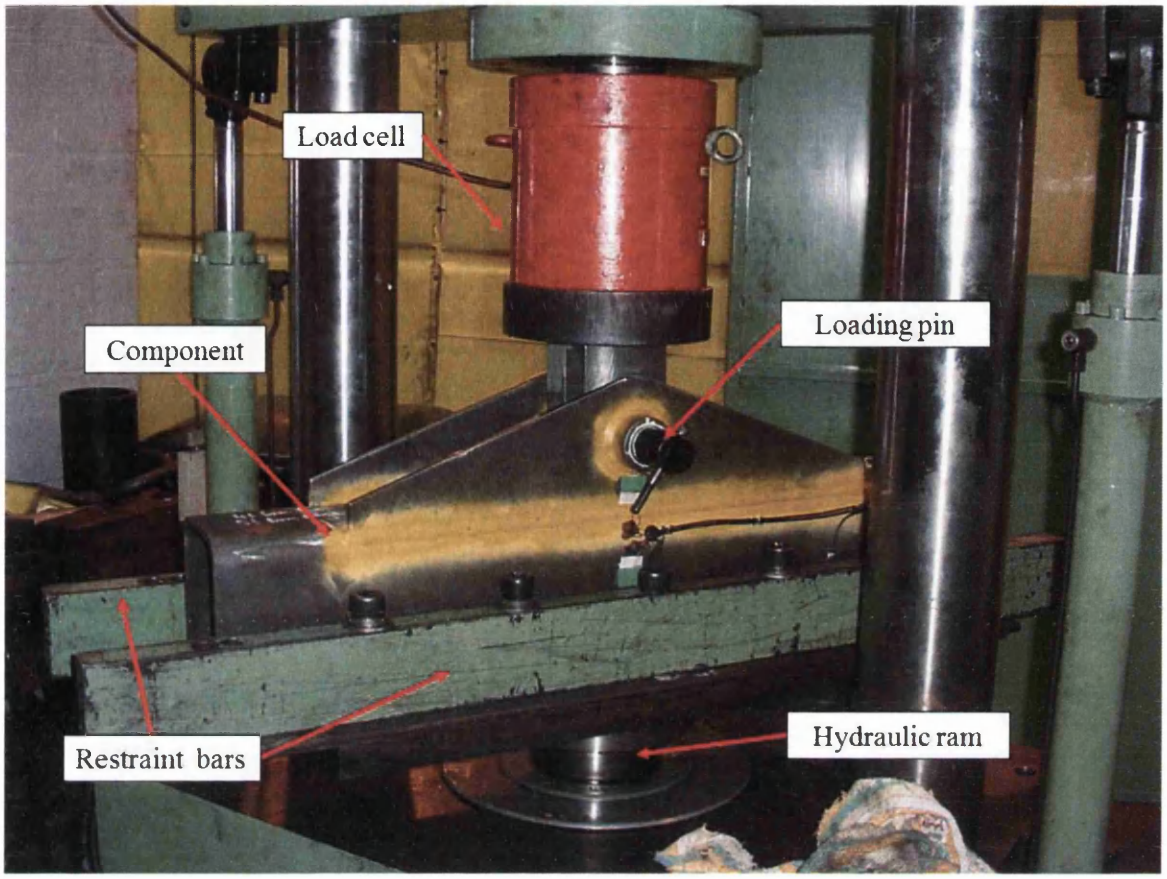

Figure 254: Test component sample 2 - twin column loading frame test set-up

Samples 2, 3 and 4 did not fail at the intended weld crack initiation feature. All three samples failed from fatigue crack initiation through the welded boss tube as shown in Figure 255 and highlighted by the scribe (the vertical cut was made, post-testing, to enable removal of the section and analyse the fatigue surface fracture area). Samples 2, 3 and 4 failed at 1,865,859 cycles, 136,320 cycles and 936,829 cycles respectively. The fatigue crack location on the test components was not suitable for validation of the type of analysis undertaken (weld fatigue life prediction). In a further attempt to obtain weld failures for fatigue life prediction comparison, the failed test components were modified to accept a direct loading method.

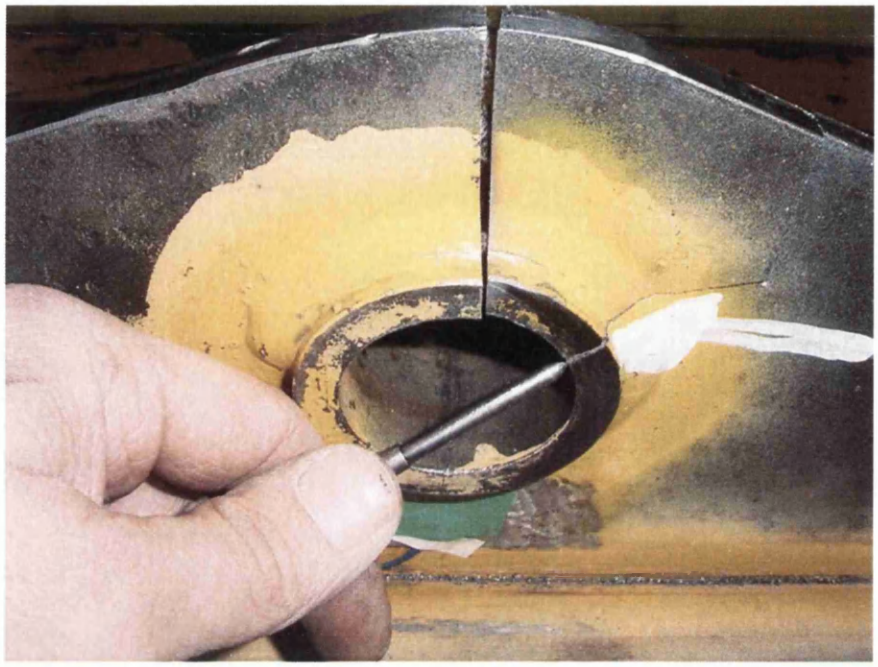

Figure 255: Test component sample 2 - fatigue failure through boss tube

The welded attachment plates on the test component were removed and holes manufactured in the top of the U-pressed section to allow direct bolting to the loading frame fixture, Figure 256.

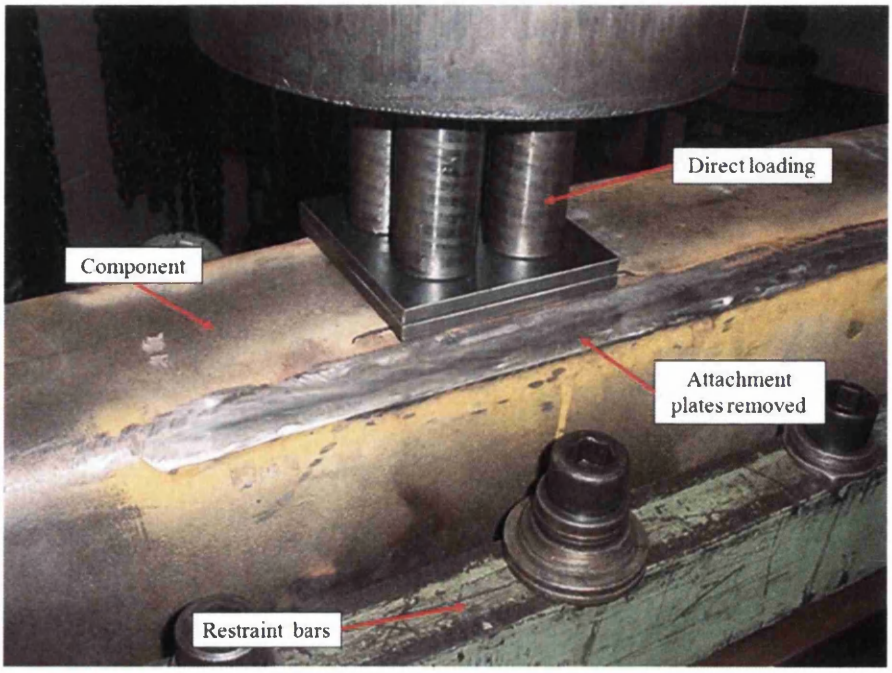

Figure 256: Test component sample 3 - direct loading to pressed U-plate

The direct loading test set-up resulted in a fatigue crack occurring on the top of the U-plate top-hat section, Figure 257. This again is not an idealised failure mode for the weld fatigue life prediction method.

Figure 257: Test component sample 3 - direct load test set-up failure

Several attempts were made to obtain additional weld fatigue failures. Ultimately, there is only one single weld fatigue failure available for comparison and validation of the structural stress method. This is a significant limitation to the quality and confidence in the validation of the structural stress method. It was not possible to achieve any further weld fatigue failures using new or alternative components and test fixtures due to the project timescale.

4.7.2 FE Stress analysis

A finite element model of the test component was generated using solid brick elements as shown in Figure 258. The model was generated based on the as-designed test component assuming no distortion occurred during welding and cooling. The model portrays the component as having symmetric and perfectly vertical attachment plates and U-pressing sidewalls. Only a solid element mesh was considered, as there is some cause for concern

when generating welded geometry using shell elements. The accurate representation of thick plate welded sections seriously tests the limitations of the shell element and its capabilities. The welded coupons in chapter 4.3 show good correlation between solid and shell element models for most of the results. However, there are some areas that can give erroneous results. Considering modern day computing power and advanced modelling software, there is little or no benefit in creating a mesh employing shell elements, especially when a sacrifice in accuracy is compromised.

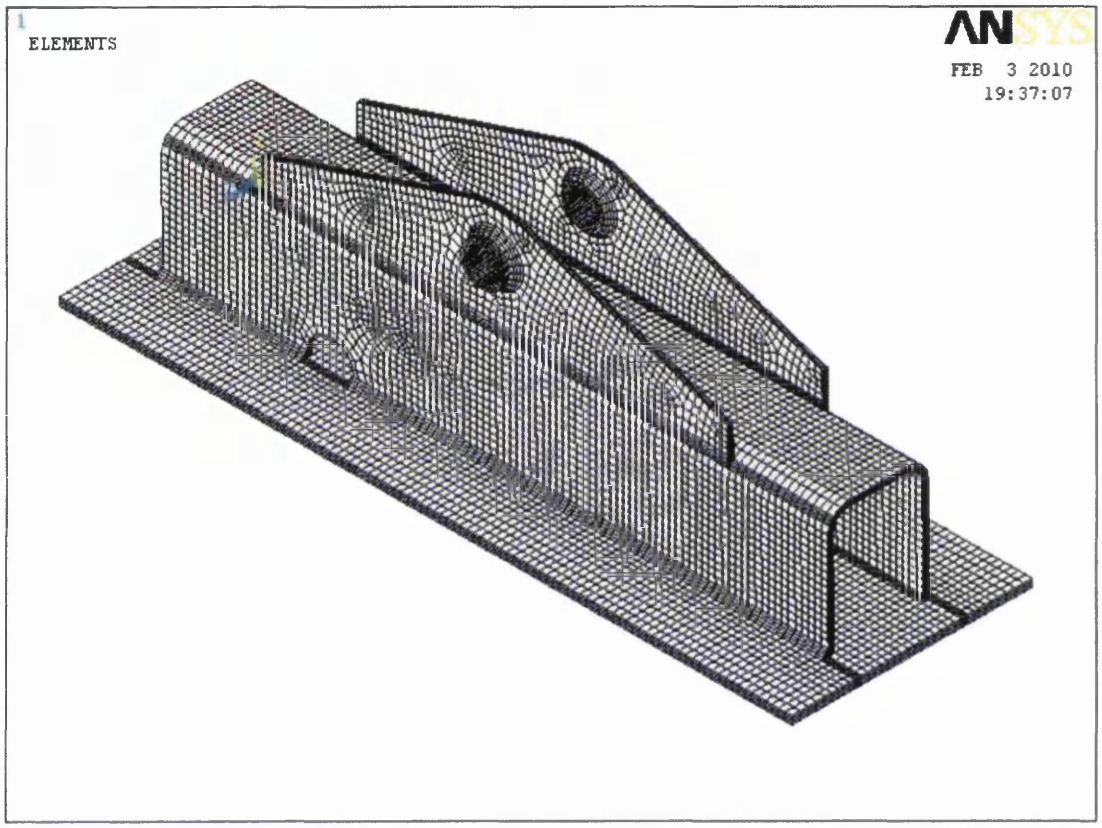

Figure 258: FE-model 1 - undistorted test component

To replicate the test fixtures and loading configuration experienced by the test component, boundary conditions consisting of fixed translations, rotations and forces were applied, Figure 259. Fixed restraints were used on the top surface of the base plate to represent the restraining clamping bars. Beam element models were used to represent the loading between the hydraulic loading ram and the bosses on the test component. The pin beam elements were connected to the test component solid elements using beam elements. The elements were only created where the pin and component came into contact, on the upper circumference area inside the boss, Figure 260. This was done to avoid over constraining the lower boss inside circumference and area, where there was no contact between pin and component. Fixed

restraints were applied to the lower inside edge of the boss to replicate the packing blocks used between the ram eye end and the component, Figure 261. A 200kN load was applied to the pin beam elements across the width of the ram eye end.

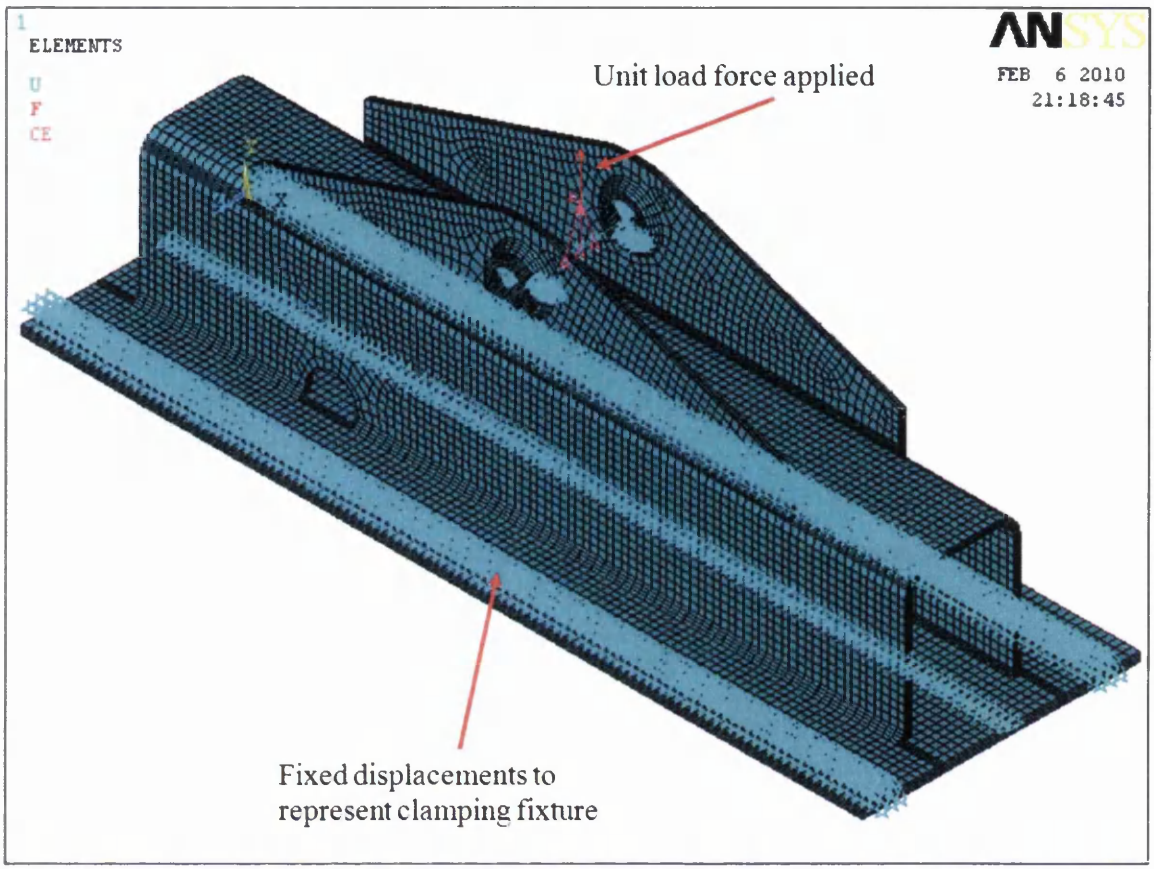

Figure 259: FE-model 1 test component – test set-up representation

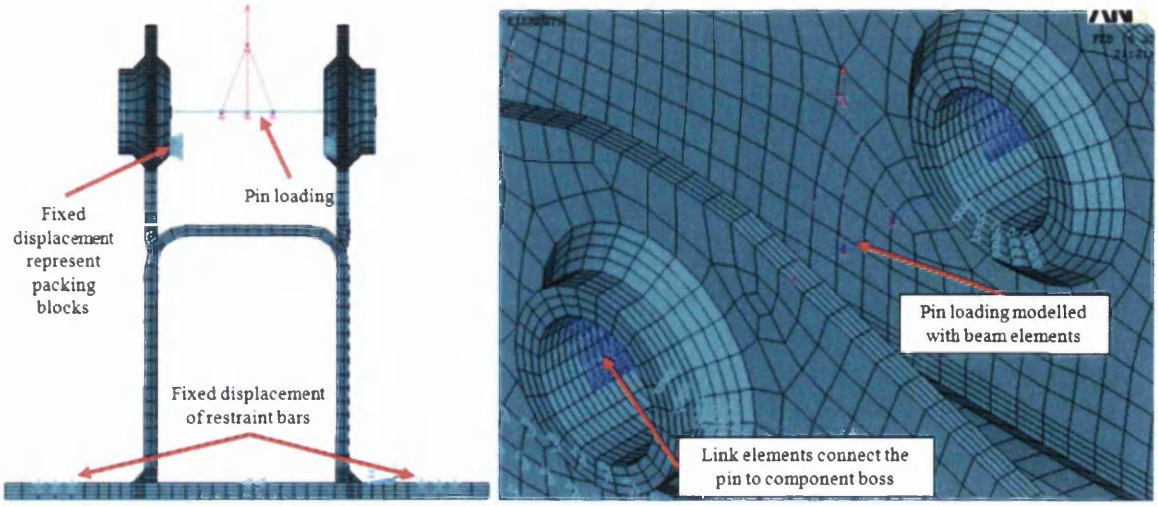

Figure 260: FE-model 1 test component - cross section and welded boss area

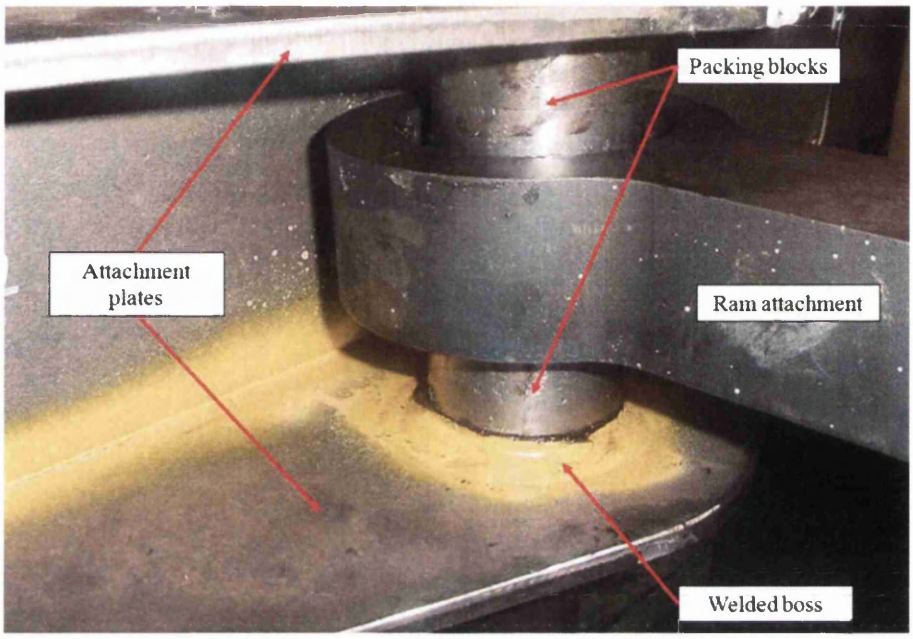

Figure 261: Test component fixture set-up - packing blocks between component and ram

An FE model solution was obtained for the test component analysis using both a full and reduced integration method. A linear 8-noded brick element was used for both solution types. The deformation results of the model 1 reduced integration solution are shown in Figure 262.

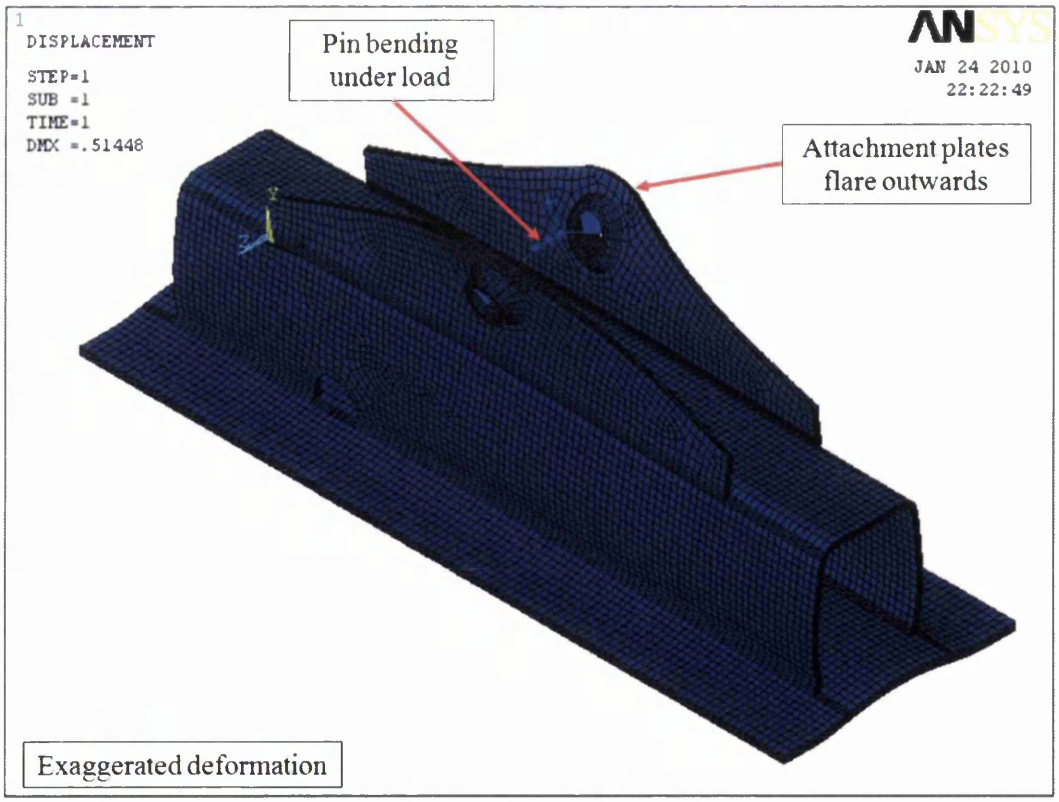

Figure 262: FE-model 1 - Displacement results reduced integration

A cross-section of the deformed model is shown in Figure 263. The deformation results in Figure 262 and Figure 263 are multiplied by 100 to allow easier interpretation of the loading path and deformation.

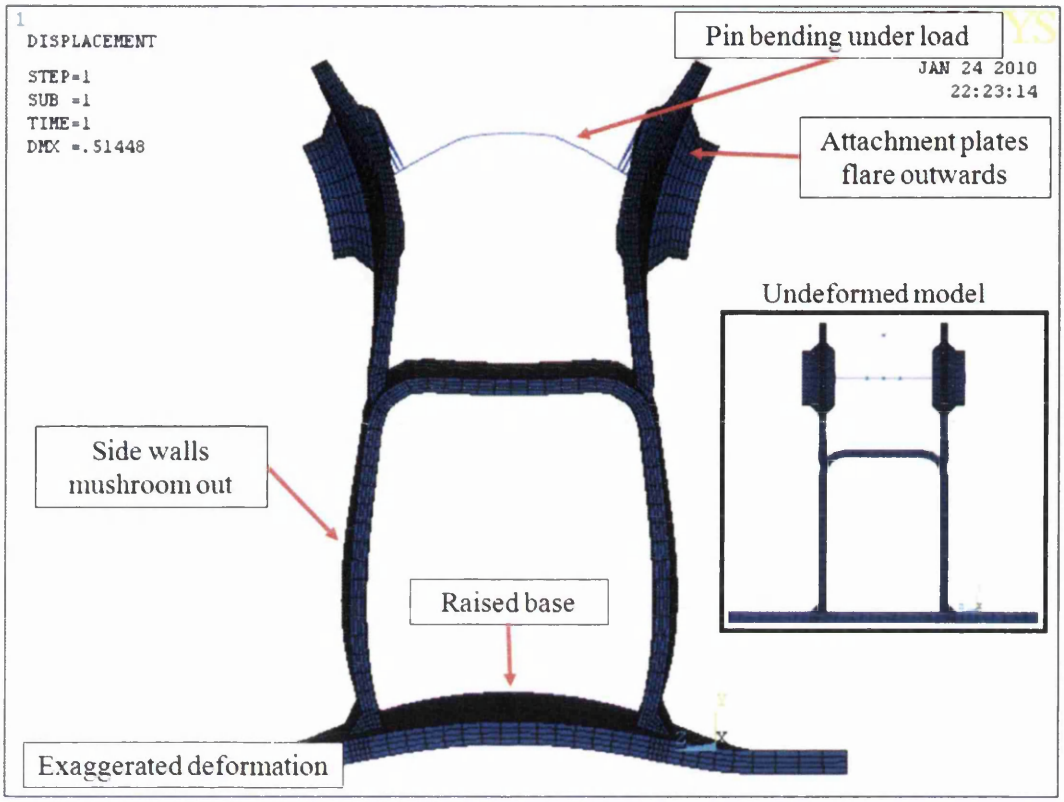

Figure 263: FE-model 1 - Displacement results reduced integration cross section

Contour plots of the calculated maximum principal stresses for test component model 1 are shown in Figure 264 and Figure 265. It is evident that due to the pin loading and bending, the attachment plate lugs are bent outwards and undergo high tensile stresses on the inside of the attachment plates. The loading method creates high stresses approximately 120MPa around the welded boss feature. The load is transferred through the attachment plate and down the sidewalls of the pressed top hat section. High stresses of 150MPa are seen at the upper edge and centre of the attachment and directly above the welded boss. A strain gauge positioned in the same area on the test component proved to be useful in confirming this result. The maximum stress in the model occurs on the inside of the boss tube at approximately 45 degrees to the vertical centre line of the component. This is similar to the failure location of samples 2, 3 and 4.

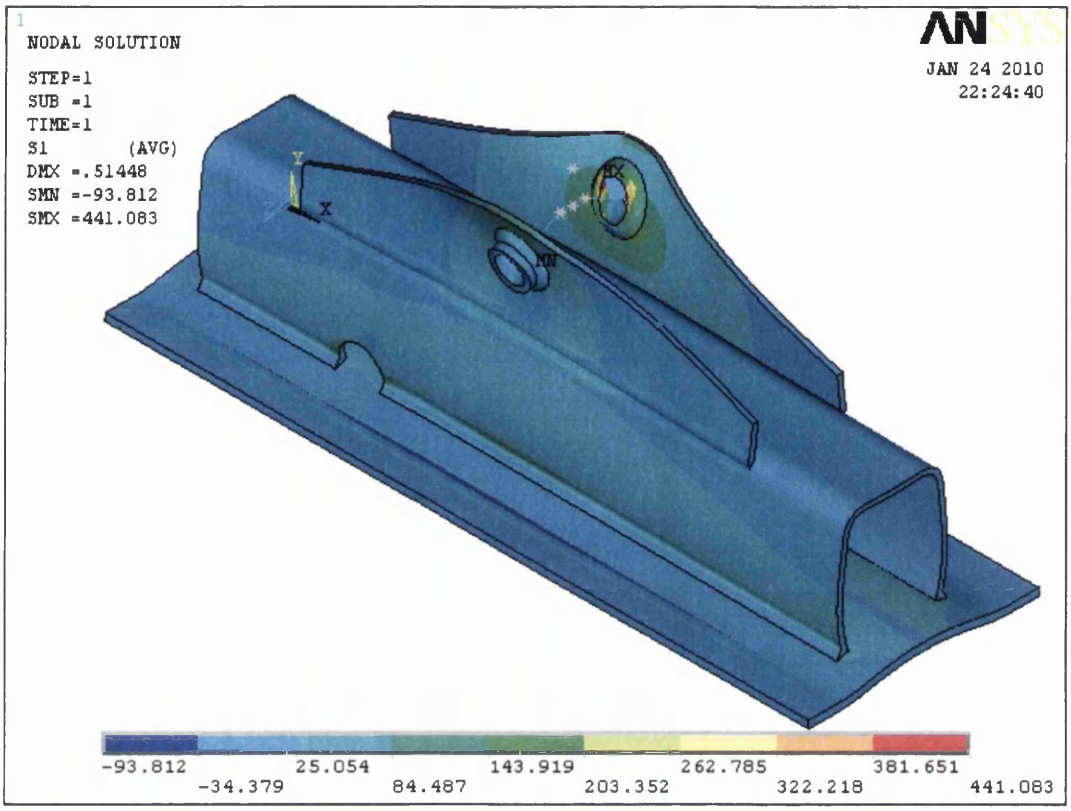

Figure 264: FE test component model 1 - maximum principal stress contour plot, (MPa)

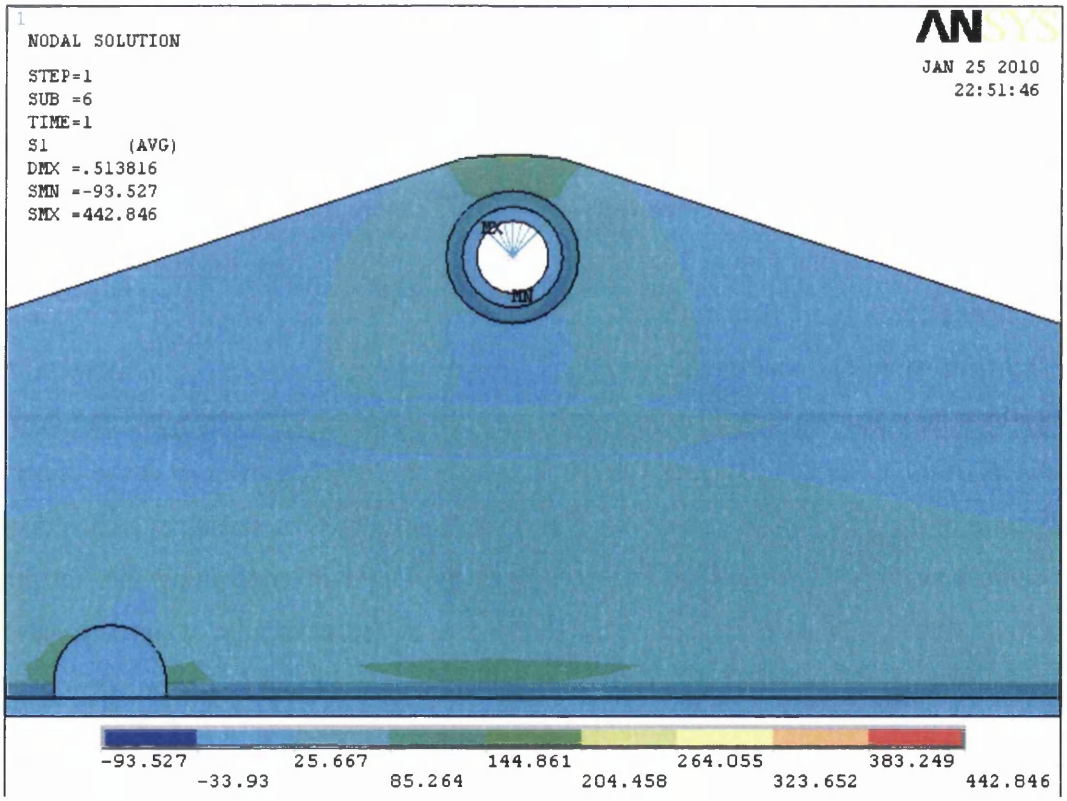

Figure 265: FE test component model 1 - maximum principal stress contour plot side view, (MPa)

There is a high stress contour in the centre of the component by the top hat to base plate fillet weld. Here most of the load is distributed into the test fixture and clamping arrangements, Figure 265. There are high, localised stresses at the end of the weld runs and plate edges on the left and right hand side of the mouse hole feature.

In order to improve the modelling of the component and test configuration, a second FE model was generated, Figure 266. The test component geometry created simulated the distortion levels achieved in the manufactured part. Exact values for each dimension could not be readily achieved in a timely and efficient manner. Rough estimates were made on the free standing component using a steel rule, set square and digital protractor. The measurements were confirmed when the component was in the test configuration. The levels of distortion (looking down the x-axis in Figure 266) were such that the sidewalls of the top-hat section and attachment plates were approximately 0.5 degree offset to the vertical centre line as shown in Figure 267.

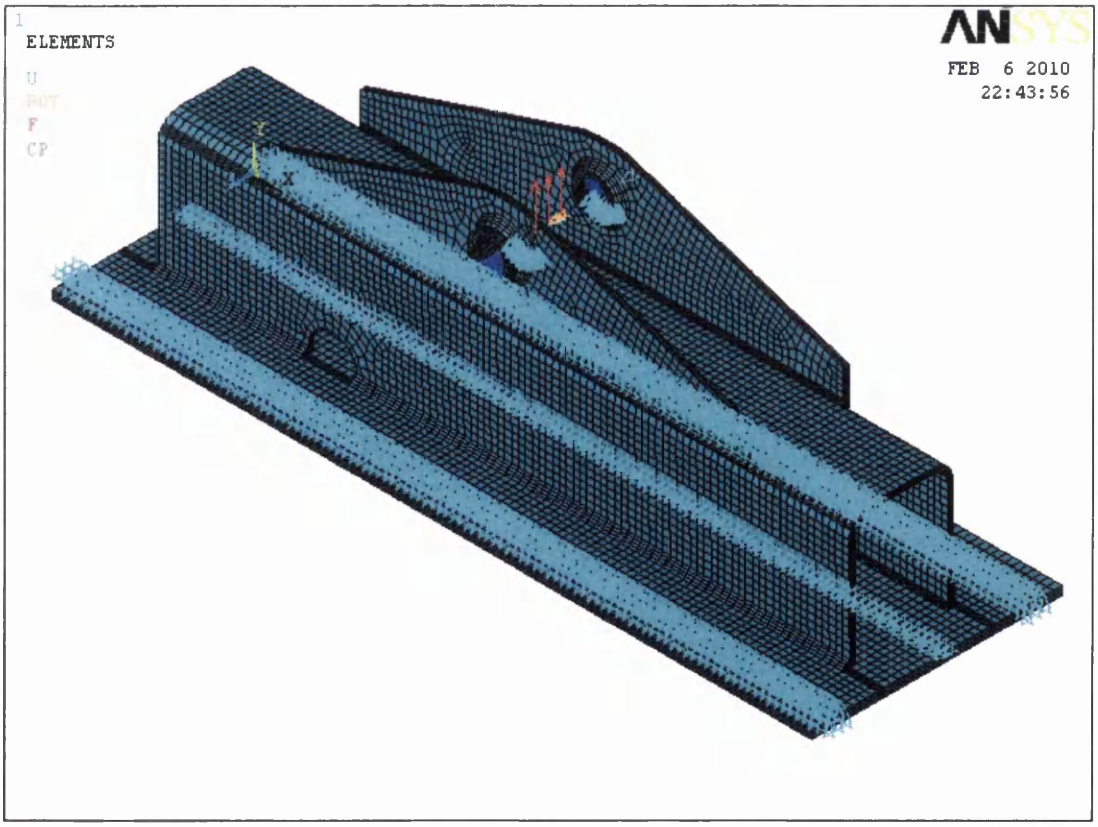

Figure 266: FE-model 2 distorted test component – test set-up representation

Fixed restraints were applied to the top surface of the base plate to represent the restraining clamping bars. Beam elements were used to represent the loading between the hydraulic loading ram and the bosses on the test component.

A 200kN load was applied to the pin beam elements across the width of the ram eye. When the component was installed in the test fixture, the hydraulic ram was off centre by approximately 8mm in the positive z-axis direction (i.e. towards the mouse hole side of the component), as shown in Figure 267.

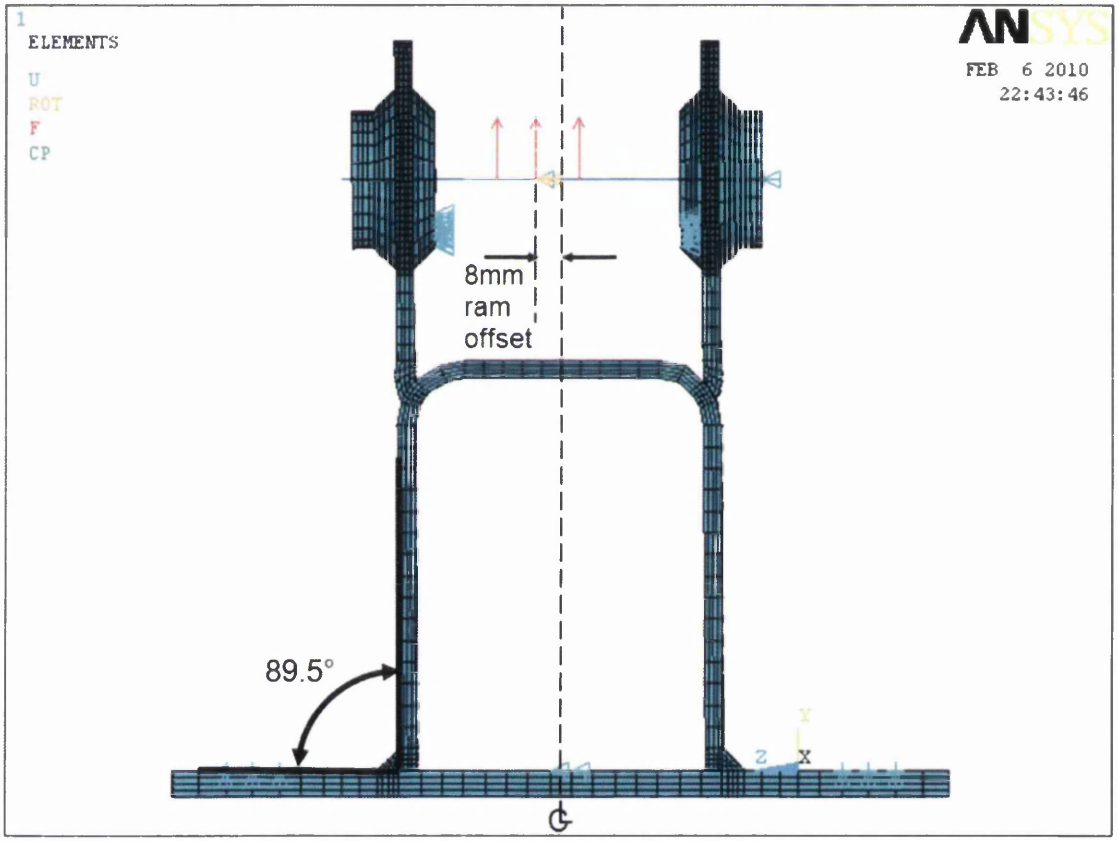

Figure 267: FE-model 2 distorted test component - 0.5 degree distortion

As in model 1, fixed restraints were used on the top surface of the base plate to represent the restraining clamping bars. Fixed restraints were applied to the lower inside edge of the boss to replicate the packing blocks used between the ram eye end and the component. In addition to the beam and link element used to represent the pin loading in the component bosses, lower link elements were added to the outer ends of the pin. This is because on bending the pin comes into contact with the lower surfaces of the boss and allows part of the load to be transferred. The elements above are deleted (any elements in tension are removed). A cross section of the elements used to represent the pin loading is shown in Figure 268. If a full

array of link elements were used to connect horizontal 'pin' the beam elements to the component, some would be in tension and the remainder in compression. In reality the vertical link elements will be transferring load to the component and hence should be in compression, i.e. pushing. If a full array of link elements were used the link elements would be both pushing and pulling on the component boss. Hence, any links in tension were removed from the model.

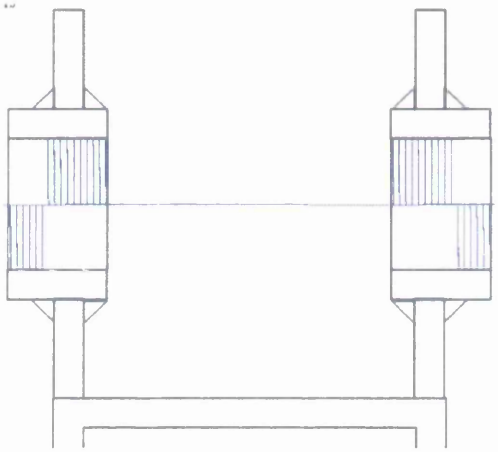

Figure 268: Cross-section of beam elements representing the loading pin

An FE solution was obtained for the distorted test component model using both full and reduced integration methods. A linear 8-noded brick element was used for both solution types. The deformation results of the model 2 reduced integration solution are shown in Figure 269.

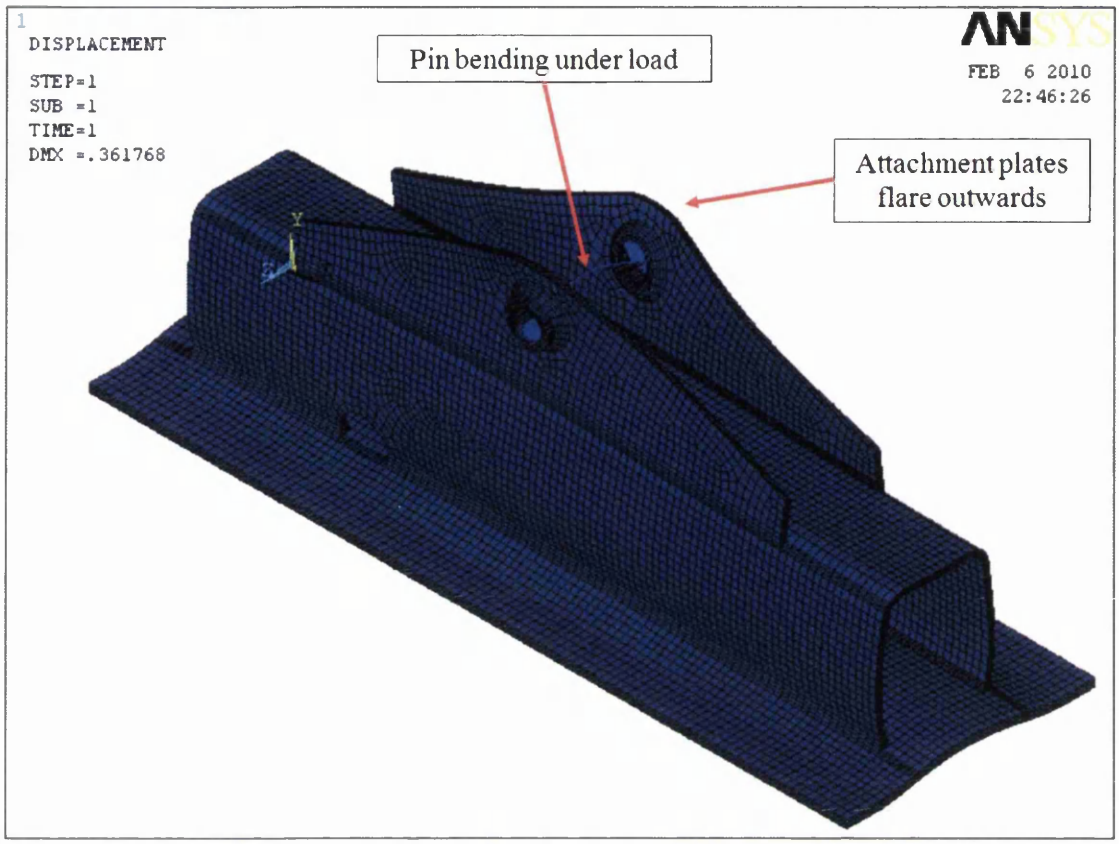

Figure 269: FE-model 2 distorted component - Displacement results reduced integration

There are similarities between the model 2 deformation results and model 1 symmetric results. There are differences, though, the most significant being that more load is passed through the boss and attachment plate on the left hand side, in the case of model 2 as shown in Figure 270. This is due to the offset load applied. The exaggerated displacement of the deformed model shows an increase in node and element translation in the y-axis. The offset loading creates a more tensile applied load and a reduced bending moment about the LHS welded boss.

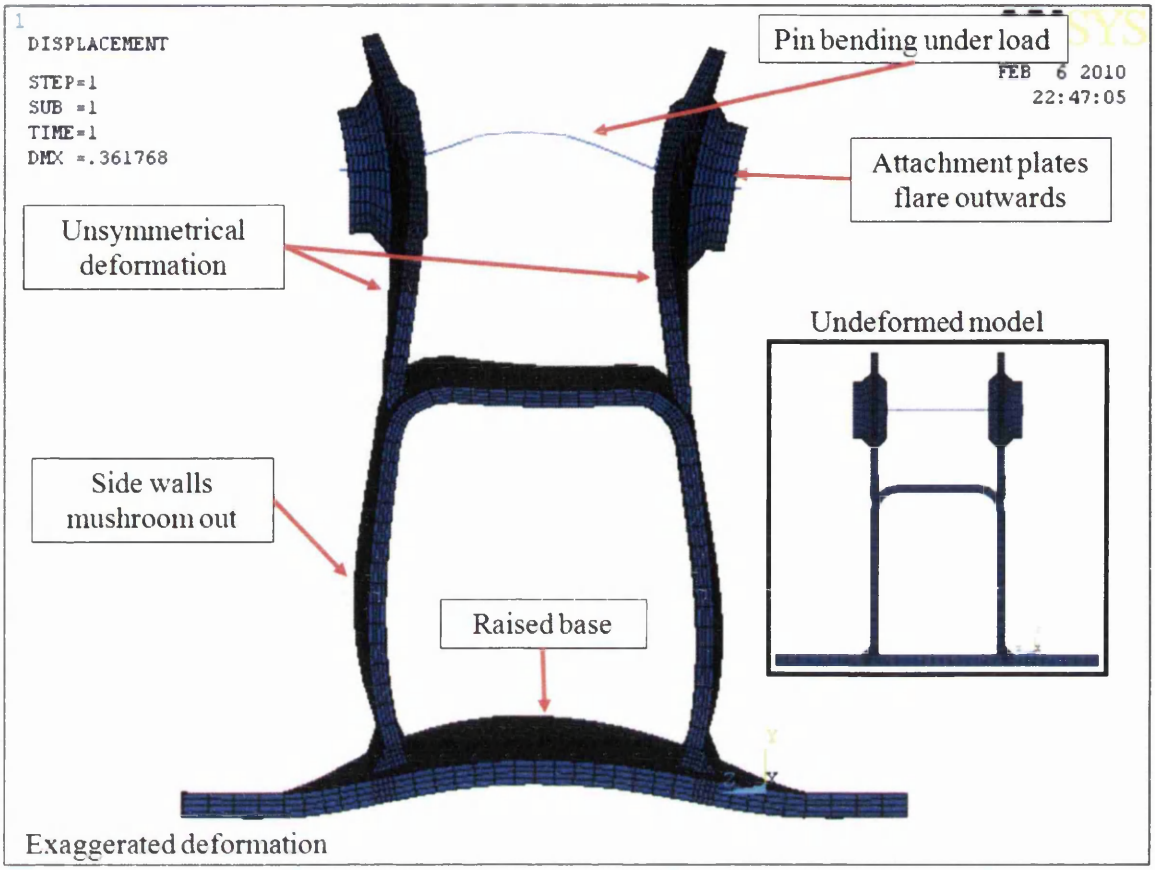

Figure 270: FE-model 2 distorted component- Displacement results reduced integration looking down the x-axis

A contour plot of the calculated maximum principal stresses for test component model 2 (distorted geometry) are shown in Figure 271 and Figure 272. As in the previous model, high stress contours of approximately 100MPa are evident at the weld toe in the centre of the top-hat section and at the plate edge on the left and right hand side of the mouse hole feature. A major difference between the model 1 and 2 solutions, is the stress distribution around the welded bosses and attachment plates. In model 1, the attachment plates experienced a high bending moment which displaced the plates outwards and away from each other. This created tensile stresses on the inside and compressive stresses at the outside below the welded boss. In contrast and most noticeably, model 2 displays a higher tensile stress on the outside of the welded attachment underneath the toe of the welded boss. This is shown in Figure 273.

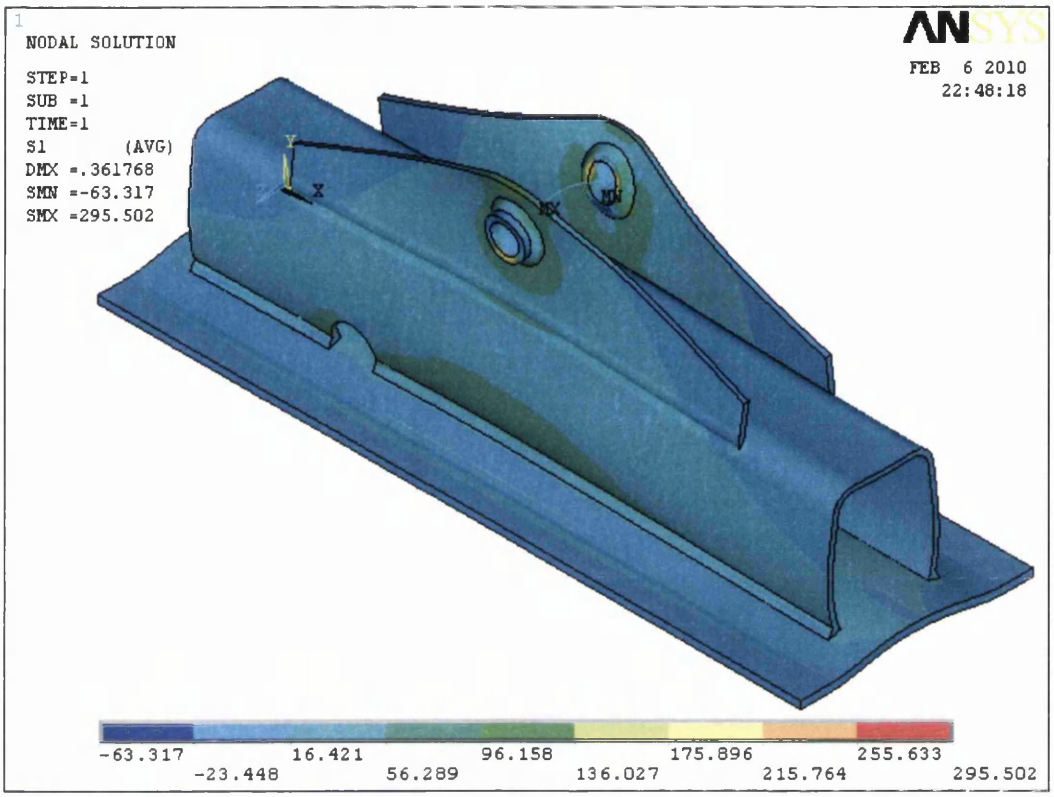

Figure 271: FE-model 2 distorted component - Maximum principal stress contour plot 1 (MPa)

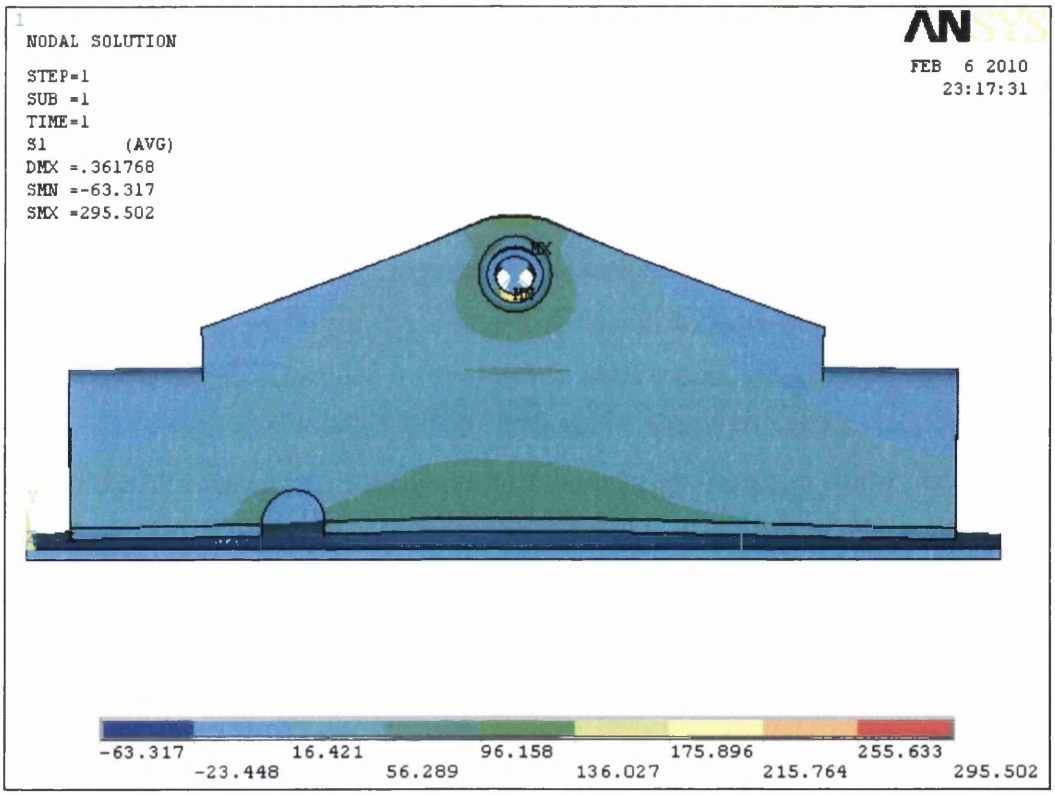

Figure 272: FE-model 2 distorted component - Maximum principal stress contour plot 2 (MPa)

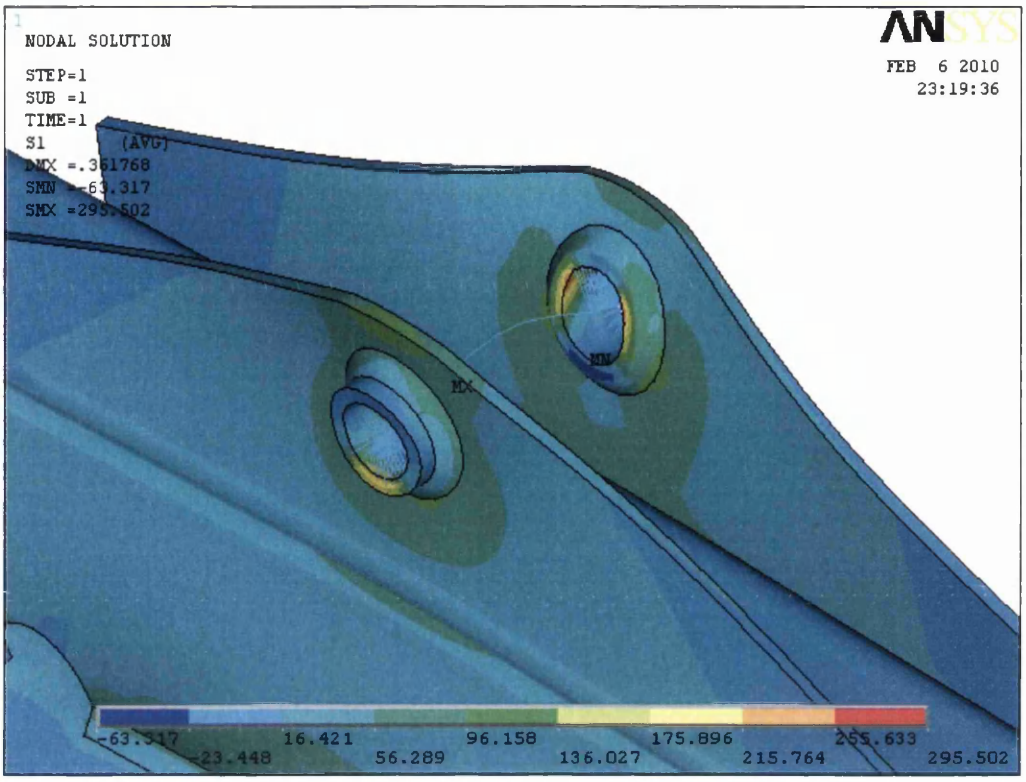

Figure 273: FE-model 2 distorted component - Maximum principal stress contour plot 3 (MPa)

4.7.3 Recorded strain readings vs. FE-model strains

To validate the accuracy of the test component analysis and model, virtual strain gauges were created with the use of a local coordinate system. Strain readings were obtained from the virtual strain gauge locations from the FE models. The FE strain gauge locations simulate those of the real test component gauge locations as shown in Figure 245.

		FEA micro strain (με) readings at 195kN	
	Pseudo component Model 1 - symmetric	Full integration	Reduced integration
1	top edge on attachment	637	571
2	45° at boss LHS	107	123
3	10mm from boss toe - CL	-13	-20
4	45° at boss RHS	281	306
5	10mm from middle weld top toe	130	112
6	10mm from middle weld lower toe	177	169
7	centre line of U-plate pressing	192	185
8	10mm from bottom weld toe CL	311	327
9	RHS of Hole	196	212
10	LHS of hole	343	377
12	opposite gauge 3 (same attachment plate)	448	394
13	mirror of gauge 3 (other attachment plate)	-12	-13

Figure 274: Test component model 1 – micro-strain (με) readings at virtual strain gauge location

The calculated static micro-strain (με) readings are shown in Figure 274 and Figure 275 for model 1 and model 2 respectively. In a similar manner to the stress contour plots, gauges 3 and 13 have a low tensile loading in model 1 compared with a high tensile loading at the same location in model 2.

		FEA micro strain (με) readings at 195kN	
	Pseudo component Model 2 - distorted	Full integration	Reduced integration
1	top edge on attachment	554	504
2	45° at boss LHS	369	363
3	10mm from boss toe - CL	377	364
4	45° at boss RHS	333	325
5	10mm from middle weld top toe	245	225
6	10mm from middle weld lower toe	220	211
7	centre line of U-plate pressing	239	229
8	10mm from bottom weld toe CL	344	361
9	RHS of Hole	209	224
10	LHS of hole	372	408
12	opposite gauge 3 (same attachment plate)	360	340
13	mirror of gauge 3 (other attachment plate)	185	185

Figure 275: Test component model 2 – micro-strain (με) readings at virtual strain gauge location

Under static loading, the test component strain gauge measurements shown in Figure 246 display some non-linear effects. A non-linear geometry solution technique was explored in the test component FE analysis, but made no difference with respect to the deformation or strain against load results compared with the linear models described in chapter 4.7.2. In a non-linear analysis the total load is applied in a number of load increments. A graph of the stress or strain against load for increments over the complete load history should highlight any non-linear effects. This is not the case for the non-linear component model, which suggests that the non-linear loading is due largely to the non-linear contact between the pin and component. However, the development of complex pin contact models would require a significant increase in both effort and time. The linear FE model of the distortion does correlate sufficiently with the known strain and load distributions, providing results that are similar to the strain gauge measurements on the tested component. This makes the extra complexity unnecessary.

Several critical strain gauge locations are selected for comparison using the cyclic strain range readings. At gauge location 1 the measured micro-strain values on the component sample 1 were 610με at 195kN. The equivalent strain values in the FE models 1 and model 2, using a full integration solution method, were 637 με and 554 με respectively. The reduced

integration models gave 571 με (model 1) and 504 με (model 2). Using the worst case scenario, all the model results are within 17% of the measured strain values on the top edge of the attachment plate; strain gauge location 1. Alternatively, the measured values are higher by a factor of 1.2. At gauge location 3 the measured micro-strain values on the component sample 1 were 512με at 195kN. The equivalent strain values in models 1 and model 2, using a full integration solution method, were -13με and 377με respectively. The reduced integration models gave -20 με (model 1) and 364 με (model 2). Model 1 calculated strain values at gauge 3 as compressive strains, not tensile as seen in the measurements. Model 2 results were slightly better with the distorted geometry and strains calculated as tensile, but incorrect by a factor of 1.4. At gauge 10 the measured strain values were approximately 345με at 195kN. The equivalent values in models 1 and model 2, using a full integration solution method, were 343με and 372με respectively. The reduced integration models gave 377με (model 1) and 408με (model 2). The FE model results are within 8% of the measured strain values (factor of 0.92) on the left hand side of the mouse hole. At strain gauge 12 the measured strain range values recorded were approximately 406με at 195kN, but had a maximum and minimum value of 150με and -256με respectively (giving a loading ratio of R=-1.7). The equivalent strain values in models 1 and model 2, using a full integration solution method, were 448με and 360με respectively. The reduced integration models gave 394με (model 1) and 340με (model 2). The FE models compare well in total strain range with the measured values, although a different R ratio is evident. The linear elastic analysis cannot represent the positive to negative loading regime at gauge location 12. At gauge location 13 the measured strain values on the test component sample 1 were 110με at 195kN. The equivalent strain values in the FE models 1 and model 2, using a full integration solution method, were -12με and 185με respectively. The reduced integration models gave -13με (model 1) and 185με (model 2). There is a significant difference at gauge 13 between the cyclic and static measured strain values at 110 με and 400 με respectively. This suggests that type of loading or loading rate has an effect on the strain experienced. The cyclic strain ranges are used here for comparison. The FE model 1 symmetric geometry calculates a compressive strain. The modified FE model 2 with a distorted geometry calculates a tensile strain with a factor of 1.7 difference from the measured values.

A number of possible sources of error must be taken into consideration: uncertainties in the material properties, load measurement errors, test equipment and fixture constraints, strain gauge misalignment and calibration errors, limitations in the finite element modelling and

boundary conditions. In view of these factors, it can be claimed that adequate correlation between the model 2 (distorted geometry) and test component strain readings is achieved.

Displacements were measured on the test component during testing. The measured locations are shown in Figure 276 and Figure 277. A dial test indicator (DTI) was placed on the component in the same location as the green circle shown in Figure 276. The DTI was zeroed at 0kN load and maximum displacement value taken. The values of the test measurements are compared with the FE model displacements in Figure 278.

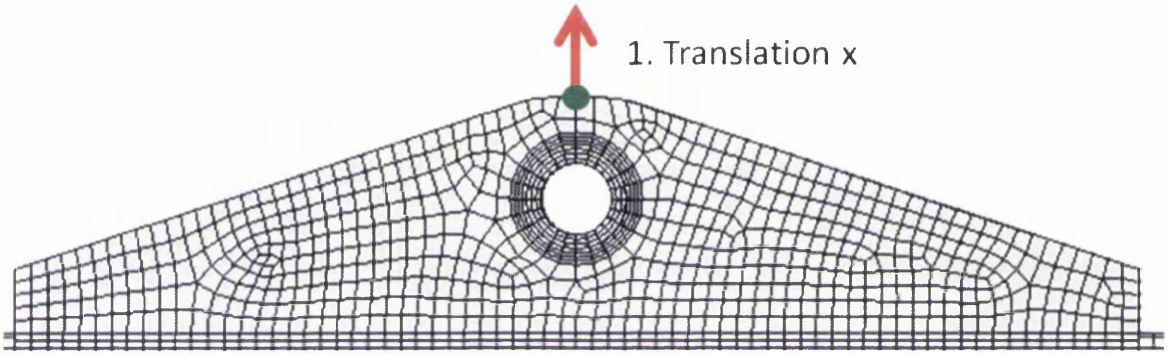

Figure 276: Displacement of attachment plate - x translation

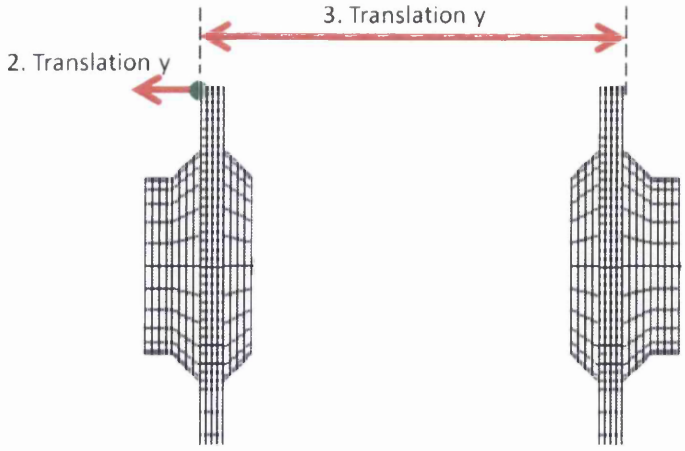

Figure 277: Displacement of attachment plate top outside edge (mouse hole side) and displacement between two attachment plates outer surfaces.

A DTI was also used on the outside edge of the attachment plate of the test component to record a maximum value. A digital calliper was used to measure the displacement between the outer surfaces of the two attachment plates as shown in Figure 277.

	Displacements - mm	FEA Model 1		FEA Model 2		Recorded - Sample 1
	Dimension	Full	Reduced	Full	Reduced	Dial test indicator
1	attachment plate translation x	0.234	0.285	0.247	0.302	0.23
2	attachment plate translation y	0.289	0.285	0.087	0.0885	0.17
3	displacement between attachment plates translation y	0.58	0.591	0.201	0.2085	0.3

(Full and reduced integration types)

Figure 278: Displacement values (mm) - FE-model 1 symmetric, FE-model 2 distorted and test recorded values

The model 2 displacements display a better correlation with the test data, compared with model 1 and the test data. This is primarily due to the improved accuracy and representation of the distorted test component model and geometry.

4.7.4 Structural Stress Calculation

The structural stress calculation procedure as described in chapter 4.3 was applied to the test component FE model. The structural stress was calculated in an Excel spreadsheet for the three weld runs on the same side of the mouse hole:

1. Boss to attachment plate weld
2. Attachment plate to top-hat section weld (middle weld)
3. Top-hat section to base plate fillet weld (lower weld mouse hole region)

The three weld locations are displayed in Figure 279, Figure 280 and Figure 281 respectively. The structural stress calculation procedure was carried out for both the model 1 symmetric geometry and model 2 distorted geometry test component. For each weld profile the structural stress is calculated and displayed on a line plot graph where the structural stress (MPa per unit load) is plotted on the y-axis against the distance along the weld (mm) on the x-axis. In the case of the circumferential welded boss (weld run 1) the x-axis parameter is the angle around the welded boss (0-360 degrees), and the results of which are displayed on a radar plot graph.

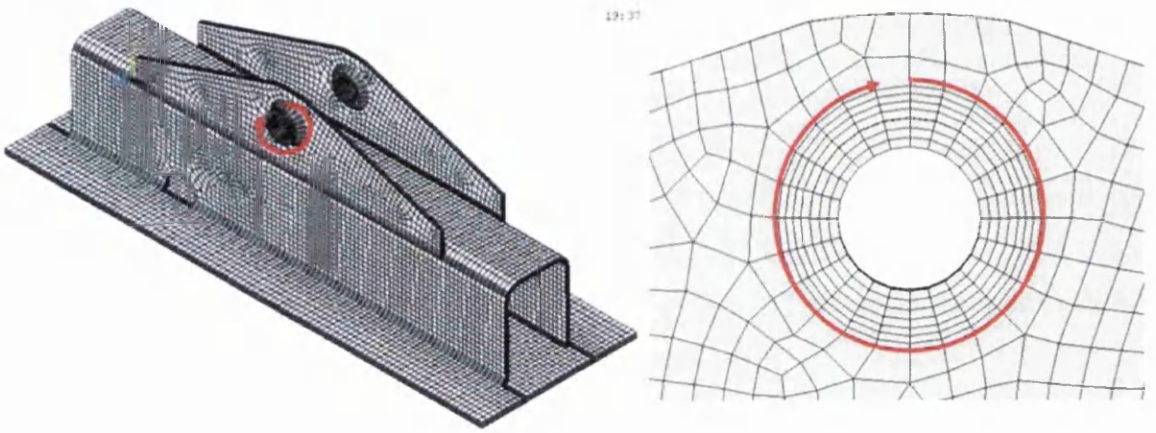

Figure 279: Boss weld toe location for structural stress calculation – Boss to attachment

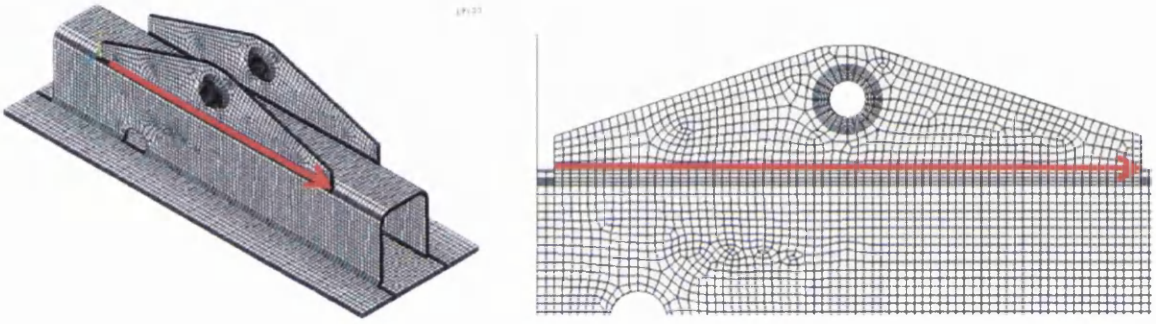

Figure 280: Middle weld upper and lower toe for structural stress calculation - attachment plate to top-hat section

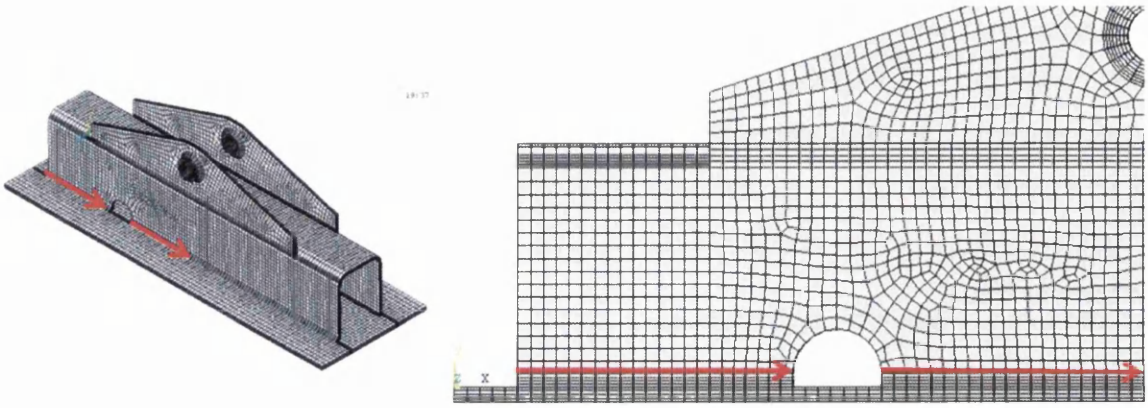

Figure 281: Base plate weld toe at mouse hole region for structural stress calculation - top-hat section to base plate fillet weld

The results of the structural stress calculation for the test component model 1 boss weld (symmetric geometry) are shown in Figure 282. The calculated profiles shown are for the inside and outside weld toe using full and reduced integration solutions. Due to the circular feature of the welded boss, it is helpful to plot the structural stress (MPa per unit load) on the y-axis against the angle around the welded boss (0-360 degrees) in a radar plot graph, as shown in Figure 283. Peak structural stresses of 1.1MPa occur at approximately 105 degrees and 255 degrees around the boss (0 degrees - Top Dead Centre (TDC)). The actual test component test failure occurred at 180 degrees. There is good correlation between the full and reduced integration approaches.

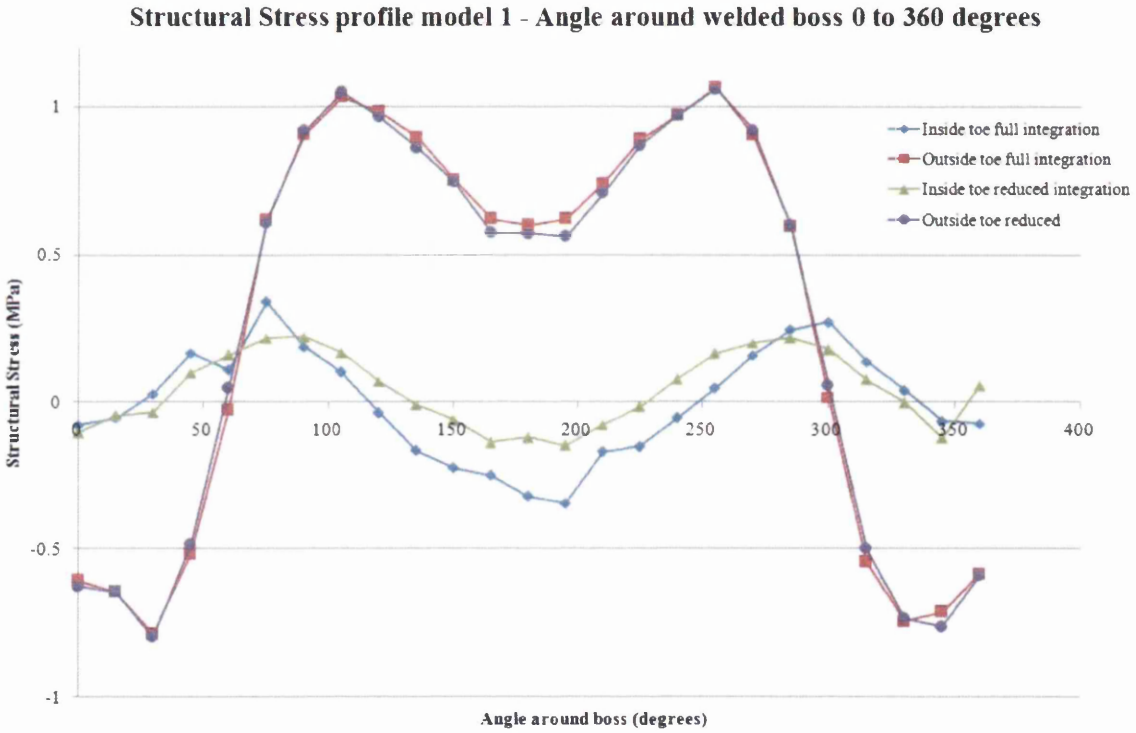

Figure 282: Calculated structural stress profile model 1 - Welded boss line plot

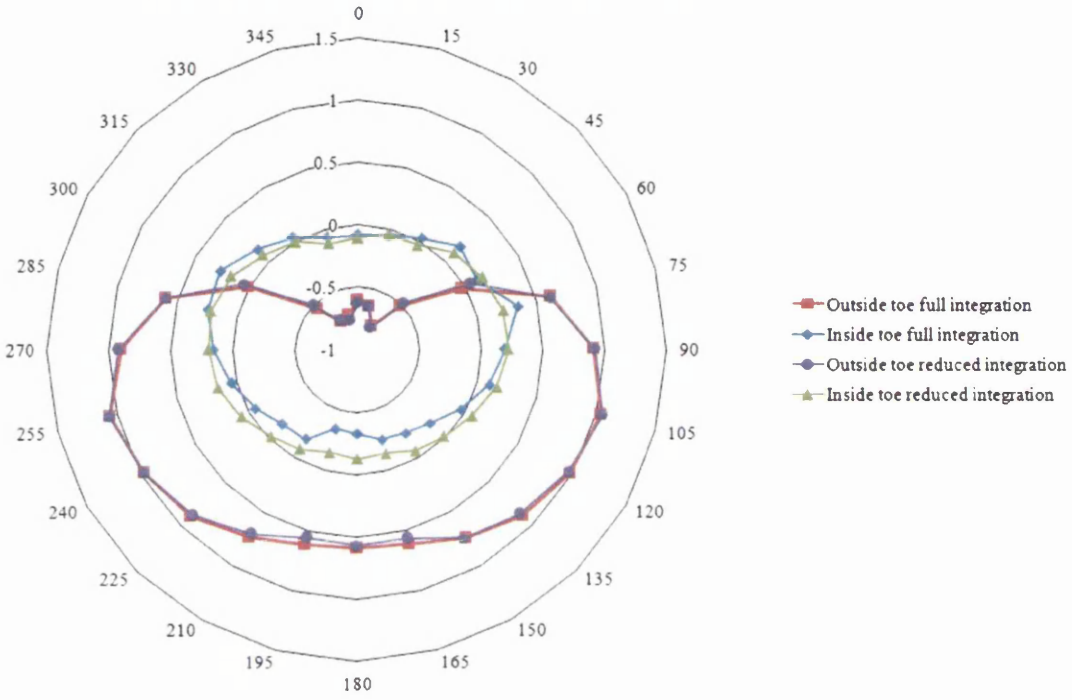

Figure 283: Calculated structural stress profile model 1 – Welded boss radar plot

The structural stress profile of the test component model 1 middle weld run is shown in Figure 284. The calculated profiles shown are for the upper and lower weld toes using full and reduced integration solutions. Peak structural stresses of 0.4MPa occur at the centre of the attachment plate to top hat section weld where the load is distributed, primarily through the centre of the component. The calculated structural stresses are higher for the upper weld toe. This is due to a reduction in thickness for the section and more flexible or less restrained material inducing higher bending stresses at the weld toe. The lower weld geometry is a slightly thicker section with increased stiffness.

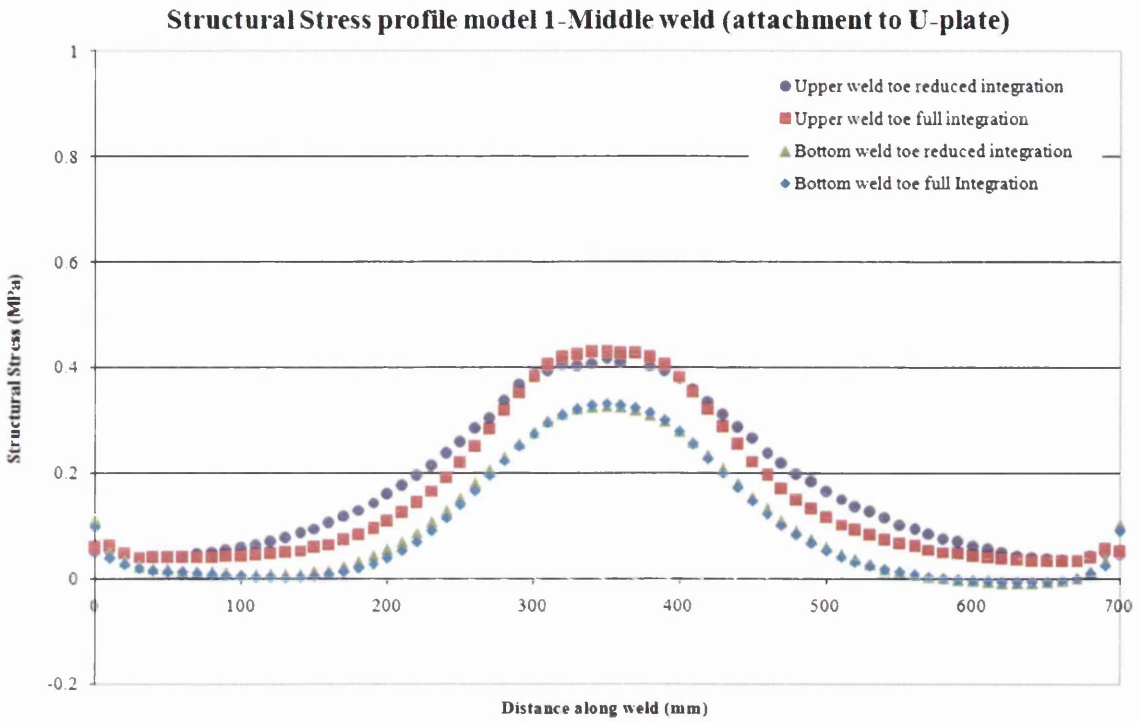

Figure 284: Calculated structural stress profile model 1 - Middle weld

The structural stress profile of the test component model 1 lower weld run is shown in Figure 285. The structural stress profiles are calculated for the LHS and RHS upper weld toes using full and reduced integration solutions. The mouse hole feature occurs at 215mm to 285mm along the x-axis. Peak structural stress of 0.6MPa and 0.7MPa occur at the plate/weld run edge on the LHS and RHS of the mouse hole respectively. There is a prominent increase in the structural stress profile on the RHS section using a full integration solution.

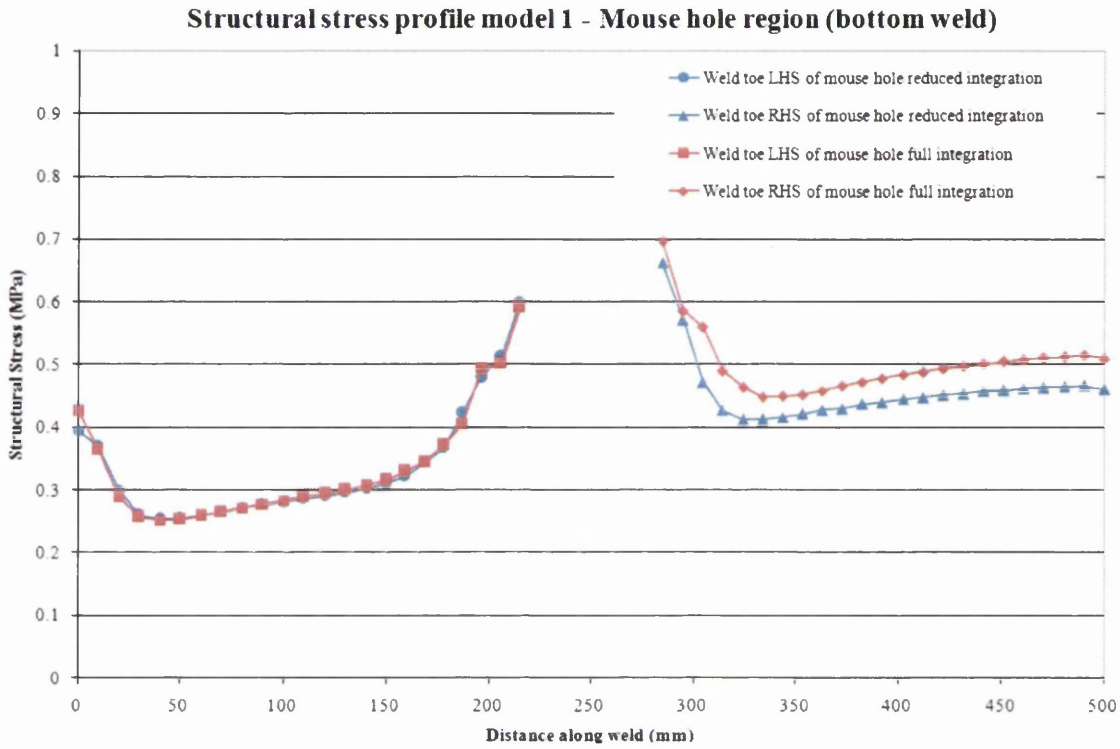

Figure 285: Calculated structural stress profile model 1 - Base plate weld mouse hole region

The results of the structural stress calculation for the test component model 2 boss weld (distorted geometry) are shown in Figure 286. The structural stress (MPa per unit load) is plotted on the y-axis against the angle around the welded boss (0-360 degrees) on the x-axis (line plot). The calculated profiles shown are for the inside and outside weld toe using full and reduced integration solutions. The structural stress profile is also shown on a radar plot in Figure 287. The structural stress (MPa per unit load) is plotted on the y-axis against the angle around the welded boss (0-360 degrees) circumference. Peak structural stresses of 1.1MPa occur at approximately 180 degrees around the boss from TDC. This stress profile shows good correlation with the actual test component test failure. There is very good correlation of the structural stress profiles between the full and reduced integration types. Due to the modified geometry and boundary conditions, the stress correlates well with the test failure location, unlike model 1 in Figure 282.

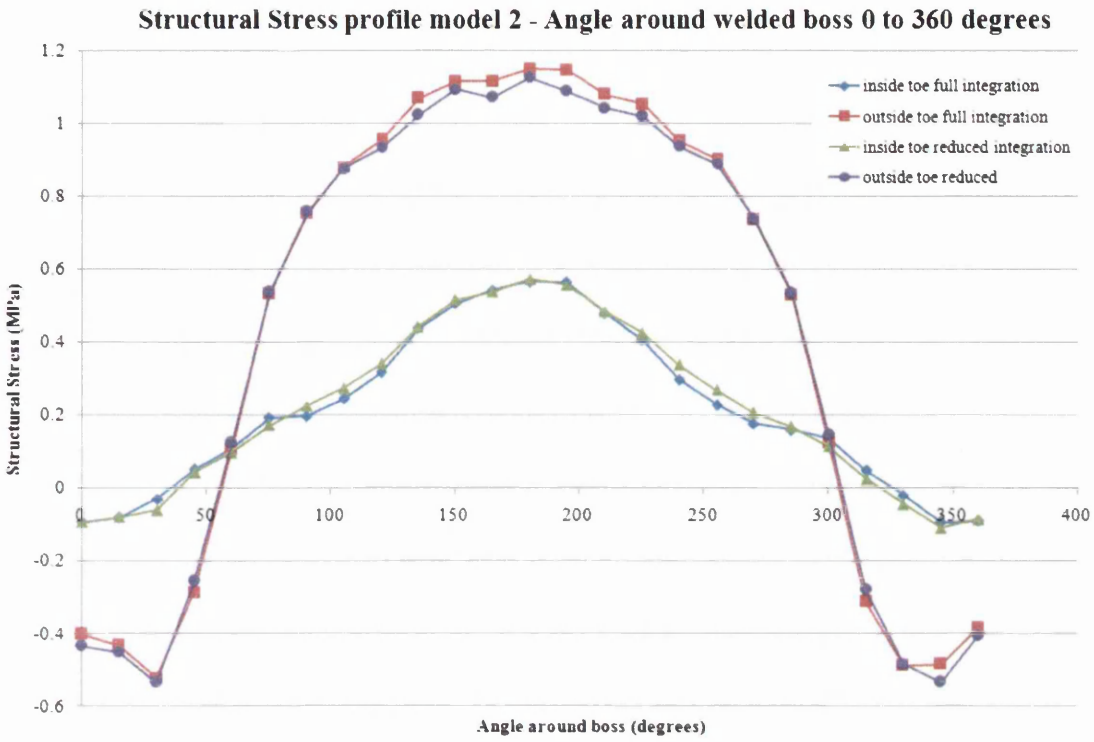

Figure 286: Calculated structural stress profile model 2 – Welded boss line plot

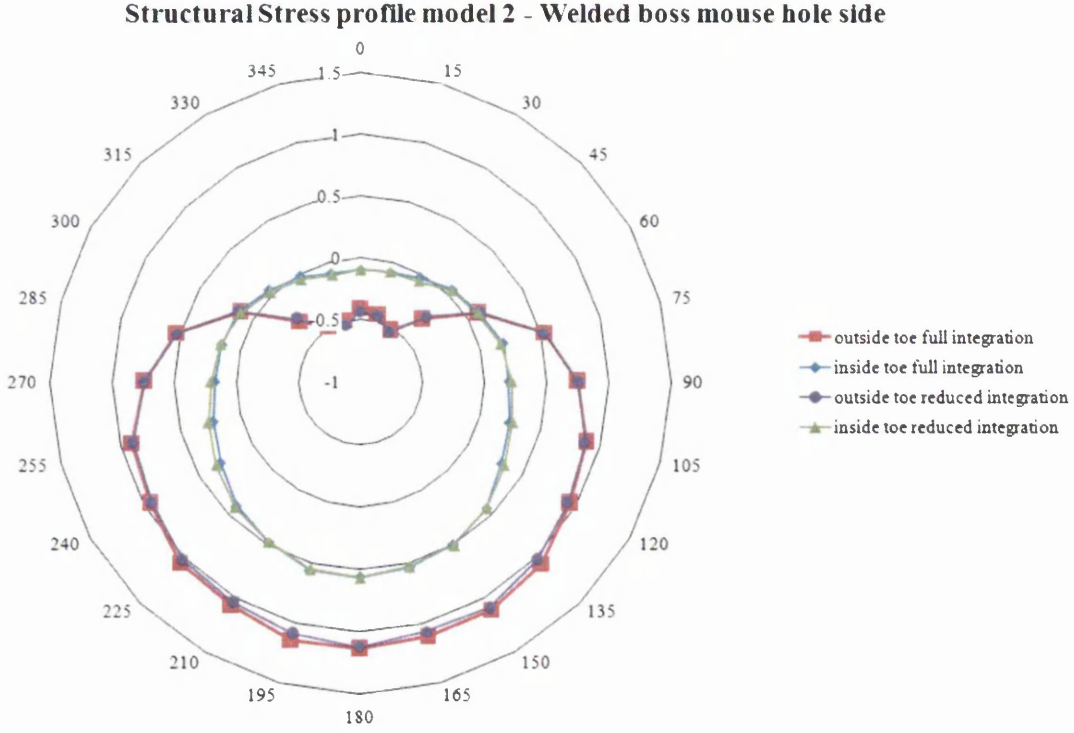

Figure 287: Calculated structural stress profile model 2 - Welded boss radar plot

The structural stress profile of the test component model 2 middle weld run is shown in Figure 288. The calculated profiles shown are for the upper and lower weld toes using full

and reduced integration solutions. Peak structural stresses of 0.55MPa occur at the centre of the attachment plate to top-hat section weld with a similar stress distribution to the model 1 analysis. However, the peak stresses are of a higher value because of the misalignment ram loading. The calculated structural stresses are higher for the upper weld toe, again, due to the reduction in section thickness and a more flexible member with higher bending stresses.

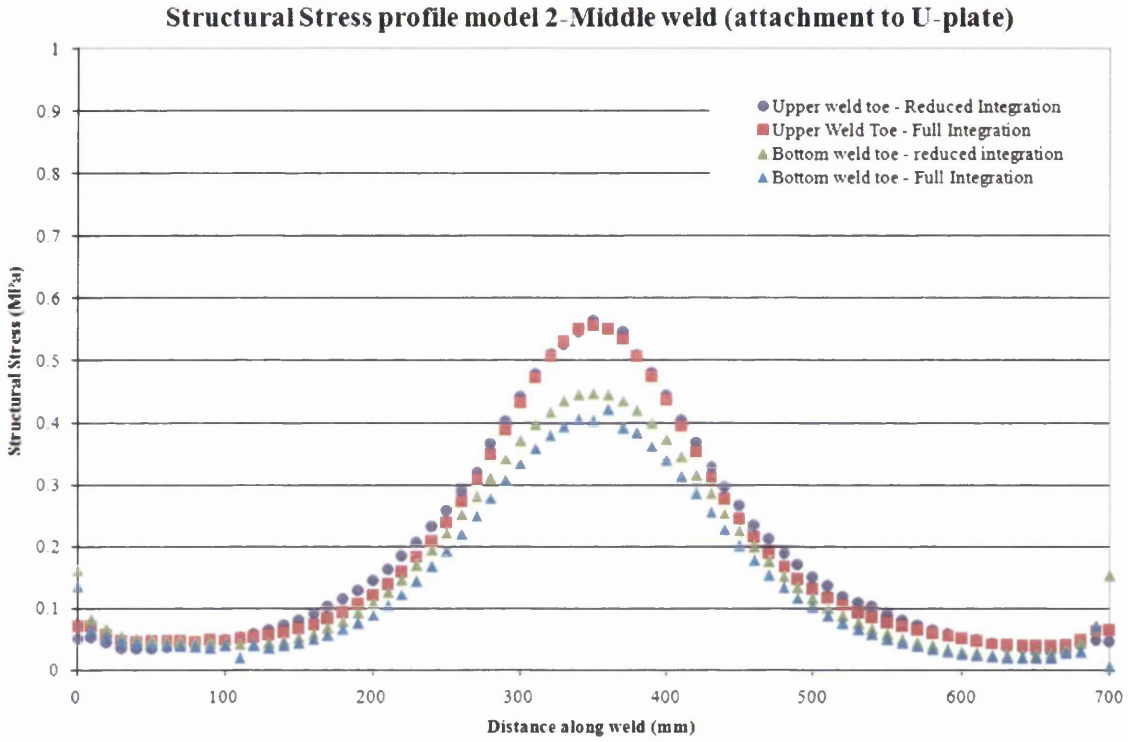

Figure 288: Calculated structural stress profile model 2 - Middle weld

The lower weld run structural stress profile for model 2 is shown in Figure 289. Peak structural stresses of 0.65MPa and 0.75MPa occur at the plate/weld run edge on the LHS and RHS of the mouse hole respectively. There is a slight increase in structural stress on the RHS with the full integration solution compared with the reduced method. The calculated stress is also higher than the model 1 structural stress profile. This is due to the misaligned hydraulic ram loading distributing higher forces down the mouse hole side (LHS) of the component.

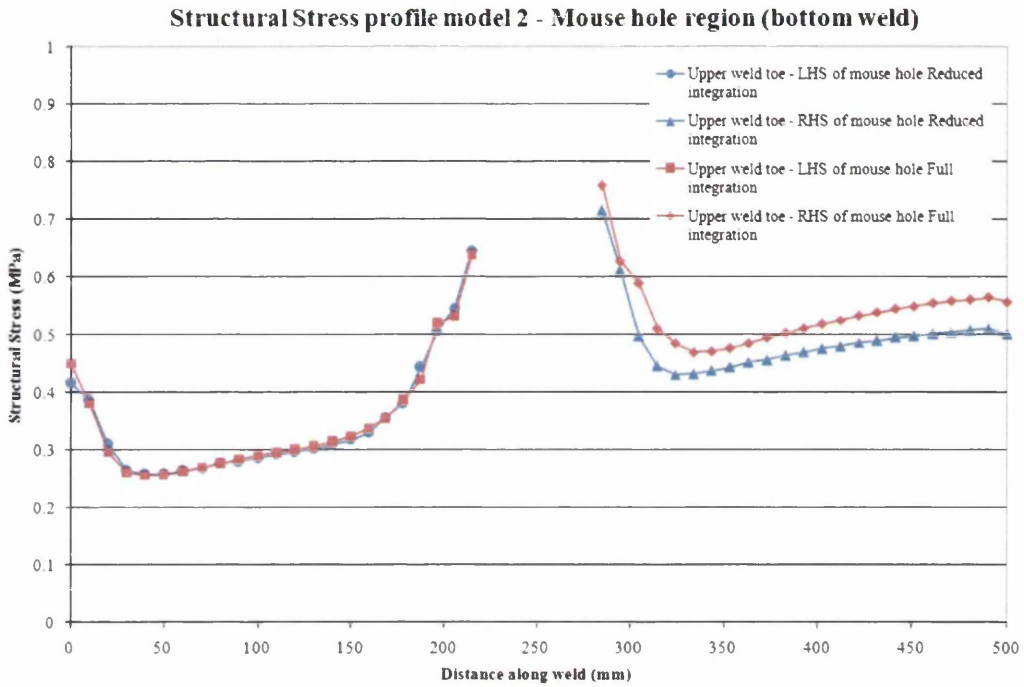

Figure 289: Calculated structural stress profile model 2 - Base plate weld mouse hole region

There are significant differences in the structural stress profiles calculated, between the symmetric model 1 and distorted geometry model 2. These are largely related to the load distribution around the welded boss and attachment plates. An important difference in principal stress between the symmetric and distorted models was shown for the stress analysis in chapter 4.7.2. Similar effects are observed here in the structural stress calculation. Furthermore, the calculated peak structural stress in the symmetric model 1 does not correlated well with the crack location in the fatigue test. On the other hand, the distorted model 2 provides an excellent correlation. For these reasons, only the distorted model 2 is taken forward for further analysis and fatigue life prediction.

The structural stress profile from the test component distorted geometry model 2 was used to calculate an equivalent structural stress profile (the method as shown in chapter 4.6). The equivalent structural stress parameter is simply a scaling parameter based on the structural stress profile (although not directly comparable). The stress profile itself is not altered, only scaled depending on any effects due to thickness and loading mode. The equivalent structural stress profile for the Model 2 welded boss is shown in Figure 290. The equivalent structural stress (MPa per unit load) profiles are, again, plotted on the y-axis against the angle around the welded boss (0-360 degrees) or distance along the weld (mm) on the x-axis, for weld runs 1, 2 and 3.

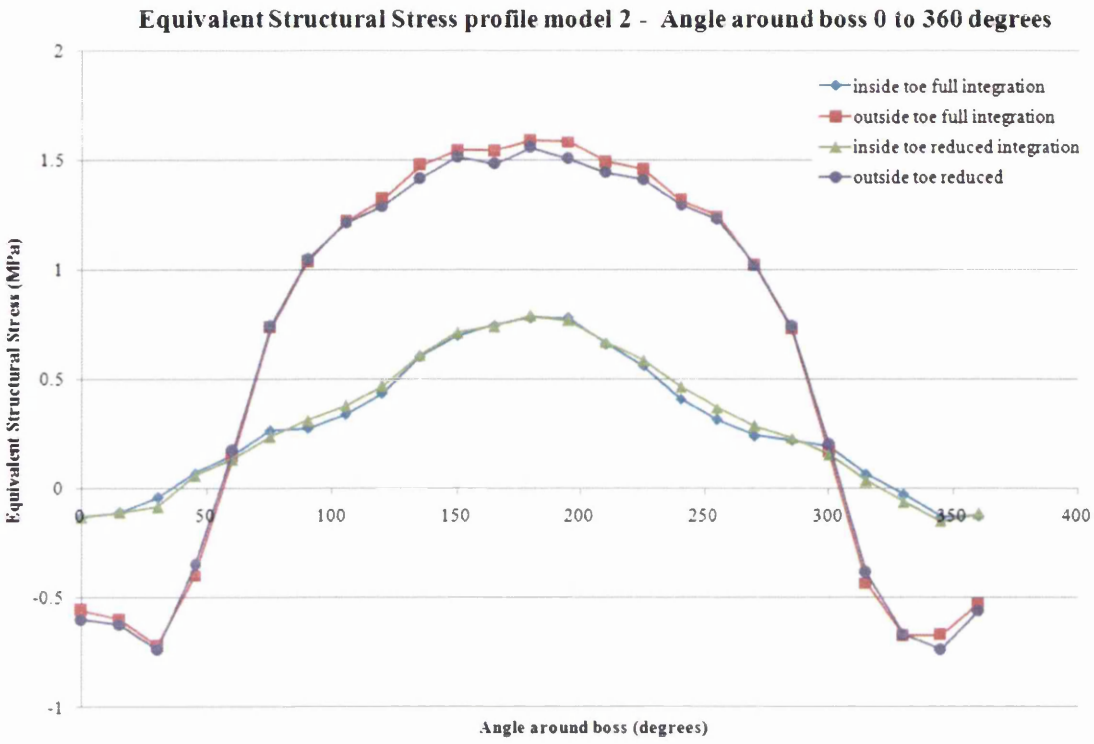

Figure 290: Calculated equivalent structural stress profile model 2 - Welded boss line plot

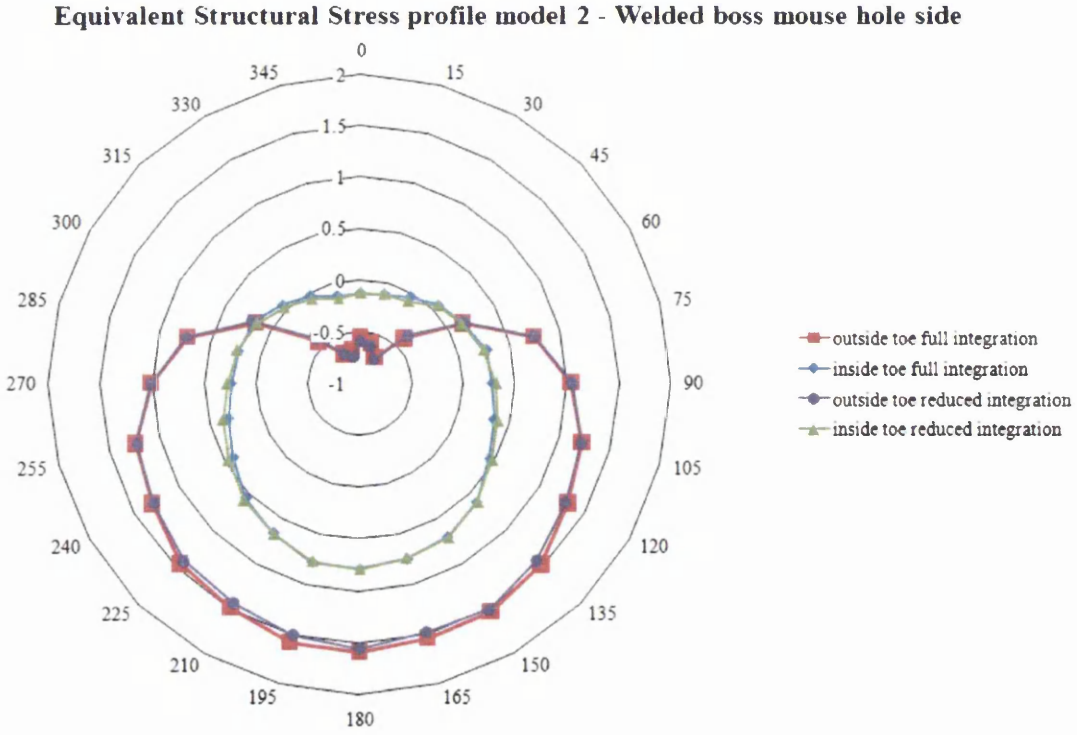

Figure 291: Calculated equivalent structural stress profile model 2 - Welded boss radar plot

The welded boss equivalent structural stress profile is also shown in Figure 291 on a radar plot. Peak equivalent structural stresses of 1.5MPa occur at approximately 180 degrees around the welded boss. There is excellent correlation between the full and reduced integration solutions used.

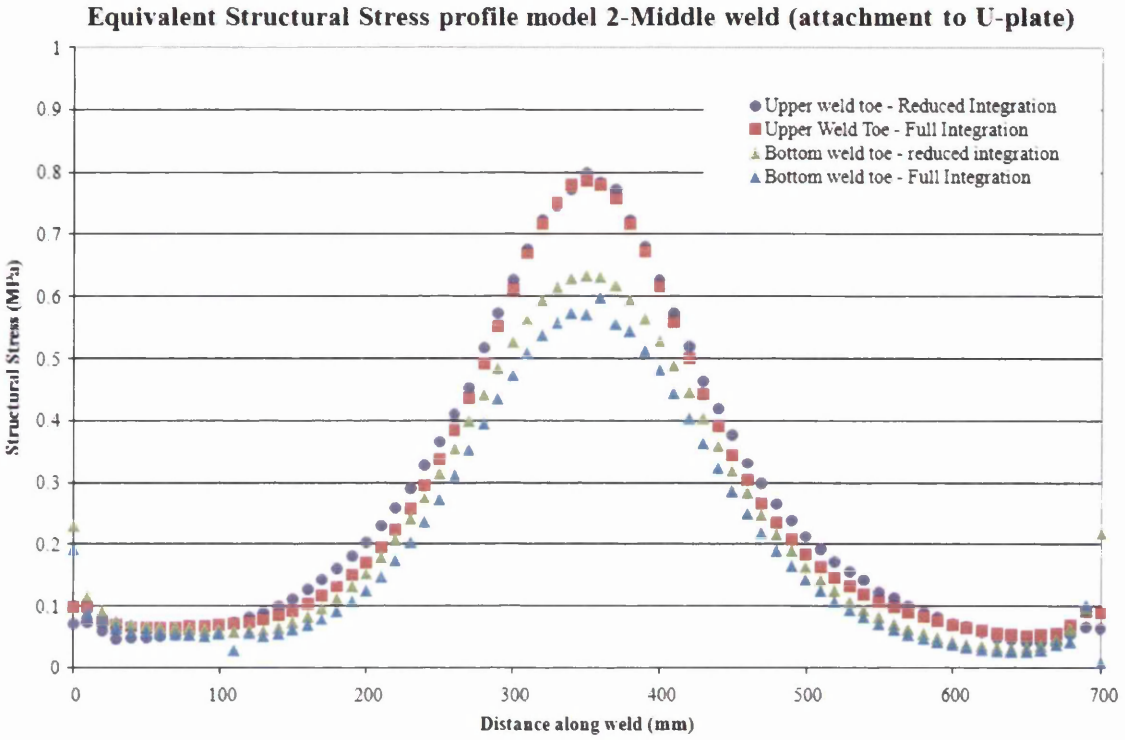

Figure 292: Calculated equivalent structural stress profile model 2 - Middle weld

The equivalent structural stress profile of the test component model 2 middle weld run is shown in Figure 292. The equivalent structural stress (MPa per unit load) is plotted on the y-axis against the distance across the attachment plate (mm) on the x-axis. The calculated profiles shown are for the upper and lower weld toes using full and reduced integration solutions. Peak structural stresses of 0.8MPa occur at the centre of the attachment plate to top hat section.

The equivalent structural stress profile of the test component model 2 lower weld run is shown below in Figure 293 for the LHS and RHS upper weld toes. The structural stress is calculated using full and reduced integration solutions. As found in the structural stress parameter, peak structural stress of 0.9MPa and 1.1MPa occur at the edge of the plate/weld run on the LHS and RHS of the mouse hole respectively. Again, there is an increase in structural stress on the RHS with a full integration solution.

Figure 293: Calculated Equivalent structural stress profile model 2 - Base plate weld mouse hole region

The only difference in the equivalent structural stress compared with the previous structural stress is a scaling factor. There is no change in the stress distribution or profile. The critical difference between the two damage parameters becomes apparent later in the prediction of fatigue life using a range of different master curves and how well it is able to condense a range of different test data.

4.7.5 Fatigue life predictions

Using the test component structural stress weld profiles calculated under a 1kN unit load from the previous chapter, a fatigue analysis is now executed using the elastic scaling and a super-positioning technique. The fatigue analysis method is discussed and described in detail in the literature review chapter 2.3.3.

In the fatigue testing of the component, two separate load ranges were applied. Firstly, at a load range of 95kN the component achieved 2,000,000 cycles. Secondly, on increasing the load range to 195kN the component attained 841,789 cycles with failure at the base of the outside boss weld toe. The observed 20mm long crack satisfied the predetermined failure criterion.

The total damage D at failure completed by a component is = 1. This is known as Miners hypothesis [45] for the analysis of variable amplitude loading. In the present case, summation of the total damage endured is described as D1+D2 where each load or damage case will use up a fraction of the total life, 1.

D_1 = damage from 95kN load cycles

D_2 = damage from 195kN load cycles

D is described as:

$$D = \frac{n_1}{N_1} + \frac{n_2}{N_2}$$

Eq 4.7.1

Where:

n_1 = completed number of cycles for D_1 – 95kN load

N_1 = prediction number of cycles for D_1 – 95kN load

n_2 = completed number of cycles for D_2 – 195kN load

N_2 = prediction number of cycles for D_2 – 195kN load

For completion of the damage equation, n values are taken from the completed fatigue test cycles and N values are generated from the equivalent stress range from the fatigue master curve. So taking the unit load structural stress value at the boss weld toe failure location (1.1MPa) and multiplying by the test load ranges 95kN and 195kN, applied stress ranges of 105MPa and 215MPa are calculated. The number of cycles is read off the fatigue curve for the corresponding stress range. The structural stress master curve used here is the 50% mean curve generated using the weld toe failure distorted solid element coupon models from chapter 4.5 (excluding the bend tee joint data) described by the equation $\sigma = 20419 N_f^{-0.347}$.

The calculated damage summation of $D_1 + D_2$ for the structural stress parameter at the weld boss toe on the distorted geometry model 2 (full integration) is shown in Figure 294. The damage is plotted on the y-axis against the angle around the welded boss (degrees). The damage calculation is completed for each weld run using the structural stress and equivalent structural stress damage parameters. In each case, the damage summation is plotted on the y-axis against the distance along the weld (mm) (or angle (degrees) around the boss) on the x-axis. For the weld run in Figure 294, the maximum damage from the structural stress parameter is 2.5 at 180 degrees around the boss weld toe. This correlates well with the test component failure location; at the base of the boss weld toe.

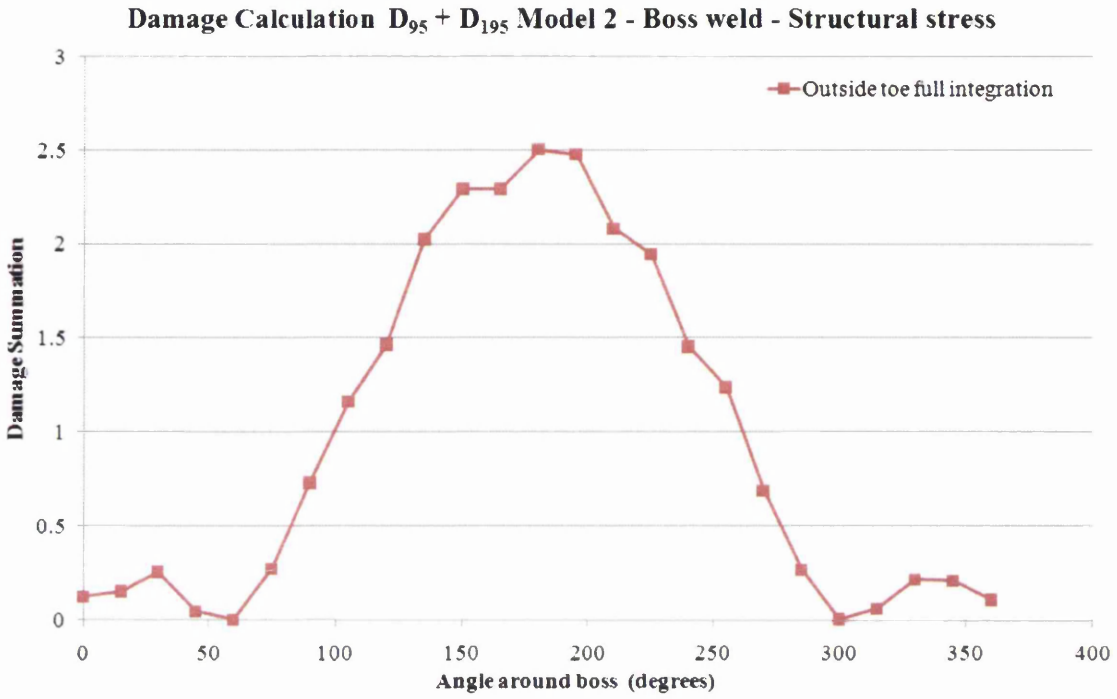

Figure 294: Model 2 structural stress fatigue life - Number of repeats D_1+D_2 at welded boss outside toe

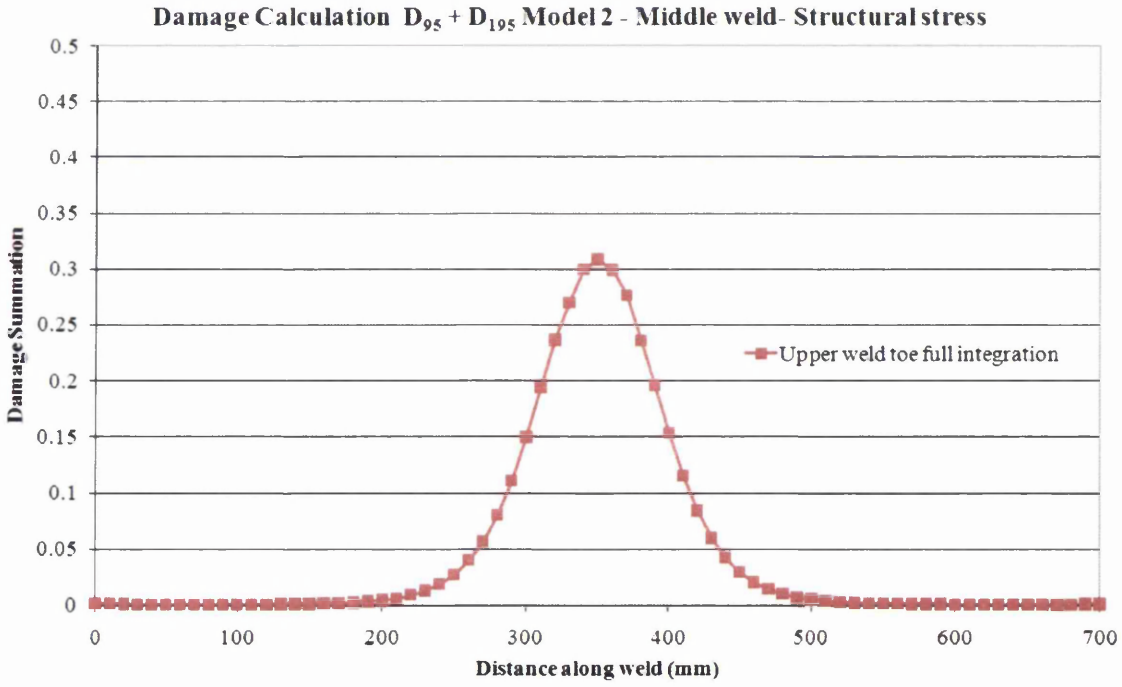

Figure 295: Model structural stress fatigue life - Number of repeats D_1 + D_2 at upper toe middle weld

The structural stress damage summation of the middle weld, upper toe (attachment to top hat section weld) for the distorted geometry model 2 is shown in Figure 295.

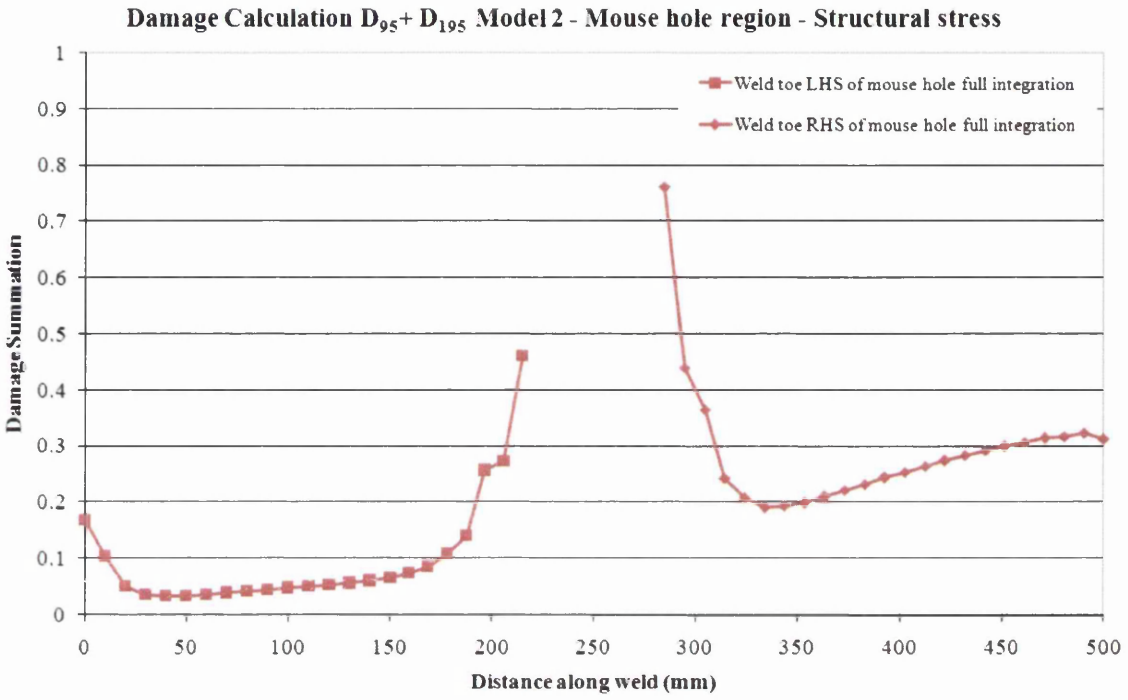

Figure 296: Model 2 structural stress fatigue life - Number of repeats D_1+D_2 at lower weld mouse hole

The structural stress damage summation at the lower weld (mouse hole region) on the distorted geometry model 2 is shown in Figure 296. The maximum damage is calculated at the weld and plate edge on the RHS of the mouse hole due to the high localised stresses.

Miner's hypothesis proposes that the total damage of a failed component is equal to 1. It is reported that this is not always the case and values of 0.25 to 7 have been recorded [46]. It is found that typical values of Miners are between 0.7 and 3. There are some concerns when using this method as it assumes damage is linear and proportional for each load amplitude, and independent of the time at which the loads are applied. This is the main concern when using the hypothesis on this test component. In terms of design, failure will not occur (at least theoretically should not occur) when the calculated damage is < 1. From the structural stress weld damages above, the maximum occurrence is found at the base of the boss weld toe. This shows excellent correlation with the recorded test component failure. The maximum damage value of 2.5 is above the assumed Miner's rule of 1. If failure is supposed to happen at 1, this suggests that either a more severe damage is experienced in the test component than in the FE model. Or, alternatively, the linear damage summation is incorrect. It is possible that at the lower stress ranges a flatter fatigue curve exists. Hence, the hypothesis assumes the lower stress ranges are more damaging than the damage experienced by the actual test component. Both scenarios are a possibility, however, since the maximum damage correlates with the test

component and is within similar values of referenced damage summations [46], the method is considered effective in this application.

The damage summation approach is also applied using the structural stress calculated damage parameter. Since the stress profiles are largely similar, compared with the original structural stress, the summation is only carried out for the weld boss toe failure location. This is done using the distorted geometry Model 2 and a full integration method, shown in Figure 297.

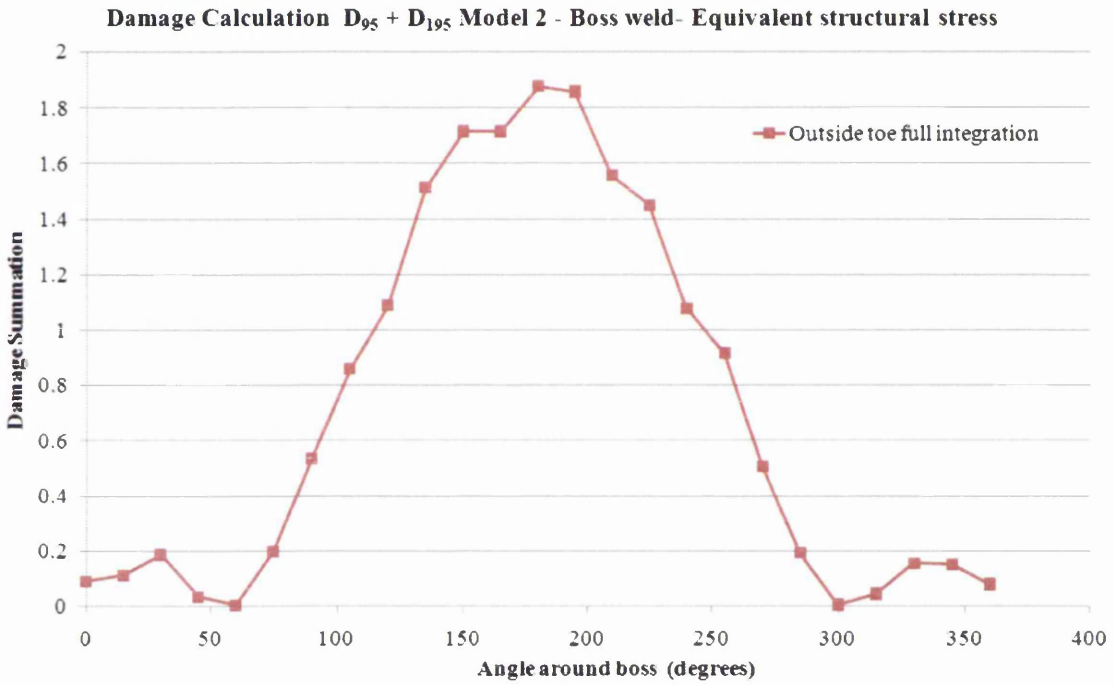

Figure 297: Model 2 equivalent structural stress fatigue life - Number of repeats (D_1+D_2) at welded boss outside toe

As recorded in the structural stress parameter summation, the equivalent structural stress also captures the weld fatigue crack location. This time, however, the total damage summation is calculated as 1.85. The master curve used is based on all of the test data including the bend load tee joint unlike the structural stress calculations. This suggests the equivalent structural stress damage parameter is more robust in condensing the fatigue data into a single scatter band. The calculated fatigue life damage is more precise, being nearer to a summation value of 1 than the structural stress with a value of 2.5.

4.7.6 Comparison of Predicted vs. Measured Fatigue Lives

In the previous chapters (section 4.7.4 and 4.7.5) it was shown that the maximum calculated structural or equivalent structural stress (and the maximum damage) occurs at 180 degrees around the welded boss outside toe (corresponding side to the mouse hole feature) and correlates with the crack initiation location in the component fatigue test, Figure 298.

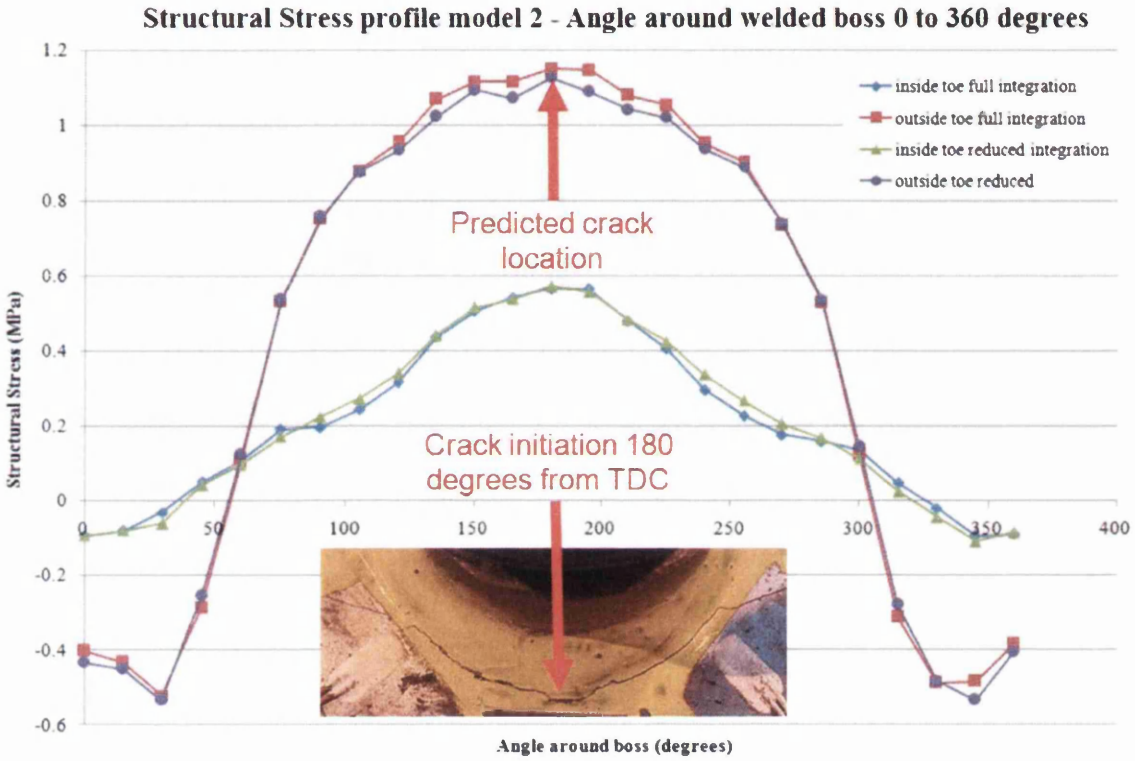

Figure 298: Maximum calculated structural stress comparison with test component fatigue test crack initiation site

The crack initiation location is now considered in the fatigue life prediction process and analysed with the range of different master curves generated in chapter 4.5 and chapter 4.6. This allows the sensitivity of the analysis approach and the effectiveness of the different master curves on fatigue life prediction to be assessed.

The structural stress master curves generated and used in the analysis are based on calculations using:

1. Curve generated using solid element models with undistorted coupon geometries.
2. Solid element models with distorted coupon geometries.
3. Measured structural stresses

4. Solid element undistorted models – without bending load tee joint data
5. Solid element distorted models – without bending load tee joint data
6. Measured structural stresses - without bending load tee joint data

The bending load tee joint data had a distinctively different fatigue curve and slope. This implies that structures experiencing a predominantly bending load mode must be assessed using a separate master curve.

The equivalent structural stress master curves have been developed in order to condense disparate fatigue curves further and to encompass thickness and loading mode effects such as the bending load tee joint data described above. The master curves generated and used in the analysis are based on calculations using:

1. Curve generated using solid element models with undistorted coupon geometries.
2. Solid element models with distorted coupon geometries.
3. Measured structural stresses
4. Solid element undistorted models – without bending load tee joint data
5. Solid element distorted models – without bending load tee joint data
6. Measured structural stresses - without bending load tee joint data
7. Solid element distorted models – with optimised Equivalent structural stress equation parameter; I(r) value = 1.6

The damage summation of D_1+D_2 (95kN and 195kN load range) was calculated, as described in chapter 4.7.5, at the boss weld toe failure location using the structural stress damage parameter. The damage summation has been calculated for each of the 6 different structural stress master curves created and the corresponding 99%, 50% and 1% certainty of survival curve from their statistical analysis. The results are plotted in Figure 299 with the damage summation on the y-axis (Log scale) against the different types of master curve on the x-axis. The damage summation, or damage endured by a component at failure is considered to be equal to 1. The quality of prediction can be assessed based on the total damage calculated. Acceptable values of the total damage D are between 0.7 and 3.

The most accurate 'structural stress' fatigue life prediction is based on the master curve calculated with the solid element distorted models without the bending load tee joint data. A damage summation of 2.75 is calculated. The next closest prediction is the master curve

calculated using the solid element distorted models (including the bending load tee joint data) with a damage summation value of 3.1.

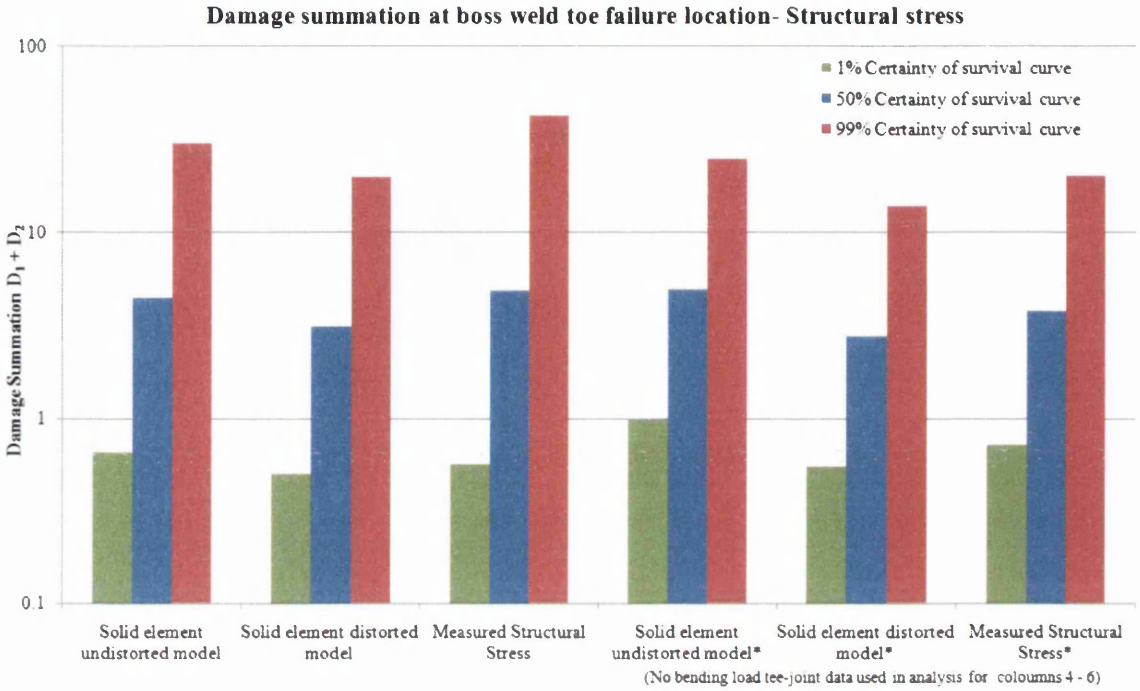

Figure 299: Damage summation at failure location (outside toe boss weld) - comparison of structural stress curves

The damage summation is again determined at the boss weld toe failure location, however, now using the equivalent structural stress damage parameter. The damage summation has been calculated for each of the 6 different equivalent structural stress master curves created and the corresponding 99%, 50% and 1% certainty of survival curve from their statistical analysis. The damage summation values are plotted in Figure 300.

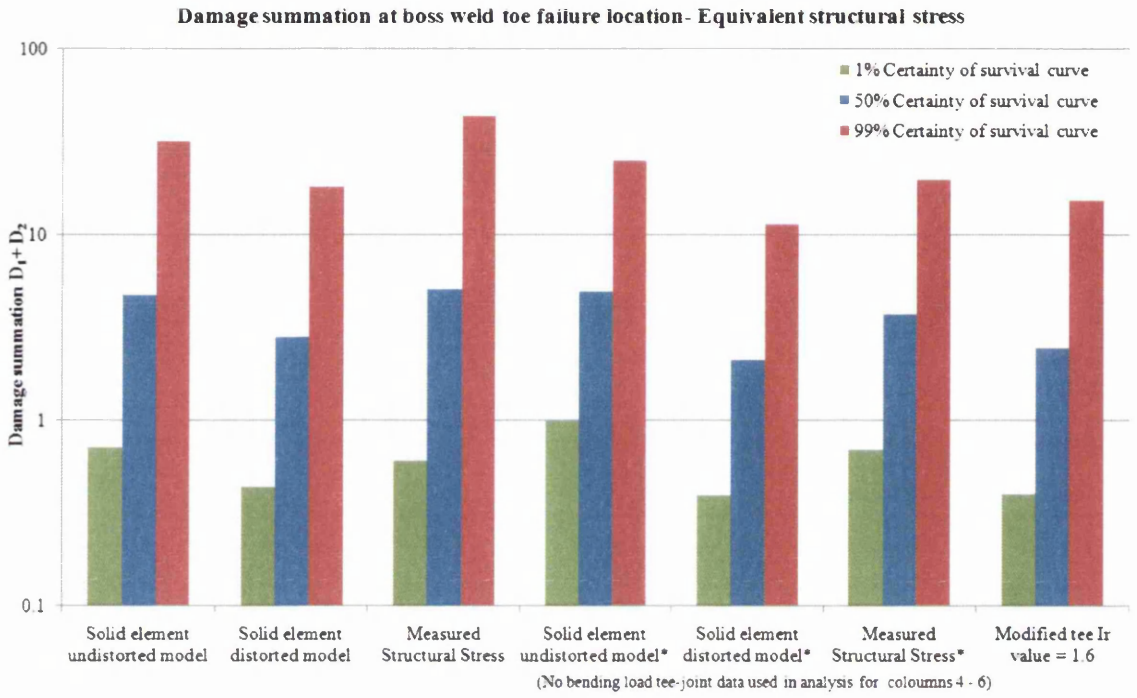

Figure 300: Damage summation at failure location (outside toe boss weld) - comparison of equivalent structural stress curves

As seen in the structural stress damage summation, the most accurate and closest fatigue life prediction is found when using the solid element distorted models without the bending load tee joint data followed by the solid element distorted models with the bending load tee joint data. This is based on the damage calculations using the 50% mean curve and compared with the total damage for component failure equal to 1. There is some variation in the calculated damage because of the different modelling techniques used. The approach proves robust and consistent for all fatigue master curves used.

An alternative way of presenting the fatigue life prediction data is shown in Figure 301. The predicted fatigue life is plotted on the y-axis log scale against the measured life on the x-axis log scale. This is done, again, using the damage calculation Miner's rule:

$$D = \frac{n_1}{N_1} + \frac{n_2}{N_2}$$

Where:

n_1 = completed number of cycles for D_1 – 95kN load (2,000,000)
N_1 = prediction number of cycles for D_1 – 95kN load
n_2 = completed number of cycles for D_2 – 195kN load (841,789)
N_2 = prediction number of cycles for D_2 – 195kN load

Where the total damage D = 1, rearranging the equation to predict N_2 we get:

$$N_2 = \frac{n_2}{1 - \frac{n_1}{N_1}}$$

Eq 4.7.2

Entering the *n* fatigue test result values and the predicted master curve value for the structural stress at 95kN load range, the fatigue life prediction for N_2 is calculated. This is completed for the structural stress master curves at the boss weld toe failure location. Each master curve N_2 predicted value is correlated against the single test component test failure at 841,789 cycles. The six data points in Figure 301 represent the different master curve prediction. This displays the range in fatigue life prediction value based on the various master curves (50% mean curve) against the single failure measurement. Correlation within a factor of 10 is acceptable, a factor of 5 is good and a factor of 3 is very good. At worst, all of the N_2 fatigue life prediction values are within in acceptable correlation. The predicted lives of each master curve (50% mean curve) are plotted on the y-axis log scale against the measured lives on the x-axis log scale.

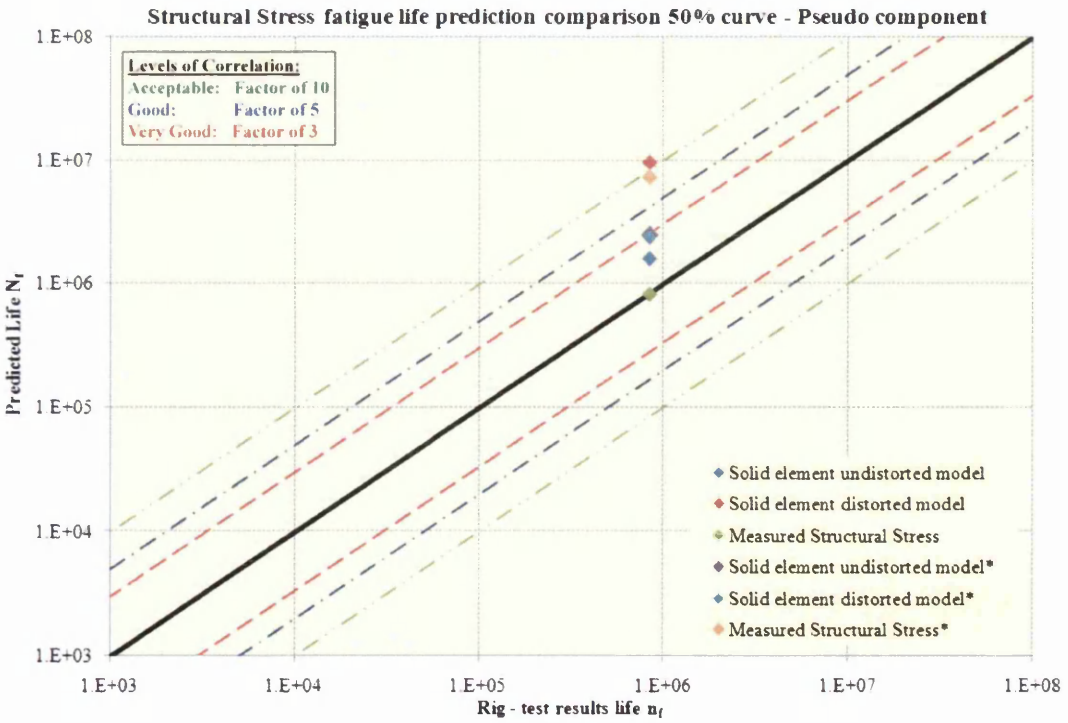

Figure 301: Structural stress fatigue life prediction of D_2 at welded boss outside toe failure location - comparison of different fatigue curves prediction vs. measured life

The fatigue life prediction calculation is repeated for the equivalent structural stress damage parameter and compared with the single component test result in Figure 302.

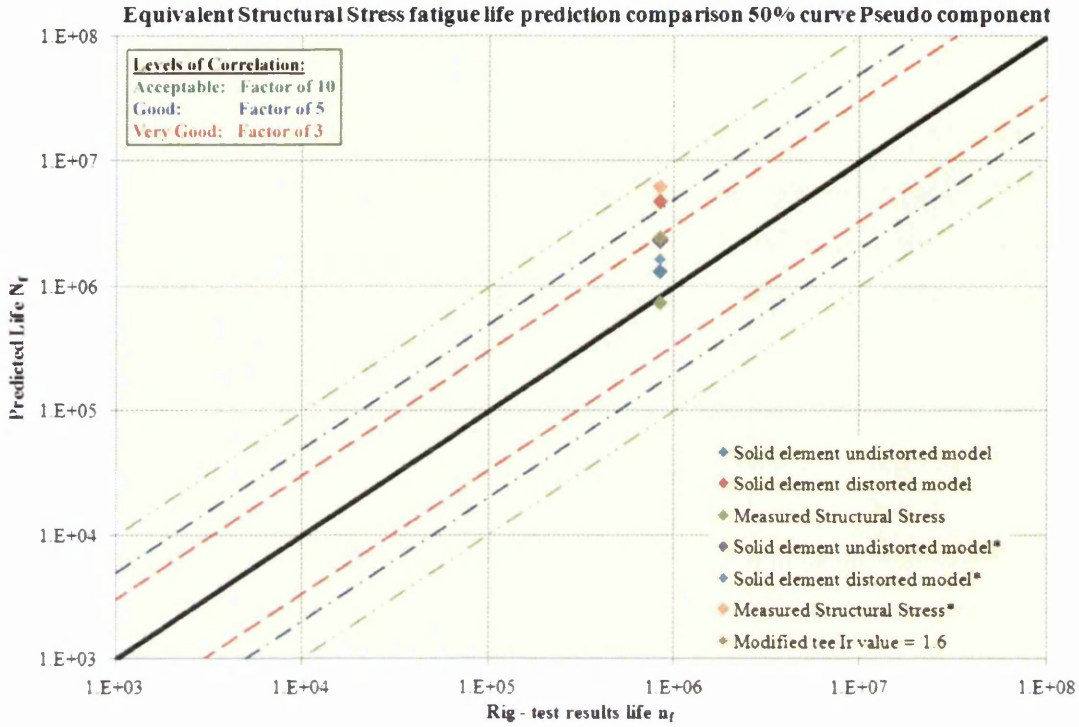

Figure 302: Equivalent structural stress fatigue life prediction of D_2 at welded boss outside toe failure location - comparison of different fatigue curves prediction vs. measured life

The predicted structural stress and equivalent structural stress N_2 values are plotted on a line plot graph in Figure 303. The predicted fatigue lives are displayed on the y-axis on a log scale against the range of structural and equivalent structural stress master curve. The test component fatigue test failure at the boss weld toe is highlighted at 841,789 cycles. There is an acceptable level of correlation between the predicted and the measured fatigue lives, all results being within a factor of 10. Most accurate fatigue life predictions are for the measured structural stress and equivalent structural stress, 50% certainty of survival master curves.

For comparison purposes, a master curve equation based on the 50% certainty of survival was extracted from the Safe Technology fatigue software vendor's FE-Safe Verity® module. The equation of the curve is $y = 19931N_f^{-0.31}$. Using the above calculation method for N_2, the structural stress unit load value at the boss weld toe failure location was used (1.2MPa) and a fatigue life prediction was calculated. N_2 was calculated at 936,425 cycles. This correlates well with the test failure at 841,789 cycles.

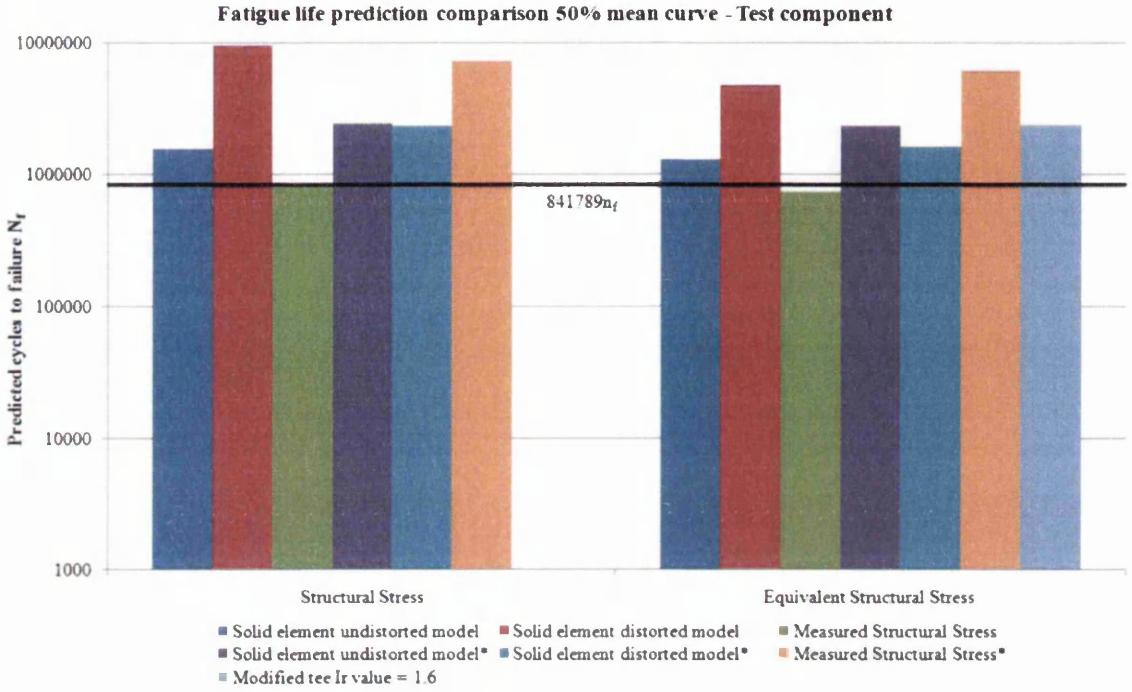

Figure 303: Comparison of structural stress and equivalent structural stress master curves on the fatigue life prediction of D_2

4.7.7 Fatigue life prediction – Failure mode master curves

It was shown in Chapters 4.5.6 and 4.6.4, for both the structural stress and equivalent structural stress damage parameter that a failure mode dependency exists upon separating the coupon fatigue test data into different failure modes. This is not to say a universal failure mode master curve is not achievable (as shown in the fatigue life predictions above), however improved correlation was seen for the throat and toe failure test results and the associated failure mode master curve. There was a clear difference in fatigue strength between the 50% mean master curves generated from the weld throat failure and weld toe failure test data, the weld toe failure master curve displaying a higher fatigue strength. The master curves are generated from the solid element distorted geometry models that are most representative of the actual coupon test samples.

The above damage and fatigue calculation (chapter 4.7.6) has been repeated for the outside boss weld toe failure location using the weld toe failure master curve (for both structural stress and equivalent structural stress damage parameter). A linear damage summation was

carried out using Miner's rule and a fatigue life prediction calculated for the N_{195kN} applied load. The master curves used and their respective parameters are summarised in Table 9.

	Chapter 4.5 Structural Stress	b	a	predicted N_{195}
1	Weld toe failures - all toe data	-0.40	43905	**2695273**
2	Weld toe failures - no bending load tee data	-0.34	20419	**1717655**
	Chapter 4.6 Equivalent Structural Stress			
3	Weld toe failures - all toe data (I(r) 1.11 to 1.13)	-0.40	58121	**2674887**
4	Weld toe failures - no bending load tee data	-0.34	28147	**1446312**
5	Weld toe failures - modified I(r) value 1.6 bending load tee data	-0.32	22233	**1263974**

Table 9: Toe failure master curves - summary of structural stress and equivalent structural stress parameters

The N_{195} calculated fatigue life predictions for the boss weld toe failure are shown in Figure 304. Fatigue life predictions are shown for all 50% mean structural stress and equivalent structural stress master curves. The n_2 number of recorded repeats from the component failure is highlighted at 841,789cycles.

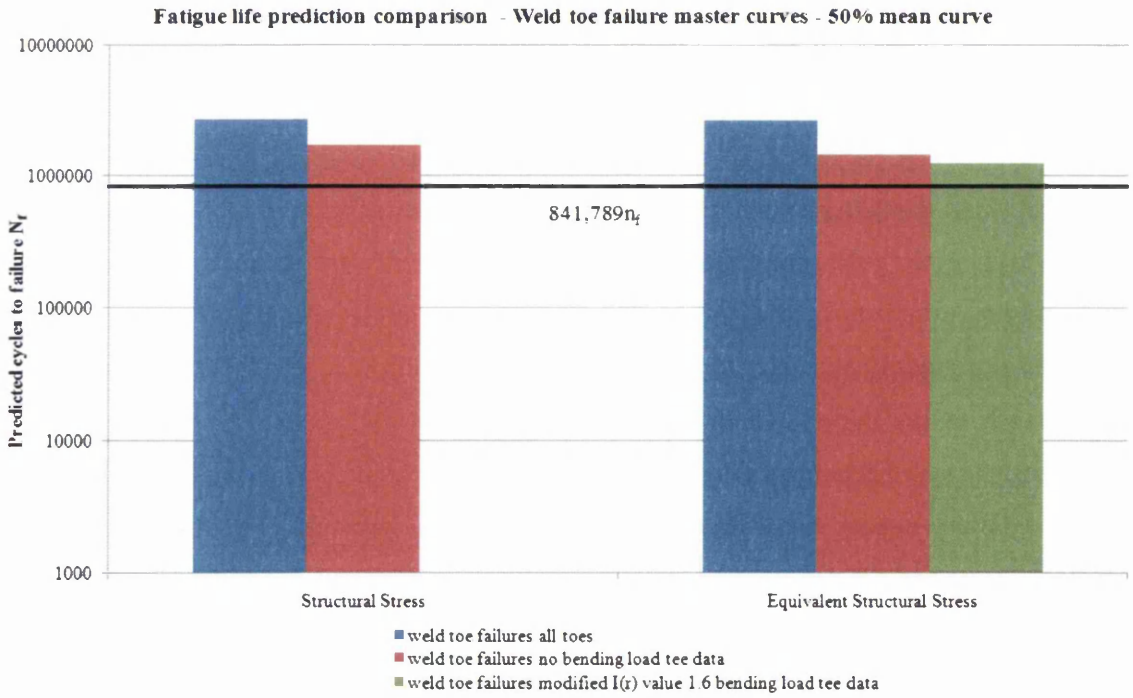

Figure 304: Comparison of structural stress and equivalent structural stress toe failure master curves on the weld boss failure fatigue life prediction

Calculated fatigue lives are over predicting when compared with the recorded component test failure. It is evident some sensitivity exists between the different structural stress and equivalent structural stress master curves generated. The equivalent structural stress fatigue life predictions are to some extent more accurate compared with the structural stress predictions. The accuracy of the fatigue life prediction is further improved when using the equivalent structural stress toe failure based master curve with the modified I(r) value for the bending load tee data. Compared with the prediction with the suggested I(r)value, there is a factor of 3.1 difference. Compared with the prediction of the master curve with no tee data there is a factor of 1.5 difference. This shows that there is a significant driving force to use the modified I(r) value from the suggested values. When the bending load tee joint data are removed, there is only a slight effect on the curve and prediction ($1.2x10^6$ cycles with modified I(r) vs. $1.4x10^6$ cycles with toe failures and no bend load tee data).

4.7.8 Summary

Both the structural stress and equivalent structural stress calculation method have shown excellent correlation of fatigue failure location predictions and also acceptable calculation of cycles to first crack. It is important to appreciate that the quality of this prediction is constrained by the fact there is only one component test result for comparison. It is evident from the above fatigue life predictions using structural and equivalent structural stress master curves, that the predictions over-estimate the measured lives. Whether the component test failure is at the upper or lower end of the scatter band cannot be established.

Less error is evident in the equivalent structural stress fatigue prediction correlations compared with the structural stress parameter. A slight improvement in fatigue life predictions was achieved, particularly when using a toe failure mode master curve. It was also shown that sufficient merit exists to use a modified equivalent structural stress I(r) parameter. Subjectively, in this case when using the modified I(r) value the extra step to calculated the equivalent structural stress parameter is justified through the more accurate fatigue life predictions.

It is promising that there is only a small level of scatter in fatigue life predictions between the range of master curves used for the structural and equivalent structural stress and that they consistently predict the correct failure locations.

4.8 Yellow goods component analysis

To further validate and investigate the effectiveness of Structural Stress based fatigue life predictions, the method was applied to a welded component from a construction equipment manufacturer. The study explored the fatigue performance of a sheet steel fabrication for a backhoe loader excavating machine.

Figure 305: Backhoe loader - Front end loading shovel and a rear excavating arm

A backhoe loader has a wide range of applications including construction and agricultural use. It is a versatile vehicle consisting of an underlying tractor chassis with hydraulically powered attachments. There is a loading shovel at the front of the vehicle and an excavating arm to the rear (the backhoe), Figure 305. Major structural components are manufactured from strip sheet steel and fabricated using fusion welding.

The rear excavating arm is primarily used for digging and the removal of soil or other materials. The excavating arm is made up of a bucket and a two part articulated arm. The bucket is connected to the middle component known as the dipper. The boom component is connected to the dipper and rear of the vehicle chassis via an articulated joint. Two distinct loading modes experienced by the excavator arm are the cause of high stresses at welded areas making weld fatigue life prediction of this structure a major design consideration. The first is the digging operation, known as excavating, where material is dragged towards the machine and picked up (as opposed to lifting or pushing material away as in a dozer). Secondly, moving the arm and bucket with its contents to the left or right of the machine (about the articulated joint) is known as slewing. The hydraulic system consists of 3 ram actuators. The bucket ram is connected to the bucket and dipper and when extended, the bucket is scooped and filled with material. The dipper crowd ram is connected between the

dipper and boom to actuate the dipper arm movement. The final boom ram is connected between the boom and the vehicle chassis to alter the pitch of the boom.

The boom component was selected for analysis by the structural stress method. The boom is an intricate welded structure with a high dependency on strength and durability. At the same time, and as is the case of many industries, high raw material and labour costs are driving the emphasis towards cost-saving opportunities in order to maximise profit margins. Fortunately, due to the way the boom is fabricated and the materials used, there are a number of potential areas for optimisation. These include down-gauging (reduction in thickness) and up-grading (higher strength) materials and the removal of costly and time-consuming post-weld heat treatments. However, the impact of such changes on weld fatigue performance must be assessed. The availability of an accurate and efficient FE-based weld fatigue life prediction method would be highly beneficial in making that assessment.

4.8.1 Historic fatigue test data

A significant amount of work and resources are employed in the design of construction equipment. Weld fatigue life prediction is an expensive and time-consuming requirement that must be established for the engineer to have full confidence in the design. The boom of an excavating arm is a mature component. It has an efficient and effective design that has evolved through extensive previous research and development. The research work in this thesis is able to draw upon that previous experience and to build upon an existing database for the characterisation of fatigue damage hot spots [47].

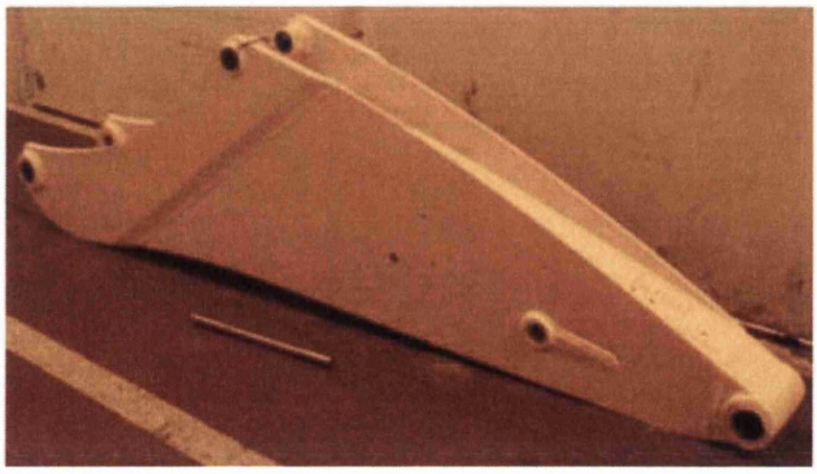

Figure 306: Backhoe loader excavating arm - boom component

The boom component selected is manufactured from strip and plate in a high strength, low alloy (HSLA), structural steel ranging in size from 6mm to 25mm thick, Figure 306. The sections are pressed and welded together using MAG fusion welding carried out at 30V, 300A and 11metres/min. Pivot bosses and castings are welded to the steel strip sections to facilitate transfer of hydraulic ram forces and loading through the structure via pins.

The structural integrity of the boom component is determined using a load-controlled fatigue rig. The in-field conditions are simulated in order to obtain accurate component failure locations but in a shorter time frame than expected service lives. The 2-part boom and dipper arm (in the non stress-relieved state) are positioned at a 90 degree angle so the dipper is at its maximum digging moment. Forces are applied to the excavating arm to replicate the digging (excavating load) and moving (slew load) of materials. Two hydraulic actuators are connected to the bucket to provide a force in two axes replicating the slew and excavating action.

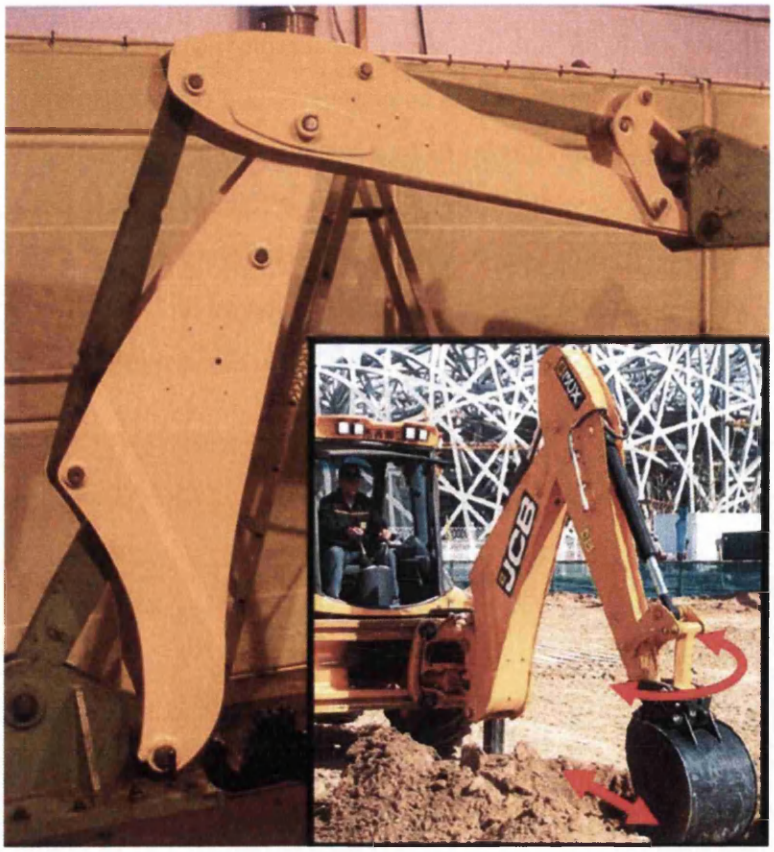

Figure 307: Component test configuration simulating in-field conditions (insert) consisting of excavating (digging and dumping of soil) and slewing (moving the bucket to the left or right)

Secondary parts of the structure, which are not the subject of analysis, are replaced with replica components and fixtures, Figure 307.

The purpose of the boom component structural stress analysis is to predict the hot-spot areas and weld fatigue failure locations. The structural stress profiles and damage summations calculated will be assessed through historic fatigue test data and known failure locations. As a boom component test programme was not completed in conjunction with this project, it is not possible to validate FE models against strain gauge readings or displacements. The weld crack locations are predicted on the basis of the historic test data along with a comparison of the number of cycles to failure.

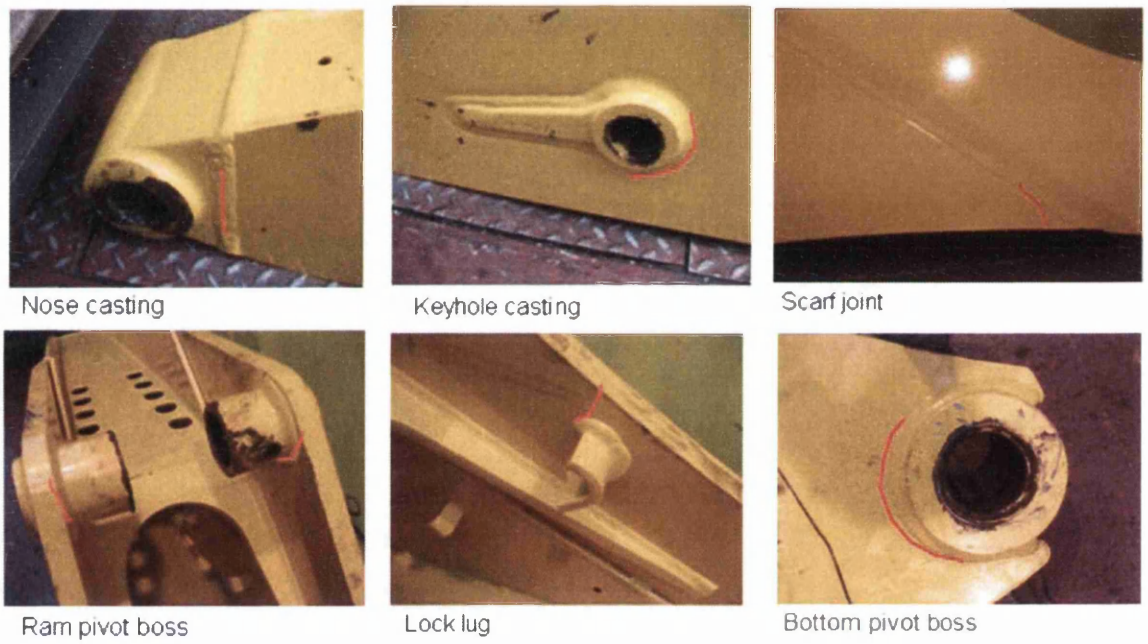

Figure 308: Boom component weld failure locations highlighted in red

The boom component has several weld details that require specific attention in the design and durability assessment. Six weld locations were selected for the structural stress analysis, Figure 308.

1. Nose casting to side plate butt weld throat
2. Keyhole casting to side plate weld toe
3. Scarf joint transition weld toe – scarf plate to side plate
4. Top pivot boss weld toe – boss tube to scarf plate
5. Lock lug attachment weld toe – attachment to scarf plate
6. Bottom pivot boss weld toe – boss tube to scarf plate

4.8.2 Boom component modelling

CAD geometry data for the boom component was imported into the FE software Altair Hypermesh. Subsequent modelling was required to create a weld seam as the imported data only contains the parent plate materials. Weld runs are not sketched or modelled at the design stage. Weld seam profiles were created acting as an interface and connection between the parent plates. These are critical in the accurate simulation of loading paths. The weld seam geometries were based on the final weld profile for the boom component. In reality the weld areas are complex and some basic simplification of the weld geometry is made in order to create a representative model within a reasonable time scale. This is feasible and a necessity since two components fabricated by the same operator can often have slightly different weld seam appearances. A finite element mesh was generated using 8-node solid brick elements for representation of the boom structural parts and weld runs using the Altair Hypermesh software package. Subjective assumptions were made to eliminate minor details of the component geometry that were deemed not to have a direct effect on the FE results. Small locating holes (drilled threaded holes for attachments) and fixture alignment features (pressed locating indents) were removed from the parent plate materials: this is called defeaturing.

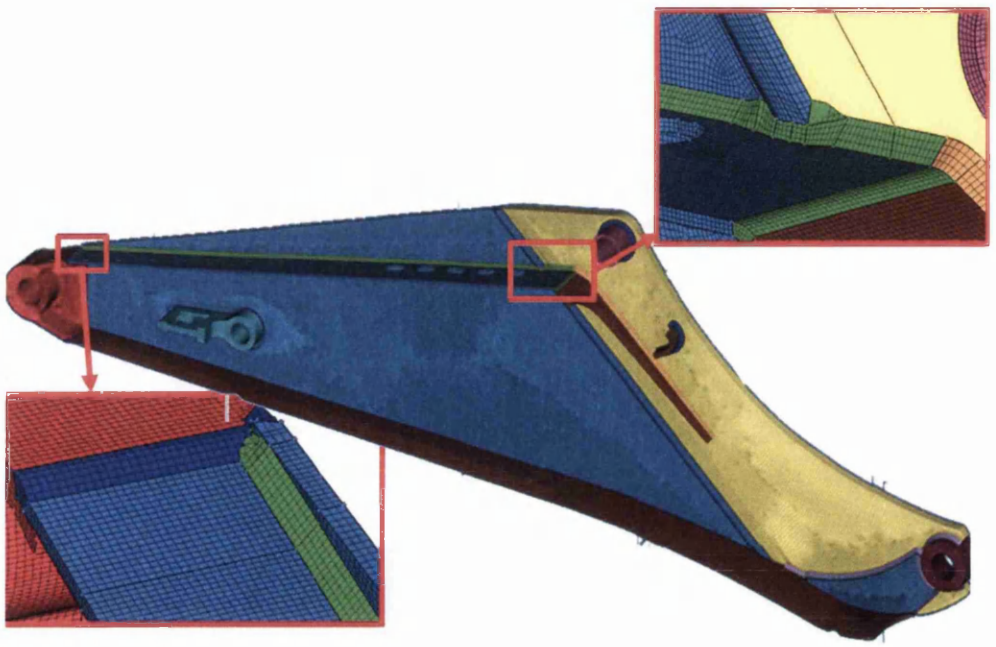

Figure 309: Component modelling - weld run mesh generation

A mesh of the boom was generated assuming some basic guidelines in order to develop an accurate model. A generic mesh element size of ¼t, where t is the material thickness, was used to represent bending through the component. In some cases this was changed to $^1/_3$t to minimise the total number of elements in the model. A $^1/_3$t mesh element size is considered the minimum through thickness mesh density. These parameters resulted in a global element mesh size of 2mm. A symmetric half model was meshed and mirrored to create the final meshed component with a total of 2 million nodes.

A significant amount of time and effort was given to the generation of the weld CAD geometry and mesh. It is clear that meshing the boom model was not an efficient step in the fatigue life prediction process. Further consideration will be given to this in the discussion in chapter 5.3.

4.8.3 Boom component FE stress analysis

The boom was chosen for the weld fatigue life prediction assessment. The whole excavating arm of the backhoe loader had to be modelled in the FE analysis. The bucket, dipper, hydraulic rams and pivot pins were modelled using simplified beam elements to minimise the solution effort required and time taken. The final excavating arm model is shown in Figure 310.

In the first load case, Figure 310, a force of 46.8kN is applied to the end of the bucket in the positive z-axis to simulate the loading of the excavating test arrangement. A force of 10kN is applied to the centre of the bucket along the negative z-axis direction to represent the contents and mass of the bucket. The pin joints connecting the bucket, dipper and boom components are modelled using beam and link elements in a similar manner to the test component in chapter 4.7. The use of a beam element as the pin with connections to the pivot boss using link elements in a spider web formation is a useful means of representing pin bending in a linear analysis. The end of the boom ram that is connected to the vehicle chassis has fixed displacements in the x, y and z directions. The pin in the bottom pivot boss is fixed in the y and z directions, while the boom is able to rotate around the pin. The centre of the pin is fixed in the x direction to stop it from sliding out of the boom assembly.

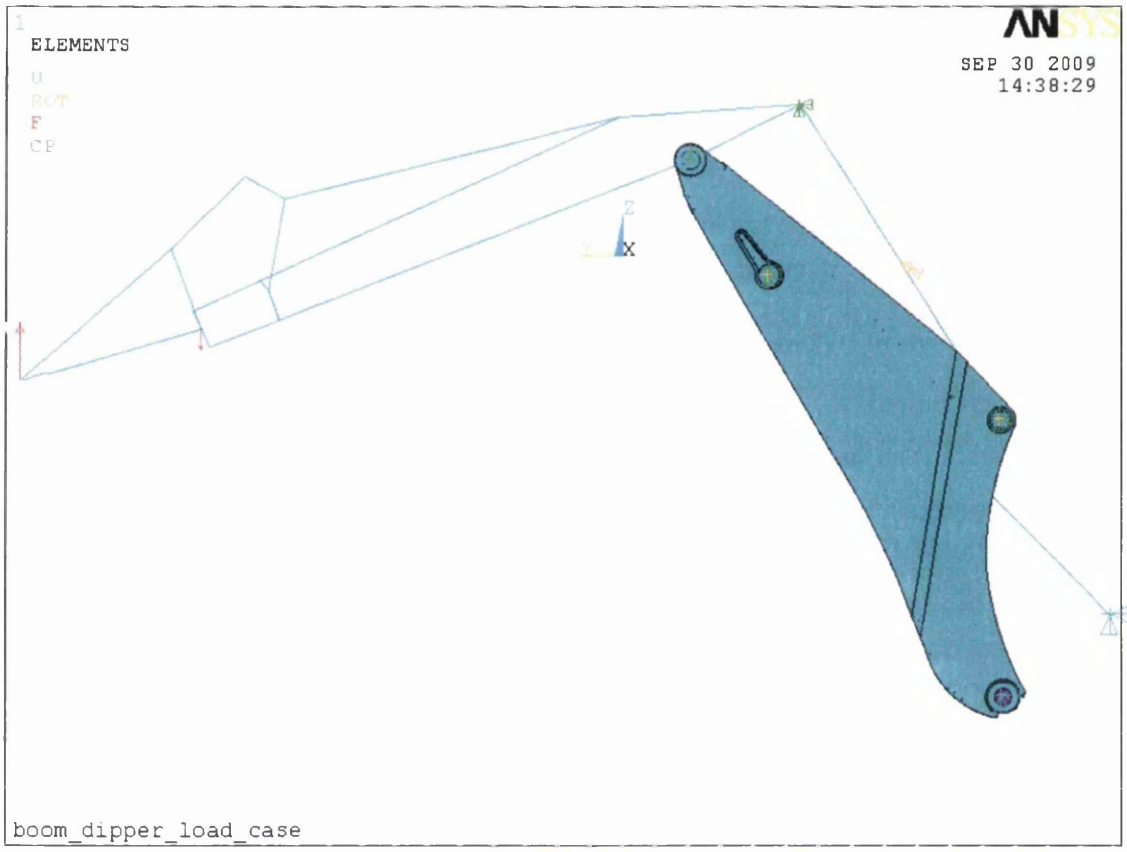

Figure 310: FE-model boom component boundary conditions - excavating load case

Due to the large model size, the FE software required modifications to the default solution parameters. An alternative matrix solution method was selected which is suggested for larger size models. The FE model only achieved a successful solution using a reduced integration method. The full integration method produced a file size of 30GB during solving and filled the computer hard drive causing the program to stop (crash). The maximum principal stress contour results are displayed in Figure 311. As the force is applied to the bucket, the dipper is displaced upwards and creates tensile stresses on the LHS edge of the boom. Stresses are approximately 120MPa in this region. The maximum stress is at the bottom pivot boss where the boundary conditions and beam elements are acting on the elements in the model. This is a localised singularity due to the boundary conditions and should be disregarded.

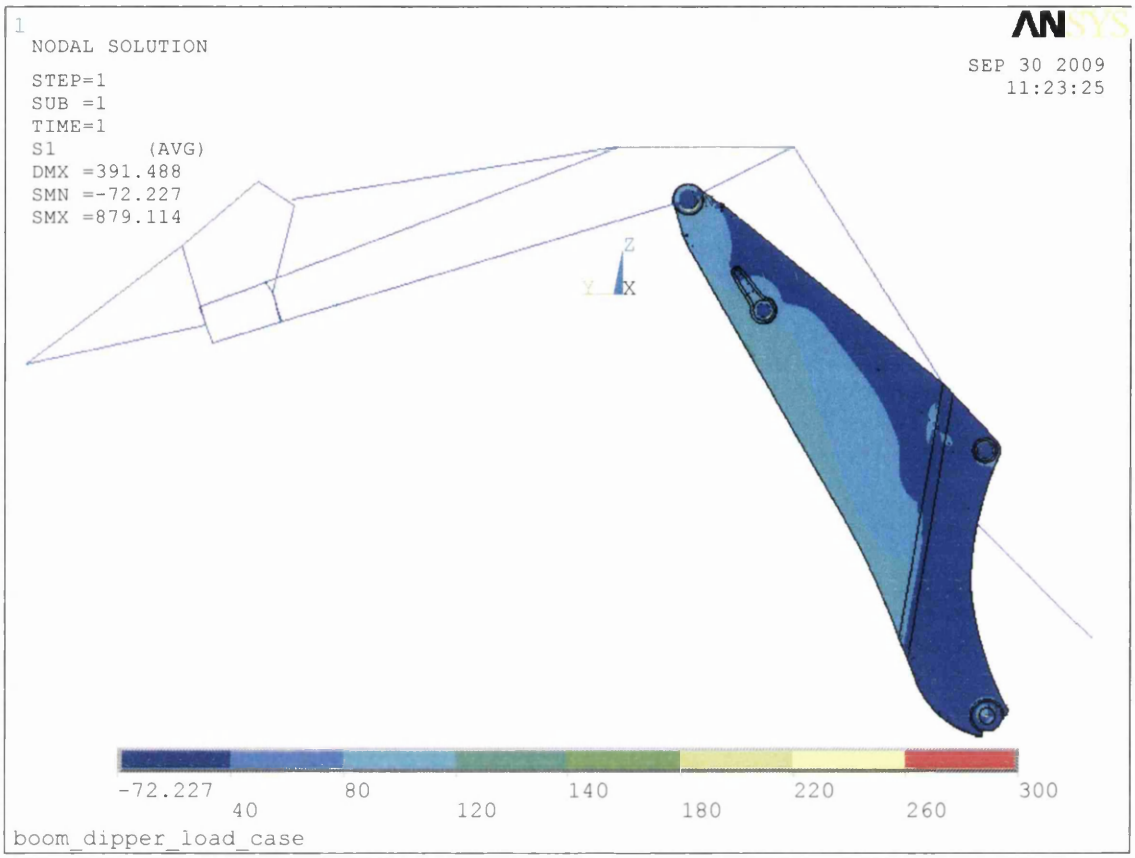

Figure 311: FE-model maximum principal stress (MPa) contour plot- excavating load

The minimum principal stress contour results are displayed in Figure 312. The minimum principal stress hot spots occur at the base of the boom towards the scarf joint region at approximately -100MPa. Similarly, compressive principal stresses occur at the top pivot boss weld and around the keyhole casting boss weld due to bending effects from the pin loading. The peak minimum principal stress at -1092MPa occurs around the keyhole casting but is purely a localised effect of the boundary conditions applied and should be disregarded as a singularity.

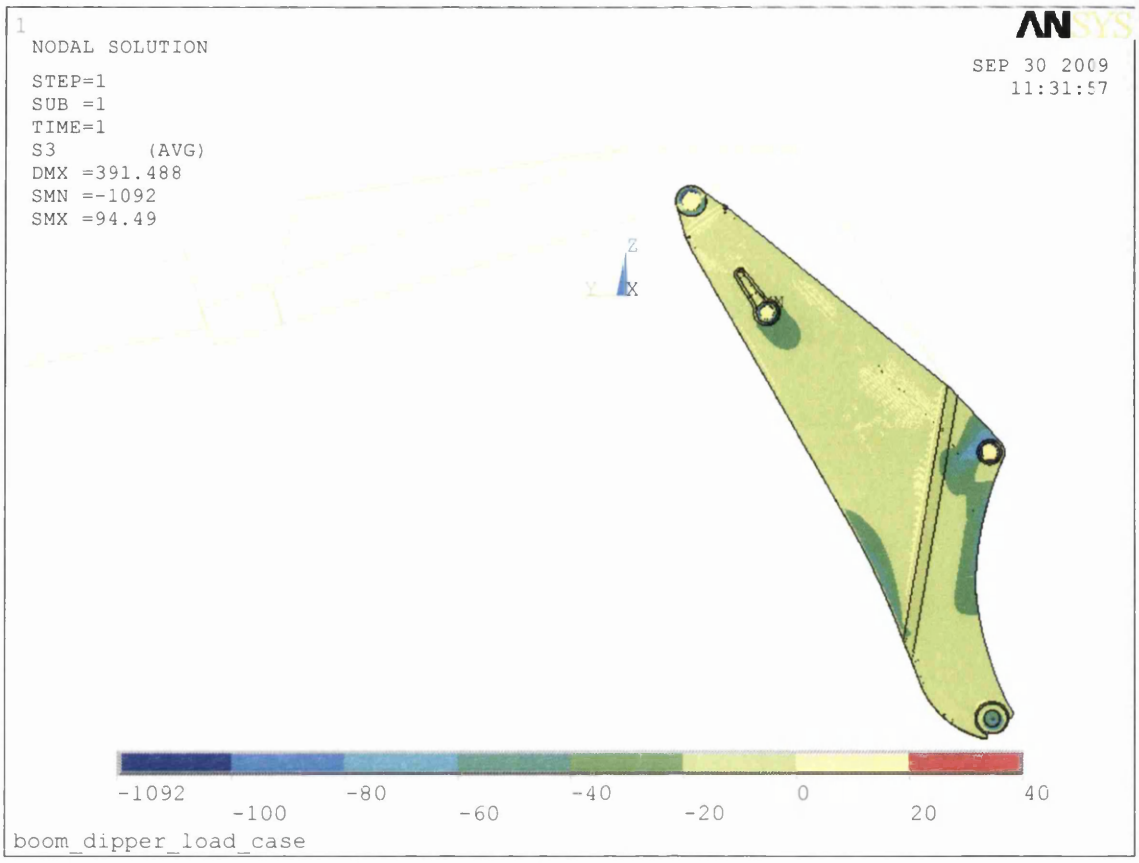

Figure 312: FE-model minimum principal stress (MPa) contour plot- excavating load

In the second load case, a force of 8.1kN is applied to the centre of the bucket tip in the positive x-axis direction (into the page in Figure 313) to simulate the loading of the slewing test arrangement. A force of 10kN is applied to the centre of the bucket in the negative z-axis direction to represent the contents and mass of the bucket. The remaining boundary conditions of the assembly are the same as the excavating load case described at the beginning of this section, chapter 4.8.3. The maximum principal stress contour results for the slew load are displayed in Figure 314. As the force is applied to the bucket, the dipper is displaced creating a torsion moment about the boom component. High tensile stresses are endured on the LHS scarf joint region of the boom. Stresses are approximately 125MPa. A side view of the component is also displayed in Figure 314 and highlights the displacement of the bucket in the positive x direction.

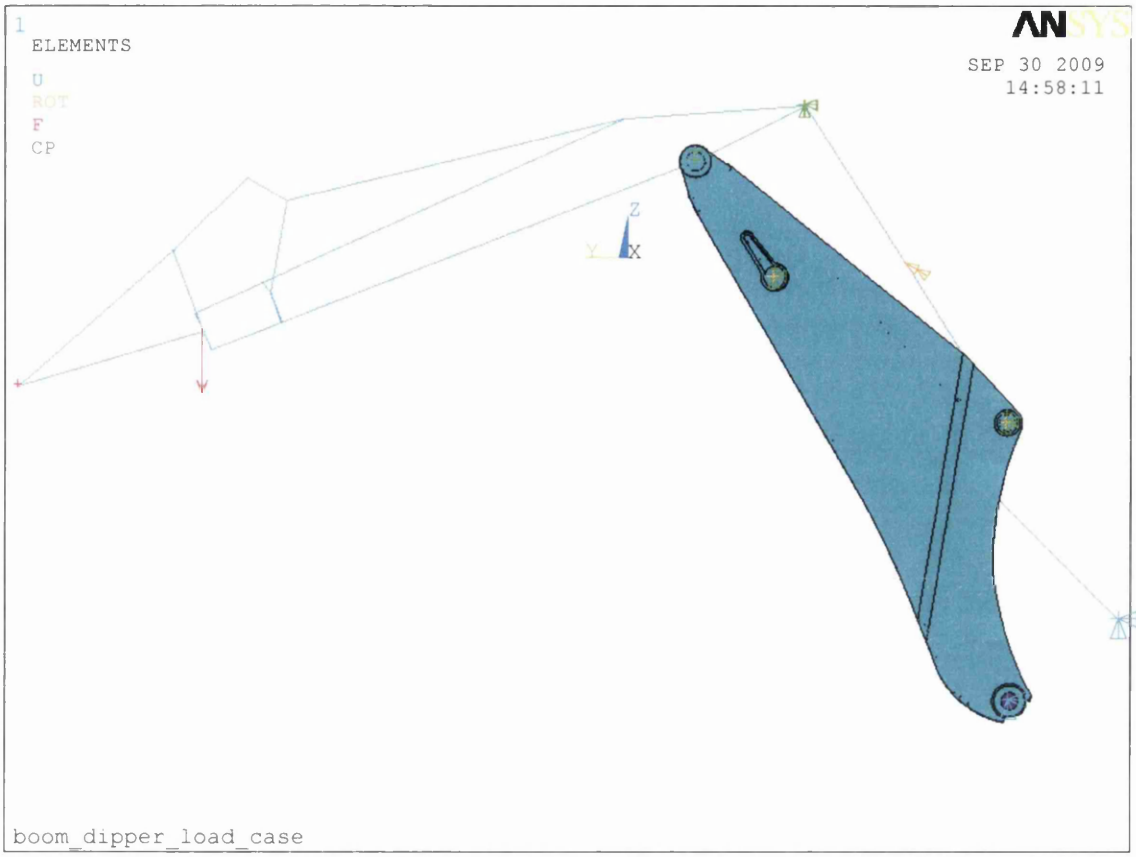

Figure 313: FE-model boom component boundary conditions - slew load case

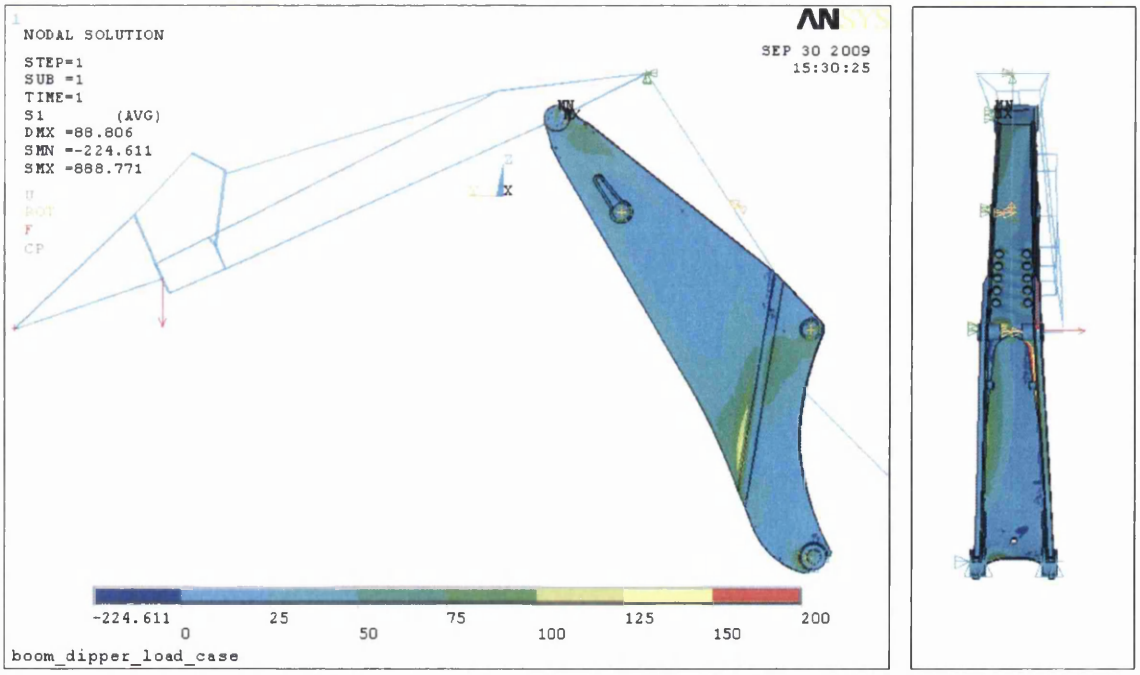

Figure 314: FE-model maximum principal stress (MPa) contour plot- slew load

The minimum principal stress contour results for the slew load are displayed in Figure 315. Compressive stress hotspots occur at the bottom pivot boss, the boom bottom edge towards the scarf joint and at the nose casting. Stresses in these regions are approximately -200MPa.

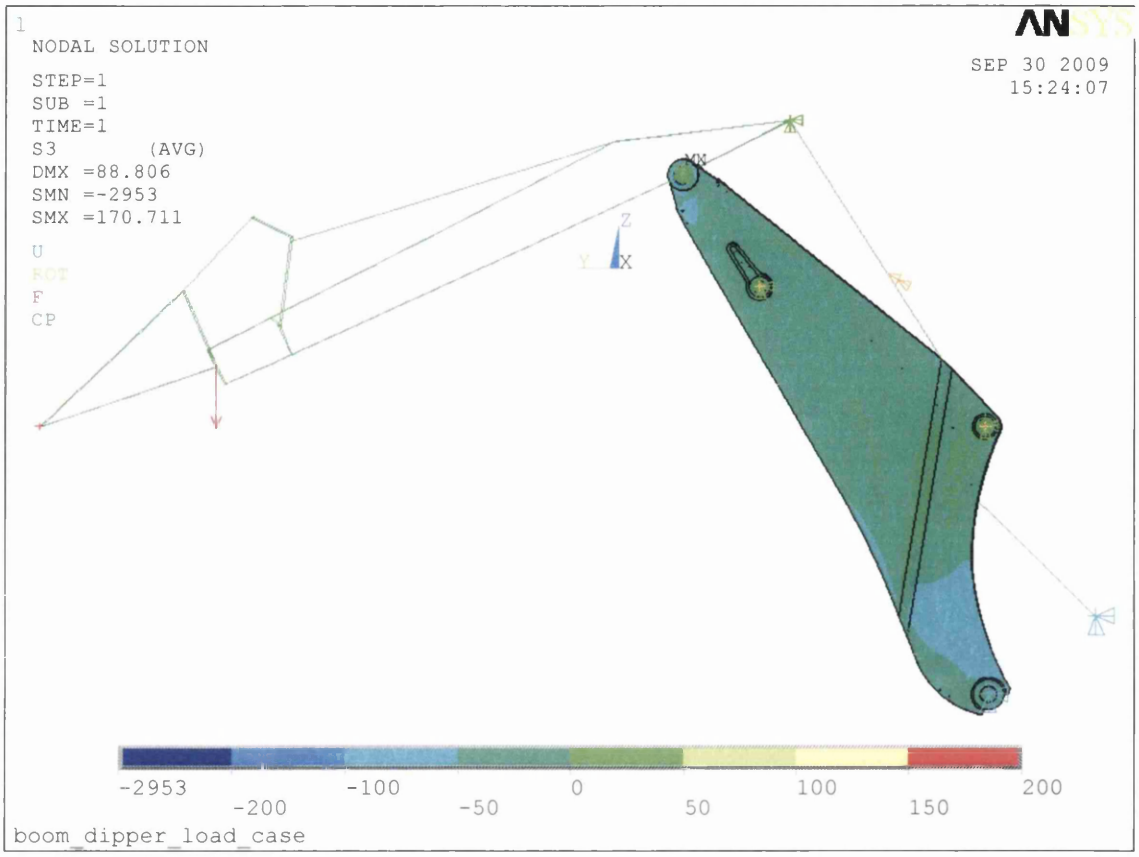

Figure 315: FE-model minimum principal stress (MPa) contour plot- slew load

Although it is not possible to have a direct comparison of FE strains against recorded measurements, the displacements at the bucket location (where the forces are applied) compare well with the actuator stroke measurements from the test data. This offers some assurance that the FE model and solution obtained is representative of the test conditions.

4.8.4 FE-based structural stress calculations

After completing the boom component stress analysis, the next step is to extract nodal forces and moments and calculate the structural stress per unit load factors at the weld regions of interest. This is a stress super-positioning step calculated for each load case applied. Given the large model size, it is a difficult task to manually extract the nodal forces and moments and input them into a spreadsheet calculation. Firstly, this is because there is a large amount

of data to input in a spreadsheet. Secondly, the selection of the necessary elements and nodes in the FE interface can be particularly time consuming and possibly sensitive to human errors. Manipulating and viewing the boom model is difficult and demands a significant amount of computer processing power to display the selected entities. The task of manually selecting the required FE information and determining the structural stress calculation was considered too time-consuming. A trial licence was obtained for the Safe Technology FE-Safe™ software and Verity® add-on module. Verity® is a commercially available post-processing FE software package for predicting the fatigue life of welded joints. Its underlying calculation method is based on the structural stress theory as discussed in this thesis. The Verity® module is used in this chapter for calculation of the structural stress (per unit load) profiles for welded areas of interest on the boom component. The software package requires an FE results file and definition of the elements on the weld crack plane and nodes on the weld toe path. The nodal forces and moments are automatically extracted from the FE model results file and a structural stress is calculated. An output solution is given with the calculated structural stress at each node of the weld toe.

Figure 316: Nose casting weld - structural stress weld line path at throat

The first weld region of interest is the boom nose casting to side plate weld shown in Figure 316. The structural stress damage parameter is calculated for a throat failure. The weld line path starts at the lower weld end continuing for 190mm until the weld run finishes,

highlighted by the red arrow. As a result of the test fixture configuration, the component assembly experiences high bending moments and torsional forces under loading. Thus, a complex multi-axial stress state is created at the weld crack plane. A bi-axial stress state along a weld can be detrimental to the fatigue performance, compared with a uni-axial stress [48]. Unlike previous calculation where coupons experienced a uni-axial stress with negligible shear stresses, here both normal and shear stresses were considered for the Yellow Goods production component. The FE-Safe Verity® software calculates both normal structural stresses and shear structural stresses on a weld crack plane. The structural stress profiles per unit load (calculated using Verity®) at the nose casting are displayed in Figure 317. The structural stresses (normal and shear (MPa)) are plotted on the y-axis against the distance along the weld throat on the x-axis. The slew load and excavating load stress profiles are displayed.

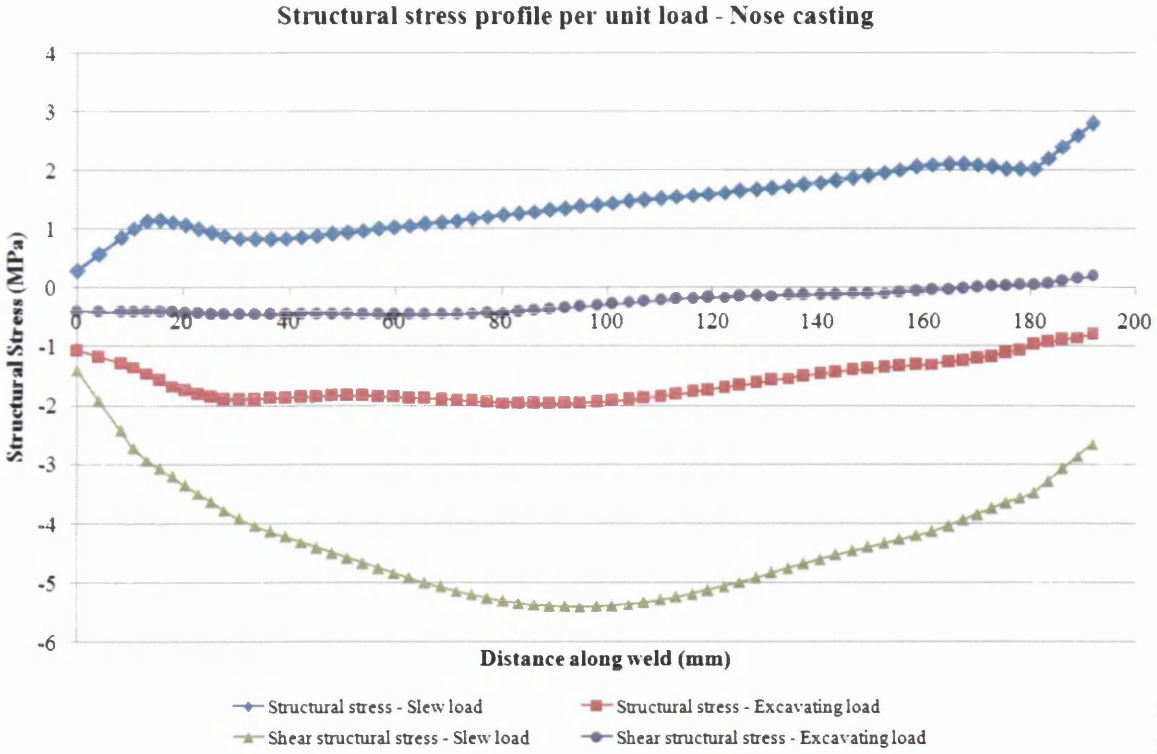

Figure 317: Nose casting weld throat - Structural stress profiles for slew and excavating load

A shear structural stress value of -5.5MPa is found under the slew load at 95mm along the weld line. This highlights the significance of shear stresses acting in the weld crack plane. Therefore, both normal and shear structural stresses should be considered when calculating the final stress state. The shear structural stress levels are greatly reduced when calculated for

the excavating load. This is expected, as forces are primarily acting through the weld, or normal to the weld crack plane. Only with the slew load is the component skewed and hence high shear stresses are experienced. Normal structural stresses under the slew load are found at the end of the weld line at 2.75MPa.

The crack path for the keyhole casting weld toe is defined in Figure 318. The path for the structural stress calculation begins at the tip of the casting, closest to the front of the boom, and works around the casting anticlockwise.

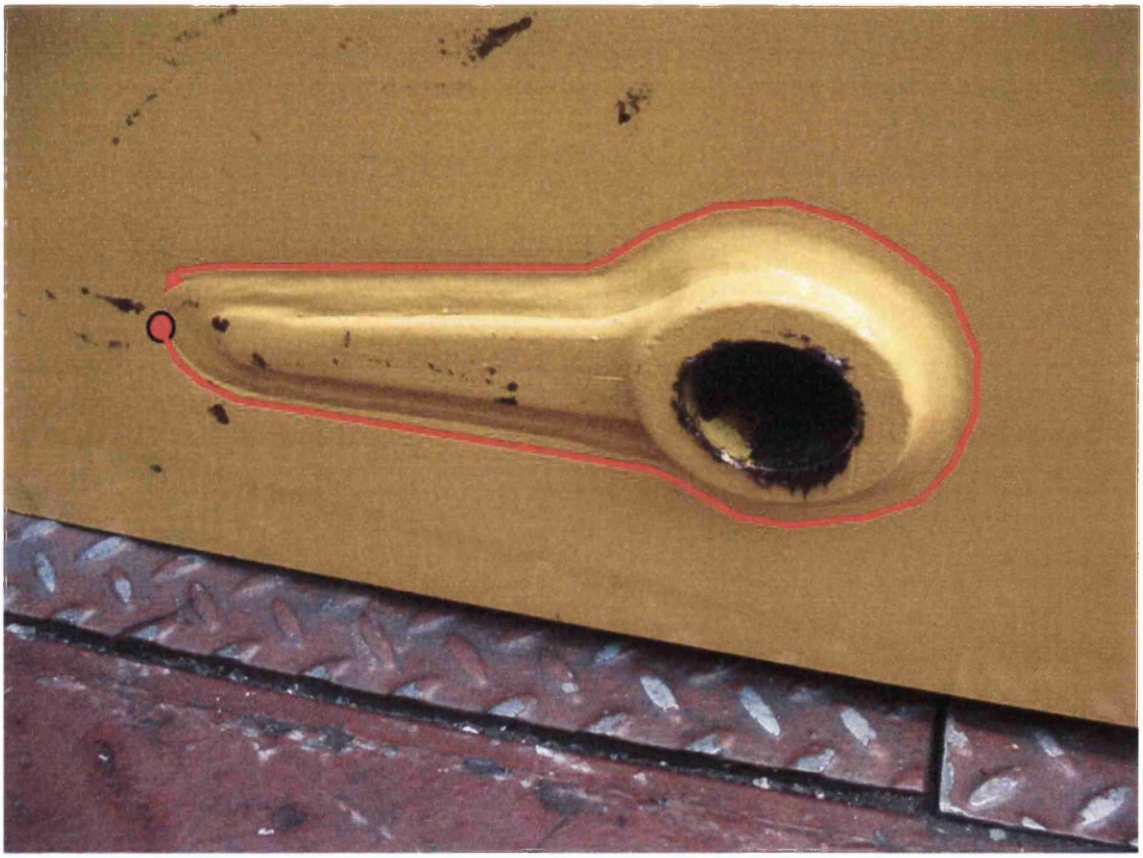

Figure 318: Keyhole casting weld - structural stress weld line path at toe

Normal and shear structural stresses are calculated for a weld toe failure. The structural stress profile per unit load at the keyhole casting is displayed in Figure 319. The structural stress (MPa) is plotted on the y-axis against the distance along the weld toe on the x-axis. The stress profiles for the slew load and excavating load are displayed.

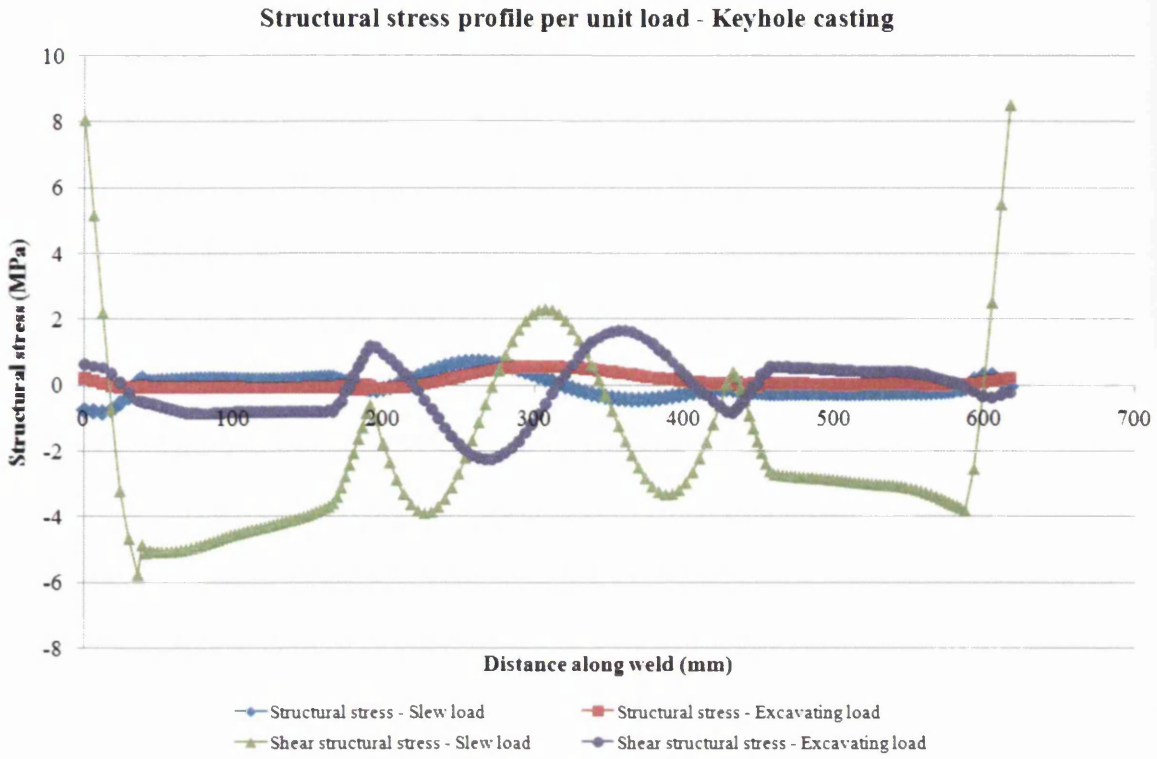

Figure 319: Keyhole casting weld toe - Structural stress profiles for slew and excavating load

The calculated normal-structural stresses are small and almost negligible compared to the shear-structural stresses experienced. This is true for both the slew and the excavating loads. High shear stress gradients are calculated around the circumference of the pinhole region from 170mm to 430mm along the weld toe path. Along this circumference, the shear structural stress fluctuates between -4MPa and 2MPa for the slew load and between -2MPa and 2MPa for the excavating load. This is due to the fact that the maximum shear stress plane is changing, with respect to the applied load, as the calculation travels along the weld circumference of the circular section of the keyhole casting. Similarly, high stresses are calculated at the tip of the keyhole casting, i.e. at the start and end of the weld calculation path. The shear structural stress fluctuates between -6MPa and 8MPa for the slew unit load. Compressive normal structural stresses of -0.8MPa occur just below the tip of the keyhole casting under the excavating load. The tip of the keyhole casting is not considered as a known failure location. In the FE model a uniform weld section is used and based on this crack area, it should be considered as a weld fatigue hot spot. The keyhole casting tip is where the weld seam run starts and finishes. At this location under manufacturing conditions, there might be a tendency from the operator to overfill or increase the amount of weld metal laid down, thus, increasing the size of the load-carrying area and reducing the risk of a fatigue crack failure.

Peak normal-structural stresses under the slew load of 0.7MPa (MPa per unit load) are found directly below the base of the casting hole (Bottom Dead Centre (BDC) where a pin is inserted) at 260mm along the weld toe path. A normal structural stress value of 0.5MPa is found at 305mm along the weld toe line (half way along the 610mm weld toe path) for the excavating load.

The crack plane for the scarf joint transition weld is defined in Figure 320, and highlighted by the red arrow. The path for the structural stress calculation begins at the base of the boom and scarf joint travelling up the full length of the boom. The normal and shear structural stresses are calculated for a front weld toe failure. The structural stress profiles for the slew and excavating unit loads at the scarf joint weld are displayed in Figure 321. The structural stress (MPa) is plotted on the y-axis against the distance along the weld toe on the x-axis.

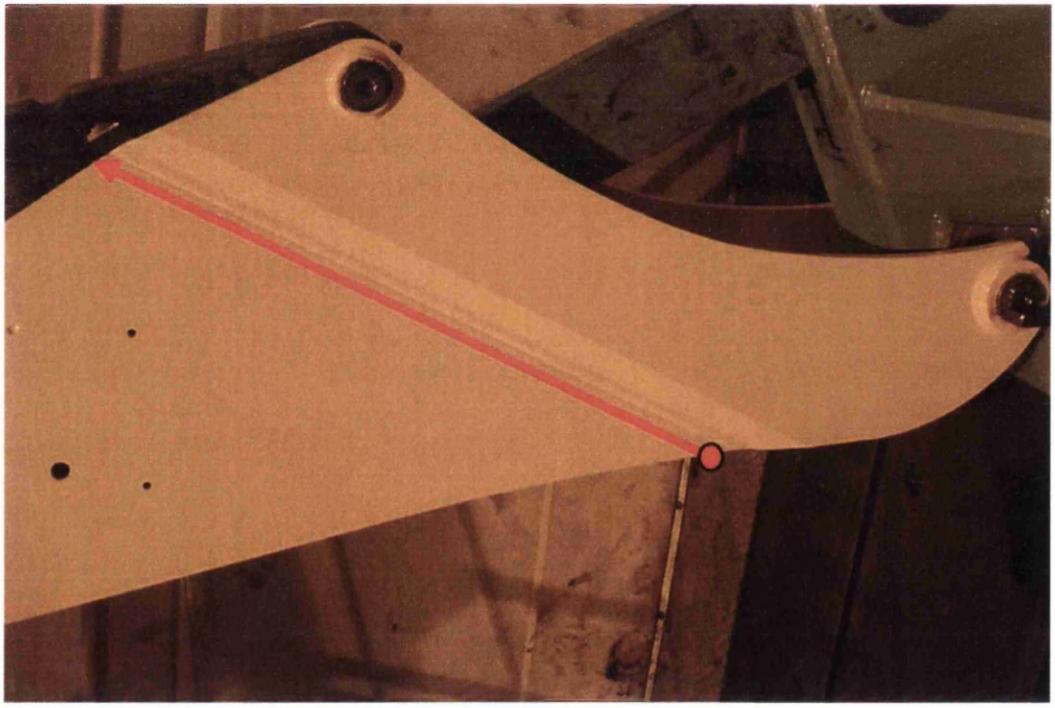

Figure 320: Scarf joint transition weld - structural stress weld line path at toe

It is evident from the structural stress profiles, that both the normal and shear slew load stresses are the most important and damaging of the two load cases (slew and excavating). A peak value of 8MPa for the shear structural stress is found at the base of the component. Peak normal structural stresses under the slew load of 15MPa (MPa per unit load) are found at 170mm from the boom base.

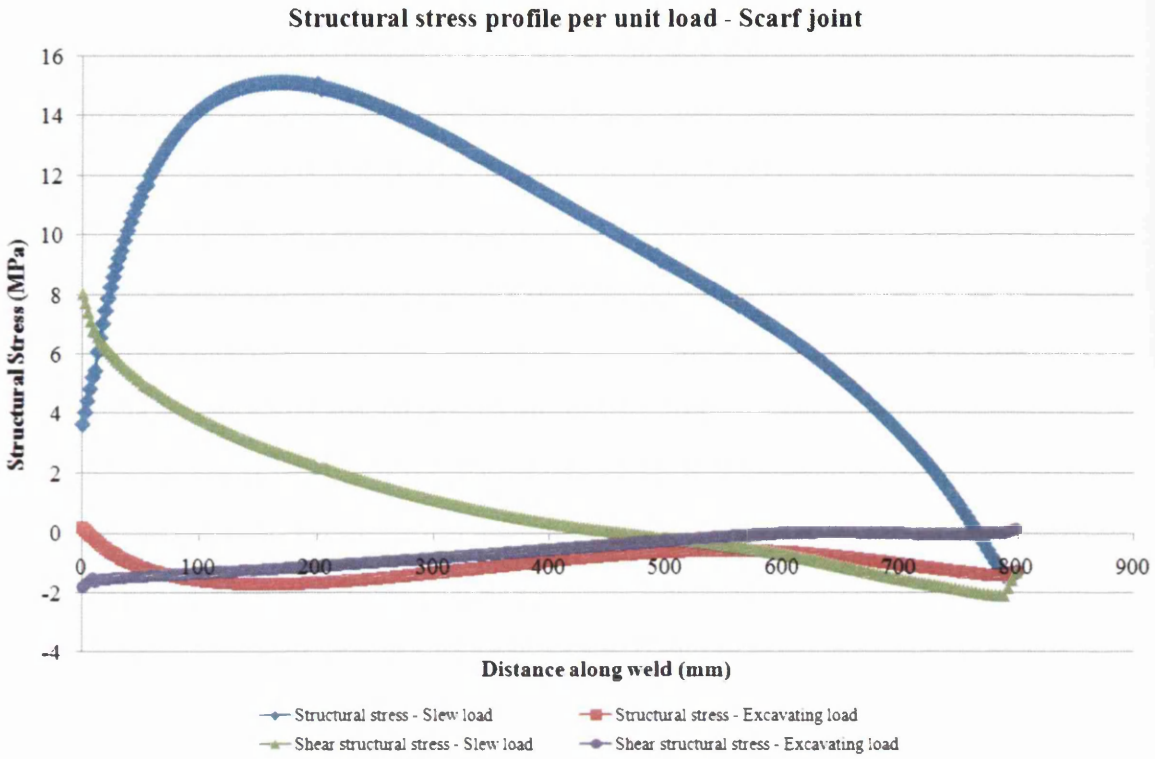

Figure 321: Scarf joint transition weld toe - Structural stress profiles for slew and excavating load

For the scarf joint excavating load, a peak compressive normal structural stress occurs at 150mm along the weld from the base of the boom with a value of -1.7MPa. The peak shear structural stress of -2MPa is found at the base of the boom component.

The crack plane for the top pivot boss (inside weld toe) is defined by the red arrow in Figure 322. The start point of the structural stress is 90 degrees from the TDC of the weld seam. The weld line travels around the weld boss toe clockwise (the dashed weld line in Figure 322 is hidden by the weld boss tube). The normal and shear structural stress parameters are calculated for the inside weld toe failure. This is repeated for the slew load and excavating load case.

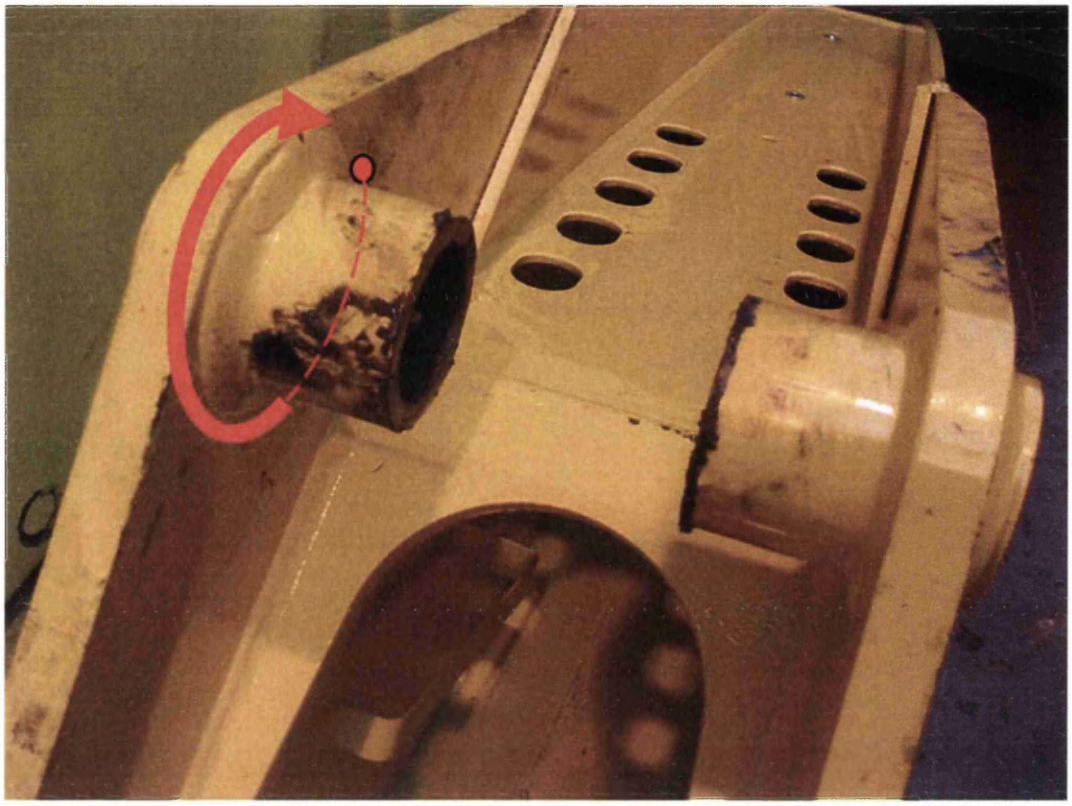

Figure 322: Top pivot boss weld - structural stress weld line path at inside toe

The structural stress profiles per unit load at the top pivot boss weld toe are displayed in Figure 323. The structural stress (MPa) is plotted on the y-axis against the distance along the weld toe on the x-axis. The structural stresses, normal and shear, appear very abrupt and sensitive to the calculation. The variation in stresses is worse for the slew load case. There is no explicit reason as to why this is found. One observation is the low stress levels calculated in comparison with the other weld crack planes in the component. The top pivot boss is an area that experiences high stresses from the load transferred through the pin joint. The onset of failure in this location is recorded early on in the fatigue life of the component, and always before the scarf joint weld. However, the scarf joint weld calculates significantly higher unit load stresses. It is possible that a more representative pin to component contact model is required to calculate the structural stress profiles experienced in this area. This aspect was researched in the test component analysis in chapter 4.7. It was established that a linear beam element model was sufficient to simulate the pin to boss contact. The fatigue test arrangement consisted of a fully tensile uni-axial load. For the production component analysis, complex bi-axial stress states and loading exists, and this assumption might not be satisfactory.

Under the slew loading, normal and shear structural stress values of 0.7MPa and -0.4MPa occur at 135mm round the weld toe. This is at approximately 140 degrees around the boss weld toe from TDC. Peak structural stresses for the excavating load occur, as per the slew load, at approximately 140 degrees around the weld toe from TDC with a value of -0.3MPa and 0.1MPa for the normal and shear structural stresses respective. High normal structural stresses are experience for both slew and excavating loads at the start of the weld path calculation, at 0mm (45 degrees from TDC).

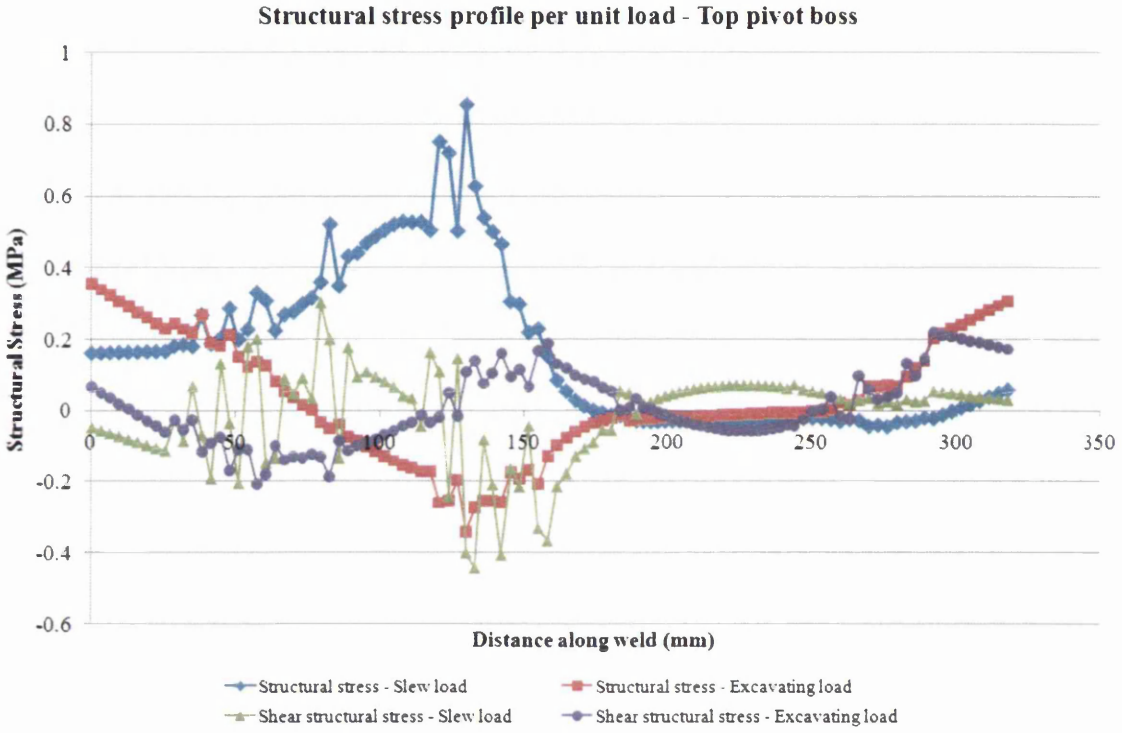

Figure 323: Top pivot boss weld toe - Structural stress profiles for slew and excavating load

The structural stress profile has been calculated for the weld toe at the lock lug attachment. The weld toe crack plane is defined by the red arrow in Figure 324. The structural stress, normal and shear, profiles per unit load for the slew and excavating cases are displayed in Figure 325. A plan view of the weld toe path is shown, insert in Figure 325, and typical weld failure crack locations are highlighted by the black underline. The structural stress (MPa) is plotted on the y-axis against the distance along the weld toe on the x-axis.

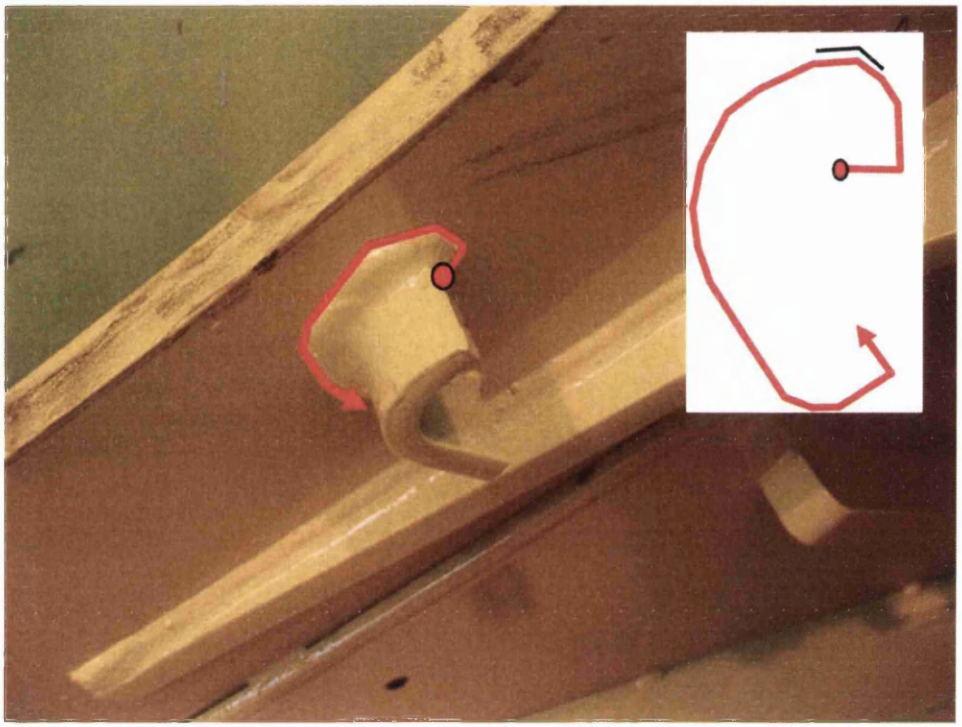

Figure 324: Lock lug attachment weld - structural stress weld line path at toe

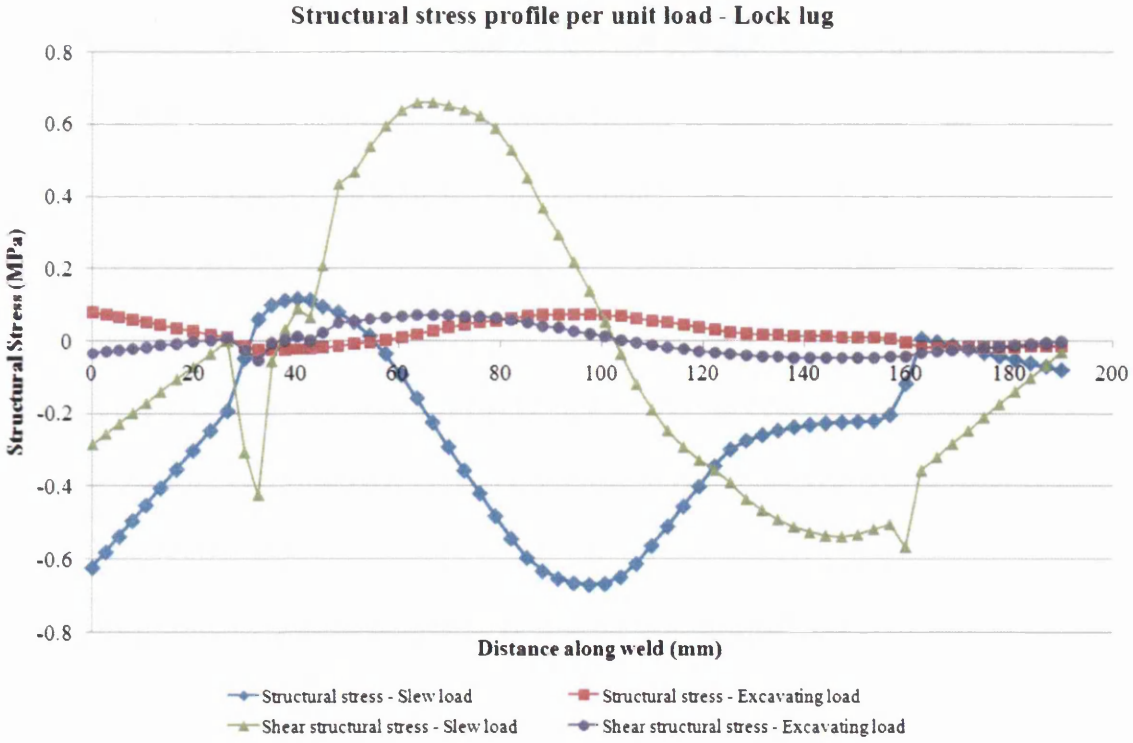

Figure 325: Lock lug weld toe - Structural stress profiles for slew and excavating load

Normal and shear structural stresses of -0.6MPa and -0.3MPa are found at the start of the weld line crack path under the slew load. The values at these locations are 0.08MPa and

0.07MPa respectively. The non-load-bearing attachment failure locations are recorded at approximately 20mm up to 60mm along the weld toe path. From 20mm along, high stress gradients are calculated for the slew load normal and shear structural parameters. This is a result of the high forces and stresses experienced by the load-carrying parent plate material that the lock lug is welded to. The parent plate is constrained at the base and an offset load is applied to the opposite end, hence, the plate is attempting to skew and twist. Despite the fluctuations, the stress levels are considerably lower than the levels seen in other weld crack planes. The calculated structural stresses for the excavating load are very low and almost negligible.

The final structural stress profiles are calculated for the weld toe around the bottom pivot boss. The weld toe crack plane around the pivot boss is indicated by the red arrow in Figure 326. This is the outside weld toe of the pivot boss where recorded failures originate.

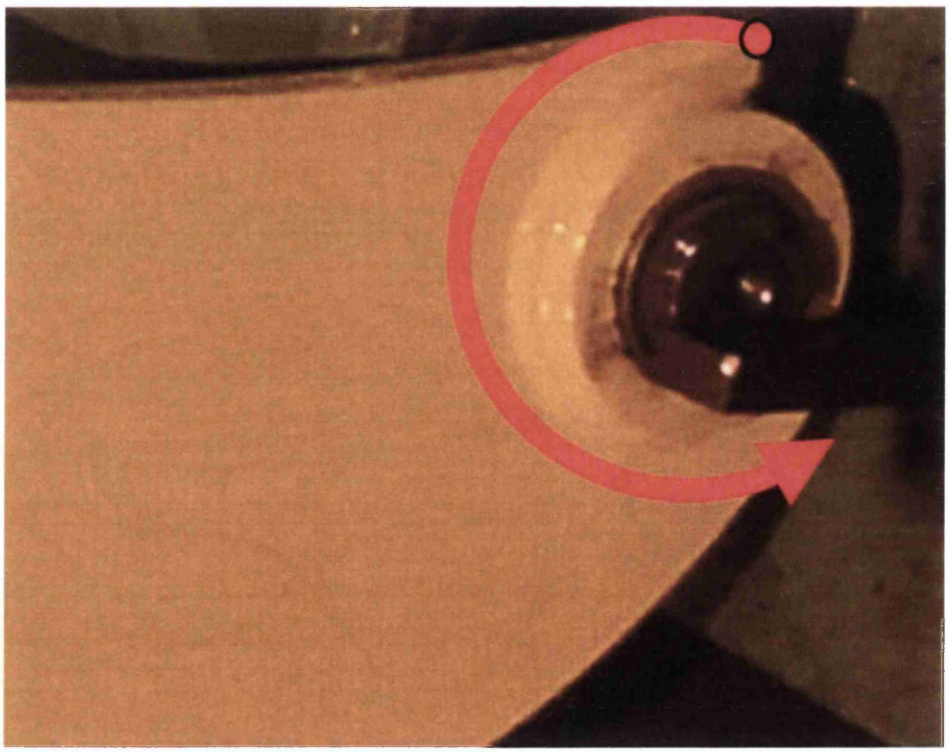

Figure 326: Bottom pivot boss - structural stress weld line path at outside toe

Normal and shear structural stress profiles are calculated for the slew and excavating load case, displayed in Figure 327. The structural stress (MPa) is plotted on the y-axis against the distance along the weld toe on the x-axis.

As observed in previous weld runs, the excavating structural stresses are very low and the slew structural stresses are the most damaging. Peak normal structural stresses are calculated for the slew load at 100mm along and at the end of the weld seam with values of -11MPa and 11MPa respectively. The high stress ranges are expected considering the fixed constraint pin in the boss and the high bending moment experienced through loads applied to the bucket end. The slew load shear structural stress fluctuates between 3MPa at 75mm and -5MPa at 160mm along the weld run.

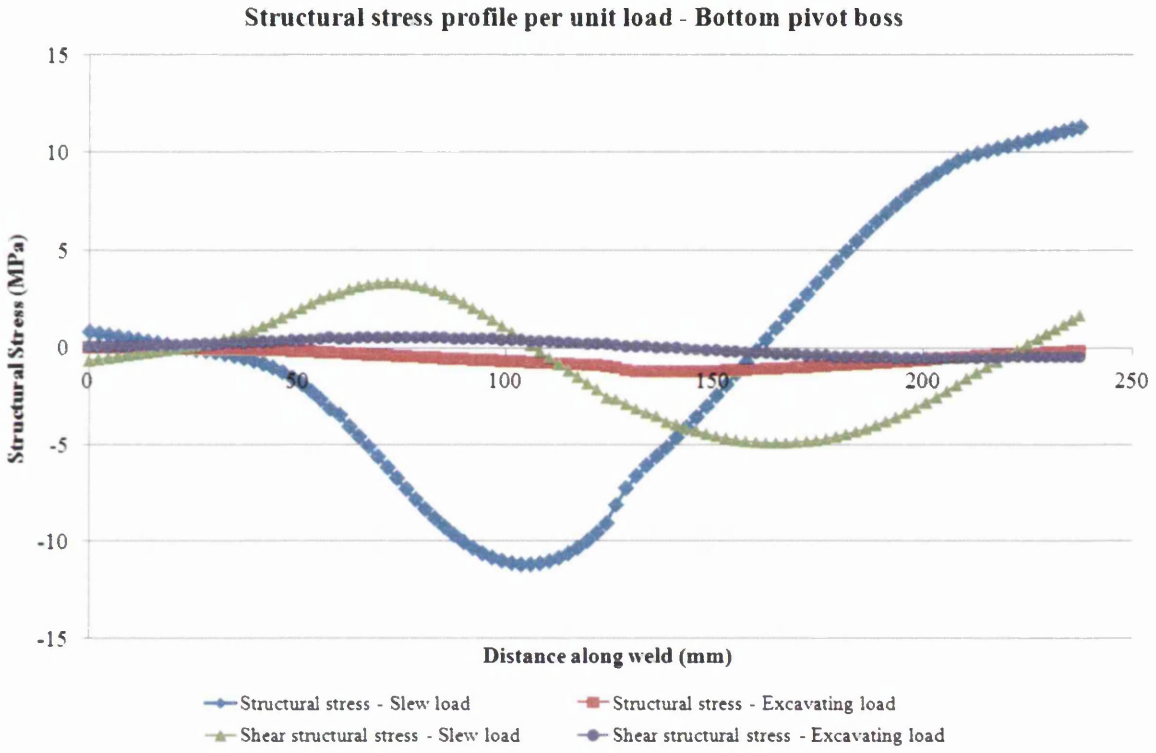

Figure 327: Bottom pivot boss weld toe - Structural stress profiles for slew and excavating load

4.8.5 Structural stress fatigue calculations

On the basis of the structural stress super-positioning for the elastic analysis excavating and slew load cases, damage calculations and fatigue life predictions can be obtained. The unit load structural stress calculations in chapter 4.8.4 illustrate that the component experiences considerable normal and shear structural stresses. Multi-axial fatigue can often be a vital damage mechanism easily overlooked in analysis environments. To predict realistic fatigue lives, the structural stress damage parameter must measure normal and shear stresses. The Von Mises damage hypothesis [49] is used to calculate a final 'structural stress' damage parameter. Fatigue life predictions calculated consider crack propagation into the plate

material (normal) and also in-plane crack propagation (shear). The Von Mises hypothesis used to calculate the total structural stress is defined as:

$$= \sqrt{(\Delta\sigma_s^2 + 3\Delta\tau_s^2)} \qquad \text{Eq 4.8.1}$$

$\Delta\sigma_s$ = Normal structural stress range
$\Delta\tau_s$ = Shear structural stress range

The Von Mises structural stress summation was calculated for the slew and excavating load case to give two total structural stress unit load values. The summarised unit load values are used in the elastic scaling and super-positioning fatigue calculation.

Structural stress based fatigue life predictions were obtained for each weld path:

1. Nose casting to side plate butt weld throat
2. Keyhole casting to side plate weld toe
3. Scarf joint transition weld toe – scarf plate to side plate
4. Top pivot boss weld toe – boss tube to scarf plate
5. Lock lug attachment weld toe – attachment to scarf plate
6. Bottom pivot boss weld toe – boss tube to scarf plate

The fatigue damage calculations and predictions are based on Miner's hypothesis as discussed in chapter 4.7.5. The fatigue calculations were carried out assuming the linear summation of both the excavating damage interaction, D_{exca} and the slew loading damage, D_{slew}. The number of repeats, $D_{exca}+ D_{slew}$, is calculated along each of the boom weld runs of interest.

The calculated number of repeats of $D_{exca}+D_{slew}$ load spectrum at the nose casting weld is displayed in Figure 328. The number of repeats is plotted on the y-axis against the distance across the crack plane (mm) of the nose casting weld on the x-axis. The minimum number of repeats is 339,145 at 90mm along the weld toe. The master curve used in the prediction is that generated from coupon throat failures and distorted solid models.

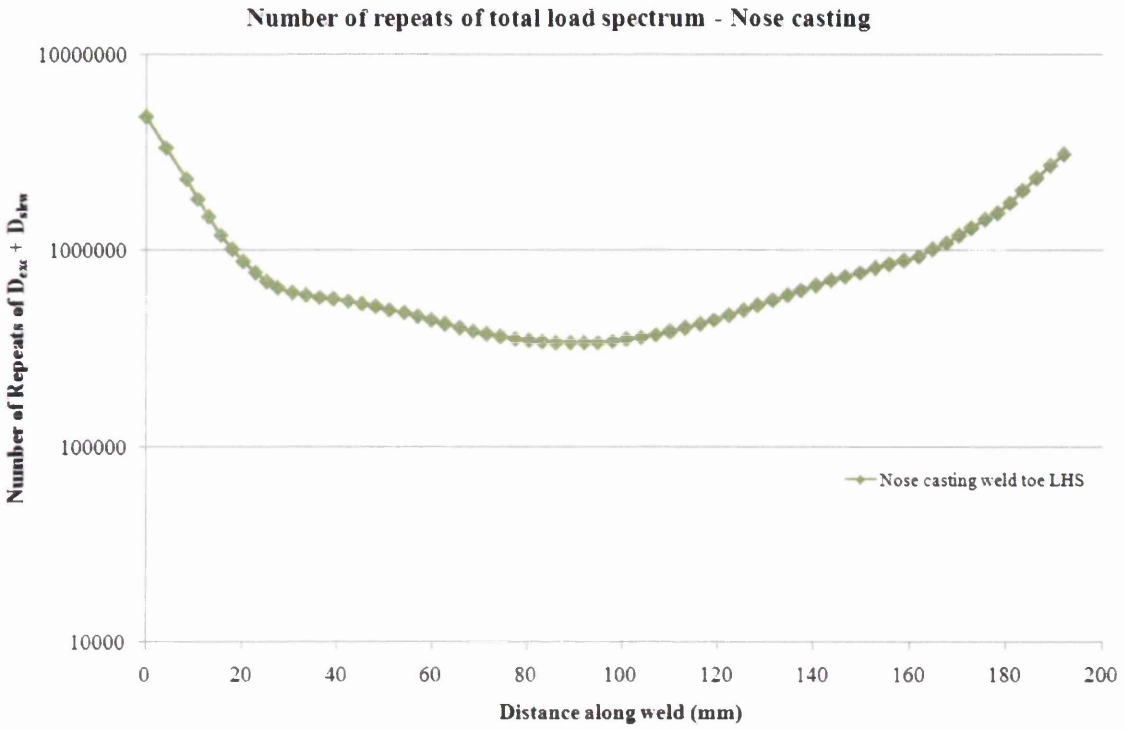

Figure 328: Nose casting weld throat – Number of repeats of loading D_{exca}+D_{slew}

The minimum number of repeats at 90mm correctly identifies the crack location recorded in the fatigue test data, towards the centre of the weld run.

The fatigue life prediction of the number of repeats at the keyhole casting weld is displayed in Figure 329. The number of repeats is plotted on the y-axis against the distance around the crack plane (mm) for the keyhole casting weld on the x-axis. The most damaging area calculated is approximately 265mm along the weld toe path with a value of 210,786 repeats. The keyhole casting tip also calculated a similar low fatigue life prediction of 226,714 repeats. At this region, there is a sudden difference in predicted lives from the three previous, and following nodal calculation points. The predicted lives change from 44 million cycles to the stated 226,714 cycles over a relatively short distance. It is possible that the prediction is erroneous and sensitive to the calculation method. Further to this, there were no historic test results recording a weld fatigue crack or failure in this region.

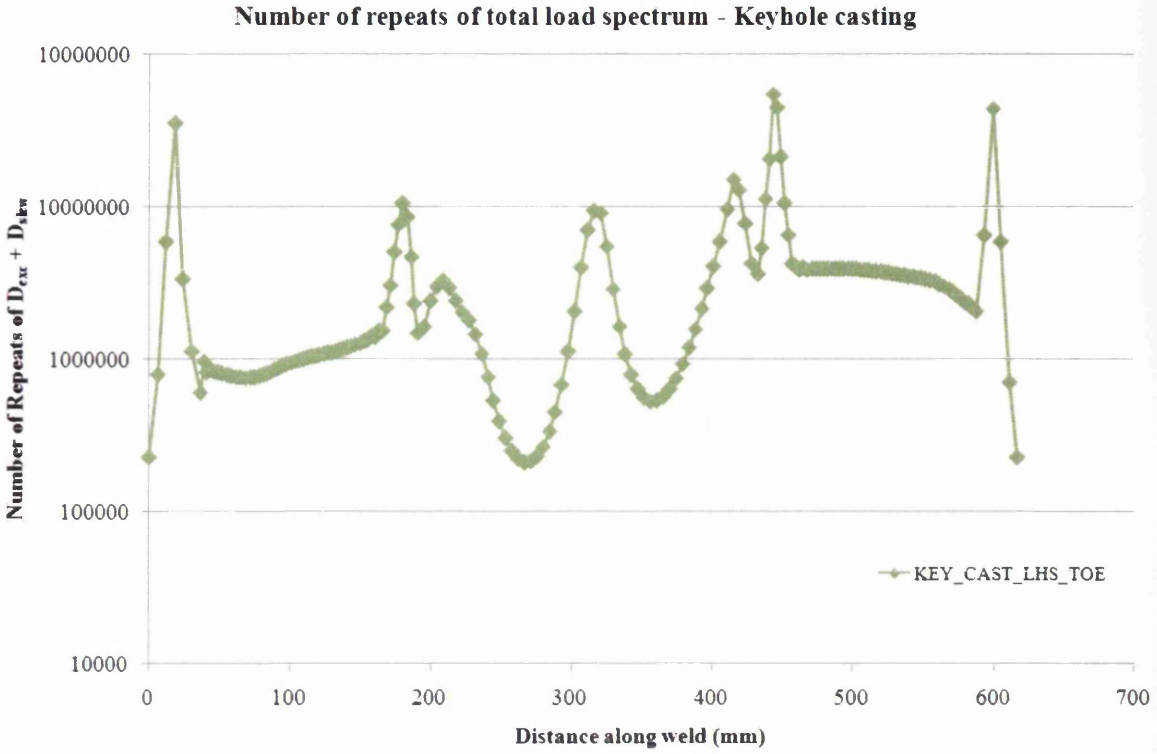

Figure 329: Keyhole casting weld – Number of repeats of loading $D_{exca}+D_{slew}$

Two prominent peaks are calculated at approximately 180mm and 440mm along the weld toe. At these locations the weld run path moves away from the straight weld run and travels around the circumference of the pin hole section on the keyhole casting, Figure 322. As the maximum shear plane changes angle along the weld path, a lower shear stress is calculated. The two troughs at 200mm to 300mm, and 300mm to 400mm are the lower and upper halves of the weld run around the pin hole section. The crack location identified directly beneath the pin hole on the keyhole casting correlates with recorded failures from component fatigue tests.

The calculated number of repeats ($D_{exca}+D_{slew}$) for the scarf joint transition weld toe is shown in Figure 330. The number of repeats is plotted on the y-axis against the distance along the crack plane (mm) for the scarf joint weld on the x-axis. The calculated location with the minimum number of repeats is at approximately 130mm up from the base of the boom component with a value of 125,688.

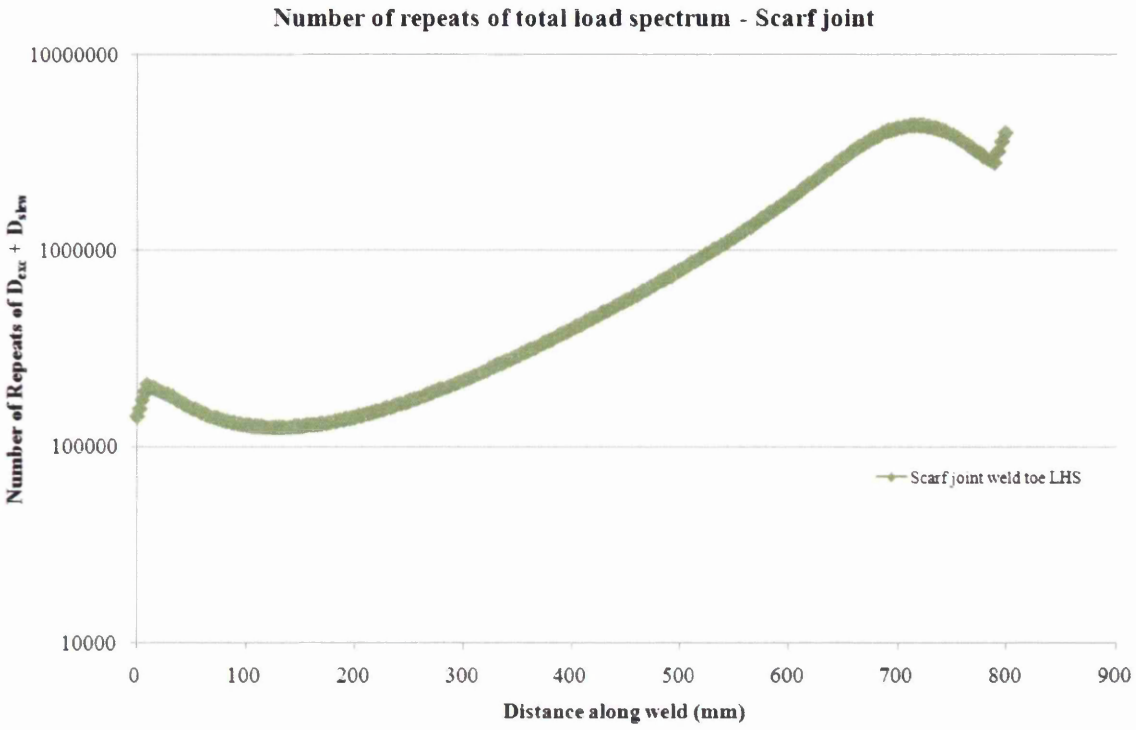

Figure 330: Scarf joint transition weld – Number of repeats of loading D_{exca}+D_{slew}

A low fatigue life is calculated along the 100mm to 200mm section of the scarf joint transition weld. This appears mainly because of the normal structural stresses experienced from the slew load. At the start of the run (0 to 75mm), an underlying cross member is welded, stiffening the section and thus able to carry the load more adequately. As the slanting transition weld is sloping towards the restrained bottom pivot base, stress levels increase at the lower end of the weld run due to the increase in the bending moment i.e. the weld is located further away from the applied load and a greater mechanical advantage is created. This highly stressed area was also recorded in the maximum principal stress plot of the boom component analysis in Figure 314.

The top pivot boss weld calculated a minimum number of repeats at approximately 240 degrees around the weld from TDC with a value of 123,198,501 (where TDC is at 233mm along the weld path). The predicted number of repeats for the top pivot boss is shown in Figure 331. The number of repeats is plotted on the y-axis against the distance along the crack plane (mm) on the x-axis. The location of the minimum number of cycles (240 degrees from TDC and 130mm along the weld path) correlates with the fatigue test failures recorded. The predicted life of 123,198,501 repeats is much greater than that recorded in the component test, approximately 82,000 cycles. This is a serious error in the calculation, and although the

fatigue prone areas are correctly identified, the results suggest the FE model does not correctly capture the loading and pin component interaction seen in the test.

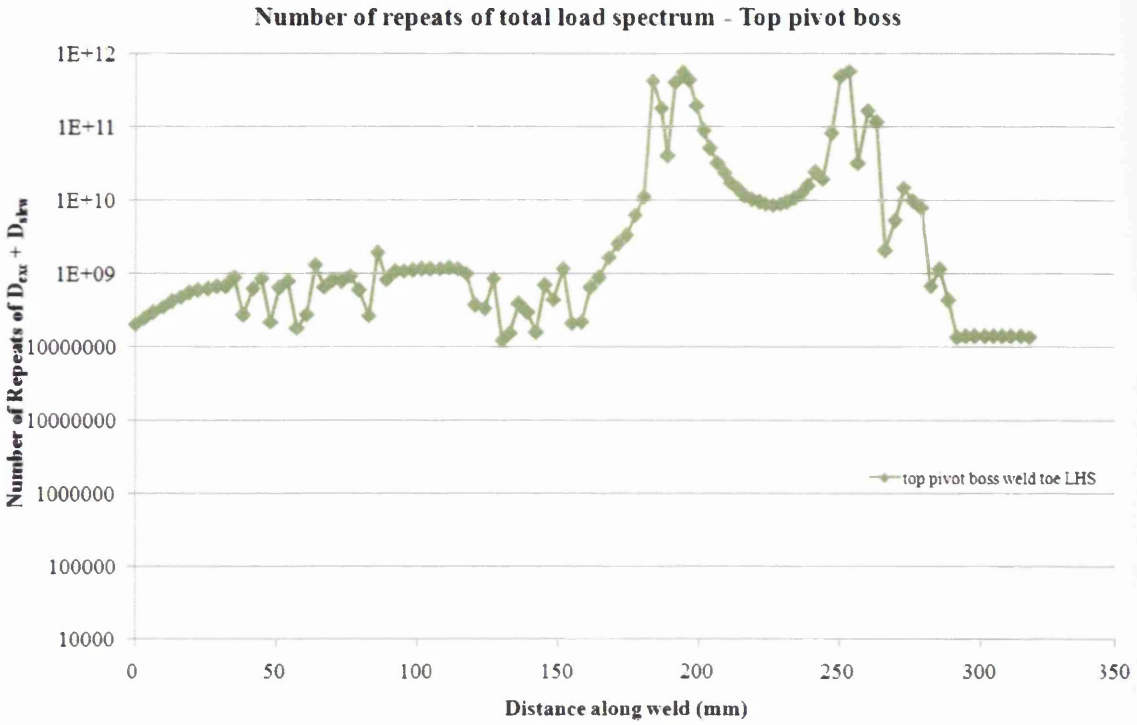

Figure 331: Top pivot boss weld – Number of repeats of loading D_{exca}+D_{slew}

The top pivot boss fatigue life predictions in Figure 331 and the structural stress calculations in Figure 323 both display very sensitive and irregular profiles. It is evident from the results that the top half of the boss circumference, the 150mm to 300mm section along the weld path, calculates a higher fatigue strength than the lower section at 0-150mm. Within the lower and upper circumference areas, further erratic peaks and troughs exist (at 35mm to 80mm and 120mm to 150mm along the weld path). It is possible these appear due to sensitivity in the calculation method when only low forces and moments are transferred through the weld. In other weld crack planes analysed, a smooth structural stress and fatigue prediction was calculated along the weld. When a large step or jump in the calculations did exist, the change was transitional and could be identified easily, such as a modified weld path direction. Despite this, there is no clear explanation for the small peaks and troughs in the top pivot boss calculations. The most concerning point to consider is the very high fatigue life calculated in the area where known failures exist early on in the component life.

The number of repeats (D_{exca}+D_{slew}) calculated for the lock lug weld toe is shown below in Figure 332. The number of repeats on the y-axis is plotted against the distance around the lock lug weld toe (mm) on the x-axis.

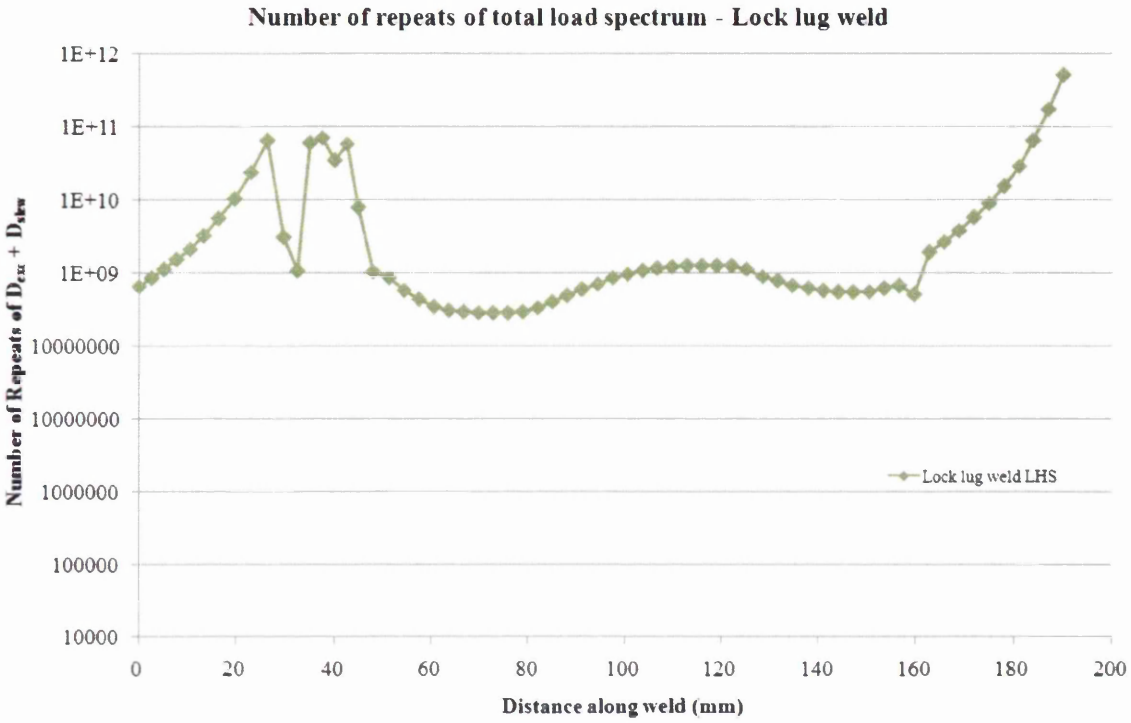

Figure 332: Lock lug weld – Number of repeats of loading D_{exca}+D_{slew}

The minimum number of repeats is calculated at 70mm along the weld toe path with a predicted life of 286,599,020 repeats. There is a striking profile in the calculation at 25mm to 45mm along the weld toe. This large step was also recorded in the shear structural stress profile calculated for the slew load in Figure 325. The trough coincides with location number 1 highlighted in the weld toe calculation path in Figure 333. It is at this location where recorded fatigue cracks originate in the component test. It is likely that at this point in the weld run, the in-plane shear stress mode is at its maximum angle to the slew load applied and, hence, a critical location for shear crack propagation.

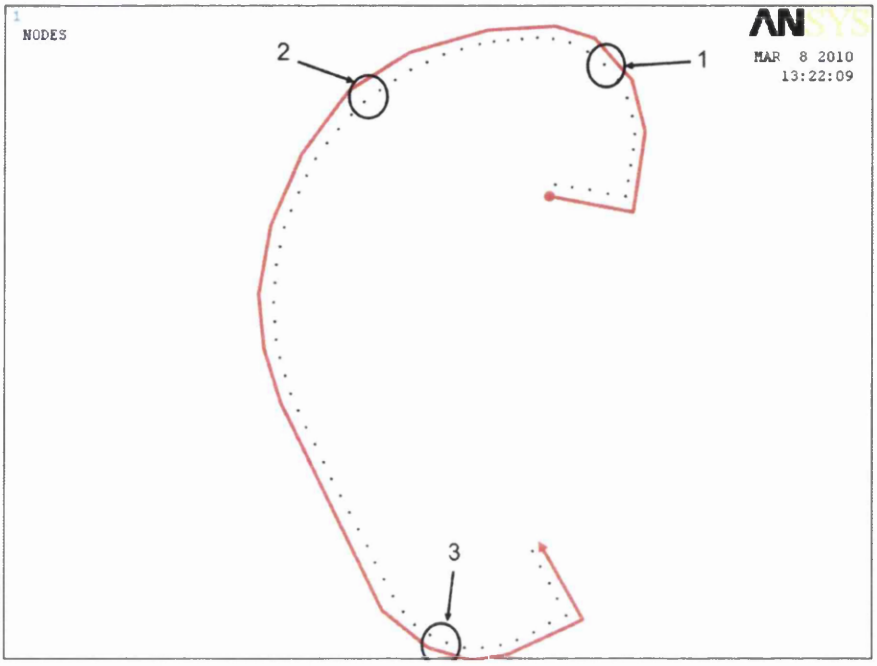

Figure 333: Lock lug weld toe path

Despite the minimum number of repeats not being at location 1 (35mm along the weld toe path), the calculation is robust enough to highlight the potential fatigue prone area. The minimum number of repeats is calculated at location 2 (70mm along the weld toe path). A higher fatigue life calculated at 1 can also be attributed to the simplified weld profile, whereas in manufacturing conditions, the lock lug attachment is a very difficult weld profile to achieve and is susceptible to errors. It is sound welding practice to move the operators' body along with the weld run and keep hand movements to a minimum. At the start of the lock lug weld the profile sweeps around the attachment and the operator must rotate with it. This is a difficult operation to complete and hence a different weld profile can be, and is, achieved each time from component to component. It is plausible that these inconsistencies will play a role in the attachment attaining a reduced fatigue life than is calculated here.

The fatigue life calculations for the entire lock lug weld are enormously inaccurate when compared with the recorded component fatigue lives. Despite only a non-load-bearing attachment, the lock lug weld is particularly prone to fatigue cracking. It is possible that the FE model, again, has failed to capture welding induced factors such as distortion levels and residual stresses.

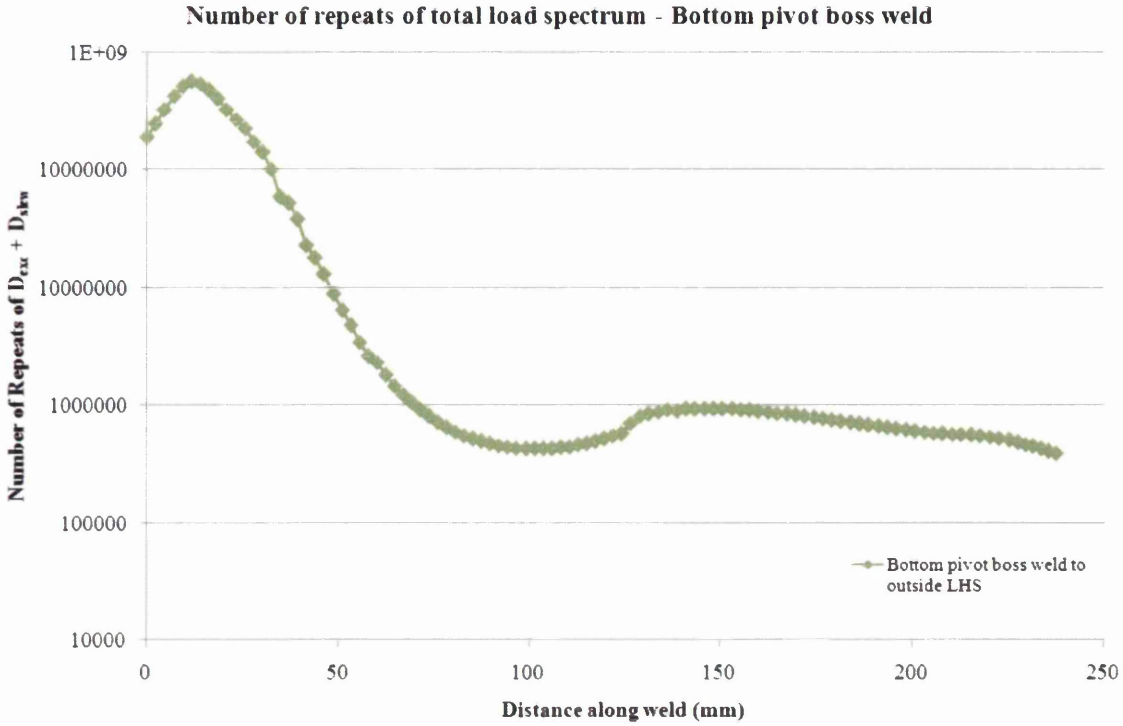

Figure 334: Bottom pivot boss weld – Number of repeats of loading $D_{exca}+D_{slew}$

The calculated number of repeats ($D_{exca}+D_{slew}$) for the bottom pivot boss weld toe is displayed above in Figure 334. The number of repeats is plotted on the y-axis against the distance around the pivot boss weld toe crack plane (mm) on the x-axis. The most damaging area calculated is at approximately 100mm around the weld toe with a predicted 388,850 repeats. The crack location at 100mm around the boss weld correctly identifies fatigue prone areas recorded in the historic test data. As per previous weld crack planes, it was the slew loading mode that proves most damaging to the fatigue calculation. Although relatively low forces are exerted on the bucket while moving material from left to right, it is the mechanical advantage and offset load that causes the pin joint and boss restraint to experience high bending moments and stresses.

4.8.6 Comparison of prediction vs. historic test data

The fatigue damage calculations in the previous section predicted the number of repeats of the loading spectrum each weld region can withstand before a first crack appears. A summary of the minimum number of repeats and its location is given for each weld in Table 10.

		Predicted cycles	Recorded cycles
1	Nose casting weld	**339,145**	**116,000**
2	Keyhole casting weld	**210,786**	**52,000**
3	Scarf joint transition weld	**125,688**	**300,000**
4	Top pivot boss weld	**123,198,501**	**82,000**
5	Lock lug attachment weld	**286,599,020**	**85,000**
6	Bottom pivot boss weld	**425,469**	**82,000**

Table 10: Yellow Goods production component fatigue life comparison - Predicted vs. recorded lives

The structural stress based fatigue calculations suggest the first weld location to fail is the scarf joint transition weld with a total of 125,688 repeats. This does not correlate with the historical test data held for the boom component failure sequence. However, this is a respectable correlation of predicted lives although, under estimating the fatigue life by a factor of 0.4. As seen in the stress analysis in chapter 4.8.2, the scarf joint weld is a highly stressed region under both the excavating and slewing load cases. The boom component in the non-stress relieved state would be expected to fail primarily at the keyhole casting weld area with the top and bottom pivot bosses and lock lug regions following soon after. There are promising levels of correlation when comparing the scarf joint weld structural stress profile (minimum number of repeats at 150mm along weld) with the locations of scarf joint failures (approximately 150mm-250mm along the weld toe). Since the scarf joint is calculated with the lowest number of repeats in the non-stress-relieved state, this might suggest that levels of distortion and/or high residual stresses are not modelled sufficiently, and correctly calculated or considered in the welded regions. In contrast, a higher fatigue performance is calculated for the keyhole casting weld, which would traditionally be the first location to fail under fatigue loading.

Despite the poor correlation in the weld location for the first crack in the boom component, it is worth noting the structural stress profiles calculated for each weld region individually. Comparing the structural stress profile along the weld crack plane with the boom fatigue test data for all 6 weld regions the minimum number of repeats along the weld correlates well

with the failure locations from the test data. For example, at the nose casting weld the minimum number of repeats is calculated 90mm along the weld. This correctly defines the location of cracks in the boom component. As another example, the keyhole casting failure location is around the larger radius of the pin hole and once again, this is the same region in which the minimum number of repeats is calculated. This level of correlation is repeated for all 6 weld locations studied.

As each of the fatigue prone areas along the six weld runs are correctly identified, reviewing each weld failure location also provides some comparison with the recorded fatigue failure measurements, Table 10. Firstly, the top pivot boss and lock lug weld are exceptions. The calculated fatigue life is completely erroneous with no correlation of recorded fatigue lives. Secondly, good levels of correlation are recorded for the nose casting, keyhole casting and bottom pivot boss welds. The fatigue life predictions are over estimating the recorded values within factors of 2.9, 4, and 5.2 respectively. The scarf joint transition weld under estimates the recorded life by a factor of 0.4.

Given the calculation does not highlight the failure sequence correctly suggests the welding process effects have not be adequately represented in the FE model. Furthermore, in comparison with the recorded fatigue lives, the structural stress calculation method is predominantly over predicting fatigue lives. It is believed the FE model has not captured the behaviour of local range and long range of residual stresses acting on the component. Further to this, there are no levels of distortion modelled into the FE geometry. All factors that can play a vital part in correctly transferring load through the FE model, and as experienced in the test configuration.

5. Discussion

5.1 Data Generation - Master Curve

Load-life weld fatigue curves have been generated for a range of different joint configurations and presented in chapter 4.1. The original or baseline fatigue curves clearly displayed a geometry dependency. As a consequence, traditional FE stress analyses based on nominal stress are severely challenged when predicting the fatigue life of such welded structures. On this basis, the effectiveness of an alternative fatigue damage parameter known as Structural Stress was explored. The structural stress has the capability to remove the geometry dependency and thereby condense the weld fatigue data onto a single Master S-N Curve.

An important aspect to emerge from the literature review was the consideration of residual stresses in small size welded coupons. It was discussed that there are potentially insufficient weld-induced residual stresses to replicate the high levels (equal to the parent material yield strength) found in a full-scale welded structure. The high residual stress state will cause even small applied load ranges to be detrimental to the fatigue performance. This will also cause the fatigue strength response of a welded component to be independent of the mean stress ratio applied. In some cases it was shown that in small welded coupons there are insufficient welding induced residual stresses. This statement was explored for the non-load-bearing cover plate and load-bearing lap coupons. A majority of the coupon fatigue test were completed at a load ratio of R=0.1, fully tensile loads. Fatigue tests for both coupon geometries were completed at a load ratio of R=0.5. The results of the high mean ratio tests showed a similar fatigue strength response, close to that of the R=0.1 results. This suggests there are sufficient residual stresses withheld in the small coupons to accurately represent the fatigue performance of full size welded structures.

5.1.1 FE-based Structural Stress coupon calculations

Structural stress unit load factors were calculated using a range of different FE model parameters for each coupon geometry. Broadly consistent results were obtained using both solid brick and shell plate elements at the centre of the coupon (peak structural stresses) for weld toe, throat and root failures. The range of different FE model parameters included comparisons between different types of FE software packages – 3 in total. The FE models displayed no sensitivity to the element type and size used. The mesh density used in these

models varied over a range such that the global element size across the width of the coupons took on values of 3.125, 5, 10, 16.67, 25 and 50mm. The through thickness element size included values of ¼, ½ and 1t, with 't' the thickness of the parent plate. Both parabolic and linear (1st and 2nd order) element types were modelled, together with reduced and full integration solution methods. It was shown that irrespective of these differences there was no or negligible variation in the unit load factors calculated. It was evident that the coupon calculations in this work support the mesh insensitivity theory observed in previous work carried out by Dong [44].

There was one important exception to the broad correlation of the results. The shell element calculations for the cruciform throat failures were not as consistent as the solid element models. Shell cruciform models were very poor compared with the best solid element model. This is due to the inability of the shell element to represent accurately the load path in this test coupon. This is a problem for symmetric cruciform models where the load is predominantly tensile; little or no load is transferred or passed through the lower weld toe node. In contrast, successful calculations and comparisons were obtained for the shell element throat failures in the tensile load tee joint (the results were comparable to those from the solid element models). This suggests that accurate shell element structural stress calculations can be made for weld throat failures where the load path passes through the complete weld bead (i.e. through the upper and lower weld toe, where load is transferred through a vertical upright to a horizontal base plate) such as in the case of unsymmetrical single-sided fillet welds. This is supported through a comparison of the nodal forces and moments extracted at the shell model weld crack plane with solid model equivalents. It can also be demonstrated through analysing the load path of the solid models, shown using a vector plot of the principal stresses, Figure 335. The red dots in the solid models (upper diagrams) are the superimposed location of the lower node of the weld throat element in the shell model (lower diagrams). The cruciform shell calculations are ambiguous compared to the solid models because the load path is not correctly modelled. In the shell model the load path is transferred through the lower nodes (red dots). However, in reality, a very small amount of the load path is passed through the node location.

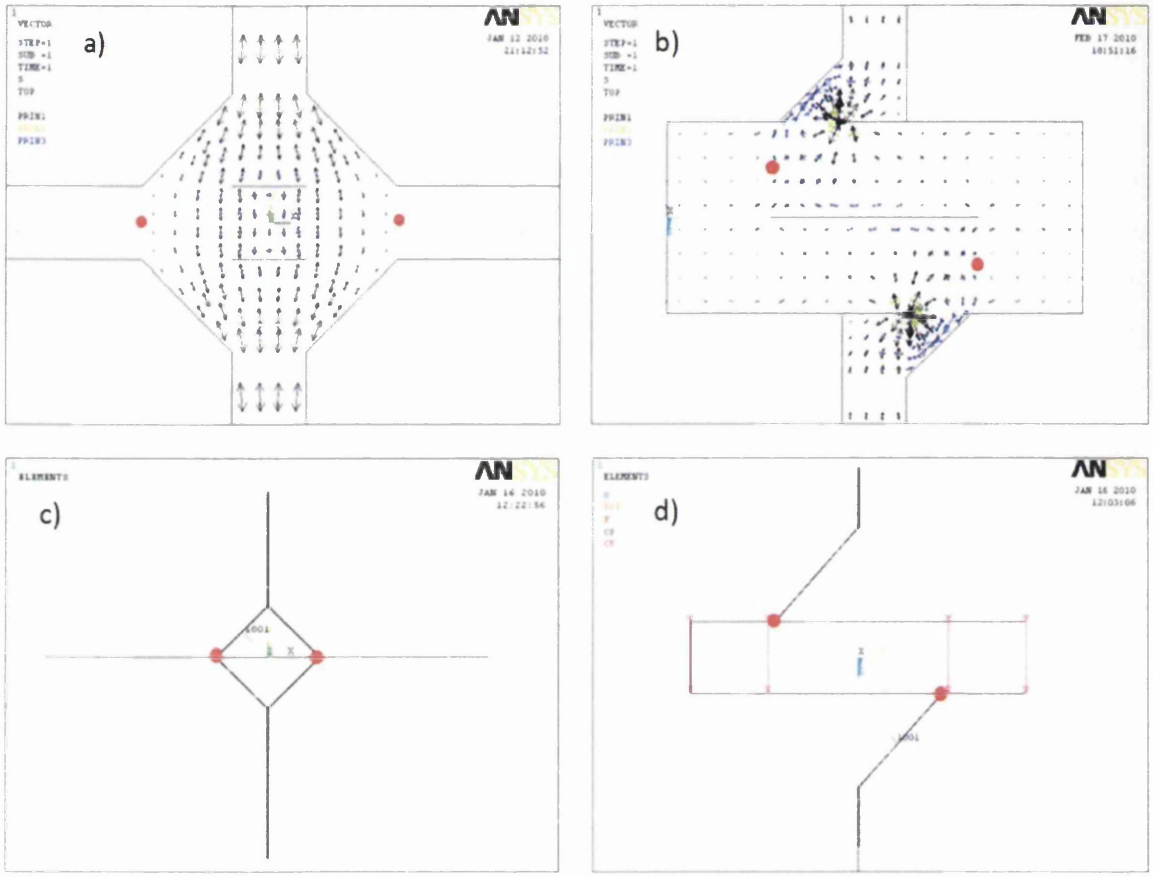

Figure 335: Throat failure coupons - Solid and shell element models a) Cruciform solid element model, b) tee solid element model, c) cruciform shell element model and d) tee shell element model.

An attempt was made to rectify this problem by including an additional element in the model in order to transfer the load more accurately, but the results were inconclusive. The extracted nodal forces and moments at the weld throat failure location did not compare with the solid element models. Shell element modelling of welded connections is a useful and viable application for automotive structures with thin sheet ('shell' like) materials up to approximately 3mm thick. The modelling of a weld with a node adjacent to the weld toe has practical and useful results [44] but based on the results in this work, the use of shell elements has significant limitations.

The shell models did achieve results at the centre of the coupons that were consistent with the solid element models (except for the cruciform throat failure modes). However, there is some erratic behaviour in the structural stress distribution and profile at the edge of the coupon. It was found that the finer the mesh, the greater the fluctuations. They were even more pronounced for a full integration method (as opposed to reduced integration). Similar results have been reported by Dong [43]. A proposal was put forward in his work to smooth out the

structural stress distribution at weld line ends. The solution makes use of a 'virtual node' placed on the weld line midway between the final two nodes of the last element. Exact details of the method are not well documented and possibly included sensitive material due to inclusion of the method in the commercial software Verity®. From the information that is available, it appears that a virtual node is placed away from the edge. This allows the forces and moments to be averaged from the maximum and minimum values from each node, including the additional one. From this research work, the erratic stress profile is not as noticeable when a reduced integration solution method is selected. This is essentially completing a similar process to the virtual node method. The Gaussian integration point is further away from the edge, thereby smoothing out the final structural stress profile. Ultimately, based on the results presented here, the structural stress calculation for weld ends or plate edges using shell elements demonstrates that the method is mesh sensitive – in a similar manner to a stress singularity – to the extent that a finer mesh produces a higher stress. However, the effect of this can be avoided or at least minimised by using a coarser mesh (i.e. increasing the distance between the penultimate and last node on the weld line) and a reduced integration method.

The FE models of coupon geometries with distortion levels modelled in, gave higher structural stresses. Furthermore, the strain readings derived from these distorted coupon models compared more favourably than the un-distorted models with the experimental measurements made on coupons with strain gauges.

For single-sided, fillet weld throat failures - in the tensile load tee joint - the shell element thickness of the element at the weld throat has no effect on the calculated structural stress. The structural stress is not sensitive to the shell element throat thickness because the load path through the node/element is the same regardless of t value. Thus, extracted nodal forces and moments are the same.

Solid element models of throat failure modes proved to be sensitive to the degree of weld penetration modelled and the crack plane of the structural stress calculation. It is advisable for the penetration levels achieved in the test coupon to be modelled correctly if reasonably practical to do so. In essence, the most representative or actual geometry should be created if this can be achieved in a reasonable time frame. For toe failure modes the structural stress calculation using solid element models is not sensitive to the level of penetration modelled.

Increased effort in modelling more representative weld geometries will not improve the accuracy of the results, and ultimately reduces the efficiency of the method.

A very coarse 1t through thickness solid element (linear 1st order) mesh with the reduced integration solution produces consistent, if not as accurate, results. It has been shown, however, that there is a limitation with regard to the characterisation of bending across the coupon width. On this basis, a very coarse mesh cannot be recommended even though it is cost effective in terms of time and resources.

Shell element modelling did display consistent results in some areas. However, the capabilities of the shell elements can be questioned. The most significant issue is the accuracy of shell elements representing the load path. The first step in extracting nodal forces and moments is essentially a computer-based free body diagram that requires the output of forces and moments acting on a specific weld crack plane. The results, generally, are sensitive to the geometry modelled. Shell models gave good correlations here for toe failures. The results are not so favourable for some weld throat failure conditions. The shell elements struggle to represent the weld geometry. In larger components or sub-assembly models (i.e. not simple tensile load coupons) there will be numerous load paths that could potentially have a greater effect on the outcome of the weld throat and toe failure calculations. It is suggested that shell element models could be used for a 'quick and dirty' initial analysis, should there be a requirement for one. Given the insensitivity seen of the coarse solid element models, the use of shell elements for an initial analysis is questionable and not necessarily an aid to a convergent solution for the problem. In essence, a full solid element analysis should be used from the outset, within the constraints posed by cost, time and resources.

However, it may be perceived, that for some design engineers or certain analysis conditions, the use of shell element modelling techniques offer increased benefits over solid models. A fast convergence was seen when using shell elements for the non-load bearing cover plate example in chapter 4.3.2, suggesting shell element models may have some potential in this application. Furthermore, it is possible, that the above associated problems with throat failures and edge sensitivity can be avoided through employing shell-solid coupling techniques as documented by Osawa [50]. The main seam weld and local geometry are modelled using solid elements, while the surrounding areas of un-welded parent plate material are modelled using shell elements. An interface between the two element types is used in the form of a fictitious shell element perpendicular to the original shell element. The

applicability of this modelling technique would require further work for construction equipment components.

5.1.2 Measured Structural Stress coupon calculations

Measured structural stress values were obtained for the coupon geometries with a weld toe failure mode, through measurement using four electrical resistance strain gauges. The FE-based calculated structural stress values for the undistorted coupons, underestimated the measured values. Calculated FE-based structural stress values for the distorted coupon geometries overestimated the structural stress values obtained from the measurements. This suggests the measured values for the coupons lay between the two model types. Undistorted geometry models are too conservative and not representative enough of the true coupon geometry. The distorted geometry FE models are too pessimistic or severe calculating a higher stress than is seen in the actual coupon test. This is consistent for all the toe failure coupons except the bending load tee joints. Due to the clamping arrangement of the bending load tee joints there are more potential sources of error. The strain gauge distances from the weld toe were modified from the suggested values in the literature due to the limited space of the coupon geometry. There is also a high stress contour difference across the base plate of the coupon. This would make the calculation significantly more sensitive to any misalignments or errors in strain gauge locations.

This is not to say that the measured structural stress calculation based on strain gauge measurements is correct. A concern over the applicability of the structural stress measurement technique was found during this research work. A discrepancy was found when creating measurement based structural stresses for tensile loading of symmetrical coupons. For example, using four strain gauges in the suggested arrangement would always result in similar or symmetric strain readings i.e. all four gauges measure 800 micro-strain and give a measured structural stress value of 1MPa. Thus, if the coupon is symmetric, irrespective of the cross sectional area, a SS value of 1MPa will always be obtained. However, this is not the case for the FE-based calculated method. Similar structural stress per unit load calculations on symmetrical coupon models are weld area dependent. Thus for a weld area of $800mm^2$, the force/area is $1000kN/800mm^2$ = 1.25MPa SS value but for an area of $1200mm^2$ it becomes $1000kN/1200mm^2$ = 0.83MPa SS value. However, measurement based SS values are 1MPa for both $800mm^2$ and $1200mm^2$ weld area sizes.

It was shown above, that the structural stress measurement technique has limitations in the calculation of symmetrical geometries. Furthermore, any component under analysis would require up to four times as much time and resources than a traditional 'weld classification' analysis. As a result, this demands increased resources, time and money for the gauge installation, data collection and data analysis. The method also assumes access is possible to the upper and lower faces of the plate section under analysis. In many off-highway construction vehicles, enclosed box sections and single-sided fillet welds exist as prominent features, restricting the access to a majority of parent material faces. The measurement technique application for this type of welded structure appears impracticable, near impossible, without enduring increased time and costs.

In a design environment, having completed a structural stress weld fatigue assessment, there is little benefit in developing and proving the chosen design with the structural stress measurement technique. Counsel would be given to complete a traditional 'stress-life' analysis using the established 'weld classification method', focusing on the fatigue prone areas highlighted by the structural stress FE-based fatigue analysis.

5.1.3 Structural Stress Master-curve

A structural stress based master curve was achieved for all welded coupon geometry types. It condensed all the data into a tight band on the basis of σ_{ss} range against life, particularly for solid element models. A master curve was also achieved for shell element models but with some concern over cruciform throat failures. The overall method supports the mesh insensitivity and geometry independent theories proposed by Dong. The master curve created was largely insensitive to failure modes, loading modes and FE modelling parameters and variables discussed in the chapter 5.1.2. The one exception was the bending load tee joint data, the results of which sat away from the main scatter band and had a distinctively different slope to the usually observed 1 in 3 gradient. In the tests completed by *Taylor et al* [51] similar bending load tee joints were tested using a clamped base set-up with a 100mm grip-to-grip distance (low load-high stress). The fatigue curve showed a similar fatigue slope (-0.13) to the tee joints tested in this work (-0.11). This suggests the results here are not a unique occurrence or singularity. *Fermer et al* [52] applied an alternative structural stress based theory to the fatigue analysis of welded structures. In that research it was reported that weld fatigue data fell into 1 of 2 separate master curves based on loading modes. Separate curves are generated for flexible and stiff members that are under predominantly bending or

tensile loading modes. The results of the tee joints here would support that. In fact, the placing of the bending load tee joint data suggests that the structural stress master curve as defined by Dong is loading mode dependent. However, other high bending moment coupons such as the tensile load tee joint and load bearing lap joint still condensed well into the main scatter trend.

Although the structural stress parameter has condensed all of the weld fatigue data into a single scatter band (largely insensitive to failure modes and loading modes - excluding the bending load tee data), there is some merit in separating the fatigue curves into failure modes. For the throat failure coupons the statistical analysis gave a 50% certainty of survival curve with an R^2 value = 0.793 and standard error = 0.255. The equation for the curve is expressed as $y = 8151.18N_f^{-0.287}$. The optimum toe failure statistics were calculated by excluding the bending load tee joint data set. Using solid element distorted models a 50% certainty of survival curve was calculated with an R^2 value = 0.814 and standard error = 0.219. The equation for the curve is expressed as $y = 19918N_f^{-0.343}$. The scatter of data for individual failure modes is a marked improvement over the R^2 = 0.6 for the master curve for all data sets.

Where distorted coupon geometries were modelled, an increase in fatigue strength was seen compared with the undistorted models.

A master curve was also created based on the measured structural stress values (an FE calculated value was used for throat failures). The measured structural stress master curve showed similar trends to the FE-based calculated SS master curve – i.e. condensing of the data, and reducing the scatter – except, that is, for the bending load tee joint data.

5.1.4 Equivalent Structural Stress Master Curve

Equivalent structural stress based fatigue master curves have been generated. Many of the considerations and issues highlighted for the structural stress parameter are applicable and stand true also for the equivalent structural stress parameter. The equivalent structural stress curves are calculated considering through thickness material effects and loading modes. The loading mode and thickness correction parameters in the Equiv. SS equation do little to further condense the fatigue data compared with the original structural stress parameter. The minimal effect of further condensing is due to similar material thicknesses and tensile loading paths used in the coupon geometries.

This is true for all except the bending load tee joint coupons. The loading mode parameter, r, is defined as 0 for pure tensile loading and 1 for bending dominated loading. Recommended values of the complete I(r) value for loading controlled fatigue tests are given as 1.1 for tensile loads and 1.13 for bending loads. An I(r) value of 1.13 for the bending load tee joint coupons alters the data set which is moved closer towards the main scatter band. The redistributed tee joint data placement is still distinct and separate from the main scatter band. Changing the I(r) value outside the suggested (1.1 to 1.13) and using a value around 1.6 as recommended for strain/displacement-controlled tests (1.2 to 1.6), the fatigue data correlation is significantly improved for other coupon geometries. The tee joint data is clearly redistributed around the main scatter band for all the other fatigue test data. This supports the theory of condensing different failure mode fatigue curves into a single master curve, as proposed by Dong. However, this is only achievable upon changing the value of the equivalent structural stress equation parameters. Having shown for the structural stress fatigue curves that improved correlation is achieved using a curve for each failure mode, and recognising that there is some sensitivity associated with the bending load having some sensitivity to the results, the Equiv. SS parameter is useful in eliminating the loading mode dependency. In essence structural stress based fatigue predictions could make use of failure mode and loading mode based fatigue curves. As a contribution to more efficient modelling, the equivalent structural stress parameter is able to eliminate the need of separate loading mode fatigue curves.

5.2 Yellow Goods Test Component

5.2.1 Component Testing

The structural stress fatigue life prediction method was applied to a yellow goods test component. The test component was manufactured from similar materials and using welding parameters to those used on construction, agricultural and materials handling equipment. Four components were made in total and fatigue tested under load-controlled conditions. Only a single weld fatigue failure was recorded, at the base of the pin loading boss location on the outside weld toe.

5.2.2 FE Stress Analysis

FE stress analyses of the test component were performed to establish the structural stress at weld locations. 'As-designed' un-distorted and 'as-welded' distorted FE models were created using solid brick elements. The two FE models were created and solved with boundary conditions replicating the fatigue test set-up. The validity of the FE model was checked by comparing micro-strain values obtained from the FE model against those measured by strain gauges at various prescribed locations on the test component. It was discovered that welding-induced distortion of the component affected the elastic strain distribution significantly. Only by including the welding distortion of the test component into the FE model could a good correlation be achieved between the FE calculated and strain gauge measured micro-strains. It is therefore essential to take welding-induced distortion into account in weld fatigue assessments.

There were indications of non-linearity when plotting the test component micro-strain values against the applied load. A modified FE stress analysis of the test component was completed using a non-linear geometry function in the FE software but the stress results were no different to the original linear analysis. It was assumed the non-linear effects were due to the loading configuration and the contact between the pin and component. To keep the FE weld fatigue assessment method practical and efficient, beam and link elements were used to model this non-linear contact between pin and component, whilst using a linear FE solution. Ultimately, the stress ranges derived from the distorted model were comparable to those experienced by the fatigue loaded test component.

5.2.3 Structural Stress Calculation

Static unit load structural stress profiles were calculated for both the un-distorted and distorted test component models. These were calculated for two FE analysis solution types – reduced and full integration. The structural stress profile was calculated along each weld run. Only the distorted component model identified the maximum/peak structural stress at the same location as the crack developed in the test component. The structural stress profiles calculated were largely insensitive to the reduced and full integration types. Based on a sensitivity assessment of the structural stress calculation for the test component and coupons, it appears that the approach provides a more accurate fatigue life assessment in the modelling of real component geometries.

5.2.4 Structural Stress Fatigue Life Predictions

Damage calculations were completed for the undistorted and distorted geometry models using Miner's linear summation hypothesis. The total number of repeats of the loading spectrum was then calculated. The minimum number of repeats was correctly identified in the distorted geometry model and there was also excellent correlation with the test component failure location. The stress profiles correctly correlated other highly stressed areas such as the mouse hole region. Although no fatigue failures were obtained at this weld, the stress distribution correlates well with the strain gauge recordings.

Further to the damage calculations, fatigue life predictions were made for the boss weld toe crack location. This calculation was completed for the range of master curves generated using different FE model parameters (such as structural stress and equivalent structural stress, un-distorted and distorted coupon models, measured or FE-based calculations) and used to determine the sensitivity of the fatigue life prediction results. The different master curves used are summarised in Table 11 together with a fatigue life prediction for the 195kN load based on the 50% certainty of survival mean curves, for both structural stress and equivalent structural stress damage parameters.

Master curves 1, 2 and 3 were generated based on all of the weld fatigue test data using solid element undistorted models, solid element distorted models, and measured structural stress values respectively. Master curves 4, 5 and 6 were generated using the same parameters found in curves 1, 2 and 3 respectively. However, the bending load tee joint data was excluded from the analysis due to the fact that the fatigue curve fell outside of the main

scatter band for the other coupons. Master curve 7 is derived from the unit load equivalent structural stress values obtained from solid element distorted geometry models, using all of the fatigue test data, as for curve 3. However, this time the equivalent structural stress equations are modified with I(r) = 1.6, to further condense the tee bend data into the main scatter band. Master curves 8, 9 and 10 considered only the weld toe fatigue failures. The toe failure master curves generated used all of the toe failure data (8), toe failure data without the bend tee results (9) and all toe failure data but with a modified I(r) value (10).

Fatigue life prediction - Test component weld boss crack location - 841,789n_{195kN}

		Damage Parameter prediction of N_{195kN}	
	Master curve	**Structural stress**	**Equivalent structural stress**
1	**Solid element undistorted model - all data**	**1580808**	**1304677**
2	**Solid element distorted model - all data**	**9538500**	**4732033**
3	**Measured structural stress - all data**	**818510**	**740957**
4	**Solid element undistorted model - no bend tee data**	**2449196**	**2344460**
5	**Solid element distorted model - no bend tee data**	**2361181**	**1658736**
6	**Measured structural stress - no bend tee data**	**7219108**	**6172089**
7	**Solid element distorted model - modified bend tee I(r) value = 1.6**	n/a	**2414009**
8	**Solid element distorted model - all weld toe failures only**	**2695273**	**2674887**
9	**Weld toe failures no bending load tee data**	**1717655**	**1446312**
10	**Weld toe failures modified I(r) value 1.6 bending load tee data**	n/a	**1263974**

Table 11: Summary of Master S-N curves generated

The number of repeats calculated for each different master curve (50% mean cure), at the weld failure location, did produce some scatter in predicted fatigue lives, N_f However, all predictions were within an acceptable factor of 10 of the failed component. This could be considered a practical and valuable approach to fatigue life prediction as, despite the wide variations in generating the master S-N curves, realistic and feasible predictions are calculated throughout. Should there be a requirement for a fast assessment early on in the design process, and as an initial step just to obtain a general indication of fatigue prone areas, the techniques explored do provide an efficient prediction of fatigue life albeit with some

inaccuracies. In contrast to this, a more accurate fatigue life prediction can be achieved with more time spent in generating and selecting the correct curve for the analysis.

From the predicted fatigue lives, it appears that the measured structural stress master curve produces the most accurate results. Although the predictions correlate with the measured values, additional features of the master curve should still be considered. With the bending load tee data included in the master curve, the data points were placed away from the main scatter band. The master curve has an uncharacteristic slope of -0.6, whereas a slope of around -0.3 is typical for welded steels. Further to this, upon calculating fatigue lives using the structural stress master curve based on measurements and excluding the bending load tee data, the predicted fatigue lives are then within a factor of 7 of the test component (compared with a factor of 1 initially), making it a very sensitive approach. A robust fatigue assessment method should be consistent and not sensitive to the removal of a single data set. Ultimately, the measured structural stress master curve including the bend tee data provided erroneous results and should be disregarded.

The solid element un-distorted model master curve, number 1 in Table 11, also appears to predict accurate fatigue lives. However, again due to the prominence of the bending load tee data, the 50% mean curve is a misrepresentation of all test data. The mean curve has an abnormal slope of -0.48 and a very poor correlation with all fatigue data points. Again, these results should not be considered as an accurate representation and the fatigue curve type should be disregarded. Using the solid element distorted model master curve (curve 2), inclusive of the bending load tee data, there is an improvement in data correlation and a slightly more characteristic fatigue curve slope of -0.41. Calculated fatigue lives are over predicting by a factor of 10, with the bending load tee data still creating an undesirable effect. The calculation shows a master curve is achievable for all data types, although, with a compromise in prediction accuracy. This further suggests that a separate fatigue curve is required depending on the load mode, or alternatively the equivalent structural stress damage parameter should be used.

The master curves 1 and 2 were analysed with the same parameters except the bending load tee joint data was not included (master curves 4 and 5). Fatigue life predictions were calculated for the test component without the bending load tee data, to explore the sensitivity of the method and master curves generated. The 50% mean curves for both the undistorted and distorted geometries displayed improved correlation with good condensing of data and

curve gradients of -0.39 and -0.35 respectively. The fatigue life predictions of 2,449,196 cycles and 2,361,181 cycles were calculated for the solid element undistorted model and solid element distorted model master curves. Provided the bending load tee data are excluded, only a slight difference exists in fatigue predictions using un-distorted and distorted coupon models. As consistent results are achieved within a factor of 2.8, the argument is strengthened for considering the bend tee data separately or for using the equivalent structural stress parameter.

The fatigue master curves were divided into separate failure mode mechanisms. Master curves were condensed into separate scatter bands for weld toe and weld throat failures. The 50% mean curves of each were distinctly different. The weld toe curves displayed a higher fatigue strength and steeper gradient. Fatigue life predictions were calculated from the toe failure master curves generated using solid element distorted models, since the distorted and un-distorted show little dependency on results calculated previously. Two master curves were generated: one with all data for toe failure coupons and the other, with toe failure coupons but excluding the bending load tee data. The fatigue life predictions were 2,695,273 cycles and 1,717,655 cycles for the toe failure master including and excluding the bend load tee respectively. A significant improvement in the fatigue life predictions is seen in both master curves. Calculated lives, including the distinct bend load tee data in the master curve are within a factor of 3 of the recorded component life. Further to this, excluding the tee data improves the prediction to a factor of 2. This demonstrates an improved prediction can be achieved when separating the master curves into different failure modes. A master curve assuming a single format for different loading modes can provide useful predictions. However, it is beneficial to separate the data into separate loading modes.

Assuming the term 'efficiency' is used to describe the outcome of time or effort against accuracy, ideally, manufacturers would prefer the minimum time spent to obtain the most accurate results. Efficiency can reduce when added time and effort is spent only to yield a small increase in results accuracy, i.e. the convergence curve starts to plateau. In the case of the structural stress damage parameter, extra effort is required to analyse the distorted geometry of the test component and correctly select the optimum master curve. In this case it was found that the toe failure master curve without the bend load tee data, curve 9, produced the most accurate and efficient results. Although extra effort is required throughout the analysis, the 'efficiency' is never compromised. This curve was selected as it is known that a

dependency on both the loading mode and failure mode exists so that master curve 9 provides the optimum choice. Despite the sensitivity to loading and failure mode parameters, accurate (not necessarily efficient) 'structural stress' fatigue life predictions can be achieved from any of the master curves produced above, highlighting the robustness of the technique.

5.2.5 Equivalent Structural Stress Fatigue Life Predictions

The 'equivalent structural stress' damage parameter was used to calculate fatigue lives in a similar approach to the previous 'structural stress' method. The damage parameter is expected to further condense weld fatigue data by considering through thickness material effects and different loading regimes. The different master curves generated have similar parameters to the previous structural stress as well as the additional equivalent structural stress equation optimised parameters. The curves are summarised in Table 11 together with the fatigue life prediction of the 195kN load from the 50% certainty of survival mean curves.

The unit load measured structural stress values were used to calculate the 'equivalent' damage parameter, while fatigue life predictions were obtained, the results were not considered credible as per the previous chapter 5.2.4. The equivalent structural stress parameter did show a slight improvement in condensing the fatigue data. However, a very high measured unit load value for the bend load tee joint (12.5MPa measured, compared with 8.9MPa FE-based calculation) still positioned the data away from the main scatter band. It is probable that the measurement technique is very sensitive to the placement of the strain gauge locations, creating a large error in the results. Due to the unique clamping arrangement a cantilever style beam is created with a very high tensile to very low compressive stress distribution across the base plate and over a relatively short distance, 35mm. Thus, due to the difference in measured structural stress values and poor correlation of all the fatigue data, the fatigue life predictions are neglected.

Observing the equivalent structural stress predictions obtained from the solid element undistorted model and solid element distorted model based master curves, there is less sensitivity between the two conditions, with fatigue lives calculated at 1,304,677 and 4,732,033 cycles respectively. This is compared with previous fatigue life predictions of 1,580,808 and 9,538,500 cycles for the same coupon model but using the structural stress damage parameter. The extra 'equivalent' calculation step, using the default suggested parameter values, improves the sensitivity of the coupon models used to generate the fatigue master curves. Mirroring the results of the structural stress analysis, upon removing the

bending load tee data, there is only a slight difference in the predicted lives between the undistorted and distorted coupon based master curves with predictions of 2,344,460 and 1,658,736 cycles respectively.

The main aspect of the equivalent structural stress method is the ability to condense different loading mode fatigue data. Throughout the structural stress master curve analysis the bending load tee data has had a detrimental effect on the unified condensing of fatigue data. Improved fatigue life predictions were calculated using the default suggested equation parameters, but were not significant enough to increase the efficiency of the extra calculation step. The calculation has been explored through modifying the equation parameters and scrutinising the fatigue data used. The equivalent structural stress master curve 7 employs all fatigue test data with an alternative modified I(r) of 1.6. The premise behind this was discussed in chapter 4.6.1. Further judgment is made on the effectiveness of the claim to use a modified I(r) with an increase in accuracy of the fatigue life prediction. The predicted life of 2,414,009 cycles shows an improved correlation with the measured component fatigue test result. The results are still slightly sensitive as on removing the bending load tee data, as shown in master curve 5, the prediction is lower at 1,658,736 cycles.

Due to the different weld failure mechanisms in the fatigue data generated, master curves 8, 9 and 10 considered only the weld toe fatigue failures. The toe failure master curves employ the fatigue data as following: all of the toe failure data (8), toe failure data without the bend tee results (9) and all toe failure data but with a modified I(r) value (10). The equivalent structural stress master curve 8 predicted a life of 2,674,887 cycles to failure at the weld boss toe crack location. This is using all of the toe failure data including the bending load tee data. The I(r) loading value used was the suggested 1.13 for the bend tee data. There is some further condensing of the data compared with levels seen in the structural stress approach. Upon removal of the bending load tee data, master curve 9, the fatigue life prediction calculated was 1,446,312 cycles, showing the degree of sensitivity compared with the equivalent structural stress prediction from master curve 8. Upon using the fatigue master curve presented in curve 10 with the alternative I(r) of 1.6 and including the bend load tee data, the equivalent structural stress prediction is 1,263,947 cycles. This is a comparable prediction to that obtained from curve 9 where no bending load tee data was used. This suggests that using the modified I(r) value has little or negligible effect due to the loading mode, proving that the equivalent structural stress damage parameter is an effective and

robust approach. However, in these results, a modified I(r) is required and the fatigue data master curves should be separated into different failure modes.

5.2.6 Structural vs. Equivalent Structural Stress Damage Parameter

The structural stress based fatigue life predictions were more sensitive to the different parameters used in calculating the master curve (i.e. un-distorted or distorted, calculated or measured) than the equivalent structural stress. The structural stress predictions ranged from 818,510 cycles for the measured parameter, to 9,538,500 cycles for the distorted solid element models. The equivalent structural stress predictions ranged from 740,957 cycles for the measured parameter, to 6,172,089 cycles for the distorted solid element models.

The equivalent structural stress fatigue life predictions were less sensitive to the different parameters used to generate the master curves, than the structural stress predictions. The structural stress predictions ranged from 1,580,808 cycles for the solid element undistorted model, to 9,538,500 cycles for the distorted solid element models. The equivalent structural stress predictions ranged from 1,304,677 cycles for the solid element undistorted model, to 4,732,033 cycles for the distorted solid element models.

Further to this, in the fatigue calculations discussed above it was clear that the 'equivalent structural stress' damage parameter is more robust. This was proven for a wide range of parameters used to generate the master curve, principally down to the ability to condense and correlate the distinctly different bending load tee joint data using a modified I(r) value. The most favourable and accurate predictions were calculated using the equivalent structural stress parameter for separate failure mode master curves. The inability of the 'structural stress' damage parameter to condense all data would require separate fatigue master curves for loading mode dependency. Although the equivalent structural stress creates an additional calculation step, this would be a more efficient process than employing separate tensile and bending load master curves in the fatigue life prediction using 'structural stress'.

The results of the fatigue life predictions of all master curves generated are displayed in a convergence graph in Figure 336. In the convergence graph the 'structural stress' predictions closely follow that of the 'equivalent' parameter. The results of the measurement based master curves in curves 3 and 6 should be ignored for the reasons discussed above. The equivalent structural stress prediction in curve 10 displays a general increase in accuracy from curve 1, compared with the recorded test component fatigue life. Curve 10 in this case is

considered the most efficient as accuracy of results is increased with each curve iteration run, whilst also incorporating more complex fatigue test data in the master curve.

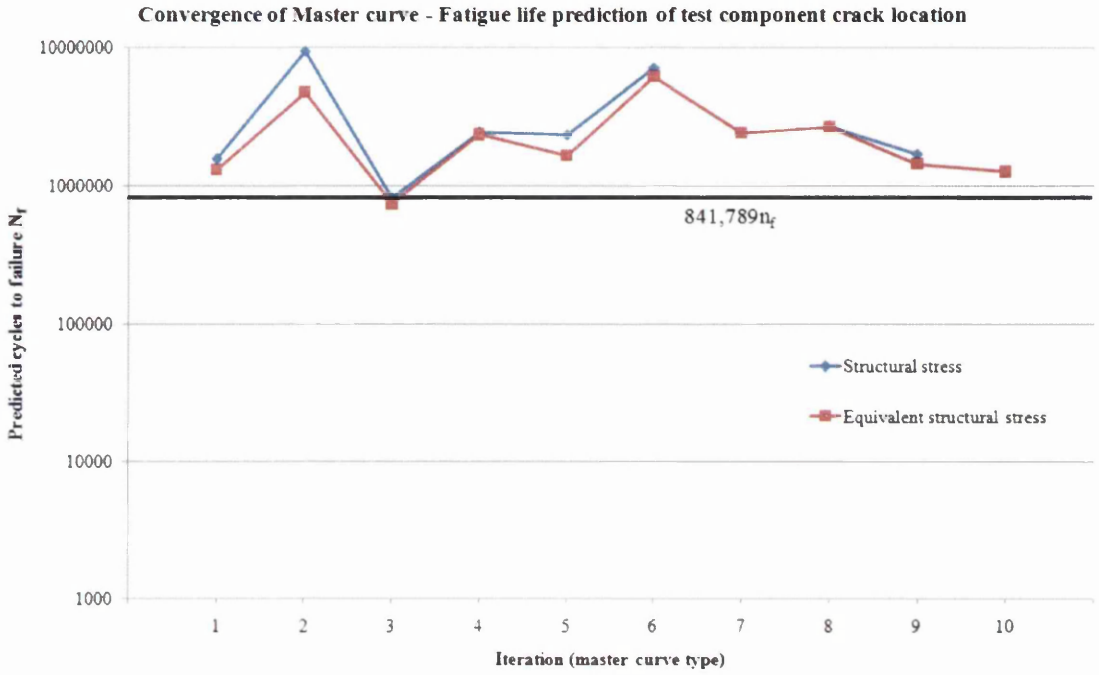

Figure 336: Convergence graph - Test component fatigue life predictions using different master curves

5.2.7 Quality of fatigue life predictions

The master S-N curve method has been explored for use on thick plate welded Yellow Goods structures. A representative FE model was validated and comparable results were obtained within a factor of 1.5 for the test component failure using the equivalent structural stress damage parameter. The technique and calculation method has been explored and proven as a robust FE analysis tool. Despite this, the levels of confidence and quality of predictions are limited as only one weld fatigue test result failure was recorded for comparison.

This does leave an element of uncertainty in the research work presented. Fatigue life predictions from all types of master curve and both 'structural' and 'equivalent structural' stress damage parameters over predicted the component fatigue life using the 50% mean curve. It is possible that the test component failure was at the lower end of fatigue scatter band. The fatigue life prediction from the Verity® 50% master curve calculated a more accurate life of 930,000 cycles (test failure recorded at 840,000 cycles). It is possible a lower fatigue strength curve would be calculated from the Verity® software as a wider range of geometries and material thickness are used. This would create an increase in the scatter of the

fatigue data, thereby calculating a lower (and what seems like a more accurate) fatigue life for the test component. Further component tests would be required to support or discount this claim.

To consider the spread and statistical variability of the master curve data, a fatigue life prediction was calculated using a 99% certainty of survival curve with the equation $y = 13466N_f^{-0.32}$, derived from the weld toe failure solid-element distorted coupons. A fatigue life prediction of 323,709 cycles was calculated, compared with the recorded 841,789 cycles. In a welded component design stage, confidence in accurate fatigue life predictions is achievable through the 'worst case scenario' curve. This would consider fatigue strength reduction effects and scatter in fatigue variability from possible defects or differences in welded geometries, and strengthen its use as component design data.

5.3 Yellow Goods Production Component

The structural stress fatigue life prediction method was applied to a yellow goods production component, with complex geometries and loading modes, to further explore its applicability to construction, agricultural and materials handling equipment. A linear elastic FE stress analysis was completed for the rear end excavating arm of a Backhoe Loader. Two separate analyses were completed with load cases and boundary conditions representing the slewing and excavating operations. Due to the large model size, manual structural stress calculations were considered a lengthy and time-consuming process for each weld run. FE-based structural stress calculations were completed using a commercially available software package (Fe-Safe Verity®). Structural stress profiles (per unit load) were created for six weld locations on the component geometry, all critical weld locations with known failure areas. The Verity® package calculated a unit load value for normal structural stresses (stresses normal to the weld seam) and shear structural stresses (in-plane shear stresses). The final calculated structural stress parameter considered both normal and shear structural stresses for each load case. This was considered vital for accurate fatigue life prediction as bi-axial fatigue can be far more damaging than uni-axial loading alone. In the majority of the weld runs, this proved correct as the normal structural stresses were often very low or of negligible levels. High structural stress values, and particularly shear stress values, were calculated for the slew unit load. Severe component stresses are experienced due to the offset loading, mechanical advantage and skewing exerted on the subassembly.

5.3.1 Fatigue life predictions

The scaled structural stress unit load factors were used in a super-positioning analysis of the load history recorded from the component test parameters. A damage summation was calculated using Miner's rule, for the slew and excavating load cases. The number of repeats of the total load spectrum (slew + excavating) was calculated at each node along the six weld paths. Fatigue life predictions were calculated using the master S-N curve generated from distorted solid model coupons. Separate curves were used for the weld throat and weld toe failure modes.

From the fatigue life predictions, the master S-N curve approach adequately captured and identified the weld failure locations along each of the seam weld runs. That is, in all cases, the method correctly highlighted the corresponding crack location of the recorded component

failures. Furthermore, the method correctly identified the recorded fatigue prone area as the first location of crack initiation along that weld, in all bar one case. In that one exception, the crack location was closely identified as a secondary fatigue prone hot-spot. In all, the structural stress method gave good correlation with recorded fatigue crack locations and where the calculated maximum damage exists for each weld run.

In four of the six weld locations, fair component fatigue life correlations were obtained, with predictions all within a factor of five. This level of correlation was calculated for the nose casting, keyhole casting and bottom pivot boss welds (over estimating the recorded lives). The scarf joint transition weld calculated an under estimated fatigue life prediction at a factor of 0.4. Despite the correct correlation of crack location at each weld, the lock lug attachment and top pivot boss weld predictions were over estimating the recorded lives by several orders of magnitude. The lock lug and top pivot boss (located towards the top of the component) unit load calculations gave very low structural stress values. In view of the highly stressed scarf joint weld towards the base of the component, this suggests that the load path experienced by the model is not representative of the real structure. In the FE model it appears the majority of the load is transferred through the nose casting pin joint connection. The load is then taking the most direct path, along the base of the component, flowing into the fixed constraints at the bottom pivot boss. In the real component, it appears the ram connection between the dipper component and top pivot boss plays a more crucial part in the load distribution experienced through the boom component. It is likely, that under both the slew and excavating load case, an increase in forces acting through the top pivot boss are distributed down through the 25mm thick rear plate section. These coincided with the lock lug attachment welded to the 25mm thick rear plate section. In the FE model this is not the case. Hence, this would account for the over predicted fatigue lives of the lock lug and top pivot boss, and the pessimistic scarf joint predictions. The rationale behind the errors in the fatigue life predictions can be mainly attributed to the effects of the assumptions for welding and fabrication process.

When considering the statistical variability of the master curve fatigue data generated, in a fatigue life prediction using the 99% or 1% certainty of survival curves, the lock lug and top pivot boss predictions are still grossly overestimated. The predictions remain several orders of magnitude over the recorded fatigue test failures. Further suggesting the errors lie with the accuracy of the FE geometry when not modelling in true welding-induced distortion.

5.3.2 Interpretation of Results

It was confirmed in the test component and coupons that modelling of distorted geometries contributes to a modified load distribution and, in turn, improved correlation of fatigue life predictions. The yellow goods production component FE model overlooked any effects of the welded process such as distortion levels and internal residual stresses. As a consequence, factors such as component-to-component fit up and clearances will increase the variability between the component assembly and FE model. Given the size of the sub-assembly, the implications of assessing the distortion of such components is a major task and outside the scope of the work presented here.

The errors in fatigue life prediction correlation were largely due to the production component FE model not accurately representing the welding-induced distortion and residual stresses. The fit-up of parent plate material in-situ in the manufacturing jig will create long-range residual stresses. Furthermore, the welding (heating, expansion, cooling and contraction) process will create localised residual stresses. Thus, simulation of the effects of the welding processes was a vital step for reliable fatigue life predictions. In certain industries, there is a growing trend to simulate the complete welding process and its behaviour on the structures performance. In some cases, the analysis suite will consider residual stress effects from the parent material production, manufacturing steps, simulation of the welding process, and finally, assess the in-service performance (durability) of the manufactured component. This would include the weld fatigue life prediction, but with greater confidence, making an allowance of the simulated distortion levels and residual stresses. The 'cradle to grave' or product lifecycle management process is a necessity and the direction more manufacturers are aiming towards, thereby promoting efficient and robust designs and low cost solutions be created to maximise profit levels. This can be achieved with confidence, provided the simulation techniques are developed with adequate validation. In the case of the test component and coupon models in this work, it was sufficient and straightforward enough to model distortion levels. However, to achieve confidence in each CAE simulation step of large sub-assemblies, time, effort and money is a prerequisite.

Further sources of error and erroneous fatigue life predictions were attributed to the assumptions made in the FE model. Important model defeaturing steps were completed in the mesh generation and small holes and fillets were removed. This was on the basis of an engineering judgement; that the component was not redesigned and the structural

performance affected. In addition, a similar judgment was made when generating the weld seam profiles. The FE model weld geometry was significantly different from that created during the actual fusion weld process. Even the most optimistic of simulation engineers would agree it is difficult to fully replicate true-to-life weld geometries. Furthermore, each welded structure will contain slight modifications in the weld metal laid down from one component to another. Additional consideration should be given to the application of beam and link elements to model the dipper, bucket, hydraulic rams and loading pins. Although these components are secondary parts in the analysis, their behaviour and interaction with the boom could still affect the load distribution, and hence the fatigue life predictions.

Variables in fatigue test set up will arise due to a number of issues such as the material and component differences but also calibration and equipment errors in the load controlled test regime. It is not uncommon in the test setup to experience interference fit-up of parts and pins and associated tolerances, as a result of weld-induced distortion and manufacturing tolerances. All of these factors will have an effect on residual stresses and will also be different from one test to another. A lack of statistical analysis of the historic test data limited the confidence in the test results for fatigue life prediction comparisons. Although proven to identify weld areas prone to fatigue cracking (i.e. repeated/consistent recorded weld failure locations analysed) were addressed, it is possible that differences in fatigue life exist from weld defects such as overlap or undercut weld profiles.

With respect to the FE model, it is impossible at this stage to accurately and fully represent the exact parameters of the tested component. Errors arise, in part, due to the simplifications and assumptions made in the FE analysis and (to what extent is unknown) how welding-induced distortion and residual stresses affect the durability of the component. However, bearing all of these factors in mind, comparable fatigue life predictions, in part, were obtained for the Yellow Goods production component. Furthermore, the structural stress approach correctly identified the fatigue prone areas of each weld. A validated test component model also achieved reassuring correlations with the recorded component failures. The findings of this research work support the applicability of the master S-N curve approach for use in the design stage of heavy construction equipment.

5.3.3 Implementation in Yellow Goods Design Process

Given that fatigue prone areas can be correctly identified and highlighted, completing a weld fatigue analysis on proposed designs can pinpoint areas for further investigation in the development of the component prototype. This would be an iterative (CAE based) design process for establishing a confident and robust design and with adequate fatigue performance. Subsequently, the design, along with its highlighted fatigue areas would be analysed further through completing rig testing or strain gauge exercises. This would be a single process to validate the chosen design and confirm whether identified fatigue hot-spots are a potential problem or not, thus building experience and confidence.

The work completed here is a step in right direction and an advancement in capability for construction equipment manufacturers, whom are heavily reliant on iterative, time-consuming and costly strain gauge based weld classification design processes. Implementation of the method, into an already established design process, should be given due care and consideration. The conclusions drawn in this research work should be recognised and taken on board to develop efficient and mesh insensitive models in predicting fatigue prone areas, whilst acknowledging the limitations and the assumptions made in the simulation process.

At a time of increased pressure, when manufacturers are striving to achieve robust and low costs design, the use of the master S-N curve approach for thick plate construction equipment is unrestricted and very appealing. The potential applications of the method include numerous design optimisation scenarios where weld fatigue is the main design consideration. This would include the down-gauging and up-grading of material specifications. The latter refers to the use of a higher strength material with a reduced thickness. As the material thickness is the principal factor in fatigue strength, an analysis could be completed for 'what if' scenarios to investigate the fatigue performance of current designs, but with a reduced section thicknesses. This can be further adopted for current designs to provide optimisation for introducing intermittent stitch welds. Further work would be required to develop weld fatigue master curves for weld end failures. The method can also be used to investigate the effects of, and reduction in, fatigue strength, when post-weld heat treatments are, or are not used in the design process.

6. Conclusions

Based on the data from experimental coupon and component tests, and results from computer-aided finite element analyses described in Chapter 4, as well as comparisons and discussions detailed in Chapter 5, the following conclusions may be drawn:

- The 'Master S-N Curve' approach was explored and applied with limited success as an FE-based weld durability assessment method for Yellow Goods equipment.
- The approach proved effective in generating suitable weld fatigue data for both 'Structural Stress' and 'Equivalent Structural Stress' damage parameters. This was concluded for weld toe, throat and root failure mechanisms.
- A structural stress based master curve was achievable for most welded coupon geometry types, condensing into one improved σ_{ss} range against life curve particularly for solid element models and in some cases shell element models.
- The structural stress parameter suggests a separate master curve exists for pure bending modes or welded coupons with long and slow crack propagation stages and a flatter fatigue curve slope.
- The equivalent structural stress damage parameter was used to further condense all weld fatigue curves. The equivalent σ_{ss} range vs. life curve condensed coupon fatigue data including complex loading modes such as pure bending. Despite the additional calculation step, the method accurately condensed a wide range of complex data, thus proving to be a robust and efficient approach.
- There was concern when using shell element coupon models for calculating the structural stress for cruciform weld throat failures and at coupon and plate edges. Where used, tetrahedral elements also displayed limitations.
- Although a master curve was achievable and largely insensitive to the test failure mode, improved correlation was achieved and a difference in fatigue strength seen when master curves were generated individually for weld toe and throat failures.
- The overall method supports the mesh insensitivity and geometry independent theories. The master S-N curve method was predominantly insensitive to failure modes, loading modes and FE modelling parameters such as element size and type, although some exceptions did exist.

- The master S-N curve fatigue life prediction method was applied to a Yellow Goods based test component and production component with complex geometries and loading modes.
- The test component fatigue life prediction correctly identified the weld failure location using both structural stress damage parameters. However, this was only achievable after modelling welding-induced distortion of the test component.
- Consistent fatigue life predictions were calculated for the test component weld toe failure location. The fatigue life predictions had minor sensitivity to the different modelling parameters used in the generation of a master S-N curve. For a range of different master S-N curves, all fatigue life predictions calculated were within a factor of 10 of the recorded fatigue life.
- It was demonstrated that a common master curve was attainable for all coupon fatigue data but prediction accuracy was increased and improved when defining separate toe and throat failure mode curves. The equivalent structural stress parameter was found to be most effective for a toe failure mode master curve. Predictions were within a factor of 1.2 of the recorded component fatigue life.
- The master S-N curve approach adequately captured and identified the weld failure locations along each of the seam weld runs in a Yellow Goods production component.
- However, erroneous component fatigue life predictions were calculated with the FE-model unable to accurately represent the load distribution of the distorted production component. The errors seen were largely due to no representation of the welding induced distortion and residual stresses in these types of thick plate welded structures.
- Accurate capture, or representation, of such welding induced distortion is a difficult process in large assemblies. Ultimately, simulation of the effects of the welding processes was a vital step for reliable fatigue life predictions.
- FE-model building and representation of the effects of the welding process are time consuming and significantly detrimental to the efficiency of the structural stress method.
- The 'Master S-N Curve' technique has been applied and shown limited potential of its use as a reliable FE analysis tool in the early design stage of welded 'thick-plate' construction, agricultural and materials handling equipment.

7. Further Work

There are number of questions and issues identified from this thesis work that require further development and investigation in order to further establish the master S-N curve approach; they are summarised in the following paragraphs.

A 'weld analysis suite' should be developed and used in the design process to assess complete product durability and create efficient and robust Yellow Goods equipment. Furthermore, case study scenarios and cost saving exercises should be completed to optimise the material section thicknesses, intermittent stitch welding, and potential removal of post-weld heat treatment, while confirming adequate weld fatigue performance exists.

The most crucial factor to arise from the work was the requirement to capture the extent of the welding-induced residual stresses and distortion levels. This requires the master S-N curve approach established here to be utilised in conjunction with other modelling techniques to simulate the welding process and calculate levels of distortion and residual stresses.

Coupon data generation should be completed to discover the effects of post-weld improvement techniques, and consideration of how or whether a separate master S-N curve can be established for each improvement method.

Structural stress calculations based on shell element models for the fatigue life prediction of weld throat failures, require further work. The development of a robust shell modelling technique should be established, as the automotive principles applied are insufficient for the thick plate welded structures analysed here. The process of building suitable FE welded component models must be improved and developed as an efficient method.

8. Bibliography

1. Benham, P.P., Crawford, J., and Armstrong, C.G., *Mechanics of Materials.* 2nd Edition ed. 1996, Harlow, England: Prentice Hall.

2. Suresh, S., *Fatigue of Materials.* 2nd Edition ed. 2004, Cambridge, England: Cambridge University Press.

3. Rankine, W.J.M. *On the causes of unexpected breakage of the journals of railway axles and the means of preventing such accidents by observing the law of continuity in their construction.* in *Proceedings of the Institute of Civil Engineers.* 1843. London.

4. Wohler, A., *Versuche uber die Festigkeit der Eisenbahnwagenachsen.* Zeitschrift fur Bauwesen, 1860. Vol 10.

5. Higgins, R.A., *Engineering metallurgy - Applied physical metallurgy.* 6th Edition ed. 1993, London, England: Edward Arnold.

6. Duggan, T.V., *Fatigue as a design criterion.* 1979, London, England.: MacMillan Press Ltd.

7. Basquin, O.H. *The exponential law of endurence tests.* in *Proceedings of the annual meeting.* 1910: American Society for Testing Materials.

8. BS7608, *Code of practice for Fatigue Design and Assessment of Steel Structures.* 1993, United Kingdom: British Standards Institute.

9. BS3518-1, *Methods of fatigue testing-Part 1: Guide to general principles.* 1993, United Kingdom: British Standards Institute.

10. BS3518-5, *Methods of fatigue testing - Part 5: Guide to application of statistics.* 1993, United Kingdom: British Standards Institute.

11. Maddox, S.J., *Fatigue design rules for welded structures.* Progress in structural engineering and materials., 2000. Volume 2(No. 1): p. pp.102-109.

12. Newman, P.R., *British Welding Journal.* 1960. Volume 7.

13. Lancaster, J.F., *Metallurgy of Welding.* 6th Edition ed. 1999, Cambridge, England: Abington Publishing.

14. Gurney, T.R., *Fatigue design rules for welded steel joints.* The Welding Institute research bulletin, 1976. 17: p. 115-124.

15. Maddox, S.J., *Fatigue strength of welded structures.* 2nd ed. 1991, Cambridge, England.: Abington Publishing.

16. Hobbacher, A., ed. *fatigue design of welded joints and components.* International Institute of Welding. 1996, Abington Publishing: Cambridge, England.

17. BS7910, *Guide to methods for assessing the acceptability of flaws in metallic structures*. 2005, United Kingdom: British Standards Institute.

18. Gurney, T.R. *The influence of thickness on the fatigue behaviour of welded joints*. in *Proceedings of the 2nd International Conference in Behaviour of Offshore Structures. BOSS '79*. 1979. London, England.

19. Eurocode9, *Design of aluminium structures. Part 2 Additional rules for structures susceptible to fatigue*. 1999: EN1999.

20. Lawrence, F.V. *Total fatigue life prediction.* in *SAE Earthmoving industry conference and exposition.* 1998. Peoria, IL, USA.

21. Ohta, A., Suzuki, N., Maeda, Y. *Effect of residual stresses on fatigue weldment.* in *Proceedings, IIW 50th Annual Assembly Conference,*. 1997. San Fransico, USA.: Welding Research Council 1997.

22. Ohta, A., Maeda, Y., Mawari, T., Nishijima, S., Nakamura, H, *Fatigue Strength Evaluation of Welded Joints Containing High Residual Stresses.* International Journal of Fatigue, 1986. 8(3): p. 147-150.

23. Neuber, H., *Theory of Stress Concentrations for Shear-strained Prismatical Bodies with Arbitary Non-linear Stress-Strain Law.* Journal of Applied Mechanics, 1961. 28: p. 544-550.

24. Martinsson, J., *Fatigue assessment of Complex Welded Steel Structures*. Division of Lightweight Structures, Department Aeronautical and Vehicle Engineering. Vol. TRITA-AVE 2005:02. 2005, Stockholm: Royal Institute of Technology.

25. BS5400-10, *Steel, Composite and concrete bridges - Code of practice for fatigue*. BSI standard publication. 1980, United Kingdom: British Standards Institute.

26. Lotsberg, I., Larsen, K.P. *Fatigue design in the new Norwegian structural design code*. in *Proceeding of the Nordic Steel Conference*. 1998. Bergen.

27. Petinov, S.V., Reemsnyder, H.S., Thayamballi, A.K., ed. *The Similitude of Fatigue Damage principle: Application in S-N Curves-Based Fatigue Design.* Fatigue Design and Reliability, ed. G. Marquis, . Solin, J. Vol. 3rd International Symposium on Fatigue Design, Espoo, Finland, 1998. 1998, ESIS publication, Elsevier.: London.

28. Van Wingerde, A.M., Packer, J.A., Wardenier, J., *Criteria for the fatigue assessment of hollow structural section connections.* J constr Steel Res, 1995. 35: p. 71-115.

29. Zhao, X.-L., Packer, J.A., *Fatigue Design Procedure for Hollow Section Joints.* Recommendations of IIW, subcommission XV-E, 2000. Cambridge, England.(Abington Publishing).

30. Niemi, E., ed. *Recommendations Concerning Stress Determination for Fatigue Analysis of Welded Components*. ed. I.d. XIII-1458-92/XV-797-92, IIW.

31. Dong, P., *A Structural Stress Definition and Numerical Implementation for Fatigue Analysis of Welded Joints.* International Journal of Fatigue, 2001. 23: p. 865-876.

32. De Jesus, A.M.P., Ribeiro, A.S., Fernandes, A.A., *Validation of procedures for fatigue life assessment of a steel pressure vessel.* Fatigue and Fracture of Engineering Materials and Structures, 2004. 27: p. 799-810.

33. Kang, H.T., Dong,P. and Hong, J.K., *Fatigue analysis of spot welds using a mesh-insensitive structural stress approach.* International Journal of Fatigue, 2007. 29: p. 1546-1553.

34. Dong, P., Zhang, J. and Hong, J.K, *United States Patent: Structural Stress Analysis*, in *B2. Jun3 7 2005*, Patent No. US 6, 809, Editor. 2005, Battelle Memorial Institute: Columbus, OH.

35. *American Society of Mechanical Engineers*, in *ASME Section VIII.* 2007.

36. Poutiainen, I., Tanskanen, P., Marquis, G., *Finite element methods for structural hot spot stress determination-a comparison of procedures.* International Journal of Fatigue, 2004. 26: p. 1147-1157.

37. Wei, L., *Structural hot spot stress based fatigue design for welded structures using finite element analysis*, in *The Welding Institute research report*, TWI, Editor. 2006, TWI: Cambridge.

38. Fricke, W., Kahl, A., *Comparison of different structural stress approaches for fatigue assessment of welded ship structures.* Marine Structures, 2005. 18: p. 473-488.

39. Griffith, A.A., *The phenomena of Rupture and Flow in Solids.* ransactions of the Royal Society., 1921. A221: p. pp.163-197.

40. Irwin, G.R., *Fracture Mechanics.* Journal of Applied Mechanics, 1957. 24: p. 361.

41. Paris, P.C., Sih, G.C., *Fracture Toughness and its Applications.* ASTM STP 381,, 1965.

42. Gurney, T.R., *Effects of mean and residual stresses on fatigue strength of welded joints under variable amplitude loading - exploratory test.* Technology Briefing, 1992. 464/1992(7065.01/92/725.03).

43. Dong, P., *Verity Structural Stress Method for Fatigue Evaluation of Welded Structures - An introductory training course.* 2005, Battelle Memorial Institute: Battelle - Centre for welded structures research.

44. Dong, P., Hong, J.K. *THE MASTER S-N CURVE APPROACH TO FATIGUE EVALUATION OF OFFSHORE AND MARINE STRUCTURES.* in *23 rd International Conference on Offshore Mechanics and Arctic Engineering.* 2004. Vancouver, British Columbia, Canada.: ASME.

45. Miner, A.M., *Cumulative damage in fatigue.* Journal of Applied Mechanics, 1945. September 1945: p. 339-341.

46. Radaj, D., *Design and analysis of fatigue resistant welded structures.* 1990, Cambridge, England: Abington Publishing.

47. Yardley, R.A., Clayton, K., Allsop, R., *Internal report - Fatigue testing of backhoe loader excavating end.* 1998, J.C. Bamford Excavators Ltd. Structures Department.

48. Draper, J., *How to achieve valid results in durability analysis from Ansys.* 2006, Safe Technology: Sheffield.

49. Rothbart, H., Brown, T.H., *Mechanical design handbook.* 2nd Edition ed: McGraw Hill Handbook.

50. Osawa, N., Hashimoto, K., Sawamura, J., Nakai, T. and Suzuki, S., *Study on shell-solid coupling FE analysis for fatigue assessment of ship structure.* Marine Structures, 2007. Volume 20: p. 143-163.

51. Taylor, D., Barrett, N., Lucano, G., *Some new methods for predicting fatigue in welded joints.* International Journal of Fatigue, 2002. 24: p. 509-518.

52. Fermer, M., Andreasson, M., Frodin, B. *Fatigue Life Prediction of MAG-Welded Thin-Sheet Structures.* in *Proceedings of the IBEC '98.* 1998. Detroit, Michigan.: SAE International.